Advances in Karst Science

Catherine Bertrand
Sophie Denimal
Marc Steinmann
Philippe Renard *Editors*

Eurokarst 2018, Besançon

Advances in the Hydrogeology of Karst and Carbonate Reservoirs

Springer

Advances in Karst Science

Series Editor

James LaMoreaux, Tuscaloosa, AL, USA

This book series covers advances in the field of karst from a variety of perspectives to facilitate knowledge and promote interaction thereby building stepping stones in this process. Methodologies, monitoring, data analysis and interpretation are addressed throughout the wide range of climatic, geological and hydrogeological contexts in which karst occurs. Case studies are presented to provide examples of advancement of the science.

Issues to be addressed include water supply, contamination, and land use management. These issues although occurring on a local basis share many of the same features on the global stage. This book series is a critical resource to the scientific community allowing them to compare problems, results, and solutions. The presented information can be utilized by decision makers in making decisions on development in karst regions. Contributions presented may be used in the classroom and to work with stakeholders, scientists, and engineers to determine practical applications of these advances to common problems worldwide.

The series aims at building a varied library of reference works, textbooks, proceedings, and monographs, by describing the current understanding of selected themes. The books in the series are prepared by leading experts actively working in the relevant field. The book series *Advances in Karst Science* includes single and multi-authored books as well as edited volumes. The Series Editor, Dr. James W. LaMoreaux, is currently accepting proposals and a proposal document can be obtained from the Publisher.

More information about this series at http://www.springer.com/series/15147

Catherine Bertrand · Sophie Denimal ·
Marc Steinmann · Philippe Renard
Editors

Eurokarst 2018, Besançon

Advances in the Hydrogeology of Karst and Carbonate Reservoirs

Springer

Editors
Catherine Bertrand
Laboratoire Chrono-environnement
Université de Franche-Comté
Besançon, France

Sophie Denimal
Laboratoire Chrono-environnement
Université de Franche-Comté
Besançon, France

Marc Steinmann
Laboratoire Chrono-environnement
Université de Franche-Comté
Besançon, France

Philippe Renard
Centre d'Hydrogéologie
University of Neuchâtel
Neuchâtel, Switzerland

ISSN 2511-2066 ISSN 2511-2082 (electronic)
Advances in Karst Science
ISBN 978-3-030-14014-4 ISBN 978-3-030-14015-1 (eBook)
https://doi.org/10.1007/978-3-030-14015-1

Library of Congress Control Number: 2019932820

© Springer Nature Switzerland AG 2020
This work is subject to copyright. All rights are reserved by the Publisher, whether the whole or part of the material is concerned, specifically the rights of translation, reprinting, reuse of illustrations, recitation, broadcasting, reproduction on microfilms or in any other physical way, and transmission or information storage and retrieval, electronic adaptation, computer software, or by similar or dissimilar methodology now known or hereafter developed.
The use of general descriptive names, registered names, trademarks, service marks, etc. in this publication does not imply, even in the absence of a specific statement, that such names are exempt from the relevant protective laws and regulations and therefore free for general use.
The publisher, the authors and the editors are safe to assume that the advice and information in this book are believed to be true and accurate at the date of publication. Neither the publisher nor the authors or the editors give a warranty, expressed or implied, with respect to the material contained herein or for any errors or omissions that may have been made. The publisher remains neutral with regard to jurisdictional claims in published maps and institutional affiliations.

This Springer imprint is published by the registered company Springer Nature Switzerland AG
The registered company address is: Gewerbestrasse 11, 6330 Cham, Switzerland

Preface

The second edition of *Eurokarst* was held in Besançon, France, in July 2018 and involved about 180 participants from 23 countries from all over Europe and the world. All five continents were represented at this event. *Eurokarst* is the largest event on this theme in Europe.

The aim of the *Eurokarst* conference series is to continue promoting advances in research in the field of karst and carbonate reservoirs after more than 40 years of regular meetings.

Once again, the *Eurokarst* conference remains a platform where professionals, consultants, researchers and students can meet to learn about new technologies and methods but also about the practical challenges encountered in applications.

Knowing each other, sharing know-how and the latest scientific advances between the various national and international communities are the major strengths of *Eurokarst*. Among the current topics addressed during this event, and despite their recurrence, the understanding of flows in karst and carbonate formations, the protection and management of water resources are still relevant. In addition, some approaches are diversifying, particularly through the development of new sensors or methodologies applied more specifically to karst.

Eurokarst is a collaboration generator as demonstrated by the "Karst Modelling Challenge" (KMC) working group that was initiated by Pierre-Yves Jeannin at *Eurokarst 2016* in Neuchâtel (Switzerland) with the aim of identifying the most effective approach for modelling karst aquifers in different situations. Eight teams actually submitted models for the Phase 1 of the challenge, which was to model time series of spring flow. The special session dedicated to the KMC was a great success, and the discussions initiated during this session continued around poster communications (20% of the posters dedicated to this research group).

Eurokarst is also a training event, as demonstrated by the success of the workshops to familiarize participants with numerical fluid transfer modelling and new tools for protecting the resource. This day was dedicated to professionals in water resources management, as well as researchers and students. These workshops were initiated during *Eurokarst 2016* in Neuchâtel, and they met with great interest.

Finally, the frequency of this conference makes it possible to realize that the world of research in this very specific environment is progressing. It is satisfying to see that young researchers are as passionate as senior researchers. These young researchers were in the spotlight during this edition by their presence in large numbers and by their professionalism. Some of their works were highlighted by excellent presentations during the plenary sessions. As in *Eurokarst 2016*, the IAH Commission on Karst Hydrology presented awards to three of them. The choice was difficult and in no way detracts from the quality of the young researchers on the side of these awards.

In 2018, for the second edition, *Eurokarst* conference included around 160 communications covering a wide variety of topics in many fields related to karst. Among them, 27 are presented in this book. These articles provide an overview of recent progresses made in karst research. The articles are organized around five main topics:

- Karst landscape and geological control;
- Surface and groundwater interactions;
- Time series analysis;
- Karst modelling;
- Multidisciplinary regional studies.

As the organizers of the *Eurokarst* event and editors of this book, we are extremely thankful to a number of organizations and people who participated in the preparation of the event and without whom the book could not be published. First of all, we would like to thank the sponsors who contributed financially to support the conference:

- The French National Institute for Earth Sciences and Astronomy (CNRS-INSU);
- The Bourgogne-Franche-Comté region;
- The city of Besançon;
- The Communauté du savoir (CdS);
- The Laboratoire Chrono-environnement;
- Springer Verlag AG;
- The Rhone-Mediterranean Corsica Agency.

The partner organizations were the following:

- The University of Bourgogne - Franche-Comté, Besançon, France;
- The University of Neuchâtel, Switzerland;
- The University of Malaga, Spain;
- The Spanish Geological Survey (IGME);
- The SNO KARST;
- The Swiss Institute of Speleology and Karstology (SISKA);
- The International Association of Hydrology (IAH);
- The IAH Commission on Karst Hydrogeology.

We want also to thank very warmly the members of the Scientific Committee of the conference and some additional reviewers (see list on the following page) who have shared their expertise and knowledge with the authors in order to provide the best possible technical quality within the limited time frame available to publish the book. Finally, we want to thank Pierre Nevers who spent countless hours to polish the format of the papers as well as the persons in charge of the project for Springer: Jim LaMoreaux, Samuel Goodchild and Ramamoorthy Rajangam.

A special thanks to the members of the Laboratoire Chrono-environnement whose help was invaluable in organizing the conference. Thanks to Catherine Pagani, Christophe Loup and Nicolas Carry for their help throughout this organization. Thanks to postgraduate and students, especially Thibaut Garin, Justine Cagnant and Selwyna Mereatu and to the colleagues of Chrono-environment for their punctual but nonetheless valuable help.

Besançon, France Catherine Bertrand
Besançon, France Sophie Denimal
Besançon, France Marc Steinmann
Neuchâtel, Switzerland Philippe Renard
Málaga, France Bartolomé Andreo Navarro
January 2019

Reviewers

Mohammed Aliouache, University of Montpellier, France
Augusto Auler, Instituto do Carste, Brazil
Bartolomé Andreo Navarro, University of Malaga, Spain
Bruno Arfib, Aix-Marseille University, France
Vincent Bailly-Comte, BRGM, France
Michel Bakalowicz, University of Montpellier, France
Andy Baker, University of New South Wales, Australia
Christelle Batiot-Guilhe, University of Montpellier, France
James Berglund, Temple University, USA
Romane Berthelin, University of Freiburg, Germany
Catherine Bertrand, University of Franche-Comté, France
Stephane Binet, University of Orleans, France
Matej Blatnik, Karst Research Institute, Slovenia
Yvan Caballero, BRGM, France
Jean-Baptiste Charlier, BRGM, France
Pauline Collon-Drouaillet, ENSG, France
Alain Dassargues, University of Liège, Belgium
Sophie Denimal, University of Franche-Comté, France
Wolfgang Dreybrodt, University of Bremen, Germany
Juan José Durán Valsero, IGME, Spain
Fang Guo, Institute of Karst Geology, China
Dolores Fidelibus, Politecnico di Bari, Italy
Lee Florea, Indiana University, USA
Franci Gabrovsek, Karst Research Institute, Slovenia
Albert Galy, University of Lorraine, France
Nico Goldscheider, Karlsruhe Institute of Technology, Germany
Andreas Hartmann, University of Freiburg, Germany
Nicolas Houillon, University of Bordeaux, France
Peter Huggenberger, University of Basel, Switzerland
Pierre-Yves Jeannin, ISSKA, Switzerland
Alexander Klimchouk, National Academy of Sciences, Ukraine
Ronald Kozel, OFEV, Switzerland
David Labat, Paul Sabatier University, Toulouse, France
Roland Lastennet, University of Bordeaux, France
Judit Mádl-Szonyi, Eötvös Loránd University, Hungary
Oswald Malcles, University of Montpellier, France
Nicolas Massei, University of Rouen, France
Louise Maurice British, Geological Survey, UK
Philippe Meus, European Water Tracing Services, Belgium
Jacques Mudry, University of Franche-Comté, France
Chloé Ollivier, University of Avignon, France
Roger Pacheco-Castro, National Autonomous University of Mexico, Mexico

Eulogio Pardo-Iguzquiza, Geological Survey of Spain
Mario Parise, University of Bari, Italia
Nicolas Peyraube, University of Bordeaux, France
Antonio Pulido-Bosch, University of Almeria, Spain
Milan Radulovic, University of Montenegro, Montenegro
Philippe Renard, University of Neuchâtel, Switzerland
Mike Ronayne, Colorado State University, USA
Pierre-André Schnegg, University of Neuchâtel, Switzerland
Philip Schuller, Trinity College Dublin, Ireland
Vianney Sivelle, University of Toulouse, France
Chris Smart, University of Western Canada, Ontario, Canada
Marc Steinmann, University of Franche-Comté, France
Sophie Viseur, Aix-Marseille University, France
Stephen Worthington, Worthington Groundwater, Ontario, Canada
Zhang Qiang, Institute of Karst Geology, China
François Zwahlen, University of Neuchâtel, Switzerland

Contents

Part I Karst Landscape and Geological Control

Part II Surface and Ground Water Interactions

Part III Time Series Analysis

Part IV Karst Modeling

Part V Multidisciplinary Regional Studies

Part I

Karst Landscape and Geological Control

Detection and Characterization of Sinkholes Through Integration of Field Surveys and Semi-automated Techniques

M. Parise, L. Pisano, and V. Zumpano

Abstract

Sinkholes are among the most typical landforms of karst terrains. They may originate from a simple downward process, through dissolution of carbonate rocks, or through rapid, sometimes catastrophic, collapse, due to the presence of underground voids or cavities, from where the instability may eventually reach the ground surface. These two extremes imply a great variety in vulnerability of man-made structures, and damage to the population, which makes the analysis of sinkholes extremely important to society. In this contribution, we present an integrated workflow to detect, classify and analyze sinkholes. The ultimate aim is to evaluate the sinkhole susceptibility and hazard. The methodology used will be illustrated by means of an example from the karst of Apulia, south-eastern Italy.

Keywords

Sinkholes • Karst • Susceptibility • Automatic mapping • Apulia

Introduction

Different mechanisms are at the origin of the formation of sinkholes, the most typical landforms of karst terrains (Waltham et al. 2005; Beck 2007; Gutierrez et al. 2014): some start at the ground surface, as the simple action of dissolution, slowly acting in downward direction; others originate from underground, which lead to instability and to the collapse of the cave roof (collapse sinkholes), or of the overburden (cover-collapse sinkholes). The variety of mechanisms implies also significant differences in terms of velocity processes, with important effects concerning civil protection issues and impacts on the built-up environment.

In regions as Apulia, the south-eastern sector of the Italian peninsula, almost entirely built of soluble rocks, karst is definitely the main morphogenetic agent. Along the coastlines landforms are produced by the interaction between karst and sea wave actions.

Identification of sinkholes, and full comprehension of the relationships between the observed karst landforms and the hydrogeological behavior of the carbonate rock mass, is a great challenge in Apulia (Del Prete et al. 2010; Festa et al. 2012; Margiotta et al. 2012; Parise 2015a, b). Especially when working over large areas, mapping sinkholes strongly depends on the scale of the final cartographic product, and the expertise of the operator as well. Changing the scale, some features may become impossible to map, while others can be shown in a quite different way. Subjectivity and karst knowledge of the operator is also a crucial point, as maps produced by several operators for a same area may be very different.

In the last decades, sinkhole occurrence in Apulia has become the main geological hazard, and many tens of sinkholes related to karst caves and with known time of occurrence have been documented (Parise and Vennari 2017). They represent only a small part of a high number of karst features which characterize the different karst sub-regions in Apulia.

In the attempt to find a semi-automatic methodology which might integrate, but not substitute, the classical mapping approach, we present in this contribution a comparison among three inventories produced for a sample area in the karst of Apulia. The first inventory was produced by the first author through intensive field mapping, while the other two were obtained by applying a semi-automated methodology.

M. Parise (✉)
Department of Earth and Environmental Sciences,
University Aldo Moro, Bari, Italy
e-mail: mario.parise@uniba.it

M. Parise · L. Pisano · V. Zumpano
National Research Council, IRPI, Bari, Italy
e-mail: l.pisano@ba.irpi.cnr.it

V. Zumpano
e-mail: v.zumpano@ba.irpi.cnr.it

C. Bertrand et al. (eds.), *Eurokarst 2018, Besançon*, Advances in Karst Science,
https://doi.org/10.1007/978-3-030-14015-1_1

Dataset and Methods

Available Data

The study area was selected in the municipality of Ceglie Messapica (Brindisi province), in southern Apulia. It is an entirely karst area, showing some of the most typical landscape in the region, which covers a territory of 47 km^2. Choice of the area was dictated, beside the interesting karst features and the more than 50 natural caves registered in the municipality, by availability of some base data; namely, these consisted of the Regional Technical Map (topographic map, in scale 1:5000), aerial photographs from different years (nominal scale 1:32,000), 8-mt Digital Terrain Model (DTM) by Apulia Region, and 1-m resolution LiDAR DTM, produced by the local municipality.

Manual Mapping

The first inventory was obtained through intensive field mapping, by using the 1:5000 topographic map as base map; the field work was integrated by analogical stereoscopic analysis of the 1998 aerial photographs. As in many settings in Apulia, land morphology is generally flat, and the use of stereoscopic view is of great help to exaggerate the relief, in order to identify slight features created in the topography by karst processes. In the manual inventory, sinkholes were discriminated by endorheic basins, these latter being defined as terminal areas of confluence of two or more temporary water courses (named *lame*, in the local karst terminology; see Parise et al. 2003). Endorheic basins are generally of larger size with respect to sinkholes, but they show the same shape (mostly, circular to sub-elliptical), and often are located along the main *lame*. Morphologically, sinkholes produced by collapse processes are generally more well defined and recognizable, due to steeper margins and greater depth. The distinction becomes more difficult when dealing with sinkholes produced by solution processes and suffusion (Gutierrez et al. 2014), showing more subtle boundaries. Both sinkholes and endorheic basins may become partly or totally flooded after heavy rainstorms, with water remaining at the surface for hours or days, following the most significant rainfall events. This implies that from a hydrogeological standpoint the two features share the same behavior, acting as sites of concentrated infiltration of the waters underground, thus actively recharging the carbonate aquifer. However, given the different processes at the origin of sinkholes and endorheic basins, they were kept separated in the manual inventory.

Automated Mapping Using Lidar DTM and 8m-DTM

The sinkholes extraction through the semi-automatic mapping was performed by using the algorithm described by Zhu et al. (2014) and by Wall et al. (2017). This algorithm is based on the DTM exploitation in GIS environment and was successfully used to map sinkholes (dolines) in karst environment (Doctor and Young 2013; Wall et al. 2017).

We used the “Fill” tool available in ArcGIS software, that in karst topography is applied for the recognition of topographically depressed areas (Doctor and Young 2013; Jeanpert et al. 2016; Wall et al. 2017). This tool identifies the depressions in the input raster, so that it is possible to obtain a filled DTM that can be differentiated from the original to produce a depth raster. The tool can be reiterated multiple times in order to fill all the depressions with different depths in the raster. We decided to choose z-limits fills of 2-m intervals, starting from 2-m depth until we had redundancy in the number of filled depressions (Kobal et al. 2015). After obtaining the filled rasters for each z-limits, the difference with the initial raster was determined, and using the Boolean Logic the fill-differences were transformed into polygons representing the sinkholes.

Before moving to the calculation of the morphometric parameters, we decided to choose the shapefile polygons map with the z-limit better representing the real situation in the analyzed study area by using the expert opinion and field activity, but also through careful comparison with the manually mapped database (Fig. 1).

In order to make the process lighter and faster, we built a tool by using the Model Builder in ArcGis software. Once the model was set up, it required only the input DTM to perform the analysis and to provide the sinkholes polygon shapefile for the multiple z-limit.

In the case of automatic procedure, the identified features include both sinkholes and endorheic basins, regardless of the processes at the origin of these landforms. An overview of the number of features in each database can be found in Table 1.

At this point, we set up another model to smooth the polygons and calculate a series of morphometric parameters (Table 2) useful to characterize the obtained database: area; perimeter; CI (Circularity Index); nearest feature and its distance; length of the long and the short sinkhole axes (Kobal et al. 2015); azimuth of the sinkhole long axis, elongation ratio and shape (Basso et al. 2013). These parameters, well known in the literature (Basso et al. 2013; Pepe and Parise 2014; Kobal et al. 2015), are calculated for both the automatically and the manually obtained databases, and only two of them will be presented hereafter (Figs. 2 and 3).

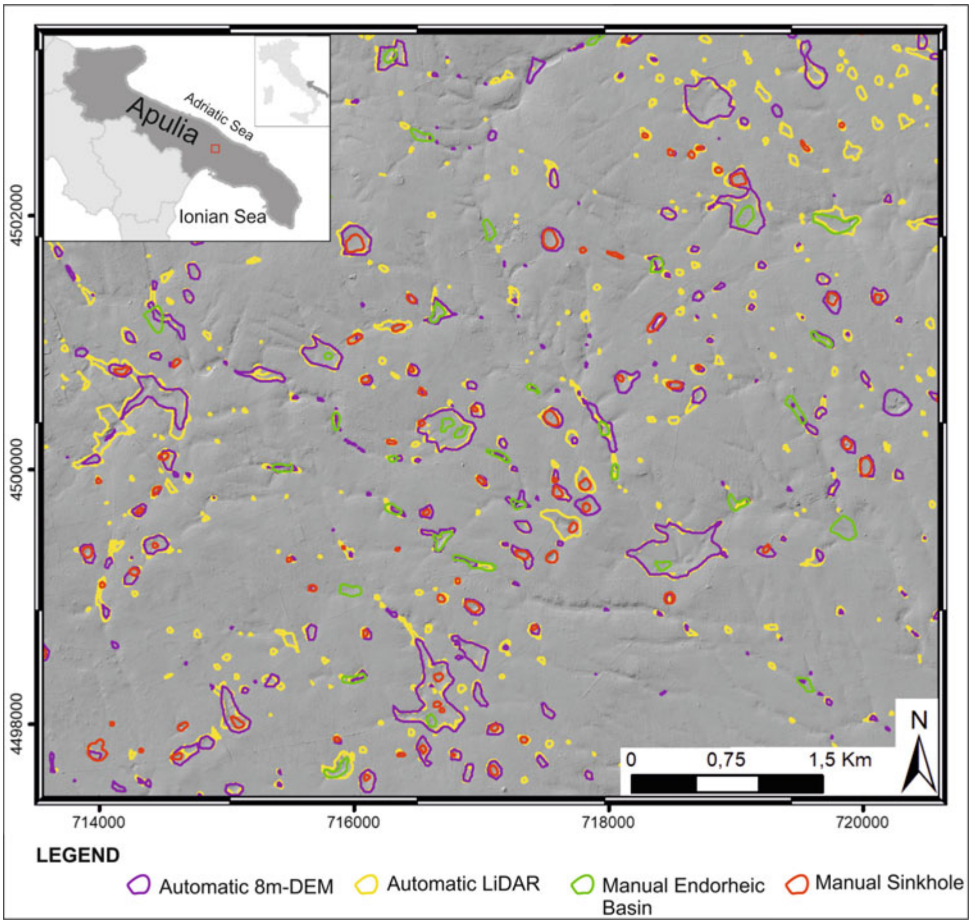

Fig. 1 Extract from the study area, showing the three datasets in different colors: green and red colors mark, respectively, the endorheic basins and the sinkholes mapped manually; yellow color indicates the sinkholes identified through the Lidar analysis, and purple color those identified through the 8m-DTM

Table 1 Summary table of the mapped features, according to the different used techniques

Mapping technique	Number
Manual mapping	131 (40 are endorheic basins)
Automated mapping (8m-DTM)	192
Automated mapping (Lidar)	523

Table 2 Summary table of the calculated morphometric parameters, the method used and the related reference

Parameter	Method	References
Area and perimeter	Calculate Geometry tool, ArcMap, ESRI ArcGIS®	–
Circularity Index (CI)	CI = 4πArea/Perimeter	De Carvalho et al. (2014)
Nearest feature	Near tool in Proximity Toolset, ArcMap, ESRI ArcGIS®	–
Distance nearest feature	Near tool in Proximity Toolset, ArcMap, ESRI ArcGIS®	–
Shortest and longest axes length	Minimum bounding Geometry in Feature Toolset, ArcMap, ESRI ArcGIS®	(Kobal et al. 2015)
Azimuth of the longest axis	Minimum Bounding Geometry in Feature Toolset, ArcMap, ESRI ArcGIS®	(Kobal et al. 2015)
Elongation Ratio (ER)	Ratio between the major and the minor axes	(Basso et al. 2013)
Shape	Circular: ER < 1.05; Sub-circular $1.05 < \mathrm{ER} \leq 1.21$; Elliptical $1.21 < \mathrm{ER} \leq 1.65$; Sub-elliptical $1.65 < \mathrm{ER} \leq 1.8$; Elongated ER > 1.8	(Basso et al. 2013)

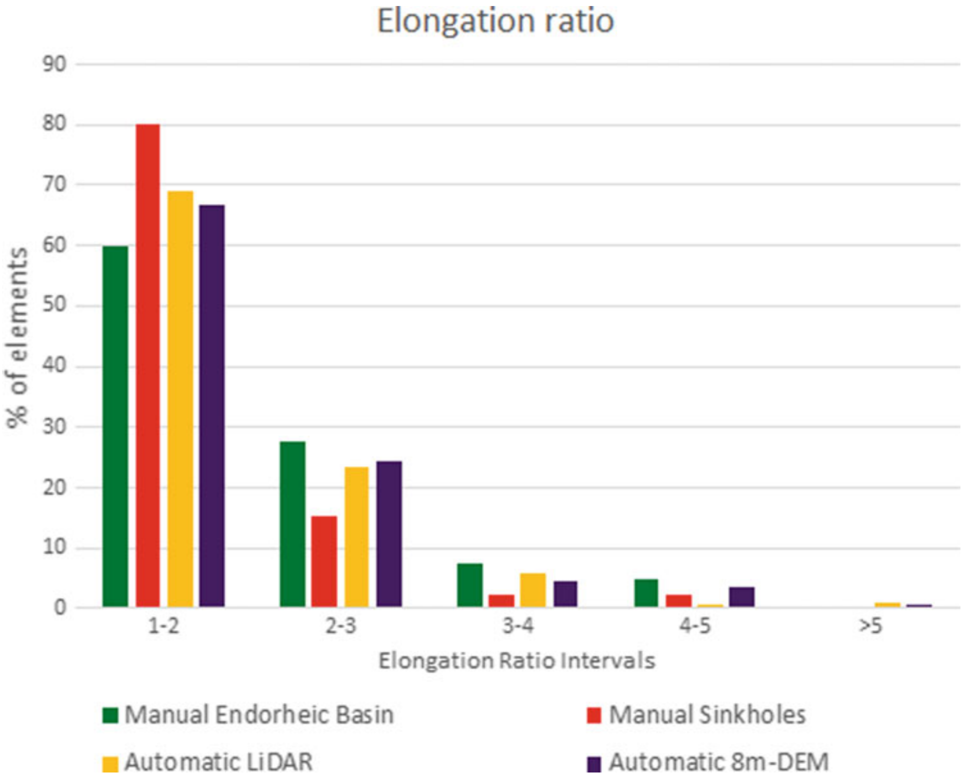

Fig. 2 Percentage of elements mapped with different elongation ratio

This procedure was applied to the 8 × 8 m resolution DTM and to 1 × 1 m Lidar DTM, giving different results in the number of mapped sinkholes (Table 1), but also in their shapes and the morphometric parameters (Figs. 2 and 3).

Finally we set up a last model to automatically clean the maps from possible artefacts attributable to errors in the DTM generation process, keeping only features significant as sinkholes. Following the published literature (de Carvalho et al. 2014; Bauer et al. 2015) the model was set up in order to operate a selection of the obtained polygons, on the basis of the diameter length and the CI. For the Lidar DTM, given its high resolution we decided to pick only the polygons with a diameter greater than, or equal to, 10 m, in order to eliminate small features probably not significant as karst forms (Kunaver 1983; Kobal et al. 2015). Furthermore, we eliminated the polygons with CI < 0.1 in order to have prevailing circular forms, and to decrease the number of elongated ones, which are typically attributable to water course segments.

For the 8m-DTM, we eliminated the polygons with a diameter smaller than 25 m, and with CI < 0.1.

The obtained databases were finally compared with the manually compiled inventory, and the differences were analyzed highlighting the strengths and weakness of each database.

Results

On the one hand, looking at the morphometric parameters considered, we evaluated that there is a certain degree of agreement in the elongation ratio (Fig. 2), showing the range 1–2 as the most common for all the considered techniques.

On the other hand, concerning the orientation (Fig. 3), there is a high heterogeneity in the data belonging to the different inventories. For the LiDAR- and the DTM-derived map, the highest count was found in the classes between 80° and 180°. In the manual inventory, the elements were almost homogeneously distributed in the entire 60–120° range (Fig. 3).

Other differences were also found in the shape of the sinkholes in the three inventories, and an example is reported in Fig. 4. In fact, it was observed that very often the accuracy of the sinkholes depicted with the automatic mapping is strictly connected with the DTM resolution, giving better results using LiDAR (the highest resolution). Further, during field observations the manual mapping was observed as the most accurate in the delineation of the correct sinkhole contouring.

Nevertheless, it is important to point out that some relevant sinkholes verified in the field were not detected by

Fig. 3 Orientation of the major axis of sinkholes and endorheic basins, with respect to the North, for a range of 180°

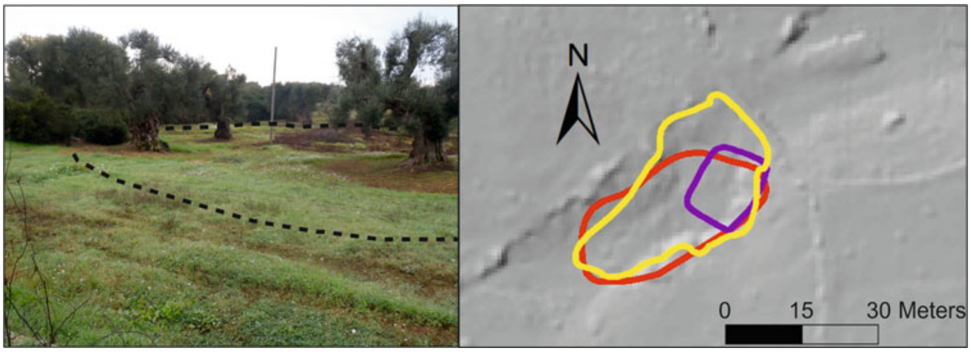

Fig. 4 Example of a sinkhole mapped by the different techniques. The "manual mapping" (through aerial photo interpretation) is shown in red, the automatic one obtained by using the Lidar DTM in yellow, and that by the DTM in purple. The dashed line in the picture to the left marks the boundary of the manual mapping

manual mapping but only by the automatic method. This indicates the understandable fallibility of the human eye in operating a complete scanning of the territory during mapping, especially in difficult conditions such as in areas with presence of a dense vegetational cover (Bauer 2015).

Conclusions

Overall the automated mapping can be considered an effective method, as demonstrated by multiple authors (i.e., Pardo-Igúzquiza et al. 2013, 2016; Wall et al. 2017), but on the basis of the evidences presented here, it cannot be considered self-sufficient to compile accurate and reliable sinkhole inventories. In fact, it was observed that automatic mapping can detect a much larger number of features with respect to the manual, this difference being commensurate with the resolution of the input topographic data.

However, considering the evidence collected during the field observations we can conclude that the automatic mapping cannot disregard the expert validation via visual interpretation and even better when it is carried out using digital stereoscopy. In some cases the automatic tool can overestimate the number of features counting morphological convergences or artifacts.

An advantage of the automatic procedure by using LiDAR is definitely the possibility to detect karst landforms in forested areas, where the vegetation covers might hinder, or completely mask, the presence of terrain features, making very difficult their identification in the field (Parise et al. 2018). In these situations, the possibility to have a look at the land without the canopy cover will certainly allow a better depiction of the landforms.

Generally, low-resolution DTMs are more easy to acquire as it is in our case study; moreover, one must take into account that the results are not fully satisfactory, especially in areas where depressions are of smaller dimensions.

On the other hand, applying the automatic mapping tool, especially over large areas, before starting the expert-based interpretation, could provide an important support in terms of time, precision and gaps reduction. In conclusion, we believe that integrating or better, anticipating, the manual mapping with the automatic one could be the right compromise for karst sinkhole interpretation and mapping.

References

Basso, A., Bruno, E., Parise, M. and Pepe, M. (2013). Morphometric analysis of sinkholes in a karst coastal area of southern Apulia (Italy). Environmental Earth Sciences 70, 2545–2559. https://doi.org/10.1007/s12665-013-2297-z.

Bauer, C. (2015). Analysis of dolines using multiple methods applied to airborne laser scanning data. Geomorphology 250, 78–88. http://doi.org/10.1016/j.geomorph.2015.08.015.

Beck, B. (2007). Soil piping and sinkhole failures. In: Culver, D.C. and White, W.B. (Eds.), Encyclopedia of caves. Elsevier Academic Press, 2nd edition, 521–526.

De Carvalho Junior, O.A., Guimaraes, R.F., Montgomery D.R., Gillespie, A.R., Gomes, R.A.T., de Souza Martins E. & Silva, N.C. (2014). Karst depression detection using ASTER, ALOS/PRISM and SRTM-derived digital elevation models in the Bambui Group, Brazil. Remote Sensing 6 (1), 330–351. http://doi.org/10.3390/rs6010330.

Del Prete, S., Iovine, G., Parise, M. and Santo. A. (2010). Origin and distribution of different types of sinkholes in the plain areas of Southern Italy. Geodinamica Acta 23 (1/3), 113–127.

Doctor, D.H. & Young, J. (2013). An evaluation of automated Gis tools for delineating karst sinkholes and closed depressions from 1-meter Lidar-derived digital elevation data. Proc. 13th Multidisc. Conf. Sink. Eng. Environ. Impacts Karst, 449–458.

Festa, V., Fiore, A., Parise, M. and Siniscalchi, A. (2012). Sinkhole evolution in the Apulian karst of southern Italy: a case study, with some considerations on sinkhole hazards. J. Cave Karst Studies 74 (2), 137–147.

Gutierrez, F., Parise, M., De Waele, J. and Jourde, H. (2014). A review on natural and human-induced geohazards and impacts in karst. Earth-Science Reviews 138, 61–88.

Jeanpert, J., Genthon, P., Maurizot, P., Folio, J.L., Vendé-Leclerc, M., Sérino, J., Join, J.L. & Iseppi, M. (2016). Morphology and distribution of dolines on ultramafic rocks from airborne LiDAR data: the case of southern Grande Terre in New Caledonia (SW Pacific). Earth Surface Processes and Landforms 41, 1854–1868. http://doi.org/10.1002/esp.3952.

Kobal, M., Bertoncelj, I., Pirotti, F., Dakskobler, I. & Kutnar, L. (2015). Using lidar data to analyse sinkhole characteristics relevant for understory vegetation under forest cover - Case study of a high karst area in the Dinaric mountains. PLoS One 10, 1–19. https://doi.org/10.1371/journal.pone.0122070

Kunaver, J. (1983). Geomorfološki razvoj Kaninskega pogorja s posebnim ozirom na glaciokraške pojave. Geogr Zb. 22, 197–346.

Margiotta, S., Negri, S., Parise, M. and Valloni, R. (2012). Mapping the susceptibility to sinkholes in coastal areas, based on stratigraphy, geomorphology and geophysics. Natural Hazards 62 (2), 657–676.

Pardo-Igúzquiza, E., Durán, J.J. & Dowd, P.A. 2013. Automatic detection and delineation of karst terrain depressions and its application in geomorphological mapping and morphometric analysis. Acta Carsologica 42/1, 17–24.

Pardo-Igúzquiza, E., Pulido-Bosch, A., López-Chicano, M. & Durán, J.J. 2016. Morphometric analysis of karst depressions on a Mediterránea karst massif. Geografiska Annaler: Series A, Physical Geography, 98 (3), 247–263.

Parise, M. (2015a). Karst geo-hazards: causal factors and management issues. Acta Carsologica 44 (3), 401–414.

Parise, M. (2015b). A procedure for evaluating the susceptibility to natural and anthropogenic sinkholes. Georisk 9 (4), 272–285.

Parise, M. and Vennari, C. (2017). Distribution and features of natural and anthropogenic sinkholes in Apulia. In: Renard, P. and Bertrand, C. (Eds.), EuroKarst 2016, Neuchatel. Advances in the hydrogeology of karst and carbonate reservoirs. Springer, ISBN 978-3-319-45464-1, 27-34.

Parise, M., Federico, A., Delle Rose, M. and Sammarco, M. (2003). Karst terminology in Apulia (southern Italy). Acta Carsologica 32 (2), 65–82.

Parise, M., Pisano, L. and Vennari, C. (2018). Sinkhole clusters after heavy rainstorms. Journal of Cave and Karst Studies 80 (1), 28–38. https://doi.org/10.4311/2017es0105.

Pepe, M. & Parise, M. (2014). Structural control on development of karst landscape in the Salento Peninsula (Apulia, SE Italy). Acta Carsologica 43, 101–114.

Wall, J., Bohnenstiehl, D.W.R., Wegmann, K.W. & Levine, N.S. (2017). Morphometric comparisons between automated and manual karst depression inventories in Apalachicola National Forest, Florida, and Mammoth Cave National Park, Kentucky, USA. Natural Hazards 85 (2), 729–749. https://doi.org/10.1007/s11069-016-2600-x.

Waltham, T., Bell, F. and Culshaw, M. (2005). Sinkholes and subsidence. Karst and cavernous rocks in engineering and construction. Springer Praxis.

Zhu, J., Taylor, T.P., Currens, J.C., Crawford, M.M. (2014). Improved karst sinkhole mapping in Kentucky using LiDAR techniques: a pilot study in Floyds fork watershed. Journal of Cave and Karst Studies 76, 207–216. https://doi.org/10.4311/2013es0135.

Karst and Vegetation: Biodiversity and Geobotany in the Sierra de las Nieves Karst Aquifer (Málaga, Spain)

Juan Antonio Luque-Espinar, Eulogio Pardo-Igúzquiza,
Víctor Francisco Rodríguez-Galiano, Mario Chica-Olmo,
and Rogelio de la Vega-Panizo

Abstract

The Sierra de las Nieves karst system is a high-relief Mediterranean karst that hosts important botanical diversity, including the unique Spanish fir *Abies pinsapo*. Vegetation is mainly controlled by the soil development and climatic conditions. In turn, the soil is controlled by lithology, fracturing, weathering and slope. There is also positive of soil and vegetation feedback in the epikarst development. This study focuses on the spatial variability of vegetation in a karst massif and its relationship with the main lithologies, karst depressions, fracturation density and slope. Contingency analysis shows degrees of association between the plant species studied and the other parameters. Thus, plant species preferences have been found for certain lithologies, degree of fracture development, karst depressions of ground slope.

Keywords

Karst • Biodiversity • Vegetation • Geology

Introduction

Only limited research has been carried out into the influence of karstic terrain lithology on vegetation (Williams 2008; Bakalowicz 2004, 2012). The spatial development of the epikarst is influenced by the interaction of different factors such as lithology, tectonic structure, density and orientation of faults and joints, degree of weathering, slope, vegetation and/or climatology (Klimchouk 2004). In addition, rainfall seeping through fractures and organic material increases the dissolution rate and fracture growth (Williams 1983; Ford and Williams 2007). Other characteristics or concentrations of different parameters related to chemical and microbial properties of soil or climate and their influence on vegetation have been analyzed by various authors (Bakalowicz 2004; Efe 2014; Liang et al. 2015; Tonga et al. 2017; Shen et al. 2013 among others). Results obtained show specifically that the chemical and microbial properties of the soil differed significantly depending on the vegetation types analyzed (Lu et al. 2014).

Factors such as topography, soil formation and vegetation distribution have been studied by several authors (Atalay 1988, 1991, 1997; Barany-Kevei and Horváth 1996). The development of soils and the successional evolution and establishment of vegetation in karst terrains are primarily conditioned by the physical and chemical properties of limestones (Shen et al. 2013).

Liang et al. (2016) studied *Arbuscular mycorrhizal fungi* that form an important part of plant growth and restoration in degraded ecosystems. Thus, soil pH shows highest in the shrub and lowest in the tussock, and the clay content is lower and the silt and sand content is higher in the primary forest than in the other three vegetation types. Liu et al. (2016) study carbon sequestration potentials of karst vegetation.

J. A. Luque-Espinar (✉)
Instituto Geológico y Minero de España, Urb. Alcázar del Genil 4, edf. Zulema bajo, 18006 Granada, Spain
e-mail: ja.luque@igme.es

E. Pardo-Igúzquiza
Instituto Geológico y Minero de España, Ríos Rosas 23, 28003 Madrid, Spain
e-mail: e.pardo@igme.es

V. F. Rodríguez-Galiano
Universidad de Sevilla. Geografía Física y Análisis Geográfico Regional, 41004 Seville, Spain
e-mail: vrgaliano@us.es

M. Chica-Olmo
Universidad de Granada, Avda. Fuente Nueva s/n, 18071 Granada, Spain
e-mail: mchica@ugr.es

R. de la Vega-Panizo
Departamento Ingeniería Geológica y Minera, Universidad Politécnica de Madrid. E.T.S. Ingenieros de Minas y Energía, Calle Ríos Rosas 21, 28003 Madrid, Spain
e-mail: rogelio.delavega@upm.es

C. Bertrand et al. (eds.), *Eurokarst 2018, Besançon*, Advances in Karst Science,
https://doi.org/10.1007/978-3-030-14015-1_2

Both biotic and abiotic factors, such as climate, site condition, species composition, community structure and human disturbance, largely influence vegetation carbon stocks (Liu et al. 2016).

In this context, the availability of the above parameters together with plant species mapping would enable us to determine which factors influence the vegetation distribution.

This paper is a first comprehensive approach to identifying the relationship between vegetation and karst in Sierra de las Nieves. To do this, vegetation maps, lithologies, fracture density, karstic depressions and slope have been used. Geostatistical methods and ArcGIS tools have been used to process the information. Contingency analysis has been used to estimate the statistical significance between the plant species and other parameters available in the study area.

Case Study

Geological Setting

The Sierra de las Nieves karst system is a high-relief Mediterranean karst in Málaga province in southern Spain (Fig. 1) with a surface area of 125 km^2. The aquifer presents a wide range of altitudes from the system base level at the source of Río Grande Spring (359 m a.s.l.) to the maximum altitude on the Torrecilla peak (1919 m a.s.l.) as shown in the digital elevation model in Fig. 2. From a geological viewpoint, the Sierra de las Nieves aquifer is part of the Nieves Unit, formed by a Triassic to early Miocene succession mainly composed of carbonate formations (Fig. 1). From base to top, the Triassic series comprises dolostones, alternating marls, marly limestones and micritic limestones. The Jurassic–Paleogene sequence is dominated by cherty limestones, nodular limestone, marly limestones and marls (Martín-Algarra 1987).

The fractures and joints are taken from Pedrera et al. (2015) to estimate the fracture density by geostatistical methods (Fig. 3).

Previous Studies and Inventory of Vegetation

The vegetation database used is produced by of the Junta de Andalucía, Consejería de Medio Ambiente y Ordenación del Territorio (JA 2017).

Sierra de las Nieves displays a wide range of vegetation of significant biological interest including *Abies pinsapo, Quercus alpestris, Juniperus Sabina, Berberis hispanica, Ulex baeticus, Pinus halepensis, Pinus sylvestris* and *Quercus faginea* (Cabezudo-Artero et al. 1998). The main plant associations or species mapped by JA (2017) are *Abies pinsapo* (Figs. 4 and 8), *Juniperus sabina* (Figs. 5 and 8), garrigue (*Berberis hispanica, Ulex baeticus*) (Figs. 6 and 8), *Quercus faginea, Quercus alpestris* (Figs. 7 and 9), mixture

Fig. 1 Geological map of Sierra de las Nieves (modified from IGME 2015)

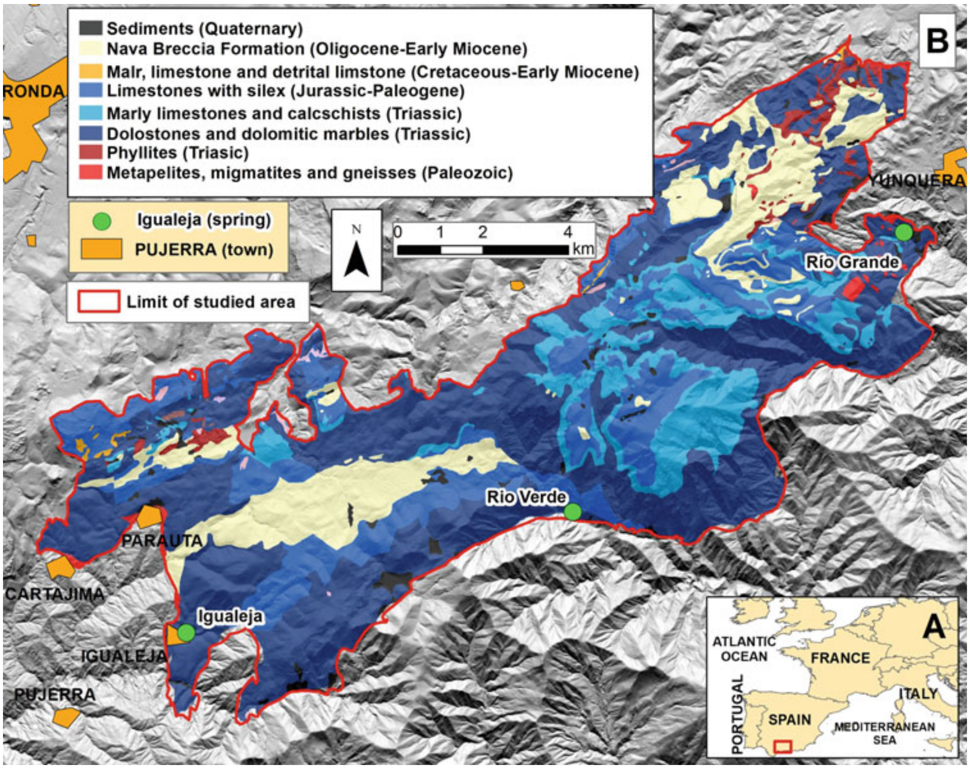

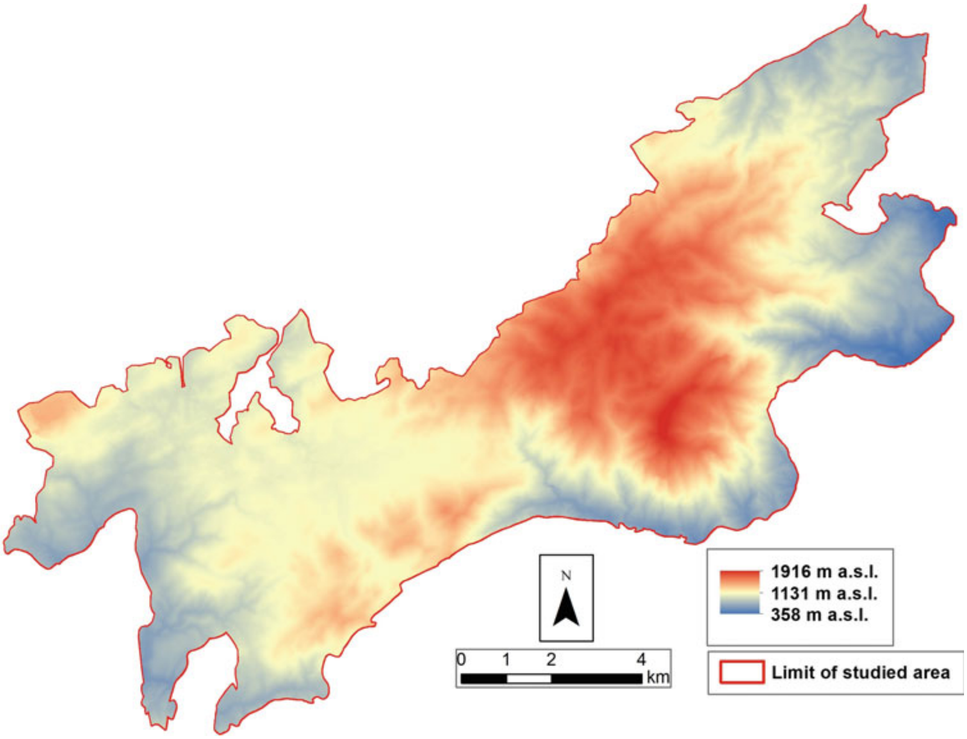

Fig. 2 Digital elevation model of the Sierra de las Nieves karst aquifer

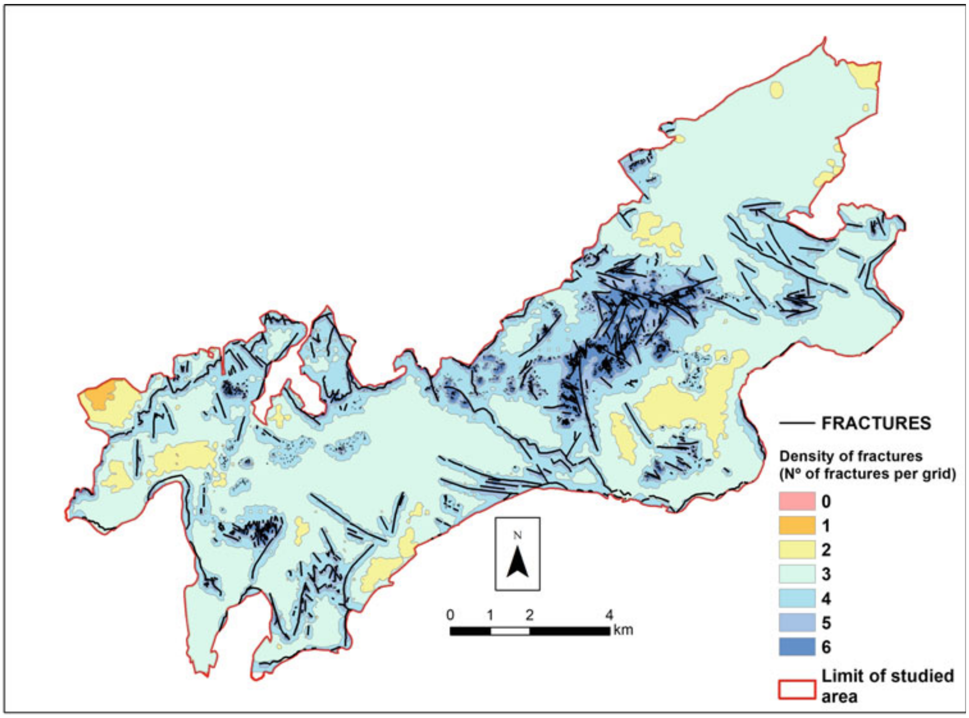

Fig. 3 Fractures and fracturing density estimated by Ordinary Kriging

of *Quercus ilex* and *Pinus genus* (Fig. 9), *Pinus genus* and high mountain scrub (*Cenista spartoides, Juniperus comunis* and *Berberis hispanica*) (Fig. 9) and *Quercus ilex* (Fig. 9).

Following observations in the study area, a four-stage conceptual model of spatial vegetation development is proposed (Fig. 10).

Fig. 4 *Abies pinsapo* forest

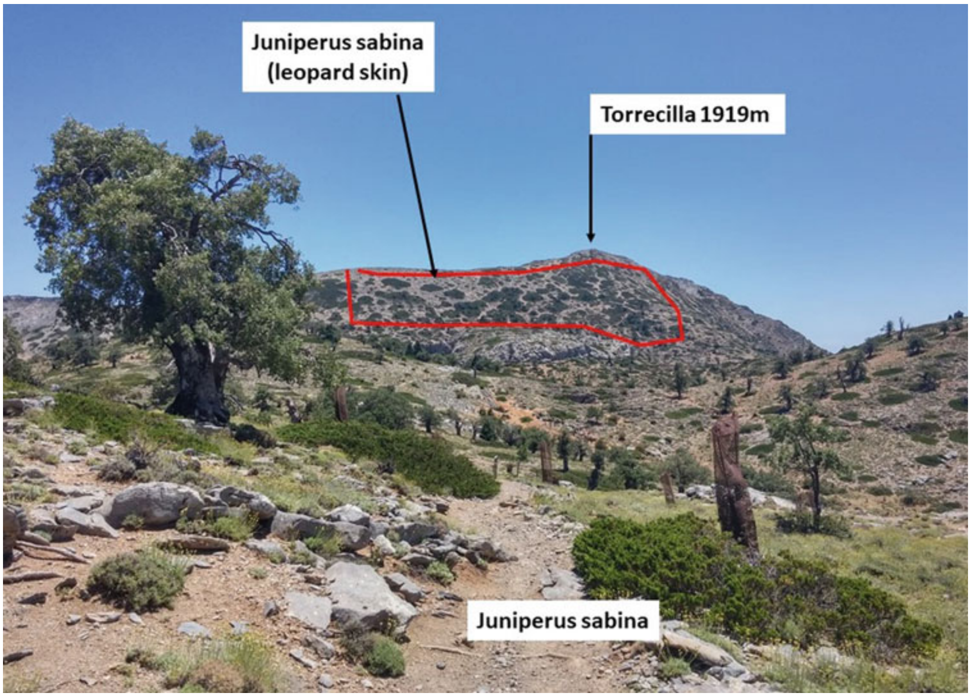

Fig. 5 *Quercus faginea* and Juniperus Sabina

Vegetation Mapping by Remote Sensing

Sierra de las Nieves shows a wide range of vegetation types: needleleaved evergreen trees (*Abies pinsapo*, *Pinus halepensis* or *Pinus sylvestris*), broadleaved deciduous trees (*Quercus alpestris, Quercus faginea* and *Quercus ilex*) and shrubland (*Juniperus Sabina*, *Berberis hispanica*, *Ulex baeticus, Cenista spartoides and Juniperus comunis*) (Cabezudo-Artero et al. 1998).

This study used spring and summer images for land-cover classification. Two Level 1C Sentinel-2 scenes of the same area in southeast Spain were downloaded (tile T30SUF). The

Fig. 6 Garrigue (*Berberis hispanica*, *Ulex baeticus*)

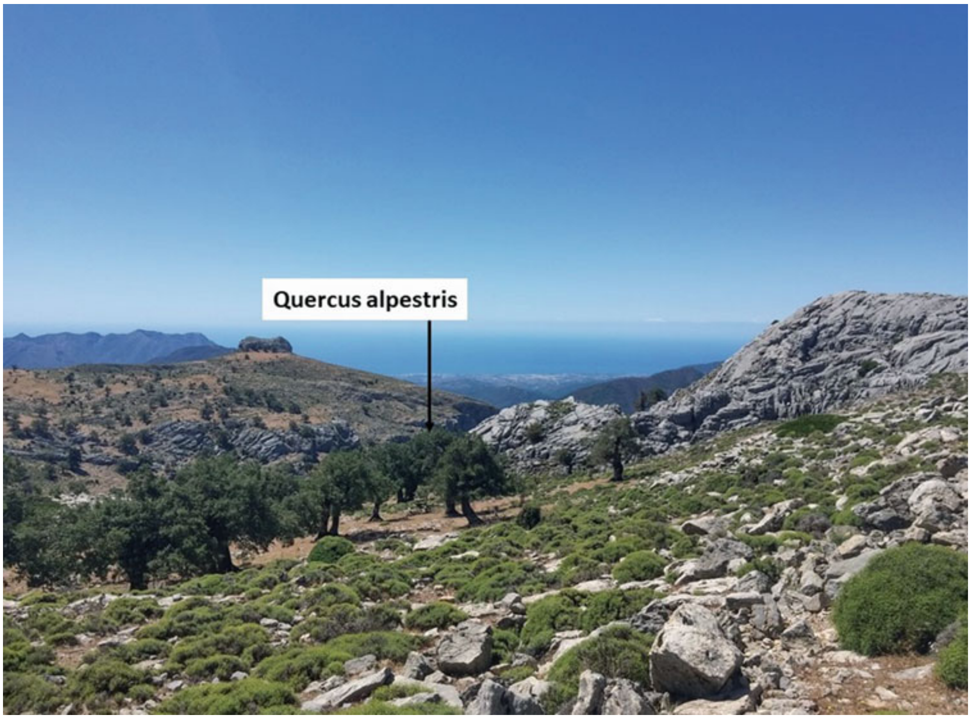

Fig. 7 *Quercus alpestris*

images were acquired on July 23 and March 20, 2017, and downloaded from the ESA Sentinels data hub. Both Sentinel-2 scenes were cloud-free and were processed from Top-Of-Atmosphere (TOA) Level 1C to Bottom-Of-Atmosphere (BOA) Level 2A reflectance using Sentinel-2 Toolbox (Sen2Cor). The spatial resolution of the red-edge and short-wave infrared (SWIR) bands was resampled to 10 m using the nearest-neighbor method to ensure integration with the 10-m visible and near-infrared (NIR) bands. Normalized difference vegetation index (NDVI) (Rouse

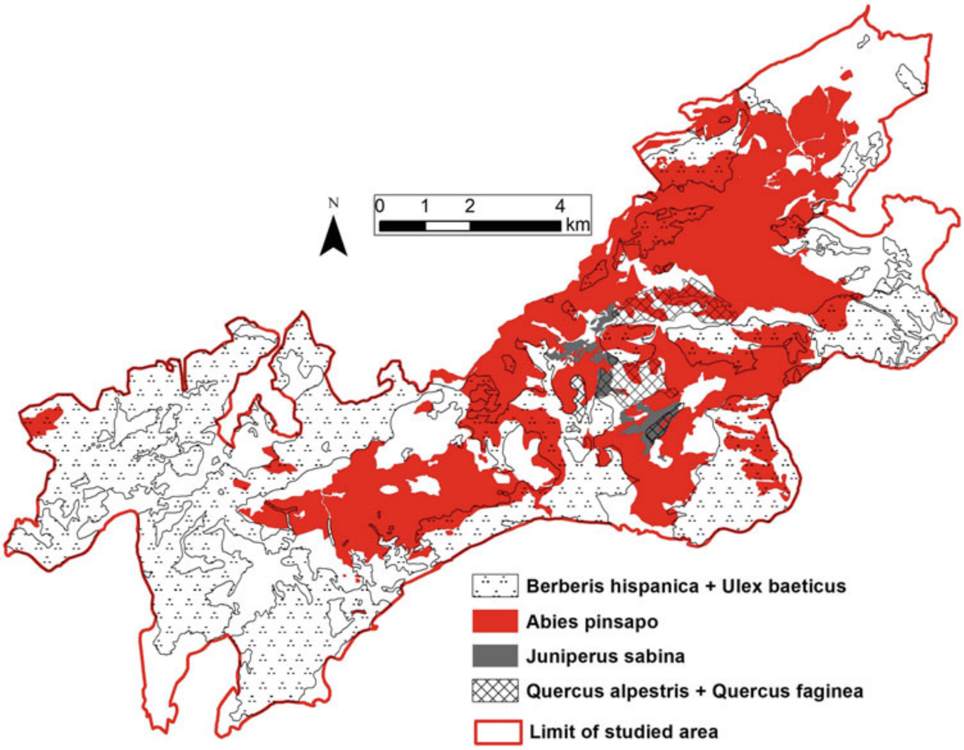

Fig. 8 Species mapped by JA (2017)

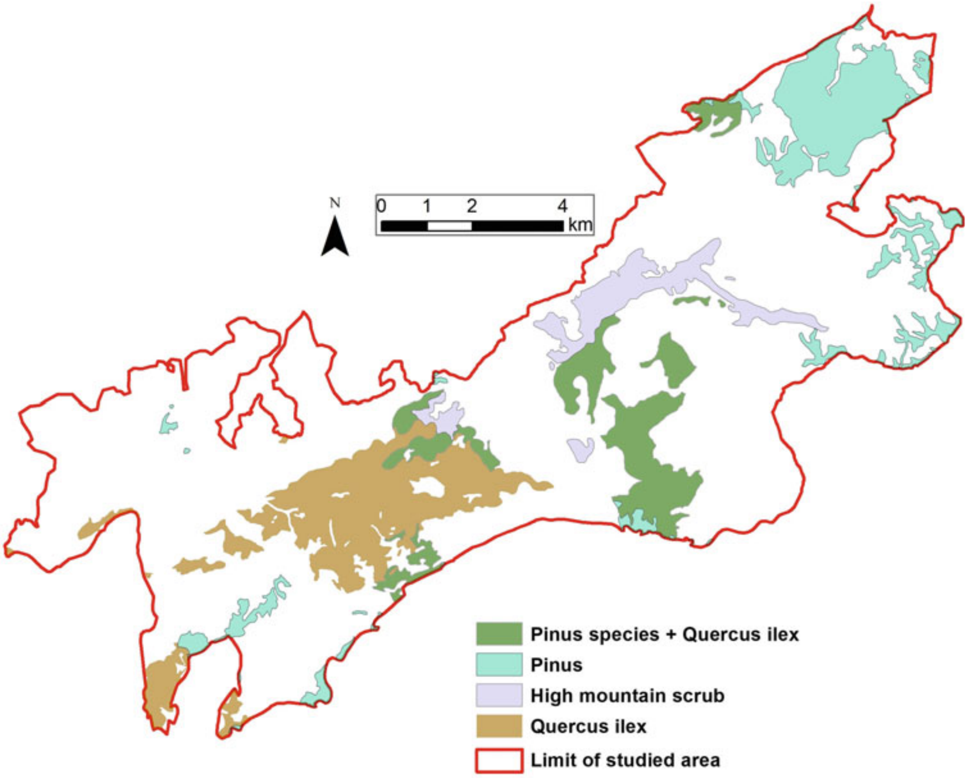

Fig. 9 Species mapped by JA (2017)

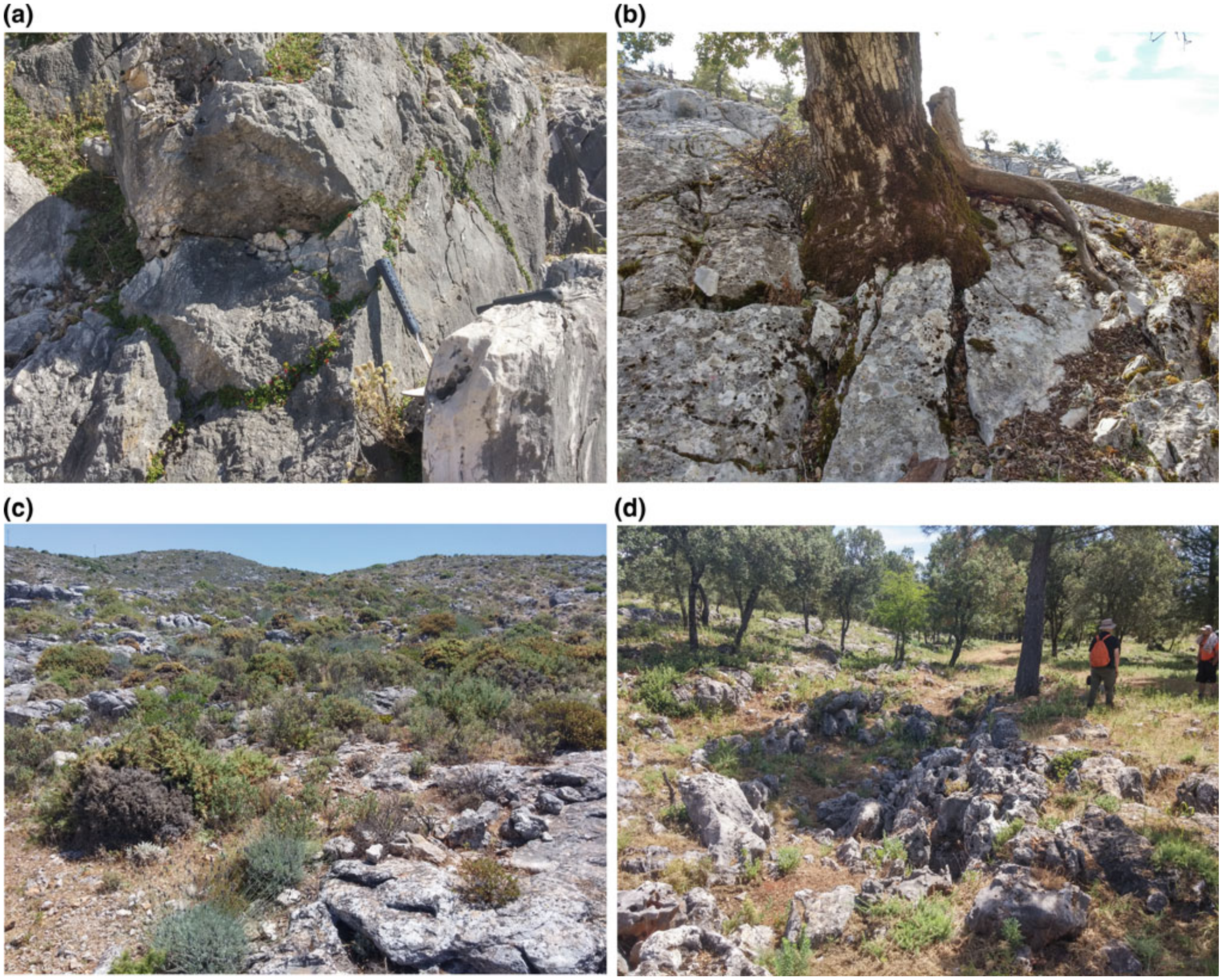

Fig. 10 **a** Early colonization of fractures, **b** the roots of shrubs and trees grow through joints. The diameter of the tree shown is approx. 50 cm, **c** increased soil and development of shrubs, **d** increased depth and forest growth (*Quercus ilex* and Pinus genus is shown)

et al. 1974) was computed from Level 2A Sentinel 2 images from the NIR (Band 8) and red band (Band 4).

$$\mathrm{NDVI} = \frac{\rho_{\mathrm{NIR}} - \rho_{\mathrm{R}}}{\rho_{\mathrm{NIR}} + \rho_{\mathrm{R}}}$$

where ρ_{NIR} and ρ_{R} are the reflectivity of the near-infrared band and red band, respectively.

Two-step ISOCLUST (Ball and Hall 1965) unsupervised classification approach was implemented in ArcGIS 10.4.1. The summer scene was initially classified to delineate the tree cover (needleleaved evergreen and broadleaved deciduous). The categories with scarce vegetation cover in summer, including shrublands, bare areas, and rainfed croplands, were extracted from the spring image. Finally, the two classifications were combined into a single map. The resulting classification can be seen in Fig. 11.

Mediterranean landscapes are difficult to classify due to the higher soil reflectance in the background of scarce vegetation land cover (Rodriguez-Galiano et al. 2012). To increase the separability between land-cover categories, information on variations in the phenological state of vegetal cover can be added by incorporating of multi-seasonal images. Several studies have shown that a combination of multi-seasonal images facilitates discrimination between certain land covers (Lunetta and Balogh 1999; Oetter et al. 2001; Wolter et al. 1995; Yuan et al. 2005). In summer images, shrublands can be confused with bare soils and outcrops. The inclusion of spring images discriminates between bare areas and evergreen natural vegetation. Additionally, shrublands, with a lower vegetation cover fraction during summer drought periods, are usually greener in springtime, allowing them to be differentiated from bare areas.

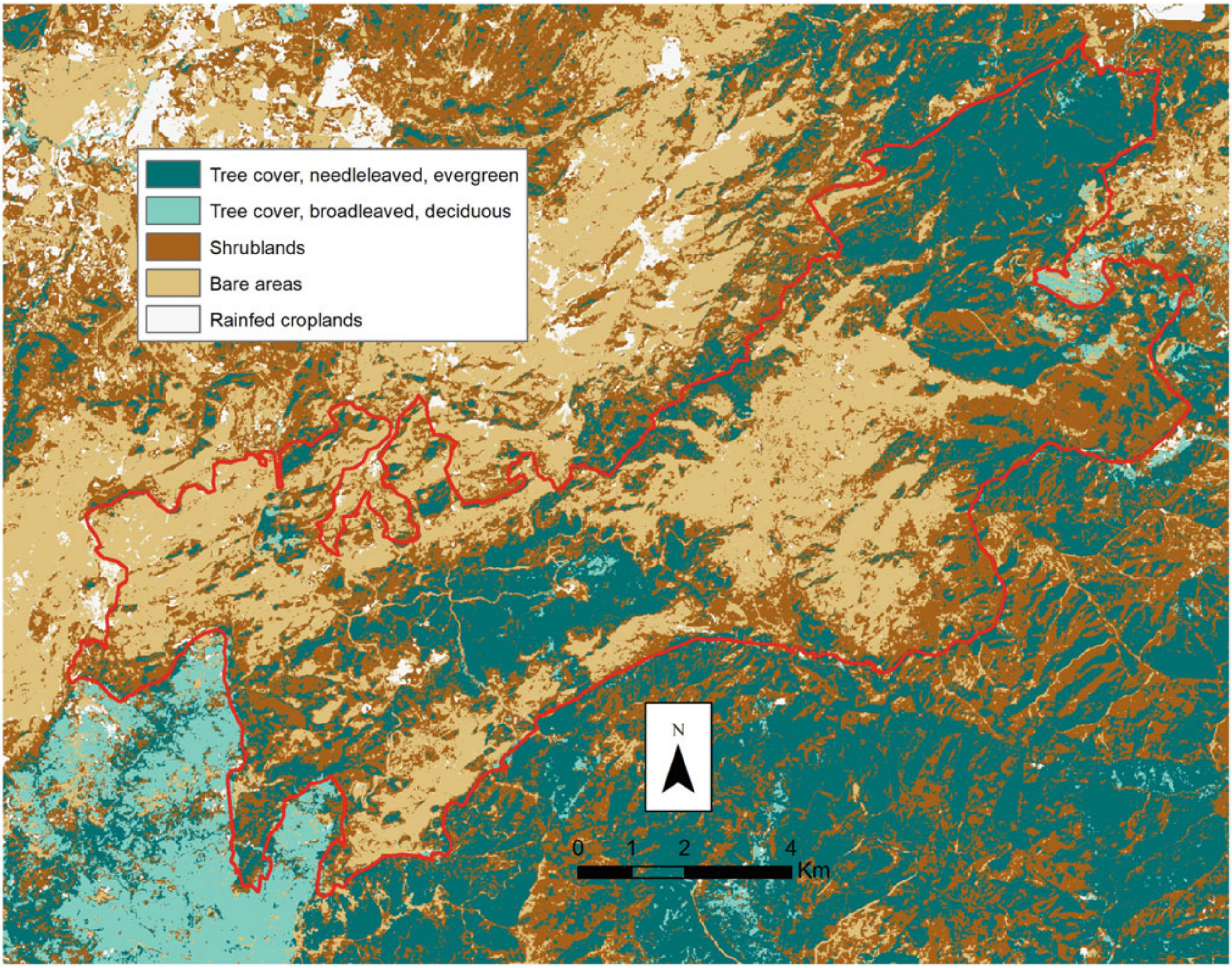

Fig. 11 Vegetation map from remote sensing images and category percentage in the study area

Methodology

The ArcGIS 10.4.1 toolbox was used to create a 100 m × 100 m grid and to merge the estimated shapes. This means that every grid shows all the parameters used to apply the contingency procedure.

The spatial distribution of fracture density (Fig. 3) was estimated by mean ordinary kriging to obtain the most probable value of a spatial estimation at any point (Journel and Huijbregts 1978). There are two main reasons for selecting this method: Ordinary kriging is easy to apply, and the data display no trend at the modeling scale. An omnidirectional variogram was estimated to obtain the fracturing density, and a spherical model was fitted with three structures. Experimental variograms can be used to detect and model different scales of variability, characterized by different variogram structures with different ranges. The ranges of use in the model were 130, 500 and 2300 m (Fig. 12).

In the next step, a contingency analysis was performed to verify spatial relationships between pairs of variables. To do this, a 100 m × 100 m grid was created to compare pairs of variables within the cells and their relationship with other parameters: lithology (the most representative) (Fig. 1), fracturation density (Fig. 3), karst depressions (Fig. 13) and slope (Fig. 14). Detailed soil information was not available. A karts depressions map (Fig. 13) was estimated from a 5-m digital elevation model Pardo-Igúzquiza (2015). The slope that was mapped has been built with ArcGIS toolbox (Fig. 14).

Association was defined by comparing pairs of variables: vegetation (presence or absence) with lithologies, depressions (presence or absence), 90th percentile of fracturation density and slope.

A and *B* are two given variables. *E* is the cutoff factor for the Chi-square (Spiegel 1998) calculation; it can be the median or can represent 90th or another more demanding percentile, e.g., 95th.

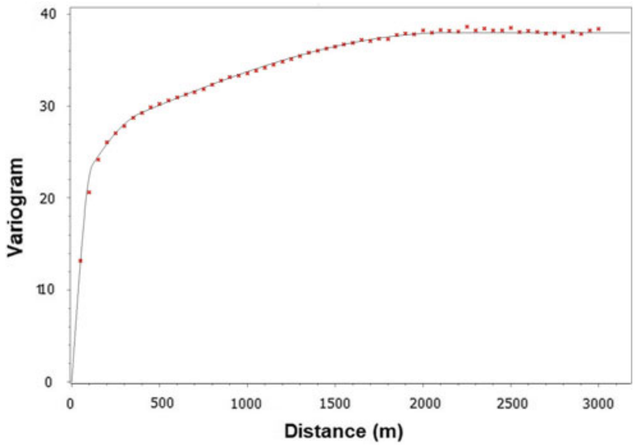

Fig. 12 Experimental variogram (red crosses) and fitted model (continuous black line)

Thus, the Chi-square statistic is calculated with the following equation:

$$X^2 = \frac{(N1 - N1E)^2 + (N2 - N2E)^2 + (N3 - N3E)^2 + (N4 - N4E)^2}{N1E + N2E + N3E + N4E}$$

	Value $A \leq E\_A$	Value $A > E\_A$
Value $B \leq E\_B$	$N1$	$N2$
Value $B > E\_B$	$N3$	$N4$

$N1 + N2 + N3 + N4 = N$ (number of pairs).

Chi-square (X^2) with 1 degree of freedom shows association with a confidence level:

$X^2 > 10.83$, the confidence level is 99.9%
$X^2 > 7.88$, the confidence level is 99.5%
$X^2 > 6.63$, the confidence level is 99%
$X^2 > 5.02$, the confidence level is 97.7%
$X^2 > 3.84$, the confidence level is 95%
$X^2 > 2.71$, the confidence level is 90%
$X^2 > 1.32$, the confidence level is 75%
$X^2 > 0.45$, the confidence level is 50%

There are other two possibilities: random relationship and relationship rejected.

Results and Discussion

The results of the contingency analysis show different degrees of affinity (Table 1). The red boxes indicate that the hypothesis is rejected.

Abies pinsapo (Fig. 5), included in category 1 (Fig. 11), shows the highest association with Nava Breccia, marly limestones and calcschists and limestones with silex (>99.9% confidence level) and with fracture density greater than 97.7%. The association with marly limestones and slope is lower than 50% and is random with depressions. The association with dolostones and dolomitic marbles has been rejected.

Pinus genus (Fig. 9) is found in small concentrations close to the boundaries of study area and is included in category 1 (Fig. 11). The best association is showed with

Fig. 13 Map of depressions (from Pardo-Igúzquiza et al. 2015)

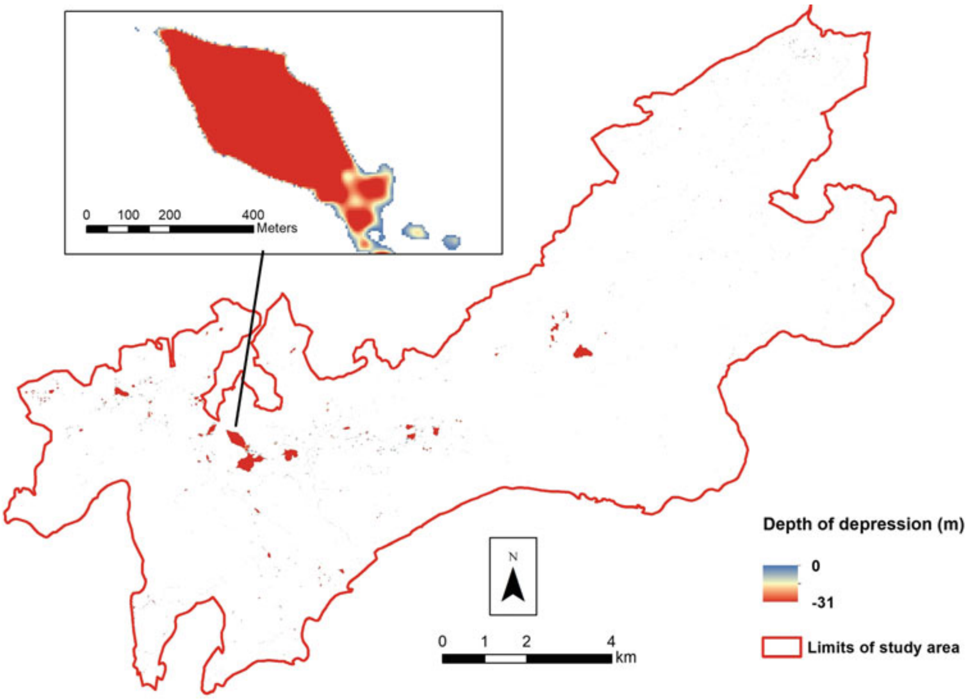

Fig. 14 Slope map of the Sierra de las Nieves Karst aquifer

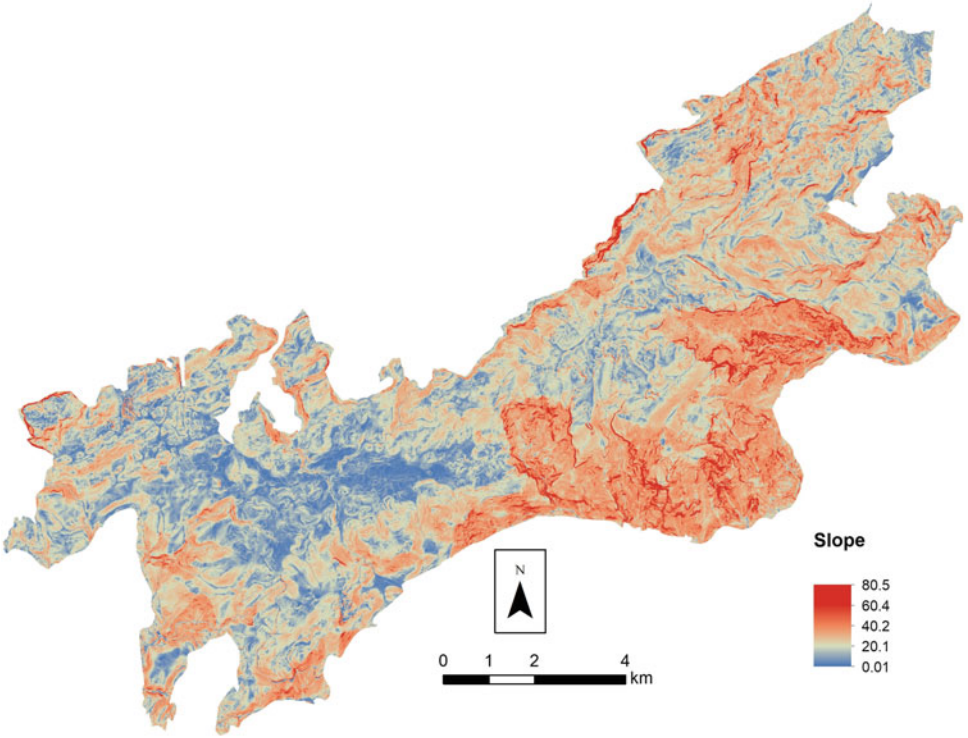

phyllite (99.5%), slope (97.7%), breccia (99%) and dolostones (99%). Association with fracture density and depressions has been rejected, and there is no overlap with marly limestones.

Quercus ilex (Fig. 9) is found to be concentrated on Nava Breccia Formation (>99.9%), limestones with silex (>95%) and depressions (>75%). This species is included in category 1 (Fig. 11). Association with slope and dolostones is rejected, and there is no overlap with phyllite, marly limestones or fracturation density.

Pinus species also grows with *Quercus ilex* (Fig. 9) with the largest forest area on the southern slope of Torrecilla peak. These species are associated with dolostones (99.9%), limestones with silex (99.9%), fracturation density (99%), marly limestones (97.7%) and slope (75%). Breccia shows random association, and the relationship with depressions is rejected between them. There is no overlap with phyllite.

Quercus alpestris and *Quercus faginea* (Fig. 8) are included in category 3 (Fig. 11). The growth in the high areas of Sierra de las Nieves scattered throughout the most fractured limestones outcrops with silex and marly limestones. Some authors consider both species are quite similar. These trees are found scattered at the highest altitudes of Sierra de las Nieves where there is no enough soil for good development. Association with fracturation density is >99.9% and with marly limestones and limestones with silex is >99.5%. Association with dolostones and dolomitic marbles is essentially random and random in the case of Nava Breccia, phyllite, slope and depressions.

Juniperus Sabina (Fig. 8) is found above altitude 1600 m on limestones with silex (>97.7%) and marly limestone (>50%) outcrops with fracturation density (>50%) and slope (>50%). This species is included in category 3 (Fig. 11). The association with dolostone, depressions and slope is random. In contrast, breccia and phyllite show no overlap. A *leopard skin* distribution can be observed in the landscape (Fig. 5).

Berberis hispanica and *Ulex baeticus* (Fig. 8) (included in category 3, Fig. 11) are spiny plants growing on calcareous outcrops and are associated with other Mediterranean shrubs as garrigue (phrygana) (Fig. 6). Other plants found in these scrubland ecoregions include thyme, gorse and Jerusalem sage. Association is best with dolostone (>99.9%) and fracturation density (>50%) and is random with marly limestone, phyllite, depressions and slope. Association with breccia and limestone with silex has been rejected.

High mountain scrub (Fig. 9) is composed of aromatic plants including thyme, oregano, rosemary, bay, pennyroyal or gum cistus. This association is included in category 3 (Fig. 11). This plant community grows on marly limestones (>99.9%) and limestones with silex (>99.5%) and outcrops showing high fracture density (>99.9%). The relationship with dolostone and slope is random, and there is no overlap with breccia, phyllite or depressions.

Table 1 (A) *Berberis hispanica* + *Ulex baeticus*. (B) *Abies pinsapo*. (C) *Juniperus sabina*. (D) *Quercus alpestris* + *Quercus faginea*. (E) Pinus species + *Quercus ilex*. (F) Pinus genus. (G) High mountain scrub. (H) *Quercus ilex*. (1) Fracturation density. (2) Nava breccia. (3) Dolostone and dolomitic marble. (4) Marly limestones and calchists. (5) Limestone with silex. (6) Metapelites. (7) Phyllite. (8) Depression. (9) Slope

	1	2	3	4	5	6	7	8	9
A	0.62	63.93	3143	8.20	67.9	2.12	6.83	0.23	3.47
B	5.72	55.30	164.2	30.91	97.4	9.53	0.82	1.30	1.19
C	0.75	no	2.19	0.88	6.55	no	no	no	0.16
D	20.33	no	9.23	7.95	8.24	no	no	no	0.12
E	6.82	3.25	14.0	5.59	15.7	no	no	no	2.51
F	38.9	7.63	7.78	no	20.76	7.96	8.45	no	5.55
G	11.18	no	5.79	10.25	9.78	no	no	no	0.09
H	0.01	44.3	40.7	no	4.83	no	no	1.66	9.39

Conclusions

The main lithologies of the Sierra de las Nieves have been analyzed together with fracture density, depressions and slopes to determine the influence of these factors on the distribution of the most significant plant species.

Ordinary kriging enabled a linear variable to be changed to continuous. ArcGIS tools were used to overlap all the information layers and generate a georeferenced table with all the variables considered.

Contingency analysis enabled a relationship to be established in statistical terms relationship between the vegetation and the lithologies of the area and with fracturation density, depressions and slope.

The lithology shows significant degrees of influence, but dolostone and dolomitic marble present the strongest contrast. Of the non-lithological variables, the fracture density shows the most difference in degrees of influence.

Additional work is needed to understand more fully the relationship between vegetation and soil properties such as pH, humidity, geochemical composition or total organic carbon composition.

This study provides information which enhances our knowledge of the biodiversity and geology in Sierra de las Nieves.

Acknowledgements This work was supported by project CGL2015-71510-R (Ministerio de Economía, Industria y Competitividad of Spain).

References

Atalay I (1988) Karstification and ecology of the karstic terrains of the Taurus Mountains in Turkey. Bulletin of Geomorphology. 16: 1–8.

Atalay I (1991) Soil forming in the karstin terrains of Turkey. Bulletin of Geomofphology. 19: 139–144.

Atalay I (1997) Red Mediterranean soils in some karstic regions of taurus mountains, Turkey. Catena. 3–4: 247–260.

Bakalowicz M (2012) Epikarst. In: White, W.B., Culver, D.C. (Eds.), Encyclopaedia of Caves, (second edition). Academic Press, 284–288.

Bakalowicz M (2004) The epikarst. The skin of karst. In: Jones, W.K., Culver, D.C. & Herman, J.S. (Eds.) – Epikarst. Special Publication 9. Charles Town, WV: Karst Waters Institute: 16–22.

Ball GH, Hall DJ (1965) Isodata: a method of data analysis and pat-tern classification. Stanford Research Institute. Menlo Park. United States. Office of Naval Research. Information Sciences Branch.

Barany-Kevei I, Horváth A (1996) Survey of the interaction between soil and vegetation in a karst ecological system at Aggtelek, Hungary. Acta Geogr. Szegediensis. XXXV: 81–87.

Cabezudo-Artero B, Pérez-Latorre A, Navas-Fernández P, Gil-Jiménez Y, Navas-Fernández D (1998) Parque Natural de la Sierra de las Nieves "cartografía y evaluación de la flora y vegetación. Junta de Andalucía, 367 pp.

Efe R (2014) Ecological properties of vegetation formations on karst terrains in the central Taurus Mountains (Southern Turkey). The 3rd International Geography Symposium-GEOMED2013. Procedia-Social and Behavio Scien. 120: 673–679.

Ford D, Williams P (2007) Karst Hydrogeology and Geomorphology. John Wiley and Sons, Chichester, UK, 562 pp.

IGME (2015). Cartografía geológica de España. http://info.igme.es/cartografiadigital/datos/geode/docs/GEOL_INFO.pdf.

Junta de Andalucía (JA) (2017) Environmental and Land Planning Counseling. http://www.juntadeandalucia.es/medioambiente/site/rediam/menuitem.04dc44281e5d53cf8ca78ca731525ea0/?vgnextoid=937b60 e749e0a210VgnVCM2000000624e50aRCRD&vgnextchannel=36faa7215670f210VgnVCM1000001325e50aRCRD&vgnextfmt=rediam&lr=lang_es.

Journel AG, Huijbregts Ch (1978) Mining geostatistics. Academic Press, New York, 600 pp.

Klimchouk AB (2004) Towards defining, delimiting and classifying epikarst: its origin, processes and variants of geomorphic evolution. In: Jones WK, Culver DC, Herman JS (Eds.), Epikarst. Special Publication 9. Charles Town, WV, Karst Waters Institute, pp. 23–35.

Liang Y, He X, Chen C, Feng S, Liu L, Chen X, Zhao Z, Su Y (2015). Influence of plant communities and soil properties during natural vegetation restoration on arbuscular mycorrhizal fungal communities in a karst region. Ecological Engineering. 82: 57–65.

Liang Y, Pan F, He X, Chen X, Su Y (2016) Effect of vegetation types on soil arbuscular mycorrhizal fungi and nitrogen-fixing bacterial communities in a karst region. Environ Sci Pollut Res. 23:18482–18491.

Liu C, Liu Y, Guo K, Wang S, Liu, H, Zhao H, Qiao X, Hou D, Li S (2016) Aboveground carbon stock, allocation and sequestration potential during vegetation recovery in the karst region of southwestern China: A case study at a watershed scale. Agriculture, Ecosystems and Environment. 235: 91–100.

Lu X, Toda H, Ding F, Fang S, Yang W, Xu H (2014) Effect of vegetation types on chemical and biological properties of soils of karst ecosystems. Eur Jour of Soil Biol. 61: 49–57.

Lunetta RS, Balogh ME (1999) Application of Multi-Temporal Landsat 5 TM Imagery for Wetland Identification. Photogrammetric Engineering & Remote Sensing 65: 1303–1310.

Martín-Algarra A (1987) Evolución geológica Alpina del contacto entre las Zonas Internas y las Zonas Externas de la Cordillera Bética (Sector Occidental). Tesis Doctoral. Universidad de Granada, 1171 pp.

Oetter DR, Cohen WB, Berterretche M, Maiersperger TK, Kennedy RE (2001) Land cover mapping in an agricultural setting using multiseasonal Thematic Mapper data. Remote Sensing of Environment 76: 139–155.

Pardo-Igúzquiza E, Durán JJ, Luque-Espinar JA, Robledo-Ardila PA, Martos-Rosillo S, Guardiola-Albert C, Pedrera A (2015) Karst massif susceptibility from rock matrix, fracture and conduit porosities: a case study of the Sierra de las Nieves (Málaga, Spain). Environmental Earth Sciences 74: 7583–7592.

Pedrera A, Luque-Espinar JA, Martos-Rosillo S, Pardo-Igúzquiza E, Durán-Valsero JJ, Martínez-Moreno F, Guardiola-Albert C (2015) Structural controls on karstic conduits in a collisional orogeny (Sierra de las Nieves, Betic Cordillera, S Spain). Geomorphology 238: 15–26.

Rodriguez-Galiano VF, Chica-Olmo M, Abarca-Hernandez F, Atkinson PM, Jeganathan C (2012) Random Forest classification of Mediterranean land cover using multi-seasonal imagery and multi-seasonal texture. Remote Sensing of Environment 121: 93–107.

Rouse JW, Haas RW, Schell JA, Deering DH, Harlan JC (1974) Monitoring the vernal advancement and retrogradation (Greewave effect) of natural vegetation, Greebelt, MD. USA, NASA/GSFC.

Shen LN, Deng XH, Jiang ZC, Li T (2013) Hydrogeochemical effects of an epikarst ecosystem: case study of the Nongla Landiantang Spring catchment. Env Earth Scien. 68 (3): 667–677.

Spiegel MR (1998) Schaum's Outline of Statistics. McGraw Hill, New York, 600 pp.

Tonga X, Wanga K, Yue Y, Brandt M, Liu B, Zhang C, Liao C, Fensholt R (2017) Quantifying the effectiveness of ecological restoration projects onlong-term vegetation dynamics in the karst regions of Southwest China. Inter J of Applied Earth Obser and Geoinf. 54: 105–113.

Williams PW (1983). The role of the subcutaneous zone in karst hydrology. J Hydrol. 61: 45–67.

Williams PW (2008) The role of the epikarst in karst and cave hydrogeology: a review. Int. J. Speleol. 37, 1–10.

Wolter PT, Mladenoff, D.J., Host, G.E., G.E., & T.R. (1995) Improved forest classification in the Northern Lake States using multi-temporal Landsat imagery. Photogrammetric Engineering & Remote sensing, 61, 1129–1143.

Yuan F, Bauer ME, Heinert NJ, Holden G (2005) Multi-level land cover mapping of the Twin Cities (Minnesota) metropolitan area with multi-seasonal Landsat TM/ETM + data. Geocarto International 20: 5–14.

Dissolution Process: When Does the Process Start

Silvana Magni

Abstract

Dissolution process is a complex phenomenon controlled by several factors as like lithology, porosity, stress orientation, environmental conditions and networks of fractures. Then, fault zone and fractures play an important role in fluid circulation and in dissolution, acting as barriers or conduits. In fact, the fault zone has a high permeability only in the early stages of the movement, but shortly the process of recrystallization and reprecipitation reduces the permeability greatly within them. Despite this, traditionally (Cucchi and Forti in In Att. e Mem. Comm. Grotte "E: Boegan" 87–93, 1988; Bini et al. in Varese Lake and the Quaternary 6:3–14, 1993; Ferrarese and Meneghel in Aspetti dell'influenza strutturale sulla morfogenesi carsica del Montello (Treviso), 45–59, 1992), the dissolution is associated with extensional structures such as faults and joints believing that they are more favorable to the water circulation. In this context, compressional tectonic structures, as like stylolites, are never been taken into consideration. In fact, the stylolites play an important role in the fluid circulation (Alsharhan and Sadd in U.A.E., Society for Sedimentary Geology Special Publicatio, 185–207 2000; Raynaud in J Struct Geol, 973–980, 1992) and in particular in the incipit of dissolution and then of the karst. The focus of the research is to investigate the starting point of the dissolution and the micromechanisms that act in the fluid/rock system. To achieve this, we performed: *field work*, *labs analysis.* The field work was carried out in a karst area in the South Italy (Alte Murge). Through a detailed structural analysis in the field and using the method of Caine (Caine et al. in Geology 1025–1028, 1996), we reconstructed the permeability of the fault zone. Our attention was focused on faults, joints and stylolites. To support the field observations we had carried out, chemical and petrographic analysis (XRD, FTIR, SEM), that are helping us to characterize the porosity and permeability near these structures. Recently, fluid/rock interactions and their impact on carbonate rocks are becoming very important as a consequence of a progressive deterioration of the quantity and quality of the groundwater due to increasing pollution phenomena. In fact, the aquifers represent about 40% of the drinking water resources and their importance will increase in coming years.

Keywords

Dissolution • Fluid/rock interaction • Permeability • Stylolites

Introduction

Fault zones and fractures play an important role in fluid circulation, acting as permeability barriers or conduits, depending on the specific conditions (lithological and structural in particular) and on the distribution of other structures associated with them. The hydraulic potential of a fault zone can be estimated by considering its thickness (Caine et al. 1996; Aydin 2000) using the parameter *Fa*, calculated as the ratio between the length of the damaged zone and the length of damaged zone plus the length of the fault gouge. For a better understanding of the role played by fault zones on fluid circulation, it is useful to investigate the structures associated with them, in particular stylolites and secondary fractures too. It is often assumed that faults, especially extensional faults, have sufficient permeability to ensure fluid flow. In reality, their permeability is sufficiently high only in the early stages of the movement (Piccini 1999) because after a short period the deposition of minerals (e.g., calcite) by fluids fills the voids resulting in a dramatic reduction in porosity/permeability.

Although different studies (Forti and Piccini 2007; Menichetti 1988; Menichetti and Galdenzi 1992;

S. Magni (✉)
University of Mainz-Institute of Geosciences, J.-J.-Becher-Weg 21, 55128 Mainz, Germany
e-mail: silmagni@uni-mainz.de

C. Bertrand et al. (eds.), *Eurokarst 2018, Besançon*, Advances in Karst Science,
https://doi.org/10.1007/978-3-030-14015-1_3

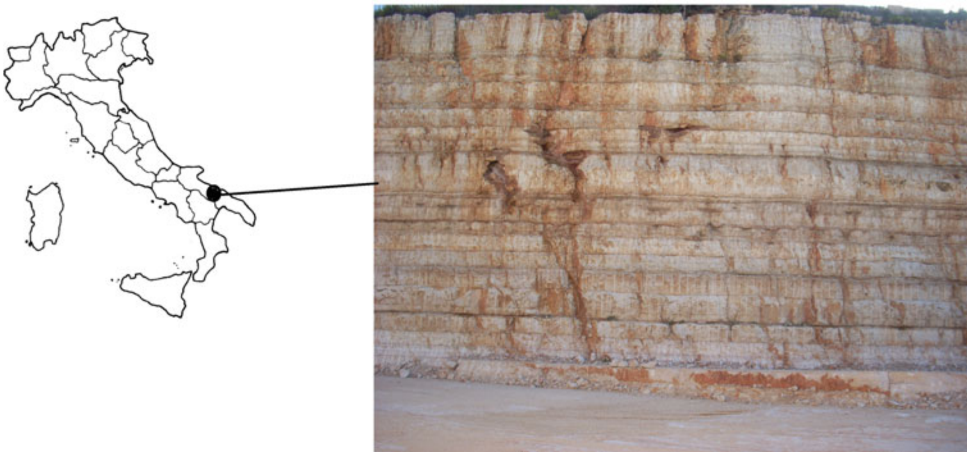

Fig. 1 Investigated area, in South Italy (Alte Murge). On the right side, the quarry where the field research was carried out

Quinif et al. 2001; Shanov et al. 2015; Tognini 1994; Vigna and Calandri 2001) have been conducted in several karst areas on the relationship between tectonic (faults, folds and joints) and karstification, little or no consideration has been given to the effective role of the compressional ones.

In this context, the stylolites play an important role. They are complex column and socket interdigitation features (Park and Schot 1968; Gratier et al. 2005) that form by variable dissolution of material along planar surface: Water dissolves the carbonate and leaves relict material, non-carbonate particles (NCP) (mostly clay minerals) along the indented stylolites planes. Stylolites play an important role in fluid circulation during carbonate deformation (Raynaud 1992). However, stylolites may also play a role as nucleation sites for karst porosity when deformation conditions change. There are few previous studies that investigate the dissolution/precipitation process along stylolites as sites of karst cavity formation (Alsharhan and Sadd 2000) and their role in deformation and permeability change (Renard et al. 2004; Koehn et al 2007, 2012; Ebner et al. 2009a). In fact, stylolites mostly form in a compressional setting probably by migration of large volumes of water that dissolves the carbonate and leaves NCP along the indented stylolite planes. It is possible that new NCP material influences the solution/precipitation process, providing starting point of dissolution.

It is presently unclear whether stylolites are barriers or conduits for fluid pathways in such cases, or whether they possibly alternate barrier/conduit behavior depending on local conditions.

Research Method

The process of dissolution along the stylolites was investigated by conducting field research and laboratory analysis. Field research was conducted in a karst area in Southern Italy (Fig. 1), where we have conducted a detailed structural analysis. Directly on the field, using the scanline method, we focus our attention on the faults, joints and stylolites and we simply separate the ones that show karst from the ones without karst. The scanline method that I followed consists using a scale on the floor and to measure systematically all our interested structures, faults, joints and stylolites that intersect the scale. We decided to indicate as *karstified* all of these structures showing dissolution that mining for us the presence of *terra rossa* (Fig. 2).

From the field results, it was clear that the dissolution is more abundant along the stylolites rather than along joins and faults.

Because of these results, we decide to focus our attention on stylolites, and therefore on them, we carried out chemical and petrographic analysis to characterize the role of NCP

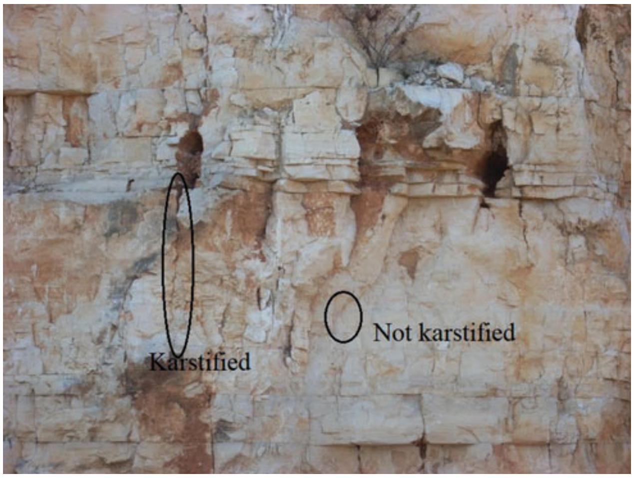

Fig. 2 Structures karstified that show terra rossa, on the left of the picture and structures not karstified

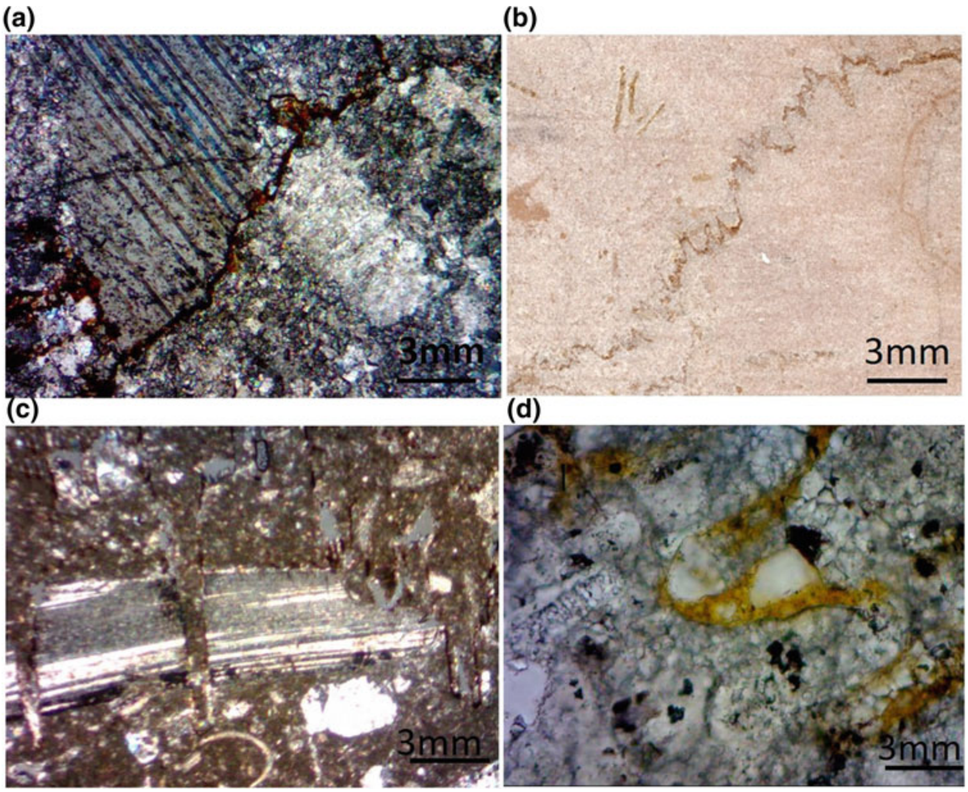

Fig. 3 Example of variable stylolite shapes; **a** sharp shape; **b** seismogram type; **c** rectangular type; **d** wave-like type (according to (Koehn et al. 2016) classification). The shape changes because of the homogeneity or inhomogeneity of the matrix that also influences the roughness amplitude

into dissolution process and fluid circulation. We have performed SEM, FTIR and XRD analysis.

XRD and FTIR analyses are until now the best method to investigate clay minerals and were carried out on the matrix and on NCP material.

SEM analysis was performed at very high resolution and has helped to investigate the size and the distribution of NCP and the host rock.

Furthermore, because of a wide variability in shape and in composition too of the stylolites, we decided to investigate a large number of samples, coming from different countries, to achieve the widest coverage of existing types.

In addition to this, because of their extreme variability in form, we are setting up a database (Fig. 3) for their classification.

Results

Field Work

The study area is affected by brittle deformation that determines mechanical discontinuity. We analyzed faults, joints, stylolites, and for each of them, we observed the presence of dissolution (Figs. 2 and 4). The relationship between these structures has allowed us to reconstruct the structural setting of the entire area and to reconstruct the permeability of the area (Caine et al. 1996) (Fig. 5). The permeability (according to Caine et al. 1996) was estimated by the value Fa that varies between 0 and 1; when Fa is closer to 1, the fault system increases the capability to act as hydraulic conductor. The data (Fig. 4) allow to observe that the karst process is the most diffused, given parity of the other conditions, along the stylolites, and this is consistent with their genesis that involves the dissolution of soluble material and enrichment of insoluble material, finer particle sizes which are more easily eroded, resulting in “expansion” of the vacuum. In situ we have seen, obviously at different sites, various stages related to the process of dissolution along a stylolite, from early stage until the formation of a true cavity.

Laboratory Analysis

We analyzed 10 samples that came from different countries (3 from Belgium, 2 from Italy, 3 from France and 2 from Spain), and on them, we did optical analysis, SEM (Figs. 6 and 7), XRD and FTIR. Both optical analysis and SEM

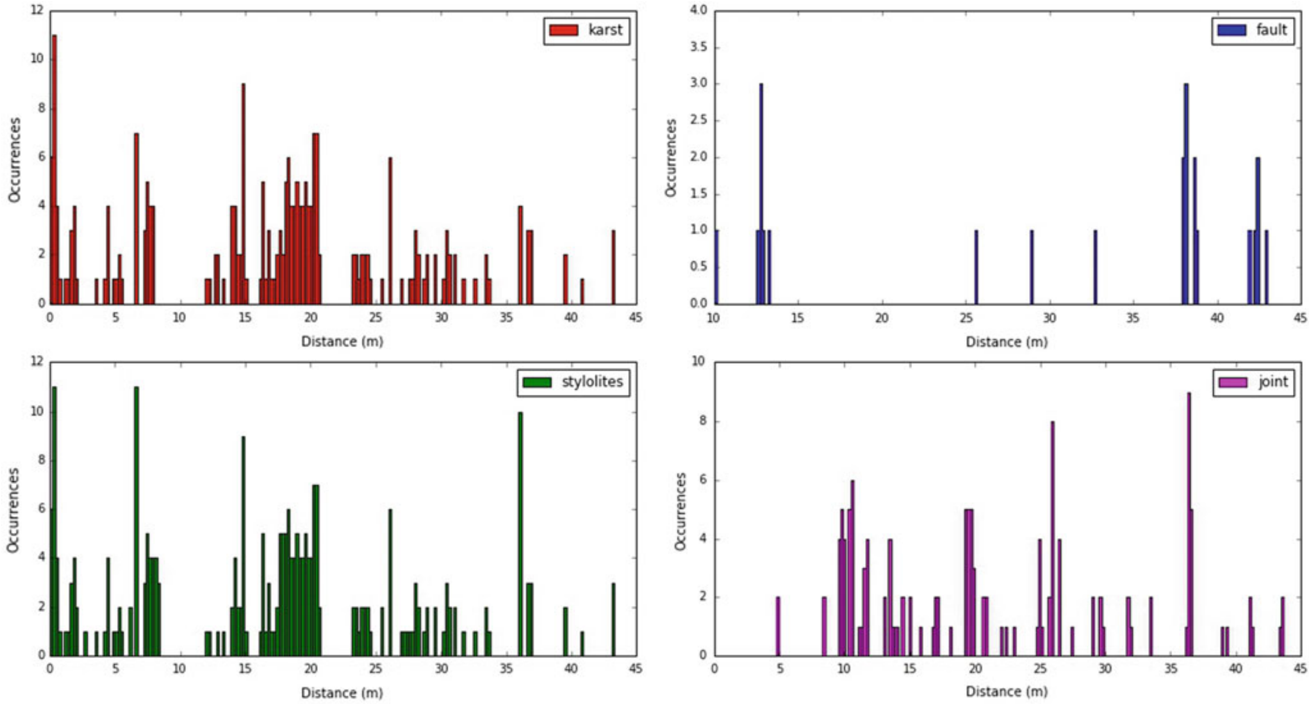

Fig. 4 Presence of dissolution along stylolites, faults and joints. On 45 m length, 27 faults; 55 joints; and 708 stylolites karst structures were measured; of them 88% of stylolites are karstified

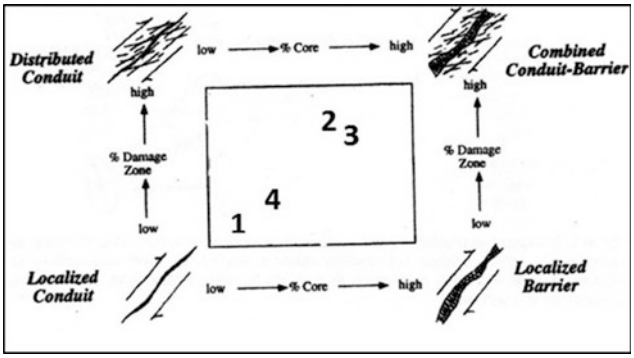

Fig. 5 Permeability reconstruction according to Caine, 1996. The numbers from 1 to 4 indicate the 4 subfaults zone investigated. It is clear how the faults zone investigated acts as a combination of conduits and barriers

show that the porosity of the area containing stylolites is always higher than the matrix of the samples. Despite the great variety (Fig. 3) of shape and composition of analyzed stylolites, we have found, from SEM, XRD and FTIR, some common characters between them:

(a) the distribution of the pores/voids is highest into the stylolites than in the matrix although this is carbonate-made rocks with a general high porosity (Fig. 6);
(b) independently of the matrix composition, Al, Mg, Fe, K are commonly present within the NCP. It means that a process that forms stylolites accumulates insoluble material into them and picks out soluble ones;
(c) hematite, pyrite and dolomitization processes are also very often found inside of the stylolites. The latter process is indicative of a significant increase in porosity due to the Ca/Mg substitution;
(d) kaolinite, montmorillonite and pyrophyllite are the most common mineral found.

The nature of stylolite formation (Ebner et al. 2009a), and the inhomogeneous stress distribution surrounding geometric asperities (Zhou and Aydin 2010), results in a complex internal structure (Fig. 6 and 7).

Discussions

Despite the constant presence of clay minerals (Fig. 6) in the stylolites, we observed an high percentage of voids and holes (Figs. 6 and 7) mostly in the contact between NCP and the other grains. This means that the presence of clay minerals does not prevent the formation of voids. The distribution, size and shape of these voids and holes started to help us to understand porosity and permeability networks around and into the stylolites.

In addition, the presence of dissolution (Figs. 2 and 4) was most abundant along the stylolites and not along faults

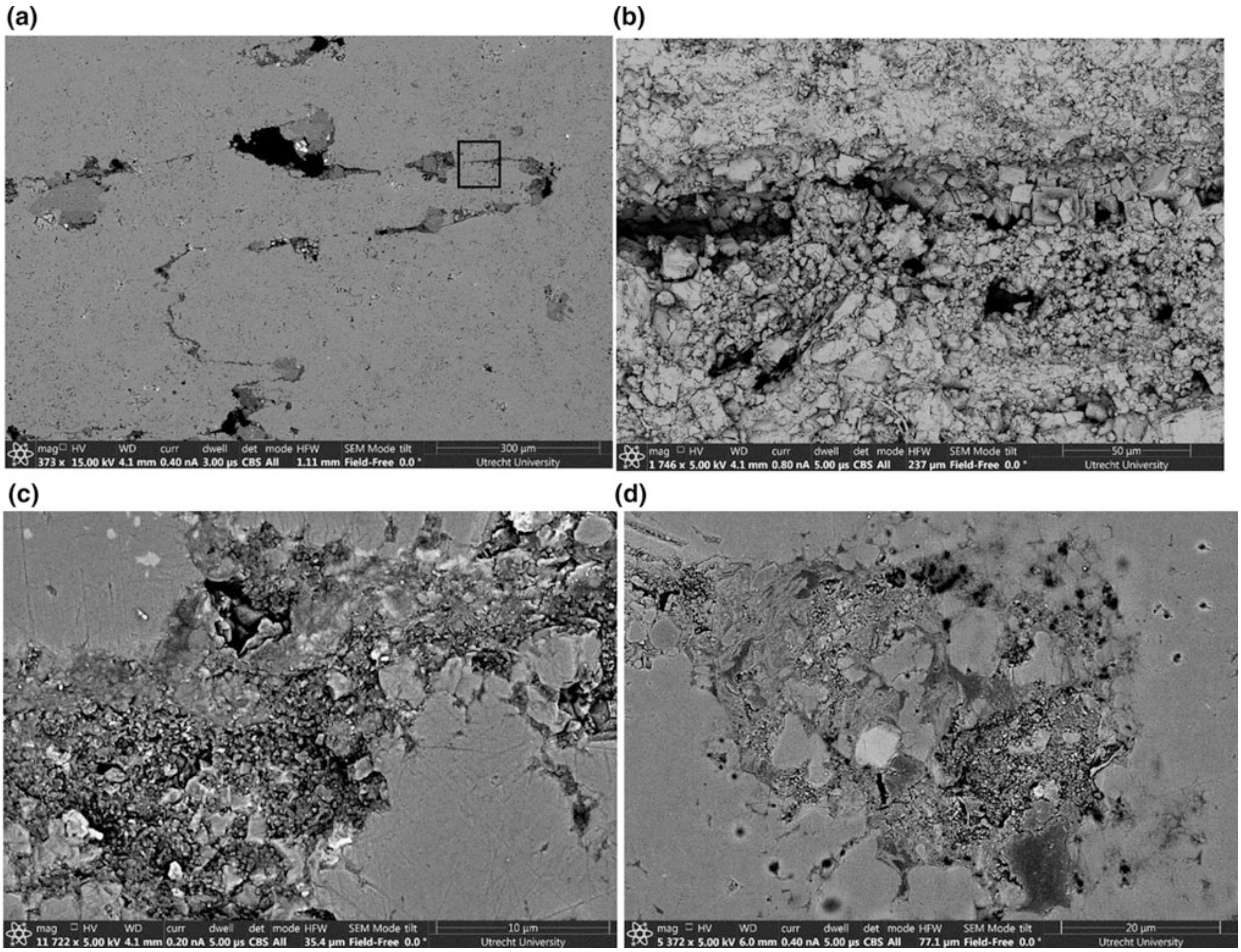

Fig. 6 SEM images of a sample from Belgium. The clayish minerals are always present along the stylolite surface. **a** Overview of the investigated area; the different distribution in porosity is already visible at this scale; **b** into the stylolite there are a lot of voids and holes that could be a possible pathway for water; **c** the contact between NCP and the other grains (calcite/dolomite/iron) into the feature; **d** evidence of dolomitization process. This analysis was performed with EPOS and NWO support

or joints. Even if along the joints the dissolution phenomena have not been observed, we cannot exclude that along them the process does not occur, since they are structures along which water could through.

Conclusions

The preliminary results obtained by our study allow us to affirm that the stylolites do not act only as barrier to fluid flow, but they can impact fluid flow in a different way than common thought.

In agreement with estimation on permeability accordingly (Caine et al. 1996) (Fig. 5), the stylolites were the preferential site of dissolution and structures with a greater permeability too.

In summary, we can confirm that there is a link between stylolites and karst, and this is the mean that is not hindered or impeded by compressive tectonic structures, such as stylolites.

To summarize then:

- The shape of stylolites does not have a strong effect on the dissolution phenomena.
- The clay mineral plays for sure a strong role on this process but is still unclear how.
- There are some other compressional structures that must to be investigated in this context.

This study is a preliminary investigation and is not exhaustive on this subject. Several aspects concerning stylolites are still unsolved, as like when they enhance or reduce porosity and permeability in and around them, and should be better investigated.

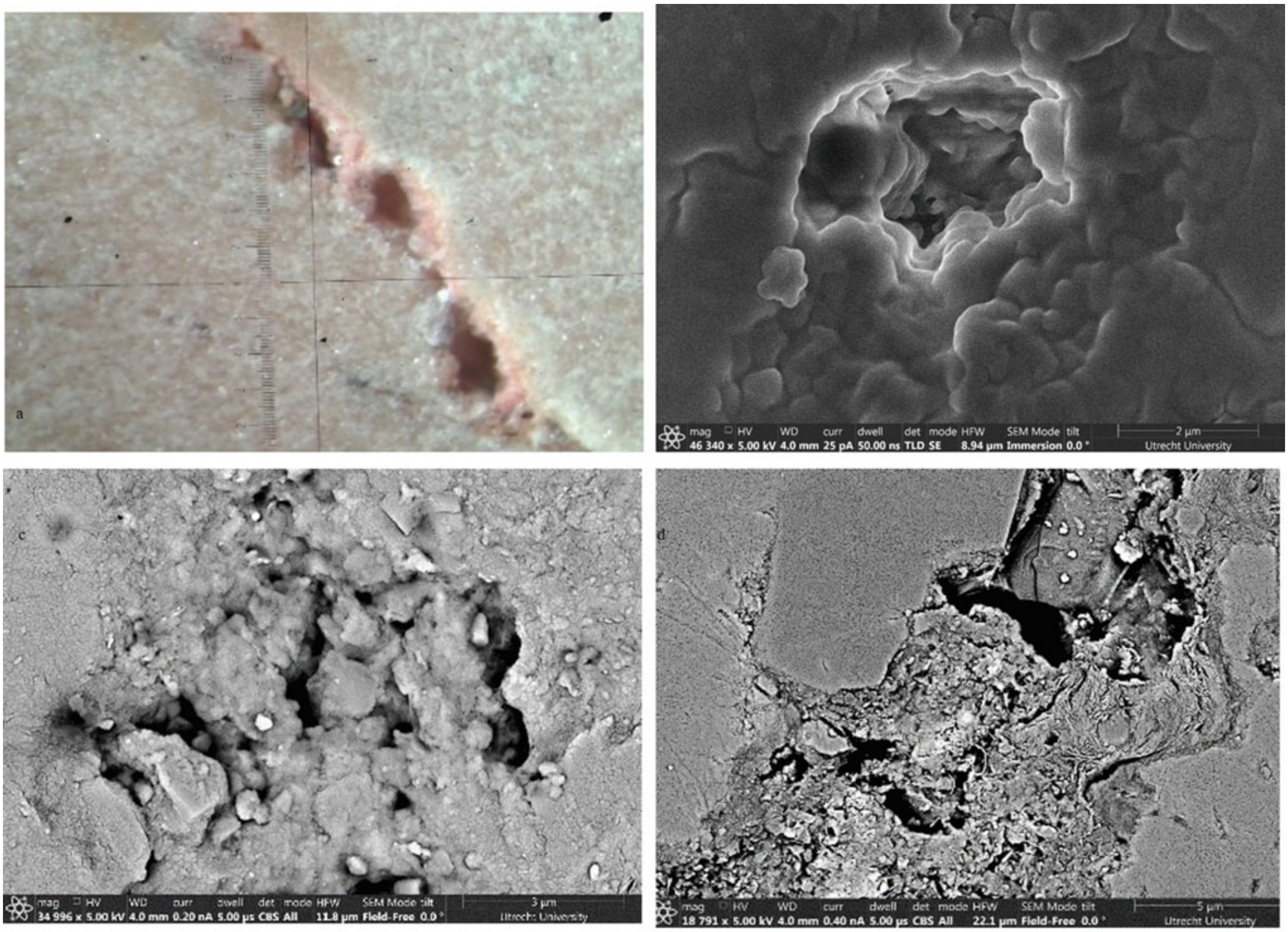

Fig. 7 Despite the idea that in a compressional setting no dissolution process is possible, along stylolite surface is quite common to observe holes with recrystallization into them. The pictures show a geometry of pores present along the stylolites at different magnifications: **a** optical image, **b** thin section image, **c** and **d** SEM images. These analyses were done with EPOS and NOW support

Acknowledgements I want to thank my Supervisor, Prof. Cees Passchier, for his support and helpful advices and, in addition, thank Dr. Mark Peternell for his collaboration on this research.

Very helpful and interesting were the discussions with Prof. Piotr Szymczak (University of Warsaw) that helped me to focus better on the still unclear aspect of dissolution.

I also want to thank Prof. Francois Renard (University of Grenoble) for interesting discussions and his availability to give me very helpful advices.

References

Alsharhan & Sadd. U.A.E, Society for Sedimentary Geology Special Publication (69), 185–207 (2000).

Aydin, A.: Fractures, faults, and hydrocarbon entrapment, migration and flow. Marine and Petroleum Geology (17), 797–814 (2000).

Bini A., Rigamonti I., Ogier A.: Evidence of recent tectonics in the plane Monte Campo dei Fiori, Varese Lake and the Quaternary 6 (1), 3–14 (1993).

Caine J., Evans J., Forester C.: Architecture fault zone structure and permeability. Geology (11), 1025–1028 (1996).

Cucchi F., Forti F.: La stazione di misura della dissoluzione superficiale a Borgo Grotta Gigante. In Att. e Mem. Comm. Grotte "E: Boegan" (27), 87–93 (1988).

Ebner M., Koehn D., Toussaint R., Renard F., Schmittbuhl J.: Stress sensitivity of stylolite morphology. Earth and Planetary Science Letters 277(3–4), 94–398 (2009a).

Ferrarese F., Meneghel M.: Aspetti dell'influenza strutturale sulla morfogenesi carsica del Montello (Treviso). In Atti e Memorie Commissione Grotte Eugenio Boegan (4), 45–59 (1992).

Forti P., Piccini L.: The Karst process. Società Speleologica Italiana. Project PPT 2007 (2007).

Gratier J.-P., Muquet L., Hassani R., Renard F.: Experimental microstylolites in quartz and modeled application to natural stylolitic structures. Journal of Structural Geology (27), 89–100 (2005).

Koehn D., Renard F., Toussaint R., Passchier C.W.: Growth of stylolite teeth patterns depending on normal stress and finite compaction. Earth and Planetary Science Letters 257 (3–4), 582–595 (2007).

Koehn D., Ebner M., Renard F., Toussaint R., Passchier C.W.: Modelling of stylolite geometries and stress scaling. Earth and Planetary Science Letters (341), 104–113 (2012).

Koehn D., Rood M.P., Beaudoin N., Chung P., Bons P.D., Gomez Rivas E.: A new stylolite classification scheme to estimate compaction and local permeability variations. Sedimentary Geology (346), 60–71 (2016).

Menichetti M.: Evoluzione spaziale e temporale del sistema carsico del Monte Cucco nell'Appennino Umbro-Marchigiano. In Atti XV Congress. Naz. Spel 1987, 731–762 (1988).

Menichetti M., Galdenzi S.: Il carsismo della Gola di Frasassi. Mem. Ist. It. Spel., Vol. 4(2), 65–92 (1992).

Piccini L.: Geomorfologia e Speleogenesi carsica. Quaderno didattico della Società Speleologica Italiana n°1, 40 (1999).

Park W. C., Schot E. H.: Stylolites: their nature and origin. Journal of sedimentary Petrology 38(1); 175–191 (1968).

Raynaud S.: Rock matrix structures in a zone influenced by a stylolite. Journal of Structural Geology (14), 973–980 (1992).

Renard F., Schmittbuhl J., Gratier J.-P., Meakin P., Merino n E.; Three-dimensional roughness of stylolites in limestones. Journal of Geophysical Research-Solid Earth (109), 1–12 (2004).

Shanov S., Kostov K. Dynamic Tectonics and Karst. Springer-Verlag Berlin Heidelberg, pp. 123, (2015).

Tognini P.: Analisi strutturale della Valle del Nosè in relazione alla carsificazione profonda. Tesi di laurea anno 1993–1994 Relatore: Prof. A. Bini; Correlatore Dott. G.B. Siletto. (1994).

Vigna B., Calandri G.: Gli acquiferi carbonatici. In quaderni didattici della Società Speleologica Italiana. Erga Edizioni Genova, pp 48 (2001).

Zhou, X. and Aydin, A.: Mechanism of pressure solution seam growth and evolution: Journal of Geophysical Research (115) B12207, 10.1029 (2010).

Quinif Y., Vandycke S.: Karst and tectonics. Geologica Belgica volume 4 (2001).

Water Isotopes, Carbon Exports, and Landscape Evolution in the Vadu Crişului Karst Basin of Transylvania, Romania

Lee Florea, Ferenc L. Forray, and Sarah M. Banks

Abstract

The karst aquifer connecting meteoric recharge entering Bătrânului Cave on the Zece Hotare karst plateau to spring discharge arising from Vadu Crişului Cave along the Crişul Repede River provides one glimpse into aquifer processes and landscape evolution occurring in the Pădurea Craiului Mountains of Transylvania. One part of this investigation looks at the stable isotopes of oxygen ($\delta^{18}O$) and hydrogen (δ^2H) measured in samples of precipitation, surface runoff, and spring water collected between October 2016 and June 2017. The second part of the investigation considers field chemistry, discrete samples, and continuous monitoring data collected between October 2016 and December 2017 and evaluates dissolved inorganic carbon (DIC), particulate inorganic carbon (PIC), total suspended sediments (TSS), and dissolved organic carbon (DOC) in water entering and emerging from the karst aquifer. Direct meteoric recharge accounts for 4–13% of observed discharge; most recharge enters the karst basin through infiltration into dolines and epikarst on the karst plateau. The local meteoric water line ($\delta^2H = 7.50 \cdot \delta^{18}O + 5.17$) exhibits significant variation and seasonally shifts between recycled continental moisture ($D_{ex} > 10‰$) during the fall and winter and marine-sourced moisture during the spring and summer ($D_{ex} < 10‰$). In contrast, samples from Bătrânului Cave and Vadu Crişului have a homogenous isotope chemistry with a local water line of $\delta^2H = 7.52 \cdot \delta^{18}O + 6.00$. The stability in water chemistry at Vadu Crişului is also seen in most other analytes. Monitoring data, however, demonstrates significant perturbations driven by storm events. The annual flux of DIC from this karst basin is from 1.37×10^5 to 1.64×10^5 kg/year. The annual flux of carbon increases by 12–22% when considering added contributions of DOC. Storm events do have a significant impact on mechanical and chemical processes operating in the karst basin; the addition of PIC and TSS flux increases landscape erosion rates by 1.1–1.2% and 7.9–8.3%, respectively, above the denudation rate computed by DIC alone (36.5–56.9 mm/ka). This illustrates the contributions of mechanical erosion in karst landscapes, particularly in high discharge conditions, when the flux of suspended sediments outpaces dissolved solutes.

Keywords

Particulate inorganic carbon • Dissolved organic carbon • Mass balance • Total suspended sediments • Pădurea Craiului • Moisture sources

Introduction

This study comprises two interrelated investigations in the Vadu Crişului karst basin of northwestern Romania: (1) stable isotopes of oxygen and hydrogen in water to evaluate sources of precipitation and partitioning of flow in the aquifer, and (2) a mass balance approach to compute chemical and mechanical weathering and, by distributing this across the surface area of the basin, arrive at an approximation of the landscape evolution in this region. Both studies provide broader insight into the hydrogeology, geochemistry, and mass transport within karst aquifers of eastern Europe and are another node in our understanding of the global carbon cycle. The water isotope data stem from a graduate student thesis (Banks 2018) and have not been previously published, but follow discussion threads from

L. Florea (✉)
Indiana Geological and Water Survey, Indiana University, Bloomington, IN, USA
e-mail: lflorea@indiana.edu

F. L. Forray
United States Geological Survey, Little Rock, AR, USA

S. M. Banks
Department of Geology, Babeş-Bolyai University, Cluj-Napoca, Romania

C. Bertrand et al. (eds.), *Eurokarst 2018, Besançon*, Advances in Karst Science,
https://doi.org/10.1007/978-3-030-14015-1_4

previous research in karst aquifers (Florea 2013). The geochemical model behind the approach has been published before (Florea et al. 2018) and uses field and lab measurements of discharge, water quality, and hydrochemistry combined with continuous monitoring data to develop time-series measurements of solute and sediment flux. For an in-depth discussion of the development of the geochemical model, please read Florea (2015) for an example from the karst of Kentucky, the USA. This paper is specific to the study location in Romania, and thus focuses on the field methodologies behind the data and the basin characteristics that lead to the interpretations of these data. For an in-depth discussion of the results of this study in the context of landscape evolution rates in Europe and as part of the global carbon cycle, please see the discussion in Florea et al. (2018).

Isotopic Signature of Oxygen and Hydrogen

The stable isotopes of oxygen and hydrogen can be an effective tracing technique in karst aquifers because of their tendency to differentiate by kinetic fractionation, such as Rayleigh distillation, according to atomic mass. The isotopic signature of water is reported as:

$$\delta = \left(R_{\text{sample}}/R_{\text{standard}} - 1\right) \times 1000‰, \tag{1}$$

where R is the ratio of heavy to light isotope—$^{18}O/^{16}O$ and $^{2}H/H$. Values of $\delta^{18}O$ and $\delta^{2}H$ within a reservoir are guided by atmospheric and hydrologic processes. So, while a linear regression of the global variation of $\delta^{18}O$ versus $\delta^{2}H$ gives the global meteoric water line (GMWL):

$$\delta^{2}H = 8 \cdot \delta^{18}O + 10 \tag{2}$$

(Craig 1961), local weather patterns produce precipitation that align on a local meteoric water line (LMWL) that produce surface and groundwater on a local water line (LWL). These regressions may quantify the influence that kinetic effects upon local precipitation and along a flow path, such as at Timavo Springs in Italy, where Doctor et al. (2006) identified the timing and mode of recharge to a portion of the classical karst of Slovenia.

The same isotope data can be used to quantify the enrichment of ^{2}H during evaporation that exceeds the ^{18}O predicted by the GMWL, called deuterium excess, D_{ex}, and computed by:

$$D_{ex} = \delta^{2}H - 8 \cdot \delta^{18}O \tag{3}$$

(Dansgaard 1964; Merlivat and Jouzel 1979). For precipitation on the GMWL, the theoretical D_{ex} = 10‰. Additional contributions of recycled continental and marine moisture can produce higher and lower values of D_{ex}, respectively (Gat and Matsui 1991). D_{ex} can help discriminate between contributing sources of moisture to local precipitation. For example, D_{ex} values change with the seasonal monsoon, such as in the Tibet Plateau (Liu et al. 2008) where D_{ex} values are lower in summer because of northward movement of warm, moist air from the Indian Ocean and values are higher in winter because of southward movement of cool, dry continental air masses.

Hydrochemistry of Karst Springs

Calculated rates of dissolved and suspended load are fundamental requirements for a mass balance study in surface water systems or groundwater aquifers. The flux at a set point in time is computed using instantaneous measurements of water discharge (Q) and the concentration of dissolved solutes and suspended sediments (c); a time series of these data $\{t = 1, 2, 3, \ldots, N\}$ can estimate the flux over a longer time interval:

$$\text{Flux} = \sum_{t=1}^{t=N} Q_t c_t. \tag{4}$$

However, in karst aquifers, low-frequency sampling misses the effects of high-frequency events of short duration. Therefore, remotely deployed probes are used to fill in the gaps for some hydrochemical parameters between field campaigns.

The hydrographs and chemographs produced by these probes are a basic tool for understanding the response of a karst basin to hydrologic inputs (Dreiss 1982), and the shape of the hydrograph or chemograph reveals some detail of processes in the karst basin that transform the input signal within the aquifer framework (Hobbs and Smart 1986). Hydraulic driving forces, basin and aquifer characteristics, land use, geochemical interactions, weathering processes, and microbial respiration along the flow path all may greatly influence the chemical character of spring flow in karst (Scanlon 1989).

Geochemistry of Carbon in Epigenetic Karst Aquifers

In epigenetic karst aquifers, meteoric waters convey dissolved solutes, including dissolved inorganic carbon (DIC), dissolved organic carbon (DOC), particulate inorganic carbon (PIC), and total suspended sediments (TSS). This flux may originate from discrete, allogenic waters conveyed by sinking streams originating from beyond the area of carbonate exposure, or diffuse autogenic recharge through the epikarst in the carbonate exposure (White 1988; Ford and Williams 2007; Palmer 2007). The discharge arising from karst springs accumulates the DIC, DOC, and TSS along the flow path in the karst basin and manifests as a signature response of the aquifer. Carbon dioxide sourced from the atmosphere or microbial respiration reacts with carbonate bedrock by way of the carbonate equilibrium reaction,

$$\begin{aligned} & \mathrm{H_2O} + \mathrm{CO}_{2(\mathrm{aq})} + [(1-x)\mathrm{Ca}, x\mathrm{Mg}]\mathrm{CO}_{3(\mathrm{sol})} \\ & \leftrightarrow (1-x)\mathrm{Ca}^{2+}_{(aq)} + x\mathrm{Mg}^{2+}_{(aq)} + 2\mathrm{HCO}^{-}_{3(aq)} \end{aligned} \tag{5}$$

where the variable x represents the fraction of dolomite in a karst aquifer. In Eq. 5, one mole of CO_2 in solution reacts with one mole of carbonate bedrock to release two moles of DIC and one mole of Ca^{2+} + Mg^{2+} into solution (Dreybrodt 1988; White 1988; Dreybrodt et al. 2005; Ford and Williams 2007). Thus, a regression between [Ca^{2+}] + [Mg^{2+}] and the concentration of DIC in a closed system would return a slope of 0.5 (Florea 2015).

Groundwater chemistry in epigenetic karst aquifers is dominantly influenced by the effects of Eq. 5; values of pH are related strongly to the balance between PCO_2 and [HCO_3^-], and the specific conductivity (SpC) of the water is directly proportional to each solute (Krawczyk and Ford 2006). Thus, the time-series SpC data from a probe at a karst spring can be used to model the time variation of [Ca^{2+}], [Mg^{2+}], and DIC using regressions based on the chemistry of a set of discrete samples. Modeling other dissolved ions using this method works to a lesser degree, if they are influenced by similar processes of recharge or chemical weathering.

Thus, it is possible to use regression models of dissolved solutes and time-series values of SpC and Q to model the DIC flux at a karst spring using Eq. 4 and partition the DIC between the atmosphere/soil and carbonate bedrock. However, this method overlooks the flux of inorganic carbon via suspended sediment and bed load, which are mobilized during events having high Q (Herman et al. 2008; Paylor 2016) when mechanical erosion may far outpace the rate of chemical weathering in karst aquifers (Newson 1971; Covington et al. 2015). Direct measurements of turbidity using a probe can provide one measurement of time-series PIC values when calibrated against concentrations using alkalinity titrations of unfiltered water and laboratory-weighed TSS in discrete samples. This method also misses the contributions of DOC to net carbon exports (Kolka et al. 2008), which are leached from organic matter and transported into groundwater by surface ponors or from direct seepage through the epikarst. Direct measurements of fluorescent dissolved organic matter (fDOM) using a probe can provide one measurement of time-series DOC values when calibrated against concentrations measured in discrete samples.

Physical Setting

The Vadu Crișului karst basin is part of the Zece Hotare karst plateau, a mixed pasture and mountain beech forest landscape punctuated by deep dolines. The Zece Hotare is one of several northwest sloping karst plateaus at elevations of 500–700 m above sea level (a.s.l.) comprising 330 km^2 of carbonate outcrop in the Pădurea Craiului Mountains, a northwest extension of the Bihor uplift (Papp et al. 2013). The valley of the Crișul Repede River borders the mountains to the north at elevations of 270–300 m a.s.l., and has incised a defile between the towns of Şuncuiuş and Vadu Crișului (Fig. 1).

The Pădurea Craiului Mountains include more than 680 caves (Onac 1996), including Romania's longest cave, Vântului Cave (~50 km), and Vadu Crișului Cave (VC) (N46.96193; E22.51079), which has ~3 km of mapped passages. Water emerges from VC at 305 m a.s.l. (Goran 1982) in Lower Cretaceous limestone and has formed a broad travertine terrace with a 10-m waterfall overlooking the west bank of the Crișul Repede. Dye tracing in the Pădurea Craiului (Rusu 1981; Orășeanu and Iurkiewicz 2010) defines a karst basin of approximately 1250 ha that also includes a hydrologic connection between VC and Bătrânului Cave (PB) (N 46.93888; E 22.46566), the latter located in the Piştireului Valley (4.25 km southwest of VC) (Fig. 1). The entrance to PB is a ponor at 550 m a.s.l. (Goran 1982) at a fault between Lower Middle Jurassic calcareous clastics and Upper Jurassic carbonates. Allogenic recharge enters the ponor, cascades through the carbonates, and flows down the axis of a syncline toward VC.

Northwest Romania is a continental humid climate with temperatures on the Zece Hotare that vary from −6 to 25 °C with peak temperatures in July and August. In 1982–1983, annual precipitation measured 843 mm, with peak monthly precipitation in May–June and variation from 800 to 1200 mm in the Pădurea Craiului (Orășeanu 1991). The recharge from this rainfall turns into a variable Q at VC, ranging from 27 L/s (November 1982) to 232 L/s (February 1983) (Orășeanu and Iurkiewicz 2010). Mean Q was greater (110–360 L/s) from 1957 to 1974. The time of travel of dye between PB and VC was 89 h, which translates to a velocity of approximately 47.8 m/h (Viehmann et al. 1964).

Samples and Analytical Methods

The data in this study were collected between October 14, 2016 and September 20, 2017, for the water isotope samples, and from October 14 to December 23, 2016 for all other data that include continuous monitoring data from VC, weekly field measurements and discrete samples at VC, and field

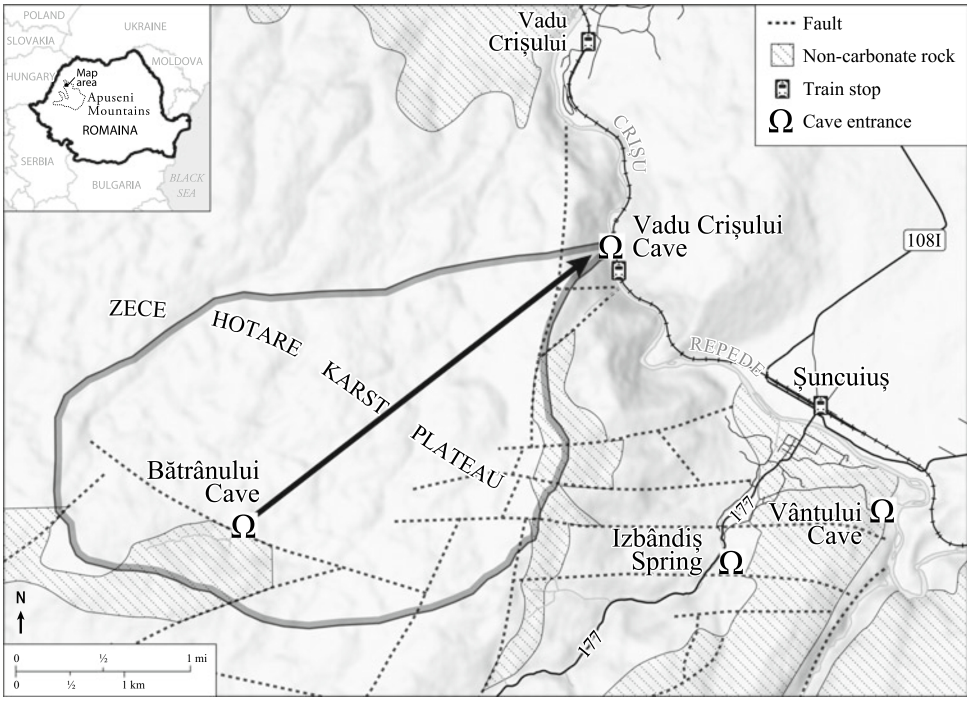

Fig. 1 Map of the Vadu Crişului karst basin in Transylvania, Romania (inset). The dark gray line is the approximate outline of the karst basin based upon dye trace data for the region. The black arrow indicates the flow direction between Bătrânului Cave (PB) and Vadu Crişului Cave (VC). Modified from Florea et al. (2018)

measurements and discrete samples from PB collected every two weeks. Analyses were conducted at Ball State University (BSU), Indiana University-Purdue University Indianapolis (IUPUI), and Babeş-Bolyai University (UBB). Geochemical modeling was adapted from spreadsheets available in Florea (2015) and included analyses in AquaChem to compute the saturation index with respect to calcite (SI_{cal}).

Values of $\delta^{18}O$ and $\delta^{2}H$ were computed using Eq. 1 and measured at the Babeş-Bolyai University Stable Isotope Laboratory in Cluj-Napoca (Romania) using a Picarro L2130-*i* (typical precision <0.025‰ for $\delta^{18}O$ and < 0.1‰ for $\delta^{2}H$) and vaporizer and following the method described by Wassenaar et al. (2013, 2018). The reproducibility of the measurement was ~0.08 and 0.20‰ for $\delta^{18}O$ and $\delta^{2}H$, respectively. Internal laboratory standards used for calibration were normalized to the VSMOW–SLAP scale.

Continuous monitoring included two calibrated probes collecting data every 15 min. An In Situ Aqua Troll 200 deployed in the underground stream of VC collected values of water level, SpC, and temperature. An adjacent YSI EXO2 measured turbidity and fDOM. pH values were not measured on the EXO2 as the probe failed and no replacement was available. Short gaps in data coverage from instrument maintenance were interpolated from bounding data. Regression models were applied to correct for instrument drift between calibrations, when appropriate.

Field measurements include pH, SpC, and temperature collected using a calibrated YSI ProPlus probe. At VC, measurements were carried out in the underground stream. At PB, samples and measurements were taken at the ponor where the surface stream sinks. Instantaneous *Q* was measured by determining stream depth and velocity in incremental segments using a Global Water handheld flowmeter. A HACH digital titrator using 1.6 N H_2SO_4 supplied titrations for alkalinity to an accuracy of approximately 4%; concentrations of carbonate species were determined by the inflection point method. Titrations were used to measure the concentration of DIC (using a filtered sample) and total inorganic carbon (TIC—using an unfiltered sample). The difference between TIC and DIC quantifies the additional contributions of PIC to alkalinity (Paylor 2016).

Discrete samples were filtered to 0.45 µm and kept at 4 °C. Principal ions (60 mL HDPE bottles with a 6 N HNO_3 preservative for cations) were measured using a Dionex ICS 1100 AS-DV for SO_4^{2-}, Cl^-, and a PerkinElmer Optima 7000 DV-OES for Ca^{2+}, Li^+, K^+, Mg^{2+}, Na^+ at IUPUI. Total nitrogen (TN) (40 mL septum-capped glass vials) and DOC were analyzed on a TOC-L Shimadzu TOC analyzer at BSU. Concentrations of TSS were measured at UBB by the pre–post-dry mass of a 0.45 µm filter used to process 1 L of raw water sample.

Analytical Results

Sample data are summarized in Table 1. Water temperatures at VC during the study were very stable; they cooled from 10.3 to 10.1 °C as winter approached with marked drops coinciding with significant rainfalls centered on November 07, 2016 and

Table 1 Field and analytical data from discrete samples

		Field parameters						
		T(°C)	pH	SpC (µS/cm)	DO (mmol/L)	Q (m^3/s)	WL (m)	TSS (mg/L)
Peştera de la Vadu Crişului								
LF101416A	10/14/16	10.3	6.9	435	0.63	0.09	0.40	0.93
LF102316A	10/23/16	10.3	6.8	429	0.67	0.23	0.49	3.80
LF102716A	10/27/16	10.3	6.8	415	0.65	0.19	0.46	–
LF110216A	11/02/2016	10.3	6.8	415	0.65	0.13	0.41	0.30
LF111116A	11/11/2016	10.2	7.0	413	0.67	0.28	0.52	1.71
LF112016A	11/20/16	10.1	6.9	427	0.67	0.26	0.51	0.57
LF120416A	12/04/2016	10.1	6.9	427	0.67	0.15	0.42	0.40
LF121816A	12/18/16	10.1	7.0	423	0.69	0.18	0.45	0.27
LF122316A	12/23/16	10.1	7.0	432	0.71	0.14	0.42	0.50
Peştera Bătrânului								
LF101416B	10/14/16	9.8	7.4	129	0.63	0.01	0.09	0.93
TT102916A	10/29/16	–	7.0	101	0.59	–	–	2.00
LF111116B	11/11/2016	6.7	6.5	43	0.77	0.02	0.14	5.33
LF112016A	11/20/16	6.1	6.5	44	0.76	0.02	0.07	1.71
LF122316B	12/23/16	0.1	5.9	49	0.83	0.01	–	2.00

		DIC_{unf} (mmol/L)	DIC_{fil} (mmol/L)	PIC (mmol/L)	NO_3 (mmol/L)	DOC (mmol/L)	Cations (mmol/L)					Anions (mmol/L)		SI_{cal}	Chrg bal (%)
							Ca	Li	Mg	K	Na	CI	SO_4		
Peştera de la Vadu Crişului															
LF101416A	10/14/16	4.11	3.88	0.24	0.015	0.33	2.12	0.02	0.01	0.03	0.08	0.03	0.05	−0.19	3.3
LF102316A	10/23/16	4.12	4.16	–	0.014	0.34	2.05	0.02	0.01	0.03	0.07	0.04	0.06	−0.19	0.5
LF102716A	10/27/16	4.00	3.80	0.20	0.014	0.34	1.97	0.02	0.01	0.03	0.08	0.04	0.06	−0.24	3.2
LF110216A	11/02/2016	4.12	4.00	0.12	0.015	0.35	2.02	0.02	0.01	0.03	0.07	0.04	0.06	−0.21	1.7
LF111116A	11/11/2016	4.14	3.82	0.32	0.014	0.33	2.00	0.02	0.01	0.03	0.07	0.04	0.06	−0.24	2.9
LF112016A	11/20/16	4.19	4.02	0.16	0.015	0.35	1.95	0.02	0.01	0.03	0.08	0.04	0.06	−0.23	−0.5
LF120416A	12/04/2016	4.05	3.92	0.13	0.041	0.35	2.07	0.02	0.01	0.02	0.09	0.23	0.07	-0.22	1.0
LF121816A	12/18/16	3.86	3.78	0.09	0.014	0.35	–	0.02	–	–	–	0.15	0.08	–	–
LF122316A	12/23/16	3.97	3.78	0.19	0.015	0.36	–	0.02	0.01	0.02	0.10	0.06	0.07	–	–

(continued)

Table 1 (continued)

		DIC_{unf} (mmol/L)	DIC_{fil} (mmol/L)	PIC (mmol/L)	NO_3 (mmol/L)	DOC (mmol/L)	Cations (mmol/L)					Anions (mmol/L)		SI_{cal}	Chrg bal (%)
							Ca	Li	Mg	K	Na	CI	SO_4		
Peştera Bătrânului															
LF101416B	10/14/16	1.28	1.06	0.23	–	0.10	0.52	0.02	0.03	0.02	0.05	0.02	0.03	−1.29	2.3
TT102916A	10/29/16	0.81	0.89	−0.08	–	0.07	0.37	0.02	0.03	0.02	0.08	0.10	0.03	−2.32	9.8
LF111116B	11/11/2016	0.29	0.27	0.02	0.001	0.03	0.17	0.02	0.02	0.02	0.04	0.02	0.04	−2.46	17.0
LF112016A	11/20/16	0.21	0.21	0.00	–	0.03	0.16	0.02	0.02	0.02	0.05	0.02	0.04	−2.36	16.4
LF122316B	12/23/16	0.27	0.21	0.06	0.003	0.03	0.20	0.02	0.02	0.01	0.05	0.08	0.04	−1.50	−6.6

November 13, 2016. In contrast, the water temperatures at PB cooled from 9.8 to 0.1 °C over the course of the study. Values of SpC (435–475 μS/cm) and pH (6.8–7.0) are very stable at VC; they are inversely proportional to measured *Q* (94–276 L/s). Values of field SpC (43–129 μS/cm) and pH (5.9–7.4) at PB reflect meteoric runoff from noncarbonate terrane with lower values in cold temperatures. Discharge measurements comprise 4–13% of the total emerging from VC (8–22 L/s) during each measurement period.

Concentrations of TSS measured at VC (0.27–3.8 mg/L) are directly proportional to measured *Q* and indicate a suspended sediment load of 38–882 mg/s emerging from the karst basin. The PIC portion of this sediment at VC (0.09–0.32 mmol/L) is directly proportional to TSS. The remaining carbon emerged from VC as DIC (3.8–4.2 mmol/L) or DOC (0.33–0.36 mmol/L). At PB, the TSS concentrations are higher (0.93–5.3 mg/L); however, the suspended sediment load (7.8–117 mg/s) is a fraction of what emerged from the aquifer at VC during that same time. The PIC concentrations at PB vary over two orders of magnitude (0.002–0.23 mmol/L), but having values of DIC (0.21–1.1 mmol/L) and DOC (0.03–0.1 mmol/L) significantly lower than at VC; the PIC represents a larger fraction of carbon flux into the aquifer.

Solute concentrations are quite stable at VC with charge balance errors of <3.3% except for samples in the second half of December 2016. Those two samples returned anomalously high measurements of all cations on December 18 and anomalously low Ca measurements for December 23. Solute concentrations are more variable at PB with charge balance errors up to 17%. Except for $[Mg^{2+}]$, which decreases from PB to VC (0.02–0.006 mmol/L), solutes increase in concentration from PB to VC as a result of water–rock interactions: $[Ca^{2+}]$, 0.28–2.0 mmol/L; $[Na^{+}]$, 0.05–0.08 mmol/L; $[K^{+}]$, 0.02–0.03 mmol/L; $[Cl^{-}]$, 0.05–0.08 mmol/L; TN, 0.002–0.009 mmol/L; and $\left[SO_4^{2-}\right]$, 0.04–0.06 mmol/L. Expectedly, values of SI_{cal} increase from PB (−2.0 ± 0.5) to VC (−0.21 ± 0.02) and are directly proportional to SpC, a sign of water–rock interactions with carbonates.

Results for $\delta^{18}O$ and $\delta^{2}H$, along with computed values of D_{ex} computed using Eq. 3, are presented in Table 2. The isotopic signature of PB ranges from −10.26 to −9.56‰ for $\delta^{18}O$, from −68.50 to −63.35‰ for $\delta^{2}H$, and from 12.43 to 13.94‰ D_{ex}. The isotopic signature of VC has a similarly narrow range from −10.43 to −10.00‰ for $\delta^{18}O$, from −70.43 to −67.85‰ for $\delta^{2}H$, and from 11.37 to 13.44‰ for D_{ex}. We exclude the November 20, 2016, sample from VC and consider it an outlier, but cannot dismiss the influence of a specific storm event. In contrast to the surface and groundwater, the isotopic signature of precipitation ranges from −15.68 to −3.05‰ for $\delta^{18}O$ and from −112.80 to −17.97‰ for $\delta^{2}H$. D_{ex} values of precipitation range from 2.66 to 17.14‰.

Table 2 Isotopic data of surface water, groundwater, and precipitation collected from the vadu crişului karst basin

	Sample date	$\delta^{18}O$ (‰)	SD (‰)	$\delta^{2}H$ (‰)	SD (‰)	D_{ex} (‰)
Bătrânului Cave	10/14/2016	−10.06	0.03	−68.05	0.08	12.43
	10/29/2016	−9.96	0.02	−66.26	0.09	13.42
	11/11/2016	−9.80	0.04	−65.51	0.05	12.89
	11/20/2016	−9.98	0.02	−66.80	0.06	13.04
	12/23/2016	−10.09	0.02	−67.86	0.16	12.86
	2/12/2017	−10.22	0.03	−68.34	0.09	13.42
	3/9/2017	−10.26	0.01	−68.49	0.13	13.59
	4/9/2017	−10.26	0.04	−68.50	0.19	13.58
	5/6/2017	−10.13	0.04	−67.10	0.21	13.94
	6/12/2017	−9.85	0.00	−65.78	0.04	13.02
	7/8/2017	−10.03	0.04	−67.30	0.13	12.94
	8/18/2017	−9.56	0.04	−63.55	0.15	12.93
	9/20/2017	−9.63	0.02	−63.80	0.23	13.24
Vadu Crişului Cave	10/14/2016	−10.28	0.01	−69.48	0.10	12.76
	10/23/2016	−10.09	0.02	−68.59	0.08	12.13
	10/27/2016	−10.09	0.03	−68.27	0.05	12.45
	11/2/2016	−10.07	0.04	−68.69	0.09	11.87
	11/11/2016	−10.00	0.01	−67.85	0.06	12.15
	11/20/2016	−8.09	0.02	−62.96	0.07	1.76
	12/4/2016	−10.06	0.02	−69.11	0.07	11.37
	12/18/2016	−10.09	0.03	−68.81	0.01	11.91
	12/23/2016	−10.12	0.02	−69.14	0.07	11.82
	2/12/2017	−10.23	0.04	−69.27	0.18	12.57
	3/9/2017	−10.31	0.05	−69.48	0.22	13.00
	4/9/2017	−10.41	0.01	−70.02	0.03	13.26
	5/6/2017	−10.43	0.04	−70.00	0.14	13.44
	6/12/2017	−10.34	0.02	−69.96	0.10	12.76
	7/8/2017	−10.40	0.01	−70.43	0.19	12.77
	8/18/2017	−10.38	0.01	−70.01	0.04	13.03
	9/20/2017	−10.37	0.03	−69.87	0.08	13.09
Precipitation	10/26/2016	−9.82	0.04	−64.96	0.09	13.60
	11/9/2016	−15.68	0.01	−112.80	0.15	12.64
	11/12/2016	−11.42	0.02	−79.69	0.12	11.67
	11/27/2016	−9.93	0.02	−62.30	0.13	17.14
	2/23/2017	−8.13	0.02	−59.05	0.15	5.88
	2/22/2017	−8.09	0.01	−58.84	0.06	5.99
	3/18/2017	−14.25	0.03	−111.34	0.10	2.66
	5/16/2017	−3.05	0.03	−17.97	0.20	6.43
	6/7/2017	−10.40	0.03	−70.61	0.15	12.59
	6/8/2017	−10.43	0.03	−70.44	0.13	13.00

Samples are normalized to the VSMOW–SLAP scale

Moisture Sources

Isotopic values of $\delta^{18}O$ and $\delta^{2}H$, and the derivative value of D_{ex}, were collated by site and compared to other sets of regional measurements and the GMWL (Fig. 2). Time-series plots of these data are presented in Fig. 3.

Precipitation at VC follows LMWL of $\delta^{2}H = 7.50 (\pm 0.45) \cdot \delta^{18}O + 5.17(\pm 4.96)$ [$R^2 = 0.96$] (Fig. 2), which lies between the Romania GNIP data (IAEA/WMO 2018) and a more arid vapor source—the Mediterranean meteoric water line (MMWL) of $\delta^{2}H = 8.32 \cdot \delta^{18}O + 15.37$ published by Giustini et al. (2016).

PB and VC follow a combined LWL of $\delta^{2}H = 7.52 (\pm 0.20) \cdot \delta^{18}O + 6.00(\pm 2.27)$ [$R^2 = 0.97$] (Fig. 2). Other regional LWLs have only slight differences and include $\delta^{2}H = 7.9 \cdot \delta^{18}O + 8.14$ for the Apuseni Mountains (Bojar et al. 2009), $\delta^{2}H = 7.9 \cdot \delta^{18}O + 8.14$ for Scărişoara Cave (Perşoiu et al. 2007), and $\delta^{2}H = 7.87 \cdot \delta^{18}O + 11.72$ for Roşia Montană (Cozma et al. 2017).

$\delta^{18}O$ and $\delta^{2}H$ of precipitation are modulated (Fig. 3). Precipitation isotopes are not time-weighted by rainfall amount, and no simultaneous evapotranspiration was computed. It is thus not possible to apportion $\delta^{18}O$ and $\delta^{2}H$ data to specific events where surface runoff results in aquifer recharge (Florea 2013).

The D_{ex} values in this study suggest that: (1) fall precipitation may strongly contribute to recharge—D_{ex} values are akin to surface and groundwater values at that time, and (2) precipitation D_{ex} may cycle between a continental moisture source in the fall and winter ($D_{ex} > 10‰$) and marine moisture in the spring and summer ($D_{ex} < 10‰$) (Fig. 3).

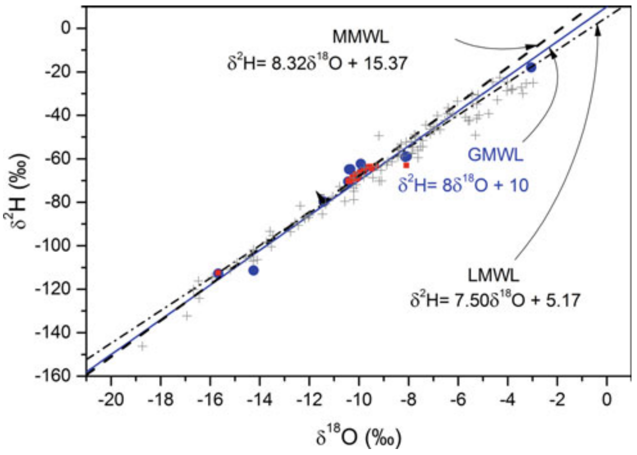

Fig. 2 Relationship between GMWL (solid line; Craig 1961) and the local meteoric water line (LMWL, dash dot line) constructed based on δ18O and δ2H values of rain water collected at Vadu Crişului (VC, dotted line). Also plotted are the stream data from both caves (squares), GNIP data (IAEA/WMO 2018) for Romania (crosses), and Mediterranean Meteoric water line MMWL (dashed line; Giustini et al. 2016). Samples are normalized to the VSMOW–SLAP scale

Derivative Values

A set of rating curves and regression models were used to convert continuous monitoring data (Fig. 4) to a time series of concentration and measurements of flux. The following are applied and presented in Figs. 5, 6 and 7:

Concentrations of dissolved solutes are directly proportional to measured SpC, most clearly visible with DIC and [Ca^{2+}]. The x-intercepts for DIC and [Ca^{2+}], SpC = 14 and 18 µS/cm, respectively, are typical of meteoric recharge. Correlation coefficients are strong for DIC = 0.99 and [Ca^{2+}] = 0.99 and TN = 0.94, and weak for [Mg^{2+}] = 0.66, [Na^{+}] = 0.69, [K^{+}] = 0.77, [Cl^{-}] = 0.05, and $\left[SO_4^{2-}\right] = 0.74$. Values of SI_{cal} from AquaChem are proportional to measured SpC as a logarithmic function.

Measured Q is linearly proportional to water level over the range of measurements. Modeled Q using the probe data ranges from 79 to 1153 L/s and has a mean Q of 198 L/s.

The concentration of TSS is proportional to turbidity as a second-order polynomial. Modeled values of TSS flux, when combined with Q, range from 28 to 2.75×10^5 mg/s, and a modeled PIC flux comprising a linear fraction (4.0–3.9×10^4 mg/s).

The proportionality between the concentration of DOC and fDOM values is weakly linear; the modeled DOC flux, when combined with Q, ranges from 322 to 4.62×10^3 mg/s.

Geochemical Modeling

The derivative rating curves and regression models form the basis of the geochemical model are presented in detail within Florea et al. (2018) and available as a supplementary online archive that accompanies that paper. In brief:

Replicate models account for potential error based upon manufacturer recommendations and method accuracy ($T \pm 0.1$ °C, water level ± 0.1%, SpC ± [0.5% + 1 S/cm], fDOM ± 1%, turbidity ± 2%, $Q \pm 5\%$, DIC/PIC ± 4%), the 5.4% average charge balance for dissolved solutes, and the weak correlation between DOC and fDOM (±32%).

Modeled solute relationships combine with the SpC from the probe to provide concentrations for each solute at every time interval. These modeled solute concentrations and temperatures from the probe were used to compute SI_{cal} for each time interval using the carbonate equilibrium reactions.

Apportioning DIC between atmosphere and bedrock is quantified by comparing the molar ratio of modeled [Ca^{2+}] + [Mg^{2+}] to DIC concentration having a value of 0.53. In this geochemical model, DIC contributions from the atmosphere are 89% as large as contributions from bedrock.

Fig. 3 Time-series variation of δ^{18}O, δ^{2}H, and Dex values from October 2016 to October 2017 for precipitation (black circles and solid black line), Vadu Crişului Cave (gray squares and solid gray line), and Bătrânului Cave (black triangles and dashed black line)

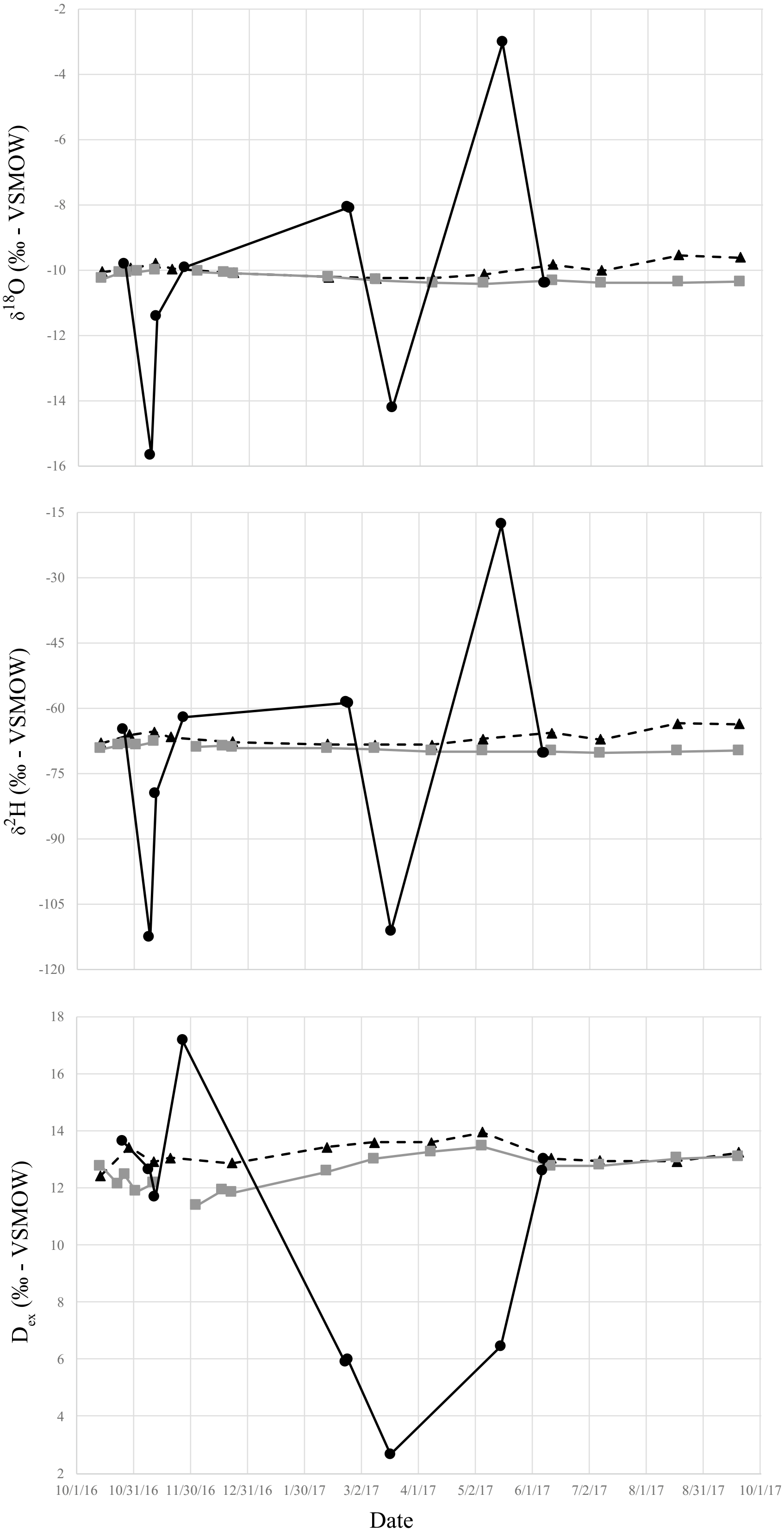

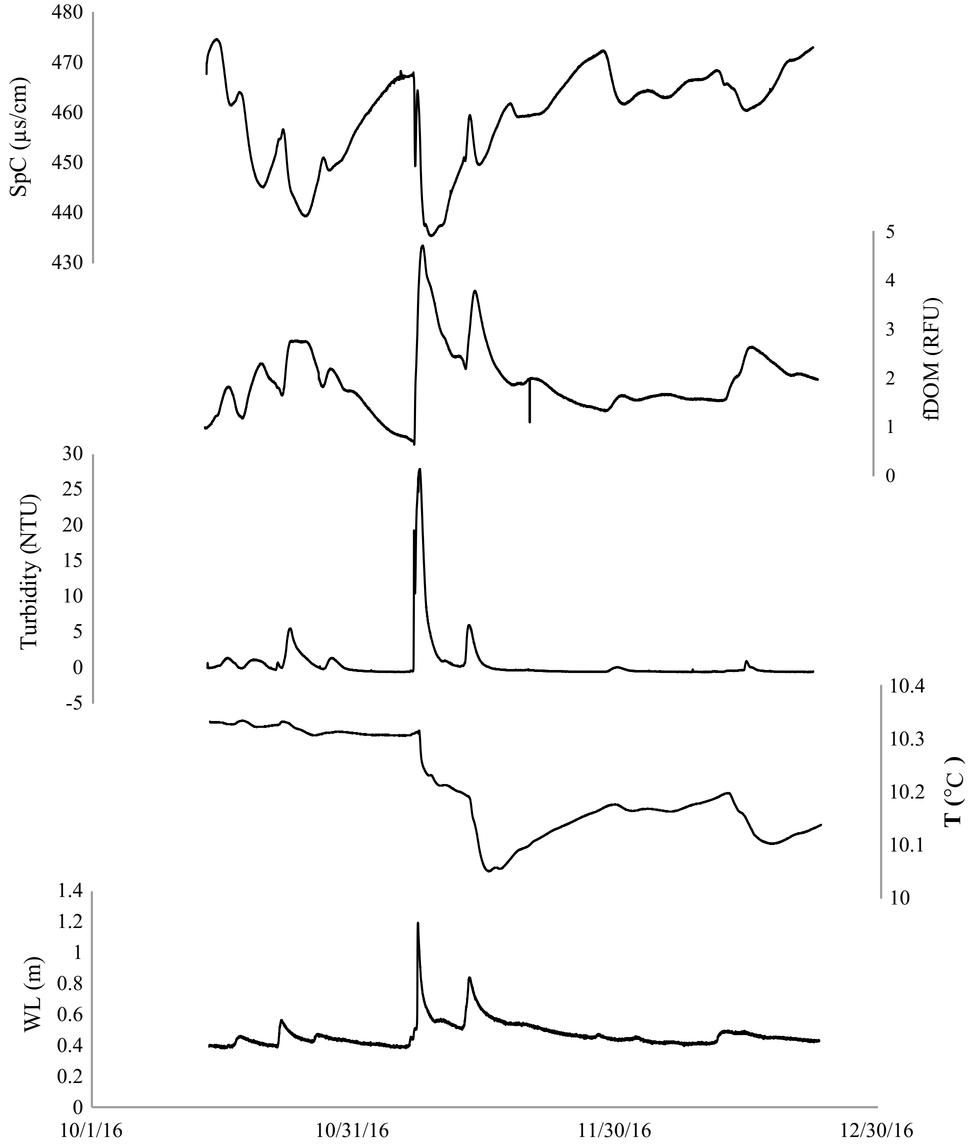

Fig. 4 Continuous monitoring data obtained at Vadu Crişului Cave. Modified from Fig. 5 of Florea et al. (2018)

Contributions from dolomite are calculated by the molar ratio of $2[Mg^{2+}]/([Ca^{2+}] + [Mg^{2+}])$. Ignoring atmospheric deposition and clastic weathering, modeled results suggest that 0.5% of $[Ca^{2+}]$ and $[Mg^{2+}]$ may result from dolomite.

The modeled values of SI_{cal} were used to compute the approximate pH of the original solution (7.17 ± 0.001) to within 5% of the field measurements.

The modeled PCO_2 in solution (0.61 ± 0.01 mmol/L) is a significant fraction of the DIC and was derived using Henry's Law and the temperature-dependent pK_{CO2}, pK_1, pK_2, and pK_c (Garrels and Christ 1965; Plummer and Blusenberg 1982; Ford and Williams 2007).

The modeled values of Q, $\left[HCO_3^-\right]$, and PCO_2 combine using the equation,

$$\text{DICflux} = \int_0^t Q \cdot [CO_2]\,dt + \int_0^t Q \cdot \left[HCO_3^-\right]dt, \qquad (6)$$

to give the molar DIC flux at VC.

The modeled atmospheric DIC flux during this study ranges from 2.62×10^4 to 3.14×10^4 kg in the geochemical model—9.61×10^4 to 1.15×10^5 kg of CO_2. Adding DOC flux increases the carbon flux from 12 to 22% (2.94×10^4–3.83×10^4 kg)—1.08×10^5 to 1.40×10^5 kg of CO_2. Partitioning the lithospheric DIC flux using the average densities of calcite (2710 kg/m^3) and dolomite (2850 kg/m^3) results in one measure of the flux of carbonate bedrock through the karst basin during the period

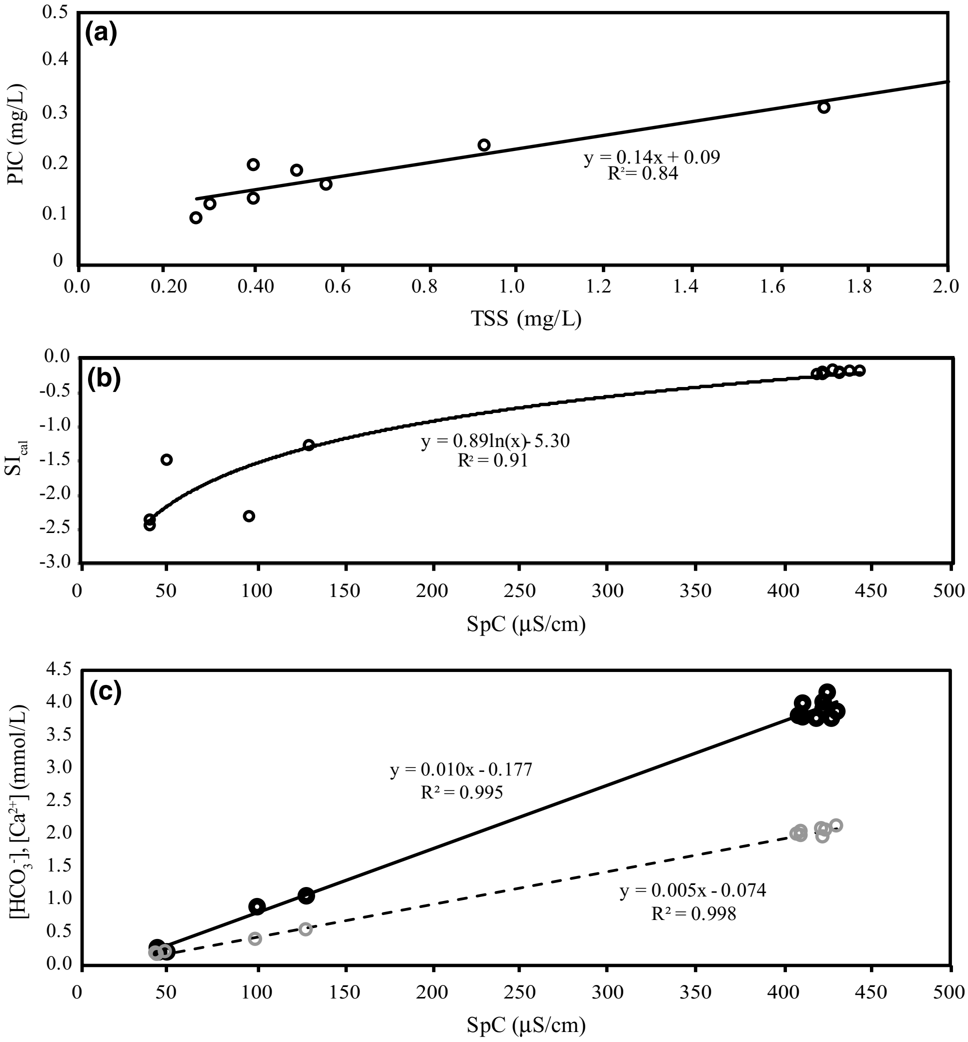

Fig. 5 Regression curves relating the measurements of **a** PIC from titration data to values of TSS measured in the lab, **b** the calculated SIcal compared to the SpC values measured in the field, **c** lab-determined concentrations of $\left[\mathrm{HCO}_3^-\right]$ (black circles and solid line). Modified from Fig. 3 of Florea et al. (2018), which includes regression models for other dissolved ions

of study from 87.7 to 109.4 m^3. Distributing the bedrock flux across the area of carbonate exposure and the entire Vadu Crişului karst basin results in modeled landscape evolution rates, based upon DIC alone, that range from 36.5 to 56.9 mm/ka. Including PIC modestly increases these rates from 1.1 to 1.2% (36.5–57.6 mm/ka). The addition of all TSS (2760 kg/m^3 for non-PIC contributions) produces rates that are 7.9–8.3% larger (39.4–61.6 mm/ka). Values of temperature and modeled pH have a limited impact on derivative products owing to their narrow range of values.

Synthesis

Groundwater flow in the karst aquifers of the Pădurea Craiului Mountains of northwest Romania is guided by geologic structures. Flow systems have a strongly concave profile, ponors with allogenic recharge cascade steeply through caves toward the regional water table and include extensive near horizontal galleries connected to springs. Autogenic recharge through the epikarst and dolines contributes to base flow of springs. Gravity flow dominates the regime with phreatic loops in lower galleries that modulate storm pulses.

The proportion of allogenic to autogenic recharge, and thus the transfer of sediments and organic matter, varies for each karst basin. The geochemistry of springs and, therefore, the flux of solutes depend upon the proportion of allogenic recharge and water–rock interactions along the flow path. We consider what the data from the Vadu Crişului karst basin reveal about moisture sources, carbon flux, and the rate of landscape evolution in the karst landscapes of this part of Eastern Europe, subject to the modeled range resulting from analytical error and the following limitations of the method:

- extrapolating to significantly longer time scales (Gardner et al. 1987),
- estimating the proportion of the landscape participating in the hydrochemical processes,

Fig. 6 Rating curves developed to relate lab measurements of DOC versus continuous monitoring data of fDOM (**a**) lab measurements of TSS versus continuous monitoring data of turbidity (**b**) and field measurements of Q versus continuous monitoring data of water level (**c**). Reprinted with permission from Fig. 4 of Florea et al. (2018)

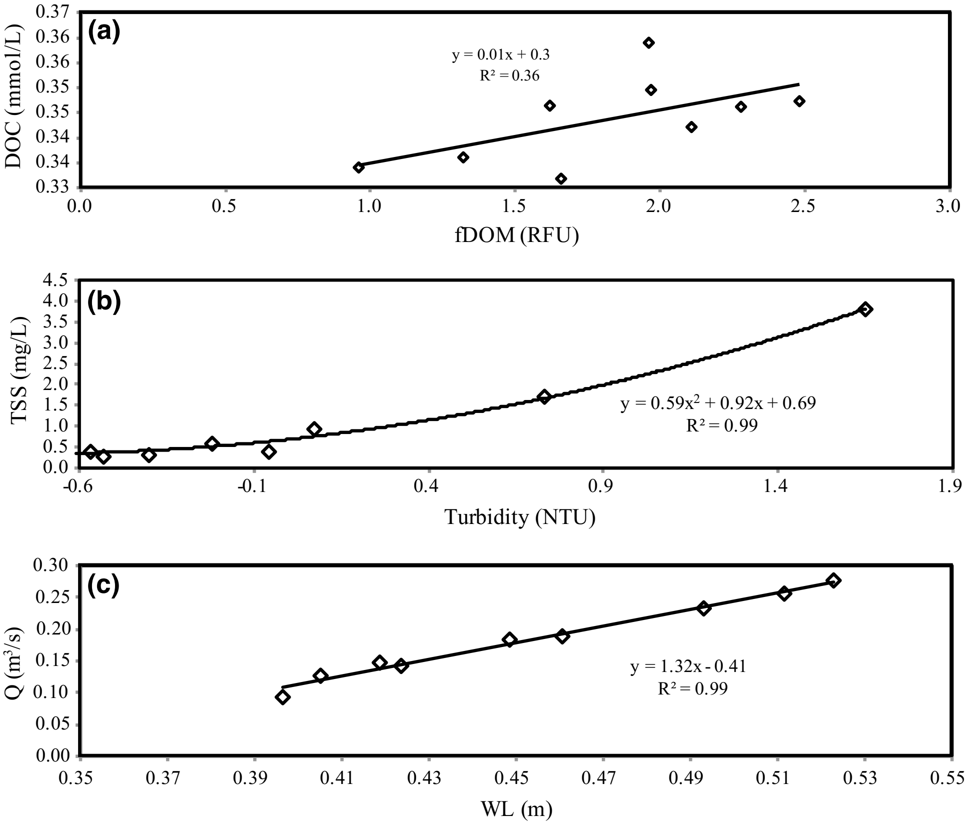

Fig. 7 Modeled time-series data combined rating curves in Fig. 4 with continuous monitoring data from Fig. 5 to compute flux using Eq. 4. Error bars are based upon the resolution of the measurement method and the R^2 value in the regressions from Fig. 4. Reprinted with permission from Fig. 6 of Florea et al. (2018)

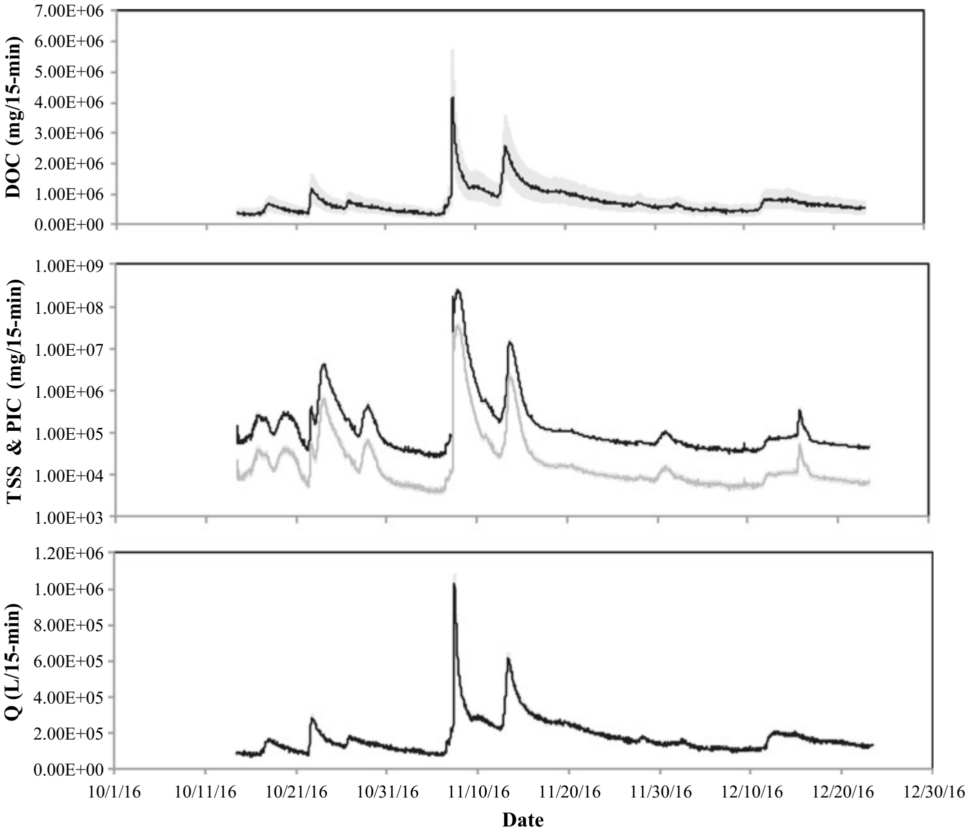

- generalizing solute flux in an aquifer to the surface area of the landscape (Priesnitz 1974),
- and disregarding changes in climate, hydraulic gradient, and conduit morphology.

Mean monthly values of Q in the modeled data (October = 150 L/s, November = 256 L/s, December = 159 L/s) are greater than data from 1982–1983, a drought year, and like data from 1957 to 1974, years having higher than average rainfall (Spinoni et al. 2015). Modeled Q also includes more than one significant storm event having peak Q = 1153 L/s that is near the peak Q = 1270 L/s published by Orăşeanu and Jurkiewicz (2010). Thus, models of carbon flux have the appropriate order of magnitude although the data span 10 weeks from what is typically the drier season. Results are presented as a range accounting for analytical error and that cover expected inter-annual variation.

Isotopic Signal

Isotopic measurements in this study do not provide the spatial or temporal density needed to quantify the translation of rainfall to runoff and from runoff to spring discharge. However, two distinct events in the time series of $\delta^{18}O$, $\delta^{2}H$, and D_{ex} (Fig. 3) lend some insight. The first occurs in November 2016, following two periods of significant rainfall, when $\delta^{18}O$ and $\delta^{2}H$ values become more depleted (−15.68 and −112.80‰, respectively) alongside a dip in D_{ex} between higher values (11.67‰). The second occurs in March 2017 and includes depleted $\delta^{18}O$ and $\delta^{2}H$ values of −14.25 and −111.34‰, respectively, alongside the lowest D_{ex} value of the study period (2.66‰) within a broader period of lower D_{ex}.

The first event follows an 'amount effect' associated with the progression of long-lived storm tracks and cloud rainout where the progressive removal of the heavier isotope from condensation through kinetic processes (Dansgaard 1964) generates negative isotopic shifts in precipitation (Clark and Fritz 1997). Interestingly, the isotopically depleted precipitation only translates to a small depletion in the isotopic values at PB and VC (Fig. 3) which is consistent with only minor changes in water chemistry (Table 1). Thus, the significant increase in water level seen in Fig. 4 from these storms may represent a transient storm pulse of water arriving from PB with minimal lasting impact on aquifer chemistry.

The second event is more consistent with a 'continent effect' where depleted isotopic shifts in precipitation are related to increased distance from an oceanic moisture source (Clark and Fritz 1997). The sinusoidal pattern precipitation D_{ex} in the study data (Fig. 3) illustrates this process and connects to weather patterns, and thus moisture sources that contribute to rainfall. Contributions from drier, inland, higher latitude climates to initial vapor formation can result in increased precipitation D_{ex}—seen in the data from late summer through early winter (October: 13.60‰, November: 11.67–12.64‰, December: 17.14‰, and June: 12.59–13.00‰, Table 2). During these times, the position of the jet stream over eastern Europe sets up synoptic weather patterns that usher in arctic air and weather from the northeast—56% of days in 2015 (Banks 2018). In contrast, lower D_{ex} values occur in winter and spring precipitation (February: 5.88–5.99‰, March: 2.66‰, and May: 6.43‰, Table 2) when westerlies sweep in Atlantic moisture from the west—44% of days in 2015 (Banks 2018).

In samples from PB and VC, almost all isotopic variation is muted and $\delta^{18}O$ and $\delta^{2}H$ values (Fig. 3) are similar at both sites during the cold season (December–March). From spring through fall, the differences increase. The isotopic values at PB become more enriched in ^{18}O and ^{2}H, most probably due to partial evaporation of the surface water that sink at PB, encompassing 4–13% of discharge at VC. Recharge through the epikarst comprises significantly more aquifer discharge and is not subject to that evaporative fractionation.

More specifically, we can consider three sources for aquifer water, the ponor at PB, autogenic recharge, and aquifer storage. The water that is sinking at PB has a transit time of about 89 h (Viehmann et al. 1964) and an average $\delta^{18}O = -9.99 \pm 0.23$‰. Autogenic recharge infiltrating through the limestone massif would have an isotopic value like precipitation if the infiltration rate is high. Because isotopic values at VC are quite stable, it is likely that autogenic infiltration becomes part of aquifer storage in the epikarst. Orăşeanu and Jurkiewicz (1987) approximated aquifer storage to be 0.27–0.48 × 10^{6} m^{3} based upon measurements at VC. This stored water, including the epikarst and providing baseflow to VC, would have homogeneous isotope values close to the average $\delta^{18}O = -10.23 \pm 0.15$‰ of the samples.

Hydrochemical Behavior

In the Vadu Crişului karst basin, allogenic recharge from noncarbonates at PB composes 4–13% of the discharge from the aquifer (Table 1); the proportion is likely higher, but unmeasured, during storm events. Each storm event translates to a measurable change in water level at VC. Increased autogenic recharge from cumulative precipitation results in an increase in base flow.

The geochemistry of waters emerging from VC is relatively stable; autogenic recharge clearly controls long-term aquifer water chemistry. Storm events produce measurable changes in SpC and temperature, though the effects are clearly buffered by mixing within the aquifer. DIC, $[Ca^{2+}]$, and [K^+] at VC from this study are like the average for regional springs (Vălenas and Iurkiewicz 1980–1981). Limited dolomite along the flowpath results in [Mg^{2+}] lower than other regional springs. Reduced atmospheric deposition since earlier campaigns (OGHE 2017) results in lower [Cl^-] and $\left[SO_4^{2-}\right]$ than in earlier studies.

Carbon Flux

The geochemical model in this study suggests that 47% of DIC that emerged from the Vadu Crişului karst basin during this 10-week study is sourced directly to the atmosphere. Thus, there was a net export of 2.94×10^4 to 3.83×10^4 kg of atmospheric carbon from the Vadu Crişului karst basin comprising DIC (78–88%) and DOC (12–22%). This is equivalent to 1.08×10^5 to 1.40×10^5 kg of CO_2. The model predicts that during similar years, 1.67×10^5 to 2.19×10^5 k/year of atmospheric carbon will emerge annually from the Vadu Crişului karst basin, translating to 5.63×10^5 to 7.33×10^5 kg/year of CO_2.

Landscape Evolution

The remaining 53% of modeled DIC in solution, 2.85×10^4 to 3.56×10^4, is sourced directly to the bedrock. Computing denudation rates requires this DIC to be distributed across the participating landscape. Including the entire basin may overestimate the surface area over which geochemical reactions occur. Using the carbonate outcrop (~80% of the basin) ignores interactions between meteoric recharge and bedrock in the noncarbonate fraction of the basin. Thus, both areas are included to provide low and high estimates, 87.7–109.4 m^3 of dissolved bedrock.

When distributed over the surface area of the basin, the bedrock DIC data translate to landscape erosion rates of 36.5–56.9 mm/ka, well within the wide range of published rates for locations in Europe (2–98 mm/ka) that vary according to location, method, and basin characteristics. Adding the modeled PIC and TSS flux modestly increases the bedrock removed by 1.0–1.4 m^3 and 5.9–7.7 m^3, respectively. TSS, which increases as the square of Q in this dataset, is not proportional to DIC flux, which is linear with Q over the range

Fig. 8 DIC flux (open circles), PIC (open squares), and TSS (open triangles) versus Q for each 15-min time interval as computed in the geochemical model. X-axis error bars based upon field uncertainty in measuring discharge. Y-axis error bars based upon uncertainties for analytical measurements. Reprinted with permission from Fig. 8 of Florea et al. (2018)

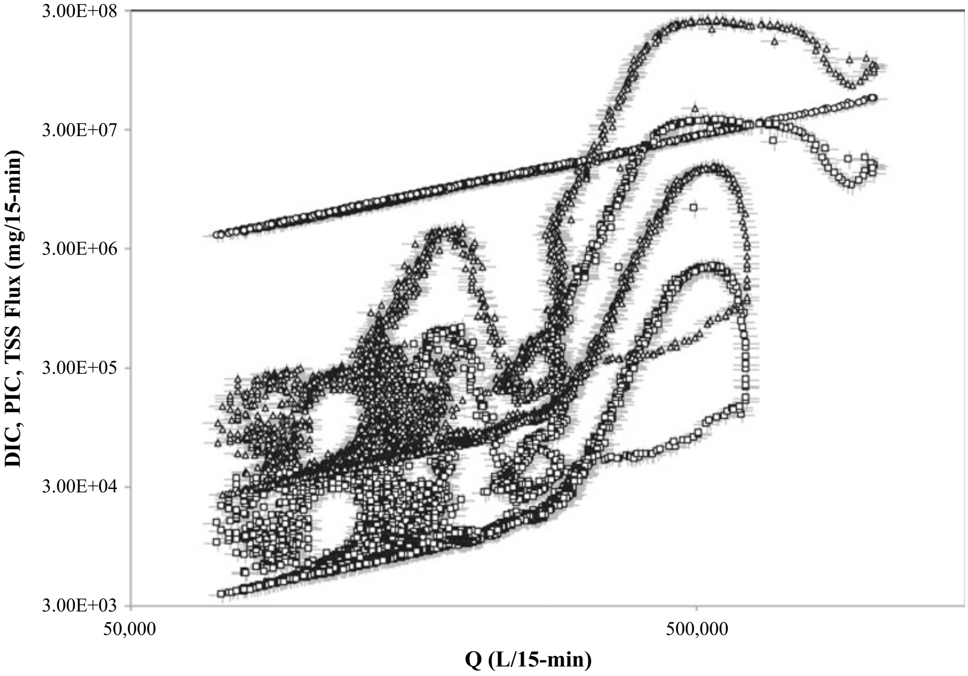

of measurements (Fig. 8). Therefore, more suspended than dissolved solids may emerge from the spring during high *Q*, the product of mechanical erosion. Like results from Cheddar Gorge spring, England (Newson 1971) and Blowing Cave in Kentucky, USA (Paylor 2016), TSS from storm events cause mechanical erosion that may exceed the rate of chemical erosion in karst aquifers (Covington et al. 2015).

Acknowledgements Financial support provided by the Fulbright Scholar Program and the Romanian-U.S. Fulbright Commission. Site Natura 2000 Defileul Crișului Repede—Pădurea Craiului (ROSCI0062) and Speleological Heritage Committee granted permission to collect samples from Bătrânului and Vadu Crişului Caves. The δ18O and δ2H analyses were carried out on equipment funded by the Integrated Network of Interdisciplinary Research-RICI grant no. 6/PM/I 2008 (MECS—ANCS) from Capacities Program Module I—Investment in Research and Infrastructure Development at Babeș-Bolyai University. Gregory Druschel of IUPUI and Michael Purdue and Eric Lange of BSU provided laboratory access and training. Colleagues at the Indiana Geological and Water Survey, the editors of this volume, and three anonymous reviewers improved this manuscript.

References

Banks, S.M., 2018. Karst processes, isotopic analysis, and contributions to global carbon cycle modeling from the Vadu Crisului karst basin, Romania. MS Thesis, Ball State University, Muncie, Indiana, 82 p.

Bojar A-V, Ottner F, Bojar H-P, Grigorescu D, Perşoiu A (2009) Stable isotope and mineralogical investigations on clays from the Late Cretaceous sequences, Haţeg Basin, Romania. Applied Clay Science 45:155–163. https://doi.org/10.1016/j.clay.2009.04.005

Clark, I., Fritz, P., 1997. Environmental isotopes in Hydrogeology: Lewis Publishers. New York, 352 p.

Covington, M.D., Gulley, J.D., Gabrovšek, M., 2015. Natural variations in calcite dissolution rates in streams: Controls, implications, and open questions. Geophysical Research Letters 42, pp. 2,836–2,842. https://doi.org/10.1002/2015GL063044.

Cozma A, Baciu C, Papp DC, Roșian G, Pop CI. 2017. Isotopic composition of precipitation in western Transylvania (Romania) reflected by two local meteoric water lines. Carpathian journal of earth and environmental sciences 12 (2):357–364.

Craig H. 1961. Isotopic variations in meteoric waters. Science 133 (3465):1702–1703.

Dansgaard, W., 1964. Stable Isotopes in Precipitation. Tellus 16, 436–468.

Doctor, D.H., Alexander, E.C., Petrič, M., Kogovšek, J., Urbanc, J., Lojen, S., Stichler, W., 2006. Quantification of karst aquifer discharge components during storm events through end-member mixing analysis using natural chemistry and stable isotopes as tracers. Hydrogeology Journal 14(7), 1171–1191.

Dreiss, S., 1982. Linear Kernels for Karst Aquifers. Water Resources Research, 18(4), pp. 865–876.

Dreybrodt, W., Gabrovsek, F., Romanov, D., 2005. Processes of Speleogenesis: A Modeling Approach. Karst Research Institute, ZRC SAZU, Postojna.

Dreybrodt, W., 1988. Processes in Karst Systems. Physics, Chemistry, and Geology. Springer, Berlin, 288 pp.

Florea, L.J. 2013. Selective recharge and isotopic composition of shallow groundwater within temperate, epigenetic carbonate aquifers. Journal of Hydrology 489: 201–213. https://doi.org/10.1016/j.jhydrol.2013.03.008

Florea, L.J., 2015. Carbon flux and landscape evolution in epigenic karst aquifers modeled from geochemical mass balance. Earth Surface Processes and Landforms 40(8), pp. 1,072–1,087. https://doi.org/10.1002/esp.3709

Florea, L.J., Banks, S.M., Forray, F.L., 2018. Importance of suspended sediments and dissolved organic carbon to carbon exports in karst–the Vadu Crişului karst basin in the Pădurea Craiului Mountains, Romania. Chemical Geology. https://doi.org/10.1016/j.chemgeo.2018.04.015.

Ford, D.C., Williams, P.W., 2007. Karst Geomorphology and Hydrogeology. John Wiley & Sons, 562 pp.

Gardner, T.W., Jorgensen, D.W., Shuman, C., Lemieux, C.R., 1987. Geomorphic and tectonic process rates: Effects of measured time interval. Geology 15(3), pp. 259–261. https://doi.org/10.1130/0091-7613(1987)15%3c259:gatpre%3e2.0.co;2.

Garrels, R.M., Christ, C.M., 1965. Solutions, Minerals, and Equillibria. Harpers' Geoscience Series. Harper and Row, New York, 450 pp.

Gat J.R., Matsui E., 1991. Atmospheric water balance in the Amazon Basin: an isotopic evapo-transpiration model. Journal of Geophysical Research 96, 179–188.

Giustini F, Brilli M, Patera A. 2016. Mapping oxygen stable isotopes of precipitation in Italy. Journal of Hydrology: Regional Studies 8:162–181. https://doi.org/10.1016/j.ejrh.2016.04.001.

Goran, C., 1982. Catalogul sistematic al peşterilor din România 1981 (Systematic catalog of caves in Romania) Consiliul Naţional pentru Educaţie Fizică şi Sport, Bucureşti, 496 pp.

Herman, E.K., Toran, L., White, W.B., 2008. Threshold events in spring discharge: Evidence from sediment and continuous water level measurement. Journal of Hydrology 351(1–2), pp. 98–106. https://doi.org/10.1016/j.jhydrol.2007.12.001.

Hobbs, S.L., Smart, P.L., 1986. Characterisation of carbonate aquifers: a conceptual base. In Proceedings of the Environmental Problems in Karst Terranes and Their Solutions Conference. National Water Well Association, Dublin OH, pp. 1–14, (Vol. 1986).

IAEA/WMO. 2018. Global network of isotopes in precipitation. The GNIP Database. Accessible at: http://www.iaea.org/water.

Kolka, R., Weisbarnpel, P., Froberg, M., 2008. Measurement and importance of Dissolved Organic Carbon. Field measurements of forest Carbon monitoring, pp. 171–176.

Krawczyk, W.E., Ford, D.C., 2006. Correlating specific conductivity with total hardness in limestone and dolomite karst waters. Earth Surface Processes and Landforms 31(2), pp. 221–34.

Liu, Z., Tian, L., Yao, T., Yu, W., 2008. Seasonal Deuterium Excess in Nagqu Precipitation: Influence of Moisture Transport and Recycling in the Middle of Tibetan Plateau. Environmental Geology 55(7), 1501–1506.

Merlivat, L., Jouzel, J. 1979. Global Interpretation of the Deuterium-Oxygen 18 Relationship for Precipitation. Journal of Geophysical Research 84, 5029–5033.

Newson, M.D., 1971. A model of subterranean limestone erosion in the British Isles based on hydrology. Transactions of the Institute of British Geographers, pp. 55–70.

Observatoire Hydro-Géochimique de l'Environnement (OHHE), 2017. http://ohge.unistra.fr, data accessed October 17, 2017.

Onac, B.P., 1996. Mineralogy of speleothems from caves in the Padurea Craiului Mountains (Romania), and their palaeoclimatic significance Cave and Karst Science 23, pp. 109–120.

Orășeanu, I., 1991. Hydrogeological map of the Pădurea Craiului Mountains (Romania). Theoretical and Applied Karstology 4, pp. 97–127.

Orășeanu I, Jurkiewicz A. 1987. Hydrological karst systems in Pădurea Craiului Mountains. Theoretical and Applied Karstology 3:215–222.

Orășeanu, I., Jurkiewicz, A., (Eds.), 2010. Karst hydrogeology of Romania. Belvedere Publishing House, Oradea, 444 pp.

Palmer, A.N., 2007. Cave Geology. Cave Books: Dayton, Ohio, 454 pp.

Papp, D.C., Cociuba, I., Lazăr, D.F., 2013. Carbon and oxygen-isotope stratigraphy of the Early Cretaceous carbonate platform of Pădurea Craiului (Apuseni Mountains, Romania): A chemostratigraphic correlation and paleoenvironmental tool. Applied Geochemistry 32, pp. 3–16. https://doi.org/10.1016/j.apgeochem.2012.09.005.

Paylor, R.L., 2016. Particulate inorganic carbon flux and sediment transport dynamics in karst: Significance to landscape evolution and the carbon cycle. Ph.D. thesis, Louisiana State University.

Perşoiu A, Bojar AV, Onac BP. 2007. Stable isotopes in cave ice: what do they tell us? Studia UBB Geologia 52 (1):59–62.

Plummer, L.N., Busenberg, E., 1982. The solubilities of calcite, aragonite and vaterite in CO_2-H_2O solutions between 0 and 90 °C, and an evaluation of the aqueous model for the system $CaCO_3$-CO_2-H_2O. Geochimica et Cosmochimica Acta 46(6), pp. 1,011–1,040. https://doi.org/10.1016/0016-7037(82)90056-4.

Priesnitz, K., 1974. Lösungsraten und ihre geomorphologische Relevanz. Abh. Akad. Wiss. Göttingen, Mathematisch-Physikalische Klasse 3. Folge 29: 68084.

Rusu, T., 1981. Les drainages souterraines de Monts Pădurea Craiului. Travaux de l'Institut de Spéologie "Émile Racovitza" XX, pp. 187–205.

Scanlon, B.R., 1989. Physical controls on hydrochemical variability in the inner bluegrass karst region of central Kentucky. Groundwater, 27(5), pp. 639–646.

Spinoni, J., Naumann, G., Vogt, J.V., Barbosa, P., 2015. The biggest drought events in Europe from 1950 to 2012. Journal of Hydrology: Regional Studies 3, pp. 509–524. https://doi.org/10.1016/j.ejrh.2015.01.001.

Vălenaş, L., Iurkiewicz, A., 1980–1981. Studiul complex al carstului din zona Suncuiuş-Mişid (Munţii Pădurea Craiului). Nymphaea VIII–IX, pp. 311–378.

Viehmann, I., Pleşa, C., Rusu, T., 1964. Peştera de la Vadul Crişului. Lucr. Inst. Speol. E. Racoviţă, Bucureşti III, pp. 49–81.

Wassenaar LI, Coplen T, Aggarwal PK. 2013. Approaches for achieving long-term accuracy and precision of δ18O and δ2H for waters analyzed using laser absorption spectrometers. Environ Sci Technol 48 (2):1123–1131. https://doi.org/10.1021/es403354n.

Wassenaar LI, Terzer-Wassmuth S, Douence C, Araguas-Araguas L, Aggarwal PK, Coplen TB. 2018. Seeking excellence: An evaluation of 235 international laboratories conducting water isotope analyses by isotope-ratio and laser-absorption spectrometry. Rapid communications in mass spectrometry: RCM 32 (5):393–406. https://doi.org/10.1002/rcm.8052.

White, W.B., 1988. Geomorphology and hydrology of karst terrains. Oxford University Press, New York, 464 pp.

Geological Setting of the Païolive Karst (Ardèche, South of France): Consequences on its Genesis and Vertical Development

Céline Baral, Michel Séranne, and Séverin Pistre

Abstract

A combined geological–geomorphological analysis of the Païolive area, Ardèche, southern France, allows to discuss the extension, origin and chronology of the karst that affects late Jurassic limestone. Results point to paleo-surface abandonment, river incision and karst formation resulting from a late Miocene and pre-Messinian uplift of the area. The epigene karst does not extend below the present-day base level.

Keywords

Karst • Incision • Paleo-surface • Base level • Geomorphology

Introduction

Intensely karstified landscapes of Ardèche (southern France) attract many tourists, rising seasonal problems of water supply. Underground water resources, especially karstic reservoirs, provide most of the supply for the region, such as the Païolive karst, located between the Chassezac and La Baume rivers. This karst constitutes a strategic aquifer of this area; however, its geometry and vertical development are poorly known.

This preliminary study of the geological setting of the Païolive karst (Fig. 1a, b) aims at testing a combined geological and geomorphological approach, in order to document the karst extension and to improve the understanding of its formation. This will, in turn, bring important constraints on its hydrological modeling with water resource objectives, which is not the scope of this contribution. Although karsts related to the incision of the Mesozoic carbonate platform by the Ardèche river (Ardèche canyon, Fig. 1a) have been analyzed (Mocochain et al. 2006a, b; Tassy et al. 2013), karsts of the upper reaches of the area, along the Cevennes margin, are much less investigated (Bakalowicz 2008). The proximity of both areas could argue for a common origin of their respective karst networks; however, our results point to significant differences in the genesis of rivers and karst incisions, as well as an original development of the Païolive karst.

We first analyze the structural framework and geological cross sections, in order to localize the karstic massif in relation with the tectonic structures resulting from regional geodynamics. Lithostratigraphic analysis is used to distinguish reservoir and seal formations, and to date some geodynamic events, crucial for the karst formation. Then, geomorphological analyses of Païolive and surrounding areas, correlated with sedimentological observations of residual deposits, lead to (i) identify paleo-surfaces and their subsequent deformations; (ii) determine the upstream sources and (iii) constrain the downstream position of each paleo-surface. Finally, the numerous available speleological data (Chabaud and Lhomme 2016) are plotted with respect to the paleo-surfaces and present-day base level and analyzed as first-order approximation of the karst vertical development.

Lithostratigraphy and Structural Analyses

The Païolive karstic aquifer develops in Late Jurassic (Kimmeridgian–Tithonian) to Early Cretaceous (Berriasian) limestones. It rests on Early to Middle Jurassic alternating marls and marly limestones which constitute the aquifer substratum. It is covered and sealed by Valanginian marls and limestones (Elmi et al. 1989).

Earlier structural studies across the Ardèche margin, along strike 15 km further north (Bonijoly et al. 1996) and several exploration borehole data, provide the base for the

---

C. Baral · M. Séranne (✉)
Géosciences Montpellier, CNRS, Université de Montpellier-Université de Guadeloupe, Montpellier, France
e-mail: michel.seranne@umontpellier.fr

S. Pistre
Hydrosciences Montpellier, CNRS-IRD-Université de Montpellier, Montpellier, France

C. Bertrand et al. (eds.), *Eurokarst 2018, Besançon*, Advances in Karst Science,
https://doi.org/10.1007/978-3-030-14015-1_5

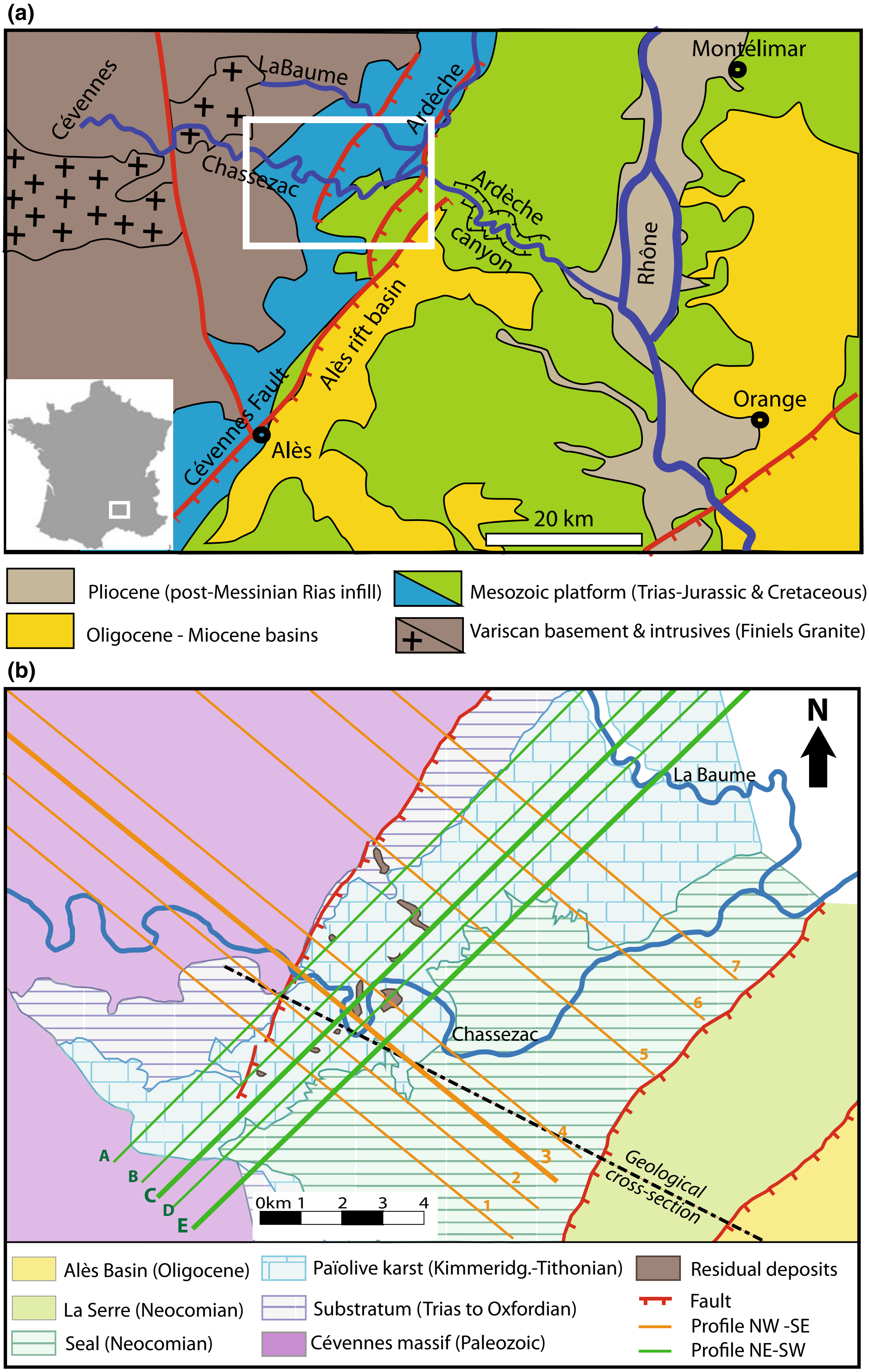

Fig. 1 **a** Geological setting of the study area (white frame). **b** Geological map showing the structure of the Païolive aquifer (substratum, karstic aquifer, seal) and localizing residual deposits. Locations of the geological cross section (Fig. 2) and of all analyzed elevation profiles are indicated; bold lines indicate the profiles shown in this contribution (Figs. 3 and 4)

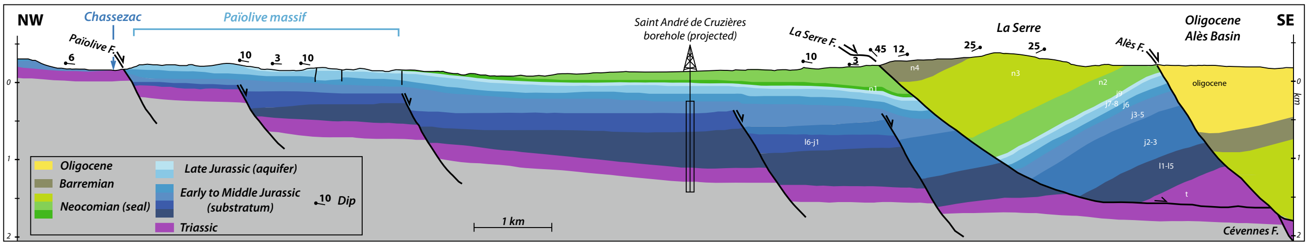

Fig. 2 Geological cross section of the studied area locating the karstic massif in relation with the tectonic structures. Note that Late Jurassic to Early Cretaceous formations are slightly dipping SE and that Neocomian was overlying Jurassic–Early Cretaceous limestones

geological cross section (Fig. 2). It shows that Late Jurassic to Early Cretaceous formations are slightly dipping SE. These are affected by low-amplitude anticline flexures oriented NE-SW, responding to a post-deposition reactivation of basement faults (Séguret et al. 1997). To the southeast, the studied reservoir is sealed at depth against the Hauterivian marly formation, across a listric fault bounding the tilted block of La Serre. This fault is a splay of the Cevennes fault reactivated as an extensional fault during the Oligocene rifting and formation of the Alès rift basin (Fig. 1a) (Sanchis and Séranne 2000). Structural and stratigraphic restoration of the Neocomian formation (the marly seal) indicates that it was overlying and thus preserving Jurassic–Early Cretaceous limestones from epigene karstification, prior to its erosional denudation.

Geomorphology

We use the base level concept as defined by Wheeler (1964); it is a theoretical, dynamic surface, which undulates around the topographic surface and is linked downstream to a still water surface (lake or sea). Where and when base level surface is below topography, rocks located between the two surfaces are unstable and prone to erosion, weathering or karstification. Where and when base level surface lies above topography, sediments may be deposited and preserved. Where and when the two surfaces meet, there is neither erosion nor deposition: It corresponds to sediment bypass. As a first-order approximation, base level surface can therefore be correlated with a steady-state, physical, topographic surface, which combines erosional, bypass and depositional surfaces. Epigene karst formation depends on base level variations in space and time and occurs when base level drops below topography, leading to carbonate dissolution in limestone areas. Base level drop also leads to river network incision and abandonment of surfaces, which may be covered with residual fluvial sediments. Such paleo-surfaces can be interpolated across present-day landscape, and they characterize paleo-base levels. In cross sections, base level surface can be assigned to an upstream–downstream profile. The methodology is based on the analysis of such profiles extracted from *Google Earth* application and displayed with a highly exaggerated vertical scale. This implies that only variations (not the values) of slopes are relevant in the analysis. Profiles display concave upward segments topping relative highs, which can be correlated downstream in a consistent way as an almost asymptotic curve, and interpreted as sections across paleo-surfaces. We have investigated 5 parallel elevations profiles trending NE–SW and 7 profiles trending NW-SE, Figs. 3 and 4 represent three of such orthogonal profiles.

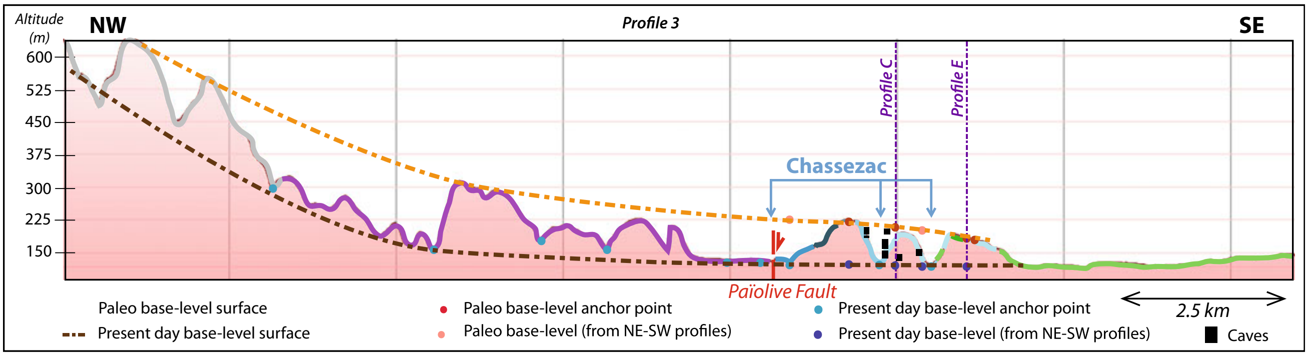

Fig. 3 Elevation profile trending NW–SE showing the interpreted paleo- and present-day base level surfaces. The colors on the topographic surface show the lithologies with the same code as in the geological cross section (Fig. 2). In section, the paleo-surface shows an concave upward upstream–downstream profile with an upstream in the Cévennes Paleozoic basement

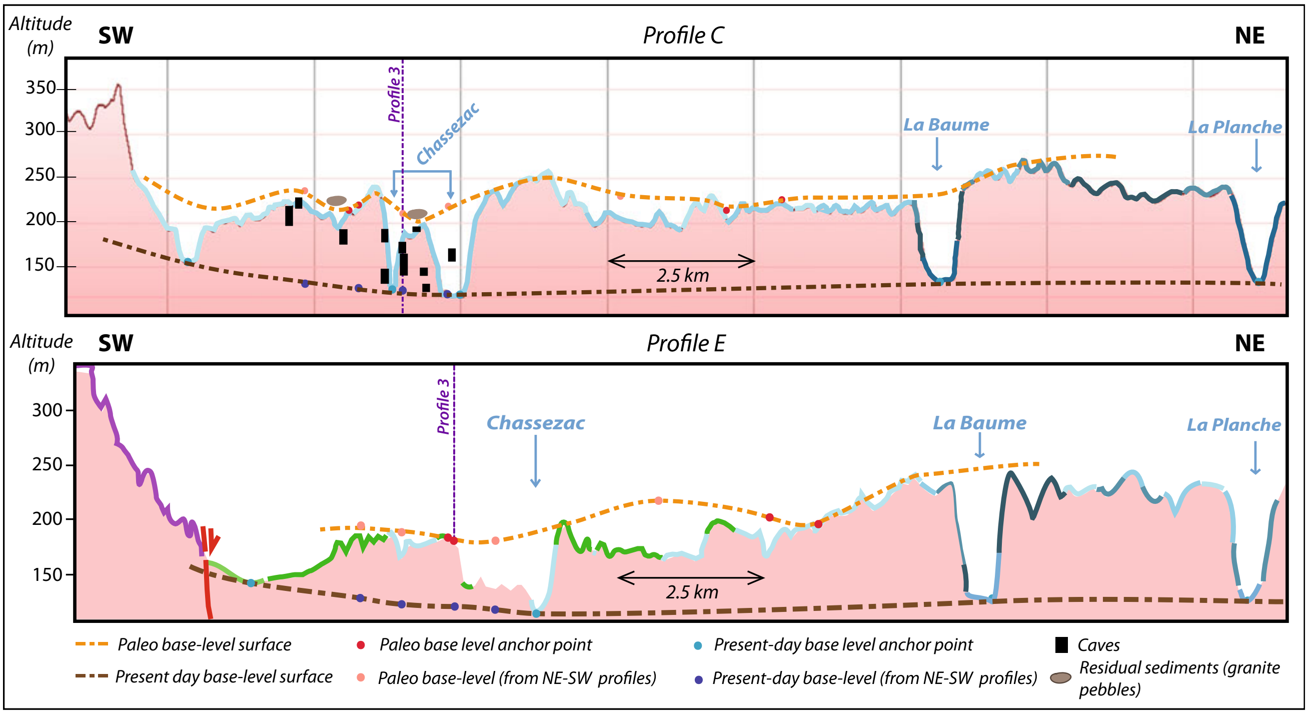

Fig. 4 Elevation profiles trending SW–NE showing the interpretation of paleo- and present-day base level surface. The colors on the topographic surface show the lithologies with the same code as in the geological cross section. Note the SE-trending ridges and gullies affected by the paleo-surface. The residual sediments are located in the gullies, i.e., the paleo-valleys. Anchor points (red dots) correspond to occurrences of residual sediments found on the paleo-surface. The paleo-surface is slightly tilted to the SW and river incision is deeper in the NE than in the SW, as a sign of surface uplift and bending

Geology and occurrence of residual sediments are plotted on the profiles, in order to map the paleo-surface.

The present-day base level is plotted as the surface interpolated between local topographic lows, such as the intersection of the elevation profile with the Chassezac and La Baume rivers, and it is compared with the paleo-surface. Smaller extension, linear, fluvial terraces found close to present-day river network have not been distinguished from present-day base level. The entrance elevation and vertical development of karst cavities (Chabaud and Lhomme 2016) are also plotted on the profiles.

A distinctive paleo-surface intersects different lithologies (Fig. 3): Its upstream lies in the Cévennes Paleozoic basement and it cuts the gently SE-dipping monocline of Triassic to Valanginian sequences, while downstream it is located against the tilted block of La Serre, which forced the river to flow northeastward, i.e., normal to the section. This paleo-surface presents an almost asymptotic profile as seen in a NW–SE section, while it displays a corrugated geometry across orthogonal profiles, with a succession of SE-trending ridges and gullies (Fig. 4). Paleo-valleys are characterized by the presence of residual sediments deposited in the gullies, which are mapped across the study area (Elmi et al. 1989), as well as south of it (Clerc 2009). In the Païolive karst, detrital elements include allochthonous pebbles and boulders of quartz, schists, hematite lateritic crust fragments and distinctive granites boulders that can be correlated with the late Variscan intrusive (Fig. 1a). Detrital allochthonous sediments indicate the source and confirm the presence of a paleo-Chassezac river, which drained the Paleozoic Cevennes basement, including late Variscan granite exposed in the watershed.

The interpretation of the paleo-surface on the NE–SW profiles (Fig. 4) is constrained by (i) the crossing with NW–SE profiles, (ii) relative highs and (iii) presence of detrital fluvial sediments found in perched valleys. The interpreted paleo-surface shows a general southwestward tilt, opposite to the NE-flowing present-day Chassezac river. This paleo-surface is cut by a more significant incision of La Baume and La Planche rivers (>150 m) to the NE, than the Chassezac river (<80 m) to the SW (Fig. 4).

Discussion

The paleo-surface has been deeply incised by the Chassezac and La Baume rivers, as well as all their tributaries, in response to the lowering of the base level. Consequently, the karstic network has sunk into the carbonate massif exposed at that time, or shortly after, depending on the rates of karstic

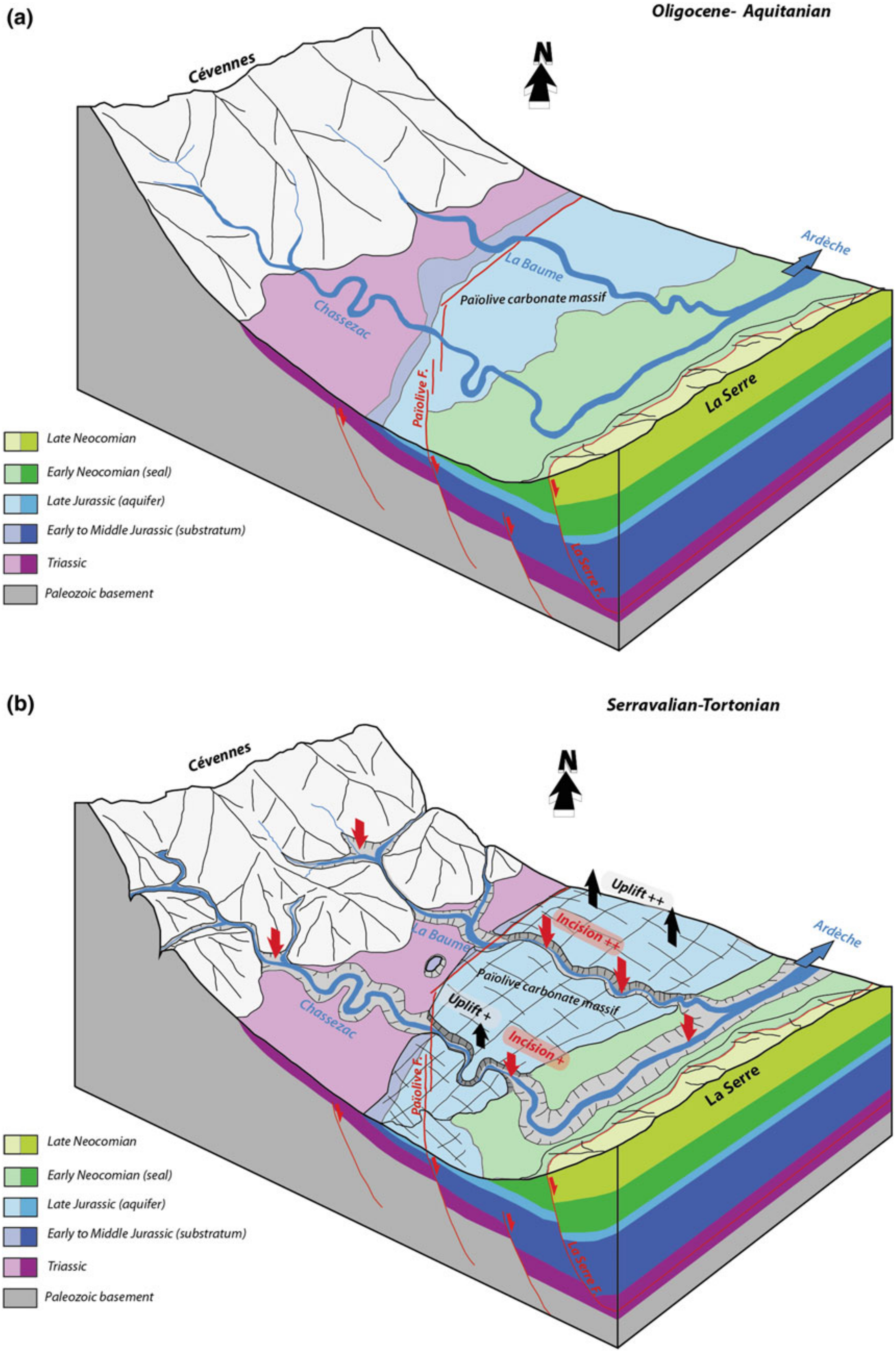

Fig. 5 Schematic 3D diagrams illustrating the geological setting and the genesis of the Païolive karst: **a** Oligocene—Lower to Middle Miocene: formation of a paleo-surface linking the Cévennes Paleozoic basement high to La Serre tilted bloc. **b** Late Miocene (pre-Messinian): differential uplift produced bending of the area, which induced abandonment of the paleo-surface, incision of the river network and karstification of the carbonate uplifted plateaus

incision. No evidence of epigene karstification below the present base level has been found in the speleological record (Chabaud and Lhomme 2016), which provides the lower boundary and vertical extension of the epigene karstic aquifer.

Datation of this paleo-surface is a key point of this study, but it is poorly constrained. However, it can be noted that: (i) the downstream paleo-surface onlaps onto the tilted bloc of La Serre, formed during Oligocene rifting (Sanchis and Séranne 2000), and (ii) the river network belongs to the Rhône river drainage that flows to the Northwest Mediterranean, which was formed during the Oligocene–Aquitanian rifting of the Gulf of Lion (Séranne 1999). This suggests that the paleo-surface was developed after Oligocene–Aquitanian rifting. The age of the paleo-surface abandonment must be discussed in the light of the origin of base level lowering. Surface abandonment, rivers incision and karstification could result from upstream regressive incision of the Ardèche river during the Messinian salinity crisis in the Mediterranean Sea, followed by the Pliocene transgression (Pliocene Rias, Fig. 1a) well documented some 20 km downstream of the study area (Mocochain et al. 2006b). Alternatively, it could be related to the Late Miocene uplift (Serravallian–Tortonian) referenced in neighboring areas of Languedoc (Séranne et al. 2002). The NE–SW elevation profiles (Fig. 4) show a southwestward tilting of the paleo-surface and a long wave, low-amplitude (±100 m) up-warping in the eastern part of the study area. The observed increasing amount of incision in a downstream direction contradicts an upstream, regressive, erosional process, as expected in response to sea-level drop. Our observations favor a tectonic origin (uplift) rather than a base level lowering by desiccation of the Mediterranean Sea during Messinian. Finally, this provides the youngest boundary for the paleo-surface abandonment, which was formed after the Aquitanian and before the Serravallian–Tortonian.

Conclusion

As a result of the Oligocene–Aquitanian rifting of the Gulf of Lion, a fluvial drainage network was established, flowing toward the Mediterranean Sea, which led to the formation of an erosional/depositional paleo-surface in the Païolive area (Fig. 5a). During the Serravallian–Tortonian interval, a differential uplift led to a long wave, low-amplitude uplift and bending in the north-east of the study area. This event induced river network incision, abandonment of the paleo-surface and karstic network sinking into the Late Jurassic carbonate massif (Fig. 5b). Such karstification therefore predates the canyon incision of the lower reaches of the Ardèche and the related karst formation in the Ardèche plateau (Fig. 1a).

Such preliminary geological and geomorphological combined study sheds new light on the extension, genesis and chronology of an epigene karst, which bring constraints on its future hydrological modeling.

Acknowledgements We are thankful to the three anonymous referees who provided detailed and constructive reviews that helped improving this work. We are also grateful to Catherine Bertrand who invited this contribution and for her editorial work.

References

Bakalowicz, M., 2008, réflexions sur la genèse du karst du bois de Païolive: Les Cahiers de Païolive, v. 1, p. 87–94.

Bonijoly, D., Perrin, J., Roure, F., Bergerat, F., Courel, L., Elmi, S., Mignot, A., and GPF-Team, 1996, The Ardèche paleomeargin of the South-East Basin of France: mesozoic evolution of a part of the Tethyan continental margin: Marine and Petroleum Geology, v. 13, no. 6, p. 607–623.

Chabaud, M., and Lhomme, M., 2016, Païolive souterrain: Cahiers de Païolive v. 2, 352 p.

Clerc, C., 2009, Structure et fonctionnement du système karstique de Saint André de Cruzières : Master 2, Université Montpellier 2 - SupAgro Montpellier, 65 p.

Elmi, S., Brouder, P., Berger, G., Gras, H., Busnardo, R., Bérard, P., and Vautrelle, C., 1989, Carte Géologique de la France à 1/50000e Feuille de Bessèges - n° 888: BRGM.

Mocochain, L., Bigot, J.-Y., Clauzon, G., Faverjon, M., and Brunet, P., 2006a, La grotte de Saint-Marcel (Ardèche) : un référentiel pour l'évolution des endokarsts méditerranéens depuis 6 Ma: Karstologia, v. 48, p. 33–50.

Mocochain, L., Clauzon, G., Bigot, J.-Y., and Brunet, P., 2006b, Geodynamic evolution of the peri-Mediterranean karst during the Messinian and the Pliocene: evidence from the Ardèche and Rhône Valley systems canyons, Southern France: Sedimentary Geology, v. 188–189, p. 219–233.

Sanchis, E., and Séranne, M., 2000, Structural style and tectonic evolution of a polyphase extensional basin of the Gulf of Lion passive margin: the Tertiary Alès Basin, southern France: Tectonophysics, v. 322, p. 243–264.

Séguret, M., Benedicto, A., and Séranne, M., Structure profonde du Gard Rhodanien, Apport du retraitement et de la réinterprétation de données sismique régionales, in Proceedings Journées Scientifiques ANDRA, Bagnols sur Cèze, 1997, Volume Atlas des Posters, ANDRA / CNRS, p. G.G.15.

Séranne, M., 1999, The Gulf of Lion continental margin (NW Mediterranean) revisited by IBS: an overview, in Durand, B., Jolivet, L., Horváth, F., and Séranne, M., eds., The Mediterranean

Basins : Tertiary extension within the Alpine Orogen, Volume Special Publication 156: London, The Geological Society, p. 15–36.

Séranne, M., Camus, H., Lucazeau, F., Barbarand, J., and Quinif, Y., 2002, Surrection et érosion polyphasées de la bordure cévenole - Un exemple de morphogenèse lente: Bulletin de la Société Géologique de France, v. 173, no. 2, p. 97–112.

Tassy, A., Mocochain, L., Bellier, O., Bruacher, R., Gattacceca, J., and Bourlès, D., 2013, Coupling cosmogenic dating and magnetostratigraphy to constrain the chronological evolution of peri-Mediterranean karsts during the Messinian and the Pliocene; example of Ardèche Valley, southern France: Geomorphology, v. 189, p. 81–92.

Wheeler, H. E., 1964, Baselevel, lithosphere surface, and time-stratigraphy: Geological Society of America Bulletin, v. 75, no. 7, p. 500–609.

From Jovan Cvijic to Alain Mangin or How a Karst Landscape Was Transformed into a Complex Karst Hydrosystem

Michel Bakalowicz

Abstract

Until the 1970s, karst was considered by a variety of approaches, often not easily reconcilable. As a place of exploration, it was regarded as a set of pipes through which man and water could pass. Because it is generally an arid surface landscape, it was seen as a combination of forms resulting essentially from climatic actions. As a groundwater reservoir discharging to often spectacular springs, it was considered as a fractured or fissured aquifer medium, in which cavities play a negligible role. The approach to karst proposed by Alain Mangin was very innovative, because it was based on a hydrogeological and functional view of karst, and no longer on a geological and geomorphological view, which did not make it possible to prioritize the forms or phenomena involved, but simply to draw up a catalogue that had previously been interpreted in terms of either geological context or climate context. Mangin's scientific contribution to the knowledge and study of karst and its aquifers is analyzed and placed within the broader framework of karst studies.

Keywords

Karst • Hydrogeology • Epistemology • History of science • Alain Mangin

Introduction

Originally, in the nineteenth century, the study of karst was the work of hydrologists, Austrian civil engineers in charge of draining the hinterland of Trieste, the Karst, to allow the development of a food-producing agriculture (e.g., see von Mojsisowics 1880). Austrian hydrogeologists together with Grund (1903), involved in the development and enhancement of the Karst region in Slovenia, considered karst as an aquifer, capable of storing water at depth. But in this type of aquifer, underground cavities were only considered as local phenomena, without any real hydrogeological function.

At the same time, the first works on the Karst and neighboring regions (Cvijic 1918; Penck 1904), relying mainly on speleological explorations and the study of their surface morphology, favored a very different conception, which was reinforced by Martel's conception (1905, 1921). According to them, caves play an essential, if not unique, role in the underground flow in karst; this led them to deny karst its role as an aquifer. This approach, taken to its extreme, led Martel to reject the French term "sources" to karst springs and to always associate their permanent flow during the low-water season with surface flows feeding swallow holes rather than with the existence of real underground reserves. Moreover, Martel (1921) did not fail to mock groundwater, Grundwasser in German, as "Grund wasser," considering that it was a myth. Following this, some geomorphologists have gone so far as to use mechanisms that have never been verified, such as the absence of evapotranspiration (Nicod 1972, concerning the Vaucluse catchment area) or occult inputs, such as underground condensation (Trombe 1952, pp. 116–117).

Is Karst an Aquifer?

These two resolutely opposed conceptions constituted a form of "karstoschizophrenia" (Bakalowicz 2006) which led the two communities to work without real exchanges between them. They have served as a reference, explicit or not, for those who, since then, have sought to understand the processes of establishing karst landscapes (karstification) in the hope of inferring the mechanisms of groundwater flow within it (karst hydrogeology). This concept, which can be described as "speleocentric," has led, among other things, to

---

M. Bakalowicz (✉)
HydroSciences Montpellier, CC57 Université de Montpellier,
163 rue Auguste Broussonnet, Montpellier, 34090, France
e-mail: michel.bakalowicz@gmail.com

C. Bertrand et al. (eds.), *Eurokarst 2018, Besançon*, Advances in Karst Science,
https://doi.org/10.1007/978-3-030-14015-1_6

the study of caves as geomorphological and geological objects (see, for instance, the work of Renault 1967a, b, 1968).

While recognizing the originality of surface karst landscapes, the other conception has made karst a common aquifer, comparable to any fissured aquifer; in these aquifers, voids would be distributed according to the geological structure, responsible for discontinuities favoring underground flows: This is the structural design, initially developed by Kiraly (1969) in Neuchâtel, Switzerland, used again and supported by Drogue (1974). A detailed analysis of the fracture field should provide a good representation of the organization of the voids and, therefore, of the hydraulic properties of the reservoir (cf. Razack 1978). According to this approach, it becomes possible to define a representative elementary volume (REV) of the reservoir, as for porous aquifers. The REV is the minimum volume below which the permeability may be considered constant, whatever the volume, lower than the REV considered (Long et al. 1982). This is the basis for modeling the structure of voids and the functioning of the aquifer. The interest of this structural approach to karst is to be able to model the structure and functioning of a karst aquifer using grid models. It provided hydrogeology with both an overall model of the organization of karst aquifer voids, allowing all observations to be placed back into this set, and methods for studying the structure and interpreting hydrodynamical data. In this design, the considerable heterogeneity observed in hydrological data, including transmissivity and groundwater chemical composition values, is associated with the notion of observational scale.

The Karst Aquifer According to Mangin

This approach is flawed by a number of field observations. This is where Mangin comes in with his first work on the functioning of karst springs in the Pyrenees (Fontestorbes, Le Baget, Aliou), which is the starting point of his Ph.D. Mangin (1974a, b, 1975) was the first to show that the heterogeneity of the karst, for the organization of voids as for its hydrological functioning, exists whatever the level of scale of observation, unlike other aquifers, for which there is always a higher level of scale for which the aquifer appears homogeneous, in its functioning and in the distribution of its voids occupied by groundwater. It comes to introduce the notion of the karst system, comparable to that of the catchment area for surface waters, i.e., as a hydrogeological entity whose spring is the outlet (Mangin 1974c, 1978, 1994). Subsequently, Long et al. (1982) indirectly showed that Mangin's approach was correct. These authors showed that the REV does not necessarily exist, since it only makes sense in a fractured massif if the flow is associated with a constant gradient and straight flow lines in a homogeneous anisotropic medium.

This new approach made it possible to avoid a priori the difficulty posed by this supposed relationship between homogeneity and the appropriate level of observation scale. But above all, it provides on the one hand a well-defined object of study, the karst system, without any hypothesis a priori imposing a model of structure and/or functioning, and on the other hand a scientific approach allowing an objective analysis of the functioning. This approach refers directly to system analysis (Mangin 1982, 1994), using its concepts and tools; it has now become a classic in Earth Sciences. Many hydrogeological studies now refer explicitly to it.

This approach is comprehensive: It analyzes the functioning of a system as a whole, in order to deduce its structure, i.e., the organization responsible for the observed functioning, and the evolution of this structure as a result of this functioning. It is based on a reference object, the karst system, and uses all the tools at its disposal to analyze its functioning, with explicit reference to a multidisciplinary approach. This heterogeneity has been demonstrated both hydrodynamically, through geochemistry (Bakalowicz 1979) and water isotopes (Bakalowicz et al. 1974) or the dynamics of underground aquatic populations (Rouch 1984, 1986).

Karst springs in the Pyrenees have been systematically studied; their catchment areas constitute investigation catchment areas, i.e., reference karst systems. All the studies, subsequently carried out using the same methods on karst in the same region, i.e., in the same geological and geomorphological context, and in other regions of France and other countries, have contributed to demonstrating the representativeness of these reference karst systems: Alongside their own characteristics, linked to their geological and paleoenvironmental history, they all possess common characteristics that distinguish them from other aquifers.

On the basis of these foundations established in the 1970s, Mangin then focused his work on several directions. First, he adapted tools used in other disciplines to karst hydrogeology, including a diversified arsenal of statistical methods for analyzing the collected data, such as multidimensional analyses, simple and cross-correlation and spectral analyses (Mangin 1981a, b) and wavelet analyses (Labat et al. 1999). At the same time, thanks to the theses he supervised, Mangin considerably increased his knowledge of karst systems developed and operating under very different environmental conditions. This allowed him to deepen his initial analysis of the hydrological functioning of karst by showing how karst evolution acts, and what the drivers and framework for its application are. In accordance with the system analysis to which he referred from the beginning to replace concepts and methods, Mangin distinguished the three aspects of the karst system, as for any dynamic system:

(1) architecture, i.e., the geological and morphological framework within which it is embedded; (2) the karst structure, the morphological set developed by the karstification process, consisting of the conduits and associated underground and surface landforms; and (3) the present functioning of the system, which takes into account the framework in which it has developed and evolved. Thus, he introduced the concept of potential for karstification (Mangin 1978) and proposed a functional classification of karst aquifers based on the results of the spring hydrograph analysis (Mangin 1974b).

Finally, partly based on the multidisciplinary approach he had advocated, Mangin "entered" the initial black box of the karst system. Thus, he showed the existence of a discontinuous perched discontinuously saturated zone associated with what he called the epikarst (Mangin 1975; Bakalowicz 2012), storage areas in the saturated zone that he called the annex-to-drain systems or ADS (Mangin 1969, 1975). As shown by spatial analyses of groundwater levels and tracing tests, ADS are the site of complex hydraulic exchanges with the conduit organization; they are most often separated from each other by very low permeability zones that give them relative hydraulic independence, which reflects a high degree of fragmentation of the saturated zone. The analysis of abandoned karst structures and the sediments they contain confirms the validity of Mangin's initial hydrodynamic interpretation (work on the Niaux–Lombrives–Sabart cave system by Sorriaux 1982; on the Languedoc karst by Camus 2003).

Among the innovative approaches introduced by Mangin, the one concerning the protection of the underground environment, and in particular prehistoric parietal works, should be retained. Indeed, Mangin showed the great complexity of the mechanisms of infiltration in the karst, which range from direct, rapid and concentrated infiltration, from privileged absorption points (swallow holes, dolines), to slow to very slow infiltration fed by storage in the epikarst. It is this slow infiltration that generally drips in caves, building speleothems and washing the walls. In the 1970s, at the request of the Ministry of Culture, the Moulis team was mobilized to determine the causes of the alteration of the parietal works in the cave of Niaux, in the French Pyrenees (Andrieux 1983; Mangin 1988). A methodology was developed and proposed (Mangin and Bakalowicz 1989; Mangin et al. 1991), which subsequently led to systematic work for the protection of prehistorical caves and other caves with remarkable speleothems (Bourges et al. 2001, 2016). Finally, through the practice of speleology, Alain Mangin had discovered the beauty and originality of the underground world and its speleothems, which he showed with the photographic support of Patrick Cabrol (Cabrol and Mangin 2000).

Summary and Conclusions

However, it is to be regretted that Mangin was not able to disseminate his work more effectively. For him, research was first and foremost an intellectual game, which satisfied him. As the problem was never completely solved, he had to continue working, which limited his ability to write. The refusal to make any mathematical model to simulate the functioning of karst systems was part of this same conception: For him a model was a caricature, therefore always far from reality.

To summarize, the main consequences and contributions of Alain Mangin's work on karst are as follows:

1. criticism of existing tools used in hydrology and adaptation to karst hydrology (hydrograph analysis; classified flow curve);
2. the implementation of statistical data analysis tools (multidimensional analyses; time series analyses);
3. a multidisciplinary methodological approach, now accepted and implemented by all;
4. the integration of field observations (speleological data; analysis of particular phenomena) to propose an organization of voids and flows (ADS);
5. the proposition of a conceptual, functional and structural model, progressively complexified by taking into account the evolution and the different possible drivers of karstification, such as hydrothermal deep karst.

The reader can be informed of Alain Mangin's biography (Bakalowicz 2018).

References

Andrieux C (1983) Etude des circulations d'air dans la grotte de Niaux. Conséquences. Karstologia 1:19–24

Bakalowicz M (1979) Contribution de la géochimie des eaux à la connaissance de l'aquifère karstique et de la karstification. PhD Laboratoire Géologie Dynamique, Laboratoire Souterrain CNRS. Université P. et M. Curie Paris-6, 269 p

Bakalowicz M (2006) Importance of regional study site conditions in elaborating concepts and approaches in karst science. In: Perspectives on karst geomorphology, hydrology, and geochemistry—A tribute volume to Derek C. Ford and William B. White, Special Paper 404. R. S. Harmon RS, Wicks CM eds, Geological Society of America: 15–22

Bakalowicz M (2012) Epikarst. Encyclopedia of Caves and Karst. Culver DC, White WB eds, Elsevier, 1:284–288

Bakalowicz M (2018) Alain Mangin (1942–2017). Géochronique. https://www.geosoc.fr/geochronique/complement/2018/GEOC144-Mangin.pdf

Bakalowicz M, Blavoux B, Mangin A (1974) Apports du traçage isotopique naturel à la connaissance du fonctionnement d'un système karstique - teneurs en oxygène 18 de trois systèmes des Pyrénées, France. J Hydrology 23:141–158

Bourges F, Genty D et al. (2016) Monitoring prehistoric painted caves: a scientific and technical challenge for heritage preservation. 41st International Symposium on Archaeometry (ISA)

Bourges F, Mangin A et al. (2001) Le gaz carbonique dans la dynamique de l'atmosphère des cavités karstiques: l'exemple de l'aven d'Orgnac (Ardèche). C R Acad Sci Paris 333:685–692

Cabrol P, Mangin A (2000) Fleurs de Pierre. Les plus belles concrétions des grottes de France, Delachaux et Niestlé

Camus H (2003) Vallées et réseaux karstiques de la bordure carbonatée sud cévenole. PhD Institut Géographie. Université Bordeaux 3, 385 p

Cvijic J (1918) Hydrographie souterraine et évolution morphologique du karst. Recueil Travaux Institut Géographie Alpine Grenoble, 6:375–429

Drogue C (1974) Structure de certains aquifères karstiques d'après les résultats de travaux de forage. C R Acad Sci Paris, série III 278:2621–2624

Grund A (1903) Die Karsthydrographie. Studien aus Westbosnien, Leipzig. Geogr. Abhandlungen von A. Penck VII (3):1–201

Kiraly L (1969) Anisotropie et hétérogénéité de la perméabilité dans les calcaires fissurés. Eclogae Geologicae Helvetiae 62 (2):613–619

Labat D, Ababou R et al. (1999). Wavelet analysis in karstic hydrology. 1st part: univariate analysis of rainfall rates and karstic spring runoffs. C R Acad Sci Paris, IIA, Earth and Planetary Science 329 (12):873–879

Long JCS, Reiner JS et al. (1982) Porous media equivalents for networks of discontinuous fractures. Water Resources Research 18 (3):645–658

Mangin A (1969) Etude hydraulique du mécanisme d'intermittence de Fontestorbes (Bélesta, Ariège). Ann Spéléologie 24 (2):253–298

Mangin A (1974a) Contribution à l'étude hydrodynamique des aquifères karstiques. 1ère partie. Généralités sur le karst et les lois d'écoulement utilisées. Ann Spéléologie 29 (3):283–332

Mangin A (1974b) Contribution à l'étude hydrodynamique des aquifères karstiques. 2ème partie. Concepts méthodologiques adoptés. Systèmes karstiques étudiés. Ann Spéléologie 29 (4):495–601

Mangin A (1974c) Notion de système karstique. Spélunca Mémoires 8:64–68

Mangin A (1975). Contribution à l'étude hydrodynamique des aquifères karstiques. 3ème partie. Constitution et fonctionnement des aquifères karstiques. Ann Spéléologie 30 (1):21–124

Mangin A (1978) Le karst, entité physique abordée par l'étude du système karstique. Coll. Le karst, Tarbes, AGSO, 21–37

Mangin A (1981a) Utilisation des analyses corrélatoire et spectrale dans l'approche des systèmes hydrologiques. C R Acad Sci Paris, D 293 (2): 401–404

Mangin A (1981b). Apports des analyses corrélatoire et spectrale croisées dans la connaissance des systèmes hydrologiques. C R Acad Sci Paris, D 293 (2): 1011–1014

Mangin A (1982) L'approche systémique du karst, conséquences conceptuelles et méthodologiques. Reunion monografica sobre el karst, Larra 82, Larra, Spain, 141–157

Mangin A (1988) Réflexion sur les mécanismes de l'infiltration dans les karsts à partir de l'exemple de Niaux. Bull. Centre Hydrogéologie Neuchâtel 8: 3–25

Mangin A (1994) Karst hydrogeology. In: Groundwater Ecology. Stanford J, Gibert J, Danielopol D ed, Academic Press: 43–67

Mangin A, Andrieux C et al. (1991). Le problème de la conservation des oeuvres pariétales. Mesa redonda hispano-francesa, Colombres, Asturias (Spain), Principado de Asturias, 131–136

Mangin A, Bakalowicz M (1989) Orientation de la recherche scientifique sur le milieu karstique. Influences et aspects perceptibles en matière de protection. Spelunca 35:71–79

Martel EA (1905) La spéléologie au XXème siècle. Spelunca Mémoires et Bulletin 6:1–810

Martel EA (1921) Nouveau traité des eaux souterraines. Paris, O. Doin, 840 p

Nicod J (1972) Pays et paysages du calcaire. Paris, P.U.F, 244 p

Penck A (1904) Ueber das Karstphänomen. Vereines zue verbreitung naturwissenschaftlicher Kenntnisse in Wien 44 (1):1–38

Razack M (1978) Sur la contribution de méthodes d'analyse numérique appliquées à l'étude d'un champ de fractures pour une meilleure connaissance de la structure des réservoirs fissurés. C R Acad Sci Paris, D 286:1577–1580

Renault P (1967) Contribution à l'étude des actions mécaniques et sédimentologiques dans le spéléogenèse. Introduction. Ann Spéléologie 22 (1):1–17

Renault P (1967) Contribution à l'étude des actions mécaniques et sédimentologiques dans le spéléogenèse. 1ère partie. Ann Spéléologie 22 (2):209–267

Renault P (1968) Contribution à l'étude des actions mécaniques et sédimentologiques dans le spéléogenèse. 2ème partie. Les effets mécaniques à l'échelle de la cavité. Ann Spéléologie 23 (1):259–307

Rouch R (1984) Les structures de peuplement des Harpacticides dans l'écosystème karstique. Crustaceana Supplement 7:360–368

Rouch R (1986) Sur l'écologie des eaux souterraines dans le karst. Stygologia 24:352–398

Sorriaux P (1982) Contribution à l'étude de la sédimentation en milieu karstique. Le système Niaux-Lombrives-Sabart (Pyrénées ariégeoises). Thèse 3ème cycle Géologie régionale, structurale et appliquée, Université Paul Sabatier, Toulouse, 255 p

Trombe F (1952). Traité de spéléologie. Paris, Payot, 376 p

von Mojsisowics E (1880) Die Karst Erscheinungen. Zeitschrift von Vereinigung des Deutschen und des Österreichischen Alpenvereins: 115–145

Part II

Surface and Ground Water Interactions

The Shallow Subsurface of Karst Systems: Review and Directions

Romane Berthelin and Andreas Hartmann

Abstract

The shallow subsurface of karst systems (soil and epikarst) plays an important role in karst recharge processes. However, only a little research that directly characterized this zone has been conducted. In this paper, we review previous studies that focus on the soil and epikarst recharge processes, in particular on diffuse recharge processes. The literature is categorized by processes, methods and controlling factors, summarized in an overview table, and discussed in detail. Finally, new directions to advance research toward a better understanding of the hydrological dynamics in the karstic shallow subsurface are derived.

Keywords

Soil • Epikarst • Recharge processes • Review

Introduction

Karst systems represent 10–15% of land surface in the world and 25% of the global population fully or partially depends on water from karst aquifers (Ford and Williams 2013). However, the strong morphologic heterogeneities of karst systems (porous matrix, fractures, and conduits) cause difficulties in their characterization and development for water supply. In the context of climate change, growing populations and land use changes, groundwater resources availability is increasingly threatened, both in term of water quantity and quality (Wada et al. 2010). Understanding the recharge processes that renew karstic groundwater resources and their vulnerability to external changes is still a challenge for water management and protection.

As observed in different studies (Aquilina et al. 2006; Trcek 2007; Aley and Kirkland 2012), the superficial weathered part of carbonate rock, named the epikarst, plays an important role in karstic recharge functioning and water quality. Because of its high porosity and fracturing, the epikarst can store the water before redistributing it via larger fractures leading to fast transfer of water to the deeper parts of the unsaturated zone.

Despite the importance of the soil above the karst and epikarst for karst water resources, previous research mostly focused on karst groundwater. Only a few studies that directly characterized the shallow subsurface processes of karst systems have been conducted. This paper reviews previous efforts to characterize the soil and epikarst processes occurring during diffused recharge. The localized recharge through sinkholes and stream losses is not considered here. Experimental approaches to investigate soil and epikarst processes are categorized and new directions to advance research toward a better understanding of the hydrological dynamics in the karstic shallow subsurface are presented and discussed.

The Shallow Subsurface of Karst Systems

The shallow subsurface of karst systems consists of the upper part of the unsaturated zone, including the soil and the epikarst (Williams 1983). It appears as an essential interface between the biosphere and the karst system (Bakalowicz 2003). The shallow subsurface characteristics control various shallow subsurface processes as for example infiltration, storage (Fig. 1) and transport processes.

The epikarst, also referred as the subcutaneous zone, is the superficial weathered part of carbonate rock. It is considered as the main karstic zone where carbonate rock dissolution takes place (Williams 1983, 2008a, b). The soil and the shallow epikarst are a source of acidity, because of the

R. Berthelin (✉) · A. Hartmann
Chair of Hydrological Modeling and Water Resources, Freiburg University, Freiburg im Breisgau, Germany
e-mail: romane.berthelin@hydrology.uni-freiburg.de

A. Hartmann
Department of Civil Engineering, University of Bristol, Bristol, UK

C. Bertrand et al. (eds.), *Eurokarst 2018, Besançon*, Advances in Karst Science,
https://doi.org/10.1007/978-3-030-14015-1_7

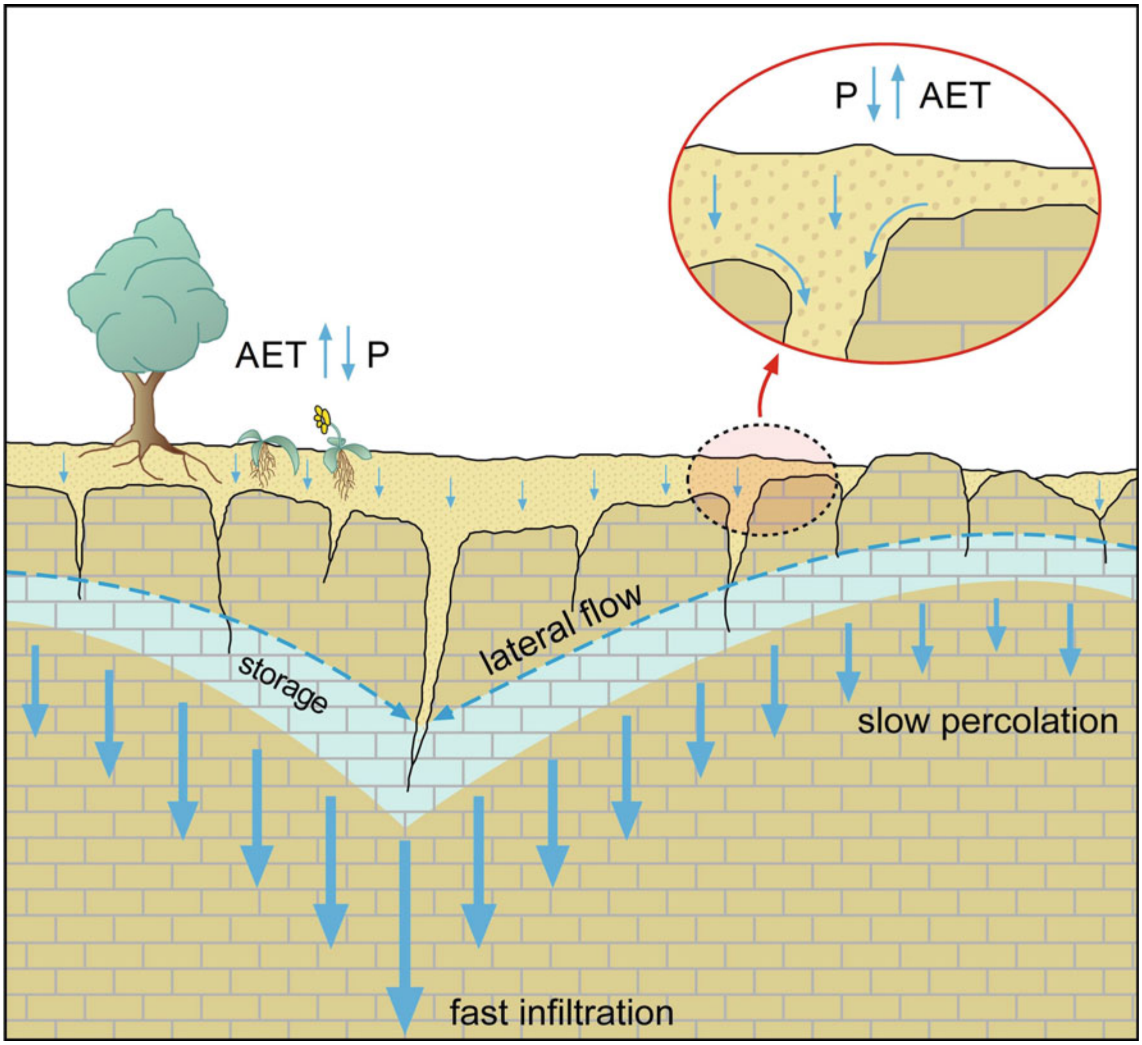

Fig. 1 Conceptual scheme of the shallow subsurface of karst systems and its dominant processes modified from Williams (1983)—P = Precipitation; AET = Actual Evapotranspiration

transformation of organic matter in CO_2. Entering into cracks and fractures, the acid water dissolves the carbonate rock and enlarges them rapidly (Dreybrodt 1990; Benavente et al. 2010). Thereby, the epikarst shows a high porosity at its surface that decreases with depth (Williams 1983) with a rather irregular interface between the soil and the rock. The thickness of the shallow subsurface can be variable depending the lithology and geomorphology evolution. In general, its thickness is estimated to be from several tens of centimeters to up to 15 m (Klimchouk 2004).

The heterogeneity of the epikarst leads to various infiltration pathways and hydrological processes. Water infiltrate into the soil and/or the epikarst where it is exposed to evapotranspiration. According to Perrin et al. (2003) and Charlier et al. (2012) the soil cover plays an important role in the velocity of infiltration and in mixing. Below, at the interface between soil and bedrock and depending on the permeability of the rock, water can flow along the rock surface and be redistributed to enlarged fractures (Fu et al. 2015). The importance of storage and lateral redistribution within the epikarst was highlighted by Király (1975) using numerical simulation. He showed the need to take into account a subsurface layer acting as a perched aquifer to represent appropriately karst aquifer. This perched aquifer evolves due to the difference of porosity between the epikarst and the non-weathered rock (Williams 2004). It can store the water for days to several months (Klimchouk 1995). Different processes can append during a rainfall event. Lateral flow can occur through the perched aquifers and lead subsurface water flow toward enlarged fissures or fractures to form fast vertical percolation. At the same time, cracks and rock porosity allow slow and diffuse vertical percolation to the rest of the unsaturated zone (Bakalowicz 2003; White 2002). In addition, in case of outcrops without soil cover, direct infiltration into the deeper karst system can take place (Bakalowicz 2003).

Processes Controlling Factors

Different factors control the hydrodynamic processes that we introduced in the previous subsection. Table 1 provides an overview of recent literature that identified controlling factors and the applied monitoring methods, classified according to the affected epikarstic processes. Below, we will discuss how the identified controlling factors affect the karst shallow subsurface processes.

Methods used to study the karst shallow subsurface can be classified in different categories: (1) hydrological methods using water balance or springs discharge; (2) hydrochemical methods using major ions analyses and physio-chemical parameters; (3) isotopic methods using for example isotopes of water or carbon as natural tracer; (4) artificial tracer tests; and (5) geophysical methods. Most of the studies were

Table 1 Literature summary of studies about the shallow subsurface of karst systems, classified in function of the investigated processes—“n.d.” = not defined

Investigated processes	Methods/Monitoring	Scale	Location and climate of the studied site	Identified controlling factors	References
Evapotranspiration processes	Energy balance measurements	Plot scale (1700 ha)	Edwards Plateau in Texas (US)—Arid climate	Soil depth and vegetation	Heilman et al. (2012)
Evapotranspiration processes Recharge dynamics (infiltration)	– GIS analysis on aerial photos, land use maps hydrological behavior analysis using numerical model (HYDRUS-2D) – Soil physical and hydraulic parameters measurements	Plot scale (139 km^2 rectangle)	Alta Murgia, Apulia Region (southeast Italy)—Mediterranean climate	Land use (stone shattering) Vegetation	Canora et al. (2008)
Recharge dynamics	Compilation of studies involving recharge assessment in 51 carbonate aquifers in SW Mediterranean	Regional scale	Betic Cordillera (southern Spain)—Mediterranean climate	Soil cover and vegetation Degree of karstification	Martos-Rosillo et al. (2015)
	– Continuous monitoring of an epikarst spring’s discharge, pH, electrical conductivity, temperature – Rainfall monitoring	Epikarst spring—hillslope scale	Maolan Karst Forest National Reserve (southwest of China)—Subtropical monsoon climate	Rainfall characteristics Epikarst characteristics as shape, size, and fractures	Jiang et al. (2008)
	Monitoring of rainfall, soil and karst water hydrochemistry analyses	Cave site scale	Crag cave (southwest Ireland)—Mild and wet climate	Soil matrix and macropores	Tooth and Fairchild (2003)
	– Major elements and dissolved organic Carbon (DOC) from soil seepage – Major ions measurements, DOC, isotopes from an epikarstic spring – Discharge monitoring	Epikarst spring—hillslope scale	Lascaux (western France)–Oceanic climate	Rainfall characteristics Epikarst water saturation	Houillon et al. (2017)
Recharge dynamics Storage	Natural tracer analyses (stables isotopes, DOC)	Spring catchment scale	Hubelj spring Catchment (southwest Slovenia)—Continental climate	Epikarst saturation conditions	Trček (2007)
Storage	– Discharge rate measurements – Weekly rainfall and spring water stable isotopes sampling – High time resolution flood events water stable isotopes sampling – Modeling	Catchment scale	Milandre karst aquifer (Switzerland)—Oceanic climate with a high mountain influence	Soil architecture (porosity, fractures and soil crust, lithology)	Perrin et al. (2003)
	Combination of time-lapse seismic refraction with hydrologic and petrophysical models	n.d.	n.d.	Porosity, permeability Rainfall input	Galibert (2015)
	Gravity measurements	Caves sites scale	Lamalou and Gourneyras karst system (southern France)—Mediterranean climate	Lithology	Champollion et al. (2017)

(continued)

Table 1 (continued)

Investigated processes	Methods/Monitoring	Scale	Location and climate of the studied site	Identified controlling factors	References
	– Meteorological monitoring – Rainfall and cave drip water stable isotopes and geochemistry measurements – Soil moisture, T and EC measurements	Cave site scale	Kosciuszko National Park, New South Wales (Australia)—Montane climate	Rainfall characteristics Antecedent moisture conditions	Tadros et al. (2016)
Storage Percolation Transport processes	– Tracer experiments – Monitoring of rainfall and irrigation, discharge, OC, turbidity EC, T, Cl^-, Br^-, fecal bacteria, uranine	Cave site scale	Vers-chez-le-Brandt cave, Jura (France)—Oceanic climate with a high mountain influence	Rainfall characteristics	Pronk et al. (2008)
Transport processes	– GIS treatment (DEM, Groundwater temperature) – Modeling nitrate concentrations	Regional scale	Murgia, Apulia Region (southeast Italy)—Mediterranean climate	n.d.	Fidelibus et al. (2016)
	Long-term tracer tests	Gallery cave site scale	Postojnska Jama (southwestern Slovenia)—Oceanic climate	Preceding hydrological conditions Geologic heterogeneities	Kogovsek and Petric (2014)
Transport processes Infiltration processes	– Dissolved organic carbon (DOC) monitoring from the water of soil cover, rock matrix and epikarstic spring – Modeling	Spring catchment scale	Fertans, Jura (France)—Oceanic climate with a high mountain influence	Soil cover State of hydraulic conductivity	Charlier et al. (2012)
General epikarst behavior	Rainfall simulations on a trench excavation under different moisture conditions	Plot scale (80 m trench, 4 m depth)	Mulian catchment (southwest China)—Subtropical climate	Rainfall intensity Antecedent moisture conditions Epikarst topography	Fu et al. (2015)
	Time lag lengths computation based on flow discharge series of hillslope springs using correlation and spectral analyses	Epikarst spring—cave scale	Jinfo Mountain Nature Reserve (southwest China)—Subtropical humid monsoon climate	Shallow subsurface thickness Degree of karstification Epikarst topography Antecedent moisture conditions	Zhang et al. (2013)
General epikarst behavior	Karst spring and rainwater monitoring (stable isotopes and Cl^-, Br^-) during high discharge events	Catchments scale	South of France (north of Montpellier)—Mediterranean climate	n.d.	Aquilina et al. (2006)
	Tracer tests (fluorescein) and wells monitoring	4 studies compilation (local scale)	Arkansas—England and Missouri	General epikarst characteristics—thickness	Aley and Kirkland (2012)
	– Major ions measurement and carbon 13 isotope at epikarstic springs–Temperature and P_{CO2} air caves monitoring	Caves sites scales	Lascaux and Cussac (western France)—Oceanic climate	Climate condition	Peyraube et al. (2013)

conducted on a local scale, which allows a good characterization of the hydrological processes of the shallow subsurface of karst (e.g., Fu et al. 2015; Canora et al. 2008). Only few studies were conducted at the catchment scale (e.g., Charlier et al. 2012; Trček 2007), some at the regional scale, by comparing different systems (e.g., Aquilina et al. 2006; Martos-Rosillo et al. 2015), or by studying a system having a regional dimension (e.g., Fidelibus et al. 2016). Concerning the studies' climate conditions, a big part of them was conducted in temperate climates (continental, oceanic or Mediterranean) and some of them in a subtropical climate. To our present knowledge, only one was done under arid climatic conditions (Heilman et al. 2012).

From this review, the controlling factors of the karst shallow subsurface hydrodynamic identified are: (1) climate conditions, (2) antecedent moisture conditions, (3) soil properties and vegetation, (4) rock properties and karstification, and (5) topography and thickness.

Climatic Factors

Climatic factors are identified to control the hydrodynamic in the shallow subsurface of karst. Tadros et al. (2016) analyzed drip water composition in caves fed by fracture flow from an epikarst reservoir in a region dominated by El Niño–Southern Oscillation (ENSO). It appears that depending on the phase (El Niño or La Niña), the dissolution and precipitation conditions can change, and so flow pathway too. Similarly in Zhang et al. (2013), the temperature variation, according to the altitude, influences the hydrochemistry composition of the epikarst water. This affects dissolution and precipitation conditions and karstic weathering occurs. Indeed, temperature and CO_2 as well are important parameters in karstification processes. In Peyraube et al. (2013), they demonstrated that the epikarst air P_{CO_2} which determines the water aggressiveness against carbonate rock, shows annual variations. Lower values are found in winter in comparison with summer.

Temperatures, but also precipitation input, can have an influence on the shallow subsurface processes. Galibert (2015) used geophysics and modeling to quantify water storage and residence time at shallow depth in carbonate rocks. They concluded that during the winter season, the residence times are shorter in response to the increase in the effective rainfall. From a contaminant transport point of view, Pronk et al. 2008 found that rainfall conditions can have an impact on transport processes. Indeed, an augmentation of freshly infiltrated water contributing to deep percolation is observed with increasing rainfall intensity and duration. This water can transport considerable amounts of sediments and contaminants originating from the land surface and soil. In Jiang et al. (2008), the reaction of the epikarst to different rainfall amount and intensity have been studied and rainfall was identified to play the most important role in the variation of the epikarst spring. This confirms Klimchouk (2004)'s conclusion: climatic factors, as precipitation characteristics and temperature, have an important impact on karstification and karst processes.

Antecedent Moisture Conditions

Fu et al. (2015) experimentation confirms that the rainfall intensity has an influence on the epikarst reaction, as well as the antecedent moisture conditions. They simulated different rainfall events with varying intensities on a soil–epikarst trench excavation at southwest China, under different moisture conditions. They observed that a threshold rainfall depth has to be exceeded to initiate runoff, which depends on antecedent soil moisture conditions. Dry antecedent conditions allow a higher percentage of water to be stored in the epikarst but decrease subsurface flow. In comparison, under wet antecedent conditions a larger fraction of the infiltrating water reaches the subsurface trough concentrated pathways. An influence of antecedent hydraulic conditions was also observed by Houillon et al. (2017). In their study, which was conducted at Lascaux Cave, the contribution of different types of water according to the rainy solicitation and water saturation of the epikarst was recorded using natural tracers. Also using natural al tracers, Trček (2007) concluded that epiflow, diffuse flow, and storage depend on the soil and epikarst zone water saturation. According to these observations, in case of small water storage volume, most of the water is stored in the base of the epikarst zone and the water slowly seeps through little-fractured rock. In case of large water storage volume, one part of the water could rapidly drain through large fractures, the remained water is stored and diffuse recharge process is restored. Charlier et al. (2012) also highlighted the importance of the initial groundwater storage. They interpreted it as the state of hydraulic connectivity in the unsaturated zone, which leads to the variation of the recharge area of the karst system. According to the hydrological conditions, they also identified that the soil cover plays an important role in mixing and transfer for the recharge water.

Soil Properties and Vegetation

Perrin et al. (2003) also highlighted the mixing function of soil. They show that the soil architecture (porosity, fractures and soil crust, lithology) induces various flow pathways. Under unsaturated conditions, storage occurs within the soil matrix with limited flow rate, but when recharge takes place a part of fresh water can flow through the soil macropores and the matrix water becomes mobile and mixes with the infiltrating water. Tooth and Fairchild (2003) confirm that the flow pathways in the soil influence karst recharge processes. In their experiment that was conducted at a karst cave in southwest Ireland, a significant contrast of hydrogeochemistry composition between soil matrix flow and well-connected macropore flow was observed. During dry periods, soil matrix flow seems to dominate karst water infiltration while soil macropores flow are more important during wet periods.

The vegetation can influence recharge processes in karst system, too. Canora et al. (2008) studied the impact of land use evolution due to intensive agriculture on recharge in a karstic area in southeast Italy. It appears that the modification of soil by shattering the rock does not always induce important changes in infiltration rate, at least in the short time. However, the shattered stone practice coupled with intensive agriculture reduces considerably the infiltration rate. The vegetation is, in this case, the main factor affecting the recharge processes. In Heilman et al. (2012), increasing density of woody plants does not necessarily lead to increased water consumption by the plant. This is probably due to the constraints imposed by shallow soil with limited water storage capacity.

The general importance of soil and vegetation cover in karst systems is confirmed by other studies, too. Martos-Rosillo et al. (2015) concluded by reviewing 51 carbonate aquifers recharge assessment in the south of Spain that the difference in the development of the vegetal cover-soil–epikarst system is one of the explanations for varying infiltration coefficients. Fu et al. (2015) demonstrated in their experiments that less than 30% of the water was retained by soil and vegetation and more than 70% of the water was redistributed by the epikarst attributing a secondary but still important role to the soil and vegetation.

Rock Properties and Karstification

As the epikarst plays an important role in redistributing the water, its rock properties and karstification are considered as factors controlling the shallow subsurface flow processes. Another factor that controlled the variable infiltration coefficients found by Martos-Rosillo et al. (2015) is the difference between the degrees of karstification of each studies system. Depending on the rock properties, such as the distribution of small and large fractures, preferential flow pathways can be induced. In Zhang et al. (2013), a quick response of the system to a rainfall event was found to be a consequence of water flow from large fractures and conduits, while a slow response of the system originated from small fractures. Similar to the flow dynamics, the rock properties can also affect the storage capacity. For example, Champollion et al. (2017) compared epikarst storage in dolomite and limestone. Because dolomite presents a higher matrix porosity, its reservoir capacity can be more important compared to limestone. In addition, fractures in dolomite filled by residual sand caused by mechanic alteration allow a more efficient storage of water. In Galibert (2015), numerical simulations to estimate water storage and residence time in the epikarst show that the epikarst must be divided into two layers with different seismic properties: a high permeability upper layer and a second deeper layer with low permeability. Kogovsek and Petric (2014) used tracer tests to observe that the majority of the tracer is not rapidly infiltrated through high permeability part of the vadose zone but can be stored within the less permeable parts of the epikarst for several years to be gradually flushed out.

Topography and Thickness

A last important factor is the interface between the soil/epikarst and the less weathered carbonate rock below as it can strongly influence the water flow distribution (see also the previous subsection). Fu et al. (2015) observed subsurface runoff along this interface, triggered by a contrast between soil and rock permeability, and the (subsurface) topography as well. They notice that the epikarst topography can present a stronger control than the surface topography itself. The thickness of the shallow subsurface can also strongly influence water processes and so the groundwater vulnerability. The thick epikarst zone presents a higher abundance of slow-flow components than thinner epikarst zone, which often shows fast-flow components due to a higher proportion of large fractures (Zhang et al. 2013). Aley and Kirkland (2012) highlighted that in case of potential pollution, the shallow subsurface of karst has to be considered. For example, an artificial tracer test should be done from the surface or the top of the epikarst rather than through a well, even more when a thick soil and epikarst zone as to be expected.

Synthesis and Conclusions

Our review showed that the shallow subsurface of karst systems plays an important role for karstic recharge processes. Improving the knowledge about these processes and their controlling factors will contribute to a better water resources management as recharge is an important indicator for sustainable groundwater development.

Although by far not complete, the literature summary in Table 1 shows that various methods have been applied to study soil and epikarst processes from the plot to the regional scale. However, few studies apply these to a larger scale, and most of them use information acquired from the outlet of the system (epikarst springs measurements, flow discharge, drip cave hydrochemistry analyses…). Only a few studies (e.g., Heilman et al. 2012) apply schemes that monitor the processes directly at the surface of karst systems. Furthermore, only a few studies consider more than one study site (e.g., Martos-Rosillo et al. 2015) and studies that systematically compare the shallow subsurface dynamics of different karst systems, to our knowledge, have rarely been conducted.

From this present state, the following questions arise:

- How to study recharge processes at a larger scale?
- How to characterize the spatial variability of the soil/epikarst geometry (depth, hydraulic properties…)?
- How to quantify the processes occurring in the shallow subsurface of karst?

Experimental work in hydrological systems other than karst systems (Sprenger et al. 2015; Martini et al. 2015; Dorigo et al. 2011) has shown that monitoring shallow subsurface processes by soil moisture networks with a high spatial resolution provides important information to understand evapotranspiration and recharge processes. We believe that such approaches, added to the traditional methods to explore karst systems (Goldscheider and Drew 2007), will provide promising directions to better understand the storage and flow dynamics of the soil and epikarst. Supported with environmental tracer information such as water isotopic composition, this will allow understanding temporal and spatial variations of karstic recharge.

Systematically applied at different karst systems, such approach will also provide new insights into factors that control the importance of different soil and epikarst processes. That way, spatially transferrable methods to quantify groundwater recharge can be developed. These methods can support present water management and, if integrated into simulation models, provide more accurate predictions of future karst water availability. Although our study did not address the aspect of modeling the shallow subsurface of karst systems or the aspect of water quality of karst water resources, we hope that this overview provides some helpful directions for future research on the soil and epikarst processes in karstic regions.

Acknowledgements This work was funded by the Emmy Noether-Programme of the German Research Foundation (DFG; grant number HA 8113/1-1).

References

Aley, T.J., and S.L. Kirkland. 2012. 'Down but Not Straight down: Significance of Lateral Flow in the Vadose Zone of Karst Terrains'. *Carbonates and Evaporites* 27 (2): 193–98. https://doi.org/10.1007/s13146-012-0106-5.

Aquilina, L., B. Ladouche, and N. Dörfliger. 2006. 'Water Storage and Transfer in the Epikarst of Karstic Systems during High Flow Periods'. *Journal of Hydrology* 327 (3): 472–85. https://doi.org/10.1016/j.jhydrol.2005.11.054.

Bakalowicz, M. 2003. 'The Epikarst, the Skin of the Karst'.

Benavente, J., I. Vadillo, F. Carrasco, A. Soler, C. Liñán, and F. Moral. 2010. 'Air Carbon Dioxide Contents in the Vadose Zone of a Mediterranean Karst'. *Vadose Zone Journal* 9 (1): 126–36. https://doi.org/10.2136/vzj2009.0027.

Canora, F., M. D. Fidelibus, A. Sciortino, and G. Spilotro. 2008. 'Variation of Infiltration Rate through Karstic Surfaces Due to Land Use Changes: A Case Study in Murgia (SE-Italy)'. *Engineering Geology*, Engineering and environmental problems in karst, 99 (3): 210–27. https://doi.org/10.1016/j.enggeo.2007.11.018.

Champollion, C., S. Devile, J. Chéry, E. Doerflinger, N. Le Moigne, R. Bayer, and P. Vernant. 2017. 'Estimating Epikarst Water Storage by Time-Lapse Surface to Depth Gravity Measurements'. *Hydrol. Earth Syst. Sci. Discuss.* 2017 (August): 1–27. https://doi.org/10.5194/hess-2016-355.

Charlier, J.B., C. Bertrand, and J. Mudry. 2012. 'Conceptual Hydrogeological Model of Flow and Transport of Dissolved Organic Carbon in a Small Jura Karst System'. *Journal of Hydrology* 460–461 (August): 52–64. https://doi.org/10.1016/j.jhydrol.2012.06.043.

Dorigo, W.P. Oevelen, W. Wagner, M. Drusch, S. Mecklenburg, A. Robock, and T. Jackson. 2011. 'A New International Network for in Situ Soil Moisture Data'. *Eos, Transactions American Geophysical Union* 92 (17): 141–42. https://doi.org/10.1029/2011EO170001.

Dreybrodt, W. 1990. 'The Role of Dissolution Kinetics in the Development of Karst Aquifers in Limestone: A Model Simulation of Karst Evolution'. *The Journal of Geology* 98 (5): 639–55.

Fidelibus M.D., G. Balacco, A. Gioia, V. Iacobellis, and G. Spilotro. 2016. 'Mass Transport Triggered by Heavy Rainfall: The Role of Endorheic Basins and Epikarst in a Regional Karst Aquifer'. *Hydrological Processes* 31 (2): 394–408. https://doi.org/10.1002/hyp.11037.

Ford, D., and P.D. Williams. 2013. *Karst Hydrogeology and Geomorphology*. John Wiley & Sons.

Fu, Z. Y., H. S. Chen, W. Zhang, Q. X. Xu, S. Wang, and K. L. Wang. 2015. 'Subsurface Flow in a Soil-Mantled Subtropical Dolomite Karst Slope: A Field Rainfall Simulation Study'. *Geomorphology* 250 (December): 1–14. https://doi.org/10.1016/j.geomorph.2015.08.012.

Galibert P.Y. 2015. 'Quantitative Estimation of Water Storage and Residence Time in the Epikarst with Time-lapse Refraction Seismic'. *Geophysical Prospecting* 64 (2): 431–44. https://doi.org/10.1111/1365-2478.12272.

Goldscheider, N., and D. Drew. 2007. *Methods in Karst Hydrogeology: IAH: International Contributions to Hydrogeology, 26*. CRC Press.

Heilman J.L., M.E. Litvak, K.J.McInnes, J.F. Kjelgaard, R.H. Kamps, and S. Schwinning. 2012. 'Water-storage Capacity Controls Energy Partitioning and Water Use in Karst Ecosystems on the Edwards Plateau, Texas'. *Ecohydrology* 7 (1): 127–38. https://doi.org/10.1002/eco.1327.

Houillon, N., R. Lastennet, A. Denis, and P. Malaurent. 2017. 'Hydrochemical and Hydrodynamic Behavior of the Epikarst at the Lascaux Cave (Montignac, France)'. In *EuroKarst 2016, Neuchâtel*, edited by Philippe Renard and Catherine Bertrand, 319–26. Advances in Karst Science. Springer International Publishing.

Jiang, G.H, F. Guo, J.C. Wu, H.J. Li, and H.L. Sun. 2008. 'The Threshold Value of Epikarst Runoff in Forest Karst Mountain Area'. *Environmental Geology* 55 (1): 87–93. https://doi.org/10.1007/s00254-007-0967-4.

Király, L. 1975. 'Rapport sur l'état actuel des connaissances dans le domaine des caractères physiques des roches karstiques'. *Hydrogeology of karstic terrains (Hydrogéologie des terrains karstiques) International Union of geological sciences*, no. 3: 53–67.

Klimchouk, A. 1995. 'Karst Morphogenesis in the Epikarstic Zone'. *Cave and Karst Science* 21 (January): 45–50.

———. 2004. 'Towards Defining, Delimiting and Classifying Epikarst: Its Origin, Processes and Variants of Geomorphic Evolution'.

Kogovsek, J., and M. Petric. 2014. 'Solute Transport Processes in a Karst Vadose Zone Characterized by Long-Term Tracer Tests (the Cave System of Postojnska Jama, Slovenia)'. *Journal of Hydrology* 519 (November): 1205–13. https://doi.org/10.1016/j.jhydrol.2014.08.047.

Martini, E., U. Wollschläger, S. Kögler, T. Beherns, P. Dietrich, F. Reinstorf, K. Schmidt, M. Weiler, U. Werban, and S. Zacharias. 2015. 'Spatial and Temporal Dynamics of Hillslope-Scale Soil Moisture Patterns: Characteristic States and Transition Mechanisms', 2015, Vadose Zone Journal edition.

Martos-Rosillo, S., A. González-Ramón, P. Jiménez-Gavilán, B. Andreo, J. J. Durán, and E. Mancera. 2015. 'Review on Groundwater Recharge in Carbonate Aquifers from SW Mediterranean

(Betic Cordillera, S Spain)'. *Environmental Earth Sciences* 74 (12): 7571–81. https://doi.org/10.1007/s12665-015-4673-3.

Perrin, J., P.Y. Jeannin, and F. Zwahlen. 2003. 'Epikarst Storage in a Karst Aquifer: A Conceptual Model Based on Isotopic Data, Milandre Test Site, Switzerland'. *Journal of Hydrology* 279 (1): 106–24. https://doi.org/10.1016/S0022-1694(03)00171-9.

Peyraube, N., R. Lastennet, A. Denis, and P. Malaurent. 2013. 'Estimation of Epikarst Air PCO2 Using Measurements of Water Δ13CTDIC, Cave Air PCO2 and Δ13CCO2'. *Geochimica et Cosmochimica Acta* 118 (October): 1–17. https://doi.org/10.1016/j.gca.2013.03.046.

Pronk M., N. Goldscheider, J. Zopfi, and F. Zwahlen. 2008. 'Percolation and Particle Transport in the Unsaturated Zone of a Karst Aquifer'. *Groundwater* 47 (3): 361–69. https://doi.org/10.1111/j.1745-6584.2008.00509.x.

Sprenger, M., T.H.M Volkmann, T. Blume, and M. Weiler. 2015. 'Estimating flow and Transport Parameters in the Unsaturated Zone with Pore Water Stable Isotopes', 2015, Hydrology and Earth System Sciences edition.

Tadros, C. V., P. C. Treble, A. Baker, I. Fairchild, S. Hankin, R. Roach, M. Markowska, and J. McDonald. 2016. 'ENSO–Cave Drip Water Hydrochemical Relationship: A 7-Year Dataset from South-Eastern Australia'. *Hydrol. Earth Syst. Sci.* 20 (11): 4625–40. https://doi.org/10.5194/hess-20-4625-2016.

Tooth, A.F., and I.J. Fairchild. 2003. 'Soil and Karst Aquifer Hydrological Controls on the Geochemical Evolution of Speleothem-Forming Drip Waters, Crag Cave, Southwest Ireland'. *Journal of Hydrology* 273 (1): 51–68. https://doi.org/10.1016/S0022-1694(02)00349-9.

Trček, B. 2007. 'How Can the Epikarst Zone Influence the Karst Aquifer Hydraulic Behaviour?' *Environmental Geology* 51 (5): 761–65. https://doi.org/10.1007/s00254-006-0387-x.

Wada Y., P. H. van Beek Ludovicus, C.M. van Kempen, J.W.T.M. Reckman, S. Vasak, and M.F.P. Bierkens. 2010. 'Global Depletion of Groundwater Resources'. *Geophysical Research Letters* 37 (20). https://doi.org/10.1029/2010GL044571.

White, W. 2002. 'Karst Hydrology: Recent Developments and Open Questions'. *Engineering Geology* 65 (August): 85–105. https://doi.org/10.1016/S0013-7952(01)00116-8.

Williams, P.W. 1983. 'The Role of the Subscutaneous Zone in Karst Hydrology', 1983, Journal of Hydrology edition.

Williams, P.W. 2004. 'The Epikarst: Evolution of Understanding'. In *Epikarst*, 11–15.

———. 2008a. 'The Role of the Epikarst in Karst and Cave Hydrogeology: A Review'. *International Journal of Speleology* 37 (1). http://dx.doi.org/10.5038/1827-806X.37.1.1.

Williams, P.W. 2008b. 'The Role of the Epikarst in Karst and Cave Hydrogeology: A Review'. *International Journal of Speleology* 37 (1). http://dx.doi.org/10.5038/1827-806X.37.1.1.

Zhang, Z., Xi Chen, X. Chen, and P. Shi. 2013. 'Quantifying Time Lag of Epikarst-Spring Hydrograph Response to Rainfall Using Correlation and Spectral Analyses'. *Hydrogeology Journal* 21 (7): 1619–31. https://doi.org/10.1007/s10040-013-1041-9.

Use of Chlorophyll-a Monitoring to Determine Karst–River Relationships: A Case Study in the Karstic Limestones of Ouche Valley, Burgundy (France)

Thierry Gaillard, Nevila Jozja, James Morris, and Christophe Brossard

Abstract

The study of groundwater–river relationships is a challenge for water supply management. In order to provide an indicator for Inversac (Estavelle) events in a karstic aquifer, the water and sanitation department of Dijon Metropole tested a chlorophyll-a probe in addition to pressure and temperature probes. The field tests were performed in karstic Bathonian limestones near a canal, where eutrophication occurs in summer. The study site, called Crucifix site, was chosen based on tracer tests showing a probable infiltration of surface water. The Crucifix site gave the opportunity to study simultaneously a karst system in a natural spring alimented by a karstic conduit, and in a nearby well used for drinking water supply. The survey was performed during one week, with a pumping test lasting 24 h at the beginning of the survey. The results indicated that temperature and water level monitoring were not able to detect unambiguously inflow of surface water. In contrast, the chlorophyll-a probe allowed to detect reliably surface water inflow, because chlorophyll-a is naturally absent in groundwater. This form of monitoring is therefore a promising tool for water supply management and its implementation should be generalized for karstic springs influenced by surface water.

Keywords

Karst • Estavelle • Chlorophyll-a • Pumping test

T. Gaillard (✉)
CPGF-HORIZON, Avon, France
e-mail: tgaillard@cpgf-horizon.fr

N. Jozja
Cetrahe, University of Orleans, Orleans, France

J. Morris
VALEPORT, Totnes, UK

C. Brossard
HYDREKA, Lyon, France

C. Bertrand et al. (eds.), *Eurokarst 2018, Besançon*, Advances in Karst Science,
https://doi.org/10.1007/978-3-030-14015-1_8

Introduction

Over 20% of the world's population depends on karstic aquifers for drinking water (Ford and Williams 2007). In Europe, 21% of the surface is covered by carbonate rock outcrops (Chen et al. 2017). Karst aquifers are more susceptible to climate change than other groundwater resources (Yuan 1997; Loaiciga et al. 2000) and require increased protection and a thorough understanding of their properties and functioning. Adapted hydrogeological investigations (Bakalowicz 2005), tracer tests (Golscheider et al. 2008; Dewaide et al. 2016), hydrochemical surveys (Hunkeler and Mudry 2007) and time series analyses (Mangin 1984; Padilla and Pudillo-Bosch 1995) are typically used to study karst aquifers.

Understanding the relationship between karst discharge zones and surface water is important because numerous drinking water plants are supplied by karstic springs near rivers, lakes or marine basins. Depending on water levels, the spring network (conduit or fissures) can either act as a sink where surface water can infiltrate, or as a spring where groundwater is discharged to the surface [termed "Estavelle" or "Inversac" in reference to Languedoc, France (Gèze 1987)]. In this paper, the term Estavelle is used to describe a drain hole which can either act as a discharging spring at high groundwater level, or as a sinkhole that contributes to recharge a karst aquifer at low groundwater and/or high surface water level conditions. Estavelles represent a major contamination risk for karstic groundwater resources, they should therefore be identified and qualified in order to manage drinking water supply. We will call in the following "Estavelle events" all interactions between surface water and underground karst aquifers through Estavelles.

Basically, the different chemical compositions of surface and groundwater could be used to identify Estavelle events in hydrochemical surveys, e.g. in coastal environments (Bonacci et al. 1995). However, surface and groundwater have often similar characteristics, necessitating the use of very specific parameters for differentiation. On the other hand, standard probes for continuous monitoring are limited to a restricted number of physico-chemical parameters (typically pH, conductivity, temperature, dissolved oxygen). These limitations were encountered in the karstic aquifers in Burgundy, where Callovian springs give rise to streams, which disappear in sink holes and feed the Bathonian karstic aquifer. Solar irradiation and microbial organisms can affect the chemistry of rivers and lakes through photosynthesis, leading to diurnal variations in conductivity, pH and water temperature (Montety et al. 2011). Such variations could potentially be used to identify the presence of surface water in karst aquifers. However, diurnal variations in surface water can be affected by meteorological events (Hess and White 1993) and daily peaks may be masked after infiltration into the karst due to the inertia of the system (Huang 1967). Algae, which contain chlorophyll-a, develop only in surface waters exposed to sunlight. Chlorophyll-a is therefore absent in groundwater could thus be used to discriminate between surface and groundwater and to detect Estavelle events. To our knowledge, chlorophyll has so far not been used as tracer in karstic investigations, except in illuminated areas of caves where prehistoric paintings were endangered by algae growth (Mulec and Kosi 2009). In surface water, chlorophyll is particularly interesting as an indicator for eutrophication (OECD 1982) or groundwater-dependent ecosystems (Eamus et al. 2015). Chlorophyll fluorescence is therefore a very useful tool to detect a large variety of stressors in karstic aquifers.

This paper presents an applied research project designed to test the feasibility of chlorophyll tracing for the identification of Estavelle events and to compare the results with more classical survey methods. In order to evaluate the risk of Estavelle events in its karstic drinking water resources, Dijon Metropole has tested different approaches based on classical hydrogeological investigations such as tracer tests, water level monitoring and chemicals analyses. The present study is based on continuous monitoring using a temperature–pressure probe associated with a fluorescence sensor (Valeport) and a logging/telemetry system (Hydreka). The installation of the equipment at the Crucifix spring was realized by hydrogeologists of Dijon Metropole and CPGF-HORIZON.

Chlorophyll represents an interesting parameter to identify river–karst interactions along the River Ouche. Chlorophyll-a is not easy to quantify using indirect methods such as temperature or nitrogen concentrations (Kotak et al. 1995). Direct methods are based on photometry, fluorescence or high-performance liquid chromatography (HPLC). Due to failures in laboratory analyses using water collected by samplers in the past, this new study using in situ monitoring was implemented in the Crucifix karstic system. After detailing some principles of fluorescent measurement techniques in Section "TraceFLO Probe Development", the TraceFLO probe is briefly described in Section "Description of TraceFLO probe". The test site, the TraceFLO system implementation and principal results are then described in Section "Geological Setting and Field Test".

Principles of Fluorescent Measurement Techniques

Principles of Fluorescent Spectroscopy

Fluorescent spectroscopy can be used to provide real-time in situ characterization of fluorescent substances (natural or artificial tracers). Fluorescent substances absorb light at specific wavelengths (excitation) and re-emit at longer wavelengths (emission). The usefulness of fluorescence is being constantly improved by advances in optical technology (Smart et al. 1998; Pellerin et al. 2012).

Chlorophyll fluorescence is one of the most popular techniques utilized in aquatic systems because a great deal of information can be collected at a relatively low cost: light energy absorbed by chlorophyll molecules can (i) drive photosynthesis; (ii) be re-emitted as heat; or (iii) be re-emitted as light (fluorescence). The total amount of chlorophyll fluorescence is very small in comparison with the total light absorbed (Falkowski and Raven 2007).

TraceFLO Probe Development

Description of TraceFLO Probe

In situ chlorophyll fluorometers date back to 1981 (Aiken 1981). Though refinements have been made (LEDs replace to incandescent lamps), the basic concept is unchanged. Photosynthetic cells (algae) are irradiated with an excitation beam (typically a 470-nm LED passed through an absorption bandpass filter to remove long wavelength emissions). This light is absorbed by various pigments (chlorophyll-a, b, carotenoids etc.) in the cell and the excitation energy passes down the photosynthetic chain to the reaction centres which always contain chlorophyll-a. Some of this excitation energy is lost as fluorescence (peak around 700 nm) which passes through an excitation filter (dielectric bandpass filter with additional absorption bandpass filter) and onto a photodetector (silicon photodiode). The photon energy is converted into a photocurrent which is then converted into a voltage

Table 1 Technical specifications

Performance	Chlorophyll-a
Excitation	470 nm
Detection	696 nm
Dynamic range	0–800 µg/l, 2 gain settings: 0–40 µg/l, 0–800 µg/l
Instrument detection limit	0.025 µg/l (3 × SD in RO water)
Linearity	0.99 R^2
Response time	0.03–2 s
Physical	
Materials	Titanium with glass window
Depth rating	6000 m
Dimensions	40 mm Ø × 179.5 mm (including connector)
Weight	0.5 kg
Operating temp	35 °C max

using a transimpedence amplifier. Synchronous detection methods are used to remove DC components in order to enhance ambient light rejection enabling use in daylight. The signal is digitized and output in serial mode to a suitable logger/device.

Technical specifications of the TraceFLO probe are described in Table 1 (see www.valeport.co.uk/Products/Optical-Sensors for details).

Laboratory Calibration

A gold-standard chlorophyll-a unit is calibrated in 3 solutions for each of 2 different gain settings (Chl-a derived from algae containing no chlorophyll-b diluted in 90% acetone/10% RO water) with spectroscopic evaluation of concentration (Fig. 1). As chlorophyll is both temperature and light sensitive, the temperature-sensitive sensors are temperature-stabilized prior to immersion in the calibration solution. The LED is then turned on for a brief period only, to perform the calibration, as excessive exposure to light will cause photo-degradation of the solution. The 6 spectroscopically verified chlorophyll-a solutions (typically 5, 10, 20, and 100, 200, 400 µg/l) are stored in the dark at −20 °C in a freezer (Fig. 2).

As the chlorophyll scale factor is derived using a pure chlorophyll-a solution, the absorption spectra will be much narrower than that encountered in an in situ assemblage of phytoplankton where other chlorophylls and accessory pigments enhance spectral absorption efficiency. If quantitative results are required, it is recommended that the user performs a field characterization of the instrument where it will be used to derive a scale factor (comparing the instrument output with either a known concentration of phytoplankton

Fig. 1 Calibration curve with fitted points showing linearity

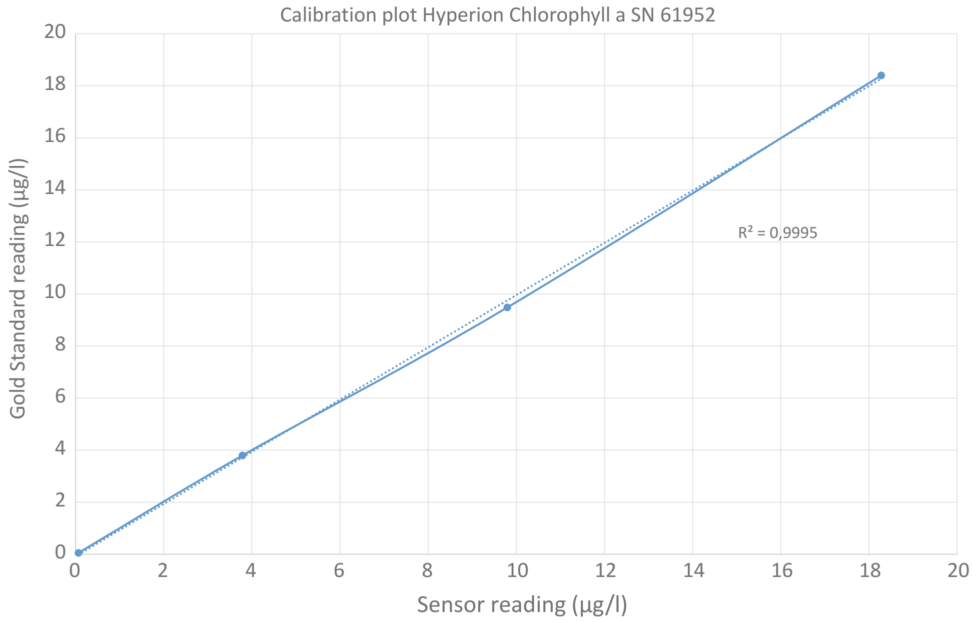

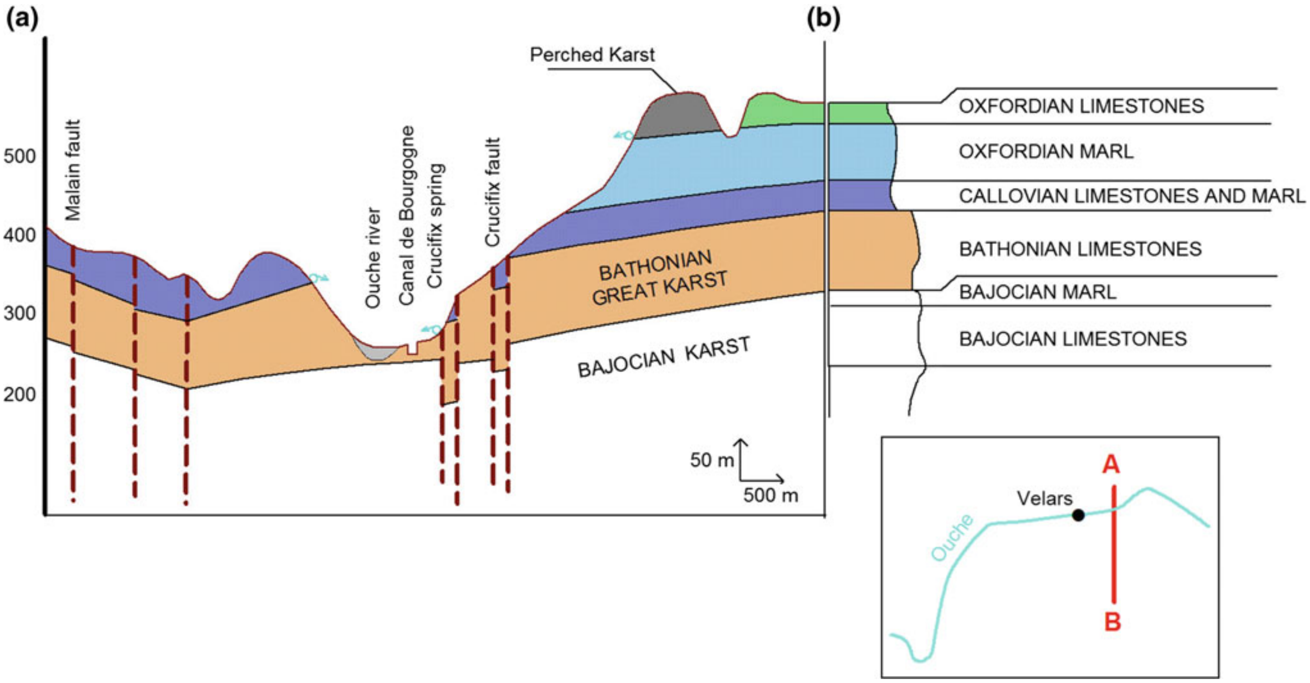

Fig. 2 Geological cross section of Ouche valley near Crucifix karst

or the chlorophyll-a concentration derived using HPLC techniques). For monitoring of events, qualitative results are sufficient and a field calibration is not required.

Geological Setting and Field Test

Geological Setting of the Ouche Valley

Dijon is situated between two geological domains separated by a major fault system: the plain to the SE is a tectonic graben filled with clastic sediments of mainly Miocene age (Bresse plain), which is delimited to the NW by a plateau with outcropping Jurassic limestones (côte de Bourgogne).

The Ouche river drains many karstic springs from Bajocian and Bathonian limestones. The river discharge increases downstream, except near Pont-de-Pany, where the river loses water. The Ouche river comes along with a canal (Canal de Bourgogne) built during the eighteenth and nineteenth centuries. The canal is fed by the Ouche river and karst springs diverted directly into the canal. The presence of the canal modifies considerably the hydrology of the valley and the underlying karst aquifer. Interactions occur all along the valley through Estavelles, acting as a discharging springs or sinking points depending on the hydrologic gradient between the karst and the canal locks.

The water for Dijon Metropole and many villages water is supplied by karstic springs from the Ouche valley; the protection of the karstic resources is therefore of fundamental importance for the city water services and its delegated manager, Suez Eau France.

Several drinking water resources in the Ouche Valley (Morcueil spring, Crucifix spring, Plombières well, Gorgets well field) are thought to be in exchange with surface water (the Ouche River and Burgundy Canal) as indicated by tracer tests (Corbier 2000).

Characterization of this karst–river relationship is challenging because surface and karstic water have very similar physico-chemical characteristics and because the karstic aquifer is dependent on meteorological conditions and water resource management. Previous studies used major (Na, Cl, SO4, Ca, Mg) and minor elements (Sr, Bo, Ba) in combination with continuous monitoring of pH, conductivity, dissolved oxygen and temperature of both river and spring waters (Corbier 2000; Gaillard and Bernard 2015). In the case of water sampling, the variations of physico-chemical parameters are often buffered during transport (pH and temperature) and the calco-carbonic equilibrium fluctuates with photosynthesis.

Study Site and Tracer Tests

Dijon Metropole decided to monitor the Crucifix karstic system in order to test whether chlorophyll-a probes can be used to detect Estavelle events (Fig. 3). Karstic water was sampled in a large-diameter well in the Comblanchien limestone (Bathonian). This well is located near the major

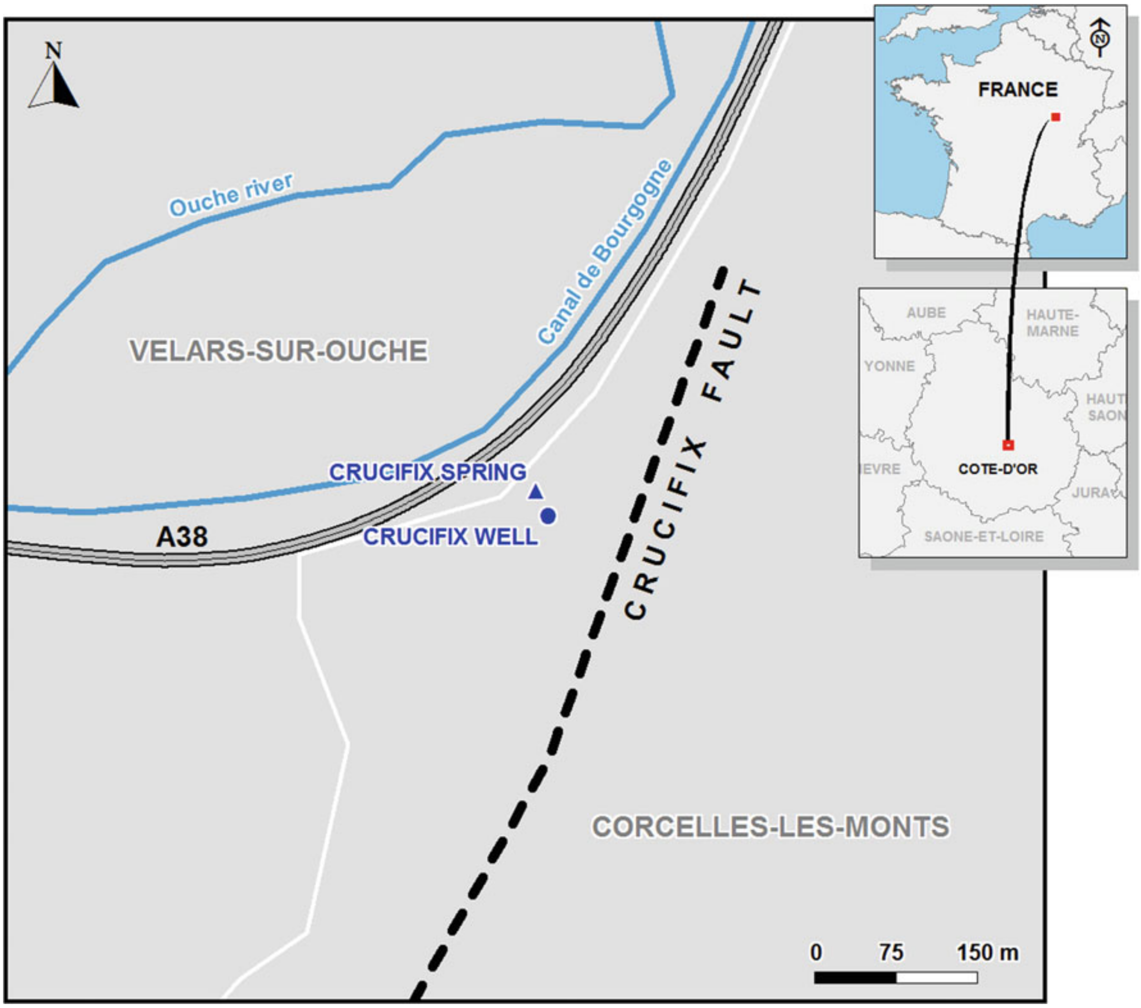

Fig. 3 Location of Crucifix karstic system

conduit that feeds the Crucifix spring. The Canal de Bourgogne runs between the karst and Ouche river. The spring and the well are located 45 and 56 m from the canal, respectively.

The Crucifix well was constructed for drinking water supply following a geophysical survey (CPGF 1969). This new well was necessary because the spring used until then for water supply was too close and situated below a new highway, the A38 built between 1971 and 1973 (Fig. 3). The primary question was how canal water might influence the quality of the karst water. During summer, eutrophication occurs in the canal and chlorophyll-a could potentially be used as a biological tracer. At the same time, chlorophyll-a in the Ouche river is very low, below the detection limit of 1 µg/l (Gaillard and Bernard 2015). The Crucifix site is thus a good candidate to test chlorophyll-a monitoring in surface and groundwater, and the site was therefore equipped with TraceFLO systems during summer 2017.

Field Implementation

The field equipment included pressure probes for water level monitoring, temperature sensors, and TraceFLO optical sensors for chlorophyll-a concentrations. The pressure/temperature sensors were programmed to sample once every 30 s. The atmospheric pressure was measured at the same rate in order to correct the water levels. The TraceFLO sensors were programmed to sample every six minutes.

The monitoring equipment was installed in summer 2017. The TraceFLO sensors in the well and the spring were located in complete darkness. In the canal, the sensor was installed at 1.5 m depth on the southern bank, beneath shady trees. All water reference levels were provided by a certified surveyor.

During the survey, a pumping test was performed in the well in order to test the relationship between the canal and karst system. A step drawdown well-pumping test was

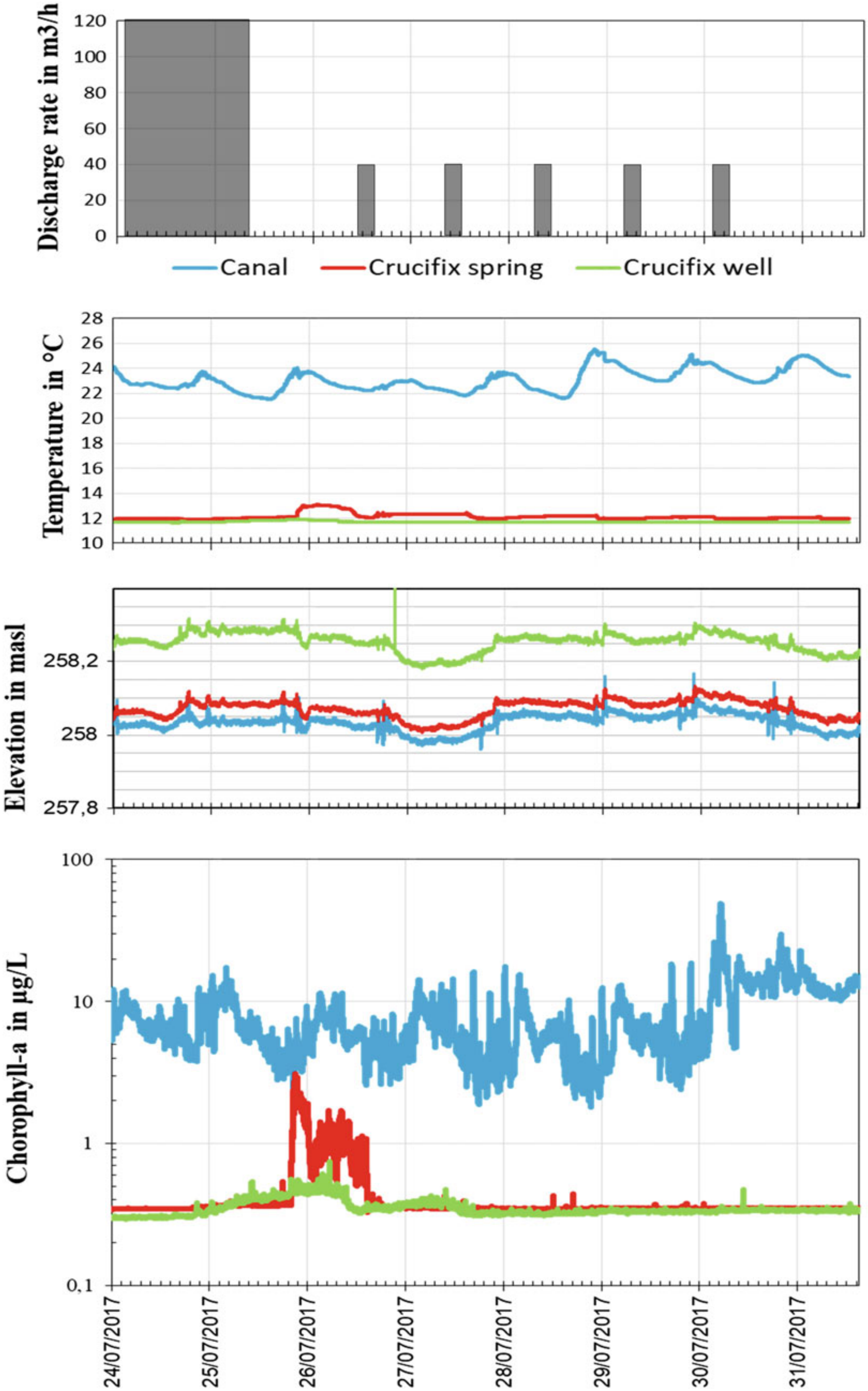

Fig. 4 Results of the Crucifix karstic system monitoring

performed between 09:00 on 24/7/17 and 14:00 on 25/7/17 (pump rates 56, 99 and 141 m^3/h for 1 h) followed by a steady state pumping test (120 m^3/h for 24 h). After 14:00 on 25/7/17, the pump rate was maintained at 40 m^3/h during 2 h per day to maintain the water supply.

Results and Interpretation

The water levels are the first main results to interpret. Figure 4 shows that the water level in the well is 20 cm above the water levels in the canal and in the spring. The canal water level controls the system and the variations observed in the canal are also visible in the karst. The step drawdown test revealed a minor drawdown in the well of only 1 cm at a pumping rate of 50 m^3/h, with level stabilization within 2 min (4 measurements). This specific drawdown discharge indicates an important well supply by a karstic conduit. The connection with a conduit was also suspected following reinterpretation of previous tracer surveys (Gaillard and Bernard 2015). The water levels in the canal and the spring were much closer (average difference between spring and canal = 3.2 cm; maximum positive difference = +10.4 cm; maximum negative difference = −5.6 cm). The absolute accuracy of levelling is about 5 cm, signifying that the water levels in the canal and spring were identical within error limits.

Analysing the temperature plots (Fig. 4b), the diurnal variation for surface water was 21.5–25.5 °C with a daily maximum at approximately 16:00. In the well, the water temperature was relatively constant, with variations of 0.1 °C on 25/7/17 at 12:00. The spring water temperature varied between 11.8 and 13 °C. Estavelle phenomena or solar radiation on the building could explain such variations. For example, the variations due to solar radiation occurred during the last days (27–31) of July with a typical trend: a slow increase following sunrise and a rapid decline following sunset. At 16:00 on 26/7/17, the temperature increased with a different trend, 26 h after the end of the pumping test. This variation could be due both to air temperature (24 °C) and canal inflow (the water temperature signal is degraded). Temperature monitoring is therefore not an ideal parameter for identifying river inflow due to a variety of competing factors.

The chlorophyll-a data are more significant. The diurnal signal in surface water varied between 3 and 45 µg/l (mean 8 µg/l). In the karstic system, the background level in water was equal to the sensor's minimum detection limit (0.025 µg/l). However, two pronounced peaks were observed: first on 25/7/17 in the well, followed by a more significant peak in the spring (3 µg/l on 26/7/17), note the logarithmic scale in Fig. 4). These two events were correlated with temperature variations. These data thus indicate that at a very low hydraulic gradient, transfers occurred from the canal to the karst conduit of the Crucifix spring. The well, thought to be fed by an annex system of the conduit or by a parallel conduit, was less contaminated than the spring, where the chlorophyll-a concentrations were closer to those in the canal. The end of the monitoring did not present the same behaviour, suggesting that the exchanges were also influenced by other parameters, which, however, have not yet been clearly identified (boundary conditions of the system, delay from the canal to the karst, chlorophyll conservation in the karst etc.).

Conclusions

The presence of Estavelles in the Ouche valley connecting surface hydrology and karst was originally proposed by Curtel in 1911. Dijon Metropole and Suez Eau France attempted to identify Estavelle events using continuous physico-chemical surveys and discontinuous chlorophyll-a analyses, however without conclusive results. The Crucifix field test presented here indicates that Estavelle interactions may occur between the canal and the karst at low hydraulic gradient. The results demonstrate that the spring drains a major conduit, whereas the well is connected to an annex system of the conduit or to another conduit. The continuous chlorophyll-a monitoring technique provides new perspectives for Estavelle studies and explains the past failures based on classical methods. Estavelle events are complex and cannot be characterized by simple physico-chemical monitoring. In contrast, chlorophyll-a concentrations in surface waters are two orders of magnitudes greater than in groundwater and, as shown by the present study, offer therefore the possibility to monitor surface infiltration in karst aquifers. Another contribution of this study are new insights into spring catchment delineation. Each tracer injection was drained by a karstic unit and appeared in downstream springs due to Estavelle interactions with the canal. Consequently, the delineation of each karstic unit could be considered with a groundwater basin and an Estavelle phenomena.

The experiment presented here is the first step of an applied groundwater research programme. In future, we plan to combine continuous chlorophyll-a monitoring by probes with automatic water samplers, in order complete the probe data with laboratory analyses of all forms of phytoplankton (chlorophyll-a and chlorophyll-b). Future applications of chlorophyll-a monitoring by optical probes may also include non-karstic environments, e.g. to identify surface infiltration during groundwater pumping in porous aquifers near rivers or abandoned quarries.

Acknowledgements This study would not have been possible without the support and the interest of Dijon Metropole and Suez Eau France. The authors dedicate this paper to Yves Lemoine, CPGF geophysicist, who first proposed the location of the Crucifix well after geophysical prospecting.

References

Aiken J (1981) A chlorophyll sensor for automatic, remote, operation in the marine environment. Marine Ecology Progress Series, 4(2): 235–239

Bakalowicz M (2005) Karst groundwater: a challenge for new resources. Hydrogeology Journal, 13 (1): 148–160

Bonacci O, Fritz F, Denić V (1995) Hydrogeology of Slanac Spring, Croatia. Hydrogeology Journal, 3 (3): 31–40

Chen Z, Auler AS, Bakalowicz M, Drew D, Griger F, Hartmann J, Jiang G, Moosdorf N, Richts A, Stevanovic Z, Veni G, Goldscheider N (2017) The World Karst Aquifer Mapping project: concept, mapping procedure and map of Europe. Hydrogeology Journal 25: 771–785. https://doi.org/10.1007/s10040-016-1519-3

CPGF (1969) Etude géophysique. Faille du Crucifix. AEP de Corcelles-les-Monts. Rapport CPGF

Corbier P (2000) Mise en évidence d'une alimentation des aquifères poreux plio-quaternaires par les massifs karstiques de bordure, Etude des relations entre la côte et l'arrière-côte dijonnaises et la plaine de Bresse, Thèse Université de Bourgogne

Curtel G (1911) Les eaux de Dijon, in Dijon et la Côte d'Or, 40ème cong. Association Française pour l'avancement des Sciences, Dijon, III: 395–421

Dewaide L, Bonniver I, Rochez G, Hallet V (2016) Solute transport in heterogeneous karst systems: dimensioning and estimation of the transport parameters via multi-sampling tracer-tests modelling using the OTIS (One-dimensional Transport with Inflow and Storage) program. J Hydrol 534:567–578. https://doi.org/10.1016/j.jhydrol.2016.01.049

Eamus D, Zolfaghar S, Villalobos-Vega R, Cleverly J, Huete A (2015) Groundwater-dependent ecosystems: recent insights from satellite and field-based studies Hydrol. Earth Syst. Sci., 19: 4229–4256, https://doi.org/10.5194/hess-19-4229-2015

Falkowski P, Raven J (2007) Aquatic Photosynthesis. 2nd Edition

Ford D, William P (2007) Karst hydrogeology and geomorphology, Wiley, Chister, UK

Gaillard T, Bernard A (2015) Etude des bassins d'alimentation des sources alimentant le Grand Dijon et Messigny-et-Vantoux: Caractérisation de la ressource et délimitation des AAC de Morcueil. SUEZ Consulting report 13DRE045, 342p

Geze B (1987) Les mésaventures des sources de l'Estavelle et de l'Inversac en Languedoc Méditerranéen. International Journal of Speleology (16): 101–109

Goldscheider N, Meiman J, Pronk M, Smart C (2008) Tracer tests in karst hydrogeology and speleology. Journal of Applied Geophysics/International Journal of Speleology, 37 (1): 27–40

Hess JW, White WB (1993) Groundwater geochemistry of the carbonate karst aquifer, southcentral Kentucky, U.S.A. Applied Geochemistry, 8 (2): 189–204, https://doi.org/10.1016/0883-2927(93)90034-e

Huang JC (1967) Quality of surface and subsurface water in a Missouri carbonate karst terrain (Dry Fork, Norman, and Benton Creek watersheds). Dissertation, University of Missouri

Hunkeler D, Mudry J (2007) Hydrochemical methods in Goldscheider N., Drew D. (2007) Methods in karst hydrogeology. Taylor&Francis, London: 93–122

Kotak BG, Lam AK-Y., Prepas EE, Kenefick SL, Hrudey SE (1995), variability of the hepatotoxin microcystin-lr in hypereutrophic drinking water lakes. Journal of Phycology, 31: 248–263. https://doi.org/10.1111/j.0022-3646.1995.00248.x

Loaiciga HA., Maidment DR., Valdes JB (2000) Climate-change impacts in a regional karst aquifer, Texas, USA. Journal of Hydrology, 227 (0): 173–194

Mangin A (1984) Pour une meilleure connaissance des systèmes hydrologiques à partir des analyses corrélatoire et spectrale. Journal Of hydrology, 67: 25–43

(de) Montety V, Martin JB, Cohen J, Foster C, Kurz MJ (2011) Influence of Diel Biogeochemical Cycles on Carbonate Equilibrium in a Karst River. Chemical Geology. 283: 31–43, https://doi.org/10.1016/j.chemgeo.2010.12.025

Mulec J, Kosi G (2009) Lampenflora algae and methods of growth control. Journal of Cave and Karst Studies, 2009, 71 (2): 109–115

OECD (1982) Eutrophication of Waters. Monitoring, Assessment and Control published in French OCDE (1982). L'eutrophisation des eaux. Méthodes de surveillance, d'évaluation et de lutte. OCDE, Paris

Padilla A, Pulido-Bosch A (1995) Study of hydrographs of karstic aquifers by means of correlation and cross-spectral analysis, J. of Hydrology, 168: 73–89

Pellerin BA, Bergamaschi BA, Horsburgh JS (2012). In situ optical waterquality sensor networks – Workshop summary report. USGS Open-File Report 2012–1044, 13 p

Smart C, Zabo L, Calvin Alexander E Jr, Worthington SRH (1998) Some advances in fluorometric techniques for water tracing. Environ Monit Assess 53:305–320

Yuan D. (1997) Sensitivity of karst process to environmental change along the PEP II transect, Quaternary International, 37: 105–113, https://doi.org/10.1016/1040-6182(96)00012-2

Karst–River Interaction, Elaboration of an Indicator of the Karst Hydrological Conditions Applied to the Cèze River (Gard, France)

Hervé Chapuis, Jordan Ré-Bahuaud, Joël Jolivet, Frédéric Paran, and Didier Graillot

Abstract

In the interest of creating a point of reference allowing to know the hydrological conditions of the karst system and for the purpose of using it as a parameter in a modeling procedure, a Hydric Indicator of the Karst (HIK) was established from the knowledge acquired on the functioning of the karstic hydrosystem of the Cèze. This indicator makes it possible to identify and qualify if at a specific moment "t" the karst is more able to contribute to the flow of the river or on the contrary to infiltrate precipitation water. The HIK is constructed from the data collected at the Ussel spring and the MétéoFrance rain gauge at the karst plateau of Méjannes-le-Clap (Gard, France). Chronic rainfall and discharge measurements from the source include two hydrological cycles. The discharge of the spring is calculated from the recordings of water amounts from autonomous water level probes. These water levels are converted into discharge through a calibration curve drawn for this study. For rain events with at least 4 mm of precipitation, ten parameters on rainfall characteristics and the flow rate of the Ussel spring are analyzed to obtain the HIK. In total, 74 events were analyzed. Finally, this indicator is a relevant entry for the simulation of flow variations in the river within its karst canyon. It is also a relevant tool for institutions which monitor the condition of the karst aquifer and thus can be a useful tool for the management of the aquifer. Our goal was to develop an approach, with which we can calculate and predict, what will be the response at karst spring, if we know current discharge of the Ussel spring and expected amount of rainfall.

Keywords

Karst • Hydrological indicator • Spring discharges • Cèze River

Introduction

Karst aquifer studies arouse a great interest given the fact that they represent important freshwater resources. According to (Ford and Williams 1989/2007), the karst rocks cover 7–10% of the Earth's surface and supply drinking water to about 25% of the world's population and most of studies mention larger areas underlain by carbonate rocks from 15 to 20% (WoKAM 2017; White 1988; Ford and Williams 2007). Karst systems are characterized by the underground flows (Bakalowicz 2005). In order to understand the underground flows, many models integrate data of karst system (Kiraly 1998; Jourde et al. 2007; Johannet 2011; Fleury et al. 2011; Bailly-Comte et al. 2010 and Bailly-Comte et al. 2012), but this work focuses to elaborate an indicator which represents the hydrological condition of the karst. The results of this work can give perspectives for future modeling of the karst system.

The interactions between the karst system and the river, in terms of flow quantities, vary during a hydrological cycle. Identification of responses of karst aquifers is very important to protect people from flooding and for sustainable development of groundwater management.

H. Chapuis (✉) · F. Paran · D. Graillot
UMR EVS 5600, Department Process for Environment and Georesources, Saint-Etienne School of Mines, University of Lyon, 158 Cours Fauriel, CS 62362 42023 Saint-Etienne, France
e-mail: h.chapuis@groupeginger.com

F. Paran
e-mail: paran@emse.fr

D. Graillot
e-mail: graillot@emse.fr

J. Ré-Bahuaud
UMR EVS 5600, University of Lyon, 18 rue Chevreul, CS 69362 Lyon, France
e-mail: jordan.re-bahuaud@emse.fr

J. Jolivet
UMR 7300 ESPACE, University of Nice-Sophia-Antipolis and CNRS, Nice, France
e-mail: joel.jolivet2@wanadoo.fr

C. Bertrand et al. (eds.), *Eurokarst 2018, Besançon*, Advances in Karst Science,
https://doi.org/10.1007/978-3-030-14015-1_9

Hydrogeological Context of the Studied Area

Located in a large karstic area in the South of France between the Ardèche and the Cèze Rivers, both tributaries of the Rhône River (Fig. 1), the study area is the subject of a multidisciplinary study which aims to characterize exchanges between aquifer and Cèze river (Ré-Bahuaud et al. 2015). This study area is an attempt to meet a territorial policy, in order to obtain a sustainable management of streams and aquifers. In this location, the Mediterranean climate induces a period of drought in summer and high flood in autumn. The karst area is a calcareous plateau incised by the Cèze River. Sometimes, during drought period the Cèze River may dry up and the water from the river infiltrates into the calcareous aquifer (Chapuis et al. 2017). This calcareous plateau is geologically and hydrogeologically well studied, including by borehole investigations, karstic network investigations and especially previous groundwater tracing (Jolivet 2013; Pouzancre 1971). The size of the recharge area is about 200 km^2, amount of the outflow can be estimated to 2 m^3/s for the minima flow during dry period and can rise to 200 m^3/s in winter so that average is not relevant. Highest discharge of studied springs is about 2 m^3/s (Maranade spring). Geological studies suggest interactions between river and Lower Cretaceous formations, Barremian and Lower Aptian (so called Urgonian) formations which is a highly karstified calcareous geological unit. Whether on the Cèze right bank, some springs may dry up during drought period. The interactions between the karst system and the river, in terms of flow quantities, vary during

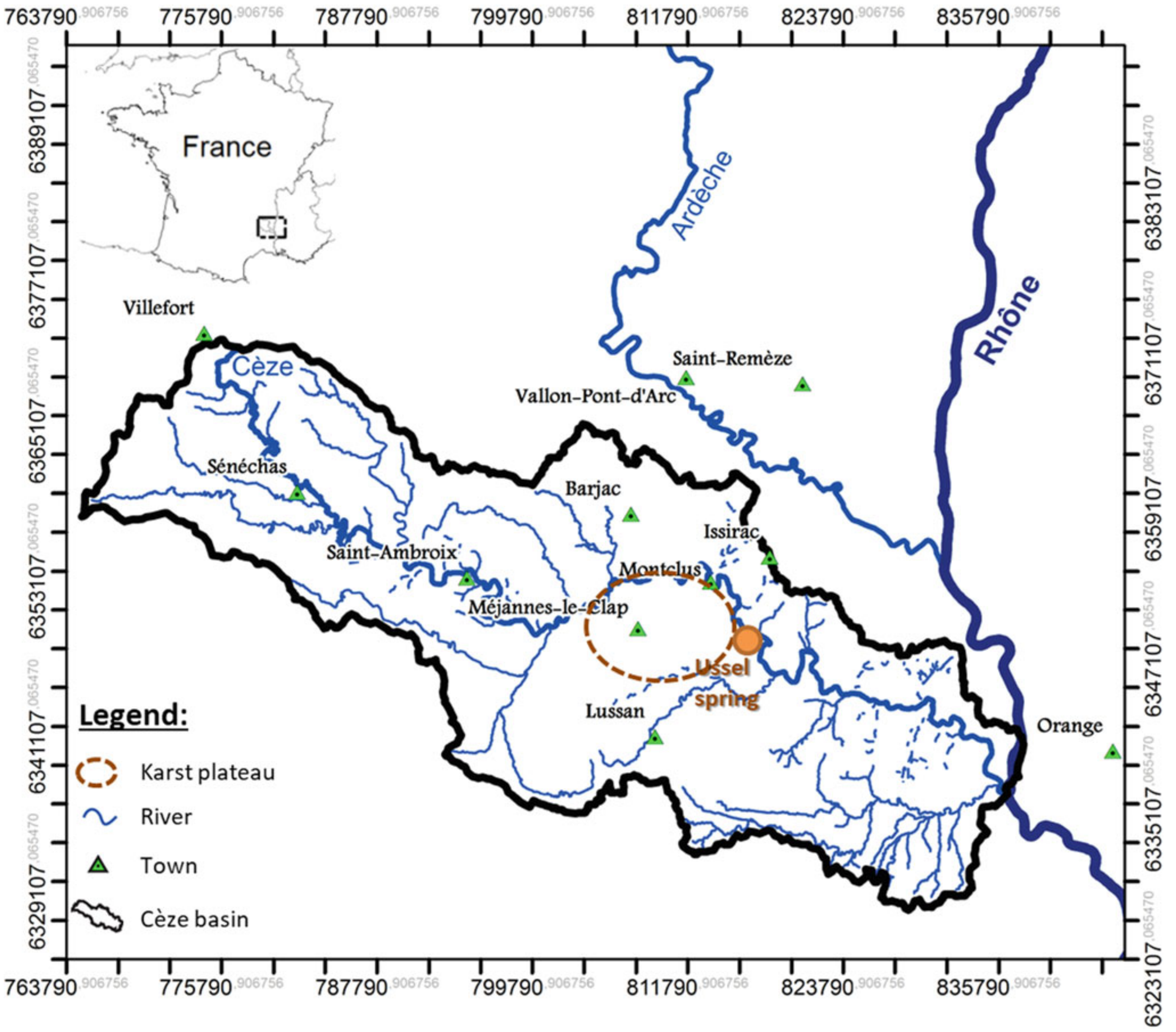

Fig. 1 Location map of the study area

a hydrological cycle. In this karst system, water sinking is caused by contacts between specific formations and fault thrust zones.

Hydrological Indicator of the Karst

The construction of the approach is based on the observation of the different parameters recorded at karst springs and rainfall events, for settings that might range from exhausted to saturated. Following the design of this indicator, the aim of the study is the construction of the model with the help of this hydrological indicator. The information about the water balance in karst aquifer can then be used for anticipating the accentuated or attenuated shape of a river or spring hydrograph after a rainfall event.

Though many data may be available, for a simplified and manageable job it is imperative to have a well-adapted time step. Representative data set of the karst hydrosystem is required to design a reliable model. For this reason, the Ussel spring data were selected, as a tracer data showing that they probably represent a large karst basin. Precipitation data from Méjannes-le-Clap Plateau also represent as well as the Méjannes-le-Clap precipitation data from MeteoFrance that represent an uninterrupted longterm data set.

These data were subjected to an event-related analysis. In fact, within these two time-related data sets, we analyzed the hydrological response of the spring for a rainfall event with at least 4 mm of precipitation. Selection of such intensive rainfall events enables identification of event that affects spring discharge. If the analysis comprises events of such a weak intensity, it is to clearly mark the distinction between rainfall events that affect spring flow, and those that are too weak and thus are buffered by the karst network and also capped by evapotranspiration. Depending on initial conditions, rain events which have less than 4 mm of precipitation have no influence on springs discharge and are not significant since there are buffered by the karst network. Such rainfall and flow rate data provide several parameters for each event:

- volume of precipitated water (in mm),
- intensity of precipitation (mm per 1, 2, 5 h and per 10 h),
- maximum intensity of precipitation,
- center of gravity of the rainfall hydrograph (in mm/h),
- cumulative rainfall several days before a remarkable rainfall event (mm in 3d, 15d and 30d),
- initial stage at the spring (in L/s),
- total water volume transiting through the spring during one high water event,
- total water volume transiting through the spring during one high water event less base volume (m^3),
- center of gravity of the spring hydrograph (m^3)
- maximum flow rate transiting through the spring (m^3/s).

These parameters are obtained by the analysis of the hydrological response at the rainfall events. The flow rate parameter of the Ussel spring results from the stage recorded with an autonomous probe. This database is converted in flow rate thanks to a tare curve.

A total of 74 events have been analyzed from 2013 to 2015.

HIK is given by the correlation curve of precipitation versus Ussel spring discharge.

Construction of the Hydrological Indicator

The hydric conditions of karst system are divided in three ranges corresponding to the colors green, yellow and black in Fig. 2.

This study was done using manual iteration (without computer assistance) and comparing the evolution of ten parameters, previously described.

The first range = HIK 1 (hydric indicator of karst) = initial flow rate of Ussel spring is lower than 220 L/s.

The second range (consider as the period of transition between HIK 1 and HIK 3) = HIK 2 = initial flow rate of Ussel spring is ranging from 220 to 350 L/s.

The third range = HIK 3 = initial flow rate of Ussel spring is higher than 350 L/s (in high level water period before one rain event).

Results Obtained with HIK

Figure 2 shows the peak flow transiting through Ussel spring (ordinate) in terms of maximum hourly rainfall over the Méjannes-le-Clap plateau (abscissa). The three colorful points in Fig. 2, green, yellow and black, are the third variable integrated from all described parameters. This third parameter called “HIK” calculates the karst-system water balance. An example on Fig. 2 shows the initial flow rate before the rain event begins. According to spring discharge, HIK is divided to three classes and represented with aforementioned colors. From HIK 1 to HIK 3, this parameter represents a karst network passing from a drying-up stage to a saturated stage. The result shown in Fig. 2 shows that the Ussel spring behaves differently according to rainfall intensity, as shown by the green, yellow and black points. In fact, HIK 1 represents the group of events, where the maximum flow rate of the spring does not increase strongly, even though the rainfall is strong. Even though the green points

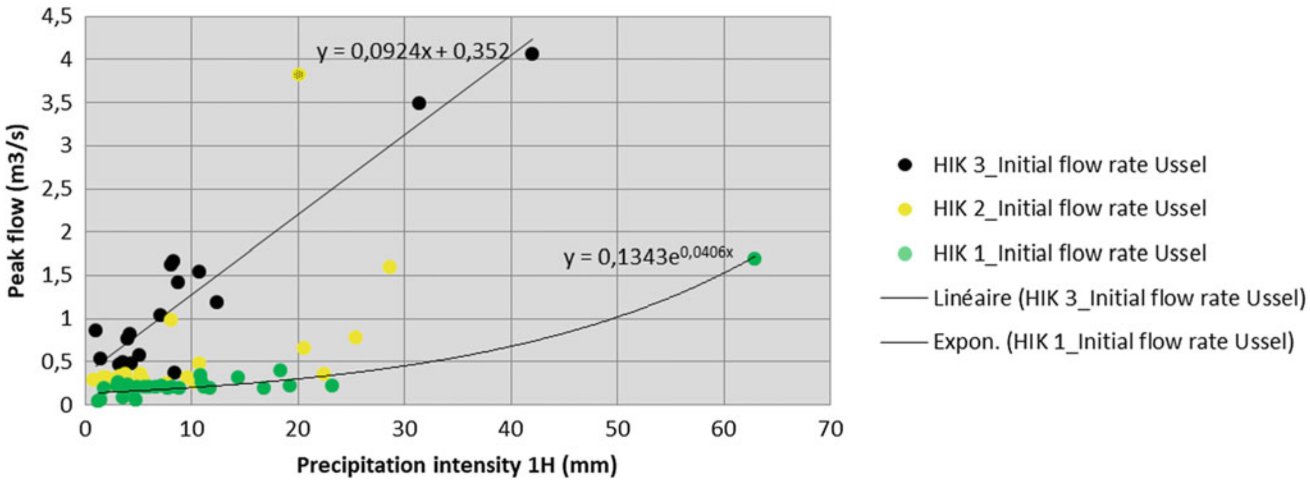

Fig. 2 Representation of the maximal flow rate of the Ussel spring as a function of precipitation intensity in 1 h; this result is represented in three ranges (green, yellow and black) each range corresponding at the hydric state of the karst: green dots represent a dry period with a karstic system unsaturated; black dots represent a saturated karstic system; some dots (events) are in the middle of green or black cloud represent intermediate (unsaturated) hydrological conditions

follow an exponential curve, only more than 60 mm of rain in one hour increases the spring flow (1.7 m^3/s), which normally does not exceed 0.5 m^3/s (current measurements of the Ussel spring discharge should confirm the exponential shape of the curve). Distribution of events, belonging to class HIK 3 (black points) shows a more-or-less linear curve where the maximum flow rate of Ussel spring increases by about 1 m^3/s for an amplification of 10 mm of precipitation in one hour.

Presented results enable qualitative expression of hydrological conditions of the karst system, and we can design an indicator for the water balance of karst. After construction of the indicator, we can predict the reaction of the Ussel spring, if its initial discharge and predicted amount of the rain (by MeteoFrance) are known.

Conclusion

The creation of karst spring database in response to the precipitation events gives many possibilities for interpretation of hydrological conditions of the karst system and its response to rainfall event.

In our case, this database allows to identify the hydrological conditions of studied karst system. This information is important because it's the crucial parameter which determines the groundwater dynamics in the karst system. The proposed methodology can be very useful and applied in further studies or in other karst systems under the same availability of data.

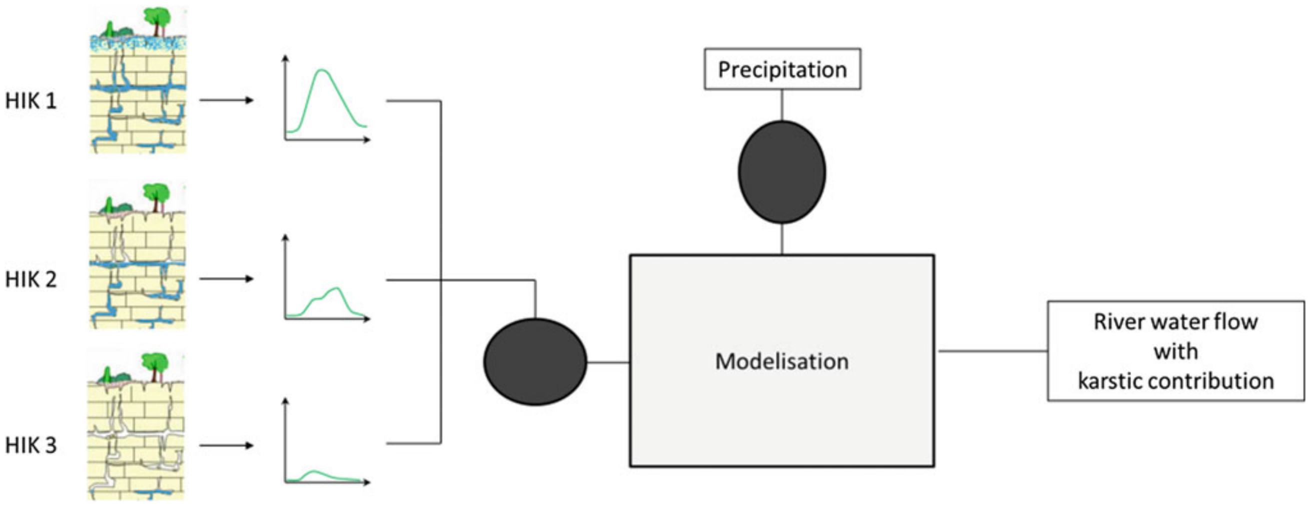

Fig. 3 Example of modeling possible with this hydric indicator of karst (HIK)

Indeed, hydrological indicator is needed to integrate relevant data into a groundwater model. In that case, this could be possible to use also this approach for other karst systems with well measured water level (discharges) of springs and rain precipitation. This indicator can be integrated in a hydrological model in order to provide a relevant parameter on the interactions between the karst system and the river. The hydrological indicator of the karst informs the model if the karst system has a less restitution of the infiltrated water (HIK 1) or conversely the karst system is saturated and restitutes the infiltrated water by the karstic springs, see Fig. 3.

In Fig. 3 (left side), initial hydrological conditions in aquifer given by HIK and spring hydrograph for the same event will be marked.

In the middle and right side: the modeling process which provides river water flows with the contribution of the karst.

After determining the flow rate ranges corresponding to the hydric conditions of the karstic system, this indicator can be a useful tool to determine the hydrological conditions of the hydrosystem and prevent of exploitation risks of the aquifer if there is pumping in low water period.

Acknowledgements The authors would like to thank MeteoFrance Company for the precipitation database and Ms Leila ESGAIB SÁNCHEZ for her contribution in reviewing the translation of this article.

References

Bailly-Comte, V., Borrell-Estupina, V., Jourde, H., Pistre, S., 2012. A conceptual semidistributed model of the Coulazou River as a tool for assessing surface water–karst groundwater interactions during flood in Mediterranean ephemeral rivers. Water Resour. Res. 48, W09534. https://doi.org/10.1029/2010W010072.

Bailly-Comte, V., Martin, J.B., Jourde, H., Screaton, E.J., Pistre, S., Langston, A., 2010. Water exchange and pressure transfer between conduits and matrix and their influence on hydrodynamics of two karst aquifers with sinking streams. Journal of Hydrology 386, 55–66. https://doi.org/10.1016/j.jhydrol.2010.03.005.

Bakalowicz, M., 2005. Karst groundwater: a challenge for new resources. Hydrogeol J 13, 148–160. https://doi.org/10.1007/s10040-004-0402-9.

Fleury, P., Charlier, J.-B., Borrell, V., Coustau, M., 2011. Appui au SCHAPI 2011 - Module 1: Mise en place d'un indicateur d'aide à la décision pour la prévision de crue en milieu karstique: les bassins versants du Lez et de la Tardoire.

Ford, D.C., Williams, P.W., 1989. Karst geomorphology and hydrology. Academic Division of Unwin Hyman London.

Ford, D.C., Williams, P.W., 2007. Karst geomorphology and hydrology. Academic Division of Unwin Hyman London.

Chapuis H., Jolivet, J., Ré-Bahuaud, J., Paran, F., Graillot, D., Guy, B., 2017. Displacement of Watershed between Two Karstic Rivers. IOP Conference Series: Earth and Environmental Science 95, 022021.

Johannet, A., 2011. Modélisation par apprentissage statistique des systèmes naturels, ou en interaction avec un environnement naturel. Applications aux karsts, crues éclair et en robotique.

Jolivet J. 2013. Nouveaux apports sur les traçages et les débits réalisés sur le bassin d'alimentation karstique de la bordure orientale du massif de Lussan, Canyon de la Cèze, Gard, France. Spelunca, p. 27–34.

Jourde, H., Roesch, A., Guinot, V., Bailly-Comte, V., 2007. Dynamics and contribution of karst groundwater to surface flow during Mediterranean flood. Environ Geol 51, 725–730. https://doi.org/10.1007/s00254-006-0386-y.

Kiraly, L., 1998. Modelling karst aquifers by the combined discrete channel and continuum approach. Bulletin d'Hydrogéologie 16, 77–98.

Pouzancre, H., 1971. Contribution à l'étude hydrogéologique des bassins d'alimentation de la Cèze, cours moyen et inferieur, Gard. Centre d'études et de recherches géologiques et hydrogéologiques.

Ré-Bahuaud, J., Jolivet, J., Marmonier, P., Johannet, A., Graillot, D., Paran, F., Chapuis, H., Guy, B., Faroux, J., Creuzé des Châtelliers, M., Olivier, M.-J., Jacquy, M., Lawniczak, M., Novel, M., Savary, M., Salze, D., Vayssade, B., 2015. Caractérisation des échanges entre eaux superficielles (rivière) et eaux souterraines en domaine karstique. Exemple d'un affluent du Rhône, la Cèze (30). Rapport provisoire année 2 (2014–2015) (Action n°43 du Programme 2014 (action 49 en 2015) au titre de l'accord cadre Agence de l'Eau ZABR).

White, W. B., 1988. Geomorphology and hydrology of karst terrains. New York: Oxford university press. (Vol. 464).

WoKAM, 2017. World Karst Aquifer Map (WoKAM) 1: 40 000. Published in 2017 and presented at the 44th Congress of the International Association of Hydrogeologists (IAH). Dubrovnik/Croatia.

Dynamics and Fluxes of Nutrients in Surface and Groundwaters in a Cultivated Karstic Basin in the Jura Mountains

Jean-Baptiste Charlier, Aurélien Vallet, Didier Tourenne,
and Guillaume Hévin

Abstract

This study aims at characterizing spatiotemporal variability of the fate of nutrients in the karst basin of the Loue River in the French Jura Mountains. The long-term temporal analysis (40 years) shows that the NO_3 increase from 1970s to the 1990s followed by a no-trend period in 2000s. The changes are linked to the usage of mineral fertilizers. The short-term analysis shows that the degree of aquifer saturation at the beginning of the hydrological cycle is a key factor to assess NO_3 mobilization during the recharge events. Contrary to nitrate, the PO_4 concentrations are disconnected from agricultural practices and are probably the consequence of point-source contaminations from domestic wastewater. Annual loads were estimated on 5 sub-basins in order to characterize the spatial variability of water contamination. Difference in fluxes for each sub-basin highlighted the most impacted reaches, providing information on hydrological units where anthropogenic pressure is highest. A correlation of NO_3–N loads with the surface area of main crops using highest level of fertilization and tillage (field crops, temporary grasslands) is proposed, highlighting the environmental impact of most intensive agricultural practices (inventoried in a small area covering less than 10% of the whole basin). This study illustrates complex interactions between agricultural practice and hydrological function and gives first insight into the fate of nutrients in karst environment.

Keywords

Water quality • Nitrate • Phosphate • Land-use • Trend • River

Introduction

Excess nitrogen (N) and phosphorous (P) in surface water and groundwater cause chronic changes in aquatic ecosystems. Despite some studies in the last decade (Mahler et al. 2008; Huebsch et al. 2014; Lorette et al. 2018), the case of karst basins is generally poorly documented in the literature. Morphological and hydrological properties of karst aquifers can limit retention and remediation, and favor fast transfers at the outlet. Environmental consequences of anthropogenic pressures are then likely to be intensified in karst basins.

Rivers in the Jura massif (Eastern France) are fed mainly by karst springs that drain the plateau. That context favors complex karst–river interactions, making difficult the understanding of hydrological behavior of basins (Dörfliger et al. 2004; Charlier et al. 2014). Although population and agricultural activity are relatively moderate compared to other intensive cultivated territories in France, the water contamination seems to be promoted by the vulnerability of the karst environment.

The Loue River in the Jura massif is important for tourism, fishing, and drinking water supply (Besançon for example) and has become an observatory for the fate of nutrients in karst basins. The aim of this paper is to present first results about the characterization of dynamics and fluxes of nutrients in waters and to investigate the relationships between agricultural practice and water contamination. Based on a monitoring network surveying nutrient concentrations and water flow, a temporal analysis of concentrations at short (1 year, daily frequency) and long term (40 years, monthly to seasonal frequency) as well as (2) a spatial analysis of fluxes at the sub-basin scale in relation to agricultural practices has been carried out.

J.-B. Charlier (✉) · G. Hévin
BRGM, University of Montpellier, Montpellier, France
e-mail: j.charlier@brgm.fr

A. Vallet
BRGM, 21000 Dijon, France

D. Tourenne
Chambre interdépartementale d’agriculture Doubs—Territoire de Belfort, 25021 Besançon, France

C. Bertrand et al. (eds.), *Eurokarst 2018, Besançon*, Advances in Karst Science,
https://doi.org/10.1007/978-3-030-14015-1_10

Site and Data Available

The study site is the Loue–Lison basin (1100 km^2) in the French Jura Mountains (Fig. 1a). The climate is temperate and displays a strong influence of mountainous areas in the eastern border. Precipitation averages 1400–1700 mm/year. The recharge area is characterized by a carbonate plateau of Jurassic limestones cross cut by 150 m deep valleys (Fig. 1b). Loue and Lison rivers are mainly fed by groundwater originating from several karst aquifers (Charlier et al. 2014). Two main springs located in the upstream zone, the Loue and Lison springs with a mean annual discharge Q_{mean} of about 9 and 7.5 m^3/s, respectively, generate more than 1/3 of the river flows at the basin outlet (Q_{mean} = 47 m^3/s). In addition, numerous lateral karst springs contribute to the surface flows. Surface runoff is usually limited to small marly areas in the downstream zone of the basin. The Loue spring is partly recharged by losses from the Doubs River that lead to dry up some river reaches during low-water periods in summer.

On the overall basin, land use is dominated by forest (49%) and permanent grassland (36%) for dairy cows (milk and cheese production) (Fig. 1c). However, at the sub-basin scale, a spatial variation is observed with an increase in land uses that use mineral fertilizers in the downstream area: cereal and field crops (up to 6%), as well as temporary grassland (up to 13%). There are four main application periods of fertilization over a year (including both mineral and organic fertilizers). Applications in March–April represent about 2/3 of the total applied amount for crops and grasslands. A second application period occurs between May and July after the first hay cut. In September–October, composted or evolved manures are spread mostly before autumnal crops. In the same time, manure and slury pits are emptied before the cold season for application in grasslands. In winter, composted and evolved manures are spread on grasslands.

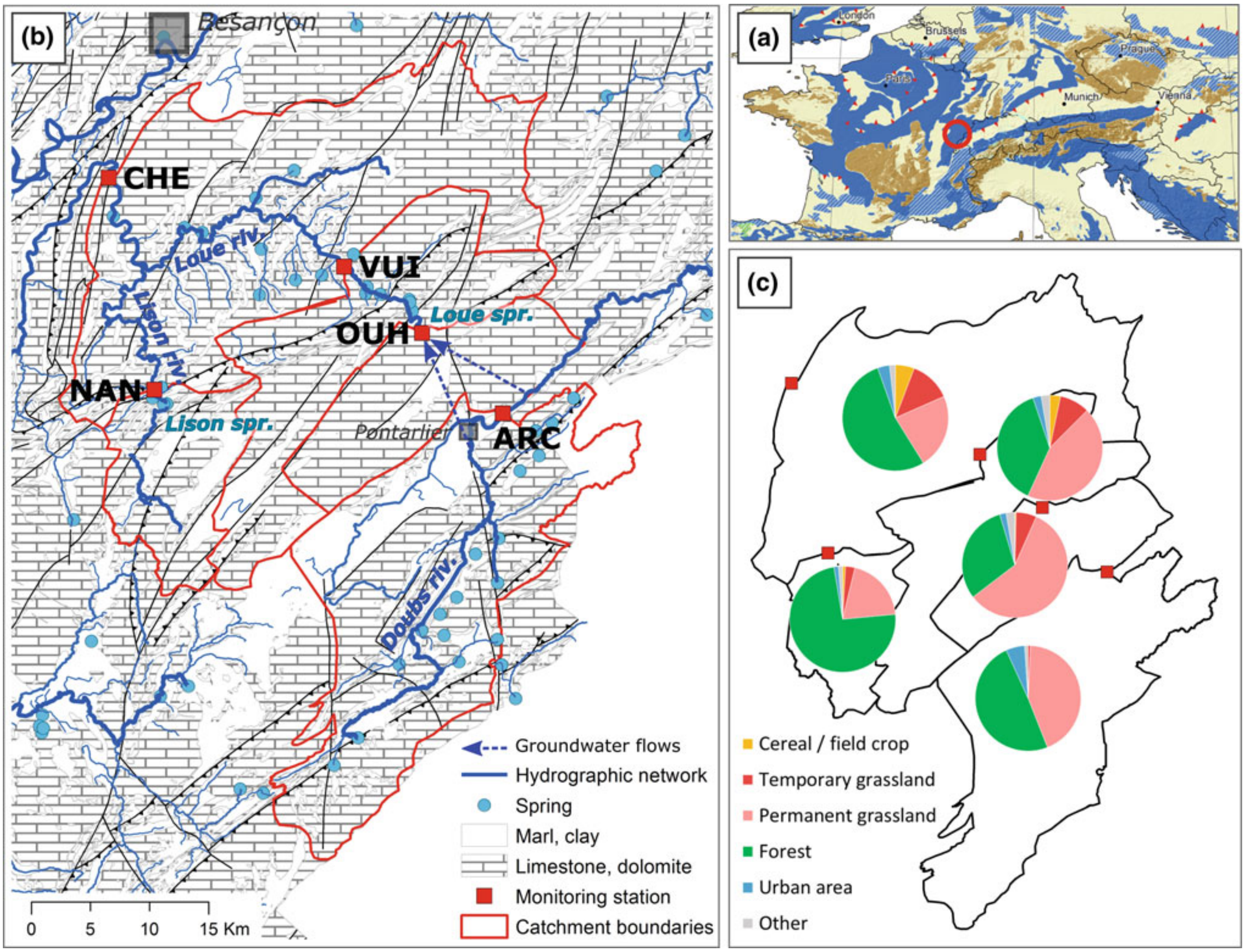

Fig. 1 **a** Location of Loue–Lison basin in the French Jura Mountains on the World Karst map (Karst aquifers in blue color—Chen et al. 2017), **b** hydrogeological map with the location of the 5 monitoring stations, **c** land use map for the 5 sub-basins

Daily precipitation and discharge are recorded by Météo-France and DREAL (*Direction Régionale de l'Environnement, de l'Aménagement et du Logement*) Burgundy Franche-Comté, respectively. Three data sets for NO_3 and PO_4 concentrations are used in this study (Fig. 2). Long-term data set (occasional analysis from 1970 to 2002) and mid-term data set (daily to biweekly analysis 2003–2012) of the Loue River at Chenecey-Buillon (CHE station) were provided by the Water Agency and the City of Besançon, respectively. Recent data set (daily to biweekly analysis from 2015 to 2017) was also collected from the QUARSTIC network (QUAlity of Rivers and Survey of nutrients in Franche-Comté; Charlier et al. 2018) at five monitoring stations (Fig. 1b): ARC station on the losing reach of the Doubs River at Arçon, OUH station at the Loue Spring at Ouhans, NAN station at the Lison Spring at Nans-sous-Sainte-Anne, VUI station on the Loue River, CHE station on the Loue River at the basin outlet. Agronomic data are provided by the Agricultural Association of the Doubs Department (CIA25-90). Spatial data of land uses are extracted from the land register (RPG 2014 database). In addition, temporal data of annual delivery amount of mineral fertilizers are estimated from data from the Union of Fertilizer Industries in Doubs department where the study site is located.

Results and Discussion

Evolution of Nutrient in Waters

At Multi-annual Scale

Figure 3 compares the annual evolution of the mean concentration of NO_3 and PO_4 at the basin outlet (CHE station) with the evolution of the delivery amount of mineral fertilizers (differencing those containing N and P). Standard deviation of concentrations indicates high intra-annual variations. Regarding the NO_3 global evolution, the increase from 3 to 7 mg L^{-1} in the 1970s to 1990s period is concomitant with the increase in delivery of mineral fertilizers. In the 2000s, NO_3 stops to increase when a significant decrease in delivery of fertilizers is observed. An unusual peak in 2003–2004 hydrological cycle appears after the extreme dry period in spring and summer 2003. No clear evolution is visible in PO_4, but two years (1982 and 2012) show high concentrations in waters (mean concentration >0.2 mg L^{-1}) without link with fertilizer amount. Indeed, contrary to NO_3, no relationships are observed with the delivery amount of fertilizers although fertilizer containing P shows a strong decrease since the 1980s.

Globally, changes to the annual NO_3 concentration may be explained partly by the intensity of crop mineral

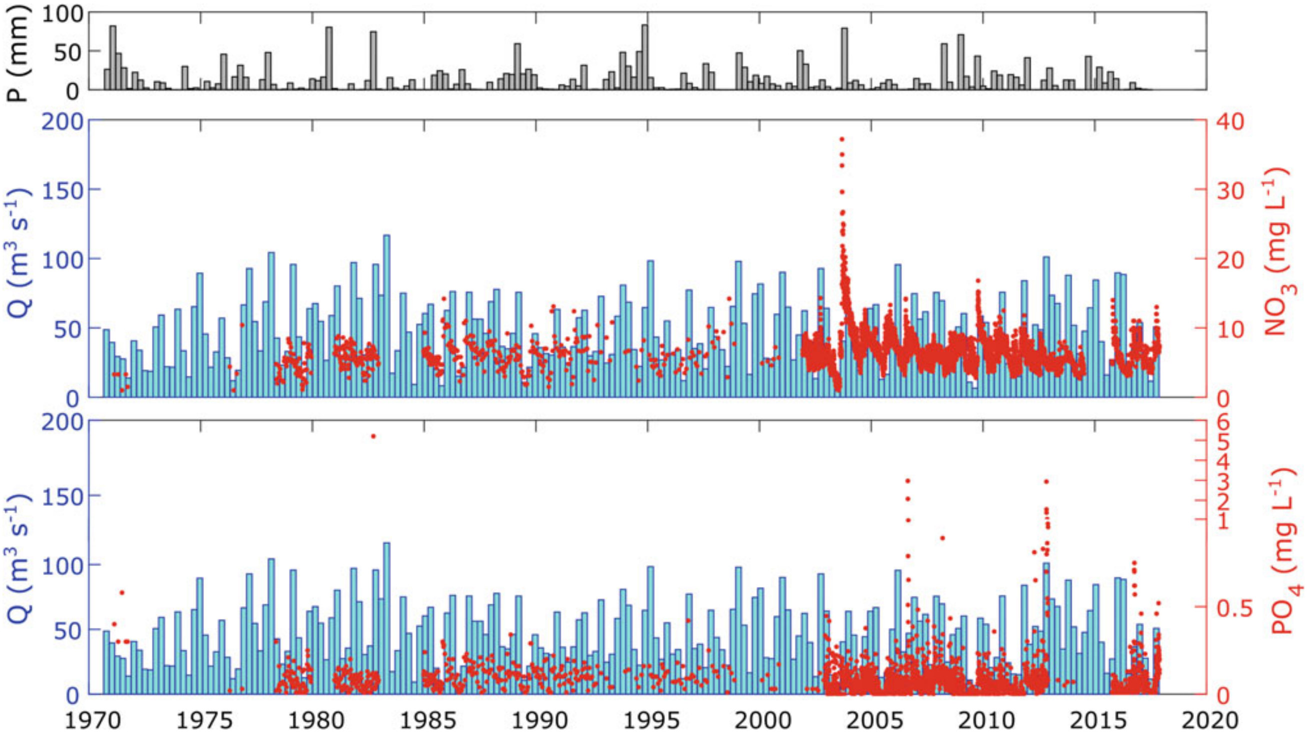

Fig. 2 Hydrological (quarterly precipitation *P* and discharge *Q*) and nutrient (punctual records) time series in the Loue River at Chenecey-Buillon over the 1970–2017 period; the interval on the *y*-scale for PO_4 is changing above 1 mg L^{-1}

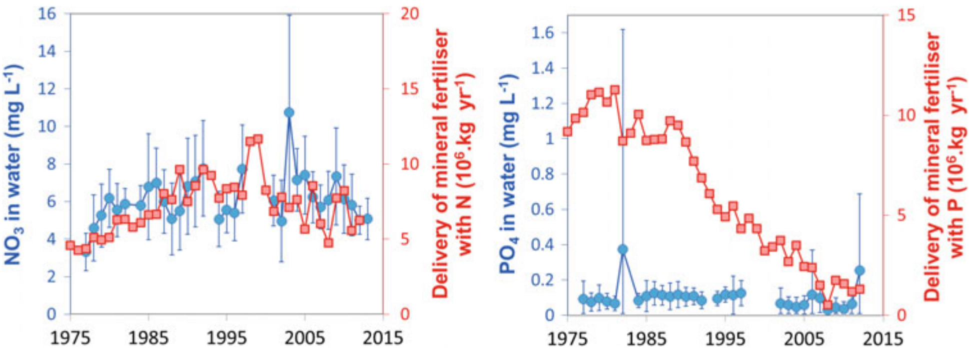

Fig. 3 Mean annual concentration (blue circles) of NO_3 (left) and PO_4 (right) at the CHE station plotted in parallel with the delivery amount of mineral fertilizer (red squares) containing N (left) and P (right) in the Doubs Department. Only years having more than 5 analyses are plotted; bars indicated s.d.

fertilization. As mineral fertilization is limited in grasslands by the cheese production (Comté) industry (cooperative union) as part of their quality insurance policy, the general NO_3 evolution observed at the basin outlet is probably the consequence of agricultural changes in only a small part of the cultivated fields used for cereals, field crops, and temporary grasslands, which represent less than 10% of the total area.

The PO_4 evolution in water is very different from NO_3 but is also different from global phosphorous trends at a larger scale. Indeed, phosphorus concentrations and loads strongly declined in main European rivers during the 1990s (Bouza-Deaño et al. 2008; Ludwig et al. 2009; Floury et al. 2012; Aguilera et al. 2015). But in our case, the severe decrease in mineral fertilization containing P is not followed by a decrease in PO_4 in water. Thus, following annual phosphorous budget given by Mainstone and Parr (2002) who showed that most of phosphorous origin is from wastewater treatment plants (WWTP), we hypothesis that the main origin of phosphorous contamination of the Loue River has a domestic origin. These results are coherent with some regional characterizations showing that the NO_3 dynamic in water was found to be a multifaceted process including agricultural practices, whereas that of PO_4 seemed to depend more on local impacts, such as urban and industrial activities (Aguilera et al. 2015).

At the Annual Scale

Two contrasted hydrological cycles have been selected to illustrate the infra-annual dynamic of NO_3 and PO_4 (Fig. 4). First, 2003–2004 (Fig. 4, left) has been chosen, because in September 2003 the highest NO_3 peak at the CHE station was recorded (37 mg L^{-1}) since the beginning of monitoring in 1970s (Fig. 2). The intra-annual NO_3 evolution shows a rapid and strong increase during first autumn recharge events, followed by a progressive decrease during winter, spring and summer to reach concentrations of few mg L^{-1} at the end of the cycle. Despite high recharge events throughout the year, main peaks are recorded during autumn. This pattern is observed every year (Fig. 2) but with various decreasing slopes and peak intensities.

Second, 2016–2017 (right) is a mean year in terms of nutrient's concentrations. In that case, the intra-annual evolution of NO_3 at CHE station shows a similar behavior with highest values in autumn–winter, but NO_3 during recharge reaches a value of 11 mg L^{-1}. The comparison with the four other stations in the Loue basin is interesting because the pattern is globally similar. However, some differences are observed. While the intensity of NO_3 peak is similar for all stations of the Loue–Lison River (OUH, VUI, NAN, CHE), it is twofold lower for the ARC station in the Doubs River, in the losing reach feeding partly the Loue Spring. Moreover, the dynamics during spring and summer shows contrasting behavior along the river. The annual decrease is higher for ARC and especially VUI stations where concentrations reach the limit of quantification (0.5 mg L^{-1}). This NO_3 depletion over several weeks during periods of low-water levels is probably linked to a NO_3 consumption in favor of a biomass production (algal development) within these river reaches. This hypothesis is supported by a concomitant COT increase in the river as mentioned by Charlier et al. (2018). The progressive summer decrease is shorter at NAN station where we observe an earlier increase in concentrations from June, leading to NO_3 concentrations in the Lison Spring higher than other stations until September.

The PO_4 dynamics at the intra-annual scale does not show a clear annual pattern. Although, PO_4 peaks occur concomitantly to NO_3 peaks, as observed during winter 2003–2004 (Fig. 4, bottom left), PO_4 shows erratic daily peak intensities throughout the year. Peaks frequently exceed 0.2 mg L^{-1} and in some periods 0.5 mg L^{-1} (as in 2016–2017; Fig. 4—bottom right). The peak occurrence and intensity is not strictly related to high-water periods and many peaks occur during the low-water period, after rainfall

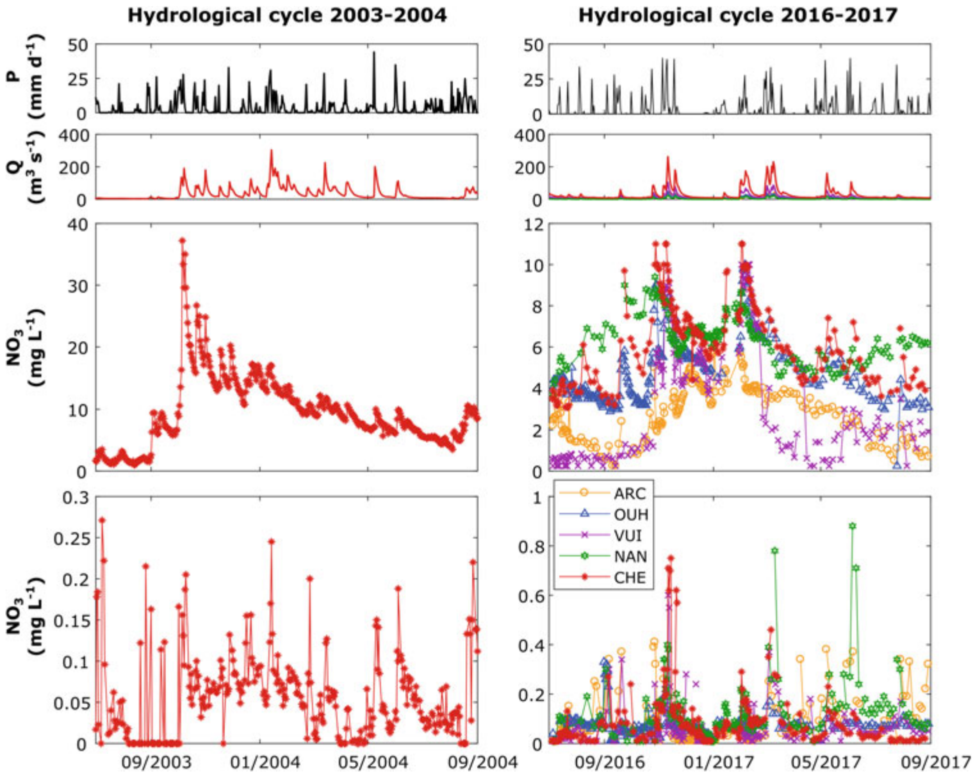

Fig. 4 Hydrological and nutrient's time series for two hydrological cycles: 2003–2004 (left) during which the highest nitrate concentration is observed at CHE station since 1970, and 2016–2017 (right) for which data from 5 stations over the basins are available. For more readability, *y*-scales for NO_3 and PO_4 are not the same for both hydrological cycles. Labels of stations referred to the map in Fig. 1b

events that have a too low intensity to generate a flood. Apart from these periods, PO_4 is generally very low, close to the limit of quantification at 0.02 mg L^{-1}. The comparison with other stations over the basin (Fig. 4 bottom right) shows that the peak occurrence varies according to the river reaches, but the concentration remains in the same range between 0.2 and 0.8 mg L^{-1}.

As the highest NO_3 concentrations are generally observed during the autumn recharge events, we ask whether the antecedent hydrological conditions may explain the temporal variability of NO_3. The relationship between the annual NO_3 peak concentration and the minimum discharge recorded at the beginning of the hydrological cycle (as an indicator of the initial groundwater storage) has been plotted from 2002 to 2016 (Fig. 5). Data show that the lower the minimum discharge, the higher the following NO_3 peak. The relationship between these two variables can be fitted by a power-law function (R^2 = 0.76). This result means that the duration of the low-water period during summer is a key factor to explain nitrate mobilization in waters. As timing and amount of organic and mineral fertilizers are almost constant over the last decade, three hypotheses can be formulated to explain this relationship. First, driest periods are generally associated with lower agricultural yields, leading to a high amount of N in soil (Bloor and Bardgett 2012). This residual N that was not consumed by plants can be leached by infiltration waters in post-harvest periods. Second, first precipitations after a warm period may favor mineralization of organic materials in soils, leading to enhance NO_3 leaching, as proposed by Mudarra et al. (2012). Third, a progressive desaturation of the karst aquifers during the summer may promote NO_3 storage in the soil/epikarst or aquifer which leaches during the first recharge events.

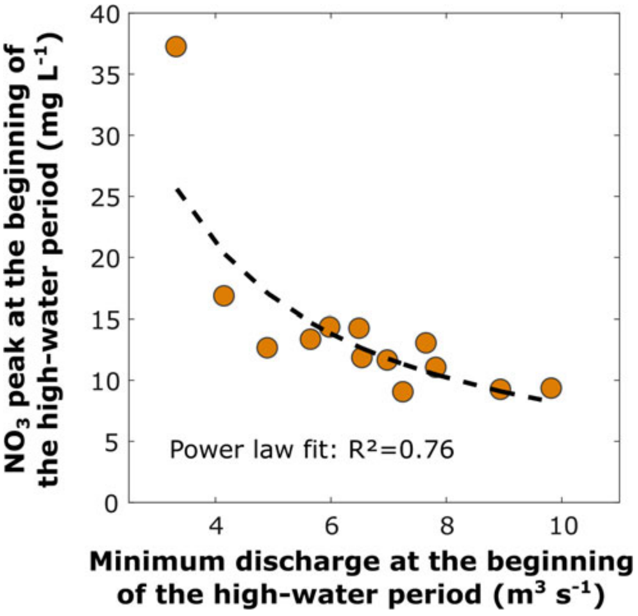

Fig. 5 Relationships between the minimum discharge and the NO_3 peak at the beginning of the high-water period (from 2002 to 2016)

Other studies carried out in the Jura Mountains (Pronk et al. 2009; Cholet et al. 2019), showed fast NO_3 increase in springs after rainfall events. Such response was attributed as the consequence of a mobilization of NO_3 stored in the soil/epikarst by Huebsch et al. (2014). Finally, these new results show that the degree of aquifer desaturation is a key factor to assess the intensity of NO_3 mobilization during the main recharge events.

Spatial Distribution of N and P Load

Annual Loads

Annual loads of nitrate–nitrogen NO_3–N and of phosphate–phosphorous PO_4–P during the 2016–2017 hydrological cycle were estimated for each sub-basin. The annual load was calculated adding up daily loads estimated from discharge and concentration data sets. For intermediate sub-basins (delimited by two successive stations in a river reach) loads were estimated making the difference of annual loads between the downstream and the upstream stations. Annual loads expressed by surface unit are presented in Fig. 6.

Regarding NO_3–N, the downstream sub-basin of the Loue River (CHE station) has the highest loads (about 17 kg ha^{-1} $year^{-1}$). This is about 1.5 times more than the intermediate and upstream sub-basins (including the both Loue and Lison Springs at OUH and NAN stations, respectively) and about 7 times more than the Doubs River in the losing reach (ARC). Regarding PO_4–P, the downstream sub-basin (CHE station) is also the one with the highest loads (about 0.5 kg ha^{-1} $year^{-1}$), but in that case, the Lison Spring (NAN station) recorded also high PO_4–P loads. This is due to high PO_4 peaks recorded in summer (see green stars in Fig. 4—bottom right).

Impact of Agricultural Practices

In accordance with our first results highlighting a water contamination related to fertilization, we expect to describe the spatial variability of annual NO_3–N loads with agriculture. Figure 7 presents the annual NO_3–N loads at the sub-basin scale as a function of the main crops using fertilizers (expressed as a percentage of the total sub-basin

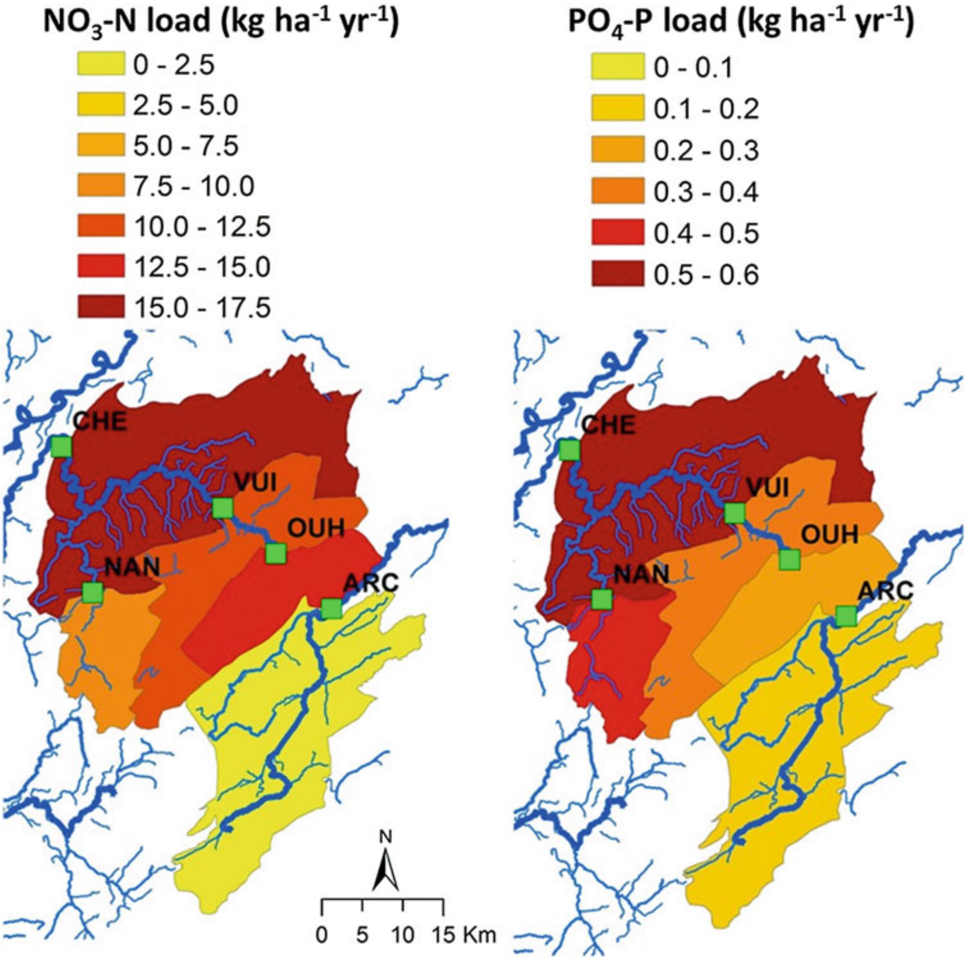

Fig. 6 Annual loads of NO_3–N (left) and PO_4–P (right) for the 5 sub-basins of the Loue–Lison during the 2016–2017 hydrological cycle

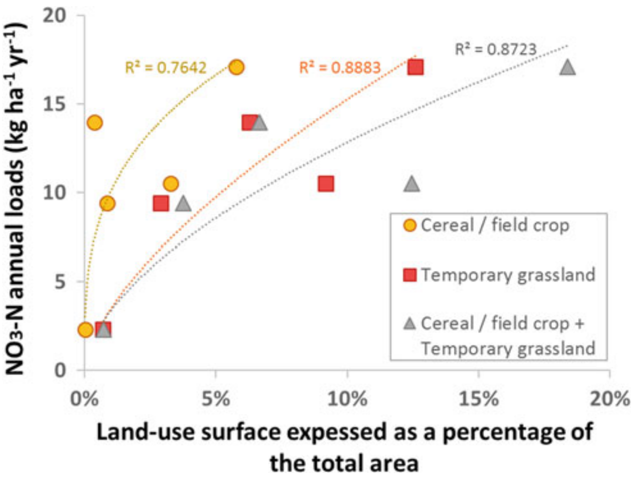

Fig. 7 NO_3–N loads during the 2016–2017 hydrological cycle versus surface of the main crops using fertilizers at sub-basin scale; R^2 refer to a power-law fit

area). The key land uses selected were those grouping cereal and field crops (yellow circle), and temporary grasslands (orange square). The combination of both was also tested (gray triangle). Good relationships were found for all three variables, but we should note that the temporary grassland seems to explain a little bit better the NO_3–N variability than cereals and field crops (r^2 = 0.89 vs. 0.76). The low number of stations (5 sub-basins) is not sufficient to characterize significantly the relationship and to conduct a thorough analysis differentiating the impact of cultural practices. However, it should be noticed that temporary grasslands cover twofold higher surface than cereal and field crops (7% against 3%), suggesting a probably high impact of those ones on the water quality of the Loue River. This result highlights the potential role of temporary grasslands (and cereals and field crops) in NO_3 leaching compared to permanent grasslands, which cover more than 1/3 of the surface basin (and for which no relationships was found with NO_3–N loads). This is coherent with observations at the field scale showing that grassland renovation (tillage) favors NO_3 leaching (Francis et al. 1995; Seidel et al. 2009).

Conclusion

Short- and long-term monitoring of NO_3 and PO_4 concentration in surface water and groundwater in the Loue basin (Jura Mountains) provides information on the evolution of the impact of anthropic activities at different time scales. The long-term NO_3 trend is related with the use of mineral fertilizers, while the short-term trend involves a more complex interaction between agricultural practices and hydrological function. The changes in PO_4 are partly disconnected from agricultural practices and illustrate more probably point-source contaminations from domestic wastewater. The estimation of annual loads for each sub-basin showed the most impacted reaches. Contrasted flux gives information on hydrological units where anthropogenic pressure is the highest. Regarding nitrates, a link with agricultural practices is proposed, highlighting the role of the main crops using fertilizers on the spatial variability of water contamination.

Acknowledgements This work was funded by the Rhone-Mediterranean and Corsica Water Agency, the Doubs Department, and the French Geological Survey (BRGM).

References

Aguilera, R., Marcé, R., and Sabater, S., 2015. Detection and attribution of global change effects on river nutrient dynamics in a large Mediterranean basin, Biogeosciences, 12, 4085–4098, https://doi.org/10.5194/bg-12-4085-2015.

Bloor, J.M.G., and Bardgett, R.D., 2012. Stability of above-ground and below-ground processes to extreme drought in model grassland ecosystems: Interactions with plant species diversity and soil nitrogen availability, Perspectives in Plant Ecology, Evolution and Systematics, 14(3):193–204.

Bouza-Deaño, R., Ternero-Rodríguez, M., and Fernández-Espinosa, A. J., 2008. Trend study and assessment of surface water quality in the Ebro River (Spain), J. Hydrol., 361, 227–239.

Charlier J.-B., Desprats J.-F., Ladouche B., 2014. Appui au SCHAPI 2014 – Module 1 – Rôle et contribution des eaux souterraines d'origine karstique dans les crues de la Loue à Chenecey-Buillon, Rapport BRGM/RP-63844-FR, 109p, http://infoterre.brgm.fr/rapports/RP-63844-FR.pdf.

Charlier J.-B., Vallet A., Hévin G., Moiroux F. 2018. Projet QUARSTIC: QUAlité des eaux et Réseau de Surveillance des rIvières Comtoises. Rapport final. BRGM/RP-68315-FR, 150p, http://infoterre.brgm.fr/rapports/ RP-68315-FR.pdf.

Chen Z, Auler AS, Bakalowicz M, Drew D, Griger F, Hartmann J, Jiang G, Moosdorf N, Richts A, Stevanovic Z, Veni G, Goldscheider N, 2017. The World Karst Aquifer Mapping project: concept, mapping procedure and map of Europe. Hydrogeol J, 25:771–785. https://doi.org/10.1007/s10040-016-1519-3.

Cholet, C., Steinmann, M., Charlier, J.-B., and Denimal, S., 2019. Characterizing fluxes of trace metals related to dissolved and suspended matter during a storm event: application to a karst aquifer using trace metals and rare earth elements as provenance indicators, Hydrogeology Journal, 27:305–319. https://doi.org/10.1007/s10040-018-1859-2

Dörfliger N., Pinault J.-L., Petit V., Jauffret D., 2004. Systèmes karstiques et crues du Doubs. Méthodologie de détermination de la contribution des systèmes karstiques aux écoulements de surface, lors de crues et des étiages. BRGM/RP-53063-FR, 182p. http://infoterre.brgm.fr/rapports/ RP-53063-FR.pdf.

Floury, M., Delattre, C., Ormerod, S. J., and Souchon, Y., 2012. Global versus local change effects on a large European river, Sci. Total Environ., 441, 220–229.

Francis, G. S., Haynes, R. J., Williams, P. H., 1995. Effects of the timing of ploughing-in temporary leguminous pastures and two winter cover crops on nitrogen mineralization, nitrate leaching and spring wheat growth. J. Agric. Sci. 124, 1–9.

Huebsch, M., O. Fenton, B. Horan, D. Hennessy, K. G. Richards, P. Jordan, N. Goldscheider, C. Butscher, and P. Blum, 2014. Mobilisation or dilution? nitrate response of karst springs to high rainfall events. Hydrology and Earth System Sciences 18 (11), 4423–4435.

Lorette G., R. Lastennet, N. Peyraube, A. Denis, 2018. Groundwater-flow characterization in a multilayered karst aquifer on the edge of a sedimentary basin in western France. Journal of Hydrology 566, 137–149.

Ludwig, W., Dumont, E., Meybeck, M., and Heussner, S., 2009. River discharges of water and nutrients to the Mediterranean and Black Sea: Major drivers for ecosystem changes during past and future decades?, Prog. Oceanogr., 80, 199–217.

Mahler B., D. Valdes, M. Musgrove, N. Massei, 2008. Nutrient dynamics as indicators of karst processes: comparison of the chalk aquifer (Normandy, France) and the Edwards aquifer (Texas, USA), J. Contam. Hydrol., 98, 36–49.

Mainstone CP, and Parr W., 2002. Phosphorus in rivers - ecology and management. Sci Total Environ, 282–283:25–47.

Mudarra, M., Andreo, B., and Mudry, J., 2012. Monitoring groundwater in the discharge area of a complex karst aquifer to assess the role of the saturated and unsaturated zones, Environ. Earth Sci., 65, 2321–2336, https://doi.org/10.1007/s12665-011-1032-x.

Pronk, M., Goldscheider, N., and Zopfi, J., 2009. Microbial communities in karst groundwater and their potential use for biomonitoring, Hydrogeol. J., 17, 37–48.

Seidel K, M. Kayser, J. Müller, J. Isselstein, 2009. The effect of grassland renovation on soil mineral nitrogen and on nitrate leaching during winter. J. Plant Nutrit. Soil Sci., 172, 512–519.

Part III

Time Series Analysis

The CO_2 Dynamics in the Continuum Atmosphere-Soil-Epikarst and Its Impact on the Karstification Potential of Water: A Case Study of the Lascaux Cave Site (Montignac, France)

Nicolas Houillon, Roland Lastennet, Alain Denis,
and Philippe Malaurent

Abstract

The aim of this work was to understand the dynamics of CO_2 in the atmosphere-soil-epikarst continuum of the Lascaux Cave site and to evaluate its impact on the hydrogeochemical signal of epikarstic waters. For these purposes, PCO_2, $\delta^{13}C_{CO_2}$ and associated hydroclimatic parameters were recorded at different depths in soil and epikarst. In parallel, hydrogeochemistry of an epikarstic emergence (SAS1 spring) located in the entrance of the cave (6 m depth) was studied. PCO_2 recorded in the soils underlines the seasonality and different levels of biogenic production according to the pedological facies and the physicochemical properties (higher in the calcisol than in the brunisol). CO_2 efflux measurements show a seasonal evolution with maximum value (25 g m^{-2} d^{-1}) in summer and minimum in winter (6 g m^{-2} d^{-1}). It decreases during rain events because of the soil moisture increases which limits CO_2 diffusivity. In the same way, seasonal processes of CO_2 accumulation (winter and spring) and CO_2 emission to the atmosphere (summer and autumn) are observed under the effect of soil moisture seasonal variations. These processes explain the very variable CO_2 concentrations (0.6–6%) and $\delta^{13}C_{CO_2}$ values (−22.1 to −24.5‰) in the superficial epikarst (0–3 m depth). This CO_2 accumulation explains the presence of higher CO_2 contents in the epikarst than in the main production area: the soil. At deeper level exists a differentiated CO_2 stock slightly variable (4–6%) with stable $\delta^{13}C_{CO_2}$ values from −22.7 to −21.7‰. Inter-annual variability of CO_2 contents is influenced by the synchronicity or not of intense production and high soil moisture. A conceptual scheme of CO_2 cycle is produced as a conclusion. The comparison with the evolution of water chemistry at the epikarstic emergence brings elements for understanding the acquisition of the karstification potential. Indeed, the seasonal evolution of the calcic carbonated mineralization of water is very well explained by the evolution of the CO_2 contents in the epikarst (PCO_2 at saturation with respect to calcite similar to the PCO_2 of the air of the epikarst). In addition, the presence of two different CO_2 compartments in the epikarst makes it possible to explain the variability of the chemical marking of water at the outlet depending on the flow conditions (transmissible and capacitive zones).

Keywords

Carbon dioxide • Continuous monitoring • Epikarst • Hydrogeochemistry • Lascaux

Introduction and Problematics

Expectations regarding the karst studies are based in part on understanding the acquisition of water chemistry under soil and epikarst air conditions. The comprehension of this mechanism could lead to a better appreciation of water chemistry entering into karstic aquifers and to evaluate the potential impact of climate change. Few studies have been conducted on CO_2 in unsaturated zone of karst (Atkinson 1977; Mattey et al. 2016). Our study aims to clarify the CO_2 dynamics in the continuum atmosphere-soil-epikarst in order to evaluate its impact on water calco-carbonic equilibrium. One of the most important objectives is to highlight the mechanisms responsible of higher CO_2 partial pressure in water than in the soil considered as the production area. In this continuum takes place the Lascaux Cave where flows are observed with an underground epikarstic emergence. This system is an ideal place to compare the hydrogeochemical behaviour of epikarstic water to epikarst air conditions. A continuous measuring device is implemented in situ to record epikarst air CO_2 contents at different depths

---

N. Houillon (✉) · R. Lastennet · A. Denis · P. Malaurent
Laboratory I2M (UMR 5295), University of Bordeaux, Allée Geoffroy Saint Hilaire, 33615 Pessac Cedex, France
e-mail: nicolas.houillon@u-bordeaux.fr

C. Bertrand et al. (eds.), *Eurokarst 2018, Besançon*, Advances in Karst Science,
https://doi.org/10.1007/978-3-030-14015-1_11

and coupled with regular water measurements to study the hydrogeochemical signal of that epikarstic emergence.

Site and Methods Backgrounds

Study Site Description

The Lascaux Cave is located in the north-east edge of the Aquitaine Basin in Dordogne 200 km east of Bordeaux (Fig. 1). The hill of Lascaux is a promontory of the Upper Cretaceous sandy bioclastic limestone. It is bordered to the West by the Vézère river valley which constitutes the local base level. The climate of Dordogne is predominantly oceanic with some continental influences. Average rainfall rate is about 880 mm per year. Air temperature, on the average, at the site of Lascaux is about 12.6 °C. With regards to the geological background, the hill is mostly constituted of a succession of Coniacian sandy bioclastic limestone from the middle and upper Coniacian, in which the karstic network including the Cave is developed. The site of Lascaux is characterized by a remarkable geomorphology composed of limestone projection notched by depressions of around 20 m deep that contain regolith resulting from ghost rock weathering. Different types of soil are present with rendosol, brunisol and calcisol according to Bruxelles et al. (2014). In terms of hydrogeological background, Lascaux Cave is located in an active karstic system hosting different types of water flows. An epikarstic emergence is located at shallow depth (6 m) in the airlock of the cave (the SAS 1 spring). This part of the cave intersects the interface between the fractured calcarenite of the epikarst and the transmission zone composed of more massive calcarenite. These epikarstic flows usually begin in late autumn (November) and end in late spring (June). Water is almost supersaturated with respect to calcite (Houillon et al. 2017).

Materials and Methods

In situ Air Measurements and Grab Sampling in Soils and Epikarst

The external atmosphere monitoring system is composed of one weather station located above the cave entrance. PCO_2 measurements are manually performed in soils at 0.30 m of depth with Dräger IR CO_2 sensor (X-am 3000, precision 0.05%). CO_2 efflux from calcisol is measured by a soil flux chamber especially designed for our application (PCO_2, atmospheric pressure and temperature measurements). Data recorded allow the calculation of CO_2 flux with a precision of 5%. In addition, an experimental zone was set up with four boreholes. These boreholes are positioned near the cave to determine the carbon dioxide dynamics in the epikarst. In situ Vaisala IR CO_2 sensors (GMP 221, 0.01% precision) are installed to record every minute the CO_2 partial pressure (PCO_2) at 1, 2, 3 and 8 m, depth respectively in the boreholes FC1, FC2, FC3 and FC4 (Fig. 1). CO_2 sensors are protected from water with a PTFE membrane. Soil moisture is recorded at 0.25 and 0.50 m of depth using ML3 Theta Probe (Delta-T, precision 1%). Air grab samples are also performed in these four boreholes to measure the $\delta^{13}C_{CO_2}$ and determine the CO_2 origins and the mixing ratio with the external atmosphere. The samples were sent to the LAB/ISO (BRGM) and analysed with a gas chromatograph coupled with a mass spectrometer (Gas Bench with Delta +XP; reproducibility of 0.03‰).

Geochemical Monitoring of the Epikarstic Emergence (SAS1 Spring)

Water samples were collected from the epikarstic emergence in the cave weekly from January 2015 to July 2017. Temperature and pH were measured in situ using a WTW model 3430 equipped with sentix 950 probe (precision 0.04 for pH, ± 0.3 °C for temperature). Bicarbonate concentration was measured at the time of sampling by digital titration using 1.6 N H_2SO_4 with a HACH alkalinity meter (precision 2.44 mg/L). Water samples were collected in 60 mL HDPE bottles and were kept at 3 °C until the analysis. Cation samples were preserved with nitric acid. Major element concentrations were measured using ICS 1500 and ICS 1100 ion chromatographs (Dionex). The analysis indicated that for the major ions, the charge balance errors of all water samples are of <5%. Other samples were collected in 120-ml glass bottles sealed and kept refrigerated until analysis of $\delta^{13}C_{CMTD}$. The analysis was performed by an Infra-Red Isotopes Spectrometer (Delta Ray Thermo Fisher, reproducibility of 0.05‰) coupled with auto sampler. Calcite saturation indices (SIcalcite), the CO_2 partial pressure at equilibrium with the atmosphere (PCO_2eq) and the CO_2 partial pressure at saturation with respect to the calcite (PCO_2sat) were calculated using Peyraube et al. (2012).

Soils and Epikarst CO_2 Dynamics

Soil CO_2 Production and Efflux

Soil PCO_2 manual measurements show typical seasonal evolution under temperature effect (Houillon 2016). PCO_2 are important from spring to late summer (1–3.65%) due to strong biogenic production and lower during autumn and

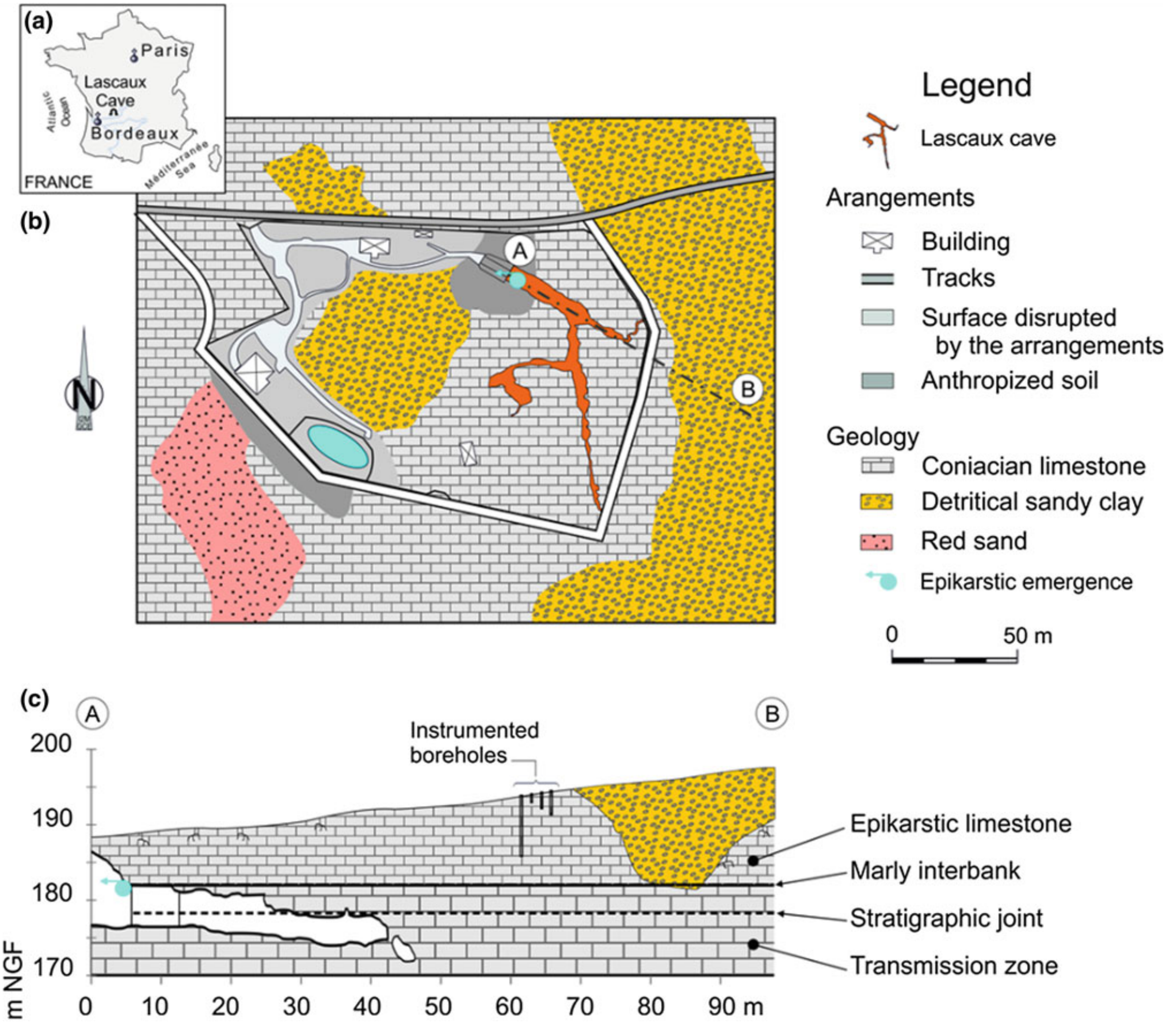

Fig. 1 Location of the Lascaux Cave in the north-east edge of the Aquitaine Basin (**a**), in the city of Montignac (Dordogne, France). Geological map of the sedimentary formations constituting the karstic system of Lascaux (**b**). Simplified geological cross section of the cave and its geological environment (**c**). Four boreholes equipped for monitoring the epikarstic air PCO_2

Table 1 PCO_2 statistics for 12 measurement campaigns (every month from March 2013 to March 2014) of 25 points in each type of soil

Soil types/PCO_2	Average (%)	σ (%)	Max (%)	Min (%)
Brunisol	0.41	0.15	1.86	0.10
Calcisol	1.18	0.67	3.56	0.11

winter (0.1–1%). Moreover, measures highlight significant differences according to the type of soils investigated as presented in Table 1. Indeed, PCO_2 are higher in the calcisol than in the brunisol (1.18% against 0.41% in average). This is explained by a lower biogenic production in the brunisol because of the physicochemical properties of this acidic soil.

Then soil CO_2 efflux from calcisol was measured continuously. Values range from 6 to 25 g m^{-2} d^{-1} with minimum in winter and maximum in summer. This seasonal trend is consistent with numerous studies. Nevertheless, the comparison between soil efflux (b) and moisture (a) under rain effect (Fig. 2) underlines an important mechanism for the CO_2 dynamics in soil.

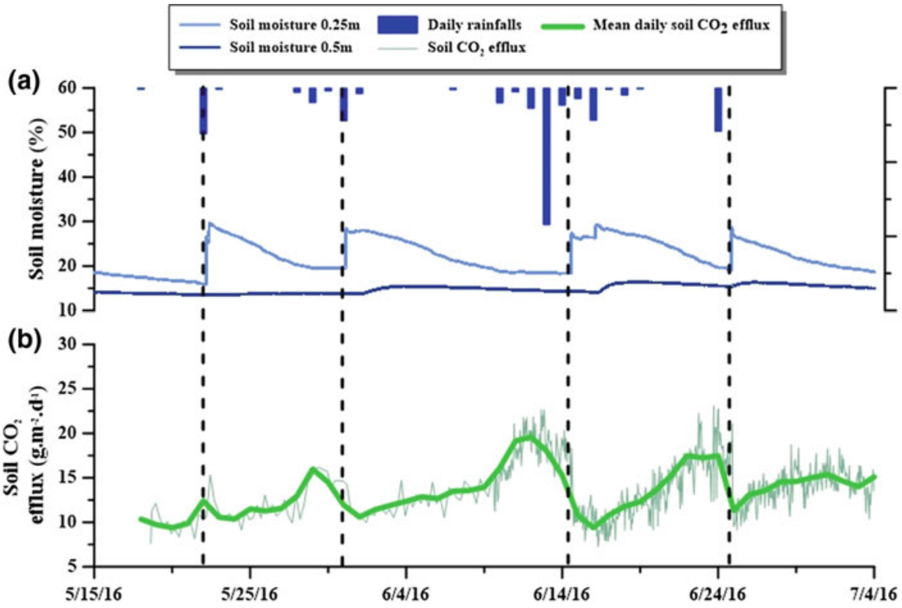

Fig. 2 Evolution of calcisol moisture during rain events (**a**) and CO_2 efflux, **b** The dash bars represent the soil CO_2 efflux decreases due to soil moisture increase under rain effect

Indeed, CO_2 efflux varies greatly with the soil moisture with high CO_2 efflux (15–22 g m^{-2} d^{-1}) when soil is dry and low CO_2 efflux (8–11 g m^{-2} d^{-1}) when soil is wet. It is explained by the effect of soil moisture on CO_2 diffusivity as shown by Maier et al. (2011). During rain events, infiltration water fills the porosity and acts as a “lid” which limits CO_2 exchanges between soil and atmosphere.

Spatiotemporal CO_2 Variations in Epikarst

PCO_2 were recorded in FC1, FC2, FC3 and FC4 during the study period (August 2014 to September 2017). The time series data are presented in Fig. 3 with the soil moisture and rainfall (a) and epikarstic air PCO_2 (b). Time periods of CO_2 accumulation (A), stabilization (S) and emission to the atmosphere (E) are also shown (c).

PCO_2 values range from 0.8% during late autumn to 6.8% during late spring. Average PCO_2 generally increase with depth because of the increase in the distance with near atmosphere. Nevertheless, two different dynamics are observed with depth: from 0 to 3 m (FC1, FC2 and FC3) and at 8 m (FC4). The first is explained by the connection degree between the shallow epikarst and the atmosphere. Three different periods are highlighted: CO_2 stabilization in winter (efflux similar to production), CO_2 accumulation in spring (efflux lower than production) and CO_2 emission in summer and autumn (efflux higher than production). During spring, the CO_2 diffusivity is reduced by the constitution of a water stock at the interface between soil and epikarstic limestone. The synchronicity of this water stock with the period of strong CO_2 production leads to CO_2 accumulation (production in a closed system). Without strong CO_2 production, CO_2 efflux and production are similar and CO_2 contents remain stable. Finally, if the soil is dry and production is low, efflux is predominant and the CO_2 is emitted to the atmosphere. At 8 m of depth, another dynamics is observed. PCO_2 are weakly variable (3.2–6%). The seasonal trend, PCO_2 increasing during summer and decreasing during autumn and winter, is controlled by advection transfer from the shallow epikarst under the thermic gradient effect. Moreover, we assume that the annual time variation of the different periods (A, S and E) is responsible of PCO_2 variation at this timescale. That is why CO_2 levels are higher in 2015 and 2016 than in 2017. Indeed, the accumulation periods (A) are longer in 2015 and 2016 than in 2017 with, respectively, 4 and 5 months against 2 months. All these mechanisms are consistent with the $\delta^{13}C_{CO_2}$ variations with depth (Table 2).

Indeed, $\delta^{13}C_{CO_2}$ is variable (−22.3 to −24.6‰) until 3 m of depth highlighting the succession of accumulation and emission phases in the shallow epikarst. It is more stable at 8 m (−22.7 to −21.7‰) because of the isolation of this compartment. $\delta^{13}C_{CO_2}$ enrichment at 8 m of depth probably results from fractionation caused by diffusion transfer since the shallower production area. To summarize, two conceptual schemes of the CO_2 dynamics (accumulation and draining phases) are presented in Fig. 4.

Impacts on Epikarstic Water Chemistry

Annual hydrological conditions were very different during the study period, with 170 m^3 discharged in 2015, 490 m^3 in

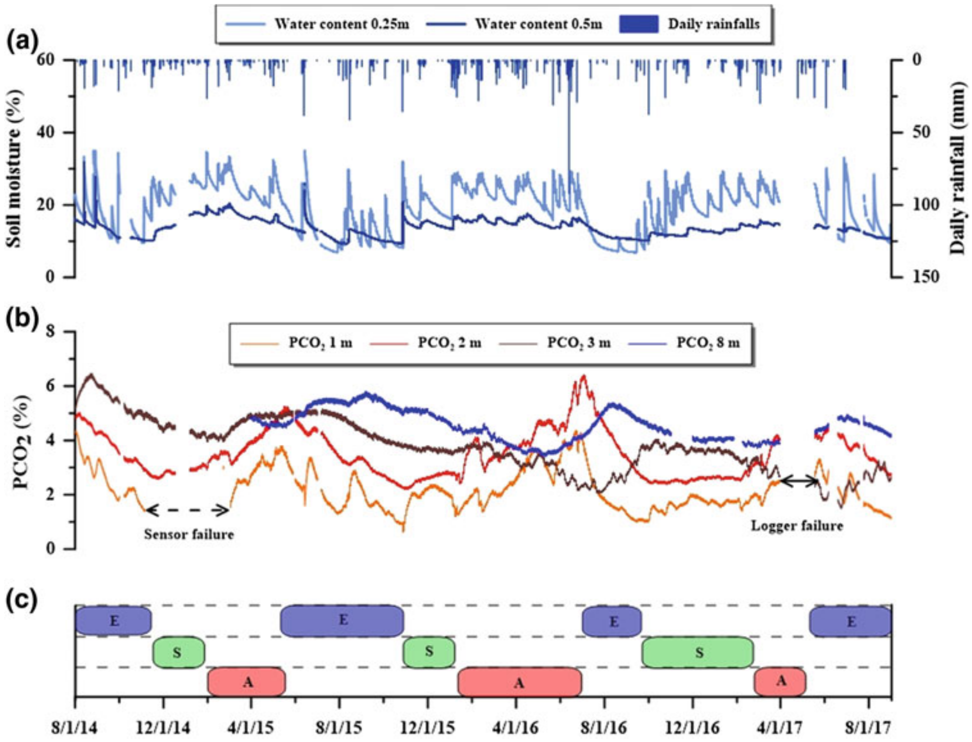

Fig. 3 Evolution of soil moisture and rainfall (**a**) and air PCO_2 at different depths in the epikarst, **b** during the study period. Blue, green and red rectangles **c** represent time periods of CO_2 accumulation (A), stabilization (S) and emission (E) in the continuum

Table 2 $\delta^{13}C_{CO_2}$ values for 2 campaigns of grab sampling in four epikarstic boreholes

Locations/Values	05/04/15 (‰)	02/23/2016 (‰)
FC1 (1 m)	−24.2	−22.3
FC2 (2 m)	−24.4	−22.5
FC3 (3 m)	−24.6	−22.4
FC4 (8 m)	−22.7	−21.7

2016 and 160 m^3 in 2017. Table 3 presents the statistical values for each point of CO_2 measurements in the epikarst and at the SAS1 spring. Annual PCO_2sat averages are different according to the hydrological cycle but coincident with epikarstic air PCO_2 annual changes. Coefficient of variation of PCO_2sat is 8, 18 and 12%, respectively, for 2015, 2016 and 2017 cycles. Varied flow conditions during 2016 cycle lead to high dispersion of PCO_2sat at the epikarst outlet.

Air PCO2 recorded in the epikarstic boreholes FC1, FC2 and FC4 and water PCO_2sat are presented in Fig. 5a. SAS 1 spring discharge is also shown Fig. 5b.

PCO_2sat values vary from 2.4 to 6.3% during the study period. The seasonal variation of this parameter is well explained by the deep epikarst air PCO_2 evolution (FC4) for the cycle 2015. Water was stored and equilibrated in the deep epikarst. Differently, PCO_2sat are more variable for the two other cycles. Low PCO_2sat values, similar to shallow epikarst air PCO_2, are observed during floods (high epikarst water saturation). It significates that water stored and equilibrated in the shallow epikarst is transferred through fissures and fractures directly to the outlet. Conversely during low water conditions, higher PCO_2sat values than epikarstic air PCO_2 are observed. The participation of water coming from high CO_2 concentrated capacitive zones of the epikarst could explain these observations.

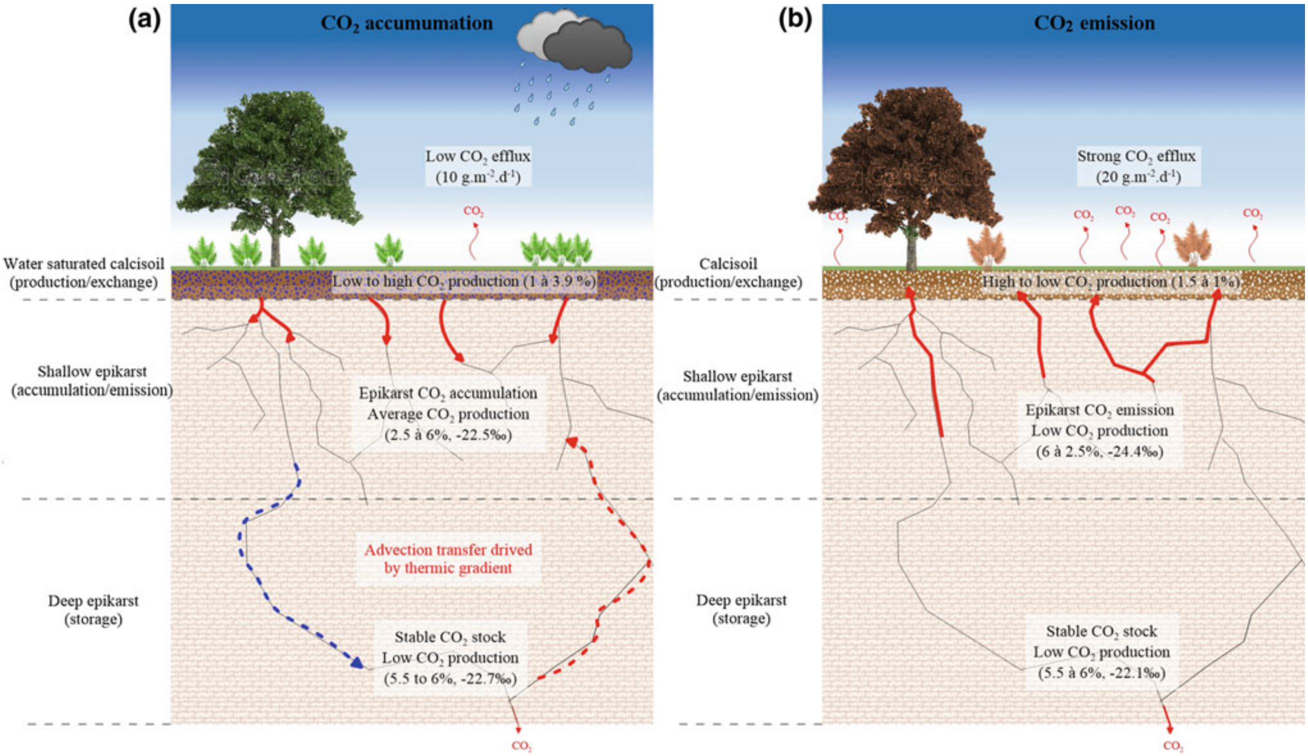

Fig. 4 Conceptual schemes of CO_2 dynamics in the continuum atmosphere-soil-epikarst according to the season (accumulation (**a**) and emission (**b**) conditions)

Table 3 Statistical values of epikarstic air PCO_2 and SAS1 spring PCO_2sat

Points/Values	2015		2016		2017	
	Average	Cv (%)	Average	Cv (%)	Average	Cv (%)
FC1 (air PCO_2)	2.87	17	2.63	31	2.15	22
FC2 (air PCO_2)	4.10	14	4.18	23	3.53	17
FC3 (air PCO_2)	4.72	7	3.13	17	2.69	21
FC4 (air PCO_2)	4.74	6	4.05	10	4.13	9
SAS1 (PCO_2sat)	4.42	8	4.07	18	3.55	12

Conclusions and Perspectives

Epikarstic air monitoring at the Lascaux site specify the CO_2 dynamics in the upper layer of the vadose zone. The analysis of soil moisture and CO_2 efflux time series data highlights the important role of soil water content on soil and shallow epikarst PCO_2. In the shallow epikarst, PCO_2 raised highest values of 6.3% when the soil diffusivity is lowered by the soil water stock at the interface between soil and epikarst. Accumulation (production higher than efflux) and emission (production lower than efflux) conditions are demonstrated as predominant mechanisms of the CO_2 dynamics in these compartments. In the deep epikarst, a stable stock of CO_2 (high PCO_2 and enriched is $\delta^{13}C_{CO_2}$) resulting from a long-time CO_2 accumulation is observed. Global PCO_2 annual variations were explained by the duration of the period of strong CO_2 production and high soil water content (accumulation process). The comparison with PCO_2sat values of SAS1 spring permits to better understand the acquisition of the karstification potential of infiltration water. Indeed, the air PCO_2 evolution explained most of the annual and seasonal PCO_2sat variations. Finally, it allowed to determine the epikarstic compartments where water acquires its chemistry depending on flow modalities. This method therefore allows the record of the climatic conditions impact on the geochemical signal of the infiltrations in the karstic systems. It will be useful for the estimation of the global warming impact on karstification through the evolution of rainfall and temperature spatial and temporal distribution.

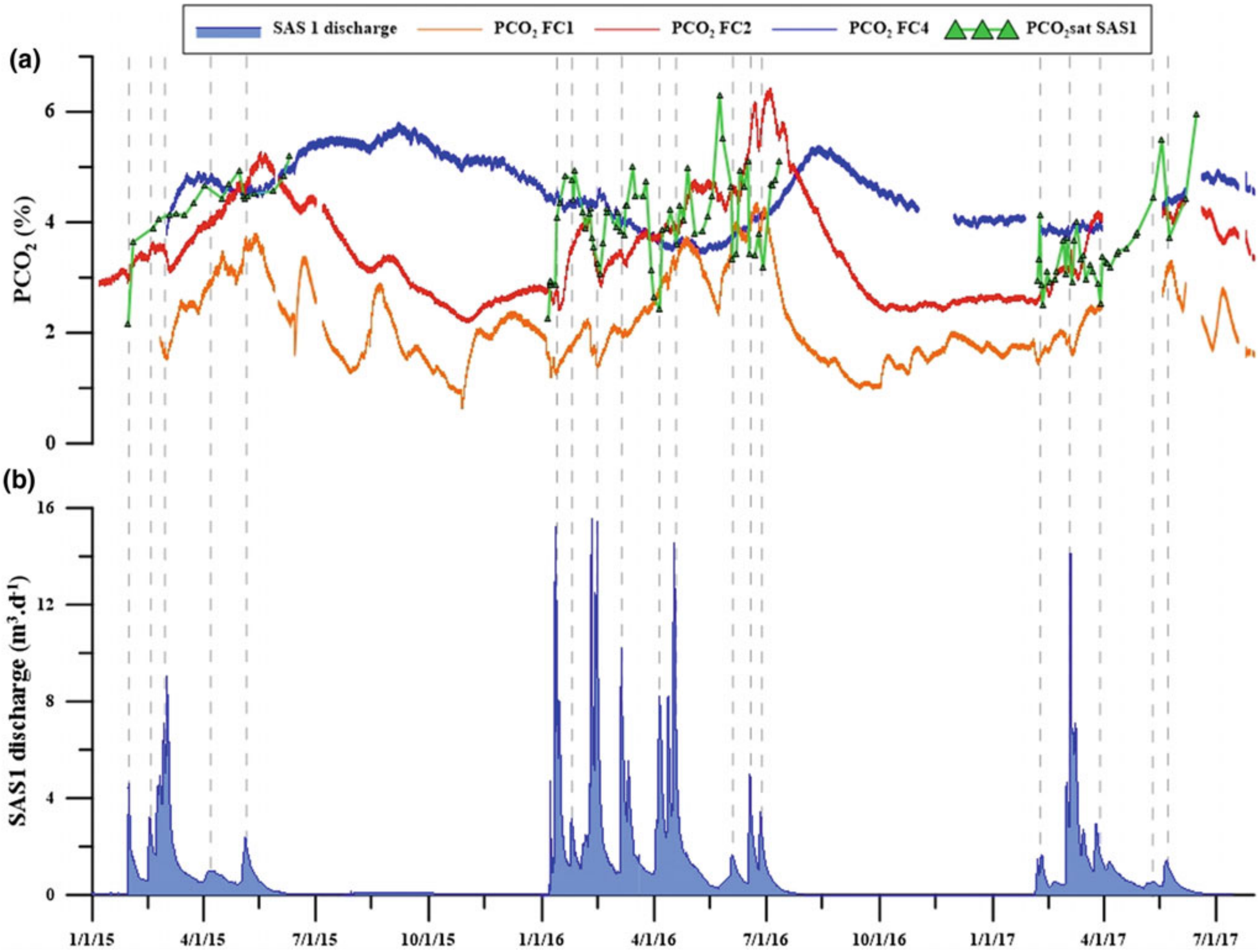

Fig. 5 Evolution of SAS 1 spring discharge (**a**), air PCO_2 in the epikarst and saturation values of PCO_2 from water (**b**) from 2015 to 2017

Acknowledgements The authors wish to thank the DRAC Nouvelle Aquitaine for its funding and support. This work benefits from scientific discussion within the Karst National Observatory Network.

References

Atkinson, T. C. (1977). Carbon Dioxide in the Atmosphere of the unsaturated Zone: an important control of groundwater hardness in limestones. Journal of hydrology 35, 111–23.

Bruxelles L., Camus H., Sirieix C., Poulenard J., Perrin J. (2014). Etude des contextes géologique, géomorphologique et pédologique de la Grotte de Lascaux. Synthèse des rapports d'étude, 64 p.

Houillon N., Lastennet R., Denis A., Malaurent P., Minvielle S., Peyraube N. (2017). Assessing cave internal aerology in understanding carbon dioxide (CO_2) dynamics: implications on calcite mass variation on the wall of Lascaux cave (France), Environmental Earth Sciences, Vol 76, 19 p.

Maier M., Shack-Kirchner H., Hildebrand E.E., Schindler D. (2011). Soil CO_2 efflux vs soil respiration: implications for flux models. Agricultural and forest meteorology, Vol 151, 1723–1730.

Mattey, D.P., T.C. Atkinson, J.A. Barker, R. Fisher, J.-P. Latin, R. Durrell, et M. Ainsworth (2016). Carbon Dioxide, Ground Air and Carbon Cycling in Gibraltar Karst». Geochimica et Cosmochimica Acta, Vol 184, 88–113.

Peyraube N., Lastennet R., Denis A. (2012). Geochemical evolution of groundwater in the unsaturated zone of a karstic massif using the PCO_2-Sic relationship. Journal of Hydrology, Vol 430–431, 13–24.

Monitoring and Preliminary Analysis of the Natural Responses Recorded in a Poorly Accessible Streambed Spring Located at a Fluviokarstic Gorge in Southern Spain

Juan Francisco Martín-Rodríguez, Mathias Mudarra,
Bartolomé Andreo, Beatrix De la Torre, José Manuel Gil-Márquez,
Javier Martín-Arias, José Manuel Nieto-López, Jorge Prieto-Mera,
and Maria Dolores Rodríguez-Ruize

Abstract

The analysis of natural responses (hydrodynamic, hydrothermal and hydrochemical) of karst springs is a well-established approach to provide insights into the hydrogeological functioning of the aquifers that they drain. However, a suitable monitoring program of these responses is often difficult to launch in poorly accessible streambed springs, due to the mixing between surface water and groundwater, in addition to topographic impediments. This work describes the installation procedure of the measurement equipment and the preliminary hydrogeological dataset collected at the Charco del Moro spring (Southern Spain) during one hydrological year (2016/17). This outlet emerges 5 m below water surface, at the bottom of a partially flooded 20–200-m-deep and 2-km-long gorge, eroded by the Guadiaro River streamflow. It is considered the largest discharge point in the region, draining groundwater from northern nearby carbonate outcrops, although its catchment area is not established yet. Continuous (hourly) monitoring of electrical conductivity, water temperature, turbidity and water level (discharge) reflects a high degree of heterogeneity in the duality of groundwater flow and storage dynamics, which is typical of karst conduit flow systems.

Keywords

Monitoring • Karst (carbonate) aquifer • Natural responses • Functioning

---

J. F. Martín-Rodríguez (✉) · M. Mudarra · B. Andreo ·
B. De la Torre · J. M. Gil-Márquez · J. Martín-Arias ·
J. M. Nieto-López · J. Prieto-Mera
Department of Geology and Centre of Hydrogeology,
University of Malaga (CEHIUMA), Málaga, Spain
e-mail: josefranciscomr@uma.es

M. D. Rodríguez-Ruize
Department of Crystallography and Inorganic Chemistry,
University of Malaga, Campus de Teatinos s/n,
29071 Málaga, Spain

Introduction

Karst aquifers provide good quality water for drinking supplies and ecosystems, and they also constitute a key strategic resource against threats such as climate change or population growth (Hartmann et al. 2014). Since an adequate knowledge about the functioning of karst systems is required for global and especially for regional water governance strategies, researchers and institutions have applied several karst-specific approaches, many of which are based fundamentally on the qualitative analyses of the natural responses of karst aquifers—hydrodynamic, water temperature, hydrochemistry, etc. (Ford and Williams 2007; Goldscheider and Drew 2007). However, suitable monitoring of natural responses in poorly accessible streambed springs is often difficult to establish due to the interaction and mixing between surface water and groundwater flowing through carbonate aquifers. In such setups, an acceptable knowledge of the hydrological settings prior to the placement of the pertinent facilities and devices is essential to effectively obtain single and/or continuous records of the natural responses during different hydrological conditions.

This work provides insights into the monitoring strategies of natural responses from karst springs located at non-friendly settings, concretely at a poorly accessible streambed outflow point (named as Charco del Moro spring) and located at the bottom of a fluviokarstic gorge in Southern Spain (Fig. 1). Recording data series of water level (up- and downstream from the spring), electrical conductivity, water temperature and turbidity during one year have

C. Bertrand et al. (eds.), *Eurokarst 2018, Besançon*, Advances in Karst Science,
https://doi.org/10.1007/978-3-030-14015-1_12

been coupled and analyzed to obtain a preliminary understanding on the hydrogeological functioning of the karst system. In addition, the degree of heterogeneity in the duality of groundwater flow and storage dynamics has been deduced from the relationships between the recorded hydrogeological variables.

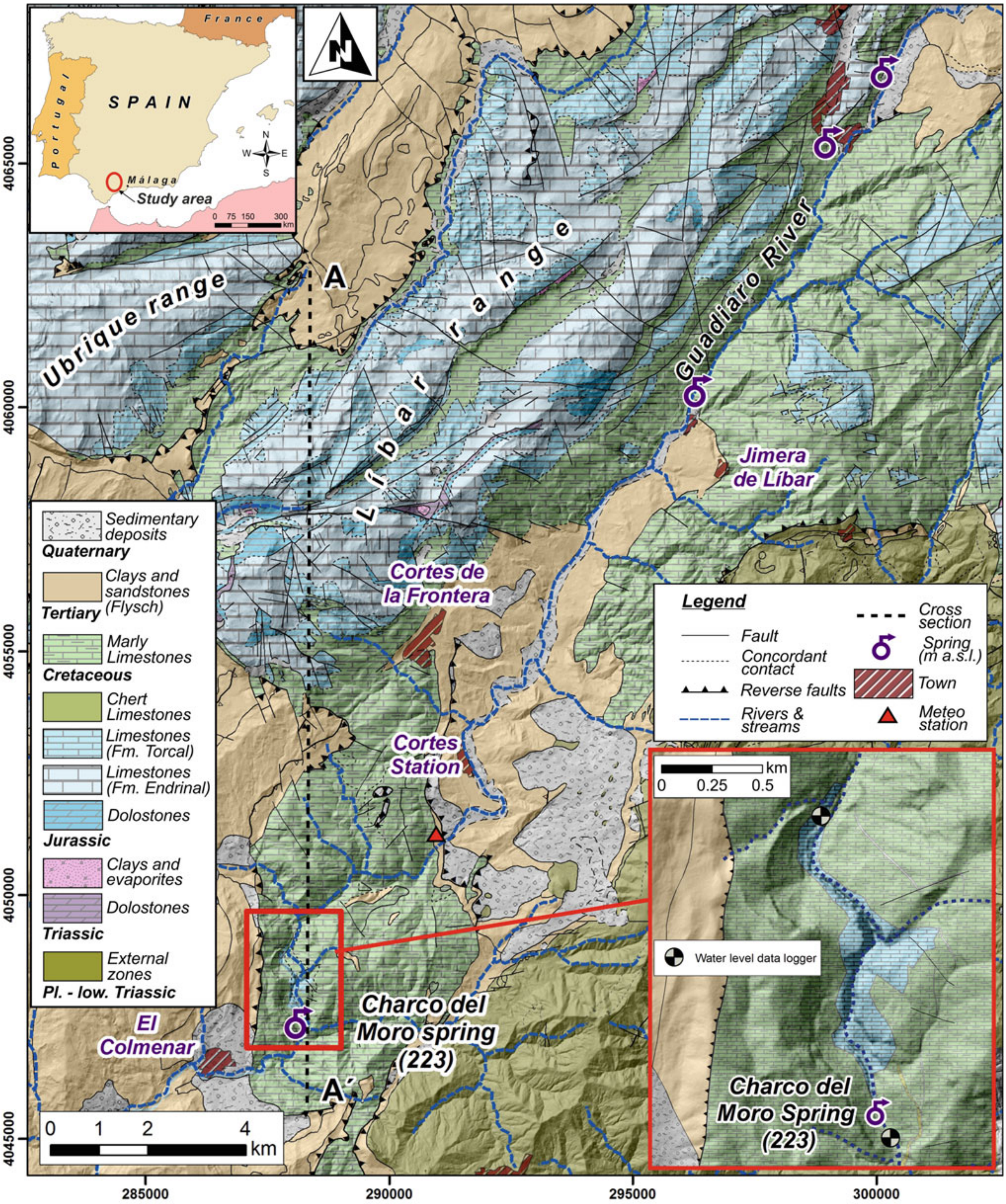

Fig. 1 Geographical location and simplified geology of the test site in the Southern Spain

Site Description

Charco del Moro spring is located 85 km WSW from the city of Malaga, in the SW edge of Ronda Mountain Range (Fig. 1). It is an outflowing cave placed at 223 m ASL, at the bottom of a partially flooded gorge (named as Las Buitreras Gorge), 20–200 m deep and 2 km long, eroded by the Guadiaro River streamflow. The terrain in this zone is rough, sometimes very steep, with altitudes ranging from 200 to 1300 m ASL (Sierra de Líbar). The prevailing climate is temperate Mediterranean, with a marked seasonal pattern in the distribution of rainfalls (mainly in autumn and winter). Climate conditions are also characterized by a dry season (very often up to 3–4 months), practically without rain, in summer. The mean historic annual precipitation and temperature values are close to 1200 mm and to 17 °C, respectively (Senciales 2007). The research period involved in this work (October 2016 to September 2017) can be considered dry and slightly warmed, with a total amount of rainfall and average air temperature of 806 mm and 17.3 °C, recorded in a meteorological station located at 335 m ASL; 3.3 km upstream from the gorge (Fig. 1).

Geologically, the pilot site and the northern carbonate reliefs are situated within the westernmost region of the External Zone of the Betic Cordillera; it consists of 450–500-m-thick Jurassic dolostones and limestones (Fig. 2), which present Upper Triassic clays, dolomitic beds and evaporite rocks (mainly gypsum) at the bottom, and Lower Cretaceous–Tertiary marly limestones and marls at the top (Martín-Algarra 1987). Neogene clays and sandstones Flysch rocks also outcrop in the area. In general, the spatial distribution and orientation of the main topographic features are strongly controlled by kilometric NE–SW folds and/or reverse faults. Anticline cores mainly occupied by Jurassic dolostones and limestones constitute the upland areas, while Cretaceous–Miocene marls appear in flanks and in the synclinal cores, defining the axes of the valleys. The previous structural control on the relief excludes Las Buitreras Gorge, characterized by the existence of an NNE–SSW anticlinorium dome, plunging southward, in whose core Jurassic limestones are exposed (Fig. 2). Outcrops of Flysch sandstones and clays are also represented in the region, overthrusting previous geological formations. The entire structure was affected by more recent strike–slip faults (NW–SE) which configure the geological structure of the area (Fig. 1).

Charco del Moro spring is considered the largest discharge point in the region, draining groundwater from the nearby northern carbonate outcrops (confirmed by tracer experiments, Andreo et al. 2004), although its catchment area is not well defined yet. In fact, the spring corresponds to a Vauclusian type cave with three outlets (located ∼5 m under the water) distributed 30 m along the left margin of the Guadiaro riverbed, on the south edge of Las Buitreras Gorge, where Jurassic limestones are bordered by low permeability materials (Cretaceous–Tertiary marls). The outlets, 3, 0.9 and 0.3 m high, are fed by a 45° steep karst conduit with at least 120 m of development (Fig. 3b), determined by speleological explorations.

Field Equipment Installation and Methods

Given the morphological characteristics of the study site, several hydrological and hydrogeological explorations in Las Buitreras Gorge were carried out at different hydrodynamic conditions before designing and installing the measurement infrastructure. The main difficulty found was introducing the recording probes deep enough in the outflowing cave for preventing disturbances by mixing of ground and runoff waters, thereby obtaining an accurate monitoring of the natural responses of the spring. A stainless steel box (1.2 m long, 0.8 m wide and 0.6 m high) was purposely designed and forged, and the different probes were fixed to it (Fig. 3a). The box was subsequently put within the 0.9-m-high outlet with the support of scuba divers.

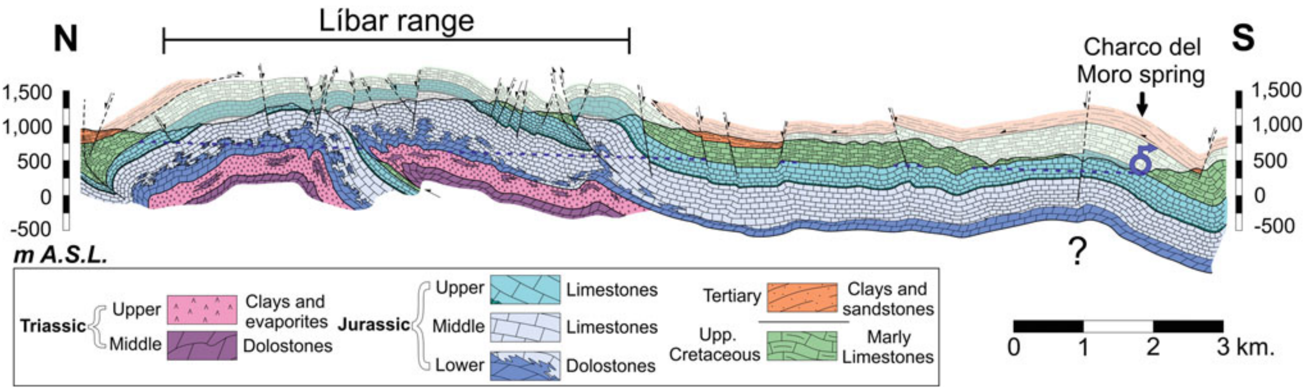

Fig. 2 Geological cross section of the study area. See location in Fig. 1

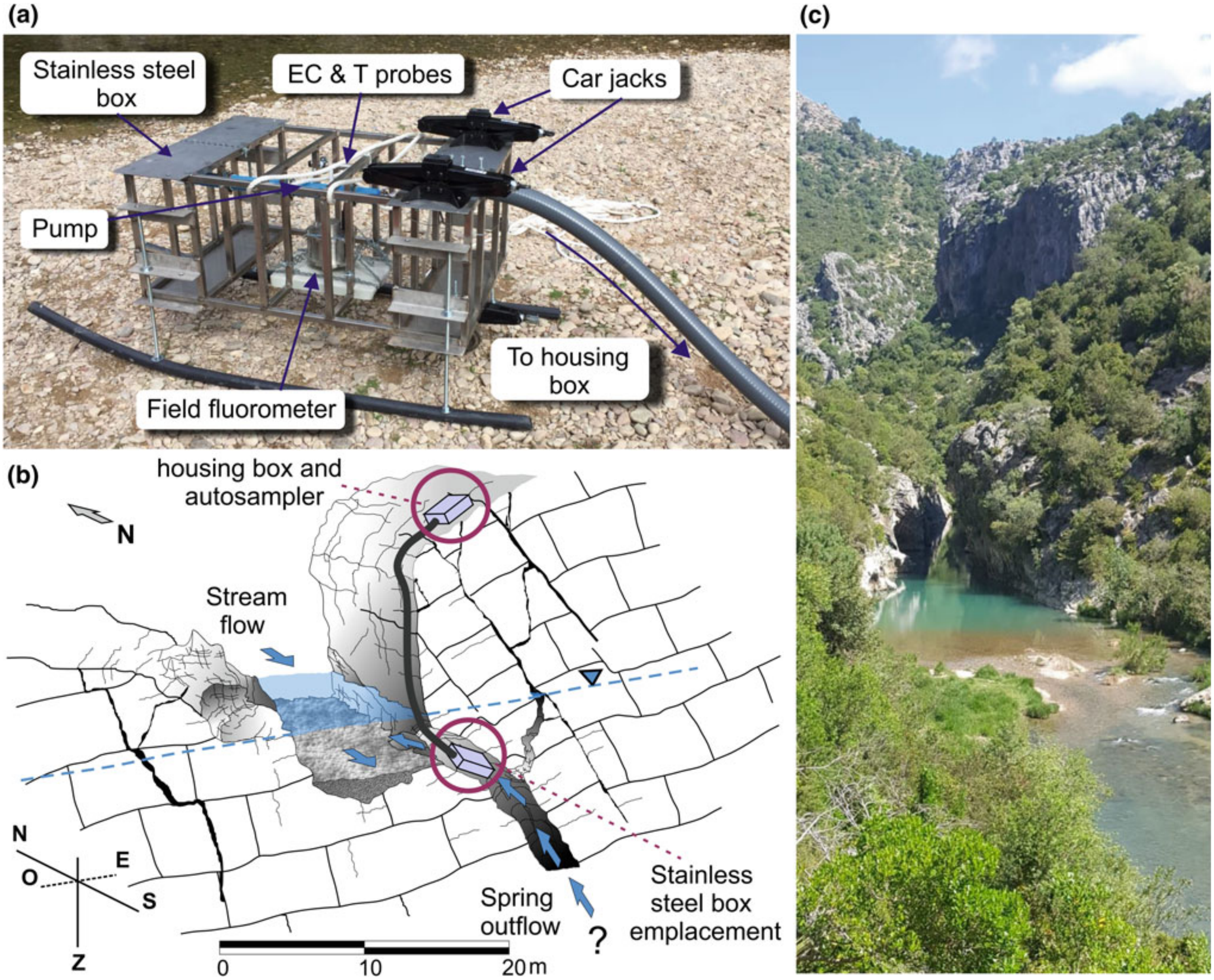

Fig. 3 Photograph of different devices installed inside steel box (**a**), and schematic section of spring and outflowing cave (**b**). Photograph of the outflowing point (**c**)

Two car jacks screwed at the upper side of the case act as mooring structure to the cave walls. A 25-m-long flexible PVC pipe attached to the rocks protects the connection cables, whereas other metallic housing box laid on the poorly accessible gorge ledge contains the data loggers and the batteries (Fig. 3b).

From October 2016 to September 2017, hourly records of water-level variations in the Guadiaro River were recorded using two *ODYSSEY® Depth & Temperature Data Recorders* (0–5 m range and ~1 mm accuracy), installed upstream and downstream from Charco del Moro spring (Figs. 1 and 4). Each probe was vertically installed and the corresponding vent tube was encapsulated inside flexible PVC pipe for protection, which were later screwed to the gorge wall (Fig. 4). Water-level variations were afterward transformed into continuous records of discharge by applying the corresponding rating curve, whose accuracy was checked from seven individual discharge flow measurements (*ETRELEC® Salinomadd* and *OTT® C2* flow meters), taken at both river locations. The discharge rate of the spring was calculated as the difference between the upstream and downstream data series, subsequently with statistical correction, whereas the mean annual discharge value of the spring was inferred through the mathematical integration of the resulting hydrograph. The performance of the upstream and downstream water-level devices is periodically verified during the data downloading tasks.

Electrical conductivity (EC) and temperature (T) of the water drained by the spring were also hourly recorded using an *OTT® EcoLog-800* data logger (accuracy of ±1 µS/cm for EC and ±0.1 °C for T) with 30 m of cable length. Probe housing was previously fixed to the stainless steel box

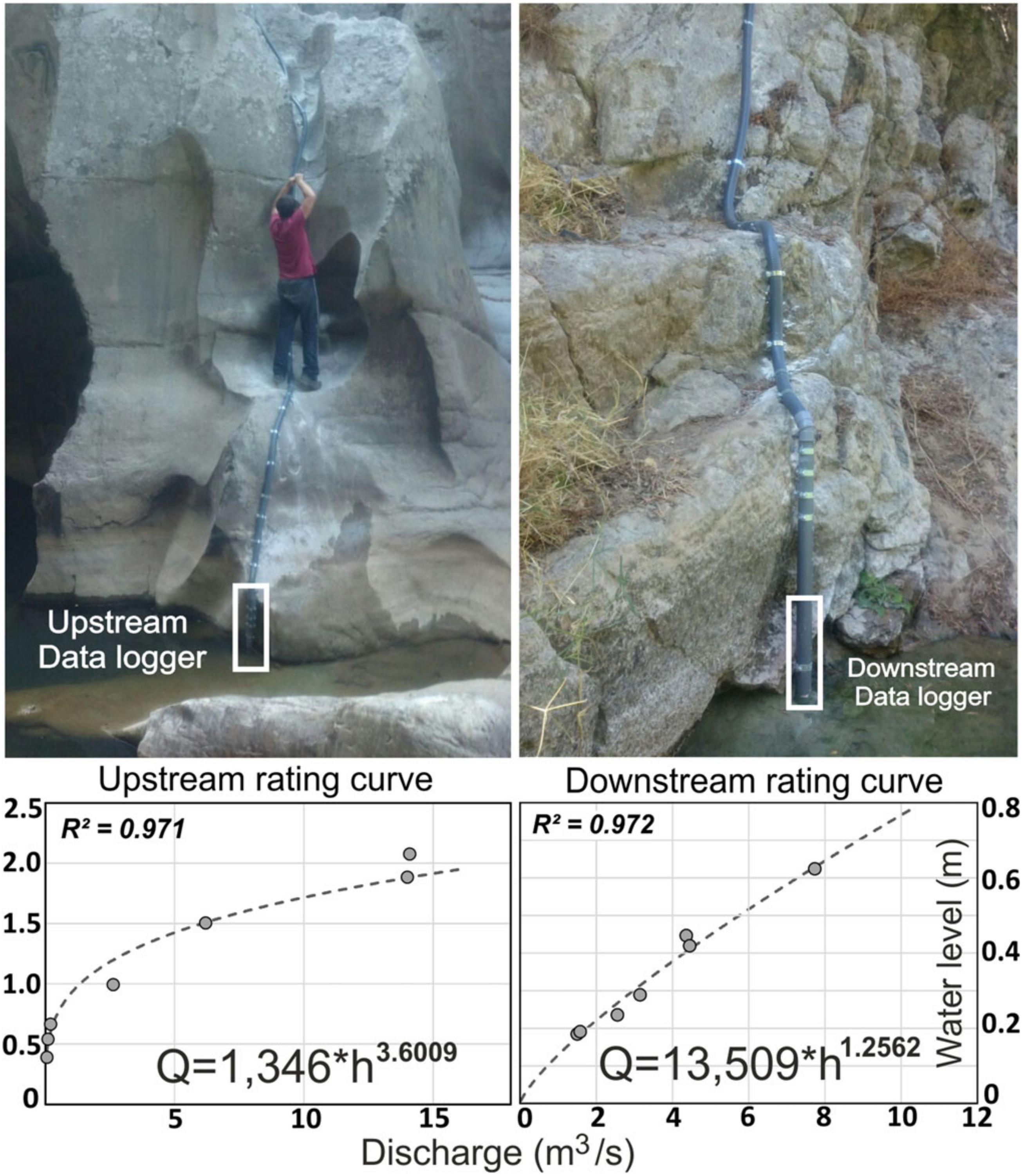

Fig. 4 Water-level data logger emplacement and their respective rating curves

(Fig. 3a). An *ALBILIA-SARL®* *GGUN-FL30* field fluorometer (accuracy of ±0.01 NTU) was also attached to the same structure in order to obtain records of water turbidity (measurement each 15 min.). A water pump for groundwater sampling routine completes the field equipment. The pump was coupled to a *HACH® Sigma SD 900* autosampler (sited at the gorge ledge). An auxiliary electronic synchronizer, specifically developed for this purpose, carried out the

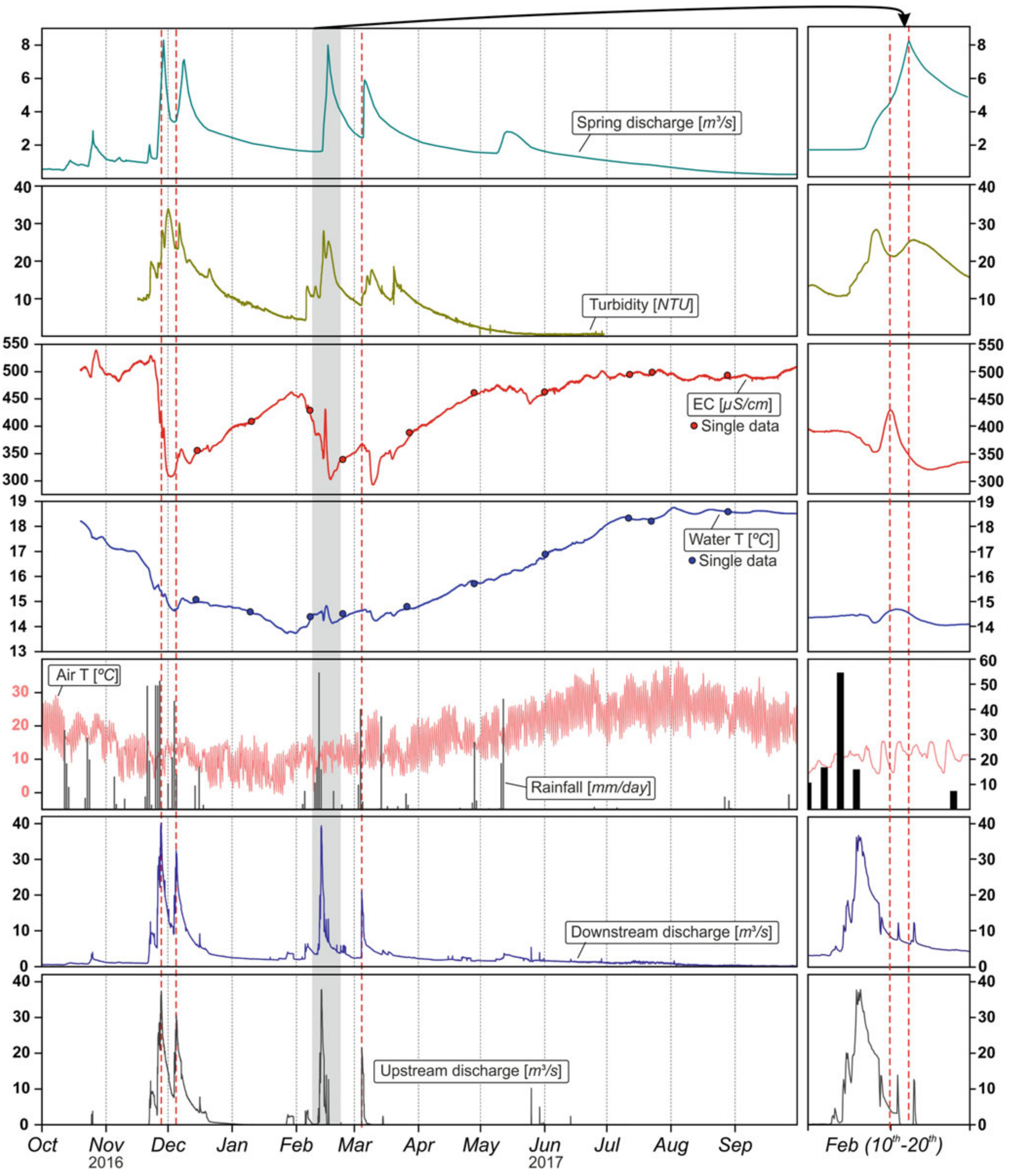

Fig. 5 Continuous record of water level (both up- and downstream), EC, T and turbidity measured in the water drained by Charco del Moro spring, with respect to the precipitation events

coordination of both instruments. All these devices and probes are annually checked and recalibrated at low flow conditions.

Results

Figure 5 shows the temporal evolution of the outflow rate, EC, T and turbidity of the water drained by Charco del Moro spring from October 2016 to September 2017, jointly with the rainfall and the air temperature recorded in the area during the same control period. This figure also displays the hydrographs inferred for the Guadiaro streamflow, both up- and downstream from the spring. During the monitoring period, relatively quick flow variations in response to the main recharge events (from 1.2 to 8.3 m^3/s) were detected in the spring, with a mean time lag of 3 days between the center of gravity of precipitation and the discharge peaks (Fig. 5).

The annual averaged discharge rate was 1.85 m^3/s. Contribution of water runoff generated at the head basin of Guadiaro River to the total streamflow rate occurred only during the rainfall period (from November 2016–May 2017); the rest of the year, the base flow of the river is exclusively supported by the groundwater drained through the spring. Regarding the temporal evolution of the physicochemical parameters (Fig. 5), relatively rapid and sharp falls of up to 200 µS/cm in EC were recorded during each recharge event. The magnitude of dilutions varied depending on the quantity and intensity of rainfall. After each dilution, mineralization progressively rose until become almost steady around 500 µS/cm, during summer months, being this trend interrupted by springtime precipitations, which caused new dilutions. Significant water temperature falls (up to 0.7 °C) slight lagged were recorded in Charco del Moro spring following main autumn and winter rainfall episodes, within a general seasonal pattern influenced by air temperature changes. When rainfalls were significantly intense, main EC and water T decreases were preceded by more mineralized and slightly warmer groundwater as shown in detail in Fig. 5. On the other hand, the turbidity values underwent quick rises during all recharge events, proportionally to the intensity and magnitude of precipitation episodes. Even limited amounts of rainfall provoked slight increases in this parameter.

Discussion

Reaching a reliable knowledge about the characteristics and behavior of karst aquifers (water resources, structure, dynamic, etc.) demands the implementation of suitable monitoring strategies. Nevertheless, the hydrogeological heterogeneity and the complexity of karst media lead to challenges in collecting sufficient information about karst system properties (spatial and temporal). Furthermore, complex setting or poorly accessible areas where observation points are located, such as the site exemplified in this work, often impose constraints on reliable field measurements and equipment installation, requiring an adequate and inventive combination of electronic data logger/probes and supplementary facilities for acceptable monitoring results. This effort has been done in numerous but singular karst spring worldwide as, i.e., Barton spring (Barker 1996), Vaucluse spring (Lastennet 1995), given the significance of these outlets, as strategic monitoring points not only for assessing the behavior of karst aquifers, but also for achieving effectiveness in groundwater management for water supply and environmental purposes.

In the case presented here, joint analysis of the data recorded in Charco del Moro spring during one hydrological year has meant a significant improvement in understanding the behavior of the pilot system, also allowing a preliminary estimation of water resources to be inferred. Thus, quick variations in discharge rate following recharge events reflect the existence of a highly developed karst network, which enables fast flows and short transit time of water within the system, from recharge areas to the spring. This is in agreement with the observed changes in EC and in T, whose values were generally lower after recharge episodes (Fig. 5) and higher at recession conditions. However, the increases in these parameters recorded before dilutions (i.e., February 2017, Fig. 5) could be caused by a “piston-flow” effect, where water recently recharged pushed groundwater previously stored in the saturated zone, with greater residence time. This provoked mobilization, toward the spring, of groundwater with higher mineralization and temperature values, suggesting the existence of ascending flows from the saturated zone. Later, recently infiltrated water coming from the surface rapidly arrived to the spring via karst conduits, leading to the mixing of both types of water.

The high development of karst conduits also favored quick and sharp variations in turbidity during recharge events. Nevertheless, unlike the other physicochemical variables, each rainfall episode was always accompanied by increases in turbidity signal, regardless of whether the episode caused “piston-flow” or dilution conditions. According to Pronk et al. (2006, 2009), the first turbidity peak (recorded before dilutions) would be due to the mobilization of sediments in the conduits, by increasing flow velocities and turbulences as a result of rises in the hydraulic head. This mobilization of particles could reach the flows within the saturated zone, since the peaks of turbidity and the maximum values of EC and T attributed to the “piston-flow” pulse coincided on time. The arrival of freshly infiltrated water at the spring, bringing sediments from the surface and diluting the water previously stored in the aquifer, could be attributed to a second type of turbidity peak. This would be in accordance with field evidences and with previous work (Andreo et al. 2004), which confirm the significant contribution of the allogenic component from non-karst areas (Flysch sandstones and clays outcrops) to the total recharge of the system. Additional methodologies using both natural and artificial tracers will be shortly applied in order to confirm these statements.

The short period of record and the fact that the results obtained during the monitoring period are not illustrative of the average meteorological conditions (considered as dry and slightly warmed) reduce the reliability of the interpretation of the system functioning. This is especially evident for the hydrodynamic response. Both upstream and downstream rating curves and, consequently the final discharge rate of the spring, might be further optimized if field hydrodynamic data were available in higher resolution, undertaken specially during high flow conditions. Anyway, it will be necessary to wait for the field equipment good functioning under other hydrodynamic scenarios.

Conclusions

The adaptation and installation of field equipment for continuously monitoring the natural responses of a poorly accessible streambed spring located at a fluviokarstic gorge in Southern Spain have provided a one-year record (2016/17), which allows performing a preliminary assessment of the hydrogeological behavior of the related karst system. Charco del Moro spring responds to precipitation events with sharp and fast increases in discharge rate and decreases in water mineralization and temperature; the last one presenting a seasonal pattern influenced by changes in air temperature. This hydrogeological behavior indicates that the system drained by the spring has a well-developed functional karstification, typical of conduit flow systems, with rapid drainage and a low capacity to attenuate the input signal. The thermal response and the mineralized water drained by the spring during piston-flow events indicate the existence of ascending regional groundwater flows, with longest residence time throughout the system. This groundwater flow coming from the saturated zone and the recently infiltrated water circulate through the karst network, and they converge at the spring. The degree of heterogeneity in the duality of groundwater movement and storage dynamics were also denoted by the increases in turbidity signal due to (1) the infiltration of surface water through sinkholes (provoking dilutions) and (2) remobilization of particles in conduits by risings of the hydraulic head and—subsequently—the flow velocities.

Further efforts are necessary to determine the hydrogeological functioning of the system, especially in order to precise the hydrodynamic response of the spring, given the significance of this outlet as one of the largest discharge points in Andalusia. This is a crucial aspect that would be considered for the evaluation and management of water resources stored in the nearby carbonate aquifers, since they have direct consequences for water supplying in the region. The monitoring infrastructure could be used for preservation of groundwater-dependent ecosystems and hydrological management in an area particularly affected by environmental changes and impacts.

Acknowledgements This study was carried out under the CGL2015-65858R project and to the Research Group RNM-308 of the Junta de Andalucía. The authors thank Raúl Cerezo, Paloma Carrasco, Marianna Mazzei and Daniel Montiel for their help during installation of devices.

References

Andreo, B., Vadillo, I., Carrasco, F., Neukum, C., Jiménez, P., Goldscheider, N., Hötzl, H. Vías, J.M., Pérez I. & Göppert, N. (2004): Precisiones sobre el funcionamiento hidrodinámico y la vulnerabilidad a la contaminación del acuífero kárstico de la Sierra de Líbar (provincias de Málaga y Cádiz, sur de España) a partir de un ensayo de trazadores. Revista de la Sociedad Geológica de España, 17 (3–4): 187–197.

Barker, R.A. & Ardis, A.F. (1996): Hydrogeologic framework of the Edwards-Trinity aquifer system, west-central Texas: USGS Professional Paper 1421-B, 61 p.

Ford, D.C. & Williams, P.W. (2007): Karst Hydrogeology and Geomorphology. Wiley Chichester, United Kingdom. 562 p.

Goldscheider N. & Drew, D. (eds) (2007): Methods in Karst Hydrogeology. International Contributions to Hydrogeology 26, International Association of Hydrogeologists, Taylor & Francis, London, 264 pp. ISBN 978-0-415-42873-6.

Hartmann, A., Goldscheider, N., Wagener, T., Lange, J. & Weiler, M. (2014): Karst water resources in a changing world: Review of hydrological modeling approaches, Rev. Geophys. 52, 218–242. https://doi.org/10.1002/2013rg000443.

Lastennet, R. & Mudry, J. (1995): Impact d'un événement pluvieux exceptionnel sur le fonctionnement du système karstique – Cas de l'orage du 22/9/92 à Vaison-la-Romaine (Vaucluse, Sud-Est de la France). C R Acad Sci Ser 2a 320: 953–959.

Martín-Algarra, M. (1987): Evolución geológica alpìna del contacto entre las Zonas Internas y Externas de la Cordillera Bética. Ph.D. Thesis, University of Granada.

Pronk M., Goldscheider N. & Zopfi, J. (2006): Dynamics and interaction of organic carbon, turbidity and bacteria in a karst aquifer system. Hydrogeology Journal, 14, 473–484.

Pronk, M., Goldscheider, N., Zopfi, J. & Zwahlen, F. (2009): Percolation and particle transport in the unsaturated zone of a karst aquifer. Ground Water 47 (3), 361–369.

Senciales, J.M. (2007): El clima en la provincia de Málaga. In: Atlas Hidrogeológico de la provincia de Málaga. Durán, J.J. (ed.). Vol. 1, 49–58. Diputación de Málaga; Instituto Geológico y minero de España. Madrid (Spain). 296 p.

Optimization of High-Resolution Monitoring of Nutrients and TOC in Karst Waters Using a Partial Least-Squares Regression Model of a UV–Visible Spectrometer

Aurélien Vallet, Fanny Moiroux, and Jean-Baptiste Charlier

Abstract

For a cost-effective survey of water quality in aquifers with a fast chemical response, such as karst aquifers, continuous high-resolution monitoring by an automatic sensor is relevant. We tested the suitability of the s::can UV–visible spectrometer for continuous measuring in a karst environment of the parameters proposed by the probe manufacturer (NO_3 and total organic carbon TOC) as well as other parameters, such as total phosphorus (TP). The spectrometer was installed at the Loue Spring (French Jura Mountains), where water was also sampled for chemical analysis of NO_3, TOC, and TP at a frequency of 1 to 4 days. A calibration model was developed based on the partial least-squares regression (PLSR) method, applied to the absorption spectra. Our method showed good results. For NO_3, both the factory calibration ($R^2_{\mathrm{VAL}} = 0.98$) and our calibration model ($R^2_{\mathrm{VAL}} = 0.99$) are very good. For TOC, except for a slight underestimation of some peaks, the low and high values are better reproduced by our model developed ($R^2_{\mathrm{VAL}} = 0.63$, or 0.23 with the factory calibration). For TP, despite a higher background noise, the overall dynamics are well simulated ($R^2_{\mathrm{VAL}} = 0.56$). Finally, our results showed that processing the raw data of the spectrum measured by the spectrometer optimizes the high-frequency monitoring of water quality and provides a better prediction of some parameters, as well as giving promising results for the calibration of non-programmed parameters.

Keywords

Monitoring • High-resolution • Nutrients • TOC • Karst • UV-Visible spectrometer • Jura moutain

Abbreviations

MSC	Multiple Scatter Correction
NCS	Non-Compensated Spectrum
PLSR	Partial Least-Square Regression
R^2	Coefficient of determination
RMSE	Root-Mean-Square Error
TP	Total Phosphorus
TOC	Total Organic Carbon
1st Der.	First derivative of the raw spectra

Introduction

Degradation of groundwater quality is a major concern in terms of environmental impact and public health problems. Anthropogenic pressure is growing in karst basins, due to agricultural pressure and sewage effluents that contribute excess nutrients to groundwater (e.g. Huebsch et al. 2013, 2014). For the efficient surveying of water quality in such an environment, the implementation of continuous high-resolution monitoring with an automatic sensor is relevant. Karst aquifers are well known for rapidly transferring infiltration water toward springs and rivers, limiting the self-purification role of the aquifer and generating fast mobilization or dilution of nutrients (Charlier et al., submitted in this issue).

The s::can UV–visible spectrometer allows reliable monitoring of certain nutrient parameters, coupled with limited maintenance (Rieger et al. 2008; Bende-Michl et al. 2010; Huebsch et al. 2015; Tournebize et al. 2015). A global factory calibration for several parameters, including nitrate (NO_3), total organic carbon (TOC), turbidity, and luminescent dissolved oxygen (LDO), designed by the manufacturer

A. Vallet (✉)
BRGM, 21000 Dijon, France
e-mail: a.vallet@brgm.fr

F. Moiroux · J.-B. Charlier
BRGM, Univ. Montpellier, Montpellier, France

C. Bertrand et al. (eds.), *Eurokarst 2018, Besançon*, Advances in Karst Science,
https://doi.org/10.1007/978-3-030-14015-1_13

on the basis of a surface water dataset, is programmed by default into the spectrometer. However, not the whole range of chemical characteristics of the surface water dataset is supplied by the probe manufacturer, and its representativeness for the karst domain is questionable. In fact, it is well known that turbidity in karst water may be high after a rainfall event, and this parameter is known to perturb data acquisition when using optical probes. A local correction proposed by the manufacturer can be applied to the global calibration results, which is based on a linear correction (rather than a new calibration) of the measurements.

Several studies have developed local calibration methods of the s::can Spectrolyser in different environments (Rieger et al. 2004; Van den Broeke 2007; Etheridge et al. 2014; Grayson and Holden 2016), but few were carried out in a karst environment (Perfler et al. 2002; Huebsch et al. 2015). In addition, some studies were interested in calibrating parameters not provided by the manufacturer, such as total Kjeldahl nitrogen (NH_4), total suspended solids, dissolved organic carbon, total phosphorus (TP), and PO_4 (Etheridge et al. 2014).

The purpose of our study was to test whether spectroscopy is suitable for measuring the NO_3 and TOC parameters proposed by the manufacturer as well as a parameter not proposed (TP), in karst waters. To this end, we developed a calibration model applied to the spectra as measured by the probe, based on the partial least-squares regression method (PLSR) and incorporating pre-processing for turbidity influence compensation and wavelength selection. Our aims were to: (1) evaluate the relevance of the factory calibration, comparing factory results with those obtained by our approach; (2) assess whether the use of wavelength selection and turbidity correction improves calibration performance; and (3) evaluate the suitability of our model for predicting non-programmed factory parameters. Our work was based on 11 months of daily nutrient monitoring in the Loue Spring of the French Jura Mountains.

Materials and Methods

Study Site and Measurements

Site Description

The spectrometer was installed in the Loue Spring, in the French Jura Mountains (Fig. 1a). The recharge area of about 200 km^2 is underlain by Jurassic limestone (Fig. 1b). Moreover, the Loue Spring is partly recharged by river losses from the Doubs River, leading to drying up of the river during low-water periods in summer (Charlier et al. 2014). The precipitation averages 1700 mm per year, and the mean annual discharge of the spring was about 9 m^3/s over the past three decades

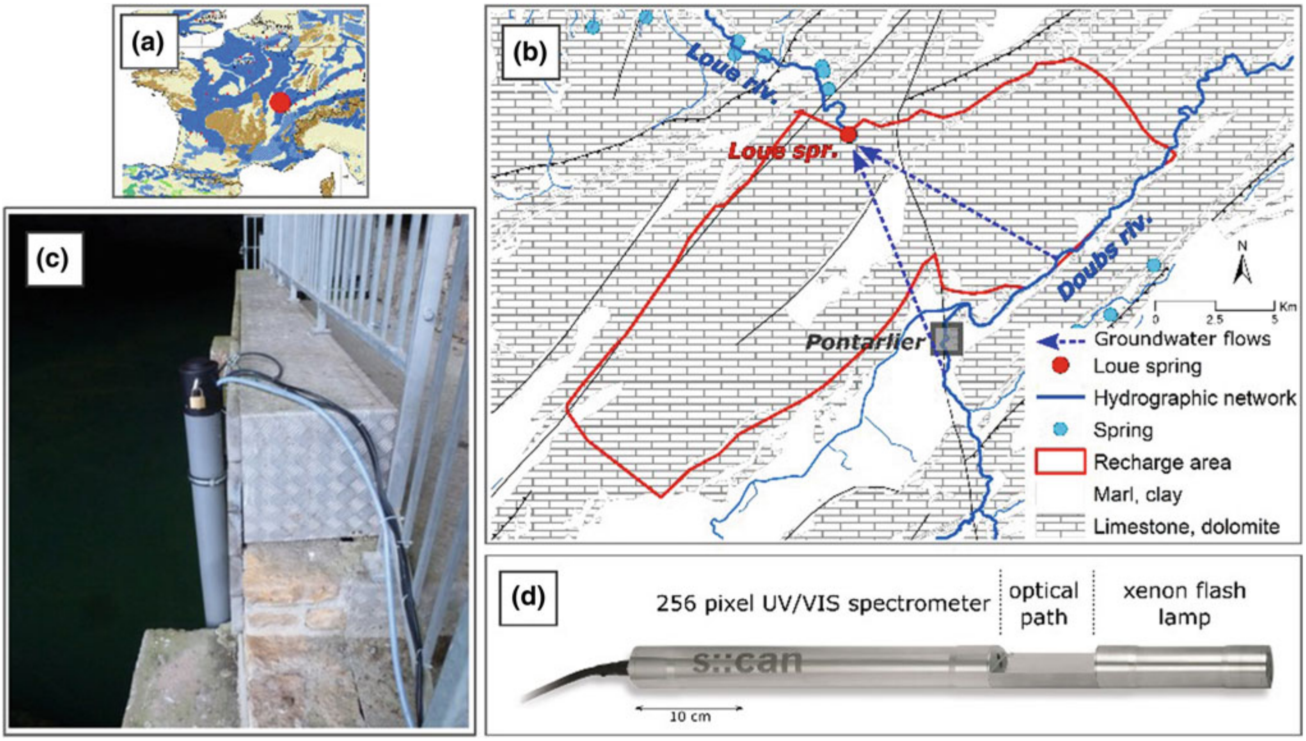

Fig. 1 **a** Location of the Loue Spring in the French Jura Mountains on the World Karst map (Karst aquifers in blue—Chen et al. 2017), **b** Hydrogeological map, **c** Photo of the monitoring station in the spring, and **d** Spectrophotometer probe (s::can Messtechnik GmbH)

Land use is dominated by permanent grazing for dairy cows (60%) and forest (30%). The main application of fertilizer occurs in March–April, and other applications are between May and July after the first hay cut. In September–October, before the cold season, manure and slurry pits are emptied for spreading on grassland, and in winter, composted manure is spread as well. The Doubs River losses thus contribute some nutrients of agricultural origin, but also from the wastewater treatment plants of Pontarlier (about 50,000 inhabitants).

Spectrometer Probe

The s::can Spectrolyser™ (Fig. 1d) is a submersible UV–visible spectrophotometer that measures the entire absorption spectrum in water between 220 and 732.5 nm with a 2.5 nm interval, i.e., a spectrum of 206 variables (Fig. 2). The raw absorption “fingerprint” of the water can be converted into nutrient elements as well as turbidity and dissolved oxygen. A measuring cycle lasts between 20 and 60 s, allowing a high measurement frequency and the detection of rapid changes in water chemistry. A self-cleaning system allows the instrument to be installed in turbid water with little maintenance. Probe sensitivity can be adapted according to the environmental context, from ultra-pure water to concentrated industrial discharge, by selecting a suitable optical path length (Rieger et al. 2004) from 2 to 35 mm. In the case of natural water with low turbidity, an optical path length of 35 mm is recommended (Huebsch et al. 2015). Thanks to the default global calibrations, the spectrometer allows the direct measurement of several pre-selected parameters by the manufacturer, from their absorbance spectra.

Data Acquisition

The time step of spectrometer measurements was fixed at 15 min, from 3 May 2016 to 10 April 2017, i.e., almost 33,000 spectrum measurements. The automatic self-cleaning system was programmed to activate every 5 min, for a cleaning cycle of 30 s with a minimum of 10 s between cleaning and measurement, to avoid any influence of cleaning on the measurement.

An automatic water sampler installed at the Loue Spring for the QUARSTIC network project (Charlier and Vallet 2016) was used during the same period for comparing the NO_3, TOC and TP probe measurements with laboratory analyses. The optical window of the spectrometer was placed directly next to the inlet of the water sampler. Water bottles were pre-acidified with sulfuric acid in order to maintain a pH = 2 for 1-week sample preservation. Water was sampled (1) at a daily rate from 4 May to 25 July 2016 and from 28 October 2016 to 20 February 2017, and (2) at a 4-day rate from 29 July to 27 October 2016 and from 24 February to 10 April 2017. A total of 215 samples were analyzed at the QUALIO Laboratory (Besançon, France) over these periods.

Calibration Models

Model Provided by the Manufacturer

A global calibration of the UV–visible spectrometer is proposed by default by the manufacturer. This is based on the partial least-squares regression (PLSR) method (presented

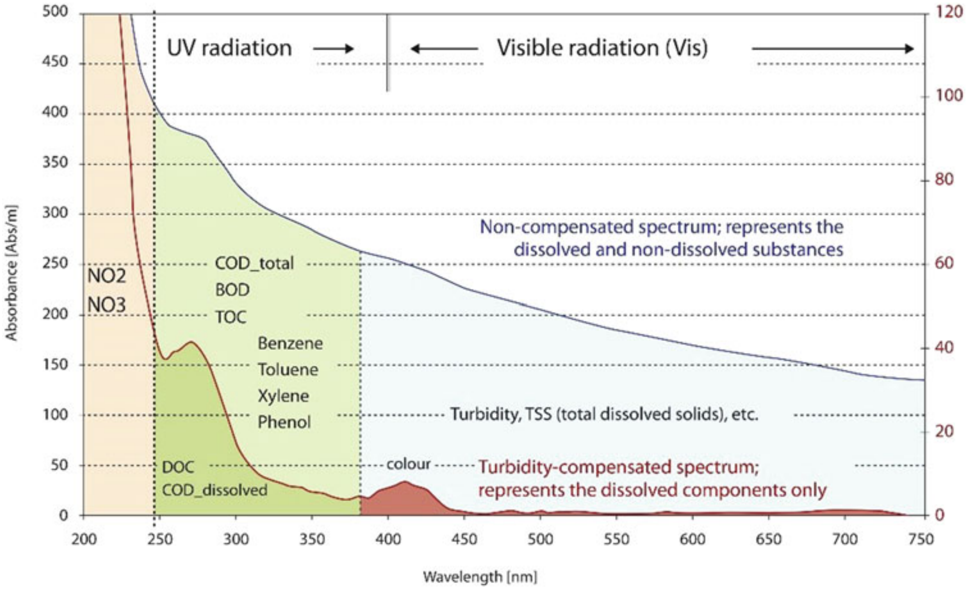

Fig. 2 Absorption of different compounds within the spectrum from 200 to 750 nm with and without turbidity compensation (s::can Messtechnik GmbH). Left-hand axis corresponds to absorbance for the non-compensated spectrum and the right-hand axis is the absorbance of the turbidity-compensated spectrum

hereafter), of hundreds of datasets of spectra and chemical analyses measured in different surface waters (rivers, lakes, etc.) (Van den Broeke 2007). This global factory calibration allows the automatic conversion of absorbance spectra data into chemical concentrations for the default parameters supplied by the manufacturer. A local calibration of the global factory model is recommended and can be carried out by users in order to improve the model performance. Such local calibration requires on-site measurements of chemical analysis and spectrum data. The local calibration proposed by the manufacturer consists in a linear adjustment of the outputs from the global calibration model, in order to minimize the errors between locally measured data on site and the default results. The local calibration does not provide a new PLSR model based on in situ measurements.

The Newly Developed Model

The local calibration model developed in this study was based on partial least-squares regression (PLSR), a statistical method combining multiple linear regression and principal component analysis (PCA). The PLSR model seeks—for a new space and based on PCA—to project the observed variables X and the predicted variables Y (latent variable approach), where the multidimensional direction in the X space explains the maximum multidimensional variance direction in the Y space. A multiple linear model is then evaluated in this new space between X and Y. The PLSR model is particularly suited to an X matrix with more variables than observations and/or multicollinear variables. For such cases, standard regression models are not suitable. In fact, PLSR can easily treat a large data matrix, extracting the relevant part of the information and producing reliable and complex models. For these reasons, this method is commonly used in spectrometry (Leardi et al. 1998; Rieger et al. 2004, 2006, 2008; Etheridge et al. 2014).

Turbidity Compensation

Turbidity due to suspended matter causes scattering of light and shading, and thus influences absorption measurements over the entire spectrum (Fig. 2). It requires compensation for determining a reliable estimate of dissolved substances, such as nutrients (Langergraber et al. 2002; Van den Broeke 2007). The importance of the dispersion phenomenon depends on the size of the suspended particles. This correction has been implemented for karst waters, which are well known to be largely impacted by turbidity especially after storms. Two methods of turbidity compensation were tested for this study:

Multiple Scatter Correction (MSC, using Andrea Candolfi's algorithm, ©1997 for ChemoAC, FABI, Vrije Universiteit Brussel). Each spectrum is shifted and rotated so that it fits linearly as closely as possible to the mean data spectrum. The correction depends on the mean spectrum of the training set.

First derivative of the raw spectra, which was successfully implemented by Etheridge et al. (2014).

Selection of Variables in a Partial Least-Squares Regression Model

The PLSR model was initially considered to be almost insensitive to noise, for which reason it was commonly thought that no feature selection at all is required (Leardi et al. 2004). Today, however, it is widely recognized that a feature selection can be highly beneficial when only spectrum variables with predictor information are considered for the model. The selection of variables improves the predictive ability of the model by reducing model overfitting, and will help producing a reliable parsimonious model.

For this study, the PLS genetic algorithm (GA-PLS) (Leardi et al. 1998; Leardi 2000) was used for selecting the variables. This algorithm was especially designed for typically multicollinear spectral data, in such a way that the final model is composed as much as possible of contiguous wavelengths.

Calibration Strategy

Our calibration strategy simulates operational water quality monitoring by a field-based spectrometric probe, routinely checked by repeated analyses of water samples for the continuous improvement and verification of the calibration model performance. To this end, the time series was split into a calibration dataset and a validation dataset, which are alternately assigned throughout the time series. Both calibration and validation intervals are thus spread over the entire variation range. This approach is different to the usual partitioning of a time series dataset into two successive periods (a calibration period followed by a validation period), as the purpose of the calibration was not to produce a predictive model, but to produce a calibration model for operational monitoring.

In addition, because of the limited 1-year measurement period, the calibration strategy had to account for various nutrient dynamics in water during low- and high-water periods. Thus, the successive assignment of calibration or validation datasets was based on sorted concentration time series, retaining a representativeness of the whole concentration range obtained for each parameter, and both calibration and validation datasets were spread over the entire variation range. In order to have enough data for calibrating the model, 75% of the dataset was assigned for calibration and 25% for validation. Outliers in laboratory analyses and/or spectra absorbance were manually removed from the dataset.

A determination coefficient (R^2) was used for assessing model performance on the calibration datasets, and model performance on the validation datasets was assessed by the root-mean-square error (RMSE). RMSE criteria range between 0 and $+\infty$, with 0 signifying a perfect fit, whereas R^2 ranges between 0 and 1, with 1 signifying a perfect fit.

Results and Discussion

Performance of Local Calibration Models

Results of the calibration models proposed in this study are presented in Table 1. For the three tested parameters, a selection of variables does not significantly improve the performance of local calibration and its implementation appears irrelevant for NO_3 and TP.

Concerning turbidity compensation, contrasted results were obtained depending upon the parameters. For NO_3, the results obtained with turbidity compensation did not improve significantly the PLSR model based on a non-compensated spectrum (NCS), in relation to the localization domain of wavelength in the UV spectrum that is less impacted by turbidity (Fig. 2).

For TOC, similar results were obtained with a good performance of the model in the non-compensated spectrum. The model obtained from compensation using MSC gave similar results as that using the first derivative of the raw spectrum, but did not improve significantly the performance from a non-compensated spectrum.

For TP, in contrast to the previous parameters, the results were globally fair to worse, with R^2_{CAL} ranging from to 0.72 to 0.49. The best model corresponds to turbidity-compensated raw spectra using MSC without a selection of variables. This result is somewhat surprising as it contradicts those of Etheridge et al. (2014), who mentioned that absorption in the visual wavelengths is important for the prediction of TP, phosphorus-bearing particles being detectable in that range. A different environmental context may explain this difference.

Comparison with Manufacturer Global and Local Calibration

Figure 3 presents the results of the calibrated models, comparing the evolution of the pre-configured parameters provided by the manufacturer (NO_3 and TOC) as well as that of the non-programmed parameter TP. The quality of the factory calibration (black curve) differs according to the parameters. Nitrate is correctly simulated ($R^2_{\mathrm{VAL}} = 0.98$) unlike TOC ($R^2_{\mathrm{VAL}} = 0.23$), for which the baseline is overestimated and many peaks are underestimated. The model developed in this study (dashed red curve) shows equal performance for surveying NO_3 ($R^2_{\mathrm{VAL}} = 0.99$), but proves much more efficient for TOC ($R^2_{\mathrm{VAL}} = 0.63$). Except

Table 1 Results of the model calibration: non-compensated spectrum (NCS), turbidity-compensated spectrum using Multiple Scatter Correction (MSC), and turbidity-compensated spectrum using the 1st derivative (1st Der.); CAL and VAL stand for calibration and validation dataset, respectively; R^2 and RMSE are the computed performance indicators of determination coefficient and root mean

Method	NO_3			TOC			TP		
	Cal.	Val.		Cal.	Val.		Cal.	Val.	
	R^2_{CAL}	R^2_{VAL}	RMSE	R^2_{CAL}	R^2_{VAL}	RMSE	R^2_{CAL}	R^2_{VAL}	RMSE
	(n.d.)	(n.d.)	(mg/L)	(n.d.)	(n.d.)	(mg/L)	(n.d.)	(n.d.)	(10^{-3} mg/L)
Without variable selection									
NCS	**0.99**	**0.99**	**0.14**	**0.86**	**0.55**	**0.35**	0.49	0.53	6.85
MSC	0.98	0.85	0.66	0.75	0.56	0.37	**0.72**	**0.56**	**6.82**
1st Der.	**0.99**	**0.99**	**0.16**	0.74	0.59	0.34	0.64	0.42	8.79
With variable selection									
NCS	**0.99**	**0.99**	**0.15**	0.82	0.50	0.36	0.58	0.57	6.60
MSC	0.96	0.89	0.54	**0.76**	**0.62**	**0.32**	Not possible		
1st Der.	**0.99**	**0.99**	**0.13**	**0.84**	**0.63**	**0.32**	0.52	0.36	9.21
Manufacturer calibration model									
Local	/	0.98	0.25	/	0.23	0.44	/	/	/

square error, respectively; the best model for each parameter is in bold-underlined, and models with performances differing from the best model by less than 0.1 for R^2 and less than 25% for RMSE are in bold

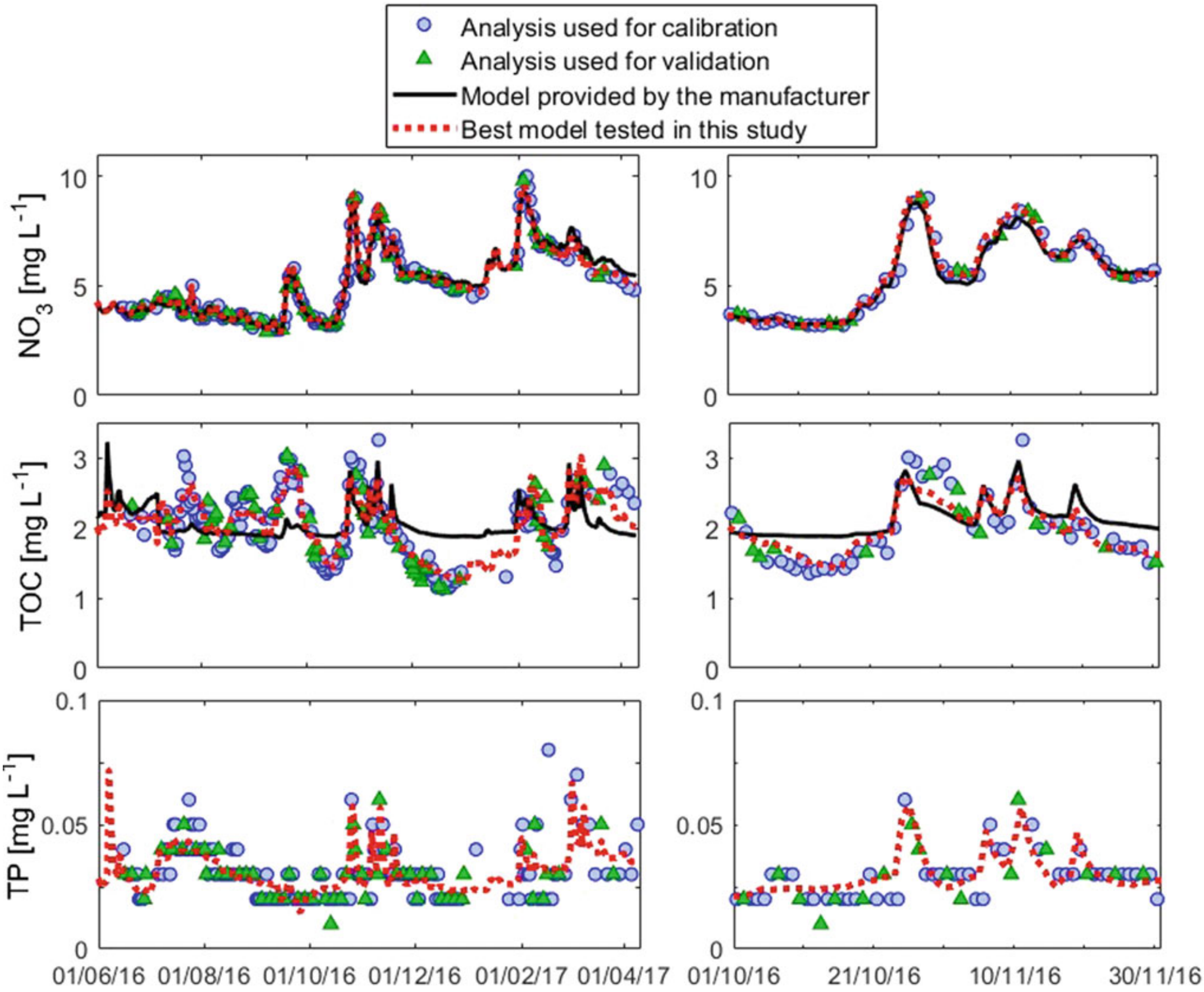

Fig. 3 Comparison of the NO_3 and TOC parameters of the calibration model used in standard mode (black curves) with the one proposed in this study (dashed red curve), and evaluation of our model for a non-programmed factory parameter (TP) for the whole period (left) and for a zoom-period of Oct.–Nov. 2016 (right). The best model tested in this study for each parameter matches with models in bold-underlined on Fig. 2

for a slight underestimation of some peaks, both low and high values are well reproduced.

Results for the TP survey ($R^2_{\mathrm{VAL}} = 0.56$) show that—despite higher background noise—the overall dynamics are well simulated. Except for some peaks that are not detected by the calibration model, the main contamination events are properly simulated.

Conclusions

Monitoring water quality during storm events with an s::can UV–visible spectrometer allows a high measurement frequency and the detection of rapid changes in water chemistry, coupled with limited maintenance. We tested the suitability of spectroscopy for measuring karst water parameters proposed by the manufacturer (NO_3 and TOC) as well as non-programmed parameters (TP). The fieldwork took place in the Loue Spring of the French Jura Mountains.

Our test results are very positive: Using the raw spectrum data measured by the spectrometer improved the high-frequency monitoring of water quality. In the case of TOC, the preconfigured parameters were well predicted. Moreover, the promising results obtained for TP allow us to consider the calibration for new parameters.

As a next step, it will be relevant to optimize the probe calibration by assessing the minimum sampling frequency required for maintaining good performance and by adapting the calibration to specific hydrological conditions, such as storm events and drought periods.

Acknowledgements The work was funded by the Rhone-Mediterranean and Corsica Water Agency, the Doubs Department, and the French Geological Survey (BRGM) under the QUARSTIC network project. The authors wish to thank the *Syndicat Mixte de la Loue* and notably Vanessa Stefani for assistance with the field work. We thank Philippe Marinot from s::can France for providing advice on the probe characteristics. The manuscript was improved by constructive comments from three anonymous reviewers.

References

Bende-Michl U, Hairsine PB, 2010. A systematic approach to choosing an automated nutrient analyser for river monitoring. *J. Environ. Monit.* 12, 127–134. https://doi.org/10.1039/b910156j.

Chen Z, Auler A, Bakalowicz M, Drew D, Griger F, Hartmann J, Jiang G, Moosdorf N, Richts A, Stevanovic Z, Veni G, Goldscheider N, 2017. The World Karst Aquifer Mapping project: concept, mapping procedure and map of Europe. *Hydrogeol. J.* 25. https://doi.org/10.1007/s10040-016-1519-3.

Charlier, JB, Desprats JF, Ladouche B., 2014. Appui au SCHAPI 2014 – Module 1 – Rôle et contribution des eaux souterraines d'origine karstique dans les crues de la Loue à Chenecey-Buillon. BRGM/RP-63844-FR. 118p. http://infoterre.brgm.fr/rapports/RP-63844-FR.pdf (accessed March 2018).

Charlier JB, Vallet A, 2016. Projet QUARSTIC: QUAlité des eaux et Réseau de Surveillance des rIvières Comtoises. Rapport de fin de 1ère année. BRGM/RP-65874-FR, 25p, http://infoterre.brgm.fr/rapports/RP-65874-FR.pdf.

Charlier, JB, Vallet A, Tourenne D, Hévin G., 2018. Dynamics and fluxes of nutrients in surface and groundwaters in a cultivated karst basin in the Jura Mountains. Springer, Eurokarst 2018. This issue (submitted).

Etheridge, JR, Birgand F, Osborne JA, Osburn CL, Burchell II MR, Irving J, 2014. Using in situ ultraviolet-visual spectroscopy to measure nitrogen, carbon, phosphorus, and suspended solids concentrations at a high frequency in a brackish tidal marsh. *Limnol. Oceanogr.: Methods*. 12, 10–22. https://doi.org/10.4319/lom.2014.12.10.

Grayson RP, Holden J, 2016. Improved automation of dissolved organic carbon sampling for organic-rich surface waters. *Sci. Total Env.*. 543, 44–51. https://doi.org/10.1016/j.scitotenv.2015.10.14.

Huebsch M, Horan B, Blum P, Richards KG, Grant J, Fenton O, 2013. Impact of agronomic practices of an intensive dairy farm on nitrogen concentrations in a karst aquifer in Ireland, *Agric. Ecosyst. Environ.*, 179. 187–199. https://doi.org/10.1016/j.agee.2013.08.021.

Huebsch M, Fenton O, Horan B, Hennessy D, Richards KG, Jordan P, Goldscheider N, Butscher C, Blum P, 2014. Mobilisation or dilution? Nitrate response of karst springs to high rainfall events. *Hydrol. Earth Syst. Sci.* 18. 4423–4435. https://doi.org/10.5194/hess-18-4423.

Huebsch M, Grimmeisen F, Zemann M, Fenton O, Richards KG, Jordan P, Sawarieh A, Blum P, Goldscheider N, 2015. Technical Note: Field experiences using UV/VIS sensors for high-resolution monitoring of nitrate in groundwater. *Hydrol. Earth Syst. Sci.* 19. 1589–1598. https://doi.org/10.5194/hess-19-1589-2015.

Langergraber G, Fleischmann N, Hofstädter F, 2002. A multivariate calibration procedure for UV/VIS spectrometric quantification of organic matter and nitrate in wastewater. *AutMoNet.* Session 1, 25–32.

Leardi R, Lupiáñez González A, 1998. Genetic algorithms applied to feature selection in PLS regression: how and when to use them. *Chemom. Intell. Lab. Syst*. 41. 195–207.

Leardi R. 2000. Application of genetic algorithm–PLS for feature selection in spectral data sets. *J. Chemom*. 14. 643–655.

Leardi R, Nørgaard L, 2004. Sequential application of backward interval partial least squares and genetic algorithms for the selection of relevant spectral regions. *J. Chemom*. 18. 486–497. https://doi.org/10.1002/cem.893.

Perfler R, Staubmann K, Hofstädter F, 2002. Real time monitoring and control of karstic drinking water sources. Proc. *XXII Nordic Hydrological Conference* 2002, Røros, Norway.

Rieger L, Langergraber G, Thomann M, Fleischmann N, Siegrist H., 2004. Spectral in-situ analysis of NO_2, NO_3, COD, DOC and TSS in the effluent of a WWTP. *AutMoNet*. Session 1. 29–36.

Rieger L, Langergraber G, Siegrist H, 2006. Uncertainties of spectral in-situ measurements inwastewater using different calibration approaches. *Wat. Sci. Techn.* 53. 187–197. https://doi.org/10.2166/wst.2006.421.

Rieger L, Langergraber G, Kaelin D, Siegrist H, Vanrolleghem PA, 2008. Long-term evaluation of a spectral sensor for nitrite and nitrate. *Wat. Sci. Techn.*. 57,. 1563–1569. https://doi.org/10.2166/wst.2008.146.

Tournebize J, Chaumont C, Fesneau C, Guenne A, Vincent B, Garnier J, Mander Ü, 2015. Long-term nitrate removal in a buffering pond-reservoir system receiving water from an agricultural drained catchment. *Ecol. Engin.*, 80, 32–45. https://doi.org/10.1016/j.ecoleng.2014.11.051.

Van den Broeke J, 2007. On-line and In-situ UV/Vis Spectroscopy. *AWE International*. 55–59.

Analysis of the Flow Recessions of the Main Outlet of the Dyr Karst (Tebessa—Algeria)

Mohammed Laid Hemila and Bilel Djoulah

Abstract

In this paper, we present the results of a characterization study of the hydraulic behavior of the Maastrichtian karst system of the Dyr perched syncline that is situated in the northern of the Algerian territory and constitutes the north horst of the Tebessa—Morsott subsidence basin. We applied the method of analysis of the flow recession curves of the main outlet, with particular reference to the decreasing part of the unitarian hydrogram. Therefore, we will analyze: the recession, during which the infiltration influences the draining of the reservoir, and drying up, which starts at the moment when the infiltration discharge becomes zero. According to the Maillet model, the drainage of the saturated karst sub-system will be described and the various physical and structural parameters of its flow will be determined. The application of this method on the flood hydrograms of the Ain Zerga spring, over a period of nine hydrological cycles (2002/2003 to 2010/2011), revealed us that this karst system is characterized by a very complex structure and hydraulic behavior. This complexity is certainly due to the hierarchy of voids and the considerable irregularity of the temporal distribution of water inflow from precipitation. The functioning of the system is always marked by slow infiltration, despite the irregular change of the climatic conditions. The duration of water infiltration for recharging the saturated zone is 6–12 days. The saturated zone is characterized by rather rapid draining, probably due to strong karstification. Its groundwater reserves are quite important, and its flow regime is influenced by losses upstream of the main outlet and the intensity of pumping in deep wells installed in this sub-system. According to the Mangin's classification, the Maastrichtian aquifer system of Dyr is effectively a karst aquifer ($K < 0.5$) with a complex internal structure.

Keywords

Karst • Hydraulic behavior • Analysis of recession curves • Ain Zerga spring • Dyr perched syncline • Tebessa • Algeria

Introduction

The Tebessa region, located in northeastern Algeria, is characterized by an autochthonous group of carbonate formations of Paleogene—Upper Cretaceous age. At the northern border of the Tebessa—Morsott subsidence basin, and over an area of 162 km^2, a karst landscape composed of two karst systems is well marked by a synclinal structure called Dyr perched syncline (Fig. 1). The Maastrichtian is the most important karst aquifer system. It is drained by the Ain Zerga spring, which has a very irregular discharge from a few liters per second at low water to a few cubic meters per second during exceptional floods (4.23 m^3/s recorded on February 17, 1974). Furthermore, during well digging upstream of the outlet, a total loss of the injected water was observed and a drill bit disappeared in an underground void. These observations confirm a well-developed karstification of the system. Consistently, the pumping tests performed on these wells revealed a high hydraulic potential.

In order to identify the hydraulic behavior of this Maastrichtian karstic aquifer system, we have applied the approach proposed by (Mangin 1970a, b). *This* ancient method of analysis was developed specifically for karst aquifers and allows to get preliminary information on the functioning of the aquifer system. In this context, we have limited our task to the processing of basic data using the theoretical concepts of these methods of the functional approach. It is an exploratory study, which will be completed in the future with more recent approaches, in particular, those proposed by Fiorillo (2014);

M. L. Hemila (✉) · B. Djoulah
Département Des Sciences de La Terre et de L'univers, Université de Tébessa, 12000 Tébessa, Algérie
e-mail: hemilamedlaid@yahoo.fr

B. Djoulah
e-mail: djoulah.b@gmail.com

C. Bertrand et al. (eds.), *Eurokarst 2018, Besançon*, Advances in Karst Science,
https://doi.org/10.1007/978-3-030-14015-1_14

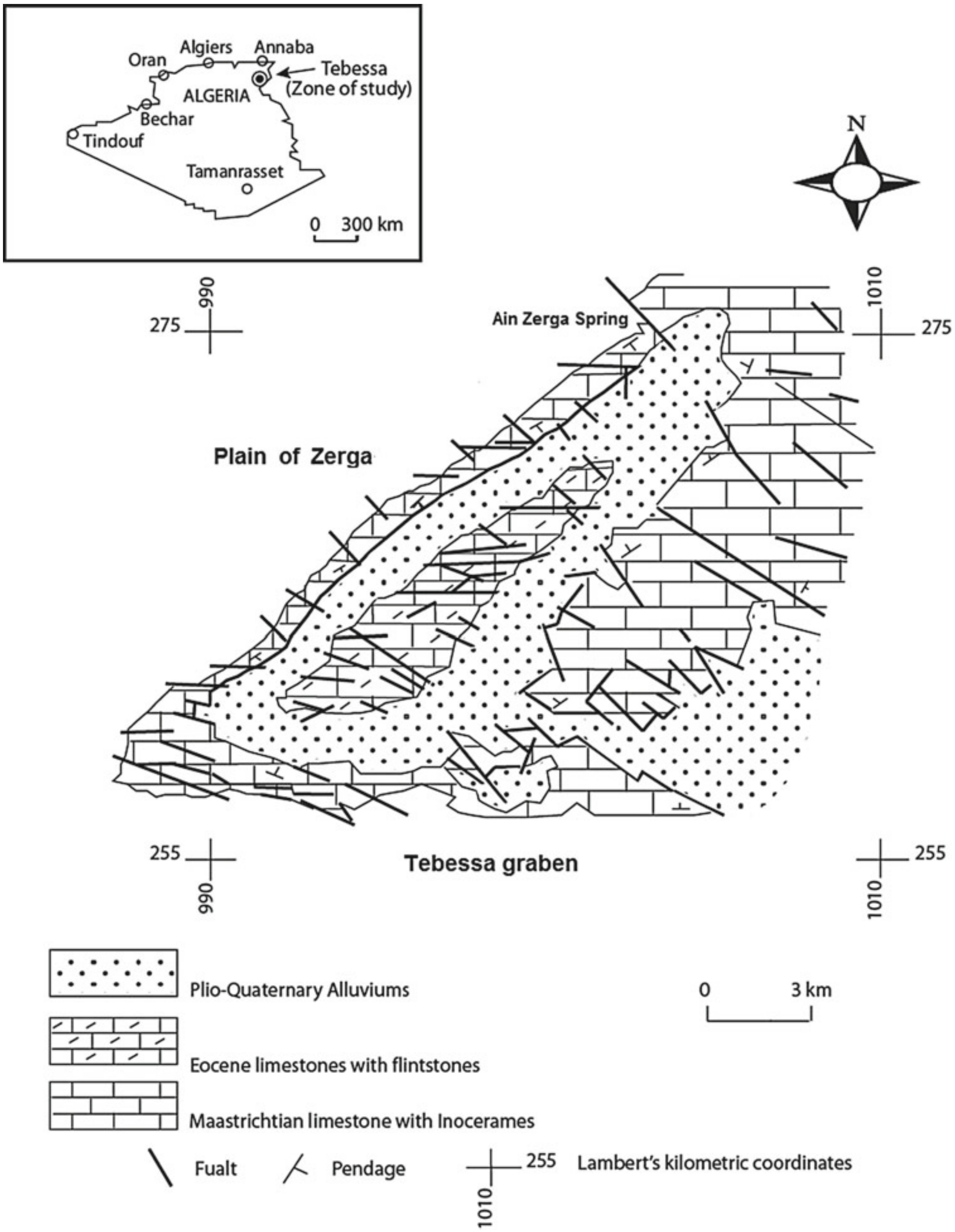

Fig. 1 Geologic sketch of the syncline of Dyr, Tebessa—Algeria

Kovács (2003); Kovács et al. (2005); Kovács and Perrochet (2008); Kovács et al. (2015). Among the results obtained from this preliminary work, we will present here the results of the application of recession curves, which allowed us to characterize the behavior of the unsaturated and the saturated zones.

Materials and Methods

Principle of Method

The method of analyzing recession curves, as described by Mangin (1970a, b) and refined by Marsaud (1996), consists in studying the portion of the unitarian hydrogram of floods, of the flow at an outlet, ranging from the peak of flood to the end of drying up. It is thus a treatment of the descent of the hydrogram from a model which, in the case of karst aquifer, takes into account the flow related to the infiltration into the unsaturated zone. The model integrates two reservoirs drained through a main outlet. The first reservoir represents the unsaturated zone, which is drained by the infiltration discharge (q_i), while the second, type Maillet, corresponds to the saturated zone drained with a discharge Q. We can distinguish:

The recession, during which infiltration (q_i) influences the draining of the reservoir, and

Drying up, which starts at the moment when the infiltration discharge (q_i) becomes zero.

The global expression used for the analytical description of the model is:

$$Q(t) = \varphi(t) + \psi(t) \tag{1}$$

The model which describes the draining of the saturated zone is defined by the following relation:

$$\varphi(t) = Q_{RO}\mathrm{e}^{-\alpha} \tag{2}$$

with α being the drying coefficient in (1/d). It defines how the drying up will be realized and informs us about the extent of the saturated zone and the losses of loads that affect its flow, Q_{R0} being the discharge at the moment t_0. It can be determined by the extrapolation of the straight line of drying up to the ordinate axis.

The model used to describe the infiltration function is a homographic function given by the relation:

$$\psi(t) = q_0\frac{(1-\eta t)}{(1+\varepsilon t)} \tag{3}$$

with q_0 being the infiltration discharge at time t_0 ($q_0 = Q_{\max} - Q_{R0}$), ε being the coefficient of heterogeneity of flow, describing the concavity of the curve according to different modes of infiltration: slow, fast, delayed, and varying between two ranges, the first (0.00–0.01) indicating a slow infiltration and the second (1–10) translating a very rapid recession ($\varepsilon = Q_{R0} - Q_i$), η being the coefficient of the infiltration speed which is equal to $1/t_i$, t_i corresponding to the moment when the infiltration ceases; it is assimilated to the average speed of infiltration. It varies between 0 and 1; when η tends to 1, it reflects a rapid infiltration with a very short duration. The drying coefficient (α) allows to calculate the dynamic volume corresponding to the volume of water in movement at the time of drying up, both above and below the outlet. It is calculated by the following expression:

$$W_d = \int_0^t Q_i e^{-\alpha t}\mathrm{d}t = Q_i\frac{C}{\alpha} \tag{4}$$

with W_d being the dynamic volume corresponding to the volume of water in movement at the time of drying up, Q_i being discharge at the moment when the drying becomes effective, t_i being the moment when the infiltration ceases, C being a constant equal grip 86,400.

In order to compare the karst systems, Mangin recommended a classification diagram to determine the functioning of the karst aquifer system (Fig. 5). This classification is based on the calculation of two coefficients: the coefficient k, which translates the ability of the saturated zone of the karst to store the precipitation and restore it gradually over time, that is to say, its regulating power. It is equal to the ratio between the maximum dynamic volume obtained over a long period ($W_{\mathrm{d.m}}$ expressed in m^3) and the average annual volume transit over the same period (W_t expressed in m^3/year) defined as follows: $W_t = 86400nQ_m$ where Q_m is the average discharge of the observation period in m^3/s and n is the number of days in the cycle. The calculation expression of k is:

$$K = \frac{W_{\mathrm{dm}}}{W_t} \tag{5}$$

where k is in accordance with an average residence time expressed in years. Depending on the coefficient k, the regulating power of the aquifer will be defined. In the case of a karst aquifer, this coefficient k is less than six months (0.5 year), whereas a value close to 0 is indicative for an almost unregulated system. The coefficient "*i*" characterizing the infiltration delays varies between 0 and 1. It is equal to the value of the homographic function two days after the flood peak. A high value >0.5 indicates a slow or complex infiltration, contributing to a better regulation of the flow. A value of i between 0.25 and 0.5 indicates a system where the delay in infiltration is important. However, a low value of less than 0.25 is the sign of rapid water transit toward the saturated zone through a developed drainage network. According to the classification diagram of Mangin, five domains of karst systems can be distinguished (Fig. 5):

A first domain *with* $k < 0.5$ and $i > 0.5$: This is a domain of complex karst systems of large size with *many* subsystems.

A second domain *with* $k < 0.5$ and $0.25 < i < 0.5$: This *corresponds to a system with* more developed *conduits* upstream than downstream *and* with alimentation delays due to slow infiltration through poorly karstified rocks or to the presence of a snow cover.

A third domain *with* $k < 0.1$ and $0 < i < 0.25$: This is a domain of systems with rapid infiltration and large *conduits* downstream. *The unsaturated zone is well developed, whereas* the saturated zone *is negligible.*

A fourth domain *with* $0.1 < \mathrm{k} < 0.5$ and $0.1 < i < 0.25$: This is a domain of systems *with* well-developed *unsaturated and saturated zones*.

A fifth domain *with* $\mathrm{k} > 0.5$ and $i < 1$: *These values are typical* for non-*karstified porous* and fissured aquifers.

Methodology of Data Processing and Analysis

As a technical procedure for the application of the recession curve analysis method, we adopted a two-step approach:

The first step is the short-term analysis of the flows chronicles of Ain Zerga spring, *monitored* by us *during* 390 days from April 01, 2010, to April 24, 2011, and

The second step is the long-term analysis of the discharge chronicles of the spring, registered by the services of the national agency of water resources (A.N.R.H) over eight hydrological cycles (2002/2003 to 2009/2010).

The processing of all available data was done using the software Excel.

Results and Discussion

Short-Term Analysis

The flow rate chronicle of the Ain Zerga from April 1, 2010, to April 24th, 2011, *included* three floods (Fig. 2), the most important of which was that of March 07 to April 24, 2011. It was generated mainly by the *melting of a snow cover* that fell on March 4, 2011, on the high altitudes of Dyr with a thickness exceeding 90 cm. The three corresponding recession curves are represented in Fig. 3. The calculation of the characteristic parameters of the functioning of the infiltration sub-system and the flow in saturated zone give the results listed in Table 1. The analysis of the values of the coefficient of heterogeneity of flow (ε) revealed a slow infiltration within the unsaturated zone of the system. Its slight increase, at the level of the third flood from March 07, 2011, to April 24, 2011, to a value of 0.052, can only be due to an important water recharge from snow melt at the beginning of the spring season. The calculated values of the speed infiltration coefficient (η) are close (0.1–0.2). *This* slow infiltration took about nine days to recharge the saturated zone.

The graphical analysis of the straight lines representative of drying ups, according to that of the exponential function, and the calculations of the hydrological characteristics, according to the fundamental equation of the recession, showed that the saturated zone was characterized by a variation in the drying up coefficient (α) between 0.01 and 0.05, yielding an average dynamic volume of 354,233 m^3. This value is indicative for relatively important water reserves in the saturated zone. The coefficient i, characterizing the delay of infiltration, has an average value of 0.745. This value indicates a slow infiltration contributing to the better regulation of the flow in the saturated zone of this karst aquifer.

Long-Term Analysis

In order to better understand the functioning and flow of the Maastrichtian aquifer system of Dyr and to compare it with other karst systems described by the classification diagram of Mangin, we have analyzed the flow hydrographs of the outlet (Ain Zerga spring) over eight hydrological cycles (2002/2003 to 2009/2010).

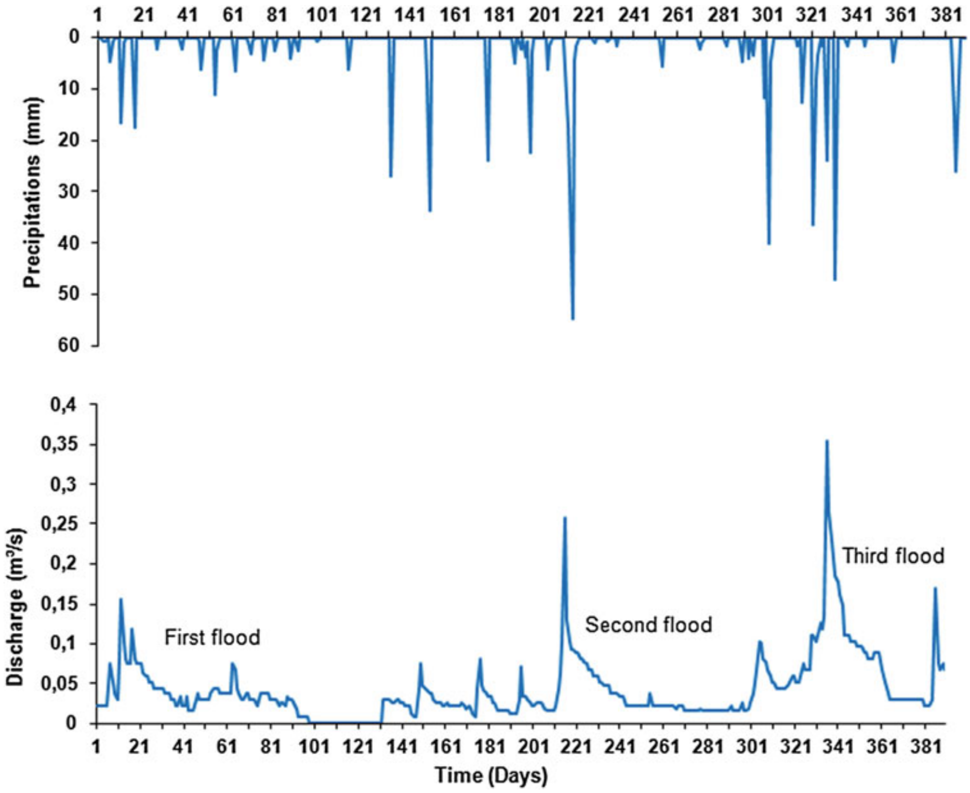

Fig. 2 Flow hydrogram of the Ain Zerga spring relative period from April 01, 2010, till April 24, 2011

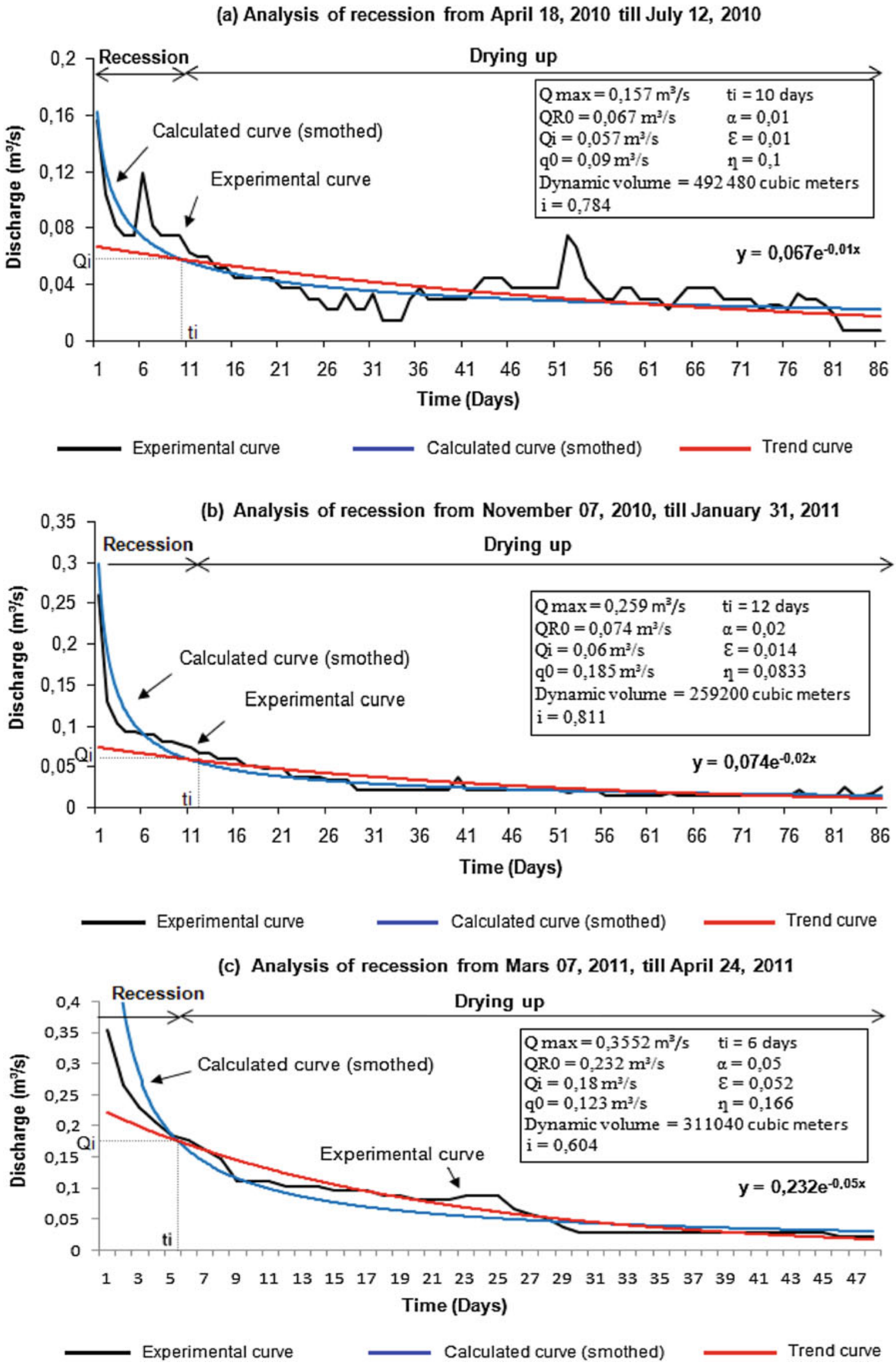

Fig. 3 Analysis of the recession curves of the flow Ain Zerga spring relative to the observation period from April 01, 2010, till April 24, 2011

Table 1 Summary table of analysis of the recession curves of the flow Ain Zerga spring relating to the observation period from 01/04/2010 to 24/04/2011

Period of recession	Q_{R0} (m^3/s)	Q_i (m^3/s)	q_0 (m^3/s)	t_i (D)	H	$\mathcal{E}$	α	W_d (10^6 m^3)	i
18/04 to 12/07/2010	0.067	0.057	0.09	10	0.1	0.01	0.01	0.4925	0.784
07/11/2010 to 31/01/2011	0.074	0.06	0.185	12	0.083	0.014	0.02	0.2592	0.811
07/03 to 24/04/2011	0.232	0.180	0.123	6	0.166	0.052	0.05	0.3110	0.64
Average values					0.116	0.025	0.026	0.3542	0.745

The application of the recession curve analysis allowed us to select seven flood hydrograms, where the *observed and calculated* recession curves *were in good agreement* (Fig. 4). The calculations of the various characteristic parameters of the functioning of infiltration sub-system and the flow of saturated karst sub-system gave the results shown in Table 2. These selected recession curves demonstrated the persistence of slow infiltration through the unsaturated zone despite the irregular change in climatic conditions in the region during *the* study period. The climate of the study area is semiarid with very cold and rainy winters and very hot and dry summers. The daily rainfall regime is very irregular, whereas average annual snowfall at high altitudes above 1400 m above sea level does not exceed ten days, followed by a rapid snow melt of only a few days. A variability of the coefficient of flow heterogeneity (ε) was observed from one flood to another but at the limit of the first for*k* (0.001–0.01). This slow infiltration is thus confirmed by the low values of the infiltration speed coefficient ($\eta < 0.167$) corresponding to approximately 6–12 days for recharging the saturated zone. *The large variability of* these parameters can only be explained by the complexity of the aquifer system probably related to the hierarchy of voids and to the considerable irregularity of the spatiotemporal distribution of the precipitations. The drying coefficient (α), reflecting the intensity of the draining of the saturated zone, *has* a rather strong average value equal to 0.016, signifying a rather rapid draining *due to strong* karstification. The calculated dynamic volume fluctuates between 241,300 and 545,600 m^3 (Table 2) and testifies the presence of important *water* reserves. According to these observations, we can admit that this sub-system of the saturated karst is in the flow influenced regime. The big losses upstream of the main outlet and the intensification of pumping at the deep wells implanted approximately 1.7–2.5 km upstream *of* the Ain Zerga *spring* are undoubtedly the main cause of this situation. The delays in the infiltration expressed by the coefficient "*i*" are high *with* values between 0.651 and 0.825, *indicating* that our karst system is *large and* complex, with slow *but constant* infiltration through the unsaturated zone. The inflow of external water has a notable effect on the regulation of the flow *at the* outlet.

Classification of the Karst System

The calculations of coefficients *k* and *i*, characterizing the regulating power and the infiltration delays, respectively, yield the following values: The coefficient k equals 0.36 year (about 131 days), and the average coefficient *i* equals 0.74. The postponement of their values on the Mangin classification diagram indicates that the Maastrichtian karst aquifer system of Dyr belongs to the first domain, i.e., the Maastrichtian aquifer is indeed a karst aquifer ($K < 0.5$) of complex geometry with numerous subsystems (Fig. 5).

Conclusions

The application of the method of analysis of the recession curves on the Ain Zerga discharge over a period of nine hydrological cycles allowed us to highlight the complex nature of the Maastrichtian karst system of the Dyr syncline with its numerous subsystems. This complexity is probably due to the hierarchy of the voids and the considerable irregularity of the temporal distribution of precipitation. The functioning of the unsaturated zone is always marked by slow infiltration. The infiltrated water reaches the saturated zone after six to twelve days. The saturated zone is characterized by a rather rapid draining, probably due to a well-developed karstification of this zone. Its groundwater reserves are quite

(a) Analysis of recession from December 13, 2005, till January 19, 2006

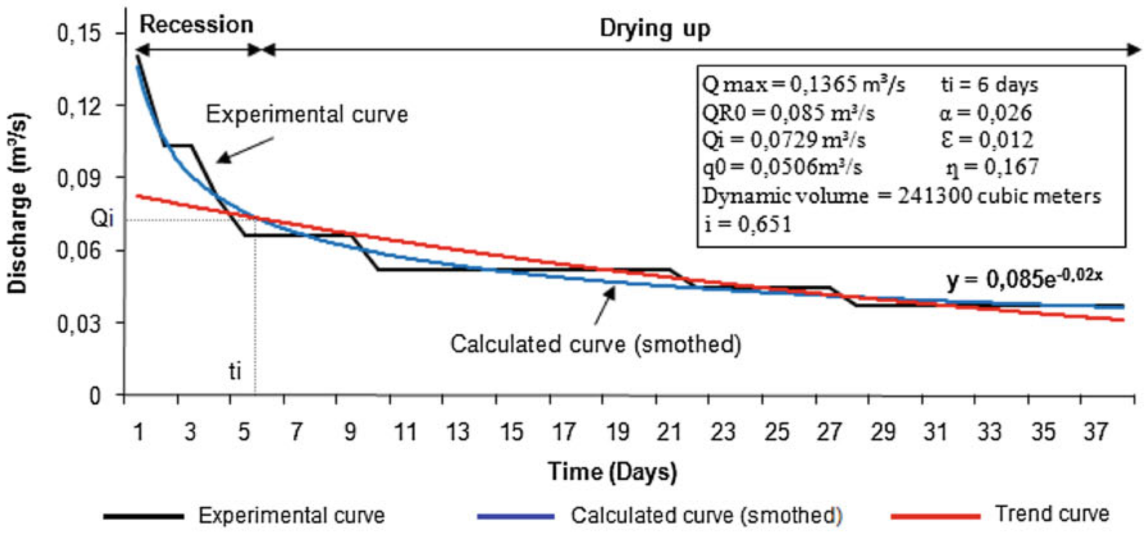

(b) Analysis of recession from Septembre 20, 2009, till December 13, 2009

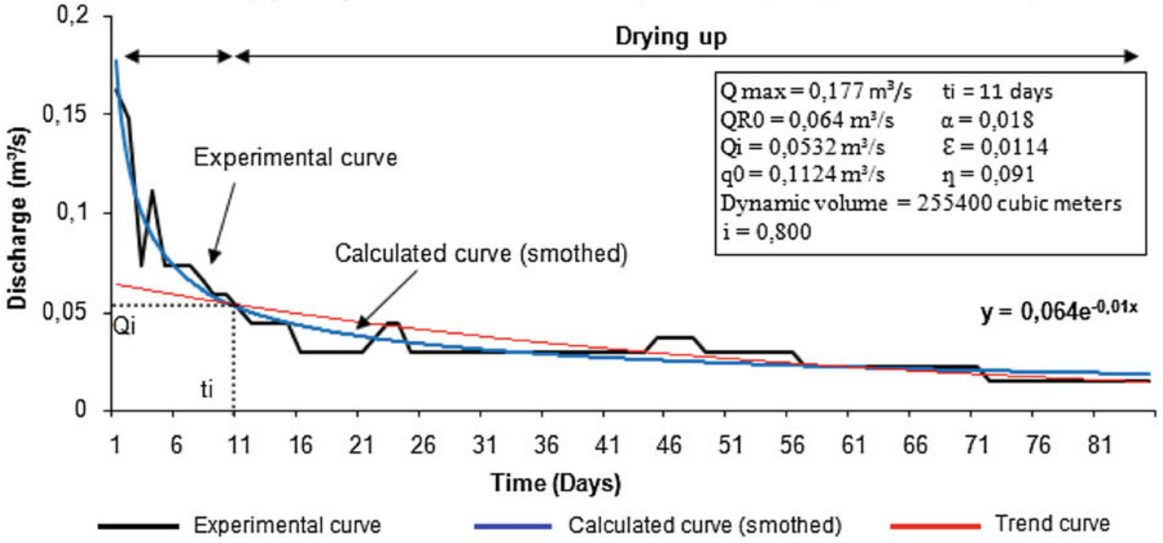

(c) Analysis of recession from April 18, 2010, till July 01, 2010

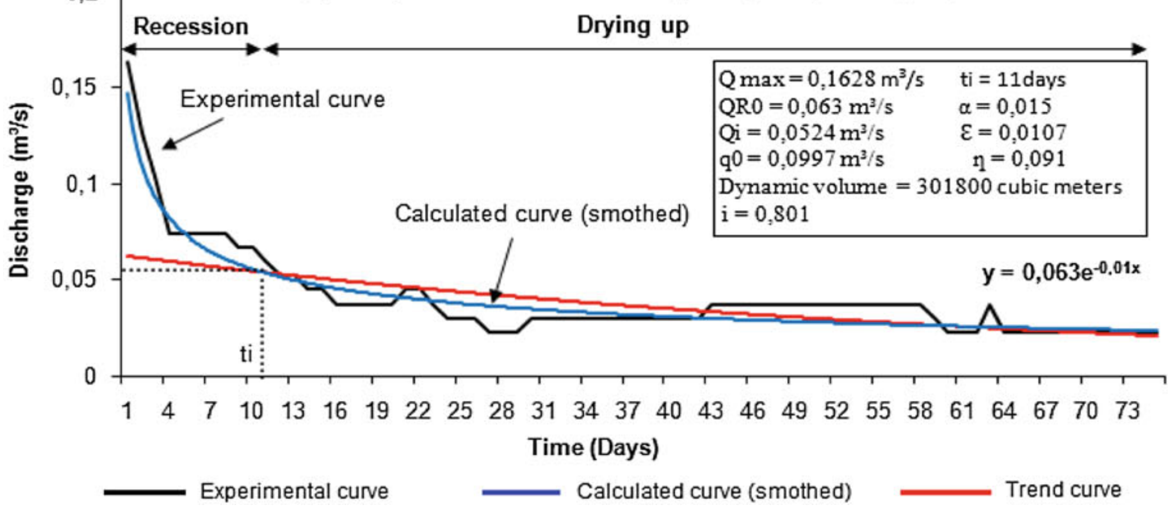

Fig. 4 Example of analysis of the selected recession curves of the Ain Zerga spring flow relative an observation period of eight hydrological cycles (2002/2003 to 2009/2010)

Table 2 Summary table of analysis of the recession curves selected of the flow Ain Zerga spring relating to the observation period from 2002/2003 to 2009/2010

Hydrological cycles	Period of recession	Q_{R0} (m^3/s)	Q_i (m^3/s)	q_0 (m^3/s)	t_i (D)	η	$\mathcal{E}$	α	W_d (10^6 m³)	i
2005/2006	13/12/2005 to 19/01/2006	0.085	0.0729	0.0506	6	0.167	0.0121	0.0261	0.2413	0.651
2005/2006	23/02/2006 to 14/04/2006	0.085	0.078	0.0353	7	0.143	0.007	0.0128	0.5265	0.704
2006/2007	18/12/2006 to 01/02/2007	0.093	0.084	0.0448	6	0.167	0.009	0.0193	0.376	0.655
2007/2008	01/04/2008 to 05/07/2008	0.046	0.041	0.0499	12	0.083	0.005	0.011	0.322	0.825
2008/2009	03/10/2008 to 03/12/2008	0.088	0.0783	0.0499	8	0.125	0.0102	0.0124	0.5456	0.735
2009/2010	20/09/2009 to 13/12/2009	0.064	0.0532	0.1124	11	0.091	0.0114	0.018	0.2554	0.800
2009/2010	18/04/2010 to 01/07/2010	0.0631	0.0524	0.0997	11	0.091	0.0107	0.015	0.3018	0.801
Minimum values						0.083	0.005	0.011	0.2413	0.651
Average values						0.123	0.009	0.016	0.3669	0.738
Maximum values ($W_{d.\max}$)						0.167	0.0121	0.0261	0.5456	0.825
Average annual volume of transit over the observation period (W_t in 10^6 m^3/year)									1.492	/

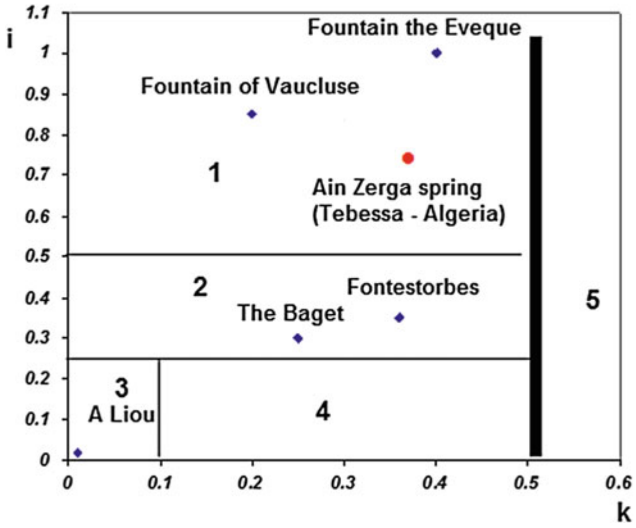

Fig. 5 Classification, according to the Mangin diagram, of the Dyr Maastrichtian karst system from the analysis of recession curves of the Ain Zerga spring flow of relative to the observation period of eight (08) hydrological cycles (2002/2003 to 2009/2010)

important, and its flow regime is influenced by the losses upstream of the main outlet and by intense pumping in deep wells within the saturated zone. According to Mangin's classification diagram, the Maastrichtian karstic aquifer system of Dyr belongs to the first domain, i.e., the Maastrichtian aquifer is indeed a karst aquifer ($K < 0.5$) of complex geometry and numerous subsystems.

Acknowledgements At the end this work, we thank the leader of sector of the national agency of hydraulic resources of Tebessa as well as all the technicians and observers for their contributions in the realization of this study. We would like to thank the anonymous reviewers and the editor for their constructive criticism and suggestions.

References

Fiorillo F (2014) The recession of spring hydrographs, focused on karst aquifers. Water resources management, 28(7), 1781–1805.

Kovács, A. (2003). Geometry and hydraulic parameters of karst aquifers: A hydrodynamic modelling approach (Doctoral dissertation, Université de Neuchâtel).

Kovács A, Perrochet P, Király L, Jeannin P Y (2005) A quantitative method for the characterisation of karst aquifers based on spring hydrograph analysis. Journal of Hydrology, 303(1–4), 152–164.

Kovács A, Perrochet P (2008) A quantitative approach to spring hydrograph decomposition. Journal of hydrology, 352 (1–2), 16–29.

Kovács A, Perrochet P, Darabos E, Lénárt L, Szucs P (2015) Well hydrograph analysis for the characterization of flow dynamics and conduit network geometry in a karst aquifer, Bükk Mountains, Hungary. Journal of Hydrology: 530: 484–499.

Mangin A (1970a) Méthode d'analyse des courbes de décrues et tarissement dans les aquifères Karstiques. (Method of analysis recession curves of flood and drying up in karst aquifers). Compte Rendus de l'académie des sciences, Paris, t. 270, 1295–1297.

Mangin A (1970b) Contribution à l'étude d'aquifères karstiques à partir de l'analyse de courbes de décrue et de tarissement (Contribution to the study of karst aquifers from the analysis of recession curves and drying up). Annales de spéléologie, t.25, 3, 581–609.

Marsaud B (1996) Structure et fonctionnement de la zone noyée des karsts à partir des résultats expérimentaux (Structure and functioning of the saturated karst zone from experimental results). Thèse de Doctorat, Université de Paris XI, Orsay.

Part IV

Karst Modeling

Limits in Using Multiresolution Analysis to Forecast Turbidity by Neural Networks. Case Study on the Yport Basin, Normandie-France

Michaël Savary, Anne Johannet, Nicolas Massei, Jean Paul Dupont, and Emmanuel Hauchard

Abstract

Approximately, 25% of the world population drinking water depends on karst aquifers. Nevertheless, due to their poor filtration properties, karst aquifers are very sensitive to pollution and specifically to turbidity. As physical processes involved in transport of solid/suspended particles (advection, diffusion, deposit…) are complicated and badly known in underground conditions, a black-box modeling approach using neural networks is promising. Despite the well-known ability of universal approximation of multilayer perceptron, it appears difficult to efficiently take into account hydrological conditions of the basin. Indeed, these conditions depend both on the initial state of the basin (schematically wet or dry: long timescale component), and on the intensity of rainfall, usually associated to short timescale component. In this context, the present paper addresses the application of the multiresolution analysis to decompose the turbidity on several timescales in order to better consider various phenomena at various timescales (flow in thin or wide fissures for example). Because of "boundary effects", usually neglected by authors, a specific adaptation was shown as necessary that diminishes the quality of results for real-time forecasting. Decomposing turbidity using multiresolution analysis adds thus questionable improvements.

Keywords

Turbidity • Neural networks • Forecasting • Multiresolution analysis • Yport

Introduction

25% of the world population drinking water comes from karst aquifers. The comprehension and the protection of these aquifers appear thus as crucial. In *Normandie* (North-West of France), the highly karstified chalk aquifer is the principal exploited aquifer. For example, the *Yport* pumping well, fed by a karst aquifer, provides half of *Le Havre* conurbation (236,000 inhabitants) tap water. Due to the karstification, connections between surface water and underground water induce turbidity occurrences that decrease the water quality. It is thus very important for groundwater managers to be able to predict the occurrence of turbidity events. Processes involved in the karst aquifer make the turbidity difficult to model because of the nonlinearity of the rainfall/turbidity relation, and the multiplicity of variables and phenomena. In this context, the aim of this work is to predict turbidity peaks and threshold overtaking in order to help managers to decrease the impact of turbidity on water treatment. Because of the lack of accurate physical description of the karst system (for example, no rating curve is available at the place of pumping), neural network models are chosen to achieve prediction as black-box models.

In previous works, the prediction of turbidity at 12-h lead time was studied using two kinds of neural network architectures: the classical multilayer perceptron and the so-called *two-branches* model. This previous work highlighted that the two-branches model was better to predict 100 NTU threshold surpassing.

In this context, the present chapter is devoted to designing a turbidity predictor using neural network models. To this end, it addresses the application of the multiresolution analysis to decompose the turbidity on several timescales in order to better

---

M. Savary · N. Massei · J. P. Dupont · E. Hauchard
Normandie University, UNIROUEN, UNICAEN, CNRS, M2C,
76000 Rouen, France

M. Savary · A. Johannet (✉)
LGEI, IMT Mines Alès, Univ Montpellier, 6 Avenue de Clavières,
30319 Alès Cedex, France
e-mail: anne.johannet@mines-ales.fr

E. Hauchard
Communauté D'agglomération Havraise, 19 Rue Georges Braque,
76600 Le Havre, France

C. Bertrand et al. (eds.), *Eurokarst 2018, Besançon*, Advances in Karst Science,
https://doi.org/10.1007/978-3-030-14015-1_15

consider various phenomena at various timescales. A focus is done on limitations of the multiresolution analysis in the context of real-time prediction. The identified limitations are discussed in order to adapt the feed-forward model. For this reason, it appears that results are not as much improved using multiresolution analysis as it is claimed in the literature.

The chapter is organized as follows: after the introduction, the first part focuses on the estimation of turbidity by machine learning; in the second part, the area of interest is presented: the *Yport* pumping well in *Normandie* (*France*). Then, the Materials and methods section presents neural networks modeling and multiresolution analysis; results are finally presented and discussed in Sect. IV.

Estimating Turbidity Using Machine Learning

Turbidity is the cloudiness of a fluid caused by suspended particles. The unit of turbidity is the Nephelometer Turbidity Unit (or NTU). Water is considered as drinkable when turbidity is inferior to 1 NTU (French public Health code: sections R. 1321-2, R. 1321-3, R. 1321-7 et R. 1321-38).

At present, physical modeling of turbidity cannot be successfully performed due to the lack of knowledge about physical properties of underground circulations. For this reason, statistical approaches in the framework of systemic modeling are valuable. First, one can note the study of discharge-turbidity relation, called *sediment-rating* curve, thanks to several tools and strategies: SVM (Kisi et al. 2012), also multilinear regression (Rajaee et al. 2009), correlation analysis (Massei et al. 2006), and finally neural networks (Rajaee et al. 2009), (Houria et al. 2014). Because of their flexibility, neural networks were applied to various kinds of relations: sediment-rating curve, chemistry–turbidity relation (conductivity, temperature, pH, ammonium concentration…). Neural networks were proved better than other methods by Darras et al. (2014), Dreyfus (2005). When discharge measurements are not available, rainfall–turbidity relation could be investigated using a rainfall–runoff model (Beaudeau et al. 2001). In synthesis, it appears that modeling the direct relation between rainfall and turbidity is little published, and for the best of our knowledge, except Savary et al. (2017), no work addresses the modeling of processes occurring at short time-steps (*e.g.,* 1 h).

Yport Pumping Well Site of Study

The Seine Maritime Regional Context and Yport Pumping Well

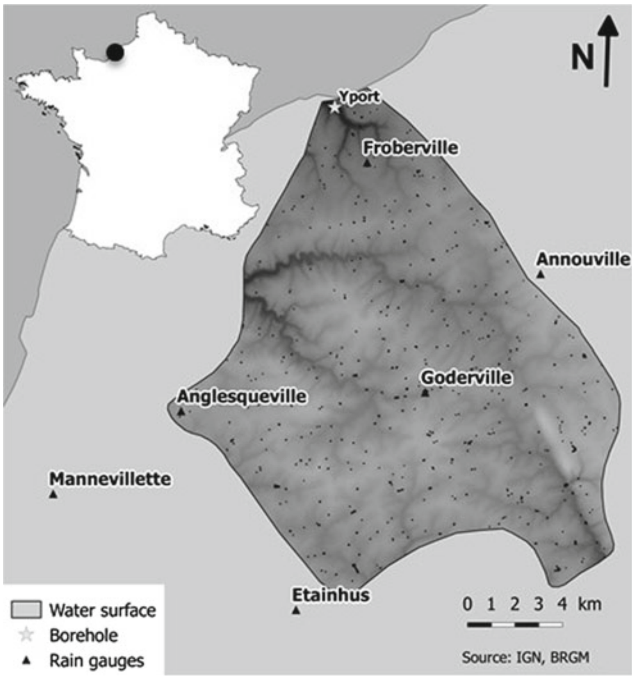

Source: IGN, BRGM

Fig. 1 Yport alimentation basin and rain gauge localizations

The *Yport* basin is localized in *Normandie* in the *Pays de Caux* at the west of the *Seine Maritime* department, France (Fig. 1). The yearly mean temperature of this region is between 10 and 12 °C. The yearly mean rainfall is between 600 and 1100 mm. The climate is both continental and oceanic. In 2012, the alimentation basin area was estimated at 320 km^2 (SAFEGE 2012).

The *Yport* pumping well is exploited by the *Communauté d'Agglomération Havraise* (CODAH) to supply *Le Havre* inhabitants. The implementation of the *Yport* water station was motivated by the *Yport* Fountain localized on the tidal zone of *Yport* beach. With a flow rate estimation of its outlet spring between 1.5 m^3/s (Hole and Roux 1978) and 2.8 m^3/s (Gaillard et al. 2012), the alimentation basin of the *Yport* Spring appears valuable for tap water exploitation. The *Yport* pumping well was thus implanted in 1994 directly in a major karst drain.

Turbidity, Water Production, and Uncertainty

At *Yport* Plant, turbidity is measured with a nephelometer considered as well calibrated. Thus, the estimation of uncertainty is the one given by the manufacturer: 2% for turbidity between 0 NTU and 40 NTU and 5% for turbidity superior to 40 NTU. When turbidity exceeds the threshold of 100 NTU, water must decant longer. This diminishes the output flow of 30–20%. Being able to anticipate the 100 NTU threshold thus would allow to anticipate by: (i) stocking more water, (ii) implementing the chain of quality control and treatment.

Then, following operational needs, prediction of turbidity peaks, and of 100 NTU threshold overtaking are presented in this paper. The necessary anticipation time should be at least 12-h lead time, or, if possible 24-h lead time.

Database

The database provided by the CODAH consists in hourly rainfall coming from six rain gauges located in the alimentation basin since 2009, and hourly turbidity, measured in the karst drain of *Yport*, since 1993. Thanks to the database, an event is selected if the cumulative mean rainfall reaches more than 3.5 mm in a sliding time-window of 24 h. Following this method, 22 events were selected: 12 events without turbidity peak and 10 events with turbidity peak (Table 1). We consider that an event presents a turbidity peak when the maximum of the turbidity reaches at least 50 NTU. Selecting events thanks to the rainfall amount is better than selecting them using only turbidity peaks, because in this case the model can learn the two configurations: (i) a rainfall event triggers a turbidity peak, and (ii) a rainfall event do not trigger any turbidity peak.

Split of the Database for Neural Network Modeling

When designing a model using a neural network, it is necessary to split the database in several subsets: training set, stop set (usually called validation set in the literature), and test set. Depending on the test set, model design stage has its own splitting and consequently a different database and a different resulting model.

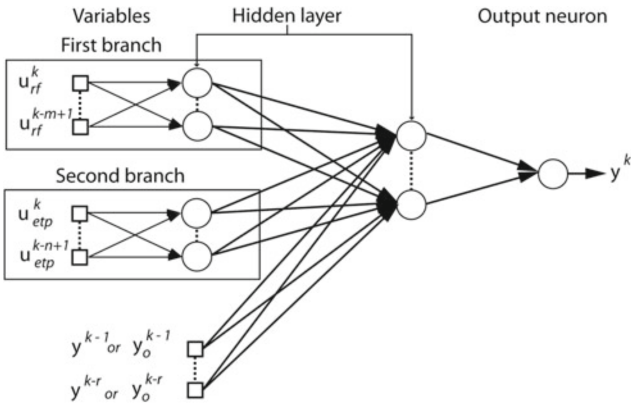

Fig. 2 Two-branches model, based on the multilayer perceptron

Materials and Methods

Neural Network Modeling

Multilayer Perceptron and Two-Branches Model

The multilayer perceptron is the most known model in hydrology because of its properties of universal approximation (Hornik et al. 1989) and parsimony (Barron 1993). Nevertheless, in order to better manage the role of evapotranspiration that is important for turbidity, another model, based on multilayer perceptron, was preferred in this study: the two-branches model Johannet et al. (2008), Savary et al. (2017). It is shown in Fig. 2. The two-branches model implements a presupposed role of the evapotranspiration: the first branch implements the rainfall–runoff relation, while the second branch implements the role of evapotranspiration that takes water in the rainfall–runoff relation.

Table 1 Simple statistics of events in the database

Events without turbidity peak					Events with turbidity peak(s)				
Event	Duration (hours)	Max	Min	Cumul	Event	Duration (hours)	Max	Min	Cumul
1	288	7	1	15.9	2	624	302	1.54	41.3
4	384	10	0.9	14.1	3	1008	135	0	26.7
5	336	8	1.5	17.5	6	720	245	1.5	42.0
8	360	27	1	22.5	7	744	85	0.1	19.2
9	384	9	1.0	20.2	10	576	256	0.9	24.9
12	456	12	0.8	28.7	11	744	308	0.9	54.8
13	576	13	0.9	30.8	16	648	405	0.8	53.8
14	384	14	0.9	23.3	17	744	157	0.5	50.7
15	600	15	0.9	31.7	18	744	87	2.2	42.8
19	504	19	1.5	30.3	22	623	53	0.8	44.2
20	576	20	0.9	40.8					
21	600	48	0.9	48.5					

Feed-Forward Versus Recurrent Model

The feed-forward model is fed by only exogenous inputs. Specifically, added to exogenous variables (*e.g.,* rainfall, temperature, evapotranspiration…), this model receives variables of the measured output, here the turbidity, at previous time-steps ($k - 1, \ldots$). In automatic control, this information can be considered as providing the state of the system. The feed-forward model can be mathematically explained as:

$$y^k(\mathrm{u}^k, \mathrm{w}) = g_{NN}(y_0^{k-1}, \ldots, y_0^{k-r}, \mathrm{u}^k, \ldots, \mathrm{u}^{k-m+1}, \mathrm{w}) \quad (1)$$

where y^k is the estimated turbidity, g_{NN} is the nonlinear function implemented by the neural network, k is the discrete time-step, $\mathbf{u}^k$ is the vector of exogenous variables (rainfall, evapotranspiration, etc.), r is the order of the model, m is the width of the sliding time-window of exogenous variables, $\mathbf{w}$ is the matrix of parameters, y_0^k is the measured (or observed) turbidity.

When turbidity measurements are corrupted by noise, the measured turbidity can be replaced by turbidity estimations calculated by the model itself, at previous time-steps. The advantage of this model is that it takes better into account the dynamics of the system. Nevertheless, it is generally less effective because its feedback is corrupted by noise Artigue et al. (2012), Dreyfus (2005).

With the same notations, the recurrent model can be stated mathematically as:

$$y^k(\mathrm{u}^k, \mathrm{w}) = g_{NN}(y^{k-1}, \ldots, y^{k-r}, \mathrm{u}^{k-1}, \ldots, \mathrm{u}^{k-m+1}, \mathrm{w}) \quad (2)$$

Bias Variance and Regularization Methods

Using neural networks, database is usually divided into three sets: a training set, a stop set, and a test set. The training set is used to calculate parameters through a training procedure that minimizes the mean quadratic error calculated on output neurons. In this study, the Levenberg-Marquardt training rule was chosen Dreyfus (2005). The training is stopped thanks to the stop set, and the model quality is measured on the remaining part of the database: the test set, which is separate from the previous sets. The stop set is chosen as proposed in Toukourou et al. (2011). The model's ability to be efficient on the test set is called *generalization*. Depending on the complexity of the model, overfitting can occur; this major issue in neural network modeling is called bias-variance trade-off (Geman et al. 1992). This trap can be avoided using regularization methods (Kong-A-Siou et al. 2012) and rigorous model selection.

Model Selection

Kong-A-Siou et al. (2011, 2012) showed that overfitting can be avoided thanks to a rigorous model selection. This consist in choosing not only the number of neurons in the hidden layers but also the order of the model and the dimension of input variables vectors using cross-validation. By this way, numerous combinations of variables are tried, and the one minimizing the variance is chosen. Also, it is necessary to choose the initialization of the parameters. This can be done thanks to cross-validation in general case. Nevertheless, it was shown by Darras et al. (2014) that a more robust model could be designed using an ensemble strategy. Ten models are thus trained and the maximum of the output, at each time-step, is taken. The model design is thus made as the following: first the hidden neurons number, then the number of input variables (selecting m), and lastly the order (r).

Multiresolution Analysis

Multiresolution analysis belongs to wavelet analysis. It is a tool used for analyzing distribution of frequencies in a signal, localized in time. To be short, multiresolution analysis allows creating several signals, called components, each one describing the content of the original signal for a range of frequencies, or, in another word, for different "timescales". In the present case, turbidity events contain 1024 samples and are decomposed in 10 components of 1024 samples. The component 1 includes high frequency and the component 10 low frequency information. The interest of this decomposition is that the different behaviors can be separated in different signals depending on their temporal scale.

As the length of the chapter is limited, we propose to interested readers to refer to Labat et al. (2000), Johannet et al. (2012) for a presentation of the technics.

Generally, neural networks and multiresolution analysis are used jointly to provide prediction of discharges. Numerous papers present how the multiresolution, used as pretreatment before prediction, helps to improve significantly the results. Nevertheless, three important issues have never been addressed: (i) the necessity to dispose of a really independent test set (not affected by training data during the low-frequency decomposition), (ii) the necessity to design decomposition using a causal filter, and (iii) the consequence of boundary effects inherent to the decomposition: boundary

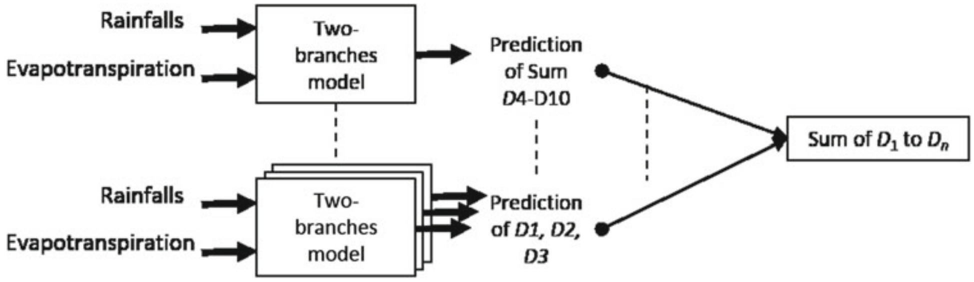

Fig. 3 Prediction strategy. The proposed strategy uses four models in conjunction: three models for the prediction of each one of the components D1, D2, D3, and one additional model for the prediction of the signal composed by the sum of the components D4 to D10. Finally, the prediction is the sum of the outputs of the four models

effects imply a modification of the signal near its beginning and near its end. Thus, when the real-time (simulated on past events) prediction is performed, the user is always at the end of the signal: the used value of components is thus different from the value used during training because decomposition used during training is done on the whole training database. This drawback is principally concerning the feed-forward models: those that are known to work very well in the literature. It is thus necessary to evaluate the influence of the boundary effect on the quality of prediction of both kinds of models: feed-forward and recurrent.

For this reason, we propose in this work to design several two-branches predictors, each one receiving the full rainfall and predicting one particular component of the turbidity, or the addition of several components. Two strategies of prediction are possible: (i) design ten models, one for each component and detail, (ii) design only necessary models in order to diminish the complexity of the whole model and to maximize the quality of generalization. After an analysis of the information included in different components (by continuous wavelets), the global architecture shown in Fig. 3 was proved more efficient (Savary 2018).

Quality Criteria

In order to assess the performance of models, we propose to use the Nash–Sutcliffe efficiency, or R^2 (Nash and Sutcliffe 1970), which is the most commonly used criterion in hydrology. The closer to 1 the R^2, the better the fit.

Results

After a rigorous design to maximize the generalization, results of different strategies are evaluated on several test events. As shown in Table 2 and Fig. 4, it appears that adding multiresolution analysis to feed-forward model degrades the performances because of the boundary effects. This effect was never cited in the literature because the wavelet decompositions were not realized in simulated real-time prediction, but on the whole past recorded data, using all the past and the future data (that are not available in prediction situation). There was thus no boundary effect at the instant of prediction. It appears also that the multiresolution improves a little recurrent models.

Table 2 Nash criteria (R^2) for several events in test

Two-branches			Using multiresolution			
Event in test	Feed-forward recurrent	Recurrent feed-forward	Model with all details		Model with grouped details	
			Feed-forward recurrent	Recurrent feed-forward	Feed-forward recurrent	Recurrent feed-forward
R^2 T2	0.93	0.63	0.84	0.52	0.94	0.75
R^2 T10	0.56	0.65	0.50	0.59	0.19	0.69
R^2 T11	0.91	0.46	0.85	0.24	0.86	0.39
R^2 T16	0.75	X	0.47	0.42	0.45	0.34
R^2 T22	0.89	0.65	0.76	0.44	0.87	0.71

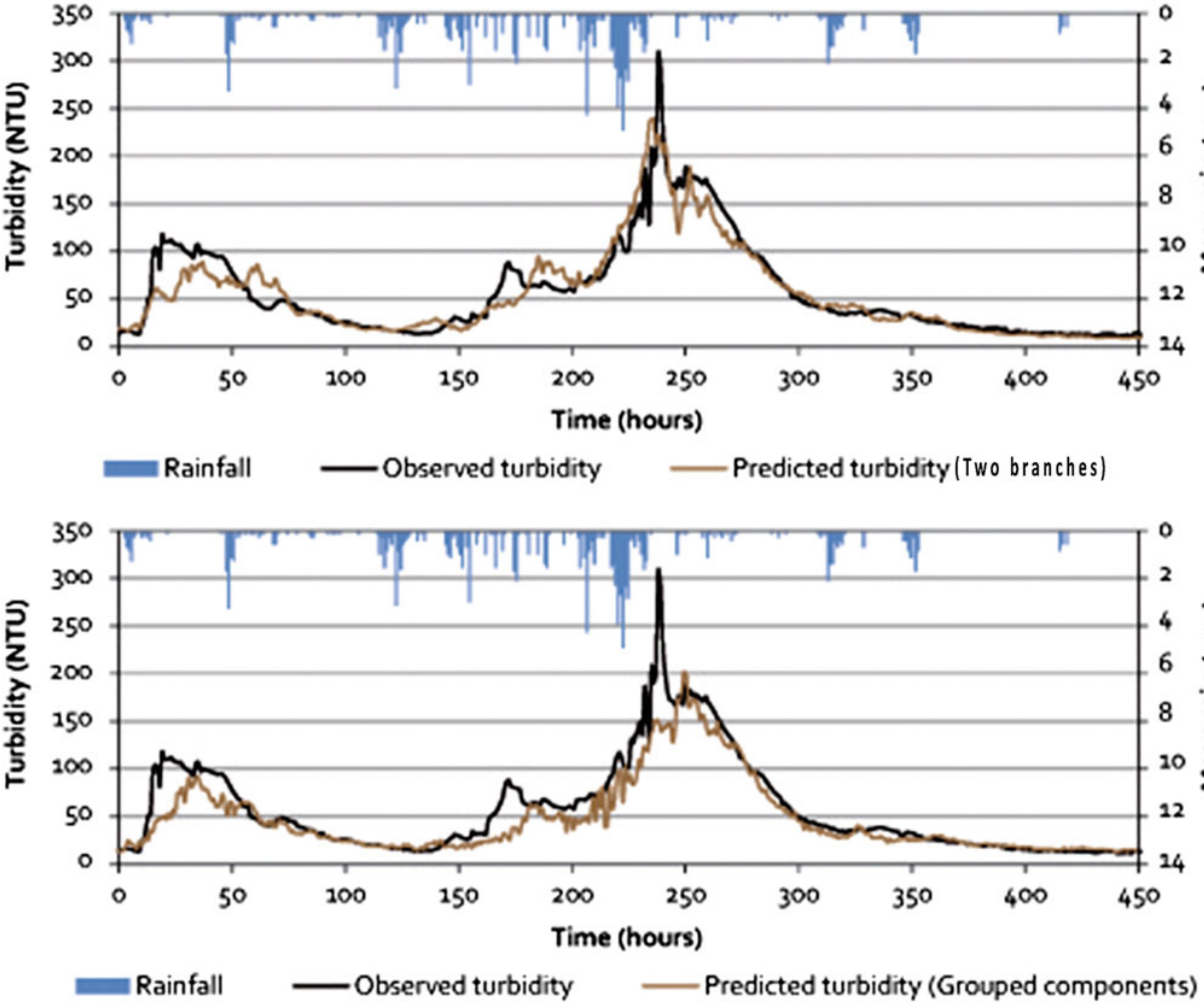

Fig. 4 Illustration of 12-h lead time predictions on the event 11: (top) Two-branches model, (bottom) Prediction using multiresolution as shown in Fig. 3 (grouped components)

Conclusion

Karst water is a valuable source of drinkable water, but karst aquifers are very sensitive to pollution transport and specifically to turbidity. The goal of this study was thus to improve the prediction of turbidity karst groundwater. Neural networks were chosen because of their ability to predict efficiently using a database without having information about physical processes. Suggested by a wide range of papers in the hydrological literature, the multiresolution analysis was used in conjunction with neural networks modeling in order to better express the information over various timescale components. After having designed models and compared the performances of models using multiresolution and the classical ones, it appeared that multiresolution degraded the performance of the feed-forward models while it improved slightly the recurrent models. The explanation concerns the boundary effects that, for the best of our knowledge, are never cited in the literature. This negative results open research to find others strategies in order to counterbalance the boundary effects and provide improved models for karst water managers.

Acknowledgements The authors would like to thank the CODAH for providing rainfall and turbidity data. The *Normandie* Region and *Seine-Normandie* Water Agency are thanked for the co-funding of the study. We are also very grateful to S. Lemarie and J. Ratiarson for the very helpful discussions they helped to organize. Our thanks are extended to D. Bertin in the design and implementation of the NN simulation tool. Finally, Marc Steinmann is thanked for careful reading of the present paper.

References

Artigue, G., et al. (2012). Flash flood forecasting in poorly gauged basins using neural networks: case study of the Gardon de Mialet basin. NHESS, 12(11), 3307–3324.

Barron, A. R. (1993). Universal approximation bounds for superpositions of a sigmoidal function. Information Theory, IEEE Transactions on, 39(3), 930–945.

Beaudeau, P., et al. H. Q. (2001). Forecasting of turbid floods in a coastal, chalk karstic drain using an artificial neural network. Ground Water, 39(1), 109–118.

Labat, D., Ababou, R., and Mangin, A. (2000). "Rainfall–runoff relations for karstic springs. Part II: continuous wavelet and discrete orthogonal multiresolution," In Journal of Hydrology, Vol. 238, pp. 149–178.

Darras, T., et al. (2014). Influence of the Initialization of Multilayer Perceptron for Flash Floods Forecasting: How Designing a Robust Model, (ITISE 2014), 687–698.

Dreyfus, G. (2005). Neural networks: methodology and applications. Springer Science & Business Media, 497p.

Gaillard, T., Hauchard, E., & Roux, J. C. (2012) Les Fontaines d'Yport (Seine-Maritime), émergences majeures du littoral normand crayeux: Exploitation et vulnérabilité de la ressource en eau. Ressources et gestion des aquifères littoraux. Cassis 2012. 235–244.

Geman, S., Bienenstock E. and R. Doursat, (1992). Neural networks and the bias/variance dilemma, Neural Computation 4 (1), 1–58.

Hole, J. P., Roux. J. C., 1978. Vulnérabilité aux pollutions du bassin hydrogéologique des sources d'Yport (Seine-Maritime), Rapport BRGM. 81.

Hornik, K., Stinchcombe, M., & White, H. (1989). Multilayer feedforward networks are universal approximators. Neural networks, 2(5), 359–366.

Houria, B., Mahdi, K., & Zohra, T. F. (2014). PSO-ANNs based suspended sediment concentration in Ksob basin, Algeria. Journal of Engineering and Technology Research, 6(8), 129–136.

Iglesias, C., et al. (2014). Turbidity prediction in a river basin by using artificial neural networks: a case study in northern Spain. Water resources management, 28(2), 319–331.

Johannet, A., et al. (2012). Prediction of spring discharge by neural networks using orthogonal wavelet decomposition. In IJCNN 2012. https://doi.org/10.1109/IJCNN.2012.6252620.

Johannet, A., Vayssade, B., & Bertin, D. (2008). Neural networks: from black box towards transparent box. Application to evapotranspiration modeling. International Journal of Computational Intelligence, 4(3), 163–170.

Kisi, O., et al (2012). Suspended sediment modeling using genetic programming and soft computing techniques. Journal of Hydrology, 450, 48–58.

Kong-A-Siou, L., et al. (2012). Optimization of the generalization capability for rainfall–runoff modeling by neural networks: the case of the Lez aquifer (southern France). Environmental Earth Sciences, 65(8), 2365–2375.

Kong-A-Siou, L., et al. (2011). Complexity selection of a neural network model for karst flood forecasting: The case of the Lez basin (southern France). Journal of Hydrology 403, 367–380.

Massei, N., et al (2006). Investigating transport properties and turbidity dynamics of a karst aquifer using correlation, spectral, and wavelet analyses. J. of Hydrology, 329 1–2, 244-25.

Nash, J. E., & Sutcliffe, J. V. (1970). River flow forecasting through conceptual models part I-A discussion of principles. Journal of hydrology, 10(3), 282–290.

Nieto, P. G., et al. (2014). Hybrid PSO–SVM-based method for long-term forecasting of turbidity in the Nalón river basin: A case study in Northern Spain. Ec. Engineering, 73, 192–200.

Rajaee, T., et al (2009). Daily suspended sediment concentration simulation using ANN and neuro-fuzzy models. Science of the total environment, 407(17), 4916–4927.

SAFEGE (2012) Étude du Bassin d'Alimentation du forage d'Yport "Phase 1 :Délimitation du bassin d'alimentation et analyse de la vulnérabilité intrinsèque du basin". 112p.

Savary M., et al. (2017) Operational Turbidity Forecast Using Both Recurrent and Feed-Forward Based Multilayer Perceptrons. In: Rojas I., Pomares H., Valenzuela O. (eds) Advances in Time Series Analysis and Forecasting. ITISE 2016.

Savary, M., PhD Dissertation (2018), Prévision de turbidité par apprentissage statistique : application au captage AEP d'Yport (Normandie). Thèse de doctorat de l'Université de Normandie en Sciences de l'univers, Ecole doctorale BISE, soutenue le 12 juillet 2018.

Toukourou M., et al.. 2011. Rainfall-runoff Modeling of Flash Floods in the Absence of Rainfall Forecasts: the Case of "Cévenol Flash Floods", Applied Intelligence, 35 2,178–189.

A Parsimonious Distributed Model for Rainfall-Discharge Simulation in the Karst Modelling Challenge (KMC)

Eulogio Pardo-Igúzquiza, Peter Dowd, Antonio Pulido-Bosch,
Juan Antonio Luque-Espinar, Javier Heredia,
and Juan José Durán-Valsero

Abstract

KARSTFLOW is a parsimonious mathematical model for simulating transient water flow in karst aquifers. It is described here and adapted to rainfall-discharge simulation in karst modelling as a contribution to the Karst Modelling Challenge (KMC). The model is designed and intended for applications in which data are scarce and a parsimonious approach is thus required to model the system to ensure that the level of complexity of the model is commensurate with the amount, type and quality of the available data. Parsimony also requires the simplest model (least assumptions and minimum number of predictor variables) that is consistent with the data, which in this and similar cases are the functional dualities of the karst system: duality in recharge (diffuse and preferential), duality in flow (slow flow across the rock matrix via fractures and fast flow along conduits) and duality in discharge (slow flow and fast flow after recharge events). The methodology, which is completely general and can be used for similar aquifers, is illustrated by application to the karst aquifer in the Milandre groundwater catchment in Switzerland. This case study shows how the recharge model plays a very significant role in the results. In general, the results are acceptable with a Nash–Sutcliffe statistic value of 72%.

Keywords

Discharge • Quick-flow • Karst aquifer • Richard's equation • Darcian flow

Introduction

This work is part of the Karst Modelling Challenge (KMC), a comparison exercise in which different water flow simulation methods for karst aquifers are applied to the same data set to evaluate the advantages and disadvantages of each methodology. In particular, this work deals with the first part of the challenge which is the simulation of discharge based only on meteorological data; no other data or information can be included. The challenge is coordinated by Jean-Yves Jeannin from the Swiss Institute for Speleology and Karst Studies.

The complexity of karst systems (Kiraly 2003) makes the mathematical modelling of water flow in a karst aquifer very challenging. Karst systems are highly heterogeneous and anisotropic due to large networks of karst conduits that have developed from networks of fractures enlarged by dissolution in a preferential and hierarchical manner. In addition, many of the hydrogeological parameters of karst aquifers, such as porosity and permeability, are scale-dependent so their values increase as the area to be modelled increases. A first approach to studying these aquifers is to use the hydrographs of the karst springs which provide important global information on the karst system. In this sense, the most basic model is one that relates an input signal (rainfall or preferably infiltration and recharge or effective rainfall) to an output signal (discharge at the karst springs). Traditionally, this type of systems approach has been modelled by convolution procedures (Padilla and Pulido-Bosch 1995), i.e. 'black-box' models. However, process-based models are arguably more suitable because they are more able to reproduce the karst hydrology. Process-based models include many types of both distributed karst simulation

---

E. Pardo-Igúzquiza (✉) · J. Heredia · J. J. Durán-Valsero
Geological Survey of Spain, Instituto Geológico y Minero de España (IGME), Ríos Rosas, 23, 28003 Madrid, Spain
e-mail: e.pardo@igme.es

P. Dowd
Faculty of Engineering, Computer and Mathematical Sciences, The University of Adelaide, Adelaide, SA 5005, Australia

A. Pulido-Bosch
Departamento de Biología Y Geología, Universidad de Almería, Edificio Científico Técnico II - B, 04120 Almeria, Spain

J. A. Luque-Espinar
IGME Granada, Urbanización Alcázar Del Génil, 4, Edificio Zulema, 18006 Granada, Spain

C. Bertrand et al. (eds.), *Eurokarst 2018, Besançon*, Advances in Karst Science,
https://doi.org/10.1007/978-3-030-14015-1_16

models and lumped karst simulation models (Hartmann et al. 2014). The lumped models are especially suited to dealing with the first task of the Karst Modelling Challenge (KMC) which is hydrological 'rainfall-discharge' modelling. In this paper, we present a parsimonious distributed model (the KARSTFLOW conceptual model) which delivers the same insights into the conceptual karst system as the lumped models, but by virtue of being a distributed model has several advantages over the latter.

Methodology

The conceptual KARSTFLOW model comprises two sub-models: the recharge model and the flow model (Fig. 1a, b). The recharge model requires the calculation of the potential evapo-transpiration time series using a procedure such as the Thornthwaite method (Pardo-Igúzquiza et al. 2012), which uses only mean air temperature, or the Eagleman (1967) method, which uses air temperature and relative humidity (Chang et al. 2015). The recharge (or effective rainfall) time series can be calculated for each cell of the spatial distributed model by using geostatistical interpolation of rainfall and temperature from data recorded at meteorological stations and secondary variables such as altitude from a digital elevation model (Pardo-Igúzquiza et al. 2012). However, in the work reported here, rainfall and temperature are considered constant over the study area and a water balance approach (Pardo-Igúzquiza et al. 2012), in which the total discharge is equated to the total recharge over a long period of time, is used to estimate the recharge. Once the recharge time series has been calculated, the flow model is applied to the study area. The area of interest is discretized into square cells with a horizontal resolution of Δx. It is assumed that there is a vadose zone from the top of the aquifer to the water table and thus there is also a vertical resolution of Δz. The result is a discrete three-dimensional model of the aquifer comprising voxels of dimension (Δx•Δx•Δz). The parsimonious KARSTFLOW conceptual model is then applied to this three-dimensional model as shown in Fig. 2. A high porosity could be assigned to the upper part of the vadose zone to simulate the epikarst. The recharge (a in Fig. 2) enters the system and travels as a vertical gravity flow described by the one-dimensional Richards equation (Richards 1943) along each column of voxels (b in Fig. 2). The one-dimensional vertical flow is coupled with a two-dimensional Darcy flow model (c in Fig. 2) that routes the water from the saturated zone to the spring output where the spring discharge (d in Fig. 2) is simulated by a drain. The quick-flow term (e in Fig. 2) allows the recharge to concentrate at preferential zones. The quick-flow term is an instantaneous recharge that does not go through the vadose zone. The coupling of one-dimensional vertical flow along each column of voxels and the corresponding cell of the two-dimensional saturated flow is done through the recharge term (Pardo-Igúzquiza et al. 2017). Both the 1D Richards equation and the 2D Darcy flow equation are solved by using finite difference approximations; the former is solved by an implicit finite difference method while the latter is solved by an iterative method using the Crank–Nicolson approach (Wang and Anderson 1982). The Dupuit approximation is used for the flow of

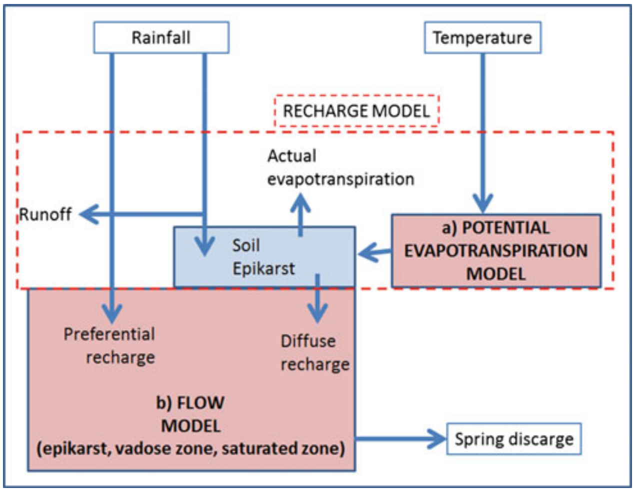

Fig. 1 **a** Potential evapo-transpiration model and **b** flow model that are required for the KARSTFLOW conceptual model

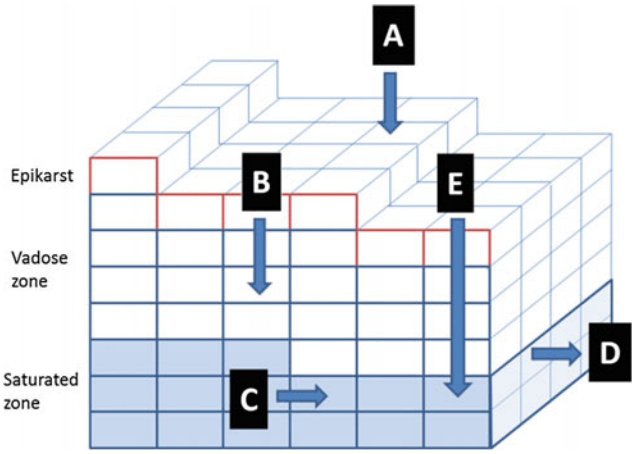

Fig. 2 Parsimonious KARSTFLOW conceptual model is a three-dimensional model of voxels with epikarst, vadose zone and saturated zone. The effective rainfall **a** enters the system and travels as a vertical gravity flow described by the one-dimensional Richards equation along each column of voxels; **b** the one-dimensional vertical flow is coupled with a two-dimensional Darcy flow **c** Model that routes the water from the saturated zone to the spring output where the spring discharge **d** is simulated by a drain. The quick-flow term **e** allows the recharge to concentrate at preferential zones

water from the phreatic zone to the karst spring. More details about the KARSTFLOW model can be found in Pardo-Igúzquiza et al. (2017).

Case Study

Experimental Data and Model Parameters

The study area is located in the Milandre test site in the Swiss Jura (Jeannin 1998; Perrin et al. 2003). The discharge point considered in this study is the Saivu-Bâme spring and the recharge is autogenic from rainfall. The model domain has a surface of 14.7 km^2 and there are three meteorological stations at Maira, Mormont and Fahy (Fig. 3). Rainfall was recorded at the three locations while temperature was recorded only at Fahy station. Rainfall data from all three stations were used to estimate the mean areal rainfall, but only the Fahy rainfall data (and temperature) were used to calculate the recharge. The reasons for this are that discharge is more highly correlated with the Fahy rainfall time series than it is for the other stations (or for the aggregated time series) and that the temperature data are only available at the Fahy station. Figure 3a also shows the area, the limits and the discretization of the aquifer. Figure 3b shows the numerical matrix used in the mathematical model. A code number greater than 0 denotes the aquifer zone. A code number greater than 1 denotes a preferential recharge area. Code numbers of 2 and 5 denote a drain to simulate the karst spring located in a cell with a code number of 4. The area and the vadose zone of the model are shown in Table 1. All required parameters (Table 1) were estimated by calibration, including the area of the catchment, the thickness of the vadose zone and areas of preferential recharge.

Recharge Evaluation

The Fahy daily rainfall and mean daily temperature used to calculate the recharge are shown in Fig. 4a, b. The period of the time series is from day 33,871 (24 September 1992) to day 34,787 (29 March 1995). Thus, there are two complete years, 1993 and 1994, plus several months from 1992 and 1995, giving a total of 917 days. Figure 5a shows the potential evapo-transpiration calculated using the Thornthwaite method and Fig. 5b shows the recharge, or effective rainfall, calculated using a water balance approach (Pardo-Igúzquiza et al. 2012). This is the autogenic water that enters the aquifer and ultimately discharges through the karst spring. Thus, over a long period of time, the total recharge must equal the total discharge. To ensure this condition, the recharge time series is calibrated by using only the total amount of recharge and thus there is no guarantee that, for shorter periods of time, the recharge would equal the discharge which may result in discrepancies between the measured and the simulated discharge peaks as shown below. In any case, the recharge time series is the input data to the flow model described in the methodology section.

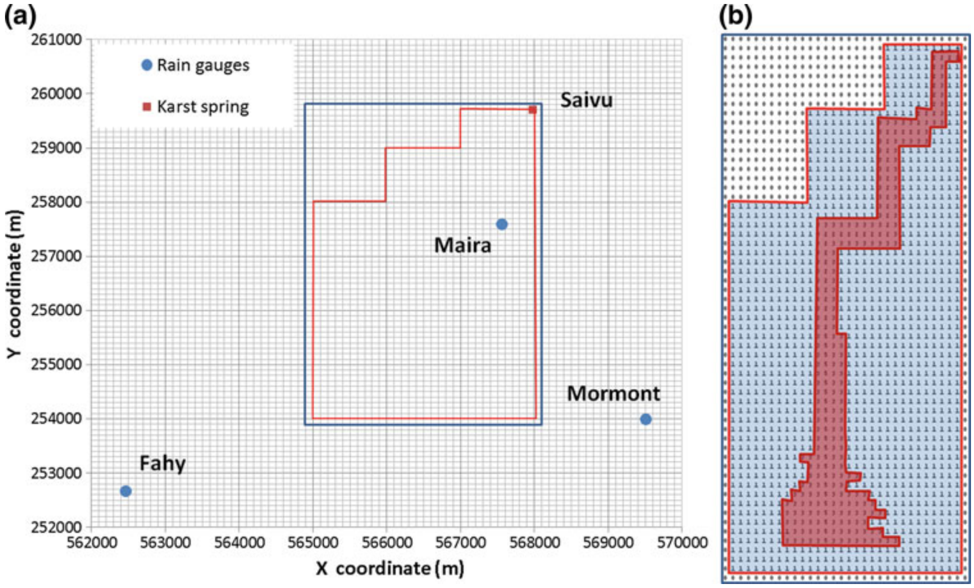

Fig. 3 **a** Mathematical model of the Milandre test site (blue rectangle) with the karstic catchment (red polygon), the main discharge at Saivu spring, and the Maira, Mormont and Fahy meteorological stations. The XY coordinates correspond to the Swiss coordinate grid **b** Numerical matrix that defines the case study: 0: no flow zone; 1: aquifer zone; 2, 3, 5: preferential recharge zone; 2, 5: drain zone, 4: karst spring

Table 1 Parameters of the mathematical model. The voxel discretization and time step are specified and the remaining four parameters are calibrated

Voxel discretization $(\Delta x, \Delta y, \Delta z)$	(100, 100, 1 m)
Time step	0.001 days
Specific yield (saturated zone)	0.001
Hydraulic conductivity (saturated zone)	0.104 m/day
Vertical saturated hydraulic conductivity	9.6 m/day
Drain conductance	$400/(\Delta x.\Delta y)$
Aquifer surface	14.7 km^2
Thickness of vadose zone	Transient (<60 m)

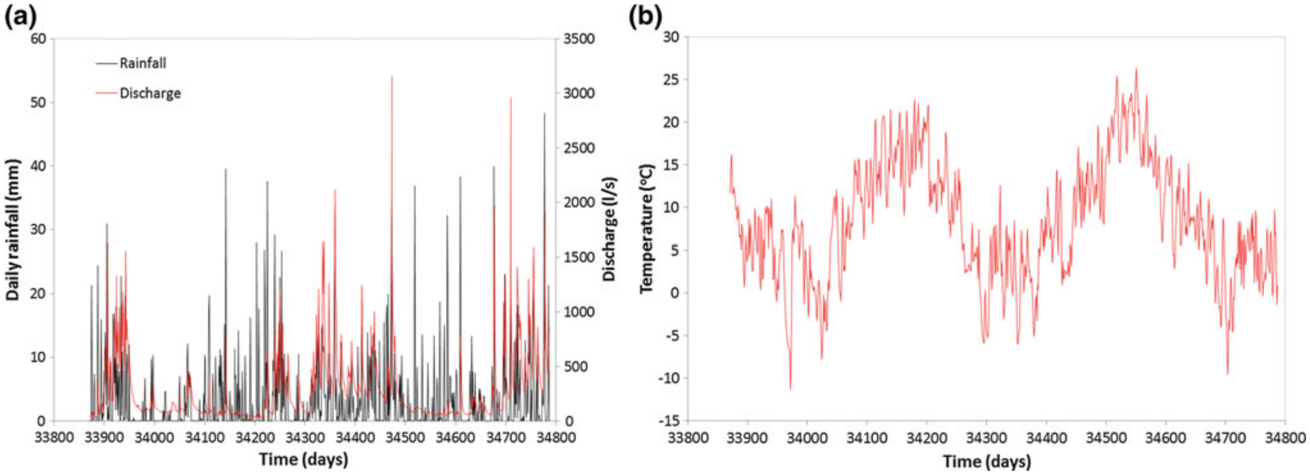

Fig. 4 **a** Discharge at Saivu spring (red line) and daily rainfall at Fahy station (black line) and **b** mean daily temperature at Fahy station. The period of the time series is from day 33,871 (24 September 1992) to day 34,787 (29 March 1995)

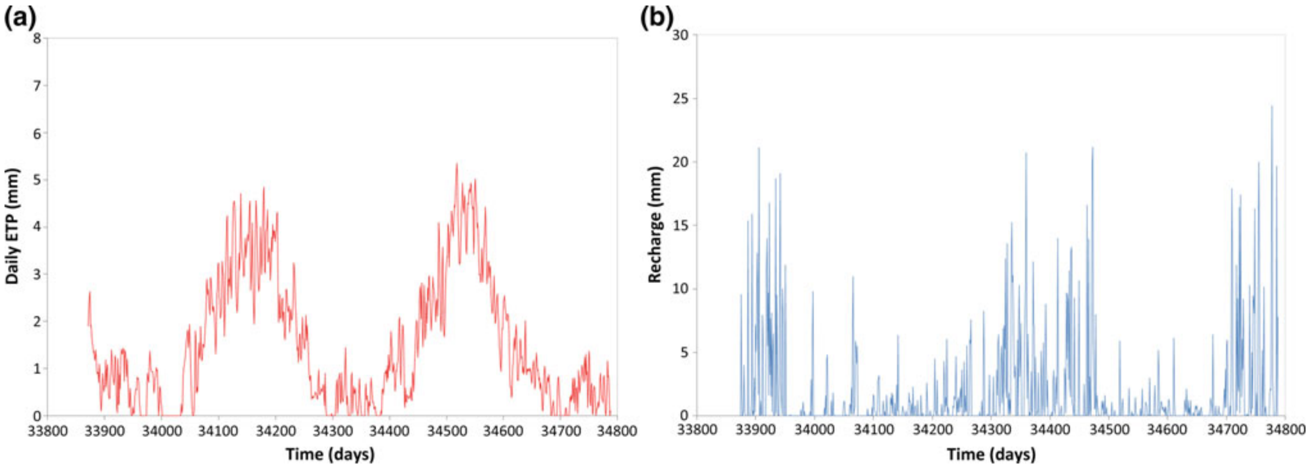

Fig. 5 a Potential evapo-transpiration calculated by the Thornthwaite method and **b** recharge, or effective rainfall, entering the aquifer

Calibration and Validation

The first 100 days were used for calibration and the selected calibration parameters are given in Table 1. Using these parameters and the catchment basin shown in Fig. 3, the model was run for the 917 days, and the simulated discharge shown in Fig. 6 was obtained. The simulation was performed with a time step of 0.001 days and the daily values shown in Fig. 6 were obtained by averaging the 1000 values within each day. This high temporal resolution in the simulation allows the simulated discharge to be compared with the original measured discharge as shown in Fig. 7. Note, that in Fig. 6, the daily ‘measured’ discharge is, in fact, the average of the values measured within each day. The original discharge data are shown in Fig. 7 for two time intervals (between days 1 and 150 in Fig. 7a and between days 450 and 600 in Fig. 7b). For all cases, the statistics used for checking the quality of the simulation were the mean error, the root mean squared error and the Nash–Sutcliffe statistic.

For the daily data in Fig. 6, the mean error (ME) is defined as:

$$\mathrm{ME} = \frac{1}{N}\sum_{i=1}^{N}\left(Q_i^s - Q_i^m\right),$$

the root mean squared error (RMSE) is:

$$\mathrm{RMSE} = \sqrt{\frac{1}{N}\sum_{i=1}^{N}\left(Q_i^s - Q_i^m\right)^2}$$

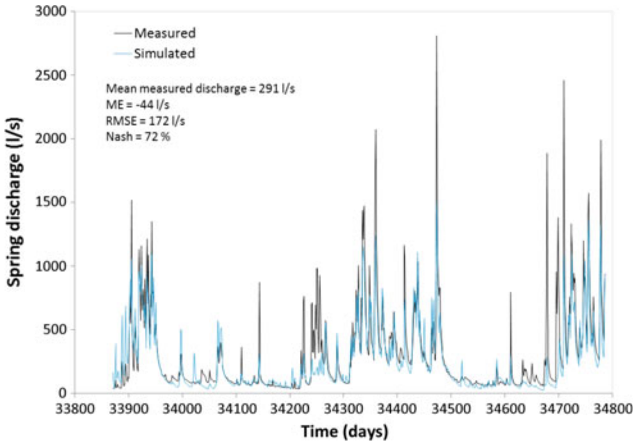

Fig. 6 Measured discharge at Saivu spring (black line) and KARSTFLOW simulated discharge (blue line). Discharge data and simulated data were averaged for the simulation step of one day

and the Nash–Sutcliffe statistic (Nash) is given by

$$\mathrm{Nash}(\%) = 100\left(1 - \frac{\sum_{i=1}^{N}\left(Q_i^s - Q_i^m\right)^2}{\sum_{i=1}^{N}\left(Q_i^m - \acute{Q}^m\right)^2}\right).$$

where Q_i^s is the simulated discharge for the ith day. Q_i^m is the measured discharge for the ith day. $\acute{Q}^m$ is the mean measured discharge.

A good simulation requires the mean error to be close to zero, the root mean square error to be as small as possible and the Nash–Sutcliffe statistic to be as close to 100% as possible. As can be seen in Fig. 6, the values of these three statistics are −44 l/s for the mean error, 172 l/s for the root mean square error and the Nash–Sutcliffe statistic is 72%. Sometimes the peaks of the discharge are overestimated as, for example, for the peaks a, b and c in Fig. 7a, and the large discharge peaks are underestimated as for peaks d, e and f in Fig. 7a. There is an acceptable agreement between measured and simulated recession curves as, for example, g in Fig. 7a.

Discussion

Although the mean areal rainfall was estimated using the data from all three rainfall stations, the Fahy rainfall data were preferred because this time series is more highly correlated with the discharge time series than it is for the other stations or for the aggregated time series. A good estimation of rainfall is essential in order to have a good estimation of recharge. Even good flow-routing methods may perform badly if the rainfall is not estimated with an acceptable level of accuracy. In addition, there are several methods for calculating recharge as there are different methods for estimating potential evapo-transpiration and a water balance equation in the soil in order to calculate diffuse recharge. Also, the areas, and percentage, of preferential recharge are parameters of the model. The differences introduced by the recharge calculation methods can be significant as shown in Fig. 8, which compares the recharge using two different methods for calculating evapo-transpiration: the Thornthwaite and Eaglman (1967) methods. It is outside the scope of this paper to study which of these methods is more reliable for the study area. The main differences are in the recharge pulses marked a and b in Fig. 8. If the KARSTFLOW procedure is repeated with the new recharge time series, the new results shown in Fig. 9 are obtained. Clearly, the deficiencies in the comparison of measured and simulated discharges shown in Fig. 6, most notably discharge pulses a

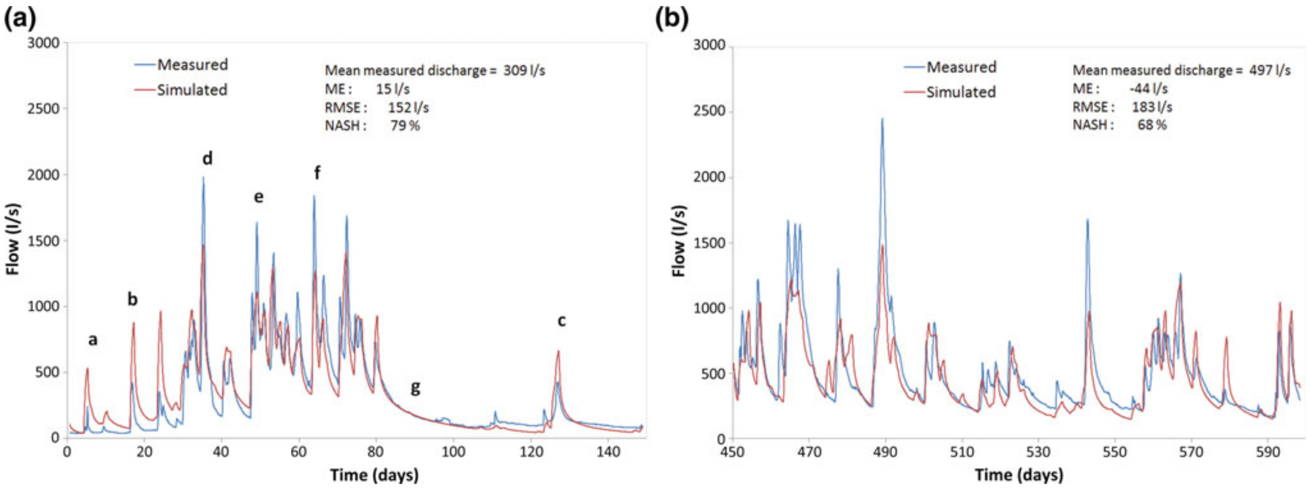

Fig. 7 Raw measured discharge (blue line) and simulated discharge (red line) at the same time positions. **a** Detail between days 0 and 150 and **b** Detail between days 450 and 600

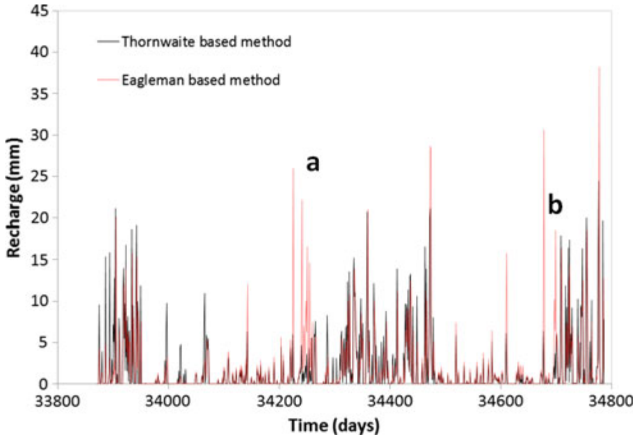

Fig. 8 Recharge calculated using two different methods based on potential evapo-transpiration calculated by the Thornthwaite method and the Eagleman (1967) method. The main differences can be seen in the recharge pulses in **a** and **b** that will have consequences for the spring flow simulation

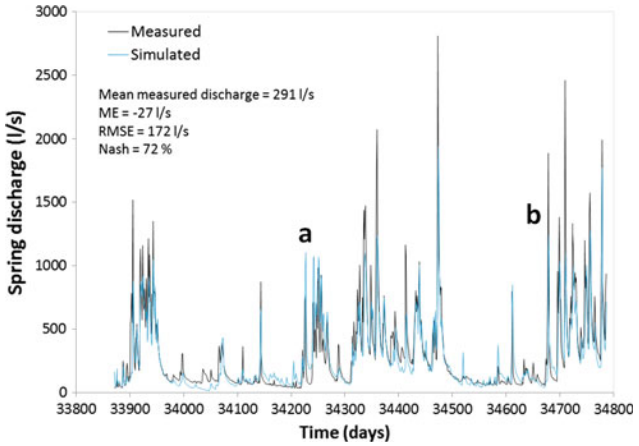

Fig. 9 Measured discharge at Saivu spring (black line) and KARSTFLOW simulated discharge (blue line). Discharge data and simulated data were averaged for the simulation step of one day. The difference between this Figure and Fig. 6 is that a different recharge time series has been used. With this new data, the peaks **a** and **b** that are not reproduced in Fig. 6 are now adequately reproduced

and b, have been corrected. The mean error has decreased considerably although the root mean squared error and the Nash–Sutcliffe statistic have not changed. The simulation results could be improved by spending more time on the calibration of both the recharge and the flow models.

Conclusions

A procedure (KARSTFLOW) has been described for simulating the rainfall-discharge flow in a karst aquifer by hydrological modelling for cases in which data are scarce. The methodology was applied to the Milandre catchment as part of the Karst Modelling Challenge (KMC) exercise. Only three time series were used: one for rainfall, one for temperature and one for discharge. Better results could be expected as more data become available. In particular, a more representative estimation of rainfall would potentially enhance the modelling results. The same can be said with respect to recharge. There are different methods for recharge evaluation and a good assessment of recharge will have a strong impact on the results.

The main advantage of the model, with respect to black-box or grey-box models used in the KMC exercise, is its immediate suitability for distributed simulation. Overall, the main structure of the measured discharge is captured by the simulation as shown in Figs. 6 and 9.

Acknowledgements This work was supported by project CGL2015-71510-R (Ministerio de Economía, Industria y Competitividad of Spain). We thank Pierre-Yves Jeannin and two anonymous reviewers for providing constructive criticism of the original version of this paper.

References

Chang, Y., Wu, J. and Jiang, G., 2015. Modeling the hydrological behavior of a karst spring using a nonlinear reservoir-pipe model. Hydrogeology Journal, 23, 901–914.

Eagleman, J.R., 1967. Pan evaporation, potential and actual evapotranspiration. Journal of Applied Meteorology, 6 (3), 482–488.

Hartmann, A., Goldscheider, N., Wagener, T., Lange, J., and Weiler, M., 2014. Karst water resources in a changing world: Review of hydrological modelling approaches. Reviews of Geophysics, 52, 218–242.

Jeannin, P.-Y., 1998. Structure et comportement hydraulique des aquifères karstiques, PhD thesis, Neuchâtel, 237 pp.

Kiraly, L., 2003. Karstification and groundwater flow. Speleogenesis and Evolution of Karst Aquifers, 1 (3), 1–24.

Padilla, A, Pulido-Bosch, A., 1995. Study of hydrographs of karst aquifers by means of correlation and cross-spectral analysis. Journal of Hydrology, 168:73–89.

Pardo-Igúzquiza E., Durán-Valsero J.J., Dowd P.A., Guardiola-Albert C., Liñan-Baena C. and Robledo-Ardila P.A., 2012. Estimation of spatio-temporal recharge of aquifers in mountainous karst terrains: application to Sierra de las Nieves (Spain). Journal of Hydrology, 470–471, 124-137.

Pardo-Igúzquiza, E., Durán, J.J., Luque-Espinar, J.A., Robledo-Ardila, P. and Heredia, J., 2017. Modelling the Hydrologic Cycle in a Mediterranean High-Relief Karst. In: Eurokarst 2016, Neuchâtel, Advances in the Hydrogeology of Karst and Carbonate Reservoirs. Editors: Philippe Renard and Catherine Bertrand. Advances in Karst Sciences, Springer, 99–107.

Perrin, J., Jeannin, P.Y. and Zwahlen, F. 2003. Implications of the spatial variability of infiltration-water chemistry for the investigation of a karst aquifer: a field study at Milandre test site, Swiss Jura.-Hydrogeology Journal, 11, 673–686.

Richards LA (1943) Capillary conduction of liquids in porous mediums. Physics 1, 318–333.

Wang HF, Anderson MP 1982. Introduction to groundwater modeling, finite dif-ference and finite element methods. W.H. Freeman, San Francisco. p 236.

Simplified VarKarst Semi-distributed Model Applied to Joint Simulations of Discharge and Piezometric Variations in Villanueva Del Rosario Karst System (Malaga, Southern Spain)

Javier Martín-Arias, Andreas Hartmann, Mathias Mudarra,
Pedro Martínez-Santos, and Bartolomé Andreo

Abstract

Numerical modeling provides well-established tools for advancing in water management. In this study, a simplified version of the semi-distributed VarKarst approach has been developed to reduce modeling routine and, therefore, the time of calculation needed for jointly simulating spring discharge and piezometric head variations in the same karst system located in southern Spain. Simulated spring outflows were compared with spring flow data derived from a previous application of the original VarKarst. Scatter correlation of spring flows yields Kling-Gupta efficiency (KGE) and a Pearson's coefficient (R^2) of 0.90 and 0.89, respectively. The modified approach includes new equations that consider the distance between sea level and the basement of the aquifer, from which the piezometric-level variations were calculated. The KGE, R^2, and the root-mean-squared error results obtained of groundwater level were 0.79, 0.85, and 3.07 m, respectively. We conclude that the simplified VarKarst numerical code can provide realistic hydrodynamic results in the karst system, as original VarKarst, concerning both discharge and groundwater level dynamics. This capacity of simulation could help to reduce uncertainty in model routines.

Keywords

Karst (carbonate) aquifer • Semi-distributed modeling • VarKarst • Hydrodynamic simulation

Introduction

Karst aquifers constitute valuable groundwater resources in many regions in the world (COST 1995). They provide good-quality water for drinking purposes and ecosystems, and they also constitute a key strategic resource against threats such as climate change or population growth (Hartmann et al. 2014). Adequate management of karst systems is required for regional water governance strategies; therefore, researchers have developed and applied several numerical modeling approaches. Nevertheless, the existence of specific karst pathways that are neither fully observable nor accurately measurable resists simplifications when flow and transport processes are numerically simulated. Moreover, inherent heterogeneity introduces additional nonlinearities and thresholds into the relation between rainfall and the hydrodynamic response, such as overflow discharge through ephemeral springs and the rapid variations in piezometric levels.

Spatially distributed models use discrete approximations of continuous phenomena, like aquifers, to provide efficient hydrogeological simulations for large study areas. However, distributed models are still difficult to implement because of the lack of available data. In contrast, lumped karst models have shown adaptability and strength in simulating karst behavior and processes under different contexts and scales (e.g., Hartmann et al. 2015), since data requirements for model inputs are less rigorous. But most of the lumped models have been applied to rainfall–runoff simulations, and

---

J. Martín-Arias (✉) · M. Mudarra · B. Andreo
Department of Geology and Centre of Hydrogeology of the University of Malaga (CEHIUMA), Universidad de Málaga, Campus de Teatinos s/n. 29071, Málaga, Spain
e-mail: j.martin@uma.es

A. Hartmann
Institute of Hydrology, Freiburg University, Fahnenbergplatz, 79098 Freiburg, Germany

A. Hartmann
Department of Civil Engineering, University of Bristol, Bristol, UK

P. Martínez-Santos
UNESCO Chair "Appropriate Technologies for Human Development", Department of Geodynamics, Stratigraphy and Palaeontology, Faculty of Geological Sciences, Universidad Complutense de Madrid, C/José Antonio Nováis 2, 28040 Madrid, Spain

C. Bertrand et al. (eds.), *Eurokarst 2018, Besançon*, Advances in Karst Science,
https://doi.org/10.1007/978-3-030-14015-1_17

karst processes and scaling are difficult to represent (Ladouche et al. 2014; Jiménez-Martínez et al. 2016).

The VarKarst model (Hartmann et al. 2013) is structured as a set of formulas and parameters used for modeling the hydrogeological and hydrochemical behavior of the aquifer, with rainfall, potential evapotranspiration, and chemical data as inputs. This model routine has a significant number of equations to make all the calculations needed. To optimize the modeling procedure of the original VarKarst code (oVK), a simplified version (sVK) of the VarKarst model has been applied to jointly simulate spring discharge and piezometric head variations in a tectonically complex and mountainous karst system located at southern Spain. oVK was already applied in the pilot site (Hartmann et al. 2014). The simultaneous application and calibration of both VarKarst routines confirm the reduction in the time of calculation, with similar modeled springflow results from oVK. The introduction of new equations to calculate water level in sVK has not disturbed the springflow calculated data significantly. Nevertheless, a small loss of accuracy in the simulation of springflow, compared to observed data, has been detected. The new version of the model provides more reliable quantitative information on the dynamics of the karst system and on its water resources availability.

Study Area

The pilot site of application is the Villanueva del Rosario karst system, located approximately 30 km north of the city of Malaga, southern Spain (Fig. 1). The topography is rugged, with altitudes ranging from 700 to 1640 m ASL. The region has a temperate Mediterranean climate, with rainfall mainly in autumn, winter and, to a lesser extent, in springtime. The historic mean annual precipitation and air temperature values are 760 mm and 14 °C, respectively (Mudarra 2012).

The geology consists of 400–450-m-thick Jurassic dolostones and limestones (Fig. 1), which are enveloped by Upper Triassic clays and evaporite rocks (mainly gypsum) at the bottom, and by lower Cretaceous-Paleogene marly limestones and marls on the top (Martín-Algarra 1987). The structure is formed by ENE-WSW oriented folds, from which overthrusts have developed toward the S–SE (Fig. 1).

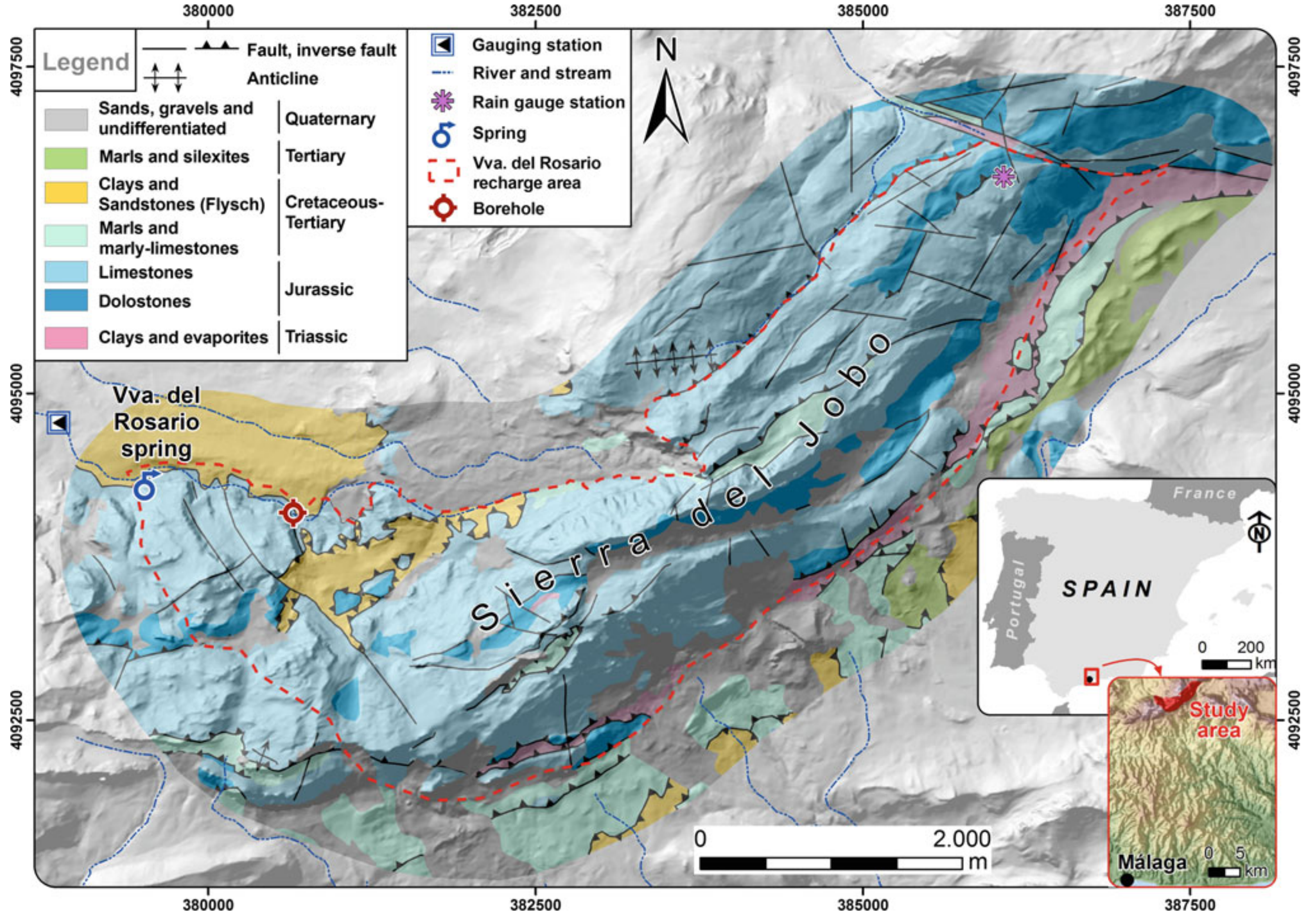

Fig. 1 Geological map of Villanueva del Rosario karst system in southern Spain

The system is surrounded by outcrops of Flysch-type clays and sandstones. The entire structure has been affected by more subsequent fractures, mainly running in NW–SE.

The Villanueva del Rosario hydrogeological system has a recharge area of around 14 km^2 (Mudarra et al. 2014), largely contained by low permeability materials (Triassic and Flysch clays and Cretaceous-Paleogene marls). Dye tracing and hydraulic head patterns indicate that the aquifer is uncontained to the southwest border. Recharge occurs by direct infiltration of precipitation (eventually concentrated), while discharge occurs mainly through Villanueva del Rosario spring (260 l/s annual mean discharge rate) situated at 770 m ASL (Fig. 1). The spring is clearly karstic based on highly variable flows in response to recharge (Mudarra et al. 2014). The Villanueva del Rosario karst system constitutes the sole source of drinking water for a nearby urbanized area. Water supply is currently satisfied by water piping from the spring. There is a borehole located 1160 m eastward from the spring (Fig. 1), but it has not ever been used. Mean static piezometric altitude in the borehole is 779 m ASL.

Methodology

Original (oVK) and Simplified VarKarst Codes (sVK)

VarKarst model (Hartmann et al. 2013) considers the variability of soil and epikarst depths, fractions of concentrated and diffuse recharge to the groundwater, epikarst hydrodynamics, and groundwater hydrodynamics (Fig. 2). Soil, epikarst, and groundwater systems are represented by a set of N compartments with varying properties.

Some equations from the original VarKarst model have been used to create the simplified VarKarst code. The model routine also was reduced caused by the simplification of the algorithm and the elimination of hydrochemical information. These aspects imply the reduction in the convergence time. Furthermore, the model parameters were identified by automatic calibration using predefined parameter ranges (Table 1).

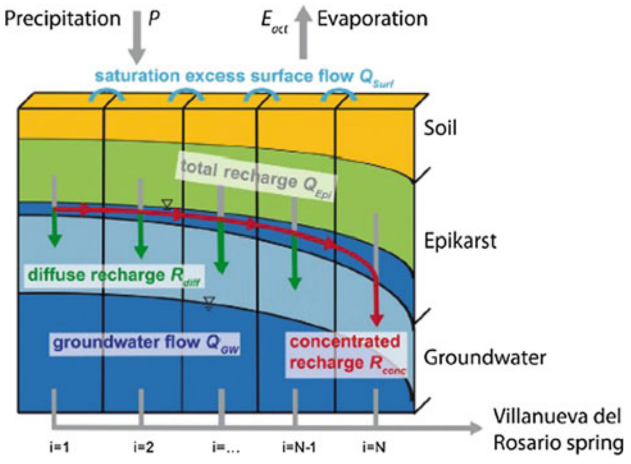

Fig. 2 Structure of both VarKarst models (Hartmann et al. 2014)

In accordance with the reservoir model, groundwater level in each compartment, $V_{gw,i}$ (m), was calculated by:

$$h_{gw,i} = \frac{V_{gw,i}(t)}{1000 * P_{gw}} + \Delta h$$

where $V_{gw,i}(t)$ is the volume of water in the groundwater compartment (mm), P_{gw} is the limestone porosity (a dimensional), and Δh (m) is the distance between sea level and the basement of the aquifer in the borehole (Adinehvand et al. 2017; Brenner et al. 2018).

Calibration and Evaluation Strategy

A three-year record (hydrological years 2006/2007–2008/2009) of spring discharge and a set of 16 instantaneous water levels within 2006/2007 hydrogeological year were used for calibration. Discharge data recorded at the gauging station of Villanueva del Rosario spring (Fig. 1) were provided by the Andalusian Water Agency, whereas piezometric records were taken for research purposes with a water-level probe in the borehole located east of the spring (Fig. 1).

For calibrations using springflow- and piezometric-level variations, a differential Evolution Adaptive Metropolis (DREAM) Markov chain Monte Carlo (MCMC) has been applied, providing global optima of parameter values needed (Table 1) in sVK simulation (Vrugt et al. 2008, 2009). The results of Table 1 reflect that, in the simplified VarKarst calibration routine, in comparison with oVK, similar values of the model parameters are obtained. This manifests that the simplification made in the sVK routine does not change the modeling results significantly. The present study does not perform model evaluation with an independent validation data set.

For the optimized parameter set, the coefficient of determination (R^2), KGE, and RMSE (only for groundwater level) have been calculated to evaluate the results of the calibration procedure.

Results

Results of the calibration of Villanueva del Rosario springflow are displayed in Figs. 3 and 4.

Table 1 Simplified VarKarst model parameters, descriptions, and ranges for calibration and uncertainty analysis routine, calibration results and oVK model calibration results for the pilot site

Parameter	Description	Unit	Parameter range (lower–upper)	Calibrated value	Normal VarKarst
P_{gw}	Effective porosity of limestones	%	0–0.01	0.01	–
Δh	Distance between the sea level and the bottom of the borehole	m	700–800	781.2	–
a_{SE}	Soil and epikarst variability constant	–	0–3	0.12	0.35
$K_{\mathrm{mean},E}$	Epikarst mean storage coefficient	day^{-1}	1–50	1	1.06
$V_{\mathrm{max},S}$	Mean soil storage capacity	mm	0–500	147.1	207.9
$V_{\mathrm{max},E}$	Mean epikarst storage capacity	mm	0–500	480.5	387
a_{recharge}	Recharge separation variability constant	–	0–3	2.93	1.14
a_{gw}	Groundwater separation variability constant	–	0–3	1.67	0.8
K_{conduit}	Conduit mean storage coefficient	day^{-1}	1–20	8.27	8.2

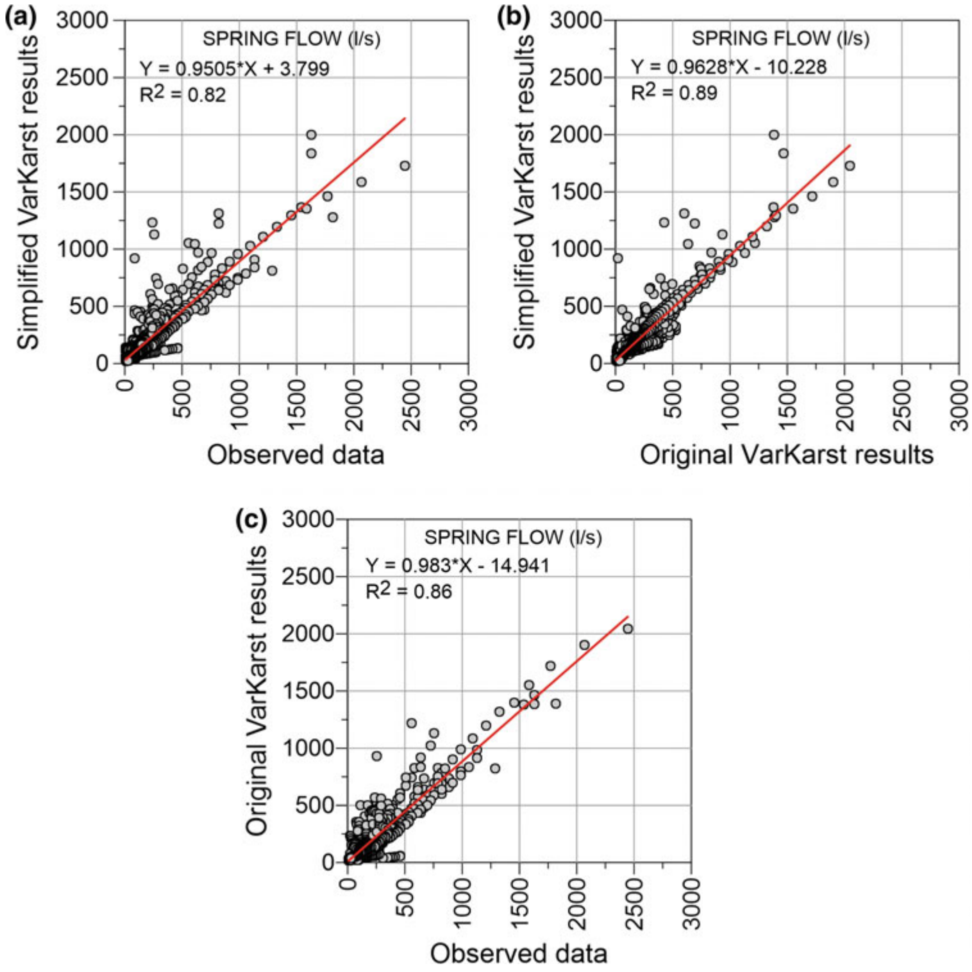

Fig. 3 Correlation of **a** simplified VarKarst modeled springflow versus observed data. **b** Simplified (sVK) versus Original VarKarst (oVK) codes results and **c** oVK results versus observed data

The calibration procedure reaches high performance concerning spring discharge, with a modified version of the KGE value of 0.90 between sVK results and observed data. In addition, coefficients of determination (R^2) obtained also prove good correlations between sVK and observed Villanueva del Rosario springflow, with 0.82 (Fig. 3a), and

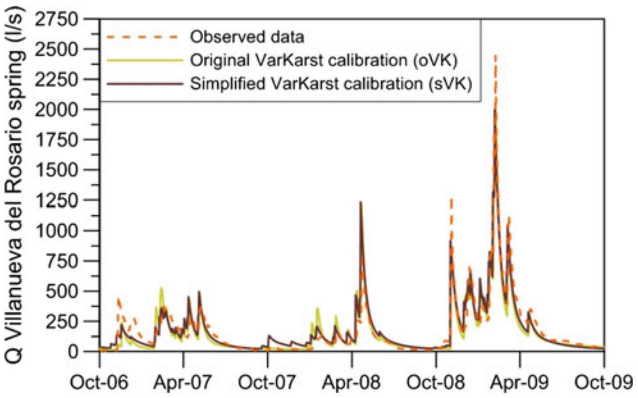

Fig. 4 Time series of observed and simulated Villanueva del Rosario springflow by original (oVK) and simplified VarKarst models (sVK)

0.89 between both VarKarst codes (Fig. 3b). High R^2 coefficients are related to similar springflow evolutions during the calibrate period (Fig. 4).

Results of the water-level calibration in a borehole close to Villanueva del Rosario spring are displayed in Fig. 5.

The calibration routine has caused a good groundwater-level correlation between sVK model and observed data, with a KGE coefficient of 0.79. Furthermore, simulated time series has an R^2 coefficient of 0.85 (Fig. 5a) and a root-mean-squared error (RMSE) coefficient of 3.07 m in relation to the observed water table (Fig. 5b).

Discussion

A simplified version of VarKarst model (sVK) has been developed in Villanueva del Rosario karst system, where original VarKarst model (oVK) has already applied (Hartmann et al. 2014). This new version provides slightly different results compared to the original VarKarst model (Fig. 4), caused by the change of the statistic coefficient applied in the calibration routine. In the sVK model of Villanueva del Rosario system, root-mean-squared error (RMSE) has been used for springflow and piezometric-level calibration, while Kling-Gupta efficiency (KGE) parameter was applied for discharge calibration in the oVK. Simplified VarKarst model parameters values (Table 1) have been similar to oVK parameters results in Villanueva del Rosario system (Hartmann et al. 2014), verifying all equations programed in the sVK code and the simplification of the program routine. Furthermore, oVK was used in other karst system located at southern Spain (Hartmann et al. 2013), with similar results of the calibration parameter values obtained in this study.

Piezometric-level correlation was also satisfactory (Fig. 5a). Water-level evolution was correctly modeled, including the trends during the calibration period (Fig. 5b). The original model is not enabled to simulate groundwater levels, which is the novelty of the simplified model that we present in this study. Nevertheless, the RMSE coefficient shows that the modeled groundwater level is overestimated, but it shows adequate performance in reflecting its dynamics. A probable cause for the systematic overestimation of the calculated water level may be the quite narrow ranges of the effective porosity parameter P_{gw}, and the assumption of a constant effective porosity throughout the aquifer, when the value of this parameter commonly decrease with depth. In other chalk areas where this linear relation was applied, the assumption of a constant porosity could account for the overestimation of high levels and an underestimation of low levels (Brenner et al. 2018).

In the calibration routine, a good model performance without a split-sample test should be handled with care. However, these preliminary results give some reasons to believe that the simplified VarKarst model can achieve a simultaneous reproduction of observed discharges and water

Fig. 5 **a** Correlation of simulated, by simplified VarKarst model, versus observed water-level records and **b** time series of observed and simulated piezometric level by simplified VarKarst model

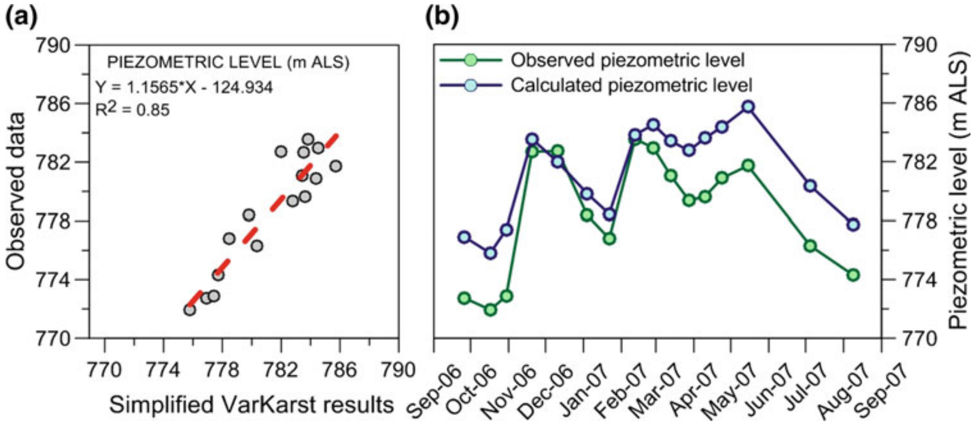

levels. Indeed, further evaluation using split-sample testing and sensitivity analysis is necessary before the model can be used for prediction.

Conclusions

The simplified VarKarst has been developed to optimize the model performance from the original version, reaching acceptable reliability in the simulation of the outflow and water level of a mountainous karst system. This kind of approach is not very common in semi-distributed groundwater models due to the heterogeneity of carbonates aquifers. Groundwater levels were simulated by translating the modeled groundwater storage into groundwater levels assuming a constant effective porosity. The calibration procedure was satisfactory, with acceptable values of the coefficients used.

Those results show that semi-distributed process-based modeling can be a valuable tool for simulating and predicting groundwater frequencies in highly heterogeneous carbonate aquifers where information is too limited for the application of distributed models. This might help decision makers in the karst regions to study the best water management strategies under possible future changes.

Acknowledgements This chapter is a contribution to the project CGL2015-65858R and to the research group 308 of Andalusian Government.

References

Adinehvand, R, Raeisi, E, Hartmann, A (2017). A step-wise semi-distributed simulation approach to characterize a karst aquifer and to support dam construction in a data-scarce environment. J. Hydrol. 554, 470–481. https://doi.org/10.1016/j.jhydrol.2017.08.056.

Brenner, S, Coxon, G, Howden, NJK, Freer, J, Hartmann, A (2018) Process-based modelling to evaluate simulated ground-water levels and frequencies in a Chalk catchment in south-western England. Nat. Hazards Earth Syst. Sci. 18, 445–461. https://doi.org/10.5194/nhess-18-445-2018.

COST (1995), COST 65: Hydrogeological aspects of groundwater protection in karstic areas, Final report (COST action 65), Rep. EUR 16547, 446 pp., Brussel, Belgium.

Hartmann A, Barberá JA, Lange J, Andreo B, Weiler M (2013) Progress in the hydrologic simulation of time variant recharge areas of karst systems – Exemplified at a karst spring in Southern Spain. Advances in Water Resources 54: 149–160, https://doi.org/10.1016/j.advwatres.2013.01.010.

Hartmann A, Mudarra M, Andreo B, Marín A, Wagener T, Lange J (2014) Modeling spatiotemporal impacts of hydroclimatic extremes on groundwater recharge at a Mediterranean karst aquifer. Water Resources Research 50. https://doi.org/10.1002/2014wr015685.

Hartmann A, Gleeson T, Rosolem R, Pianose F, Wada Y, Wagener T (2015) A large-scale simulation model to assess karstic groundwater recharge over Europe and the Mediterranean. Geosci. Model Dev., 8, 1729–1746. https://doi.org/10.5194/gmd-8-1729-2015.

Jimenez-Martinez, J, Smith, M, Pope, D (2016) Prediction of groundwater induced flooding in a chalk aquifer for future climate change scenarios, Hydrol. Process., 30, 573–587. https://doi.org/10.1002/hyp.10619, 2016.

Ladouche, B, Marechal, JC, Dorfliger, N (2014) Semi-distributed lumped model of a karst system under active management, J. Hydrol., 509, 215–230. https://doi.org/10.1016/j.hydrol.2013.11.017.

Martín-Algarra M (1987) Evolución geológica alpìna del contacto entre las Zonas Internas y Externas de la Corduillera Bética. Ph.D. Thesis, University of Granada.

Mudarra M (2012) Importancia relative de la zona no saturada y zona saturada en el funcionamiento hidrogeológico de los acuíferos carbonáticos. Caso de la Alta Cadena, sierra de Enmedio y área de Los Tajos (provincia de Málaga). Ph.D. Thesis, University of Málaga.

Mudarra M, Andreo B, Marín AI, Vadillo I, Barberá JA (2014) Combined use of natural and artificial reacers to determine the hydrogeological functioning of a karst aquifer: the Villanueva del Rosario system (Andalusia, Southern Spain). Hydrogeological Journal 22: 1027–1039, https://doi.org/10.1002/2014wr015685.

Vrugt JA, ter Braak CJF, Clark MP, Hyman JM, Robinson BA (2008) Treatment of input uncertainty in hydrologic modeling: Doing hydrology backward with Markov chain monte Carlo simulation. Water Resources Research, 44: W00B09. https://doi.org/10.1029/2007wr006720.

Vrugt JA, ter Braak CJF, Diks CGH, Robinson BA, Hyman JM, Higdon D (2009) Accelerating Markov Chain Monte Carlo Simulation by Differential Evolution with Self-Adaptive Randomized Subspace Sampling. International Journal of Nonlinear Sciences and Numerical Simulation, 10(3), 271–288.

Laboratory Experiments for Calibrating Flow Exchange Coefficient of MODFLOW CFP1

Roger B. Pacheco Castro, Ming Ye, Xiaohu Tao, Hongyuan Wang, and Jian Zhao

Abstract

A sandbox device was developed to test MODFLOW CFP1 under various conditions. The experiment represents a three-dimensional confined karst aquifer. MODFLOW CFP1 is a public-domain software developed by the US Geological Survey that is becoming popular for the simulation of karst hybrid models. Since geometry and hydraulic parameters of the matrix and conduit related to the experiments can be measured accurately, this study is focused on the flow exchange coefficient used by MODFLOW CFP1 to simulate the flow exchange between matrix and conduits of karst aquifers. The flow exchange coefficient is commonly calibrated given our limited knowledge of the underground system. In this work, we discuss the issues encountered during the calibration of this coefficient. It was found that the calibrated parameter values depend on the direction of the flow exchange something that is not considered in the current definition of this parameter. The calibration also revealed the structural inadequacy of the linear model used in MODFLOW CFP1 for simulating the flow exchange. These results are useful for further evaluation of MODFLOW CFP1 at laboratory and field scales.

Keywords

Sandbox • Karst flow modeling • Model error

Introduction

The most used groundwater flow models for karst aquifers can be divided into three categories depending on the conceptualization used for conduits and fractures. Conduits and fractures are commonly conceptualized as either equivalent continuums (the average properties of the conduits are simulated using an equivalent continuum) or discrete pipes (in which the conduits are simulated using a discrete network of pipes). The combination of the two conceptualizations with the porous media leads to the following three categories: continuum models, discrete models and combined discrete–continuum models, these types of models are also known as hybrid models (Kuniansky 2014; Hartmann et al. 2014; Shoemaker et al. 2008). The continuum models assume that the karst aquifer can be simulated by one or more equivalent continuous media where the flow can be turbulent or laminar. In the case where more than one porous media is considered, the two continua are linked by means of an exchange term. The simplest type of equivalent continuum model is the single continuum model where the aquifer heterogeneities are averaged (Hartmann et al. 2014). The flow in the porous media is modeled using the Darcy law (Bear 1972; Hartmann et al. 2014). This kind of model can be used for predictions and estimations when the scale of investigation is regional (Hartmann et al. 2014; Davis 1996; Scanlon et al. 2003). The discrete models consider that the porous media have a very low hydraulic conductivity; therefore, the groundwater flow in the porous media is negligible. This assumption simplifies the system to a discrete network of fractures. Information such as density of fractures, fracture length, and orientation are required (Sauter 1992; Kovacs and Sauter 2007). An example of the application of discrete fracture networks to a karst aquifer is given by Jeannin (2001). The author used a discrete set of pipes to model flow in a conduit-dominated system. Flow in the conduits where modeled using Saint-Venant equations.

R. B. Pacheco Castro (✉)
Sisal Academic Unit, Institute of Engineering, National Autonomous University of Mexico, Puerto de Abrigo Sisal, Yucatán, 97355, Mexico
e-mail: rpachecoc@iingen.unam.mx

M. Ye
Department of Earth, Ocean, and Atmospheric Science, Florida State University, Tallahassee, FL 32306, USA

X. Tao · H. Wang · J. Zhao
College of Water Conservancy and Hydropower Engineering, Hohai University, Nanjing, China

C. Bertrand et al. (eds.), *Eurokarst 2018, Besançon*, Advances in Karst Science,
https://doi.org/10.1007/978-3-030-14015-1_18

The combined discrete continuum models or hybrid models couple a continuous medium with a discrete network of cylindrical pipes. This kind of approach allows simulating high conductive karst channels through the integration of existent information about the conduits (Shoemaker et al. 2008; Kovacs and Sauter 2007). There are different mathematical approximations for hybrid models, depending on the equations used to simulate the flow in the conduits. Examples of this type of models are the Darcy–Stokes with Beaver-Joseph boundary condition and MODFLOW CFP1, from now on referred as CFP1 (Shoemaker et al. 2008; Faulkner et al. 2009; Cao et al. 2010). Faulkner et al. (2009) used a laboratory analog to simulate a karst aquifer and results were compared with Darcy–Stokes solution. The modeling results suggest that Darcy–Stokes is a valid model for conduit matrix systems (Faulkner et al. 2009; Hu et al. 2012). CFP1 couples the classical groundwater flow equations with pipe-flow equations by means of a linear exchange term. CFP1 has been used for simulating groundwater flow in karst aquifers (Gallegos et al. 2013; Saller et al. 2013; Mikszewski and Kresic 2015; Karay and Hajnal 2015; Giese et al. 2018), and recently was extended to simulate solute transport (Xu and Hu 2017). Gallegos et al. (2013) performed simulations at field and laboratory scales using CFP1 and evaluated the model performance by comparing the modeling results with real data obtained by Faulkner (2009) at the laboratory scale. At the field scale, the comparison was done with data from the Woodville Karst Plain, Florida (Davis 2010). According to Gallegos et al. (2013), in comparison with the classical MODFLOW, CFP1 can produce more accurate results at field and laboratory scales. Hill (2008) performed a similar comparison in a karst aquifer in West Central Florida. In this study, the authors found an improvement in the overall matching of 12–40% when CFP1 was compared to the classical MODFLOW. Saller et al. (2013) found similar results using data from the Madison Aquifer of western South Dakota, USA. The main conclusion of all these studies is that the simulation results are improved with the consideration of conduits as discrete pipes.

Applications of CFP1 always require calibrating the flow exchange coefficient that controls the amount of flow exchange between the conduits and surrounding porous media. However, calibrating the flow exchange coefficient is not straightforward given our limited knowledge about the conduit and the porous media. We take advantage of our experimental data of a simple experiment to evaluate how good the calibration of this coefficient is. The present work is part of a bigger research oriented to test rigorously the performance of CFP1 and other hybrid models. Although previous works claim improvements of CFP1 over classical approaches, we believe that this model needs more testing. The work presented by Gallegos et al. (2013) only considers laminar flow in the conduit, and the exchange flow is from the conduit to the matrix. Their conclusion is based in one simulation. Also, Kuniansky et al. (2011) argues whether the extra effort caused by data collection and computational time for CFP1 is justified, it is also discussed that CFP1 is only able to simulate average annual conditions. Wang (2010) showed that the equations of CFP1 are ill-posed. Hill (2008) estimated the exchange coefficient using field measurements —one of the sites showed a nonlinear behavior. There is also a disagreement on whether a correct characterization of the critical Reynolds number is important to have good simulations (Reimann et al. 2011; Hill et al. 2010).

This study has two objectives. The first objective is to estimate the flow exchange coefficient for different configurations of the sandbox, and the second objective is to use the calibration results to evaluate possible structure error caused by the use a linear exchange equation to estimate flow exchange. We also examined the dependence of the flow exchange coefficient on the direction of flow exchange.

Materials and Methods

CFP1

CFP1 (Shoemaker et al. 2008) couples the groundwater flow equation of continuous porous media with pipe-flow equation of a discrete network of cylindrical pipes. The equation used to simulate the flow in the porous media is the classical equation derived from Darcy law. The flow rate in the conduit is simulated using the Hagen–Poiseuille equation for laminar flow, or the Darcy–Weisbach and White–Colebrook equations for turbulent flow (Shoemaker et al. 2008). CFP1 requires that the user input two critical Reynolds numbers to check whether the flow is under laminar or turbulent flow conditions. The lower Reynolds number is used to indicate when the flow switch from laminar to turbulent, and the upper one to switch from turbulent to laminar (Shoemaker et al. 2008; Clemens et al. 1996). The flow exchange between the conduits and the porous media is given by the linear exchange equation (Shoemaker et al. 2008),

$$Q_{\mathrm{ex}} = \alpha\left(h_{\mathrm{c}} - h_{\mathrm{p}}\right), \tag{1}$$

where Q_{ex} is the volumetric flow exchange [L^3/T], α is the pipe conductance or the flow exchange coefficient [L^2/T], h_{c} is the head in the conduit [L] and h_{p} is the head in the porous media [L]. This equation was introduced by Barenblatt et al. (1960) in his study of seepage through fractured rocks. Except a few studies that estimated the flow exchange coefficient based on direct measurements (Hill 2008), the coefficient is always obtained by calibrating CFP1 with measurements of hydraulic head (Gallegos et al. 2013; Saller et al. 2013).

The software UCODE 2014 (Poeter et al. 2014) was used in this work to automatically calibrate the flow exchange coefficient. UCODE minimizes the objective function,

$$S(\theta) = \sum_{l=1}^{N} w_l \left(y_l^m - \hat{y}_l\right)^2 \tag{2}$$

where θ can be one or a set of NP parameters, $N = \text{ND} + \text{NPR}$ is the total number of available measurements (ND) plus prior information for the parameters (NPR), y_l^m are either measurements or estimated prior information, $\hat{y}_l$ is the corresponding simulated value that depends on the parameter θ and w_l is the corresponding weight (Hill and Tiedeman 2007). Equation (2) assumes that the residuals, $y_l^m - \hat{y}_l$, are independent (Draper and Smith 1998; Hill and Tiedeman 2007). The weights, w_l, reflect the relative accuracy of the data, y_l^m, and smaller weights are assigned to less accurate data (Hill and Tiedeman 2007; Poeter et al. 2014; Doherty 2016). In this study, to make Eq. (2) dimensionless, the weights are assigned as $w_l = 1/\sigma_l^2$, where σ_l^2 is the variance of the l-th observation or prior information (Hill and Tiedeman 2007). There are two options to calculate the variance by assuming that data errors are not correlated. One option is to first assign a value to the coefficient of variation (c.v.: variance divided by the mean) based on existing knowledge about the data, and then calculate the variance as $\sigma_l^2 = (\text{c.v.} \times y_l)^2$. The other option is to assume a range of variability for the data, $y_l - \in \ \le y_l \le y_l + \in$. By assuming that the error is normally distributed and that 95% of the time the error belongs to such interval, we have $1.96\sigma_l = \in$ and then calculate the variance directly (Poeter et al. 2005). In this study, the measurement variance is evaluated using the first method for heads and the second for flow rates.

Once the calibration is complete, the calculated error variance for the calibration, s^2, was evaluated via,

$$s^2 = \frac{S(\theta)}{\text{ND} + \text{NPR} - \text{NP}} \tag{3}$$

where NP is the number of calibrated parameters. The s^2 can be used to evaluate the model fit relative to the weights used for the nonlinear regression (Hill and Tiedemann 2007). A value of $s \approx 1$ is expected if the model fit is consistent with the weights used for regression (Hill and Tiedeman 2007; Lu et al. 2012). If the value of s is significantly different from one, then the value of s can be used to calculate weights that are consistent with model fit. If the new weights are unreasonable, it may indicate the presence of model error (Hill and Tiedeman 2007). The variance–covariance matrix is defined as,

$$V(\theta) = s^2 \left(J^T W J\right)^{-1} \tag{4}$$

where W is the $N \times N$ weight matrix and $J = \left[\partial y_i / \partial \theta_j\right]$ is the $N \times \text{NP}$ Jacobian matrix. The variance of the parameter θ_j is the square root of the (j, j)-element of the matrix $V(\theta)$, and can be used as well to identify model structural error. Since the data errors of the well-controlled lab experiments can be estimated accurately in this study, s^2 can reveal the model structure error associated with Eq. (1). The results can help the users of CFP1 to understand its limitations.

Laboratory Data

The laboratory experiments were conducted in a sandbox device developed to test CFP1 under controlled conditions, under which most of the CFP1 model parameters can be measured accurately. Figure 1a shows a side view of the sandbox. The sandbox was built using acrylic with a thickness of 1.7 cm. The dimension of the sandbox is $104.4 \times 41.9 \times 43.4\ \text{cm}^3$ (including the acrylic thickness). The sandbox is splitted into three sections. The left and right sections of the sandbox (20 cm each) are filled with gravel to create a uniform distribution of the pressure, two stainless steel meshes are used to keep the sand in the middle and separated from the gravel. The other four sides of the sandbox are impermeable. The length filled with sand is 80 cm, with a hydraulic conductivity of 0.788 cm/s (measured from a Darcy column). The porous media is fully saturated to represent a confined aquifer. As shown in Fig. 1, a pipe of stainless steel was placed in the center to mimic a karst conduit. The pipe length is 80 cm, external diameter 1.9 cm, and a thickness of 0.1 cm. To make possible the flow exchange between the conduit and the fine sand, holes of 0.2 cm in diameter were drilled along the pipe. The pipe was covered by a stainless steel mesh to prevent infiltration of the sand into the conduit. Four external reservoirs were used to control the inflow and outflow conditions of the laboratory experiments (Fig. 1). Two reservoirs were connected to the conduit to create conduit inflow and outflow, and the other two reservoirs were connected to the gravel-filled water sections to create matrix inflow and outflow.

A set of 13 experiments were conducted with different flow conditions created by changing the heights of the inflow reservoirs. For each experiment, when steady-state flow conditions were reached, a total of 29 variables were measured. The data included water temperature, hydraulic heads at the inflow and outflow sections, flow rates from and to the four reservoirs, and twenty hydraulic heads in the matrix at the locations shown in Fig. 1. The heads in the matrix were measured using pressure transducers. The accuracy of the

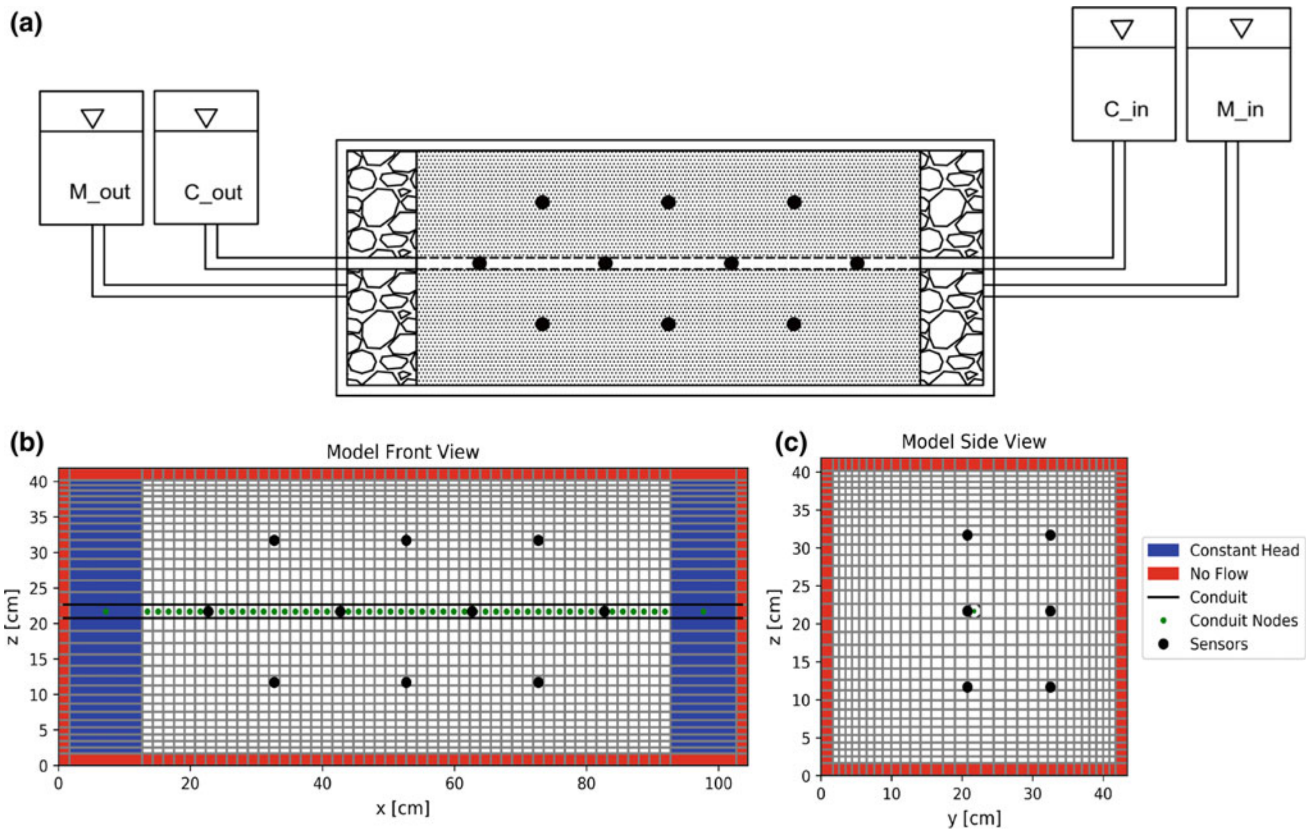

Fig. 1 Experimental design model discretization. **a** Experimental model design, *M* is used for porous media and *C* for conduit. **b** Front view of vertical cross section along row 16 where conduit is located. **c** Side view of vertical cross section along column 16

measurements is estimated to assign the weights needed for UCODE. For the sensors used to measure matrix heads, the sensor accuracy is ±0.5 cm. The flow rates were measured using the head loss on two points located on each of the hoses connecting the external reservoirs to the inflow/outflow sections. A curve between measured head loss and measured flow rate was fitted for each of the four hoses to estimate flow rate. The error of the flow estimates was estimated as the maximum change on the flow rate calculated from a variation on the measured heads by ±0.1 cm divided by the flow rate. This error was calculated for each flow rate. The errors were about 10% of the measured flow rate most of the time.

Figure 2 plots the measured inflow and outflow rates and the corresponding heads at the four reservoirs for the 13 experiments. The experiments can be classified into two cases. For Case I (Experiments 01 to 07), the head of conduit inflow was increased gradually to generate flow from the conduit to the matrix. For Case II (Experiments 08 to 13), the head of matrix inflow was gradually increased to generate flow from matrix to conduit. Detailed results of the laboratory experiments can be found at Pacheco (2017).

The forward simulation of the laboratory experiment was conducted using FloPy (Bakker et al. 2016), a software that integrates MODFLOW with the Python programming language. During the CFP1 model simulation, the entire sandbox was discretized into a computational grid with 33 rows, 54 columns, and 33 layers, as shown in Fig. 1. The conduit was located in layer 16 and row 16, between columns 3 and 52. The conduit layer height was 1.9 cm, the size of conduit diameter. The conduit was discretized by placing one node within each cell that the conduit passes through. Constant head boundary conditions were used for the porous media and conduit inflow/outflow boundaries as measured in the laboratory experiments. For the conduit, the following parameters were fixed: critical Reynolds numbers of 2000 and 4000, tortuosity was set to 1, for the diameter 1.9 cm, and 12 °C for temperature. The absolute value of the percent of discrepancy (defined as in MODFLOW) is less than 1% for all numerical simulations.

Results and Discussion

The calibration of CPF1 was conducted in two steps. In the first step, hydraulic conductivity of the matrix and roughness coefficient of the conduit were calibrated by using the data of Experiment 02, for which the flow exchange between matrix and conduit was neglected. The calibrated values of

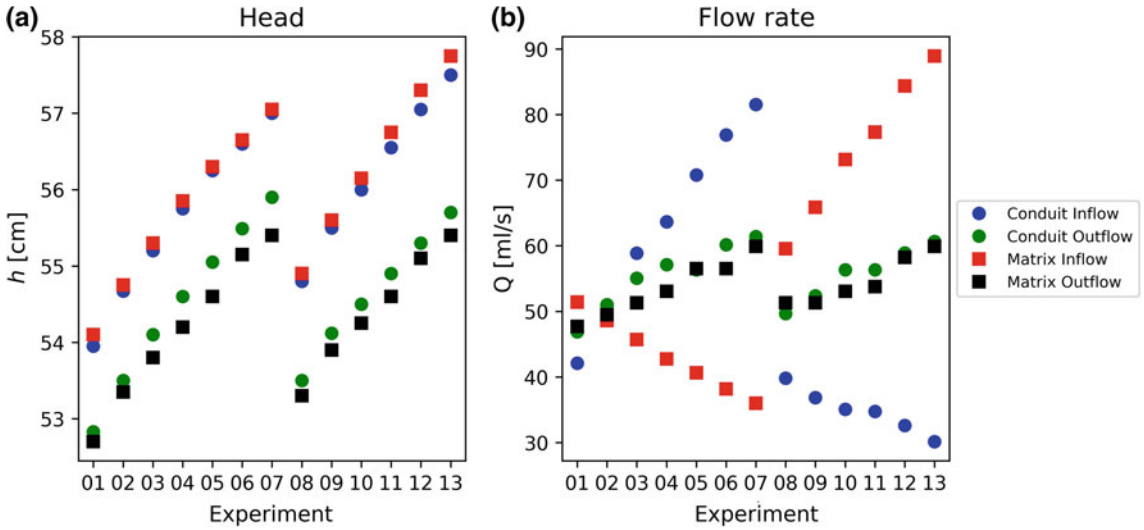

Fig. 2 Experimental results for **a** heads at the inflow and outflow of the matrix and the conduit (boundary conditions for CFP1), and **b** measured flow rates at the inflow and outflow of the matrix and the conduit. Exact results can be found in Pacheco (2017)

hydraulic conductivity and roughness coefficient were used in the second step to calibrate the flow exchange coefficient.

Calibration of Hydraulic Conductivity and Roughness Coefficient

For Experiment 2, the measurements of inflow and outflow rates (plotted in Fig. 2) gave a percent discrepancy of −1.8% for the porous media and 0.1% for the conduit. The percent of discrepancy is defined as in MODFLOW: 100 × (IN *FLOW* − OUTFLOW)/(INFLOW + OUTFLOW/2), and is calculated separately for conduit and matrix using the measured values. The small discrepancy in mass balance suggests that the net flow exchange between the matrix and the conduit is negligible. Therefore, it is reasonable to set the flow exchange coefficient (α) to be zero for this case. The calibration of hydraulic conductivity (K) and roughness coefficient (k_c) was performed using flow rate data only, because matrix heads of the steady-state flow system with homogeneous sand is not a function of hydraulic conductivity, but a linear function of boundary heads. The calibrated values for K and k_c were 2.05 and 0.34, respectively. The weights were assigned following the guidelines of Hill and Tiedemann (2007) and using the estimated measurement error. Head weights were assigned using the method 1 and flow rates using the method 2 as discussed above. The calculated standard error of this calibration is 0.99 [Eq. (3)]; thus, the corrected coefficient of variation is consistent with the measurement error. The calibrated value (2.05 cm/s) of hydraulic conductivity is larger than the measured one (0.788 cm/s) from the Darcy experiment. The calibrated value (0.34 cm) of roughness is also larger than the estimated one (0.1 cm). We estimated a value of 0.1 cm for the roughness because this was the thickness for the pipe and the holes were through the entire thickness. The difference is not unexpected because of the errors that we may have introduced when packing the sand, and the extra roughness caused by the mesh surrounding the pipe. The calibrated values of hydraulic conductivity and roughness coefficient provided information about those parameters that were used and fixed for the calibration of the exchange flow coefficient.

With the objective of checking the accuracy of the pressure transducers, a comparison between the measured and simulated heads in the porous media was performed. The mean and the standard deviation of the error were calculated, and a systematic bias of 0.55 cm was detected in the measurements of the transducers in the matrix. In the following comparisons, a value of 0.55 was added to the sensor measurements to compensate for this bias.

Calibration of Flow Exchange Coefficient

When calibrating the flow exchange coefficient, the roughness coefficient and the hydraulic conductivity were fixed at their calibrated values. First, we tried to calibrate randomly two experiments, one for each case. However, the calibration did not converge for some cases or it took too long to converge, apparently caused by a lack of sensitivity of the model to the exchange coefficient. We did plots of the objective function in terms of the exchange coefficient and

Table 1 Calibrated values for the flow exchange coefficient, 95% confidence intervals (CI) and error variance for Experiments 05 and 08

Experiment	Flow exchange coefficient [L^2/T]	95% CI	Parameter variance
05	0.829	(0, 2.65)	0.777
08	3.20	(0, 17.8)	50.002

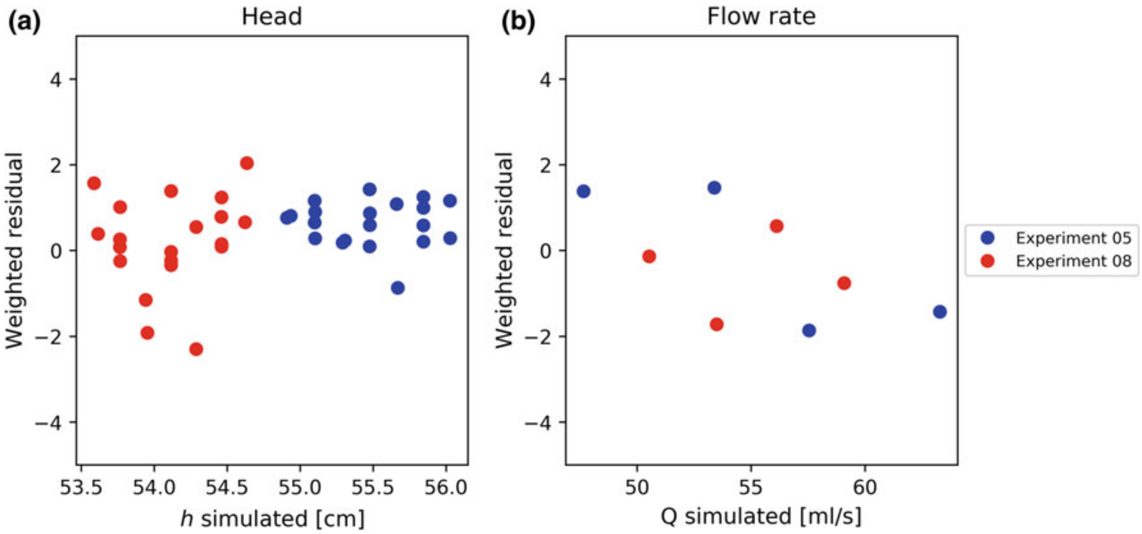

Fig. 3 Residual plots of the experiments used to calibrate the flow exchange coefficient. The x-axis is the simulated value and the y-axis the corresponding weighted residual. **a** Weighted residuals for the heads in the matrix and **b** weighted residuals for the flow rates at the boundaries

choose two cases where the calibration would be successful, Experiments 05 and 08 were then selected. We decided one for each set of experiments because this value depends only on the wall permeability and conduit geometry, and both of them do not change from one experiment to another. Table 1 lists the calibrated values, the 95% confidence interval, and the parameter variance calculated using Eq. (4). The large value of the error variance for Experiment 08 is an indicator that the model is not very sensitive to the value of the exchange for this experiment.

Figure 3 plots the weighted residuals for head and flow rates of the two experiments. For Experiment 5, the weighted head mean is larger than zero, even when the heads were corrected for the bias detected in the Experiment 02. These were the best calibrations we could get; however, the weights were modified. First, the large weighted residuals were reduced by increasing the variance. In this way, all of them became independent and randomly distributed. Then, we multiplied the observation variance by s^2 to get the error variance of the calibration close to 1 and for the residuals to be consistent with the weights used. The corrected weights corresponded to errors bigger than expected which is not reasonable (up to 20% in some cases). This may indicate the presence of model error (Hill and Tiedeman 2007). Also, the two calibrated values of flow exchange coefficient are different by one order of magnitude, suggesting that there are other factors controlling the amount of exchange between the matrix and the conduit not considered in the current definition of the exchange coefficient. With the current definition, the flow exchange coefficient depends on the conduit geometry and wall conductance (Barenblatt et al. 1960; Shoemaker et al. 2008).

Figure 4 shows the estimated error (simulated value minus measured value) for all flow rates as a function of the flow exchange coefficient. For all the experiments, except Experiments 03 to 07 at the conduit outflow, it seems that the results become insensitive to the exchange after some value (Fig. 4). This is the reason why for some experiments the model calibration took long to converge, and the variance of exchange coefficient was big (for Experiment 08 compared to Experiment 05). The bigger the flow exchange coefficient, the less sensitive the model is. Birk et al. (2003) argued that CFP1 models are very sensitive for small values of exchange. This is not observed in Fig. 4, the model is not highly sensitive for small values of exchange and for large values, the model is either not sensitive to the flow exchange coefficient or CFP1 equations did not converge. Hu et al. (2012) reported similar results for another hybrid model similar to CFP1.

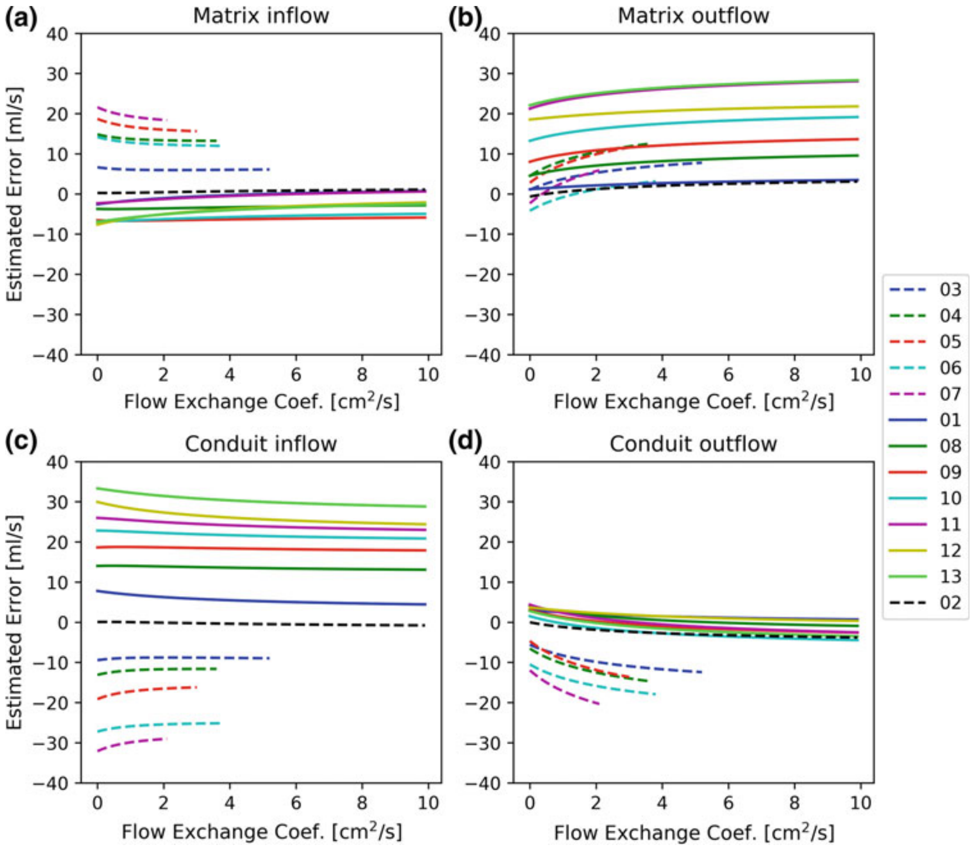

Fig. 4 Estimated error as a function of the flow exchange coefficient for all the experiments. **a** Matrix inflow. **b** Matrix outflow. **c** Conduit inflow. **d** Conduit outflow

Conclusions

An experimental device was developed to test CFP1 model. This device was used to collect information about the dynamics of the exchange between a porous matrix and a conduit in a controlled environment where most of the required parameters could be measured accurately. By using the measured heads in the lab as boundary conditions for the numerical model, we calibrated the hydraulic conductivity of the porous media, roughness, and the exchange coefficient. The following was observed about the exchange coefficient calibration: (1) different cases calibrated to different values (one order of magnitude difference) thus suggesting that may be other parameters influencing its value currently not considered in its definition, (2) the model seems to be insensitive to the flow exchange coefficient; thus, the calibration may take long time to converge and the calibrated value will have a large variance, (3) to get a good calibration weights needed to be adjusted with errors bigger than expected. Those results may suggest the presence of model error in CFP. This information should be considered when using CFP1. Also, the results of this work will be used to perform more rigorous tests in CFP1.

Acknowledgements The first author was supported by the Fulbright Scholarship for his dissertation research at the Florida State University. The laboratory experiment was supported by a travel grant from the Hohai University. The second author was supported in part by National Science Foundation grant EAR-1828827.

References

Bakker, M., V. Post, C.D. Langevin, J.D. Hughes, J.T. White, J. J. Starn, M.N. Fienen. 2016. Scripting MODFLOW model development using Python and FloPy. Groundwater, 54(5): 733–739.

Barenblatt, G., I.P. Zheltov, I. Kochina. 1960. Basic concepts in the theory of seepage of homogeneous liquids in fissured rocks [strata]. Journal of applied mathematics and mechanics 24(5), 1286–1303.

Bear, J. 1972. Dynamics of fluids in porous media. Dover Publications Inc., NY.

Birk, S., R. Liedl, M. Sauter, G. Teutsch. 2003. Hydraulic boundary conditions as a controlling factor in karst genesis: A numerical modeling study on artesian conduit development in gypsum. Water Resources Research, 39(1).

Clemens, T., D. Hückinghaus, M. Sauter, R. Liedl and, G. Teutsch. 1996. A combined continuum and discrete network reactive transport model for the simulation of karst development. Proceeding of ModelCAE96, Colorado, IAHS Pub., 309–320.

Cao, Y., M. Gunzburger, F. Hua, X. Wang. 2010. Coupled Stokes-Darcy model with Beavers-Joseph interface boundary condition. Communications in Mathematical Sciences 8(1): 1–25.

Davis, J. 1996. Hydraulic investigation and simulation of ground-water flow in the Upper Floridan aquifer of northcentral Florida and southwestern Georgia and delineation of contributing areas for selected City of Tallahassee, Florida, water-supply wells. U.S. Geological Survey, Water Resources Investigations Report 95-4296.

Davis, J., B. Katz, D. Griffin. 2010. Nitrate-N Movement in Groundwater from the Land Application of Treated Municipal Wastewater and Other Sources in the Wakulla Springs Springshed, Leon and Wakulla Counties, Florida, 1966-2018. U.S. Geological Survey Scientific Investigations Report 2010-5099.

Doherty, J. 2016. PEST model-independent parameter estimation user manual part I: PEST, SENSAN and Global Optimizers, 6th Edition. Watermark Numerical Computing.

Draper, N.R., H. Smith. 1998. Applied Regression Analysis, Third Edition. John Wiley & Sons.

Faulkner, J., B.X. Hu, S. Kish, F. Hua. 2009. Laboratory analog and numerical study of groundwater flow and solute transport in a karst aquifer with conduit and matrix domains. Journal of contaminant hydrology 110(1): 34–44.

Gallegos, J.J.; B.X. Hu, H. Davis. 2013. Simulating flow in karst aquifers at laboratory and sub-regional scales using MODFLOW-CFP. Hydrogeology Journal 21(8): 1749–1760.

Giese M., Reimann, T., Bailly-Comte, V., Marechal, J., Sauter, M., Geyer T. 2018. Turbulent and Laminar Flow in Karst Conduits Under Unsteady Flow Conditions: Interpretation of Pumping Tests by Discrete Conduit-Continuum Modeling. https://doi.org/10.1002/2017WR020658.

Hartmann, A., N. Goldscheider, T. Wagener, J. Lange, M. Weiler. 2014. Karst water resources in a changing world: Review of hydrological modeling approaches. Reviews of Geophysics 52(3): 218–242.

Hill, M.C., C.R. Tiedeman. 2007. Effective groundwater model calibration: with analysis of data, sensitivities, predictions, and uncertainty. John Wiley & Sons.

Hill, M.E. 2008. Conduit conceptualizations and model performance. PhD dissertation, Department of Geology, University of South Florida, Tampa.

Hill, M.E., M.T. Stewart, A. Martin. 2010. Evaluation of the MODFLOW-2005 Conduit Flow Process. Groundwater 48(4): 549–559.

Hu, X., X. Wang, M. Gunzburger, F. Hua, Y. Cao. 2012. Experimental and computational validation and verification of the Stokes–Darcy and continuum pipe flow models for karst aquifers with dual porosity structure. Hydrological Processes 26(13): 2031–2040.

Jeannin, P. 2001. Modeling flow in phreatic and epiphreatic karst conduits in the Hцlloch cave (Muotatal, Switzerland). Water Resources Research 37(2): 191–200.

Karay, G., G. Hajnal. 2015. Modelling of Groundwater Flow in Fractured Rocks. Procedia Environmental Sciences 25: 142–149.

Kovacs, A., M. Sauter. 2007. Modelling karst hydrodynamics. In: Methods in karst hydrogeology, N. Goldscheider, D. Drew, ed., Taylor & Francis, 201–222.

Kuniansky, E., J. Gallegos, J. Davis. 2011. Comparison of Three Model Approaches for Spring Simulation, Woodville Karst Plain, Florida. In: Karst Interest Group Proceedings, Fayetteville, Arkansas, April 26–29, U.S. Geological Survey Scientific Investigations Report 2011-5031, 169–170.

Kuniansky, E.L. 2014. Taking the mystery out of mathematical model applications to karst aquifers - A primer. In: Karst Interest Group Proceedings, E.L. Kuniansky, L.E. Spangler, eds., Carlsbad, New Mexico, April 29–May 2, U.S. Geological Survey Scientific Investigations Report 2014–5035: 69–81.

Lu, D., M. Ye, M.C. Hill. 2012. Analysis of regression confidence intervals and Bayesian credible intervals for uncertainty quantification. Water Resour. Res., 48.

Mikzewski A., Kresic N. 2015. Chapter 10. Mathematical Modeling of Karst Aquifers. In Karst Aquifers—Characterization and Engineering, Stevanovic Z. (ed.). Springer International Publishing.

Pacheco, R. 2017. Statistical analysis of karst aquifer pollution, karst flow model validation at laboratory scale, and development of seepage meter. Ph.D. dissertation, Florida State University.

Poeter, E.P., M.C, Hill, E.R. Banta, S. Mehl, S. Christensen. 2005, CODE_2005 and Six Other Computer Codes for Universal Sensitivity Analysis, Calibration, and Uncertainty Evaluation. U. S. Geological Survey, Techniques and Methods 6-A11.

Poeter, E.P., M.C. Hill, D. Lu, C.R. Tiedeman, S. Mehl. 2014. UCODE_2014, with new capabilities to define parameters unique to predictions, calculate weights using simulated values, estimate parameters with SVD, evaluate uncertainty with MCMC, and more. Integrated Groundwater Modeling Center Report Number GWMI 2014-02.

Reimann, T., Rehrl, C., Shoemaker, W. B., Geyer, T., & Birk, S. (2011). The significance of turbulent flow representation in single-continuum models. Water Resources Research, 47(9).

Saller, S.P., M.J. Ronayne, A.J. Long. 2013. Comparison of a karst groundwater model with and without discrete conduit flow. Hydrogeology Journal 21(7): 1555–1566.

Sauter, M. 1992. Quantification and forecasting of regional groundwater flow and transport in a karst aquifer (Gallusquelle, Malm, SW. Germany). Tubinger Geowissenschaftliche Arbeiten, Part C (13).

Scanlon, B.R., R.E. Mace, M.E. Barrett, B. Smith. 2003. Can we simulate regional groundwater flow in a karst system using equivalent porous media models. Case study, Barton Springs Edwards aquifer, USA. Journal of hydrology 276(1): 137–158.

Shoemaker, W., E.L. Kuniansky, S. Birk, S. Bauer, E.D. Swain. 2008. Documentation of a Conduit Flow Process (CFP) for MODFLOW-2005. U.S. Geological Survey, Techniques and Methods, Book 6, Chapter A24.

Wang, X. 2010. On the coupled continuum pipe flow model (CCPF) for flows in karst aquifer. Discrete and continuous dynamical systems-series B 13(2): 489–501.

Xu, Z., and B. X. Hu (2017), Development of a discrete-continuum VDFST-CFP numerical model for simulating seawater intrusion to a coastal karst aquifer with a conduit system, Water Resour. Res., 53, https://doi.org/10.1002/2016wr018758.

Part V

Multidisciplinary Regional Studies

The Characteristics of Karst Aquifers and the Variation of Karst Hydrological Processes in Northern China

Yonghong Hao, Juan Zhang, and Yaru Guo

Abstract

Approximately 3.44 million km^2 of carbonate rock exists in China and occupies one-third of China's territory. In general, the karst in China can be classified as two types (i.e., the karst in north China and the karst in south China) based on the paleodepositing environment of carbonate rocks and subsequent karstification processes. On the one hand, the lithology of carbonate rocks deposited between the Mesoproterozoic Era and the Mid-Ordovician in north China are micritic, which is difficult to erode compared with the sparry limestones common to south China, and deposited between the Sinian Sub-Era and the Triassic period. On the other hand, the paleoclimate during karstification processes in north China was dry and cold, and karstification occurred mainly in the subsurface, whereas the paleoclimate during karstification in south China was wet and warm, and karstification took place mostly at or near the surface. Karst aquifers are therefore characterized by fractures and conduits in the north, and by caves, tunnels, and subsurface rivers in the south. One of the significant characteristics of a karst hydrological system in the north is that the groundwater in a karst aquifer converges in a topographical depression and creates a large karst spring. To better understand the effects of climate variation and anthropogenic activity on spring discharge, the authors focused on the karst hydrological processes in north China, examined the Niangziguan Springs as a case study of karst hydrology in north China, and analyzed the spring discharge from 1959 to 2015 using statistical methods, including piecewise analysis, Wilcoxon rank-sum test, and wavelet coherence. Results indicate that the data of the Niangziguan Springs discharge can be divided into two groups: a pre-development period from 1957 to 1980 and a post-development period from 1981 to 2015. The annual average precipitation was 531 mm in the pre-development period and 462 mm in the post-development, showing a 13% decrease in precipitation. The annual mean spring discharges in the pre- and the post-development periods were 12.54 and 7.67 m^3/s, respectively, showing a 39% decline. Compared to the precipitation, the spring discharge has a 26% greater reduction on average between the periods. This fact indicates that the spring discharge was attenuated by almost 26% owing to the effects of human activity in the Niangziguan Springs basin. To see whether human activity alters the frequency (i.e., short- and long-term variations) of the discharge of Niangziguan Springs, the time series of spring discharge in both the pre- and the post-development periods were analyzed by wavelet coherence. Results indicate that although groundwater development has weakened the relation between spring discharge and precipitation, the resonant frequency between spring discharge and precipitation remain unchanged.

Keywords

Karst aquifer • Spring discharge • Climate change • Human activity • Karst in China

Introduction

Approximately 3.44 million km^2 of carbonate rock exists in China, and occupies one-third of China's territory (Zhang 1980; Li 1985). The karst in China is predominately formed

Y. Hao (✉)
Tianjin Key Lab of Water Resources and Water Environment, Tianjin Normal University, 393 Binshuixidao Road, Xiqing District, Tianjin, 300387, China
e-mail: haoyh@sxu.edu.cn

J. Zhang
Institute of Groundwater and Earth Science, Jinan University, 601 West Huangpu Road, Guangzhou, 510632, China

Y. Guo
School of Geographical and Environmental Science, Tianjin Normal University, 393 Binshuixidao Road, Xiqing District, Tianjin, 300387, China

C. Bertrand et al. (eds.), *Eurokarst 2018, Besançon*, Advances in Karst Science,
https://doi.org/10.1007/978-3-030-14015-1_19

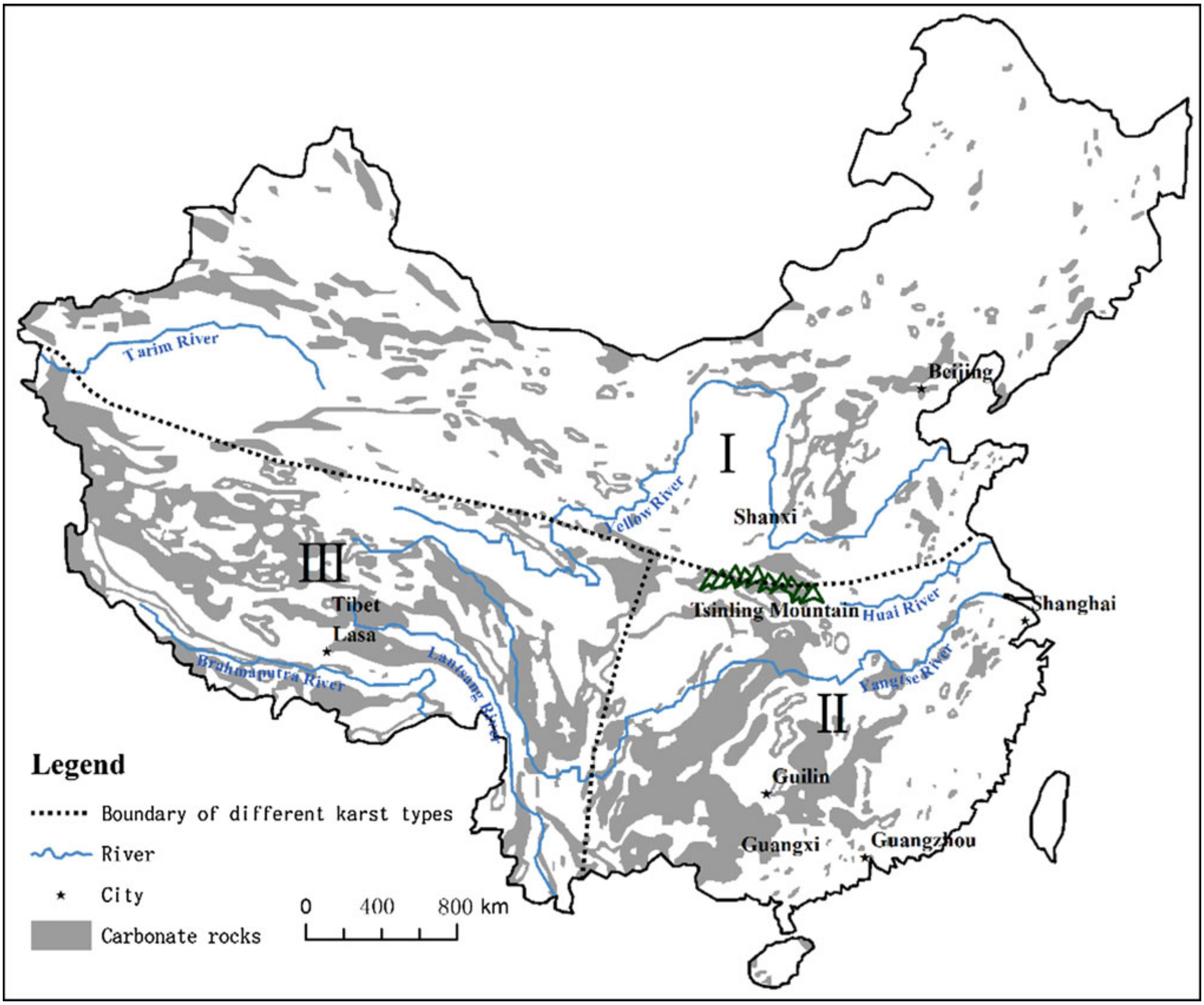

Fig. 1 The distribution of carbonate rocks and karstic classification in China (after Li 1985)

in carbonate rocks (Fig. 1). The groundwater in karst aquifer occupies 23% of all groundwater resources in China and has been an important resource for drinking water, agriculture irrigation, industrial, and municipal uses (He et al. 1997). During the most recent four decades, storage of karst groundwater has decreased in response to anthropogenic activity and climate change, and is evident in the drying up of karst springs, and the decline in groundwater levels (Guo et al. 2005; Liang et al. 2008). Many researchers have published papers on groundwater models of karst hydrology (e.g., Charlier et al. 2015; Hao et al. 2013; Fiorillo et al. 2015), but most authors focus mainly on the mathematical technique. This paucity of descriptions of karst aquifer characteristics leads to a lack of understanding of karst hydrological processes, because karst features are complicated and heterogeneous. The current paper compares karst in north China with karst in south China, by including information on the lithology of carbonate rocks, paleoenvironment, karst processes, and karst features, and also describes the different problems in northern and southern China. Because the Niangziguan Springs karst system is the representative of most karst systems of northern China (Guo et al. 2005), this paper selected Niangziguan Springs in northern China as a case study, and analyzed karst spring discharge using statistical methods including piecewise analysis, Wilcoxon rank-sum test, and wavelet coherence. Different from previous studies on karst hydrological research in north China only focused on specific issues of a karst spring (Hao et al. 2016; Miao et al. 2014; Zhang et al. 2017), this paper intends to provide full profiles of karst in China and concentrate on the difference of karst between north and south China, and subsequently investigate the effects of climate and human activity on spring discharge decline in the north.

Characteristics of Karst Aquifer Between North and South China and Their Problems

In north China, carbonate rock deposition began in the Mesoproterozoic Era (1600–1000 Ma), and ended in the Mid-Ordovician (466 Ma). While in south China, carbonate rock deposition began in the Sinian Sub-Era (825–570 Ma), and ended in the Triassic (250–200 Ma). In Qinghai-Tibetan Plateau, carbonate rock was deposited in the Late Permian (257–250 Ma). Yuan et al. (1995) classified karst in China as three categories: Karst Zone I is an arid and semiarid karst area in north China; Karst Zone II is a subtropical humid karst area in south China; and Karst Zone III is located on the Qinghai-Tibetan Plateau (Fig. 1). This paper focuses mainly on the Karst Zones I and II.

The differences of karst feature between south and north China are ascribed to internal and external causes (Hao et al. 2012). The internal cause is the lithology. At the microscopic level, the lithology of carbonate rocks is conspicuously different between north and south China (Han 1998). In the north, the carbonate rocks are micritic, which formed under conditions of continuous flow in a calm environment. The rocks are more argillaceous and dense, with low primary permeability, which can prevent the easy passage of groundwater, except in small fissures, which make dissolution or erosion difficult (Sweeting 1995; Zhang 2004). In contrast, the carbonate rocks in the south are thick and sparry, and were deposited in a more active environment of waves and tides, and their structures are easier to denude or erode compared with the micritic limestones in north China (Han 1998).

The external cause is paleoenvironmental change. The early karstification in the north occurred from the Middle Ordovician to Early Carboniferous (Zhang et al. 1981). The paleoclimate changed between the Ordovician to Early Jurassic, from warm and humid to cold and arid, which decelerated the karstification in the North China Plate (Gu 1995). The modern karstification in the north and south happened between the Tertiary (53–2.6 Ma) and the Quaternary. The first important event that affected karstification is the uplift of the east–west trending Tsinling Mountains in central China toward the end of the Middle Jurassic, which effectively separated the northern and southern ancient climate: arid and semiarid karst in the north and subtropical humid karst in the south. The second event is the uplift of the Tibetan Plateau in the Tertiary and Quaternary, which effectively blocked the incoming vapor from the southwest ocean, and changed the planetary wind system to create the monsoon system in China. The north region became drier and colder, while the south became warmer and more humid, which means interaction between water and rocks occurred less frequently in the north than in the south. Moreover, loess was deposited in the north, which partly delayed or prevented karstification in the region. Thus the karst process in north China mainly occurred in the subsurface (i.e., hypogene), which prevented carbonate rocks in the north from eroding. While in south China, the processes were epigene in the Quaternary.

Owing to the internal and external causes, the structural and tectonic settings of karst formations between the north and south are totally different. In the north the karst formation is dominated by fissures, fractures, and conduits (i.e., caves and subsurface rivers are not typically present). In contrast, the karst formations in the south are characterized by well-developed caves and highly connected underground flow channels and subsurface rivers (Yuan 1994).

Consequently, the karst aquifers are totally different between the north and south. The hydrologic characteristics of the aquifers in north China include pores, fractures, and conduits, while the aquifers in south China are mainly comprised of sinkholes, caves, and channels. The ratios of maximum to minimum spring flow in the north are generally from 1.24 to 5.89, whereas the ratios are from 10 to 1000 in the south (He et al. 1997). These ratios indicate that response of spring discharge to precipitation in the north is slower, and groundwater residence time is longer (i.e., several years) than in the south (i.e., several hours). The springs in the north are considered “slow-response” according to the classification of karst springs by White (1988).

The different karst features mean that the environmental challenges are also different between the north and south. A desperate shortage of water resources exists in the north, where groundwater from the karst aquifers has been an important water resource for local residents. Because of the obvious declining trends of spring discharge, the research on karst aquifers in the north was mainly focused on the effects of climate change and human activity on spring discharge (Hao et al. 2013). In contrast, the outstanding problem in the south is karst rocky desertification (KRD), a process in which soil is eroded substantially or even thoroughly, so that bedrock exposure is widespread, the carrying capacity of land to support humans is drastically decreased, and the landscape appears similar to a desert under violent human impacts (Yuan 1993). The studies of karst groundwater systems in south China focused primarily on environmental problems (Cai 1997).

Analysis of the Variations of the Niangziguan Springs Discharge

Geological and Hydrogeological Context of the Niangziguan Springs Basin

The Niangziguan Springs complex, the largest karst springs in northern China, is located in the Mian River Valley, Eastern Shanxi Province, China (Fig. 2). Niangziguan Springs are distributed along 7 km of the Mian riverbank with an annual average discharge of 9.68 m^3/s based on records from 1957 to 2015.

The main strata in the Niangziguan Springs basin from the top to bottom are Quaternary loss deposits and sandstone, Permian arenaceous shale, Carboniferous mud stone, sandstone and limestone with coal seams, Ordovician carbonate rocks, and Cambrian dolomite (Fig. 3). The main aquifers of the basin are comprised of Ordovician karstic limestone and Quaternary sandstone and porous sediments. The limestone and Quaternary sediment aquifers are hydraulically connected. The groundwater in karst aquifers (i.e., Ordovician carbonate rocks) flows toward the Mian River valley in the east, where groundwater perches on low-permeable strata of Cambrian dolomicrite, and eventually intersects the ground surface, thus creating the Niangziguan Springs (Figs. 2 and 3).

Rough hilly terrain with small basins and gentle sloping river valleys are the primary physiographic features of the Niangziguan Springs basin, where the elevation ranges from 362 to 2149 m above mean sea level (MSL). The western part of the basin is higher than the eastern part, with the general topography of the basin inclining to the east. The Mian River

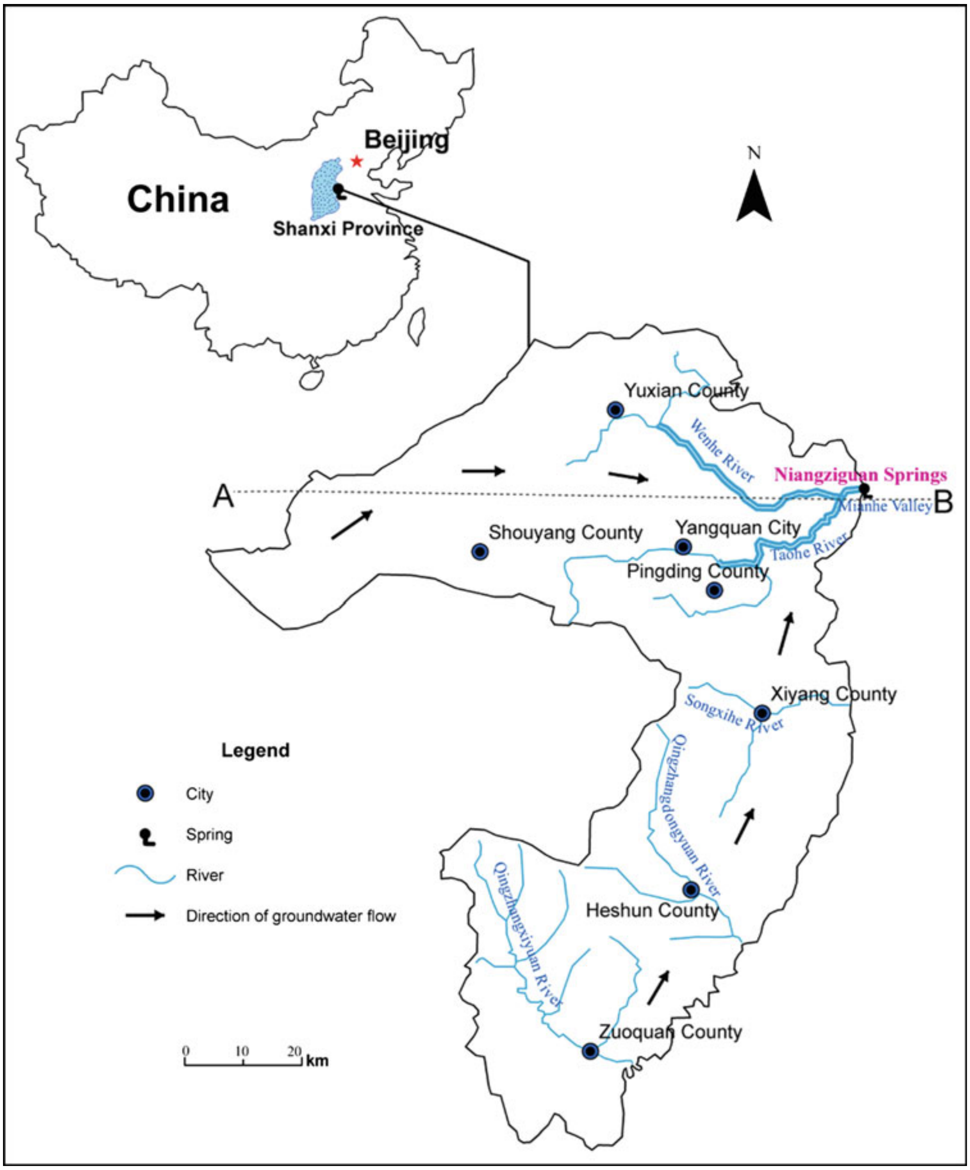

Fig. 2 Geographical map of the Niangziguan Springs basin

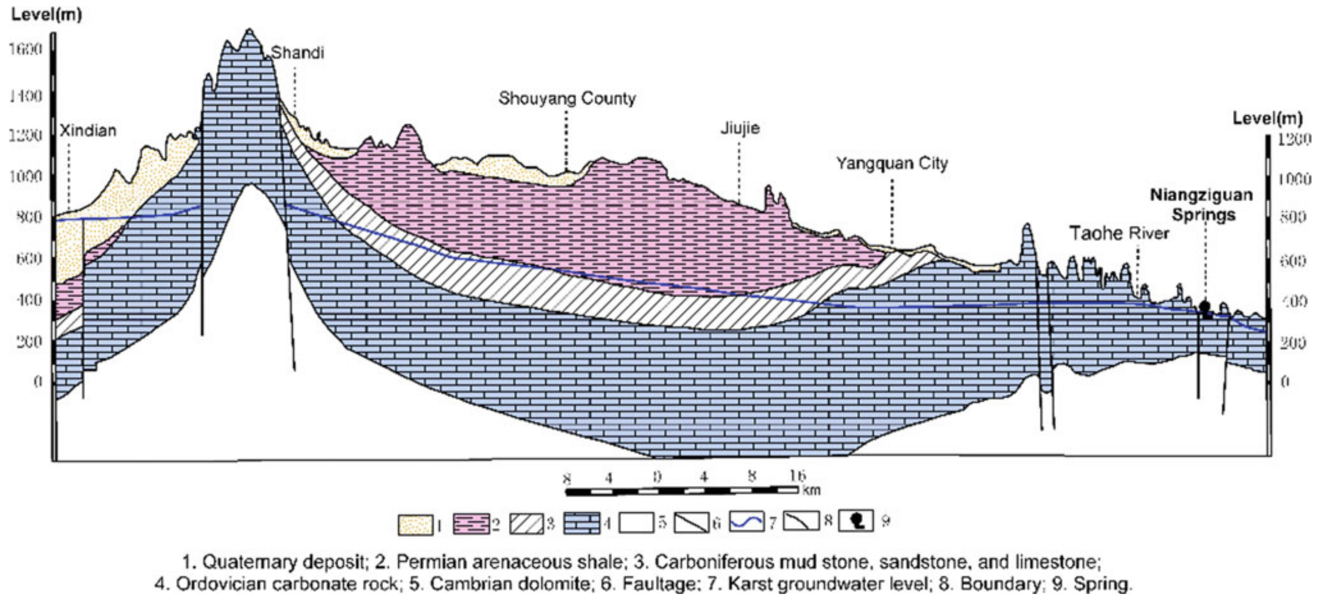

Fig. 3 Geological cross-section of A–B in Fig. 2

Valley, where the Niangziguan Springs discharges, has the lowest elevation in the Niangziguan Springs basin, ranging from 360 to 392 m above MSL (Figs. 2 and 3).

Niangziguan Springs receive water from a 7394 km^2 catchment that includes the city of Yangquan, and the counties of Pingding, Heshun, Zuoquan, Xiyang, Yuxian, and Shouyang (Fig. 2). The recharge to the aquifer in the Niangziguan Springs basin comes from precipitation (Han et al. 1993). The annual average precipitation is 490.5 mm based on the record from 1957 to 2015. Affected by Asian monsoon, about 60–70% of the annual precipitation occurs in July, August, and September.

Data Acquisition

Monthly spring discharge data of Niangziguan Springs from June 1959 to December 2015 were collected from the Niangziguan gauge station in the Mian River (Fig. 4). The observed monthly precipitation time series were obtained at seven meteorological stations (Yangquan City, and County of Pingding, Yuxian, Shouyang, Xiyang, Heshun and Zuoquan) in the Niangziguan Springs basin, spanning a time period from January 1959 to December 2015. Then the monthly precipitation of the Niangziguan Springs basin (Fig. 4) was determined using Thiessen Polygons. Monthly temperature data from January 1959 to December 2015 were collected from meteorological stations of Yangquan City.

Methods

Piecewise Analysis

The piecewise analysis is a statistical method which is based on finding one or more random thresholds to divide a continuously random sampled series into two or more time periods to identify the dominating influencing factors by comparing the statistical parameters of those different time periods (Quandt 1958; Hudson 1966; Ramos 2005). Opening up and economic reforming (around 1978) is the change point for economic development of China accompanying with extensive water resources development. Consequently, the variations of karst spring discharge were caused by climate variation only (the pre-development period), and by both climate variation and human activity (the post-development period). In this paper, the time series of precipitation and spring discharge were segmented into two time periods depending on whether variations were caused by climate variation only (the pre-development period), or by both climate variation and human activity (the post-development period). After that, the hydrometeorological processes of the two periods were analyzed by wavelet coherence. By comparing the results between the pre-development and the post-development periods, one can acquire the effects of human activities on spring discharge.

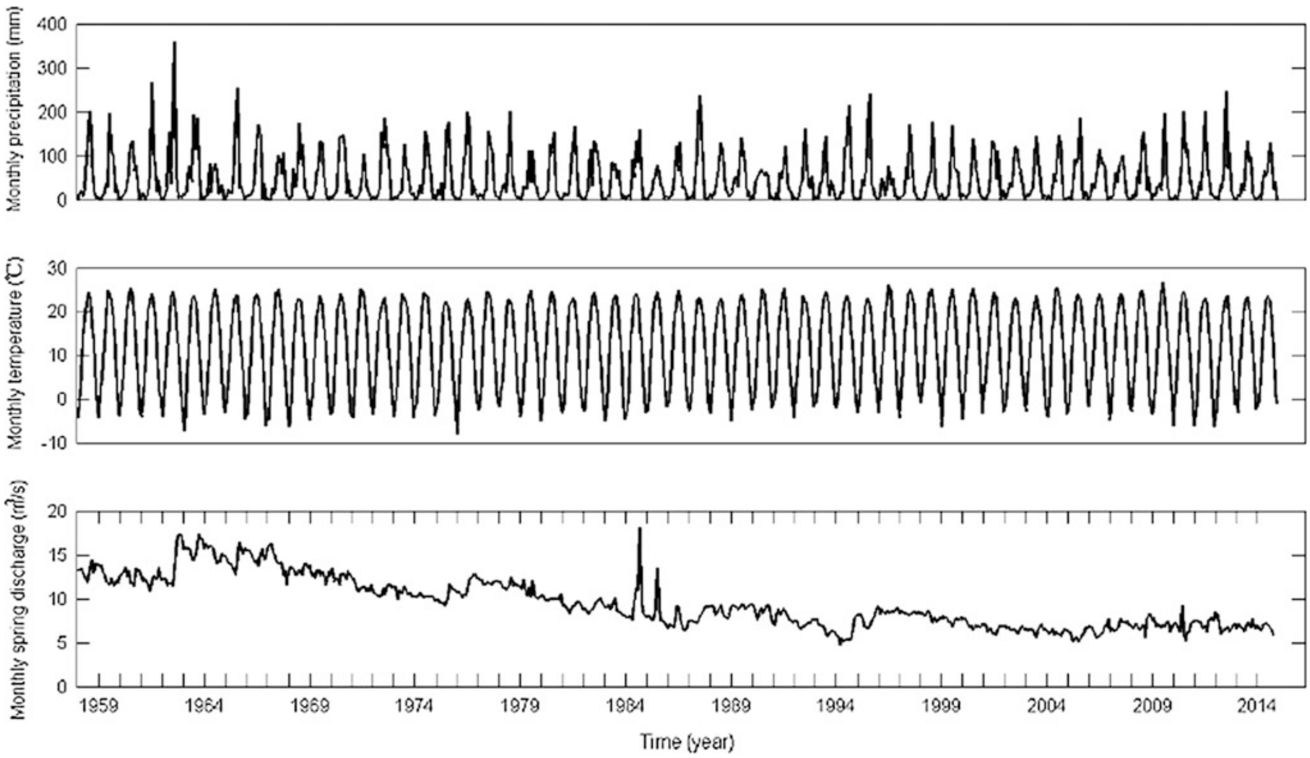

Fig. 4 Monthly precipitation, temperature and spring discharge in the Niangziguan Springs basin

Wilcoxon Rank-Sum Test

The Wilcoxon rank-sum test is a nonparametric test capable of determining whether a statistically significant discrepancy exists between two sample series, and if so, the extent and significance of the difference. The observations are ordered from smallest to largest after the two sample series are combined, and their ranks are given. The rank-sums of the observations in two samples are calculated, respectively. We calculate significant levels between the two sample series using the hypothesis test. If the p value is less than 0.05, the test is passed. We assume that a significant discrepancy between the two sample series exists (Asmita and Dhyan 2014). The Wilcoxon rank-sum test is based solely on the order of the observed values from the two samples (Wilcoxon 1945; Helsel and Hirsch 2002). Unlike the t test, it does not need to assume the normal distribution of data. It is nearly as efficient as the t test on normal distributions.

Wavelet Analysis

The continues wavelet transform of a time series $x_n, n = 1, \ldots, N$ is defined as the convolution of $x_n, n = 1, \ldots, N$ with scaled and translated version of a so-called mother wavelet $\psi_0(t)$:

$$\sum_{a}^{b} W_n^X(a) = \sqrt{\frac{\Delta t}{a}} \sum_{n'=1}^{N} x_{n'} \psi_0^* \left[\frac{(n'-n)\Delta t}{a}\right] \tag{1}$$

where ψ_0^* enotes the complex conjugate, the parameters a and n can, respectively, be interpreted as a scale expansion factor and a time shift factor to adjust the scale and location of the wavelet in the time-frequency domain. Δt is the time step of the series (Torrence and Compo 1998).

Because the wavelet function in this study (i.e., Morlet wavelet) is a complex exponential function, so the wavelet transform $W_n^X(a)$ is also complex, and can also be

$$W_n^X(a) = \left|W_n^X(a)\right| e^{i \tan^{-1}\left[I\left\{W_n^X(a)\right\}/R\left\{W_n^X(a)\right\}\right]} \tag{2}$$

where $\left|W_n^X(a)\right|$ is the amplitude, and $\tan^{-1}\left[I\left\{W_n^X(a)\right\}/R\left\{W_n^Y(a)\right\}\right]$ is the phase (Torrence and Compo 1998).

The cross-wavelet transform of the two series x_n and y_n can be defined as:

$$W_n^{XY}(a) = W_n^X(a) W_n^{Y*}(a) \tag{3}$$

$\left|W_n^{XY}(a)\right|$ is the cross-wavelet power spectrum and it reveals the cross-covariance between the two time series (Torrence and Compo 1998).

Torrence and Compo (1998) defined the wavelet coherence between time series x_n and y_n as:

$$R_n^2(a) = \frac{\left|S\left(a^{-1}W_n^{XY}(a)\right)\right|^2}{S\left(a^{-1}\left|W_n^X(a)\right|^2\right)\cdot S\left(a^{-1}\left|W_n^Y(a)\right|^2\right)} \quad (4)$$

where S is a smoothing operator and can be defined as $S(W) = S_{\text{scale}}(S_{\text{time}}(W_n(a)))$, S_{scale} and S_{time} denote smoothing the wavelet transform along the scale axis and in time, respectively (Grinsted et al. 2004).

The global coherence coefficient intuitively expresses the wavelet coherence coefficient distribution of two series at different scales. The global coherence can be written as:

$$\overline{R}^2(a) = \frac{1}{N}\sum_{n=1}^{N} R_n^2(a) \quad (5)$$

where N is the length of the time series (Torrence and Compo 1998).

Results and Discussion

The Spring Discharge Segment and Significant Test

The Niangziguan Springs basin had been an undeveloped region in China before 1980. Along with rapid economic development in the last four decades, the Niangziguan Springs basin has become one of the industrialized hubs in China for coal mining, power generation and metallurgy. Accordingly, population and Gross Domestic Product (GDP) of the Niangziguan Springs basin have increased considerably (Fig. 5). Rapid economic developments in the region consume huge amounts of water resources. Before 1980, local residents at the Niangziguan Springs basin mainly used surface water for their water supply, but the rapid economic development after 1980 mainly depended on groundwater.

Based on the piecewise analysis principle, the data of the Niangziguan Springs discharge can be divided into two groups: a pre-development period from 1959 to 1980 during which groundwater was impacted primarily by the climatic variation, with negligible anthropogenic impacts; and a post-development period from 1981 to 2015 during which groundwater was impacted by both climatic variation and human activity. Then the reasonability of the spring discharge segment at 1980 was tested by using the Wilcoxon rank-sum test. The p value for the annual average spring discharge was 2.2E−16, which is much less than 0.05, meaning that the distributions of the spring discharge of the pre-development and the post-development periods were significantly different. In other words, the segment of the spring discharge at 1980 was reasonable.

Estimation of the Spring Discharge Decline Caused by Human Activity

In the Niangziguan Springs basin, the annual average precipitation was 531 mm in the pre-development period, and

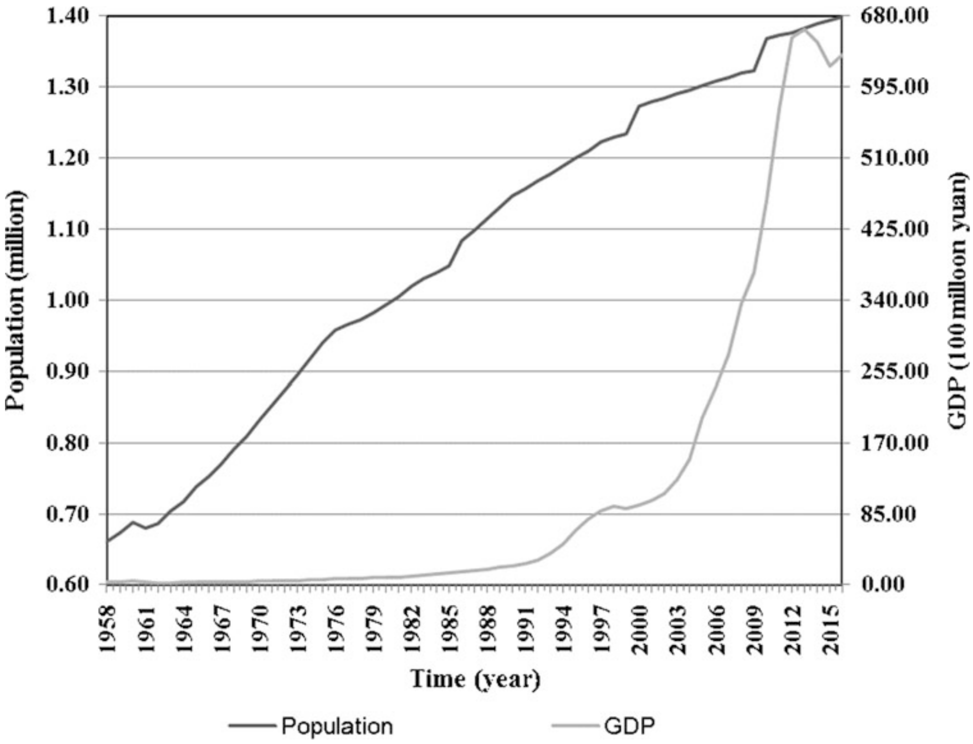

Fig. 5 Population and gross domestic product (GDP) in the Niangziguan Springs basin

462 mm in the post-development period, showing a 13% decrease in precipitation. Similarly, and the annual average temperature was 10.9 °C in the pre-development period, and 11.4 °C in the post-development period, with a 4.59% increase for temperature. The annual mean spring discharges in the pre- and the post-development periods were 12.61 and 7.67 m^3/s, respectively, showing about 39% decline. Compared to the precipitation, the spring discharge has a 26% greater reduction on average between the periods. This fact indicates that the spring discharge attenuated about 26% owing to the effects of human activity in the Niangziguan Springs basin.

Since 1980, the development and utilization of karst water in the Niangziguan Springs basin have increased rapidly (Liang et al. 2005; Guo et al. 2005) and have caused the decline of the Niangziguan Springs discharge. The increase can be attributed to four main kinds of human activities. The primary human activity pertains to dewatering for coal mining in the region. The impact of dewatering from coal mines on the decline of the spring discharge was 1.02 m^3/s (Sun 2006). The second human activities were anti-seepage channels and dam construction. Anti-seepage channels prevented surface water from infiltrating to the subsurface, and dams stored a large amount of water from the catchment, reduced the river flow, and decreased the groundwater recharge in the bare karst valley. The karst water recharge declined 0.84 m^3/s because of the anti-seepage channels and dams (Zhang et al. 2014). The third human activity was karst groundwater exploitation which caused spring discharge to decline by 0.46 m^3/s (Liang et al. 2005). The fourth human activity was groundwater exploitation of the upper unconsolidated sediment aquifers, which caused spring discharge to decline by 0.06 m^3/s (Liang et al. 2005). These previous studies reemphasized that compared with climate variation, human activity played a major role in spring discharge decline.

The Effects of Human Activity on Periodicities of the Discharge of Niangziguan Springs

In nature, the rhythm of spring discharge is controlled by regional hydrometeorological condition through recharging, converging, and discharging processes. With extensive groundwater development, the natural balances of karst hydrological processes were undermined by human. To better understand whether human activity alters the periodicities of the discharge of Niangziguan Springs, the periodicities of the spring discharge in both the pre- and the post-development periods were analyzed, and wavelet coherence plots are shown in Figs. 6 and 7, respectively. Wavelet coherence in the time–frequency domain was represented by colors ranging from blue to red, with the small coefficient in blue, and the larger coefficients trending to red. Shadow parts delineate cone of influence (COI), because of edge effects (Torrence and Compo 1998). To eliminate the edge effects, the results outside COI only were considered. The values that passed the test of a 5% significance level were encircled by black lines. In addition, in order to highlight the changes of the correlation between the spring discharge and precipitation small scale, the vertical axis of wavelet coherence is logarithmic, and the horizontal axis is linear equidistant.

Intermittent power can be detected at scales of 0.25, 0.5, 1, 2, and 5 years for the wavelet coherence between the spring discharge and the precipitation in the

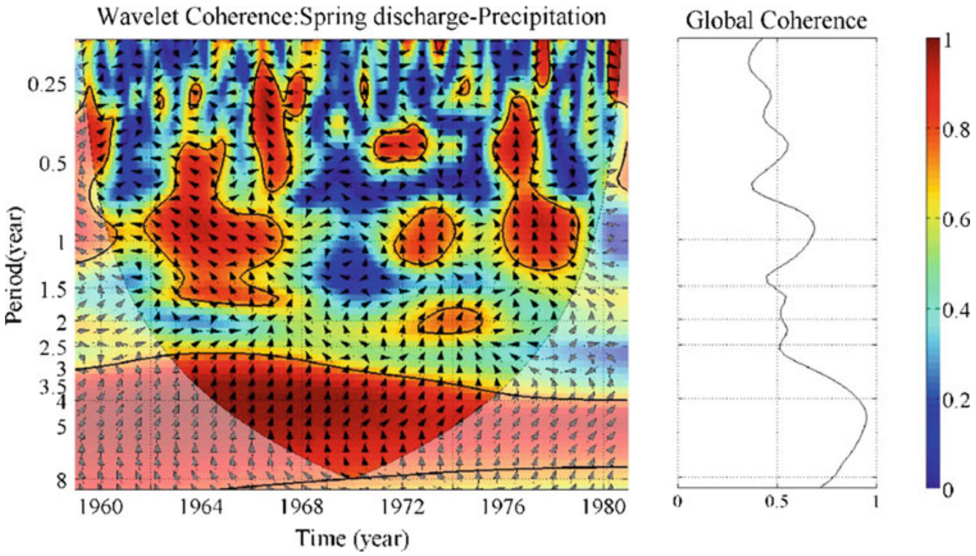

Fig. 6 Wavelet coherence and global coherence between the spring discharge and precipitation in pre-development period

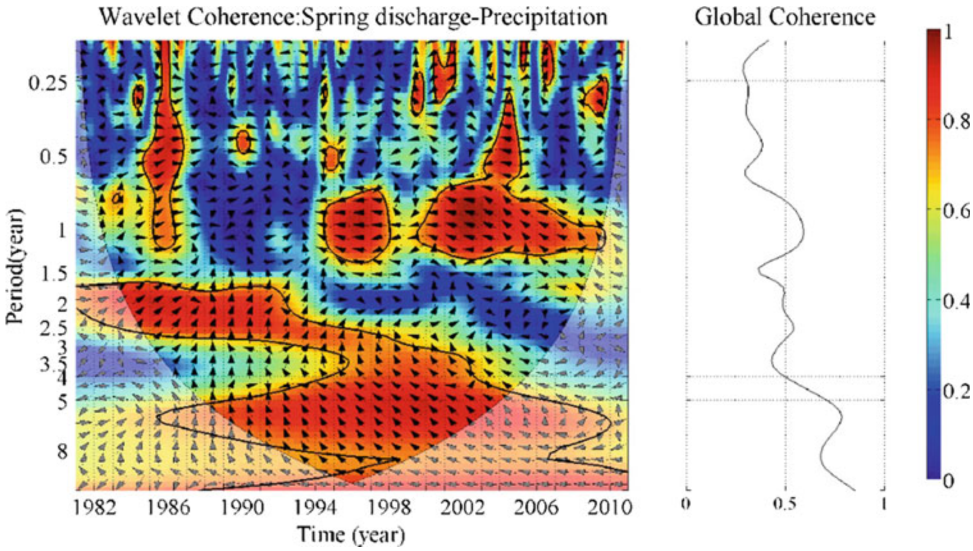

Fig. 7 Wavelet coherence and global coherence between the spring discharge and precipitation in post-development period

Table 1 Global coherence coefficients between the spring discharge and precipitation

Periodicity (year)	0.25	0.5	1	2	5
Pre-development period	0.45	0.55	0.68	0.47	0.95
Post-development period	0.38	0.42	0.59	0.49	0.78

pre-development period (Fig. 6). Similarly, the intermittent regions exhibited at the timescales of 0.25, 0.5, 1, 2, and 5 years for the wavelet coherence between the spring discharge and the precipitation in the post-development period (Fig. 7). The results indicate that the resonant periodicities of spring discharge with precipitation have not changed significantly between pre-development and post-development periods.

Simultaneously, the corresponding global coherence coefficients between the spring discharge and precipitation the two periods are listed in Table 1. The peaks of the global coefficient in the pre-development period are 0.45, 0.55, 0.68, 0.57 and 0.95 at timescales of 0.25 year, 0.5 year, 1 year, 2 year, and 5 year, respectively. Similarly, the peaks of the global coefficient in the post-development period are 0.38, 0.42, 0.59, 0.49 and 0.78 at timescales of 0.25 year, 0.5 year, 1 year, 2 year, and 5 year, respectively. The results show that the global coherence coefficients in post-development period are smaller than that in pre-development period. The results indicate that groundwater development has weakened the linear relation between spring discharge and precipitation.

The facts suggest human activity has not altered that resonant periodicities between the spring discharge and precipitation, although it has weakened the relation between spring discharge and precipitation. It appears that human activity has adapted to climate rhythms and has become consistent with climate variations.

Conclusion

The lithology of carbonate rocks in north and south China is different owing to different depositional paleoenvironments during different geologic time periods. The lithology of carbonate rocks deposited between the Mesoproterozoic Era and the Mid-Ordovician in north China are micritic, which are difficult to erode, compared with the sparry limestones in south China, which were deposited from the Sinian Sub-Era to the Triassic. Early karstification in northern China occurred from the Middle Ordovician to Early Carboniferous, but the paleoclimate became cold and arid between the Ordovician to Early Jurassic, which decelerated the karstification processes. The modern karstification in China happened between the Tertiary and the Quaternary. The uplift of the east–west trending Tsinling Mountains in central China toward the end of the Middle Jurassic caused the paleoclimate to become dry and cold in the north. Meanwhile, loess deposits partly prevented karstification in north China. Consequently, in north China, the karstification is undeveloped, and the major karst features are pores, fractures, and conduits. In contrast, the karstification of carbonate rocks in south China occurred in a wet, warm environment with exposed limestone outcrops. Accordingly, in the south, karstification is well developed, and the karst features are large basin with hills in regional scale, and sinkholes, caves, and tunnels in local scale. The karst aquifer in the north is characterized by fractures and conduits. One of the prominent characteristics of karst hydrological system in the north is that the groundwater in karst aquifers converges in topographical depressions, and creates large karst springs. The variations of karst spring discharge could reflect the dynamic feature of the regional groundwater system.

Since the 1980s, spring discharge in north China has declined largely because of the effects of human activity accompanying the opening up and economic reform in China. The data of the Niangziguan Springs discharge can be divided into two groups: a pre-development period from 1957 to 1980, and a post-development period from 1981 to 2015. The annual average precipitation was 531 mm in the pre-development period, and 462 mm in the post-development, showing a 13% decrease in precipitation. The annual mean spring discharges in the pre- and the post-development periods were 12.54 and 7.67 m^3/s, respectively, showing a 39% decline. Compared to the precipitation, the spring discharge has a 26% greater reduction on average between the periods. This fact indicates that the spring discharge was attenuated by almost 26% owing to the effects of human activity in the Niangziguan Springs basin.

Although intensive groundwater development has largely decreased the magnitude of spring discharge, the resonant periodicities of spring discharge with precipitation have not changed significantly between pre-development and post-development periods. In other words, human activity has not altered the resonant periodicity between spring discharge and precipitation. It is likely that human activity has adapted to climate rhythms and has become consistent with climate variation.

Acknowledgements This work is partially supported by the National Natural Science Foundation of China 41272245, 40972165, and 40572150, and Natural Science Foundation of Tianjin, China (18JCZDJC39500). The authors sincerely thank three anonymous reviewers for their detailed and constructive comments to improve this manuscript.

References

Asmita RM, Dhyan SA (2014) Trend and periodicity analysis in rainfall pattern of Nira Basin, Central India. American Journal of Climate Change 3(1): 60–70

Cai Y (1997) Ecological and socio-economic rehabilitation in the karst of the southwest China. The Journal of Chinese Geography 7: 24–32 (in Chinese)

Charlier J, Ladouche B, Maréchal J (2015) Identifying the impact of climate and anthropic pressures on karst aquifers using wavelet analysis. Journal of Hydrology 523: 610–623

Fiorillo F, Petitta M, Preziosi E, Rusi S, Esposito L, Tallini, M (2015) Long-term trend and fluctuations of karst spring discharge in a Mediterranean area (central-southern Italy). Environmental Earth Science 74(1):153–172

Grinsted A, Moore JC, Jevrejeva S (2004) Application of the cross wavelet transform and wavelet coherence to geophysical time series. Nonlinear Process Geophysics 11 (5/6):561–566

Gu H (1995) The Carboniferous to Jurassic bauxite deposits are symbols of paleoclimate and palaeogeography. Light Metals 6: 1–5 (in Chinese)

Guo Q, Wang Y, Ma T, Li L (2005) Variation of karst springs discharge in recent five decades as an indicator of global climate change: a case study at Shanxi, northern China. Science in China Series D: Earth Science 48: 2001–2010

Han B (1998) Study of microkarstification mechanism. Geological Publication House, Beijing, pp. 26–30 (in Chinese)

Han X, Lu R, Li Q (1993) Karst Water Systems: A Study on Big Karst Spring in Shanxi. Geological Publishing House: Beijing (in Chinese)

Hao Y, Cao B, Zhang P, Wang Q, Li Z, Yeh T (2012) Differences in karst processes between northern and southern China. Carbonates and Evaporites 27: 331–342, doi:101007/s13146-012-0116-3

Hao Y, Cao B, Chen X, Yin J, Sun R, Yeh T (2013) A piecewise grey system model for study the effects of anthropogenic activities on karst hydrological processes. Water Resources Management 27(5): 1207–1220

Hao Y, Zhang J, Wang J, Li R, Hao P, Zhan H (2016) How does the anthropogenic activity affect the spring discharge? Journal of Hydrology 540: 1053–1065

He Y, Han B, Xue C, He Y (1997) Study of karstic water in China. Tongji University Press, Shanghai (in Chinese)

Helsel DR, Hirsch RM (2002) Studies in Environmental Science 49: Statistical Methods in Water Resources. Elsevier Science Publisher Company INC: New York

Hudson DJ (1966) Fitting segmented curves whose join points have to be estimated. Journal of American Statistical Association 61: 1097–1129

Li D (1985) Explanation of the map of soluble rock type in China. Cartographic Publication House, Beijing, pp 29–35 (in Chinese)

Liang Y, Gao H, Zhang J, Huo J, Wang T (2005) Preliminary quantitative analysis on the causes of discharge attenuation in Niangziguan spring. Carsologica Sinica 24(3): 227–231 (in Chinese)

Liang Y, Han X, Xue F (2008) Water resources conservation for karst spring basin of Shanxi Province. China Water and Power Press: Beijing (in Chinese)

Miao J, Liu G, Cao B, Hao Y, Chen Yeh TJ (2014) Identification of strong karst groundwater runoff belt by cross wavelet transform. Water Resources Management 28: 2903–2916

Quandt RE (1958) The estimation of the parameter of a linear regression system obeying two separate regimes. Journal of American Statistical Association 53:873–880

Ramos JI (2005) A piecewise-analytical method for singularly perturbed parabolic problems. Applied Mathematics Computation 161:501–512

Sun Z (2006) The mechanism of Niangziguan Springs decline and conservation measures. Shanxi Water Resources 22(1): 16–17 (in Chinese)

Sweeting MM (1995) Karst in China, its geomorphology and environment. Springer Inc., New York

Torrence C, Compo GP (1998) A practical guide to wavelet analysis. Bulletin of the American Meteorological Society 79 (1):61–78

White W (1988) Geomorphology and hydrology of karst terrain. Oxford University Press, New York

Wilcoxon F (1945) Individual comparisons by ranking methods. Biometrics Bulletin 1(6): 80–83. https://doi.org/10.2307/3001968

Yuan D (1993) The karst study of China. Geology Press, Beijing (in Chinese)

Yuan D (1994) Karstology of China. Beijing: Geological Publishing House; (in Chinese)

Yuan D, Li B, Liu Z (1995) Karst in China. Episodes 18 (1–2): 62–65

Zhang H, Guo Y, Miu P, Sun K (2014) Analysis on the status of water ecological investigation in Niangziguan spring area and the cause of spring discharge attenuation. China Environmental Science Society academic essays (in Chinese)

Zhang J (2004) Variation of mechanical property of marlite in process of karstification and weathering in three gorges region. Chinese Journal of Rock Mechanics and Engineering 23: 1073–1077 (in Chinese)

Zhang J, Hao Y, Hu BX, Huo X, Hao P, Liu Z (2017) The effects of monsoons and climate teleconnections on the Niangziguan Karst Spring discharge in North China. Climate Dynamics 48(1): 53–70

Zhang K, Luo Z, Zhang Q, Yao H (1981) The evolution of continent plate of China and the basin rich in petroleum and gas. Petroleum Exploration and Development 1:13–25 (in Chinese)

Zhang Z (1980) Karst types in China. GeoJournal 4(6): 541–570

Point Dilution Tracer Test to Assess Slow Groundwater Flow in an Auxiliary Karst System (Lake of Fontaine de Rivîre, Belgium)

Philippe Meus, Jérémy Flament, Luc Willems, Luc Funcken,
Gauthier Roba, Claire A. Chauveau, Jean Godissart, and Camille Ek

Abstract

The quantification of mass transfer through auxiliary karst systems is addressed by using a specific point dilution long-term tracer test. The physical functioning of such systems is usually only inferred by hydrodynamical and environmental tracer data, whose interpretation often relies on invalidated assumptions. The new approach is a way for experimentally validating or complementing the classical approaches. The lake of Fontaine de Rivîre is an auxiliary karst system in the Frasnian limestones of the Ourthe Valley in Belgium. Its particular confinement was studied by conjunctional use of natural responses and single-point dilution tracer test, with an injection of 41 g of uranine on 22 March 2017. The tracer test was monitored during one year using fluorometers, water and charcoal samplings at five points in the lake and six points at the surface (no connection having been established outside). A slow flow (in the order of magnitude of 1 m/h) of the lake could be observed and some mixing processes identified. The dilution of the tracer along the year indicates an average discharge of only 0.16 l/s. This low discharge is compatible with the high confinement of the lake also proved by its high homogeneity and stability (temperature and conductivity). However, the level fluctuations are apparently not compatible with this renewal, and especially with the low rate of dilution of the tracer observed during winter in the lake. This can thus be explained by pressure transfers from the surroundings, without necessarily high fluxes of water. The delays for the responses have also been quantified by cross-correlations for the whole period of monitoring from 2007 to 2018.

Keywords

Dilution test • Uranine • Active charcoal • Natural tracer • Karst flow • Climate

Introduction

Since the early steps of hydrogeology, the question of the groundwater origin has always been generating a lot of controversies. At the beginning of the twentieth century, after recognizing the precipitations as the origin, the main question was changed to how water flows, and is stored, into the soil and subsoil, and on the role that fissures, especially those enlarged into karstic conduits, can play for these flows, from the infiltration processes unto the emergence of groundwater in the springs (Martel 1921). Several decades later, the duality of diffuse and conduit flow became the main topic of research for karst aquifers (Mangin 1975; Müller 1981;

P. Meus (✉)
European Water Tracing Services, Nandrin, and Club de Recherches Spéléologiques Ourthe Amblève, Sprimont, Belgium
e-mail: ewts@skynet.be

J. Flament
Institut Scientifique de Service Public, Liège, and Club de Recherches Spéléologiques Ourthe Amblève, Sprimont, Belgium
e-mail: j.flament@issep.be

L. Willems · C. Ek
Université de Liège, Liège, and Club de Recherches Spéléologiques Ourthe Amblève, Sprimont, Belgium
e-mail: l.willems@uliege.be

C. Ek
e-mail: camille.ek@uliege.be

L. Funcken
Service Public de Wallonie, Direction de la Géotechnique, Liège, Belgium
e-mail: luc.funcken@spw.wallonie.be

G. Roba · C. A. Chauveau
Club de Recherches Spéléologiques Ourthe Amblève, Sprimont, Belgium
e-mail: robbygees@hotmail.com

C. A. Chauveau
e-mail: claire.a.chauveau@outlook.com

J. Godissart
Union Belge de Spéléologie, Namur, Belgium
e-mail: godissart.jean@gmail.com

C. Bertrand et al. (eds.), *Eurokarst 2018, Besançon*, Advances in Karst Science,
https://doi.org/10.1007/978-3-030-14015-1_20

Worthington 2003), while multiple porosity behaviours were also recognized in many other aquifers. One should say that, and this remains valid today, most of the hydrogeological questions can be reduced to a main question about the relationship between the structure of voids and groundwater flows in between them. So, definitely, the early question of flow was not so trivial. What probably makes the difference nowadays is that an increasing number of methods and innovative instruments have been implemented in hydrogeology, providing data to answer the above question and to allow for better management of groundwater resources (exploitation, protection, remediation, etc.).

Mangin (1994), Jeannin (1996), Bakalowicz (1999) and Kiraly (2003) emphasized the role of a hierarchical structure for karstic flows, and they identified the role of these “somewhat hidden” auxiliary systems (the so-called annex-to-drain systems of the French terminology) in the functioning of karst aquifers.

However, a direct insight into these auxiliary systems seems not so common (or not often recognized as such) and their knowledge is mainly limited by the small panel of experimental techniques than can be implemented inside the systems. Bakalowicz et al. (1994), as well as Marsaud (1996), already attempted high-rate pumping tests in such system with quite good connection with the main karst conduits. Meus (1997) experienced a continuous tracer test in the same system. Dewaide et al. (2017) have used fluorescent dye tracing to assess where the main flow was occurring, and how it was exchanging with low flow water, in large karst conduits. Nevertheless, most of the knowledge about such systems, in most of the carbonate aquifers, is usually coming from indirect measurements using spring hydrographs, natural tracers (temperature, chemistry or isotopes), water levels, where boreholes or caves exist, or any combination of those tracers (Grasso et al. 2003).

In this study, we took advantage of a “windowing” on an underground lake, with undetected connection with any transmissive conduit. Such system could be considered as an extreme auxiliary system, offering the unique opportunity to experiment artificial tracers in conditions where natural tracers only would have normally been used, and to make a comparison between both methods. This artificial tracer test, as such, can thus be considered as a border case for natural tracing.

This long-term tracer test is also quite uncommon since it could only be qualified “from the interior”, according to a single-point dilution method (Novakowski et al. 1995), without any surface breakthrough of the tracer, and thus without any residence time distribution available for the interpretation, as it is usually the case for tracer tests (Guizerix et al. 1990).

The specificity of the dynamics of the lake and its exceptionally weak connectivity to the neighbouring parts of the aquifer helped us a lot in interpreting long-term water level and temperature variations, as well as thermal and CO_2 exchanges with the cave atmosphere.

Several methodologies experimented here revealed themselves promising tools for long-term experimentation, among others the point dilution tracer test method, the video recording of the tracer plume, the passive sampling of uranine with charcoals or its long-term measurement with fluorometers. But, for any of these methods, as for many techniques in hydrogeology indeed, the major concern remains the repeatability (or reproducibility) of long-term measurements. Today in hydrogeology, too much data series are unfortunately not fully comparable, and, however, they are compared.

The importance, for the protection of ecosystems, of the relation between flowpaths of groundwater, residence time and exposure conditions has been largely emphasized by Abbott et al. (2016), who recall that suitable tracers must be applied according to the flow, transport and reactive processes. Karst aquifers are probably the most challenging environment where natural and artificial tracers (Mangin et al. 1976; Gaspar and Oraseanu 1987; Dörfliger 2010) can be calibrated together inside the system itself, thus reducing the uncertainties that are inherent to the single use of natural tracers or to systemic lumped parameters approaches. However, this task is made particularly difficult by the high and often unpredictable heterogeneity of karstic features.

Context

The experimental site is situated along the Ourthe River, 25 km south of Liège, near the city of Hamoir, on the southern flank of the synclinorium of Dinant (Fig. 1a).

The cave of Fontaine de Rivîre (Fig. 1b, c) is a maze cave, about 1.1 km long, mostly structurally controlled by bedding and diaclases, ending by a quite unusual lake with crystalline water which has always been fascinating the generations of cavers. The lake is 50 m long, 25 m wide, with a funnel shape blocks boulder bottom, whose volume has been estimated to 19,400 m^3 (which is also approximately the volume of the air above the lake). The thickness of the limestones below the surface is estimated to be 80 m. The hall of the lake, about 15 m high, is known for its speleothem wall deposits which are correlated to the successive levels of the Ourthe River.

The cave was discovered in 1968 by the CPL (Centre de Prospection Liégeois). It was early closed and more recently, in 1997, it was given the protective status of a CSIS (Cave of Scientific Interest).

It was formed in Frasnian limestones and dolomites of the Lustin formation (Boulvain et al. 1999, Fig. 1a, b), in pseudo-vertical inverse position, striking NE-SW, as the

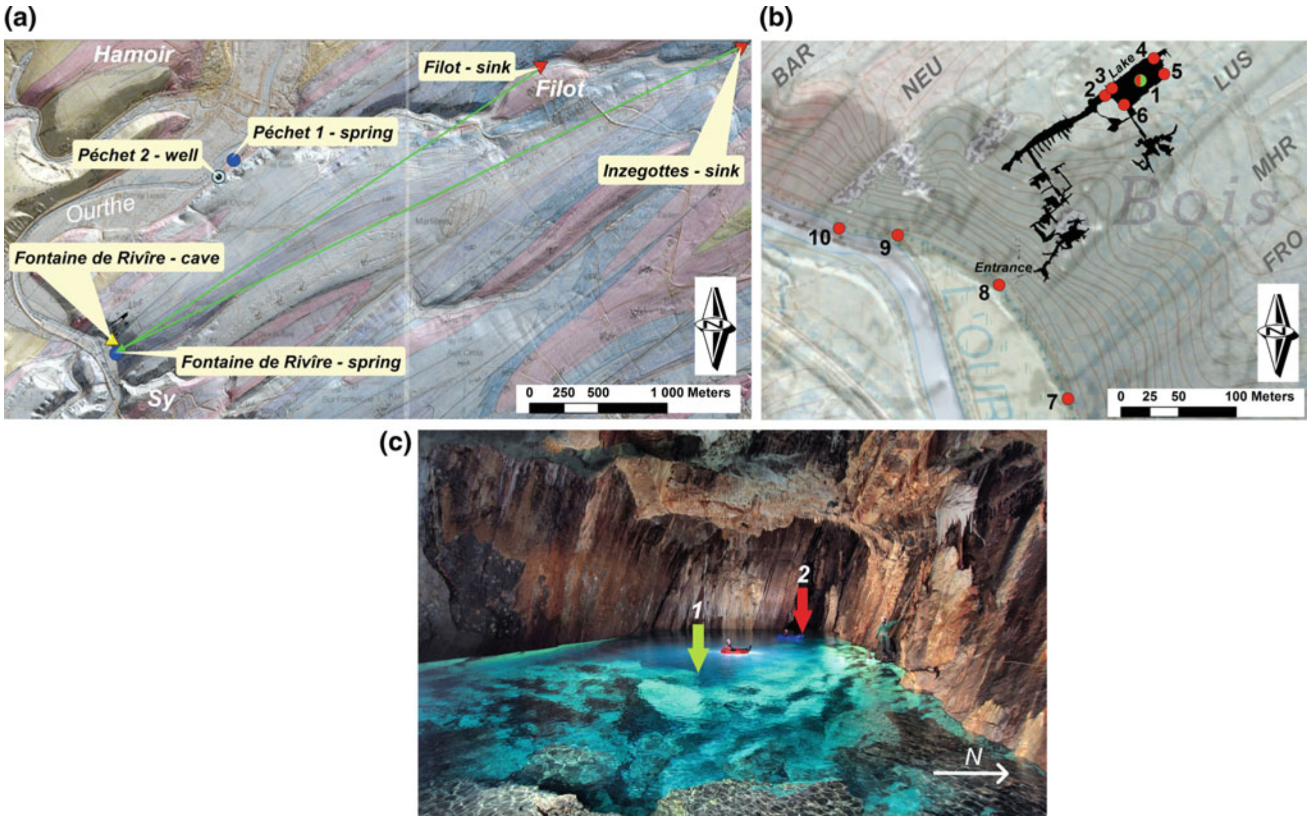

Fig. 1 Situation of the studied area and tracer test. **a** General situation with geological (after Marion and Barchy in press) and Lidar background. The green arrows indicate connections proven by previous tracer tests. **b** Situation of the tracer test in the Fontaine de Rivîre cave. 1: centre of the lake—injection point and fluorometer 1; 2: Vineyards gallery—fluorometer 2; 3 to 6: corners; 7: Fontaine de Rivîre spring; 8: stream; 9: stream at confluence; 10: Ourthe River; BAR: Barvaux formation; NEU: Neuville formation; LUS: Lustin formation; MHR: Mont d'Haurs formation; FRO: Fromelennes formation. The meteorological station of Ouffet is outside of the map (to the North) just a few kilometres from the cave. **c** Lake of Fontaine de Rivîre (photograph P. De Bie). The green arrow indicates the position of the injection point (3 m depth) and the fluorometer 1 (12 m depth). The red arrow is for fluorometer 2 (2 m depth)

general structural trend of the area (Dusar and Gullentops 1989; Marion and Barchy in press). The Lustin formation is limited by a fault bringing the limestones of the Mont d'Haurs and Fromelennes formations (of Givetian age) to the south.

The Fontaine de Rivîre spring flows out of the Fromelennes limestones some 100 m south of the entrance of the cave, with which it is now demonstrated that there is no connection. A shale layer is, however, separating the two systems.

A tracer test was done by Nys in 1929, from the Inzegottes swallow hole. This tracing was repeated in 1968 by the speleological association Centre de Prospection Liégeois. More recently (Meus 2006), in May 2006, both Filot and Inzegottes swallow holes were traced in the frame of a study for the restoration of the waterworks of Péchet 1 and 2 in Hamoir. An exclusive connection between the swallow holes and the Fontaine de Rivîre spring was established in each case, with transit velocities, in high stage of May 2006, of 52 and 73 m/h, respectively. However, no connection was ever found towards the lake in the cave, though the lake was carefully controlled by charcoal detectors.

Godissart (1994) found that the temperature of the atmosphere above the lake was higher than the average of the other Belgian caves, that is to say 11.6 °C instead of 9.2 °C. He found that the stationarity of this temperature could be due to the stationarity of thermal fluxes from the lake itself. The author also assumes some regulation exchanges of CO_2 between the lake and the air above that indicate an important confinement with a saturation of water regarding the calcite equilibrium. This confinement would be in accordance with the lack of a good connection between the lake and the surrounding aquifer.

Godissart also made several altimetric measurements with a tube level to find that the spring of Fontaine de Rivîre was 4.5 m higher than the normal level of the lake.

Ek and Godissart (2009) have recorded the evolution of the concentration of CO_2 in the air above the lake. They measured an increase in CO_2 lower than in the majority of the other caves studied in Belgium. The concentration in

2014 (Godissart, oral communication based on a last measurement done by O. Stassart) was around 10,000 ppm, that is to say twice the concentration measured in 1970. Despite the fact that measurements with such an interval should of course be considered with special care, and that continuous monitoring of the CO_2 has not been done until now, we can make the assumption that the specific confinement of the lake should also be responsible for a great stability of the air above, and thus a good coherence with climatic trends. The main intriguing questions about the lake have always been where water was coming from, where it was going to, and even whether it was moving somewhere, and perhaps during which period of the year. The great stability of the physico-chemical parameters (water temperature and conductivity), even when significant fluctuations of the water level occur, together with the latest questions, were the main reasons motivating the tracer test described in this work.

Methods

A pressure and temperature probe (In Situ, TROLL 500) was installed at the beginning of 2007 in the water of the main gallery leading to the lake (point 2 on Fig. 1b, c). This probe was doubled by a second probe between 2010 and 2014.

In 2008, a topographic survey was made with the support of the Geotechnical Direction of the Public Service of Wallonia (DGO1-61) using a differential GPS outdoor and a level tube improved by a TROLL pressure probe at the end for the underground levelling. The survey confirmed the higher level of the Fontaine de Rivîre spring (+121.92 m a.s.l. for the reference) compared to the lake (+119.46 m a.s.l. for the reference bolt where the support of the probe is attached, the lake being 1.22 m lower than the reference at that time on 26.10.2008 at 16:25). The confluence of the spring stream with the Ourthe River (point 9 on Fig. 1b) is at 118.30 m a.s.l.

The tracer used for the test was a liquid uranine (FLUORESCEIN LT SOLUTION 67%—Alpasud). The fluorescence efficiency of the tracer was calibrated against a reference uranine (FLUORESCEIN SODIUM—Fisher Chemicals) also used for calibration of the fluorescence spectrophotometer (Hitachi F-2500), and the content was in fact 41%. Two field fluorometers (GGUN-FL30 from Albillia) were recording three fluorescence signals (with an excitation LED at 470 nm for uranine detection), turbidity, temperature and conductivity. The data of these fluorometers were stored with TRMC-5 (Tetraedre) dataloggers.

The installation of the tracing material was made one week before the test, to avoid any flow disturbance of the lake during the injection. The injection tube was suspended at 3 m depth in the middle of the lake (point 1 on Fig. 1b, c). One of the fluorometer probes was suspended at the vertical of the injection point, at about 12 m depth. The other fluorometer was immersed at the same approximate depth in the main gallery (point 2 on Fig. 1b, c).

The injection of 61 g of uranine (149 g of product) was made on 22.03.2017 at 14:53, in approximately 1.5 min, with a Knf 12 V membrane pump (100 ml/min) with a pressure regulator of 3 bars at the end of the injection line.

The sampling interval of the fluorometers was set to 1 min during the day of the injection and then to 15 min until the end of the test on 4 February 2018.

Pictures of the tracer plume (Fig. 2) were taken every 5 s during 8:40 by a GoPro Hero camera (120° angle) fixed at the top of the chamber. Light was provided by five spots (4700 lm) distributed around the lake just above the surface and powered by a generator outside the cave.

Carbon detectors (charcoal activated ref. 1.02514.5000, granularity 1.5 mm, from Merck) were placed at the four

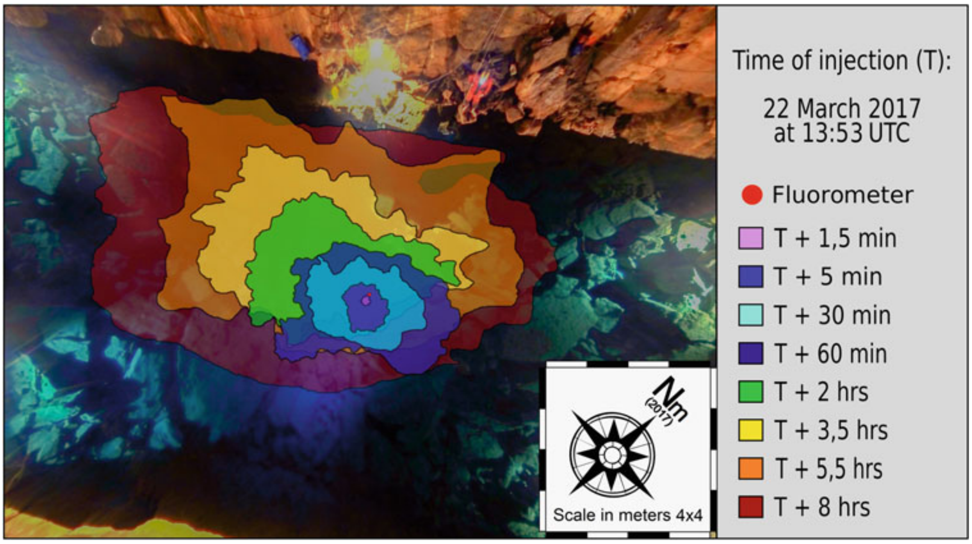

Fig. 2 Progression of the tracer plume towards WSW (processed from camera recordings)

corners of the lake (points 3, 4, 5 and 6 in Fig. 1b) and close to the fluorometer in the main gallery (point 2 in Fig. 1b, c). They were replaced with intervals between 2 weeks and more than 1 month. The water of the lake was sampled for laboratory analyses at the same place and interval as the detectors.

Outside sampling was also done at the Fontaine de Rivîre spring (point 7 on Fig. 1b), along its stream in front of the cave entrance (point 8 on Fig. 1b), in the stream just before its confluence with the Ourthe River (point 9 on Fig. 1b), along the right bank of the Ourthe River (point 10 on Fig. 1b) and at the overflows of the Péchet 1 and 2 waterworks (Fig. 1a).

The analyses of uranine were performed with a Hitachi F-2500 fluorescence spectrophotometer. All intensities at uranine wavelengths (490/591 nm) were corrected according to instrument long-term stability using a solid standard (Gaigalas et al. 2001) made of epoxy resin with addition of a fluorescent dye (epodye) in a PS supporting cell. Fluorometer intensities were calibrated according to water sample concentrations.

Extraction from charcoals was made by a solution of KOH 5%Vol in pure ethanol, followed by spectrofluorimetric quantification with the same calibrated fluorescence spectrophotometer.

Rainfall and level of the Ourthe (intervals of 1 h) were provided by DGO2 (Public Service of Wallonia), rainfall from the station of Ouffet situated a few kilometres from the cave, and level from the station of Hamoir (Fig. 1a).

Results

Tracer Test

Though the injection was as smooth as possible, the injection (at a depth of 3 m) created a mushroom cloud. It appeared rapidly that a deal of the tracer was sinking towards the bottom of the lake while a main cloud (plume) started a very slow horizontal displacement (Fig. 2) towards WSW, in the direction of the main gallery (Wineyards gallery) and the Ourthe Valley.

The fluorometer situated 9 m below detected the tracer after 12 min, reaching directly the maximum concentration of 2.991 ppm (Fig. 3a). The cloud was filmed during 8.4 h.

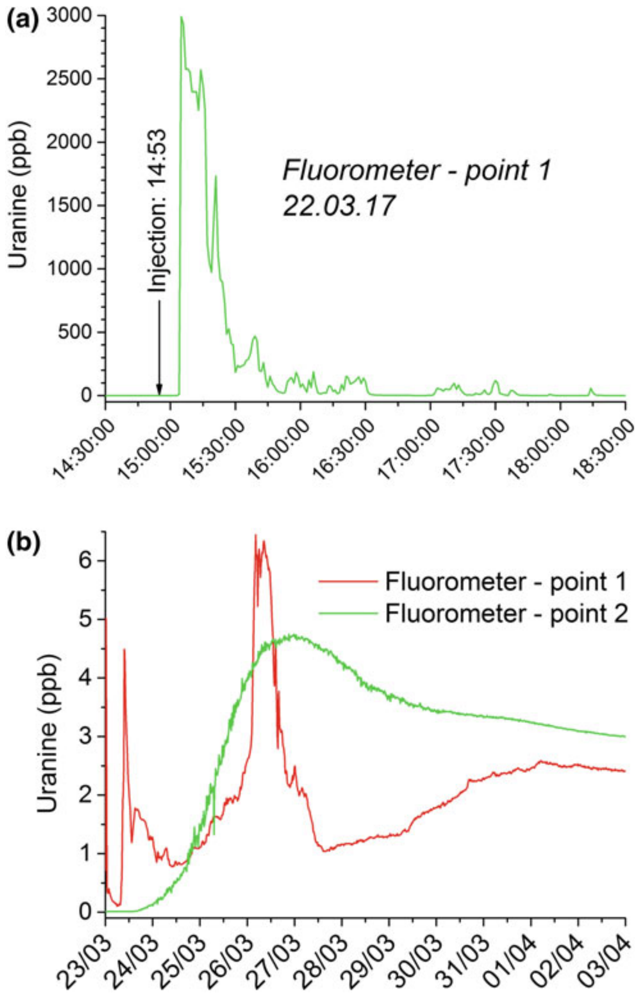

Fig. 3 Breakthrough of uranine. **a** Recorded during the first hours by the fluorometer at the centre of the lake (point 1 on Fig. 1b, c). The fluorescence was measured with excitation at 525 nm to work around the saturation at 470 nm. **b** Recorded during the first 13 days by the fluorometers at the centre of the lake (point 1 on Fig. 1b, c) and in the main gallery (point 2 on Fig. 1b, c)

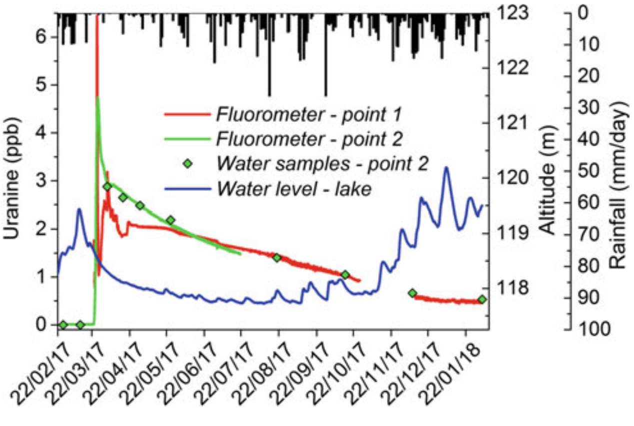

Fig. 4 Breakthroughs of uranine recorded during the whole experiment (fluorometer at the centre of the lake and manual sampling until 4 February 2018, fluorometer in the main gallery until 22 July 2017), compared with altitude of the lake and daily precipitations

At the centre of the lake, the breakthrough of the tracer remained quite chaotic (Fig. 3a, b), what can be partially due to a limited diffusion inside the cell of the fluorometer. It took about one month (Fig. 4) to reach a more homogeneous behaviour flowed by a slow concentration decrease. The breakthrough was more regular at point 2 situated at about 30 m downwards the injection point. The first arrival was 21.12 h after the injection, which gives a maximum velocity of 1.42 m/h. The peak was reached after 104.78 h (a velocity of 0.29 m/h). Assuming a section of 187.5 m^2 and a uniform velocity, this would give a flux of 54.4 m^3/h (15 l/s). Soon after the peak, there was a change in the behaviour of the tracer which followed an asymptotic trend to a linear decrease until the end of the test on 4 February 2018 (Figs. 3b and 4). We make the hypothesis that this change can be due to a change in the flow regime of the lake, which was until then under the influence of the high stage of mid-March, and whose effect finally ceased at the beginning of April, without any rain event (see responses of the lake below). One can also consider that the start of the linear trend, with the same concentration at the centre of the lake and in the gallery, would correspond to a complete mixing of the tracer in the lake and eventually connected water. Knowing the concentration at that moment (around 2 ppb), the 61 g injected would uniformly reach a volume of 30,500 m^3 which is slightly higher than the estimated volume of the lake. The additional volume involved can be stored in some inaccessible conduits, or due to an underestimated volume, but this also means that the lake is not connected to any other relevant volume of water in its vicinity, and it is in agreement with the initial hypothesis of the confinement of the lake. We assume that we observed a transitional regime of the lake with a convective component at the beginning of the experiment (displacement of the plume of tracer) followed by a diffusive phase afterwards. Anyway, this diffusive phase is a challenge for understanding. Molecular diffusion lonely cannot explain the initial evolution of the plume of the tracer. Using for instance the value of the diffusion of fluorescein in water given by Culbertson et al. (2002), 4.25×10^{-6} cm^2 s^{-1} at 25 °C, even with a correction of the effect of temperature, and using an approximated Fick's law, the mean displacement of the tracer should be less than 1 cm after 8 h, while the real displacement was in reality several metres during that time.

The concentration decreased regularly after complete mixing in the lake, so that we should assume the dilution by a given volume of external water (or another unknown effect, any degradation of uranine being not supposed to occur in the absence of light and presumably low microbiological activity, and long-term adsorption being not known as well). If we look at the behaviour of the tracer during the period of recharge in autumn and winter (Fig. 4), no variation can be seen at any moment (it even seems to stabilize at the end of the experiment). This is quite contradictory with the influence of the recharge noticed at the beginning of the test. If we assume the lake rising several times by one to two metres, this would allow for the renewal of the lake of minimum a quarter of its initial volume. So, the concentration should have decreased by at least a factor 4. This was not the case during the recharge period, and we should normally assume another mechanism for the rising of the lake (see the lake responses hereafter). We should remark here that this factor 4 would be the same as the factor of dilution that the tracer effectively underwent, but in this case during the whole year. This volume of dilution corresponds to an average annual discharge of the lake of about 0.57 m^3/h (0.16 l/s). This value is 100 times lower than what was calculated according to the velocity of the tracer at the beginning of the tracer test.

Water (Fig. 5a) and charcoals (Fig. 5b) sampled in the gallery and in the four corners of the lake are complementing the measurements made by the fluorometers. Water concentrations show that the tracer is progressively more homogeneous in the whole lake along time. The first sampling on 3 April shows that the upward side of the lake (points 4 and 5 on Fig. 1b) contains less tracer, according to the initial displacement towards SW and the lake which was not yet homogenized. The analyses of the samples of 2 July must not be taken into account because they may have suffered an instrumental problem (a lamp default).

Dunn (1961) and later Lallemand and Paloc (1964) suggested the charcoal method as a convenient sampling technique for fluorescent tracers in hydrogeology. Regarding the fluorescein, Mathey (1971) also tested the method at the laboratory scale only. Smart and Simpson (2002) reported a field study on the problem of the background (and the potential use of charcoals for sampling fluorescent compounds). Nevertheless, the charcoal method is nowadays despised (Mondain and Muet 2008) due to the possible errors when it is misused (for instance without spectral determination) or not validated through other sampling methods. In this study, we intended to test the ability of the method for a quantitative approach, for uranine specifically, at field scale, long-term scale also, and with relatively well-controlled conditions. The concentrations of uranine in the eluents of the charcoal bags immersed in the lake are shown in Fig. 5b. The analyses confirm the lower fluxes of uranine upwards at the beginning of the experiment. They also demonstrate that the duration of the immersion is a determinant factor. While the amount of desorbed uranine decreases after the injection with 2 weeks sampling interval, a longer sampling interval (above 1 month) gives again higher concentrations, proving a complex kinetic of fixation that could take longer than assumed before. Our own experience of this technique let us believe that the quite high dispersion of the results may be due to insufficiently controlled parameters (thus reproducibility) during the analytical process of extraction. The method would obviously require further validation tests to become more reliable for fluorescent dye traces.

We will close this section by mentioning that, despite regular samples and conjunctional use of water and charcoal

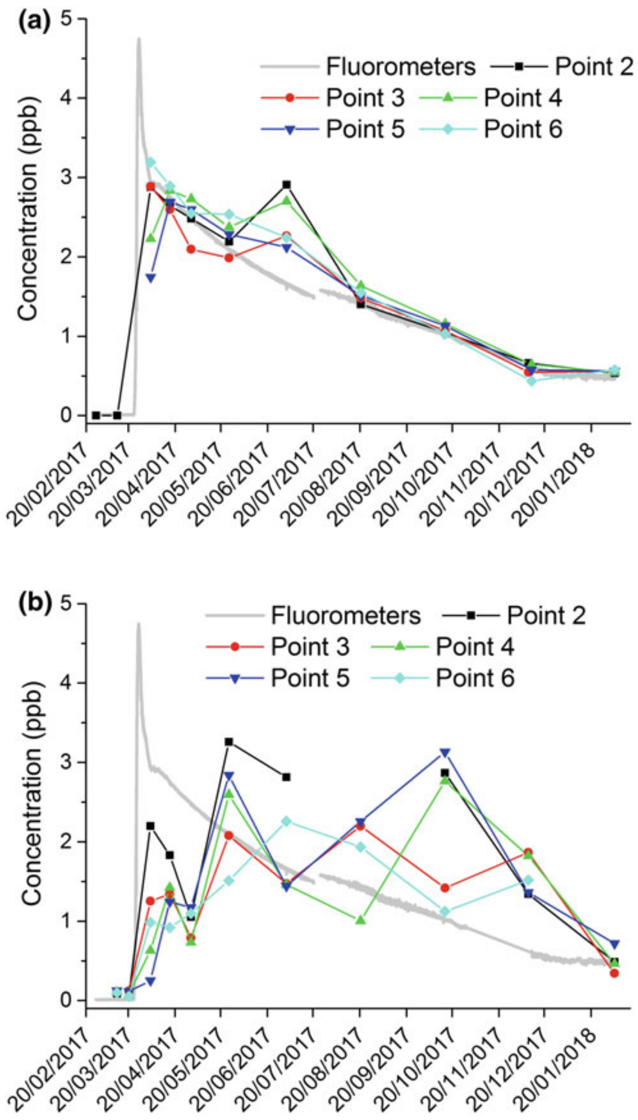

Fig. 5 Concentrations of uranine. **a** In water samples collected in the main gallery (point 2 on Fig. 1b, c) and at the four corners of the lake (points 3 to 6 on Fig. 1b during the experiment, compared with fluorometer measurements (first part from fluorometer in the gallery, second part from the fluorometer in the centre). **b** In the eluent of active charcoal detectors collected in the main gallery (point 2 on Fig. 1b, **c** and at the four corners of the lake (points 3 to 6 on Fig. 1b) during the experiment, compared with fluorometer measurements (first part from fluorometer in the gallery, second part from the fluorometer in the centre)

samples for precise detection, uranine could never be found outside, nor in the Fontaine the Rivîre spring (theoretically it was however impossible), nor in the Ourthe (where it can underflow at extremely low concentrations), nor in the Péchet waterworks. These results are obviously not surprising after what was observed in the lake.

Natural Responses

The apparent contradiction between the lake level variation and its high stability regarding any other parameter motivated the tracer test. The temperature in particular (Fig. 6) was showing a continuous increase since the beginning of its recording in 2007.

Despite the specification of 0.1 °C accuracy, obviously, the probe TROLL always kept a better sensitivity. This was proved by a second probe installed at the same point between 2010 and 2014, as well as by the temperature recorded by the fluorometers during the tracer test. The decennial increase of 4.6 °C seems compatible with the trend of 4 °C recorded at the meteorological station of Uccle for the mean annual temperature during the years before 2016 (Climat.be 2018). The advantage of the signal of the lake of Fontaine de Rivîre is obviously the total absence of background noise. This confirms the role of filter that cave environments (and aquifers) may play in a precise determination of climate change. So, caves would not only represent a tool for palaeoclimate studies but also for the present evolution. The same idea as for temperature can be advanced concerning CO_2 concentrations in such a cave. The records of temperature in the lake show that it was increasing exponentially until the years 2010–2011. Since then, the temperature follows a more linear trend. Meus et al. (2014) already noticed a break in 2010–2011 in temperature and hydrologic behaviour of several karst springs in Belgium.

The fluctuations of the lake do not significantly affect the temperature, what is in agreement with the very low renewal of the lake indicated by the tracer test. Sometimes, some fluctuations of the temperature can be observed during the most important risings of the lake but their amplitude of a few thousandths of degree is probably not significant in that case.

We can also already observe (Fig. 6) a strong apparent correlation (not only from an event point of view but also regarding the amplitudes) between the level of the lake and the level of the Ourthe River recorded downward the site.

A closer look at the responses of the lake (Fig. 7) confirms the link between the level of the river and that of the lake with a given lag and damping of the pulses. This process could be statistically quantified for the whole period of observation (2007–2018), using correlation analyses (Mangin 1984).

The simple correlograms shown (Fig. 8a), processed with R software, using a lag of 1 h (data regularly interpolated), indicate a quite high memory effect of lake level, and a lower memory of the levels in the Ourthe River. The cross-correlograms were also computed (Fig. 8b) between assumed causes and the responses. It shows maxima of responses to rainfall of 32 and 104 h, respectively, for the

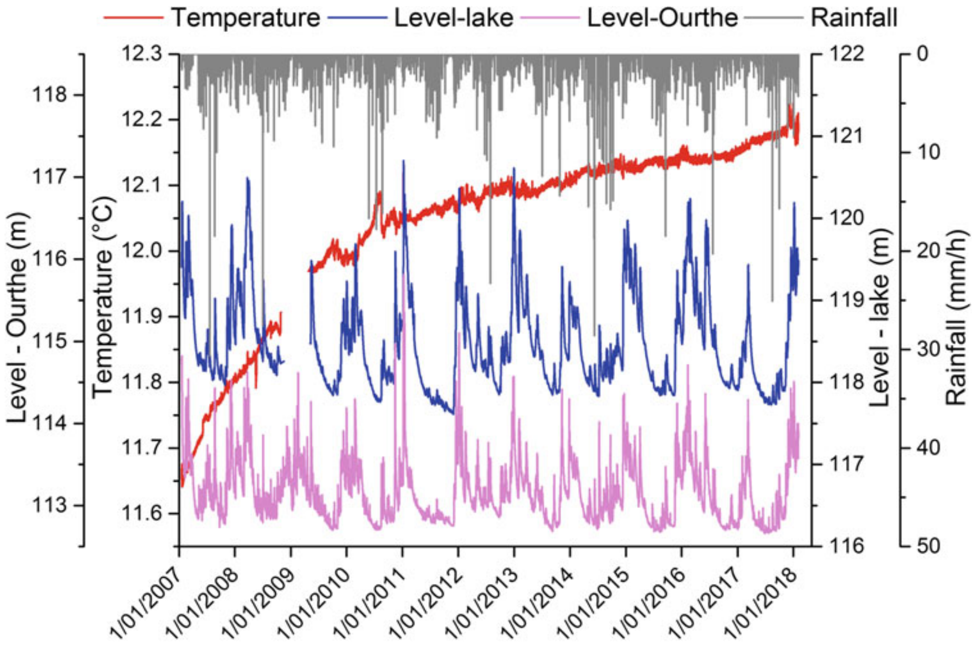

Fig. 6 Time series of the water temperature of lake, altitudes of lake and Ourthe River in Hamoir, and rainfall in Ouffet

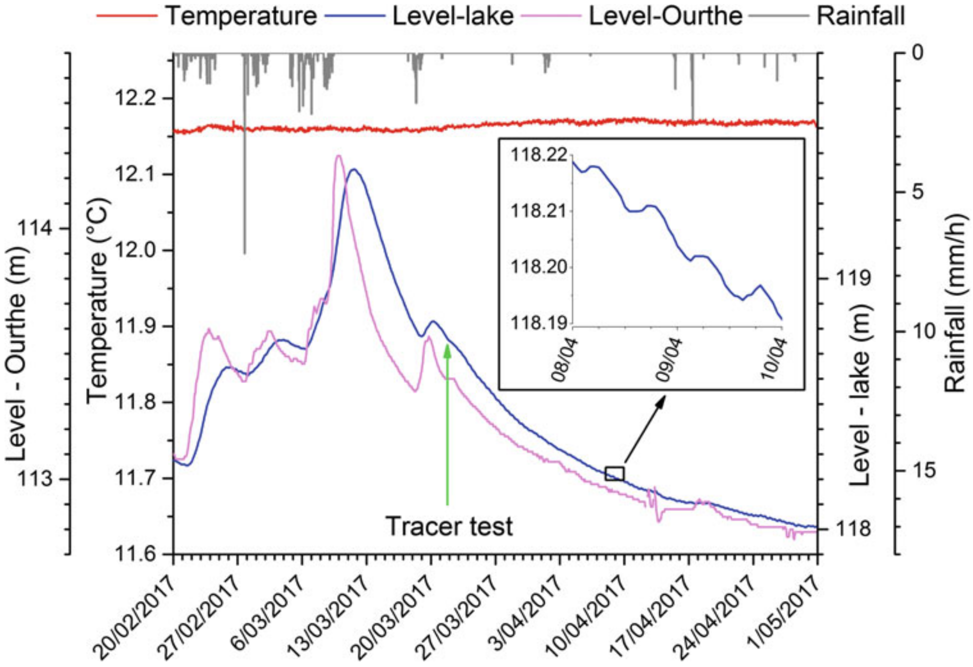

Fig. 7 Temperature of lake, altitudes of lake and Ourthe River in Hamoir, and rainfall in Ouffet for the period from 20 February until 1 May 2017. The insert shows the semi-diurnal fluctuations

level of the Ourthe and the level of the lake. The delay between the level of the Ourthe and the level of the lake is only 34 h, with a quite high correlation. This indicates most probably a causal relation between both levels and it gives us one additional element to understand the recharge of the lake. We assume that the main cause of the variations of the level of the lake is not only the recharge by water itself (through infiltration or exchanges with high transmissivity karst conduits), but it would be mainly due to a complex transfer of pressures from the neighbouring water table, with very low exchanges of matter indeed.

Another key for understanding the confinement of the lake can be the tidal variations that are clearly seen on the level recordings during undisturbed periods (insert on Fig. 7) where cyclic fluctuations of about 1 cm are detected. A Fourier analysis was computed with the Origin software for the levels of the lake. Four frequencies went out of the spectrum (Fig. 9).

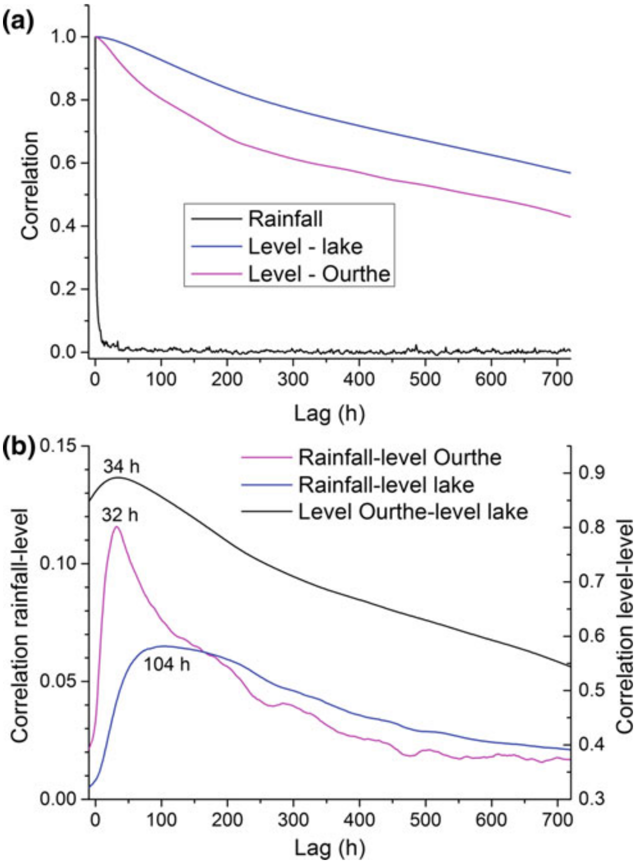

Fig. 8 **a** Simple correlograms of rainfall and water levels. **b** Cross-correlograms between rainfall and levels, and between levels of lake and Ourthe

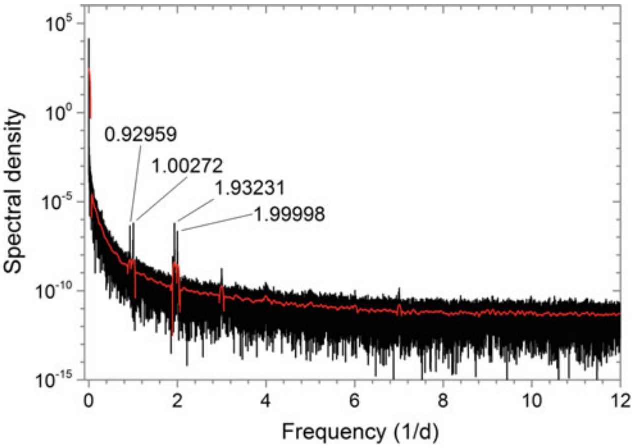

Fig. 9 Fourier analysis of water levels of the lake with gravitational semi-diurnal and diurnal frequencies

These are very close to the four main gravitational lunar and solar periodicities mostly known as responsible for tidal effects in Belgium (respectively, K1 at 1.00278, O1 at 0.92963, M2 at 1.93288 and S2 at 2.00000, Van Ruymbeke et al. 2007). Such periodicities have been found in other carbonate environments (springs, boreholes, Delvaux and Steisel 2009). The confinement of the lake of Fontaine de Rivîre is suggesting us that a detailed analysis of the tidal and barometric effects would be useful to understand how a confined auxiliary system is exchanging energy with its surroundings.

Conclusion

Single-point dilution tracer test offers an interesting alternative where classical tracer tests are no more relevant, especially for the most confined auxiliary systems of many karst aquifers. In most of these aquifers, the volume of low flow water can be far higher than inside active conduits, while playing a crucial role for the sustainability of the aquifer.

Such a tracer test was successfully achieved using a low quantity of uranine in the lake of Fontaine de Rivîre. The expansion of the tracer could be followed at different time scales during 1 year, using video recordings, fluorometer measurements, as well as water and charcoal samplings.

A slow flow (in the order of magnitude of 1 m/h) of the lake could be detected and some mixing processes identified. However, this flow probably decreased very early after the injection. The dilution of the tracer along the year indicates a mean discharge of the lake of about 0.16 l/s.

The behaviour of the tracer, together with the natural responses of the lake, indicates that the system is not physically filling and emptying during high stages. The fluctuations of the level of the lake are due to pressure transfers from the surrounding water table regulated by the base level of the Ourthe Valley, with a mean time delay of 32 h.

From a methodological point of view, this research is also a contribution to tracer sampling techniques, among others the video monitoring and the active charcoal sampling for which a quantitative validation could be done for the first time at a field scale.

Thanks to its high confinement, the lake is also a real filter for climatic responses (temperature, CO_2, etc.) at the condition that long-term recordings could be gained by insuring a good reproducibility. This lake could thus become an efficient observatory to understand both climatic evolution and resources of aquifers.

Acknowledgements This research was not supported by any fund. This is a good reason why we are especially grateful to those people who contributed to the achievement. The owner of the property Ranscelot is acknowledged for authorizing the access to the cave and allowing it to be protected for scientific studies. J.-M Marion provided great help with his feeling of "real" geologist and providing unpublished maps. Johan Derouane contributed to the GIS management. The lake has been photographed many times, but the best picture is here included thanks to Paul De Bie. Finally, I would like to express my gratitude to Alain Mangin (†) and to Michel Bakalowicz who showed me the way and motivation for understanding karst aquifers.

References

Abbott B, Baranov V, Mendoza-Lera C et al. (2016) Using multi-tracer inference to move beyond single-catchment ecohydrology. Earth-Science Reviews, 160 (2016): 19–42

Bakalowicz M (1999) Connaissance et gestion des ressources en eaux souterraines dans les régions karstiques. Bassin Rhône-Méditerranée-Corse, Guide Technique no. 3, juin 1999

Bakalowicz M, Crochet P, D'Hulst D et al. (1994) High discharge pumping in a vertical cave, fundamental and applied results. In: Basic and applied hydrogeological research in French karstic areas. Cost 65 Action. Hydrogeological aspects of groundwater protection in karstic areas. Crampon and Bakalowicz ed. European Commission, pp 93–110

Boulvain F, Bultynck P, Coen M et al. (1999) Les formations du Frasnien de la Belgique. Memoirs of the Geological Survey of Belgium, no. 44-1999: 1–125

Climat.be (2018) Le climat en Belgique. Observations en Belgique. Température. http://www.climat.be/fr-be/changements-climatiques/en-belgique/observations-en-belgique. Accessed 19 March 2018

Culbertson CT, Jacobson SC, Ramsey JM (2002) Diffusion coefficient measurements in microfluidic devices. Talanta 56 (2002): 365–373

Delvaux M, Steisel M (2009) Etude de l'influence de la marée terrestre sur les variations piézométriques de la nappe de la craie à Spiennes (Mons). Mémoire, UCL Louvain-la-Neuve

Dewaide L, Collon P, Poulain A et al. (2017) Double-peaked breakthrough curves as a consequence of solute transport through underground lake: a case study in the Furfooz karst system, Belgium. Hydrogeology Journal. Published on-line 26 Sep 2017

Dörfliger N (2010) Guide méthodologique. Les outils de l'hydrogéologie karstique. Avec la participation de Ph. Crochet, R. Guerin, N. Jozja, B. Marsaud, P.-H. Mondain, Ph. Muet, V. Plagnes. BRGM RP-58237-FR

Dunn JR (1961) Nouveau procédé de détection de la fluorescéine. Spelunca 4ème série: 1–26

Dusar M, Gullentops F (1989) Stratigraphie et tectonique dans la region d'Hamoir-sur-Ourthe. Aardkundige mededelingen vol.4 Leuven University Press 1989

Ek C, Godissart J (2009) Extreme increase of CO_2 in Belgian caves. Earth Sciences, 2009 ICS Proceedings, 15th International Congress of Speleology: 1467–1473

Gaigalas AK, Li L, Henderson O et al. (2001) The development of fluorescence intensity standards. J. Res. Nat. Inst. Stand. Technol. 106: 381–389

Gaspar E, Oraseanu I (1987) Natural and artificial tracers in the study of the hydrodynamics of karst. Theoretical and Applied Karstology, vol.3, 1987: 32–106

Godissart J (1994) Le cycle annuel des températures et du CO_2 dans la grotte de Fontaine de Rivîre à Hamoir (Belgique). Publ. Serv. Géol. Luxembourg, vol. XXVII, Comptes-rendus du colloque international de karstologie à Luxembourg, 1994: 179–185

Grasso DA, Jeannin PY, Zwahlen F (2003) A deterministic approach to the coupled analysis of karst springs' hydrographs and chemographs. Journal of Hydrology 271 (2003): 65–76

Guizerix J, Margrita R, Niemi A (1990) Tracer methodology. In: Guidebook on radioisotope tracers in industry. IAEA Vienna 1990. Technical reports series no. 316: 39–92

Jeannin PY (1996) Structure et comportement des aquifères karstiques. Thèse. Université de Neuchâtel

Kiraly L (2003) Karstification and groundwater flow. Speleogenesis and Evolution of Karst Aquifers, 1(3), September 2003: 1–25

Lallemand A, Paloc H (1964) La méthode de détection au charbon actif pour les opérations de traçage à la fluorescéine. Quelques exemples d'application. BRGM DS 64 A47: 1–15

Mangin A (1975) Contribution à l'étude hydrodynamique des aquifères karstiques. Université de Dijon. Laboratoire du CNRS Moulis. Thèse publiée dans les Ann. de Spéléologie, 1974 no. 29 (3): 283–332, 1974 no. 29 (4): 495–601, 1975 no. 30 (1): 21–124

Mangin A (1984) Pour une meilleure connaissance des systèmes hydrologiques à partir des analyses corrélatoire et spectrale. Journal of Hydrology, 67 (1984): 25–43

Mangin A (1994) Karst hydrogeology. In: Groundwater Ecology, Academic Press, pp 43–67

Mangin A, Molinari J, Paloc H (1976) Les traceurs en hydrogéologie karstique. Leur apport à la connaissance des réservoirs aquifères calcaires. La Houille Blanche No. 3–4 1976: 261–267

Marion JM, Barchy L (in press) Carte géologique de la Wallonie à l'échelle 1/25.000. Hamoir - Ferrières no. 49/5-6 et sa notice explicative. SPW/Editions, Cartes. DGARNE, Jambes (Namur). 1 carte couleur + 1 notice explicative

Marsaud B (1996) Les pompages en aquifère karstique. Une démarche d'interprétation des essais adaptée au karst. In: Pour une gestion active des ressources en eau d'origine karstique. BRGM Département Eau (1998). Rapport BRGM R 40126, pp 177–197

Martel EA (1921) Nouveau traité des eaux souterraines. Paris, Librairie Octave Doin, Gaston Doin Ed., 1921

Mathey B (1971) La méthode au charbon actif dans les essais de coloration à la fluorescéine. In: Actes du 4ème Congrès suisse de Spéléologie, Neuchâtel, septembre 1970, pp 53–61

Meus P (1997) Méthode d'évaluation de la vulnérabilité des aquifères karstiques utilisant le traçage en continu. In: La géologie de l'ingénieur et l'eau dans le sous-sol. Colloque National. Leuven. 18-20/11/1997, 22/1-10

Meus P (2006) Multitraçage sur le site de la source Péchet (Hamoir). Rapport EWTS 07-2006

Meus P, Moureaux P, Gailliez S et al. (2014) In situ monitoring of karst springs in Wallonia (southern Belgium). Environ Earth Sci (2014) 71:533–541

Mondain PH, Muet P (2008) Proposition d'une grille d'évaluation des résultats des traçages en milieu karstique (au moyen de traceurs fluorescents). In: CFH Colloque Hydrogéologie et Karst au travers des travaux de Michel Lepiller, 17 mai 2008, pp 191–205

Müller I (1981) L'eau dans les roches calcaires. Bulletin de la société Fribourgeoise des Sciences Naturelles. 70 (1/2) – 1981: 12–20

Novakowski KS, Lapcevic PA, Voralek et al. (1995) Preliminary interpretation of tracer experiments conducted in a discrete rock fracture under conditions of natural flow. Geophysical Research Letters, vol.22, No. 11, June 1, 1995: 1417–1420

Smart CC, Simpson B (2002) Detection of fluorescent compounds in the environment using granular activated charcoal detectors. Environmental Geology (2002) 42: 538–545

Van Ruymbeke M, Zhu P, Cadicheanu N et al. (2007) Very weak signals (VWS) detected by stacking method according to different astronomical periodicities (HiCum). Nat. Hazards Earth Syst. Sci., 7: 651–656

Worthington SRH (2003) A comprehensive strategy for understanding flow in carbonate aquifer. Speleogenesis and Evolution of Karst Aquifers, 1(1), January 2003: 1–8

Water Tracing Experiments in Low-pH Quartzite Karst Water, Chapada Diamantina, Northeastern Brazil

Augusto S. Auler, Philippe Meus, and Paulo F. P. Pessoa

Abstract

The existence of karst features and conduit flow in silica-rich rocks has been increasingly recognized around the world. Well-developed quartzite karst is known in tropical settings, such as southern Venezuela and eastern Brazil. However, little is known about the hydrogeological behavior of these terrains. Pioneering water tracing studies were performed in the Proterozoic quartzites of the Chapada Diamantina (Diamontiferous Plateau) of central-eastern Brazil, using the tracers amino-G and uranine. Tracer detection was performed by four in situ fluorometers, granular-activated charcoal receptors and water analysis. Hydrochemical conditions resulted in contrasting performances of the tracers, with uranine providing some positive results and yielding clear breakthrough curves. Low-pH water and high-fluorescence background levels appear to considerably inhibit tracer performance and add difficulties in the interpretation of some tracer tests. A preliminary assessment of flow routes and the main characteristics of groundwater dynamics in this quartzite area are provided, with insights on the behavior of the tracers under acidic (pH = 4–5) water conditions.

Keywords

Quartzite karst • Chapada Diamantina • Fluorescence • Water tracing

Introduction

Water tracing studies have been extensively applied in many parts of the world during the past few decades to infer groundwater flow paths, and they can now be considered as an established hydrogeological technique (Smart and Laidlaw 1977; Kass 1998). Despite the more straightforward goal of assessing flow paths, these techniques have now found applications in many other areas, such as in studies of groundwater pollution, the protection of waterworks, the delineation of groundwater basins, ocean circulation, and the quantification of discharge (Abbott et al. 2016 and references herein). The number of tracers that can be employed has increased substantially, and new potential tracers are regularly being tested and applied. With the development of sophisticated and accurate field and laboratory instruments, more detailed work can be performed, and water tracing techniques have now been expanded to many experimental and practical fields (Leibundgut et al. 2009).

The bulk of water tracing studies has been performed in carbonate areas. The behavior and dynamics of groundwater circulation in carbonate karst terrains are now better understood, and the limitations related to the use of tracers in alkaline waters have been addressed (Jones 2012). Although most of the studies have been performed in temperate areas, tracing techniques have increasingly been applied to the tropics (Smart and Smith 1976) so that the performance of individual tracers under warm conditions can be better assessed. Low-pH water, typical of quartzite karst (Wiegand et al. 2004; Mecchia et al. 2014) is known to interfere with the efficiency of tracers (Lyons 1993). In carbonate karst waters, where alkaline conditions tend to prevail, fluorescence of uranine could increase 1.3 times as pH varies from 6.9 to 8.4 (Zhu et al. 2005).

Conduit flow in non-carbonate areas is much less understood, although several studies have now identified the existence of quartzite or sandstone karst areas

A. S. Auler (✉) · P. F. P. Pessoa
Instituto do Carste, Rua Barcelona 240/302, Belo Horizonte, MG 30360-260, Brazil
e-mail: aauler@gmail.com

P. Meus
European Water Tracing Services, rue de la Chapelle, 43, 4550 Nandrin, Belgium

C. Bertrand et al. (eds.), *Eurokarst 2018, Besançon*, Advances in Karst Science,
https://doi.org/10.1007/978-3-030-14015-1_21

containing caves and underground streams (Wray 2009; Wray and Sauro 2017 and references herein). However, little is known about the hydrochemistry of quartzite karst areas, which has been addressed in only a few studies performed in Brazil and Venezuela (Wiegand et al. 2004; Mecchia et al. 2014).

The study area lies in the Chapada Diamantina (Diamantiferous Plateau), a scenic quartzite area in the state of Bahia, northeastern Brazil. The table mountains landscape comprises several important quartzite caves. The study area is close to the village of Igatu, within the municipality of Andaraí (Fig. 1). According to Almeida (1977), the area lies within the boundaries of the São Francisco Craton and was consolidated over 1.7 Ga ago during the Transamazonian orogeny. Pedreira (1997) described the region as a plateau with outcrops of Mesoproterozoic sedimentary rocks, forming a Quartzite-Pelite-Carbonate (Q-P-C) association, embracing 12 different conglomerate, sandstone and carbonate lithofacies. Our study area is entirely composed of quartzites and metaconglomerates that were subjected to low-grade metamorphism and deformation, with depositional bedding at the site-orientated N0E/10 NW (Pereira et al. 2017). Dominant fracture direction is 129°, with a secondary orientation at 35°. At Chapada Diamantina, the wet season is concentrated in the austral summer months of December, January, and February, when 50–60% of the annual rainfall occurs, alternating with the dry season during the winter in July, August, and September (Chaves and Cavalcanti 2001). Annual mean temperature and rainfall according to Brazil's Water Agency (ANA) are 23.9 °C and 1125 mm, respectively.

The area was subject to intensive diamond mining activity in the past, and localized mining still occurs. This has resulted in the modification of the landscape with the removal of fine-grained material through washing, water diversion, and the construction of numerous mining structures. Presently, the former mining village of Igatu lies upstream of the study area and may be responsible for altering water quality parameters, although this was not the focus of our research.

This study will provide a first insight into the dynamics and general characteristics of groundwater flow in a quartzite karst area in northeastern Brazil. Knowledge of quartzite karst is mostly confined to geomorphological studies, and an integrated approach that includes hydrodynamics is lacking. This study represents a pioneering effort in assessing the behavior of two commonly used tracers (uranine and amino-G) in low-pH water and in establishing groundwater flow paths, resulting in a useful baseline for future studies in similar environments.

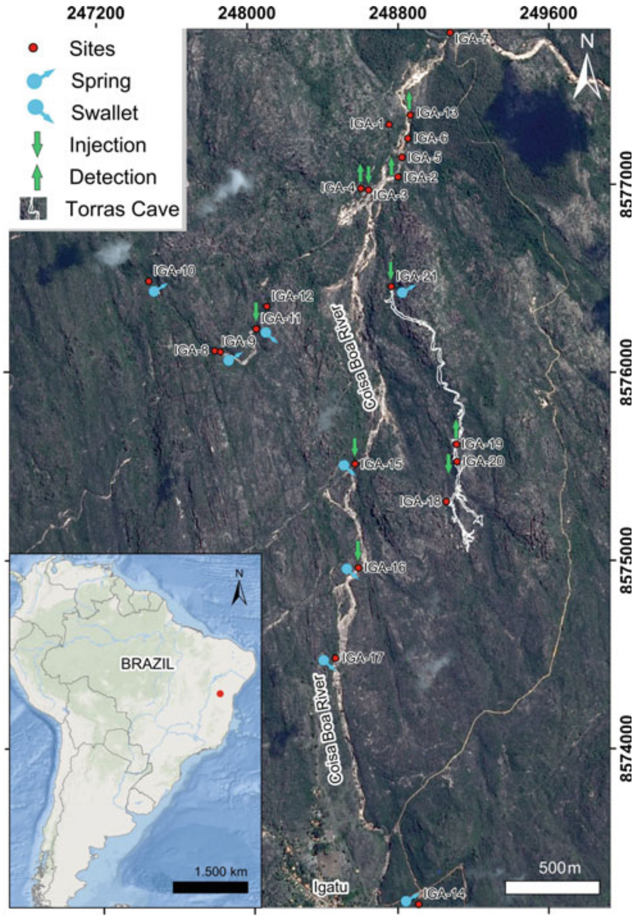

Fig. 1 Location of the study area, main hydrogeological features and sites where water was sampled and charcoal and fluorometers were deployed

Methods

Previous caving trips have assessed the speleological potential of the area and produced cave locations and maps. With the help of local guides, an initial inventory was performed, resulting in the identification of springs and swallets (Fig. 1). No hydrometric method was applied, and discharge data was obtained through tracer test data assuming a 100% recovery of the tracer at one single outlet.

Field work occurred in May 2017. Basic hydrochemistry was performed with a Hanna HI 991301 multiparameter device with electrical conductivity calibrated at 25 °C. Water samples were collected both for background fluorescence and for detecting tracers. Three GGUN-FL30 and one GGUN-FL24 field flow-through fluorometers were used, with excitation wavelength channels at 365, 470 and 524 nm. An additional portable Turner Designs AquaFluor fluorometer was also employed for fast, in situ measurements. Sulfal granulated 12 × 25 mesh activated charcoal was used as a passive detector. The charcoal was initially left in place for several days to assess background levels and then to expand our search for tracers, especially in sites where no fluorometers were deployed. Uranine ($C_{20}H_{10}O_5Na_2$—CAS 518-47-8 from Abbey Color) and amino-G (monopotassium 7-amino-1, 2-naphthalenedisulfonate hydrate—CAS 842-15-0 from Fluorochem Ltd) tracers were used. Hitachi F-2500 and Hitachi F-2700 fluorescence spectrophotometers from the European Water Tracing Services (Belgium) and Hidrovia (Brazil) companies, respectively, were used. Extraction of the tracers from the charcoal was performed using a solution of 5 wt% NaOH in ethanol. Measurements of photometry were at fixed wavelengths at EX/EM of 250/445 nm (optimum for amino G acid), 310/420 nm (usually the most representative for dissolved organic matter, DOM), and 491/511 nm (optimum for uranine). Synchronous scanning spectra were produced with an interval of 20 nm (optimum for uranine) and an interval of 95 nm (optimum for amino G) between EX and EM. Excitation emission matrix (EEM) spectra were also produced with a scan between wavelengths of 220 and 500 nm for EX and between 250 and 600 nm for EM. Experimentally buffering solutions through the addition of NaEDTA at high pH while running the sample at the spectrometer enabled assessment of the influence of low-pH water on the fluorescence.

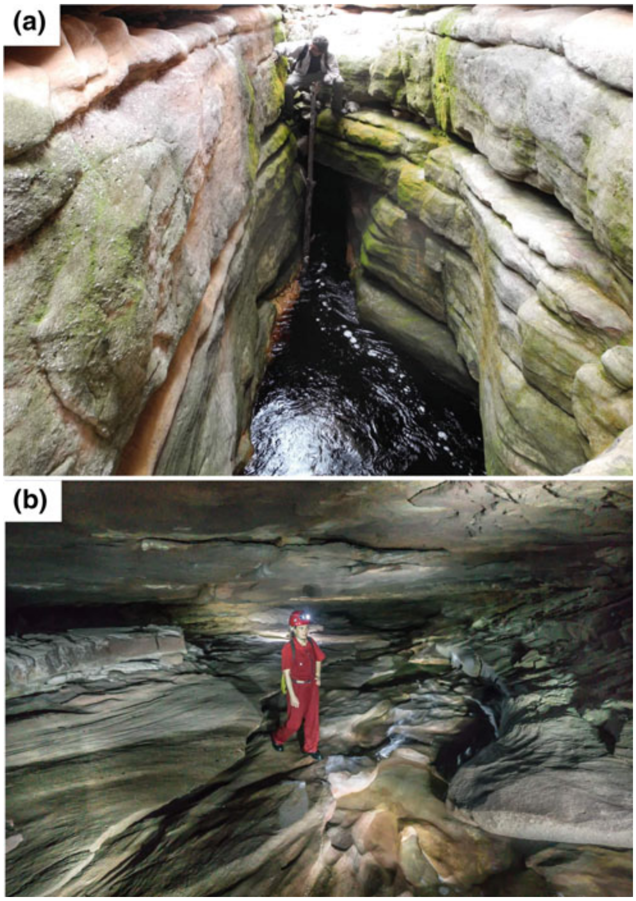

Fig. 2 **a** Karst window that represents site IGA-3. **b** Stream passage of Torras Cave. Photograph courtesy of Daniel Menin

Groundwater Hydrology and Study Design

The study area comprises a quartzite range that dips uniformly at approximately 10° westward. Throughout the area, there are numerous caves, springs, and swallets (Fig. 2). Surface water running from the upstream reaches of the area either flow through Coisa Boa River, the main stream in the area, or sinks in a series of swallets. In the now mostly dry riverbed of Coisa Boa River, three different sinking points were identified (IGA-15, IGA-16, IGA-17). Another important sinking stream is associated with Torras Cave (IGA-18), a major 3.6-km-long quartzite cave, which collects tributaries along its underground course until the passage becomes impassable. To the west, Criminoso swallet (IGA-11) collects water coming mostly from the northwestern sector. These three major systems (Coisa Boa, Torras, and Criminoso) were chosen as the main tracer injection points of our study. At the northern portion of the area, close to the limit of the quartzite outcrops, a series of springs were identified (labeled IGA-2, IGA-3, IGA-5, IGA-6). These springs discharge into the Coisa Boa River (IGA-13, IGA-14). All these springs were subject to water analysis and tracer detection. Experimental work was also performed in the surface section of the Coisa Boa River, downstream from the springs. Overall, discharges at the springs are rather small, being measured at 1.62 l/s at IGA-2 and estimated at 85 l/s at IGA-3.

Flow-through GGUN fluorometers were placed at the two major springs, IGA-2 and IGA-3. Another GGUN fluorometer was placed downstream from these two springs, at Coisa Boa River (IGA-13). Activated charcoal passive detectors were placed at all springs located in the northern discharge area, and water samples for fluorescence analyses were taken at most sites before and after injections. Tracers were injected in the three major swallets (IGA-11, IGA-15, and IGA-16) and at the mid-section and downstream end of Torras Cave (IGA-20 and IGA-21, respectively). Table 1 provides information on all injection, detection and sampling sites.

Table 1 Description of hydrogeological sites with type of sampling and injection marked by colors

Sites	Description	Water	Charcoal	Tracer injection	Fluorometer
IGA-1	Nearly stagnant water at rock shelter	🟦	▨		
IGA-2	Small spring and cave that represents the outlet of Torras Cave	🟦	▨		🟥
IGA-3 **IGA-4**	Pothole (karst window) with river flowing at bottom. IGA-4 a few meters upstream from IGA-3	🟦	▨	*100 g uranine 05/11/17 at 4:25 pm	🟥
IGA-5	Small stream known as Cabasaco	🟦	▨		
IGA-6	Small dark water stream.	🟦	▨		
IGA-7	Coisa Boa River under the bridge at highway	🟦	▨		
IGA-10	Spring of Criminoso creek issuing from a cave	🟦			
IGA-11	Swallet of Criminoso creek	🟦	▨	50 g uranine 05/07/17 at 10:20 am 383 g amino- G 05/10/17 at 12:53 pm 200 g uranine 01/02/18 at 9:33 am	
IGA-12	Criminoso cave		▨		
IGA-13	Coisa Boa river, downstream from the other sites, including IGA-1				🟥
IGA-14	Upstream from the study area, small spring by the side of the main road	🟦			
IGA-15	Downstream swallet of Coisa Boa River, below a big waterfall.	🟦		250 g amino-G 05/07/17 at 1:07 pm	
IGA-16	Upstream swallet of Coisa Boa River.	🟦		100 g amino-G 05/07/17 at 2:40 pm	
IGA-17	Swallet where the largest volume of Coisa Boa flow sinks				
IGA-18	Main entrance of Torras Cave				
IGA-19	Inside Torras Cave, site of fluorometer				🟥
IGA-20	Upstream from IGA-19, inside Torras Cave. Point of injection			*50 g amino-G 05/09/17 at 12:58 pm	
IGA-21	Downstream end of Torras Cave			50 g uranine 05/09/17 at 3:30 pm	

Injections labeled with * were performed to test tracer behavior in quartzite groundwater

Results

Natural Fluorescence and Effects of pH on Tracers

Basic physical properties of quartzite water in the study area are presented in Table 2, in addition to results of background fluorescence. Low pH and very low conductivity characterize the water, with a mean (n = 9) of 4.7 and 23 µS/cm. This value is typical of quartzite karst waters (Wiegand et al. 2004; Mecchia et al. 2014). Natural background fluorescence was measured in situ (Table 2) and in water and charcoal eluent in the laboratory (Figs. 3 and 4). All samples showed high background fluorescence intensities for natural

Table 2 Basic parameters, measured in situ

Sites	pH	Electrical Conductivity (µS/cm)	Temperature (°C)	Fluorescence background Rhodamine wt (ppb)	Fluorescence background Uranine (ppb)
IGA-1	4.78	33	23.9	0.339	0.713
IGA-2	4.45	40	22.5	0.423	1.139
IGA-3 IGA-4	4.71	19	24.0	0.508	1.029
IGA-5	4.69	13	26.0	0.193	0.728
IGA-6	5.18	8	24.9	0.019	0.397
IGA-7	4.77	15	25.4	0.098	0.550
IGA-10	4.52	35	23.0	0.987	2.522
IGA-11	4.46	29	24.7	1.172	2.415
IGA-14			23.1	0.467	1.071
IGA-15			23.7	0.548	0.881
IGA-16	4.84	15	23.4	0.395	1.128

Fluorescence obtained with a handheld AquaFluor

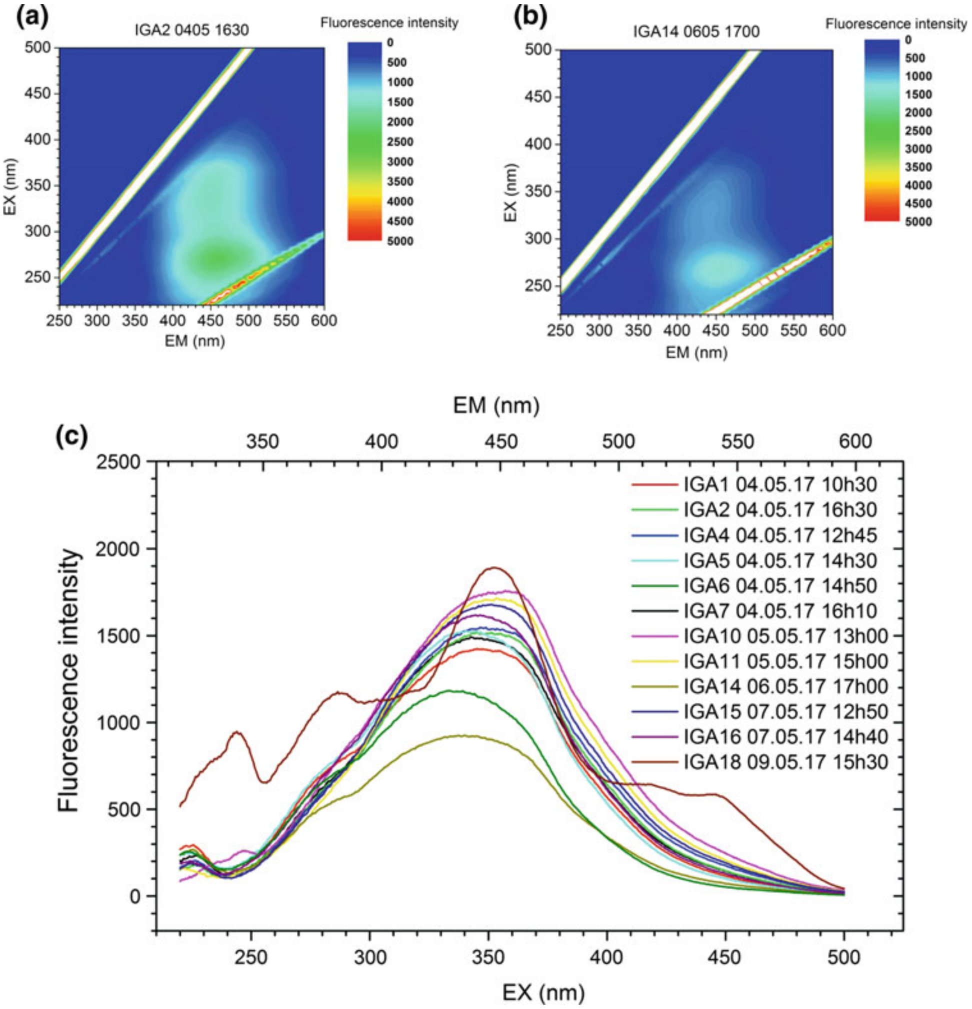

Fig. 3 **a** EEM spectra of representative downstream site IGA-2 and **b** of a smaller upstream spring IGA-14, showing differences in fluorescence intensity. **c** Natural fluorescence in the water of all sampled sites. EX and EM slits were 5 nm, and the photomultiplier voltage was 700 V. Synchronous scanning with a 95-nm interval

water. Sites with lower discharges (IGA-6) or sites located in higher elevations (IGA-14) tended to yield lower intensities. Natural fluorescence is interpreted as the result of dissolved organic matter (DOM). Natural fluorescence in charcoal showed a similar behavior (Fig. 4), although the spectra tended to be broader (with a trend toward shorter wavelengths) or narrower (again moving toward shorter wavelengths). Although anthropogenic inputs from the upstream Igatu village could be responsible for spectral differences related to the longer exposure of the charcoal to the water, this effect has also been observed in laboratory charcoal samples and perhaps reflects an intrinsic feature related to charcoal. No evidence of uranine or amino-G was found in the background samples.

Low-pH water is known to interfere with the efficiency of tracers (Lyons 1993). Oba and Poulson (2012) noted that uranine becomes increasingly non-conservative at pH < 7. Our study confirms the findings of Lyons (1993), Oba and Poulson (2012) and Zhu et al. (2005) that fluorescence decreases in low-pH situations. Figure 5 shows that at the uranine breakthrough curve at site IGA-2, a solution buffered with the results of the water samples displayed a marked increase by a factor of 5 compared to the original fluorometer curve.

Tracing Results

A total of eight injections of uranine or amino-G were performed (Table 1). Some of the short injections, intended to test tracer and fluorometer performance in quartzite groundwater, will not be further discussed. Table 3 presents details about three informative hydrologic connections. A successful breakthrough was obtained between the stream at Torras Cave (IGA-21) and the spring that issues from a small cave (IGA-2) (Fig. 6). Assuming a 100% recovery of uranine, calculated discharge at the site would amount to 1.6 l/s. This straightforward connection, although traversing a short route, implies a fast-flowing stream with limited ponding (velocity of 60 m/h). An injection made on the same day at an upstream section of Torras Cave (IGA-20), over a ripple and pool sequence approximately 92-m long

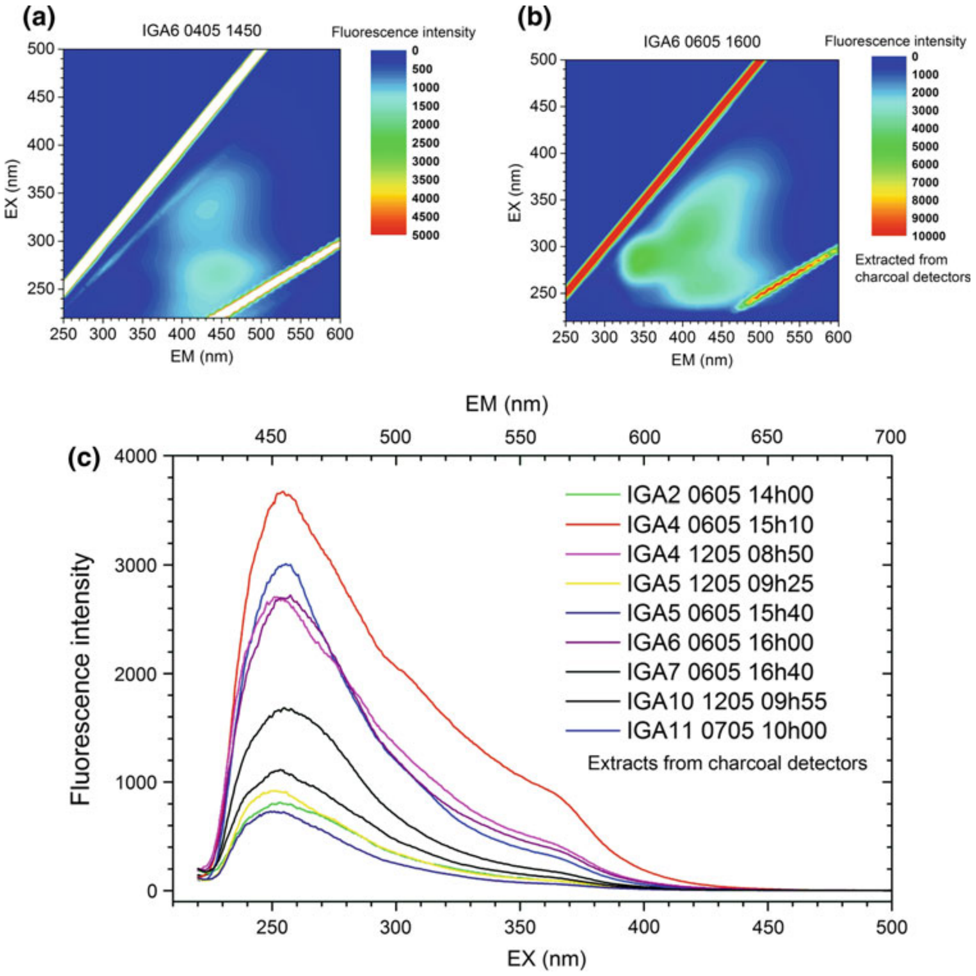

Fig. 4 **a** EEM spectra showing natural fluorescence in the water and **b** charcoal for IGA-6 site. Note that charcoal spectra show amplifications at shorter wavelengths in addition to a broader overall spectrum. **c** Natural fluorescence in charcoal of all sampled sites. Synchronous scanning with a 95-nm interval for water and 200-nm interval for charcoal

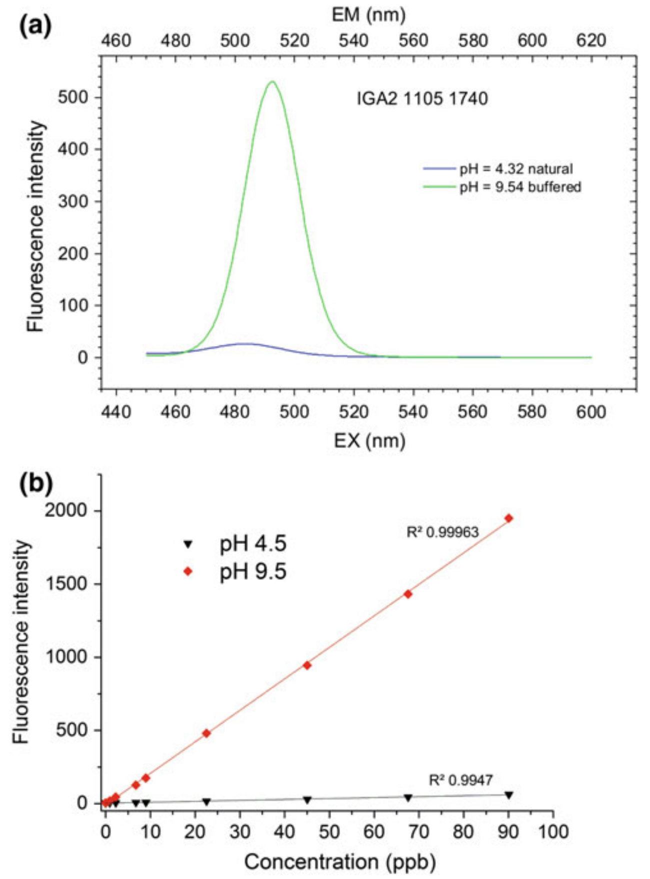

Fig. 5 **a** Uranine synchronous scan for IGA-2 displays a much more intense fluorescence when buffered at high pH than when measured with its natural pH. **b** The same strong pH dependency effect is observed for standards prepared with water from Coisa Boa River (IGA-13) buffered (pH = 9.5) or not buffered (pH = 4.5)

(comprising approximately 20 pools over 1 m in diameter), resulted in a much slower travel velocity of 21 m/h. These differences are probably related to conduit morphology. Fast flow occurs when the passage turns along the bedding dip, as appears to be the case with the IGA-21 to IGA-2 connection.

A well-marked peak at IGA-3 and, interestingly, a double peak in the downstream fluorometer placed at IGA-13 could be related to the sequential amino-G injections at the two Coisa Boa swallets (IGA-15 and IGA-16) (Fig. 6). These intriguing results could have been affected by background interference in IGA-13 (as only the main peak is clearly above the noise) or may represent a yet-unrecognized route between one of the injection points and the Coisa Boa (IGA-13) that bypasses the upstream site at IGA-3. It is assumed that the larger amount of tracer injected in IGA-15 compared to IGA-16 and the proximity between IGA-15 and the sampling sites explain the main peak at IGA-3 (and possibly at IGA-13). An alternative explanation would be differential mixing between the two amino-G injections.

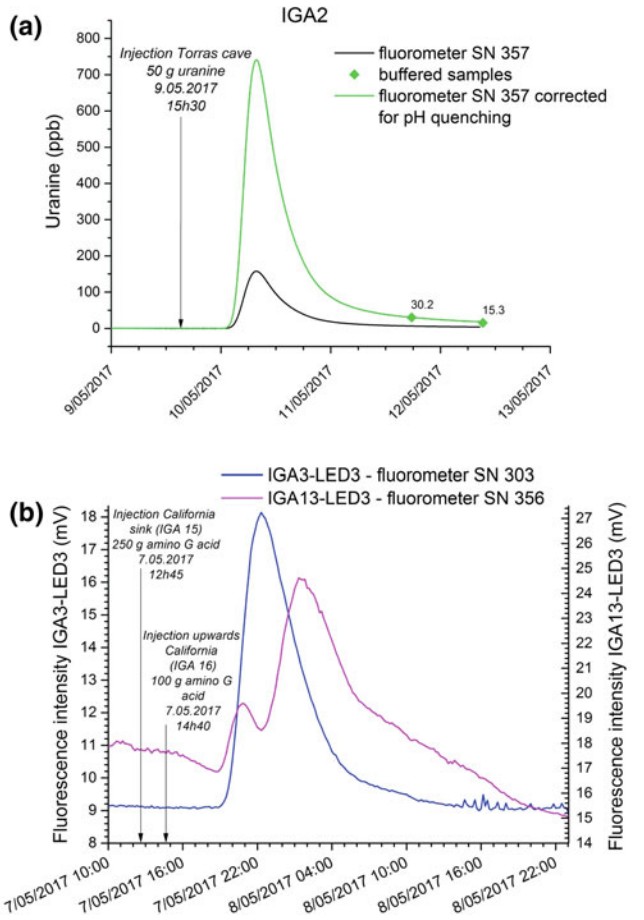

Fig. 6 **a** Breakthrough curve for connection IGA-21 to IGA-02. The recorded uranine curve is shown in black for the natural low-pH situation. The higher-concentration green curve is the same breakthrough corrected according to the concentration of two samples buffered in the laboratory. **b** Fluorometers at IGA-3 and IGA-13 recorded the presence of amino-G differently. While the upstream IGA-3 shows a clear peak, the downstream IGA-13 displays a double peak

Table 3 Straight line distance, travel time, and velocity of some tracing routes

Site injection	Site fluorometer	Travel time (h)	Distance (m)	Velocity (m/h)
IGA-21	IGA-2	9:40	581	60
IGA-15	IGA-3	5:52	1458	248
IGA-11	IGA-3	122:30	949	8

The IGA-11 to IGA-3 connection needs further experiments (see text)

Further research is needed to sort out details of this connection. Unfortunately, water samples could not be collected during this breakthrough.

Finally, a possible connection was achieved between Criminoso sink (IGA-11) and IGA-3. A first attempt using uranine was followed by an injection of 383 g of amino-G. Unfortunately, travel times were too slow to allow for a conclusive result in the fluorometer, although there is discrete evidence of uranine arrival in a charcoal detector collected on the last day of the campaign in IGA-4 (a few meters upstream from IGA-3). Therefore, we must treat this possible connection with caution until further refinements are made. Distances and travel times are shown in Table 3. Tracer velocities vary considerably and appear compatible with a ripple (fast) and pool (slow) morphology characteristic of quartzite streams in the area. Slow flow is possibly associated with the occurrence of slow moving pools, which sometimes predominate when water flows along the strike, while fast flow is expected in situations where water follows the dip, both mostly in vadose or epiphreatic conditions.

Discussion and Final Remarks

Most studies on groundwater tracing in karst terrains have been performed in limestone areas, under well-known alkaline hydrochemical conditions. Tracer behavior in such conditions is well documented and has allowed for important insights into the dynamics of carbonate karst aquifers (Goldscheider et al. 2008). However, little is known about quartzite karst hydrochemistry and conduit morphology, although recent progress has been made (Auler 2012; Mecchia et al. 2014). From observations in several caves in eastern Brazil, quartzite flow appears to occur mostly under shallow conditions, as perched streams within the vadose zone (Auler 2012). Although Wray (2009) notes the existence of phreatic conduits, most of the groundwater flow paths display marked bedding plane and structural control. No evidence of deep groundwater flow, as commonly occurs in limestone karst, has been observed. Our results show that groundwater connections in the quartzite karst of Igatu occur under velocities that vary by more than an order of magnitude. This appears to reflect considerable time delays in the numerous pools that characterize the streambed morphology. Traced flow paths that followed the main joint systems, toward the NNW, had faster travel time, while the one (IGA-11–IGA-3) that runs toward the NE had a much slower flow. It is interesting to note that the IGA-13–IGA-3 route follows the mostly dry bed of the Coisa Boa river. This river appears to have followed favorable joints, which would reflect equally favorable conditions under the riverbed. Our experiments were performed during low flow conditions. Faster velocities, decreasing the influence of ponding, would probably occur under higher discharge. Due to the shallow nature of groundwater flow in the Igatu area, surface morphology plays a significant role, and groundwater flow routes tend to be relatively short when compared to limestone areas.

Low-pH conditions characterize the local hydrochemistry, resulting in decreased fluorescence intensity, at least for uranine (the amino-G tracer should be investigated by laboratory testing). Natural background levels in the area are relatively high. Due to the pH effects and elevated natural background (and likely also due to anthropogenic contribution), the application of tracer tests in this context requires special care to avoid complications in tracer detection. Additionally, it requires the combination of several sampling and analysis techniques: in situ fluorometry, spectral analysis of water samples, and eventually passive sampling with charcoal detectors (although the charcoal approach should be better validated by laboratory tests). This study illustrates the need for a better understanding of the distinct dynamics of quartzite karst aquifers. Classical tracing methods may require adaptations, and tracer performance in acidic water needs further evaluation.

Acknowledgements We acknowledge the help of the local guide, Chiquinho, in showing us springs, swallets and caves in the study area. The staff at European Water Tracing Services (Belgium), Hidrovia Hidrogeologia e Meio Ambiente (Brazil), and Carste Ciência e Meio Ambiente (Brazil) helped with analyses and various aspects of this manuscript. Special thanks to Bárbara Zambelli, Caroline Reis, and Rafael Cruz for helping with data and figures and Daniel Menin for providing photograph.

References

Abbott BW, Baranov V, Mendoza-Lera C, Nikolakopoulou M, Harjung A, Kolbe T, Balasubramanian MN, Vaessen TN, Ciocca F, Campeau A, Wallin MB, Romeijn P, Antonelli P, Gonçalves J, Datry T, Laverman AM, Dreuzy JR, Hannah DM, Krause S, Oldham C, Pinay G (2016) Using multi-tracer inference to move beyond single-catchment ecohydrology. Earth Sciences Reviews 160:19–42

Almeida FFM (1977) O Cráton do São Francisco. Revista Brasileira de Geociências 7:349–364

Auler AS (2012) Quartzite caves of South America. In White WB, Culver DC (eds) Encyclopedia of Caves. Academic Press, Chennai, p. 635–639

Chaves RR, Cavalcanti IFA (2001) Atmospheric circulation features associated with rainfall variability over southern Northeast Brazil. Monthly Weather Review 129: 2614–2626

Goldscheider N, Meiman J, Pronk M, Smart C (2008) Tracer tests in karst hydrogeology and speleology. International Journal of Speleology 37:27–40

Jones WK (2012) Water tracing in karst aquifers. In White WB, Culver DC (eds) Encyclopedia of Caves. Academic Press, Chennai, p. 887–897

Kass W (1998) Tracing technique in geohydrology. A.A. Balkema, Rotterdam

Leibundgut C, Maloszewski P, Külls C (2009) Tracers in hydrology. Wiley Blackwell, Chichester

Lyons RG (1993) Identification and separation of water tracing dyes using pH response characteristics. Journal of Hydrology 152:13–29

Mecchia M, Sauro F, Piccini L, De Waele J, Sanna L, Tisato N, Lira J, Vergara F (2014) Geochemistry of surface and subsurface waters in quartz-sandstones: significance for the geomorphic evolution of tepui table mountains (Gran Sabana, Venezuela). Journal of Hydrology 511:117–138

Oba Y, Poulson SR (2012) Octanol-water partition coefficients (Kow) vs. pH for fluorescent dye tracers (fluorescein, eosin Y), and implications for hydrologic tracer tests. Geochemical Journal 46:517–520

Pedreira AJ (1997) Sistemas Deposicionais da Chapada Diamantina Centro-Oriental, Bahia. Revista Brasileira de Geociências 27:229–240

Pereira RF, Rocha AJD, Pedreira AJ, Etchevarne C, Nolasco M, Pascoal Junior OS, Torlay R (2017) Geoparque Serra do Sincorá, BA: proposta. CPRM, Brasília

Smart PL, Laidlaw IMS (1977) An evaluation of some fluorescent dyes for water tracing. Water Resources Research 13:15–33

Smart PL, Smith DI (1976) Water tracing in tropical regions, the use of fluorometric techniques in Jamaica. Journal of Hydrology 30:179–195

Wiegand J, Fey M, Haus N, Karmann I (2004) Geochimische und hydrochemischeuntersuchungzurgenese von sandstein-und quarzitkarst in der ChapadaDiamantina und imeisernviereck (Brasilien). Zeitschrift der Deutschen Geologischen Gesellschaft. 155:61–90

Wray RAL (2009) Phreatic drainage conduits within quartz sandstone: evidence from the Jurassic Precipice Sandstone, Carnarvon Range, Queensland, Australia. Geomorphology 110:203–211

Wray RAL, Sauro F (2017) An updated global review of solutional weathering processes and forms in quartz sandstone and quartzite. Earth Sciences Reviews 171:520–557

Zhu H, Derksen RC, Krause CR, Fox RD, Brazee RD, Ozkan HE (2005) Fluorescent intensity of dye solutions under different pH conditions. Journal of the ASTM International 2:1–7

Artificial Tracer Tests Interpretation Using Transfer Function Approach to Study the Norville Karst System

Vianney Sivelle, David Labat, Léa Duran, Matthieu Fournier, and Nicolas Massei

Abstract

Karstic aquifers are known for their high degree of nonlinearity and non-stationarity in their hydrodynamic behaviour. We used a transfer function approach (TFA) to interpret artificial tracer tests in Norville karst system (Normandy, France). The system's behaviour is modelled as a conceptual reservoir with an assumed transfer function containing an 'intrinsic' part and a 'boundary conditions dependent' part. Additionally, a relationship between spring discharge and residence time distribution characteristics can be formulated. This constitutes new perspectives for testing pollution scenarios.

Keywords

Karstic system • Artificial tracer test • Transfer function

Introduction

Karstic systems consist of limestones (carbonate rocks) in which a karstification process takes place. This generates a subterranean self-organized conduit networks and leads to typical surface landscapes with geomorphological features such as dolines and karren. Karstic formations are known for their highly heterogeneous underground structure and for the coexistence of three types of porosity: (1) matrix, (2) fissures and fractures and (3) conduits. This internal structure leads to high non-stationarity and nonlinearity in the hydrodynamic behaviour.

Artificial tracer tests are one of the most efficient ways to investigate such complex structure (Ford and Williams 2007). They consist in an injection of a known quantity of tracer and careful analysis of the tracer restitution at the outlet, often called breakthrough tracer curve (BTC). The next step is to determine the residence time distribution (RTD). Many studies have shown the ability of artificial tracer tests to give information on the internal structure through RTD shapes (Dewaide et al. 2016, 2017; Goldscheider 2008; Massei et al. 2006b). Here, we want to assess the ability of the transfer function approach (TFA) to establish a link between spring discharge and RTD characteristics.

Transfer Function Approach (TFA)

A systemic approach consists in studying a system from the signal transformation operated between input and output signals. The system is considered as a 'black box' who works as a filter between input and output. It is then possible to describe the system using a mathematical function linking input and output signals, called 'transfer function'. This approach is widely used in process engineering to describe chemical reactor behaviour from tracer tests (Levenspiel 2012; Walas 2005). In the same way, TFA has been applied to karstic system study, considering karstic systems as an assembly of reservoirs (Becker and Bellin 2013; Labat and Mangin 2015). However, these studies do not consider that transfer function might include some 'intrinsic' features as the geometry of the tracing system does not vary between successive tracing tests. Only boundary conditions show variability: rainfall events, run-off and piezometric levels. Here we want to assess the ability of the TFA to describe the RTD shape directly from boundary conditions, summarized

---

V. Sivelle (✉) · D. Labat
Géosciences Environnement Toulouse (UMR 5563 CNRS UPS IRD CNES), Université de Toulouse, France, 14 avenue Edouard Belin, 31400 Toulouse, France
e-mail: vianney.sivelle@get.omp.eu

L. Duran
Department of Civil, Structural and Environmental Engineering, University of Dublin Trinity College, Dublin, 2, Ireland

M. Fournier
Normandie Univ, UNIROUEN, UINCAEN, CNRS, M2C, 76000 Rouen, France

N. Massei
Place Emile Blondel, 76821 Mont Saint Aignan Cedex, France

C. Bertrand et al. (eds.), *Eurokarst 2018, Besançon*, Advances in Karst Science,
https://doi.org/10.1007/978-3-030-14015-1_22

through the spring discharge in case of non-reactive solute transport.

One of the methods most frequently used for artificial tracer tests interpretation is based on the advection–dispersion equation (ADE) introduced by Wang et al. (1987). It has been widely developed in the past decades with several modifications of the initial ADE model in order to give more precise information about solute transport in karst aquifers: dual advection–dispersion equation (Field and Leij 2012), mobile–immobile fluid model (Field and Pinsky 2000; Toride et al. 1993) and multi-dispersion model (Käss 1998; Leibundgut et al. 2009). These models are based on the use of dimensionless Péclet number. It is generally defined as the product of the effective advection velocity and the length of flow divided by the coefficient of hydrodynamic dispersion (Huysmans and Dassargues 2005). Despite the practical interest of ADE models, the physical significance of these parameters can be questionable when it represents the flow process in karstic systems over several kilometres because of their high heterogeneity (Labat and Mangin 2015).

However, the TFA provides a framework including all physical processes (advection, diffusion, dispersion and mixing) in a conceptual reservoir without defining any of these physical parameters. The TFA is based on the use of a Laplace transform of the RTD. This transformation counts various applications in the theory of probability. The Laplace transform is frequently used in chemical engineering to model the behaviour of chemical reactors. Then, a model of a perfect reactor can be derived from the shape of the theoretical particle distribution at the outlet. For example, one should consider the plug flow reactor (PFR) in which output has the same distribution as input, delayed in the time domain. Then, the real reactors are modelled through an assembly of perfect reactor models.

Here, the Norville karst system is assimilated into an assembly of chemical reactors in cascade including piston effect and mixing. The associated transfer function is given in Eq. (1) (Levenspiel 2012; Walas 2005). The cascade structure is given by the N value in the transfer function. It corresponds theoretically to a number of reservoirs in the same way as a Nash cascade (Nash 1957). Here, the Laplace framework allows dealing with non-integer N values.

$$H(p) = \alpha * \left[\frac{1}{1 + A * p}\right]^{N} * \exp[-\tau * p] \qquad (1)$$

where α is the area under the simulated curve, N is the «intrinsic» tracing system exponent, A is the mixing coefficient depending on the mean spring discharge during tracer recovery considered here to be integrating boundary conditions described by Duran et al. (2016), τ is the transit time and p is the Laplace complex variable.

Then, an optimization procedure allows the definition of the best parameters values for the model. This consists of the application of a genetic algorithm (Gordy 1996) to determine the best-fitting parameters. The optimization function is chosen as a classical Nash–Sutcliffe coefficient (Nash and Sutcliffe 1970) between experimental and simulated RTD curves.

Study Site and Tracer Tests Campaign

The Norville karst system is located in Normandy (France), near the Seine River (Fig. 1). The site has been studied since 1999 and is described in various publications (Dussart-Baptista et al. 2003; Fournier et al. 2008; Massei et al. 2002, 2003, 2006a, b). It is a part of a national observation network on karstic systems (SNO Karst).

In this study, 14 tracer tests were performed between 1999 and 2013 (Fig. 2) under various boundary conditions (Table 1). Duran et al. (2016) proposed a statistical study of the effect of boundary conditions on the RTD shapes considering several environmental variables: piezometric level, tidal coefficient, tide and rainfall events. Here we propose to improve the knowledge of the Norville karst system behaviour using a systemic approach (TFA) considering only spring discharge as it is the only hydrological variable needed to calculate the RTD.

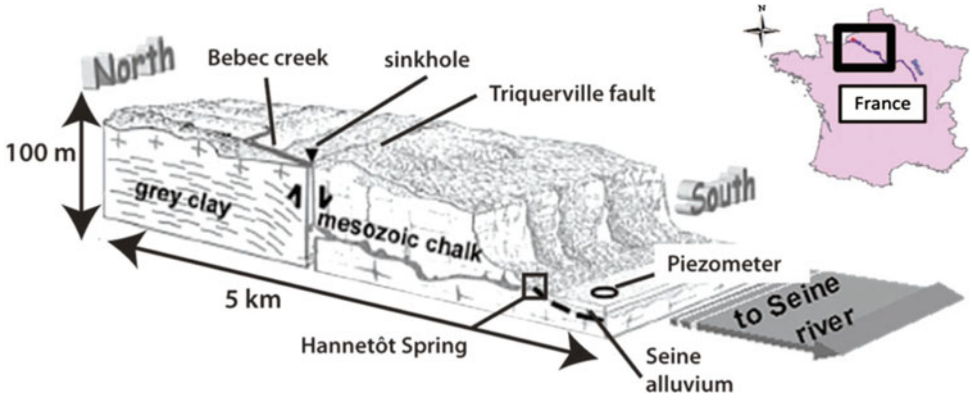

Fig. 1 Norville system (Duran et al. 2015)

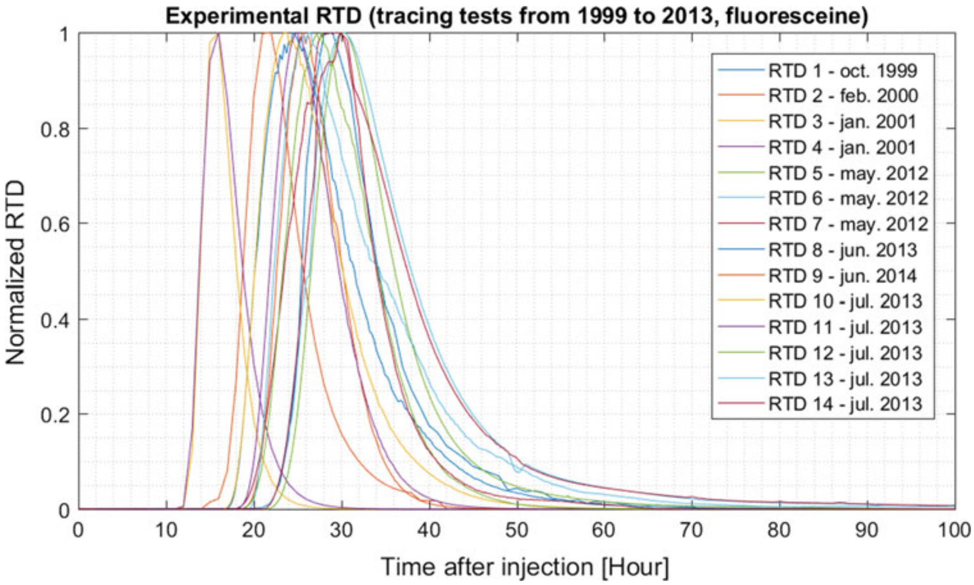

Fig. 2 Normalized residence time distribution curves (modified from Duran et al. 2015)

Results and Discussion

Parametrization of the Transfer Function

In order to determine the ‘intrinsic’ part of the transfer function, noted *N*, an optimization for *A* is done over the 14 experimental RTD considering several *N* values along a vector from 1 to 10 with a step of 0.05. An optimization function is calculated as the mean of the Nash criterion calculated over the 14 tracer tests for a given *N* value. The transfer function parameter *N* is chosen as the one that maximizes the optimization function. The ‘intrinsic’ tracing system coefficient resulting from the parametrization process is $N = 3.75$ with a mean Nash criterion equal to 97.8%, which ensure an admissible quality of the model. Table 2 synthesizes the transfer function parameters and Nash criterion for each tracer test.

Table 1 Summary of conditions for each tracer test, numbered from 1 to 14 (modified from Duran et al. 2016)

Conditions	Tracer tests
Low piezometric level	5; 6; 7
Medium piezometric level	1; 8; 9; 10 to 14
High piezometric level	2; 3; 4
High tidal coefficient	1; 2; 8; 9; 12; 13; 14
Low tidal coefficient	6; 10; 11
Low tide	4; 9; 11; 13; 14
High tide	3; 10; 12
Following rainy period	1; 2; 3; 4; 5; 8; 9
Following dry period	7; 10; 11; 12; 13
Rain during test	2; 14

The way transfer function parameters have been determined allows to describe the normalized RTD shapes but do not give information about the intensity of the peak of the RTD (so the peak of concentration) nor the time of transit in the system, as it is fixed as the experimental value. Also, the TFA enables to describe normalized RTD shapes depending on one ‘intrinsic’ parameter, noted N, and one parameter depending on the spring discharge, the mixing coefficient noted *A*.

Influence of the Mean Discharge on the Mixing Coefficient

The previous study has shown that boundary conditions (rainfall events, piezometric levels and mean discharge) are relevant to model the RTD parameters over the Norville karst system (Duran et al. 2016; Massei et al. 2006b). In this paper, we show that the TFA offers a new way to model RTD shapes from spring discharge, as it is the only hydrological variable needed to calculate the RTD.

The ‘boundary conditions dependent’ part of the transfer function (Eq. [1]) appears to be linearly anti-correlated with the mean discharge (R = −0.9), giving c (Fig. 3):

$$A_{\text{mod}} = -0.57 * \mathbf{Qm} + 311.1 \qquad (2)$$

where Qm is the mean spring discharge [l/s] during tracer restitution and A_{mod} is a theoretical value for the transfer function parameter *A* calculated from the spring discharge rate. Tracer tests 8, 9, 10 and 11 have been removed since they were done in very dry conditions (with possible dewatered drains) and appeared to be out of the area of validity of the relation between *A* and Qm (Fig. 3).

Table 2 Transfer function parameters and associated Nash criterion: α is the area under the normalized RTD curve, A is the optimized mixing coefficient, N is the tracing system exponent and τ is the transit time

Test	α	A	N	τ (min)	Nash (%)
1	649.7	160.3	3.75	1310	98.4
2	483.4	140.1	3.75	890	95.0
3	283.1	72.5	3.75	730	98.7
4	331.7	91.6	3.75	730	99.8
5	681.7	167.7	3.75	1360	99.2
6	878.4	205.4	3.75	1310	98.1
7	995.0	232.0	3.75	1135	98.9
8	783.8	164.4	3.75	1050	97.5
9	482.0	126.8	3.75	1175	98.4
10	674.9	150.5	3.75	1045	99.5
11	522.3	129.9	3.75	1135	99.6
12	687.9	170.8	3.75	1180	99.7
13	860.8	175.3	3.75	1200	88.9
14	581.0	144.2	3.75	1320	98.1

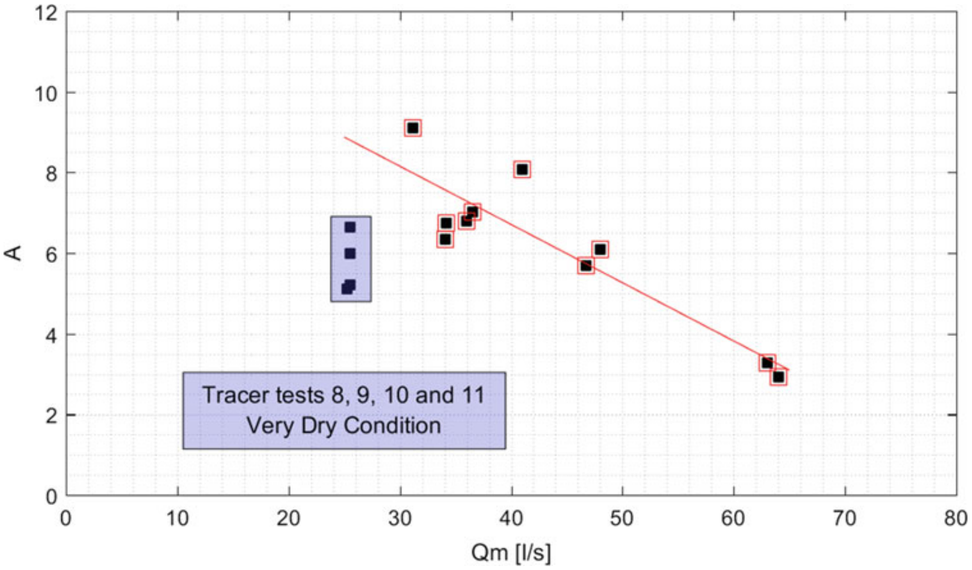

Fig. 3 Regression between mixing coefficient, noted A, and the mean discharge during tracer recovery, noted Qm: black square are experimental data, red outline are data for regression and the red line is the regression line ($R = -0.9$)

It appears that the transfer function proposed here is not well constrained for extreme discharge conditions. In case of low discharge conditions (less than 30 l/s—when the drainage system is likely to be dewatered), the mixing coefficient A shows a different relationship with discharge rate. Additionally, no tracer test has been achieved for discharge rate higher than 64 l/s, value often exceeded during winter (Fig. 4). Considering the maximal discharge over the 2013–2015 period ($Q_{\max} = 100.5$ l/s recorded on the 01/02/2015-07:00 am), Eq. (2) gives a theoretical mixing coefficient equal to 2.5, which appears to be a non-realistic value. Consequently, extrapolation appears not to be relevant to predict RTD shape in extreme conditions. Effects of change in boundary conditions on dissolved transport are well documented (Cholet 2017; Duran et al. 2016; Ender et al. 2018), but assessing these effects during flood event remains a difficult task. Several elements must be taken into consideration: (1) discharge may be subject to rapid variations during tracer transport and recovery; (2) turbulence phenomenon may occur depending on initial piezometric level (Worthington and Soley 2017) and may change transport parameters; (3) the hydraulic gradient between conduit and surrounding matrix is a key factor governing the dissolved transport. This has been investigated on a reduced scale (Li et al. 2008; Mohammadi et al. 2018) but still well misunderstood in real karst aquifers. Therefore, the limits of validity of the relation between transfer function parameter and spring discharge are here defined as the minimum and

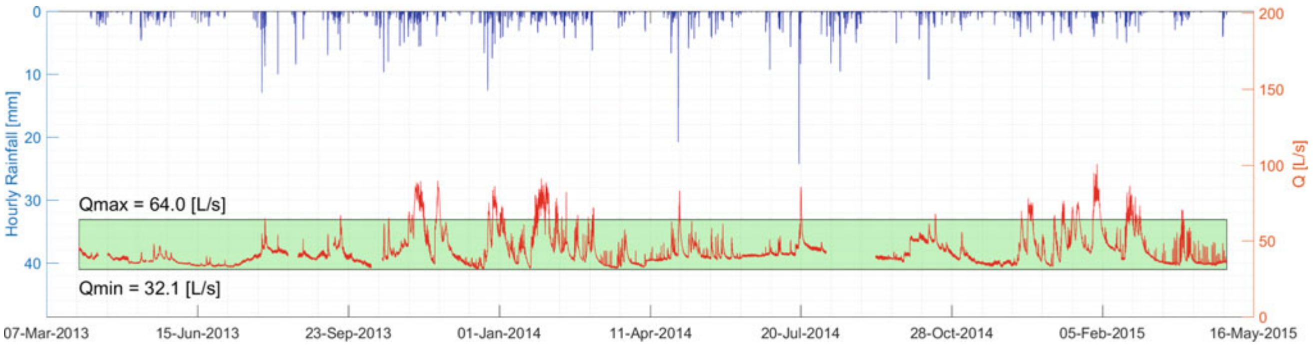

Fig. 4 Rainfall–run-off time series in Norville: green rectangle gives the domain of validity of the transfer function depending on the spring discharge

maximum discharge rates observed during the set of tracer tests considered in the regression between mixing coefficient *A* and mean discharge Qm (Fig. 4).

Discussion

Duran et al. (2016) find out that the mean discharge, associated with other environmental variables, is a relevant variable in the determination of the RTD parameters. Also, this variable is as important as a piezometric level or tide coefficient. However, we show here that using TFA, it is possible to link mean discharge to the RTD shape in a wide range of discharge values, except for extreme values (low water and floods). The linear anti-correlation between the parameters A of the transfer function and the mean discharge during tracer tests shows an anti-correlation coefficient of −0.9. It can be considered to be a great level of confidence. Nonetheless, this regression is done on a narrow number of samples (10 tracer tests), corresponding to various boundary conditions. Ideally carrying additional tracer tests would be useful to confirm the observed linear relationship. However, four tracer tests achieved in low discharge condition, with possibly dewatered drain, show a different relationship between transfer function parameter and the mean discharge.

The model has been built in a way that the parameters represent both ‘intrinsic’ and ‘boundary conditions dependent’ features. The transfer function we proposed here is calibrated on the Norville karst system for various boundary conditions in a certain range of spring discharge values. The proposed transfer function appears to be valid as long as the spring discharge is comprised between 32.1 and 64.0 l/s, that is to say, a range characteristic of the regular hydrologic behaviour of the system across the hydrological year (excepting extreme events). In order to better constrain the validity domain and to obtain a more robust model, additional data are necessary. Tracing tests carried out in extreme conditions would be useful to possibly extend the validity of the model, as an extrapolation of the model appears not to be relevant in this case.

Conclusion

Duran et al. (2016) established a model giving the expression of the RTD parameters as a function of environmental variables, including the mean discharge during artificial tracer tests. Here, we propose a new model in order to predict RTD shapes from spring discharge including an ‘intrinsic’ part and a ‘boundary condition dependent’ part.

The TFA gives a new way to deal with nonlinearity in karst aquifers behaviour. It is possible to determine the validity domain of a model based on TFA. The limits of the validity domain could be considered as a change in the aquifer behaviour. If there is a change in the transfer function, it could correspond to a change in the conceptual representation of the tracing system. In case of the Norville karst system, we show that a TFA allows describing the RTD shapes from the spring discharge in a range of values large enough to describe the behaviour of Norville karst system. Nonetheless, there is a lack of knowledge of using TFA to describe the extreme event (low and high discharge rates).

At this stage, it is important to notice that this model allows only to predict RTD shapes, but do not allow to predict the intensity of the peak of the RTD nor the transit time. Nonetheless, it has been shown that discharge could be a confident variable to predict the RTD shape of the Norville karst systems. As the discharge must be determined in order to calculate the RTD, the model proposed here can be applied to other karst systems where other hydrological variables are not monitored.

More investigations must be done to refine and validate the relationship between hydrologic variables and transfer function parameters. We encourage the karst community to test this approach in various karstic systems.

References

Becker, M., Bellin, A., 2013. A reservoir model of tracer transport for karstic flow systems. Hydrogeol J 21, 1011–1019. https://doi.org/10.1007/s10040-013-0991-2

Cholet, C., 2017. Fonctionnement hydrogéologique et processus de transport dans les aquifères karstiques du Massif du Jura (Thèse de Doctorat). Université de Bourgogne Franche-Comté

Dewaide, L., Bonniver, I., Rochez, G., Hallet, V., 2016. Solute transport in heterogeneous karst systems: Dimensioning and estimation of the transport parameters via multi-sampling tracer-tests modelling using the OTIS (One-dimensional Transport with Inflow and Storage) program. Journal of Hydrology 534, 567–578. https://doi.org/10.1016/j.jhydrol.2016.01.049

Dewaide, L., Collon, P., Poulain, A., Rochez, G., Hallet, V., 2017. Double-peaked breakthrough curves as a consequence of solute transport through underground lakes: a case study of the Furfooz karst system, Belgium. Hydrogeology Journal. https://doi.org/10.1007/s10040-017-1671-4

Duran, L., Fournier, M., Massei, N., Dupont, J.-P., 2016. Assessing the Nonlinearity of Karst Response Function under Variable Boundary Conditions. Ground Water 54, 46–54. https://doi.org/10.1111/gwat.12337

Dussart-Baptista, L., Massei, N., Dupont, J.-P., Jouenne, T., 2003. Transfer of bacteria-contaminated particles in a karst aquifer: evolution of contaminated materials from a sinkhole to a spring. Journal of Hydrology 284, 285–295. https://doi.org/10.1016/j.jhydrol.2003.08.007

Ender, A., Goeppert, N., Goldscheider, N., 2018. Spatial resolution of transport parameters in a subtropical karst conduit system during dry and wet seasons. Hydrogeol J 1–15. https://doi.org/10.1007/s10040-018-1746-x

Field, M.S., Leij, F.J., 2012. Solute transport in solution conduits exhibiting multi-peaked breakthrough curves. Journal of Hydrology 440–441, 26–35. https://doi.org/10.1016/j.jhydrol.2012.03.018

Field, M.S., Pinsky, P.F., 2000. A two-region nonequilibrium model for solute transport in solution conduits in karstic aquifers.pdf. Journal of Contaminant Hydrology 44, 329–351

Ford, D., Williams, P.D., 2007. Karst Hydrogeology and Geomorphology. John Wiley & Sons, Inc

Fournier, M., Massei, N., Mahler, B.J., Bakalowicz, M., Dupont, J.P., 2008. Application of multivariate analysis to suspended matter particle size distribution in a karst aquifer. Hydrol. Process. 22, 2337–2345. https://doi.org/10.1002/hyp.6828

Goldscheider, N., 2008. A new quantitative interpretation of the long-tail and plateau-like breakthrough curves from tracer tests in the artesian karst aquifer of Stuttgart, Germany. Hydrogeology Journal 16, 1311–1317. https://doi.org/10.1007/s10040-008-0307-0

Gordy, M.B., 1996. Genetic Algorithms toolbox for Matlab

Huysmans, M., Dassargues, A., 2005. Review of the use of Péclet numbers to determine the relative importance of advection and diffusion in low permeability environments. Hydrogeology Journal 13, 895–904. https://doi.org/10.1007/s10040-004-0387-4

Käss, W., 1998. Tracing Technique in Geohydrology, 1st ed. CRC Press

Labat, D., Mangin, A., 2015. Transfer function approach for artificial tracer test interpretation in karstic systems. Journal of Hydrology 529, 866–871. https://doi.org/10.1016/j.jhydrol.2015.09.011

Leibundgut, C., Maloszewski, P., Külls, C., 2009. Artificial Tracers, in: Tracers in Hydrology. John Wiley & Sons, Ltd, pp. 57–122

Levenspiel, O., 2012. Tracer Technology, Fluid Mechanics and Its Applications. Springer New York, New York, NY

Li, G., Loper, D.E., Kung, R., 2008. Contaminant sequestration in karstic aquifers: Experiments and quantification. Water Resources Research 44. https://doi.org/10.1029/2006WR005797

Massei, N., Dupont, J.P., Mahler, B.J., Laignel, B., Fournier, M., Valdes, D., Ogier, S., 2006a. Investigating transport properties and turbidity dynamics of a karst aquifer using correlation, spectral, and wavelet analyses. Journal of Hydrology 329, 244–257. https://doi.org/10.1016/j.jhydrol.2006.02.021

Massei, N., Lacroix, M., Wang, H.Q., Mahler, B.J., Dupont, J.P., 2002. Transport of suspended solids from a karstic to an alluvial aquifer: the role of the karst/alluvium interface. Journal of Hydrology 260, 88–101. https://doi.org/10.1016/S0022-1694(01)00608-4

Massei, N., Wang, H.Q., Dupont, J.P., Rodet, J., Laignel, B., 2003. Assessment of direct transfer and resuspension of particles during turbid floods at a karstic spring. Journal of Hydrology 275, 109–121. https://doi.org/10.1016/S0022-1694(03)00020-9

Massei, N., Wang, H.Q., Field, M.S., Dupont, J.P., Bakalowicz, M., Rodet, J., 2006b. Interpreting tracer breakthrough tailing in a conduit-dominated karstic aquifer. Hydrogeology Journal 14, 849–858. https://doi.org/10.1007/s10040-005-0010-3

Mohammadi, Z., Gharaat, M.J., Field, M., 2018. The Effect of Hydraulic Gradient and Pattern of Conduit Systems on Tracing Tests: Bench-Scale Modeling. Groundwater. https://doi.org/10.1111/gwat.12659

Nash, J.E., 1957. The form of the instantaneous unit hydrograph. International Association of Scientific Hydrology, Publ 3, 114–121

Nash, J.E., Sutcliffe, J.V., 1970. River flow forecasting through conceptual models part I—A discussion of principles. Journal of Hydrology 10, 282–290. https://doi.org/10.1016/0022-1694(70)90255-6

Toride, N., Leu, F.J., Van Genuchten, M.T., 1993. A Comprehensive Set of Analytical Solutions for Nonequilibrium Solute Transport With First-Order Decay and Zero-Order Production. Water Resources Research 29, 2167–2182

Walas, S.M., 2005. Chemical reaction engineering handbook of solved problems. Gordon and Breach

Wang, H.Q., Crampon, N., Huberson, S., Garnier, J.M., 1987. A linear graphical method for determining hydrodispersive characteristics in tracer experiments with instantaneous injection. Journal of Hydrology 95, 143–154. https://doi.org/10.1016/0022-1694(87)90121-1

Worthington, S.R.H., Soley, R.W.N., 2017. Identifying turbulent flow in carbonate aquifers. Journal of Hydrology 552, 70–80. https://doi.org/10.1016/j.jhydrol.2017.06.045

Detailed Water Quality Monitoring at Various Points of the Krásnohorská Cave System (Slovakia)

Peter Malík, Juraj Michalko, Alexandra Pažická, Branislav Máša, and Jaroslav Stankovič

Abstract

Detailed karstic water quality monitoring was performed in the Krásnohorská Cave system in the Slovenský kras Mts./Silická planina karstic plateau formed by Triassic limestones. The cave itself is 1550 m long, formed by a huge underground stream that can be followed in more than 400-m-long corridor. Here, two small visible side inlets to the stream are found. Some 100 metres above the cave entrance underground stream disappears in a siphon to emerge on the ground surface as a Buzgó karstic spring (5.3–1355.8 L s^{-1} discharge). Two other (but smaller) karstic springs are situated on the foot of the same karstic plateau within a distance of 200 m from the Krásnohorská Cave entrance, with yet unknown karstic network behind. 150-m-deep hydrogeological borehole RHV-4, exploited as drinking water source for the neighbouring village, is situated just in front of the Krásnohorská Cave entrance. Water at six monitoring points—both side inlets to the major underground stream and its end point (spring at the cave entrance), as well as smaller side springs and the borehole outside were regularly sampled for chemistry, $\delta^{18}O$, δ^2H and tritium content in the period of June 2015–June 2016. Approximate weekly samplings were accompanied by precipitation sampling in the same extent, but in two weeks interval. Surprisingly high stability of karstic groundwater chemical composition was found. Content of dissolved HCO_3^-, Ca^{2+}, Mg^{2+}, K^+, Na^+, Cl^- and NO_3^- remained unchanged even in the period of 20-fold raise of discharge of the Buzgó spring during the snowmelt period in February/March 2016. Results of 573 chemical analyses also show a great similarity of karstic groundwater chemical composition at different monitoring points. This was not the case of SO_4^{2-}. Results of analyses pointed out that one part of the water circulation system is influenced by dissolved sulphates of geogenic origin, very probably occurring in Lower Triassic shales. These were not found in the outcrops in the recharge area, but their strong influence on water chemistry is characteristic. Groundwater flow rates of partial water circuit which is passing shales with sulphates seem to be more stable. Sulphate content is then diluted at high water stages and increases with groundwater depletion in respective monitoring points. Mean values of $\delta^{18}O$ and δ^2H are very similar at all monitoring points, found in the narrow intervals of −9.48 to −9.04‰ and −64.5 to −61.3‰, respectively. Recharging precipitation in the monitored period was somewhat heavier (−8.77 and −60.6‰) although the altitudinal difference of sampling places was more than 230 m. Comparing individual samplings in time series, $\delta^{18}O$ differences may reach the range of 1.47‰ comparing to the 0.44‰ span of mean values (ranges of up to 10.7‰ in individual samplings and 3.2‰ in mean values for δ^2H). Time series of $\delta^{18}O$ and δ^2H therefore point to different patterns/different mean transit times of water circulation at individual monitoring points.

Keywords

Water quality monitoring • Karstic groundwater • Chemistry time series • Stable isotopes

---

P. Malík (✉) · J. Michalko · A. Pažická
Štátny geologický ústav Dionýza Štúra—Geological Survey of Slovak Republic, Mlynská dolina 1,
817 04 Bratislava 11, Slovakia
e-mail: peter.malik@geology.sk

B. Máša
HES - COMGEO, spol. s r.o., Kostiviarska Cesta 4,
974 01 Banská Bystrica, Slovakia
e-mail: branislav.masa@hes-comgeo.sk

J. Stankovič
Speleoklub Minotaurus, Edelényska 10,
048 01 Rožňava, Slovakia
e-mail: stankov@ke.psq.sk

C. Bertrand et al. (eds.), *Eurokarst 2018, Besançon*, Advances in Karst Science,
https://doi.org/10.1007/978-3-030-14015-1_23

Introduction

Karst aquifers may offer perspective drinking water sources for the large areas. However, high vulnerability of karstic groundwater resources requires appropriate caution in securing sustainable water quality. In general, rapid changes of groundwater dynamics and existence of conduits with concentrated flow are typical for karstic aquifers (Bakalowicz 2005; Goldscheider and Drew 2007). Thin soils on karstified surface, point recharge in dolines, shafts and swallow holes, as well as concentration of flow in the epikarst and vadose zone are decreasing the contaminant attenuation capacity of karstic aquifers. Contaminants may easily reach groundwater, where they are rapidly transported in karstic conduits over large distances. The residence time of contaminants in the system is often short and their interaction with the aquifer limited, so many processes of contaminant attenuation like filtration and adsorption, as well as chemical and microbiological decay, often do not work effectively in karst systems (Zwahlen et al. 2004). High frequency monitoring of groundwater quality contributes to better understanding of hydrogeological functioning of karst aquifer systems (Fournier et al. 2007; Mudarra et al. 2013). Having this in mind, proper and detailed groundwater quality monitoring covering all seasonal changes needs to be performed before the karstic water source can be exploited for mass consumption. This study was focused on major Buzgó karstic spring and smaller side springs Pod kameňolomom and Pri kaplnke in the area of underground hydrological system of the Krásnohorská jaskyňa cave (southern Slovakia). Together with already exploited hydrogeological borehole RHV-4 nearby, these represent an important perspective drinking water sources for the whole neighbouring region.

The objective of this study was to evaluate changes of groundwater chemical composition in time by frequent sampling for all aforementioned groundwater sources, to ensure reliability of water quality during its possible use in the future. Precipitation quality was monitored in the same analytical extent on the top of the karstic plateau on the places where the recharge of the karstic aquifer is supposed to take place. To estimate the possible patterns of water circulation between water recharge and its output from the karstic system, hydrogen and oxygen isotopes were studied at the same monitoring points. All these activities were performed within the framework of the EU LIFE+ project LIFE11ENV/SK/001023, entitled “Implementation of Sustainable Groundwater Use in the Underground Karst System of the Krásnohorská jaskyňa Cave” (acronym: KRASCAVE). Together 600 samples were taken from 6 different karst groundwater sources plus one precipitation station within approximately one-year period (May 2015–June 2016) to evaluate seasonal changes of groundwater quality.

Study Site Characteristics

Krásnohorská jaskyňa cave is located at the northern rim of the Silická planina Plateau, southeast of the village Krásnohorská Dlhá Lúka, Rožňava region, Slovakia (Fig. 1). It is 1355-m-long typical outflow fluviokarstic cave with active conduit. The cave was discovered in 1964 by lowering the water level in the output siphon as described in the works of several authors (Roda 1964; Skřivánek 1965; Erdös 1995). The most comprehensive description of the Krásnohorská jaskyňa cave is summarised in the monographic book by Stankovič and Cílek eds. (2005).

Starting from its entry through artificially excavated gallery (Fig. 1), the cave is progressing along the water course in the active length of about 400 m. In the above-situated massive vertical hall (Sieň obrov/Hall of the Giants), the visitor meets a huge speleothem—sinter column (Kvapeľ rožňavských jaskyniarov/Rožňava cavers’ column). It has a height of 32.7 m, with several separate stories. At the time of its discovery, the stalagmite was considered to be one of the largest stalactites in the world (Roda 1966). From this place, the active conduit continues in the next 100 m through a narrow corridor up to the underground lake of Marikino jazero (Lake of Marika) marked as “M” in Fig. 1. Siphon of Marikino jazero, 120 m long and 28 m deep, was surpassed in 1982 (Stankovič and Cílek 2005). Behind this siphon, cave continues in some 250 m along the underground stream. Another 15-m-long siphon leads to the cave’s terminating point in the Suťový Dome, where the stream disappears beneath a mass of collapsed blocks. Passages behind the Marikino jazero siphon are not shown on the cave map in Fig. 1.

According to Gaál in Stankovič and Cílek (2005), northern part of the Krásnohorská jaskyňa cave is cutting grey Middle Triassic Gutenstein dolomites, partly also Gutenstein limestones (passages from its entrance up to the Hall of Giants; Fig. 1), the rear (southern) part is modelled in the light grey, also Middle Triassic, Steinalm limestone. In the neighbouring parts of northern slope of the Silická planina Plateau, both to the east and west, the Szin layer aquitard is uplifted high above the alluvium (Mello et al. 1996). Such geological and geomorphological situation enables karst water output from the plateau only in an 800-m-wide corridor along the place where major karstic spring of Buzgó is located. In the cave, remnants of an

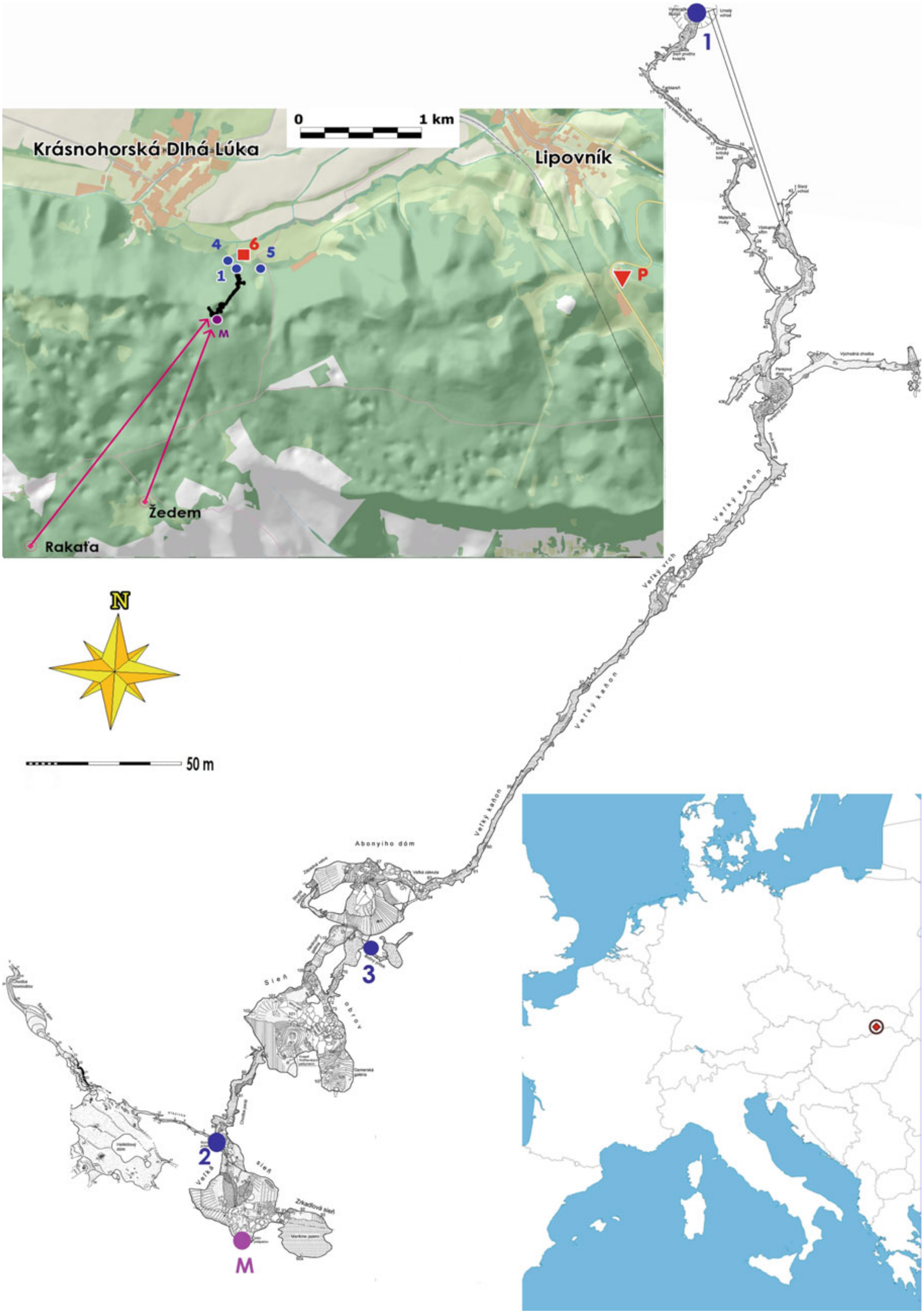

Fig. 1 Position of the Krásnohorská jaskyňa Cave in Slovakia, monitored groundwater sources (marked from 1 to 6), siphon of Marikino jazero (M), precipitation station (P) and results of referenced tracer tests (violet arrows). Cave map according to Stankovič (2003)

earlier level are preserved, located 35–40 m above the contemporary erosive base. This level also corresponds to the level of the Pleistocene terrace of Mindel period, preserved on the left bank of the Čremošná stream. The cave is located in a zone of intensive tectonic activity, a significant vertical fault of the NE–SW direction followed by the corridor of Veľký kaňon (Grand Canyon) is supposed to be recently active (Gaál 2008). Based on detailed geological mapping in the area, Kronome and Boórová (2016) found the importance of gravitational slope movements in the area and especially near the margins of the karst plateau. Here they form oblique crevasses, and the cave itself is supposed to be developed on such a gravitational slide plane.

Mean annual precipitation totals in the area slightly above 700–703 mm were recorded at the Rožňava station, 318 m a.s.l and 5 km NW from the cave, and totals of 725 mm were reported at the top of the Silica plateau, station Silica, 541 m a.s.l. and 9 km SW from the cave. Observations here were run since 1931 (Rožňava) and 1971 (Silica). Average air temperature recorded in Rožňava was 8.9 °C (1972–2016 period); in Silica at higher altitude it was 8.1 °C for the same period. Stable air temperature of 9.2 °C is preserved all over the year inside the cave (Stankovič and Cílek 2005).

The main hydrogeological feature of the Krásnohorská jaskyňa cave is represented by permanent underground stream. It is leaving the cave as a karstic spring of Buzgó. Spring's discharge and water temperature is gauged since 1958 by Slovak Hydrometeorological Institute (SHMI) having the catalogue number of 1862. Observations were briefly interrupted in the period of 1966–1967. Since 1983, weekly intervals of observations were replaced by daily observation frequency and since 2011 hourly data are available. Approximately 200 m eastwards from Buzgó, we find another karstic spring Pod kameňolomom (Under the Quarry; SHMI catalogue No. 1861; weekly observations in 1968–1992). Its mean discharge is 8.71 L s^{-1}; archived records were ranging from 0.59 to 88.0 L s^{-1}. Another small groundwater outlet is located approximately 100 m west of the Buzgó spring at a traditional Christian pilgrim place. Consequently, it has a characteristic naming Pri kaplnke (By the Chapel; SHMI catalogue No. 1863; observations in 1957–1965). Unfortunately, discharge time series are lost and only range of values was preserved: 0.10–6.5 L s^{-1}. Position of springs is shown in Fig. 1.

Karstic spring of Buzgó, outlet of the underground flow leaving the Krásnohorská jaskyňa cave, shows a high discharge variability according to the SHMI gauging monitoring through more than 50 years. The observed discharge maximum documented on August 10, 2002 was 1355.8 L s^{-1} and the minimal yield 5.3 L s^{-1} was observed in February 1987. The long-term mean yield of the Buzgó spring is 55.1 L s^{-1}. Highest discharges are usually recorded in the snowmelt period (February–April), although rainy storm events and intensive regional rainfalls may cause irregular intensive yield increase, especially from May to October. Low discharge values tend to occur in the periods of significant reduction in effective precipitation by evapotranspiration or periods of water accumulation in the snow cover, generally in the period from July to February.

Resistivimetry and thermometry on the longitudinal profile of the underground stream to identify additional inlets in the cave was performed by Malík et al. (2011). No inlets were found. Malík et al. (2014) also tried to estimate karstification degree of the surrounding limestone massif according to the discharge recession curves of Buzgó and Pod kameňolomom springs. Spatial changes of microclimatic parameters during the summer ventilation mode in the Krásnohorská jaskyňa cave atmosphere were described by Kováčová et al. (2017).

Two positive tracing tests help us to reveal the extent of the infiltration area of the Buzgó spring. The first tracer test was described by Erdös (1995). In 1967, the dye trace released near the swallow hole of Rakaťa occurred after 25 h in the cave. The second tracing experiment linking the cave with the well of Žedem was mentioned by Roda et al. (1986). On the other hand, Ščuka in Stankovič and Cílek eds. (2005), describes a repeated tracer test in the well of Žedem, aimed to distinguish infiltration areas of the Buzgó spring and Vápenná vyvieračka spring (south from the area). The tracer did not appear at any of the two springs, probably due to limited water circulation as this test was performed in a dry period.

In front of the cave entrance, 60 m NE from the Buzgó spring, 150-m-deep borehole RHV-4 was drilled to investigate local hydrogeological settings (Orvan and Vrábľová 1986). In its borehole log, at a depth of 83.5 m Lower Triassic shales underlay the limestones of Middle Triassic. The borehole is nowadays exploited as a source for public drinking water supply, with maximal groundwater abstraction of 2 L s^{-1}.

Materials and Methods

Water samples of the two side inlets of the major underground stream of the Krásnohorská jaskyňa Cave, three karstic springs (Buzgó, Pod kameňolomom, Pri kaplnke) and the RHV-4 borehole were regularly sampled for dissolved bicarbonates, calcium, magnesium, nitrates, chlorides, sulphates, potassium and sodium, δ18O, δ2H and tritium content in the period of May 31, 2015–June 30, 2016. The main output of the Krásnohorská jaskyňa Cave underground hydrologic system—karstic spring Buzgó—was sampled just at the point of the spring's orifice (No. 1 in Fig. 1). One sampled inlet to the main underground stream is bringing water from the area of the Helictite Dome from its left side

(No. 2), and one from the opposite side in the area of Abonyi Dome (No. 3). It should be noted that discharge of both inlets, proven by measurements of Bajtoš et al. (2017), does not represent more than 10% of the total discharge of the Buzgó spring, as majority of water comes out from the siphon under the Marikino jazero Lake (marked as "M" in Fig. 1). Due to its limited accessibility, this point was not sampled in the sampling campaign described here, but several samples were taken from this siphon on other occasions (Bajtoš et al. 2017). Groundwater of two smaller karstic springs, Pod kameňolom (No. 4) some 200 m east and Pri kaplnke (No. 5) some 100 m west from the entrance of the Krásnohorská jaskyňa Cave was sampled as well on their orifices. The last groundwater sampling point (No. 6) was the 150-m-deep hydrogeological borehole RHV-4. Precipitation sampling was performed using plastic funnel, hosepipe and tank (IAEA 2002) on the roof of the restaurant on the Soroška pass (Silická planina Plateau—supposed recharge area of the sampled karstic springs). This sampling place is marked as "P" in Fig. 1. Apart from this figure, position of the monitored sites with topographical information and brief description is also specified in Table 1. Approximate weekly sampling was performed on sites 1, 4, 5 and 6. Due to their accessibility, samples within the cave (2 and 3) were taken approximately in two weeks interval. This was also the case of precipitation sampling, where cumulative samples were collected also in two weeks interval.

Plastic bottles with screw cap, 1 or 2 litres in volume (dependent on laboratory material available) were used for water chemistry analyses—bicarbonates (HCO_3^-), calcium (Ca^{2+}); magnesium (Mg^{2+}); nitrates (NO_3^-); chlorides (Cl^-); sulphates (SO_4^{2-}), potassium (K^+) and sodium (Na^+). Bottles were three times flushed by the sampled water and finally filled by this up the cap that was tightly screwed afterwards. Samples were not filtrated, cation fixing by reagents and the dosage of HCO_3^- on the site were also not performed. As suggested by the laboratory, samples were stored in a cooling box and transported within the period of one day to the hydrochemical laboratory of Ingeo Envilab Žilina, Slovakia. Standardised procedures were used to analyse the individual components here: titration analysis for bicarbonates and chlorides; titration analysis to the complex for calcium and magnesium; isotachophoresis for nitrates and sulphates; atomic absorption spectrometry (AAS) in flame for potassium and sodium.

Water samples for the stable isotopes analysis were collected into glass bottles of 100 ml capacity, at a depth of 0.1 m bellow water level, if possible. Bottles were fully filled and air bubbles inside eliminated before capping. Precipitation water was cumulatively collected following the guidelines of the Isotope Hydrology Laboratory, International Atomic Energy Agency (IAEA 2002). Every two weeks, all the amount of the precipitation collected in plastic tank was transferred into a glass bottle, tightly capped and sent directly to the laboratory for analysis of its isotopic composition. Upon the arrival into the laboratory, 200 µl for δ^2H and 500 µl for $\delta^{18}O$ measurements were pipetted into vials of 12 ml capacity for triplicate stable isotope analysis per sample. For stable isotope analyses, the Gas Bench II device connected to the Continuous Flow Isotope Ratio Mass Spectrometer (CF-IRMS) Delta V Advantage from

Table 1 List of monitored sites with topographical information and brief description. IDs of monitored sites are the same as on Fig. 1

ID	Monitored site name	Altitude (m)	Lon	Lat	Description
1	Buzgó karstic spring	311	20.58894	48.61825	Karstic spring orifice at the entrance of the Krásnohorská jaskyňa Cave
2	Helictite Dome subsurface inlet	313	20.58711	48.61435	Left side inlet to the main underground stream of the Krásnohorská jaskyňa Cave from the area of the Helictite Dome
3	Abonyi Dome subsurface inlet	312	20.58775	48.61494	Right side inlet to the main underground stream of the Krásnohorská jaskyňa Cave in the area of the Abonyi Dome
4	Pod kameňolom karstic spring	311	20.59164	48.61835	Karstic spring some 200 m east from the entrance of the Krásnohorská jaskyňa Cave
5	Pri kaplnke karstic spring	310	20.58794	48.61885	Karstic spring some 100 m west from the entrance of the Krásnohorská jaskyňa Cave
6	RHV-4 borehole	311	20.58966	48.61933	150 m deep hydrogeological borehole RHV-4 drilled in 1986 some 50 m north from the entrance of the Krásnohorská jaskyňa Cave; nowadays municipal drinking water source
P	Soroška precipitation station	548	20.63201	48.61898	Improvised precipitation quality monitoring station placed on the roof of the restaurant on the Soroška pass

Thermo Fisher was used. This periphery is the system with the special Valco loop used for repetitive injection of gases and allowed δ^2H and δ^{18}O measurements based on the equilibration method, where about mill mole amount of equilibration gas (0.5% CO_2 in He for oxygen and 2% H_2 in He for hydrogen analysis) is brought into isotopic equilibration with a few µl of water sample. The minimal equilibration time for δ^{18}O measurements was 20 h, and in the case of δ^2H measurements, platinum catalysts were used for acceleration the equilibration time. The conversion of investigated compound into simple gases is the principle of isotope ratio mass spectrometry. The results of deuterium and oxygen—18 analyses were expressed by standard delta notation in ‰ as the ratio of the deuterium and oxygen—18 abundance in water samples and in the reference gas. Calibration was performed against the internal and LGR standards, and the results are reported relative to the Vienna Standard Mean Ocean Water (VSMOW). The precision of the deuterium and oxygen 18 analysis was in the range ±0.5‰ and ±0.07‰, respectively.

For tritium content detection, water samples were collected into plastic bottles of 1000 ml capacity and sent to Hydrosys Labor Analytical Laboratory Ltd. (Budapest, Hungary). The samples were analysed by MSZ 19387:1987 standard, with measurement error of ±0.05 Bq/l (±0.42 TU).

Results and Discussion

Statistic on individual water quality components in the underground hydrologic system of the Krásnohorská jaskyňa Cave and precipitation water is listed in Table 2.

Sampled groundwater within and around the Krásnohorská jaskyňa cave underground hydrological system shows very similar features. Concerning bicarbonates (HCO_3^-; Table 2) their content was varying between 293 and 405 mg L^{-1}. Systematically highest values were found in groundwater of Abonyi Dome inlet (No. 3) and lowest ones in RHV-4 borehole (No. 6). Figure 2 clearly shows that individual sampled sources keep relative stability of bicarbonate content (Abonyi Dome inlet > Buzgó spring > Pod kameňolomom spring ≈ Pri kaplnke spring > Helictite Dome inlet > RHV-4 borehole) during the low flow period. For Abonyi Dome inlet, Buzgó spring, Helictite Dome inlet and RHV-4 borehole this relative order and seems to stay undisturbed by high water stages in February 2016 when discharges of the Buzgó spring twice exceeded 1000 L s^{-1} (Fig. 2). For nearly two weeks (February 11–24, 2016) discharge was constantly higher than 500 L s^{-1}, more than 20-fold of the median discharge value of 22.5 L s^{-1} in the monitored period.

In the case of Pod kameňolomom and Pri kaplnke springs, the reaction to increased discharge is different. Bicarbonate content in Pri kaplnke springs increases with the discharge, while Pod kameňolomom seems to be diluted. Their maximal difference is of 46 mg L^{-1}. The same reaction of these two springs was visible also in minor discharge increase at Buzgó (from approximately 10 to 70 L s^{-1}) in October 2015. Again, HCO_3^- content at Pri kaplnke reacted by increase in 30 mg L^{-1}, while in water of Pod kameňolomom decreased in 20 mg L^{-1}. Interestingly, period of decrease was quite short and within 10 days, Pod kameňolomom spring was of higher HCO_3^- content than that of Pri kaplnke again, but both were in some 10–15 mg L^{-1} higher than in the preceding summer period. In the case of the Helictite Dome inlet, its reaction to major flood event cannot be evaluated as this source could not the sampled at high water stages. During the discharge recession, bicarbonate content in Pod kameňolomom gradually prevails over bicarbonate content in Pri kaplnke, although differences there are less than 8 mg L^{-1}. Effect of high water stage is visible on bicarbonate dilution (decrease in some 20 mg L^{-1}) in RHV-4 borehole, which appeared approximately with one month delay (Fig. 2).

Calcium (Ca^{2+}) and magnesium (Mg^{2+}) contents (Table 2) indicate presence of pure limestone and lesser extent of dolomitic layers in the recharge area of the Krásnohorská jaskyňa cave underground hydrological system. However, comparison of magnesium content in individual sampled sources (Fig. 3) seems to mark differences. While in Helictite Dome inlet (No. 2) the highest Mg^{2+} content is found, it is also the most variable (from approximately 15 to 32 mg L^{-1}) among all monitored sources and seems to be highly dependent on water stages indicated by Buzgó spring discharge. On the contrary, another subsurface inlet in the cave (Abonyi Dome; No. 3) is very stable in Mg^{2+} content while the lowermost median values of all sampled groundwater sources are found here (Table 2, Fig. 3). Despite the presence of dolomites, Mg^{2+} is not high (Table 2). It does not seem to vary with the same processes as bicarbonate and calcium. Then, it is possible to establish a link between Buzgó spring and Pri kaplnke spring. Observations on Table 2 can be made also on Fig. 4. There is a possible relationship between Abonyi inlet and Pod kameňolom spring (Fig. 5).

Sodium and potassium contents with their values between 0.8 and 2.0 mg L^{-1} (Na^+) and between 0.2 and 0.7 mg L^{-1} (K^+) document the minor influence of alkali sources on groundwater quality in karst areas uninfluenced by human activities (Table 2). Dissolved chloride (Cl^- content ranging from 0.1 to 5.0 mg L^{-1}) corresponds to merely atmospheric input without any sign of geogenic chlorine sources (Table 2). Nitrate content found in all sampled sources also

Table 2 Overview of groundwater quality components at different monitored sources within Krásnohorská jaskyňa Cave and its vicinity and precipitation water on the nearby Soroška pass in the period of May 31, 2015–June 30, 2016

Site no.		1	2	3	4	5	6	7
Site name		Buzgó karstic spring	"Heliktite Dome" subsurface inlet	"Abonyi Dome" subsurface inlet	Pod kameňolom karstic spring	Pri kaplnke karstic spring	RHV-4 borehole	Precipitation
HCO_3^-	Min–Max	340–384	326–345	389–405	317–369	334–375	293-323	4–18
	Avg.	372.6	338.8	398.4	357.7	356.3	313.0	8.5
	Median	374.0	340.0	398.0	359.0	356.5	313.0	8.0
	st. dev.	6.5	4.5	4.3	7.3	10.1	4.7	3.6
Ca^{2+}	Min–Max	112–133	108–190	133–143	111–130	113–126	103–123	1–10
	Avg.	126.6	140.9	138.3	122.0	120.8	112.8	2.8
	Median	127.0	138.5	139.0	123.0	120.5	112.0	2.0
	st. dev.	3.5	22.6	3.1	2.7	2.3	3.5	2.1
Mg^{2+}	Min–Max	2.9–14.1	15.1–31.9	1.0–5.4	1.0–7.8	5.4–13.6	11.7–22.4	1.0–2.4
	Avg.	9.8	23.9	3.3	5.0	9.8	17.0	1.1
	Median	10.0	23.5	3.4	4.9	9.9	17.0	1.0
	st. dev.	2.0	4.4	1.0	1.4	1.4	1.6	0.3
Na^+	Min–Max	0.8–1.3	0.9–1.6	0.8–1.5	0.8–1.5	0.9–1.4	1.3–2	0.1–1.2
	Avg.	1.0	1.2	0.9	1.1	1.0	1.6	0.3
	Median	1.0	1.2	0.9	1.1	1.0	1.6	0.2
	st. dev.	0.1	0.2	0.1	0.1	0.1	0.1	0.2
K^+	Min–Max	0.3–0.7	0.4–0.7	0.3–0.4	0.2–0.4	0.3–0.6	0.4–0.7	0.1–0.7
	Avg.	0.5	0.5	0.4	0.3	0.4	0.5	0.2
	Median	0.5	0.5	0.4	0.3	0.4	0.5	0.2
	st. dev.	0.1	0.1	0.0	0.1	0.0	0.1	0.2
Cl^-	Min–Max	1–3.9	1–5.0	1–4.0	1–4.6	0.1–3.9	1–3.9	1–3.9
	Avg.	2.2	2.8	2.3	2.3	2.2	2.4	1.3
	Median	2.5	2.8	2.5	2.5	2.5	2.5	1.0
	st. dev.	0.7	0.8	0.8	0.6	0.7	0.7	0.7
NO_3^-	Min–Max	3.9–10.5	0.3–9.5	5.9–11.8	5.7–12.8	3.7–9.5	1.2–7.3	0.3–3.2
	Avg.	7.2	5.7	8.4	7.6	6.5	5.2	1.2
	Median	7.1	5.7	8.3	7.6	6.5	5.2	1.0
	st. dev.	1.2	1.7	1.2	0.9	1.2	1.0	0.8
SO_4^{2-}	Min–Max	19.9–84.3	48.7 – 330.0	18.4–24.2	15.4–28.5	22.1–89.1	68.6–110.0	1.7–7.5
	Avg.	42.1	164.2	21.1	22.5	41.7	88.1	3.4
	Median	40.5	161.0	21.1	22.5	40.1	87.8	2.7
	st. dev.	15.6	78.3	1.1	2.0	14.7	8.9	1.6
$\delta^{18}O$	Min/Max	−10.1/−7.9	−9.8/−9.0	−9.7/−8.4	−9.5/−8.3	−10.3/−8.6	−9.9/−8.2	−16.8/−0.8
	Avg.	−9.3	−9.5	−9.2	−9.0	−9.3	−9.3	−8.8
	Median	−9.3	−9.5	−9.3	−9.0	−9.3	−9.3	−8.8
	st. dev.	0.3	0.2	0.3	0.2	0.3	0.3	3.5
δ^2H	Min/Max	−70.1/−56.9	−66.5/−61.1	−70.5/−54.6	−65.9/−53.9	−68.6/−56.7	−66.4/−56.4	−121.5/−13.5

(continued)

Table 2 (continued)

Site no.		1	2	3	4	5	6	7
Site name		Buzgó karstic spring	"Heliktite Dome" subsurface inlet	"Abonyi Dome" subsurface inlet	Pod kameňolom karstic spring	Pri kaplnke karstic spring	RHV-4 borehole	Precipitation
	Avg.	−62.7	−64.1	−62.2	−60.8	−62.8	−62.5	−60.9
	Median	−63.1	−64.5	−62.6	−61.3	−63.2	−62.8	−60.6
	st. dev.	2.0	1.4	2.6	1.9	2.0	1.8	24.8
Number of samples		114	42	43	156	110	108	29

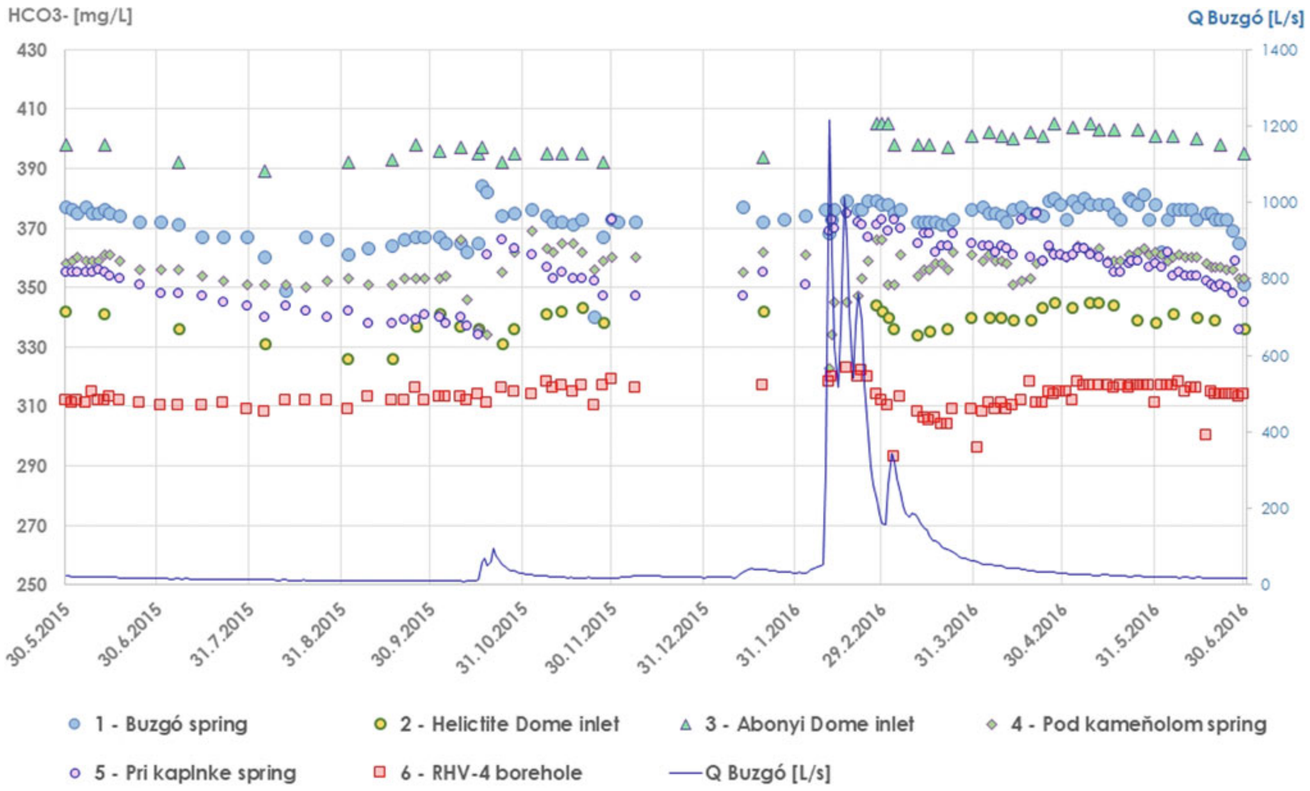

Fig. 2 Dissolved bicarbonate (HCO_3^-) content in groundwater and precipitation water at different monitored sources within Krásnohorská jaskyňa Cave and its vicinity and Buzgó karstic spring discharge in the period of May 31, 2015–June 30, 2016

shows that karstic reservoir here is still relatively untouched by agricultural production: median values in all groundwater sources are found in the interval between 5.2 and 8.3 mg L^{-1} while all values are ranging from 0.3 to 12.8 mg L^{-1} (Table 2). This is not a surprise as the surface of the Silická planina Plateau is mostly covered by young forest and only partly by pasture land. Still, the lowest values are found in the RHV-4 borehole (No. 6) where circulating groundwater is supposed to be bound to less karstified fissure system.

The most interesting, however, is the content of dissolved sulphates (SO_4^{2-}) in individual sampled sources (Table 2). The lowermost and most stable content of sulphates is both in Pod kameňolomom spring (No. 4; 15.4–28.5 mg L^{-1}; median 22.5 mg L^{-1}) and in Abonyi Dome subsurface inlet (No. 3; 18.4–24.2 mg L^{-1}; median 21.1 mg L^{-1}). As documented in Fig. 4, SO_4^{2-} content in Buzgó (No. 1) and Pri kaplnke (No. 5) springs copies the same pattern in time (median of 40.5 and 40.1 mg L^{-1}; ranges of 19.9–84.3 and 22.1–89.1 mg L^{-1}, respectively). Buzgó spring can be considered to be a mixture influenced by several end members—inlets into the subsurface system (Fig. 5). These are inlets in Abonyi Dome and from the Helictite Dome, which were sampled, and the not sampled outlet from the

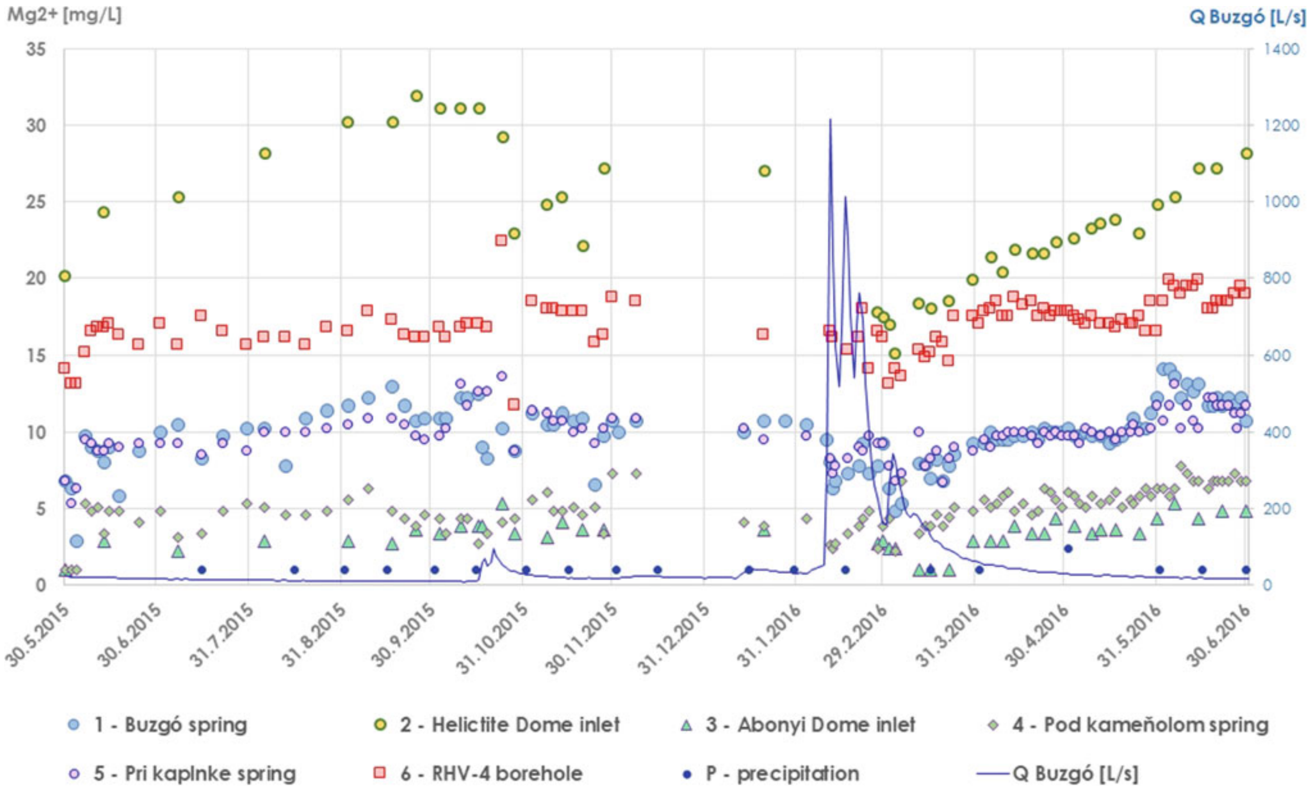

Fig. 3 Dissolved magnesium (Mg^{2+}) content in groundwater and precipitation water at different monitored sources within Krásnohorská jaskyňa Cave and its vicinity and Buzgó karstic spring discharge in the period of May 31, 2015–June 30, 2016

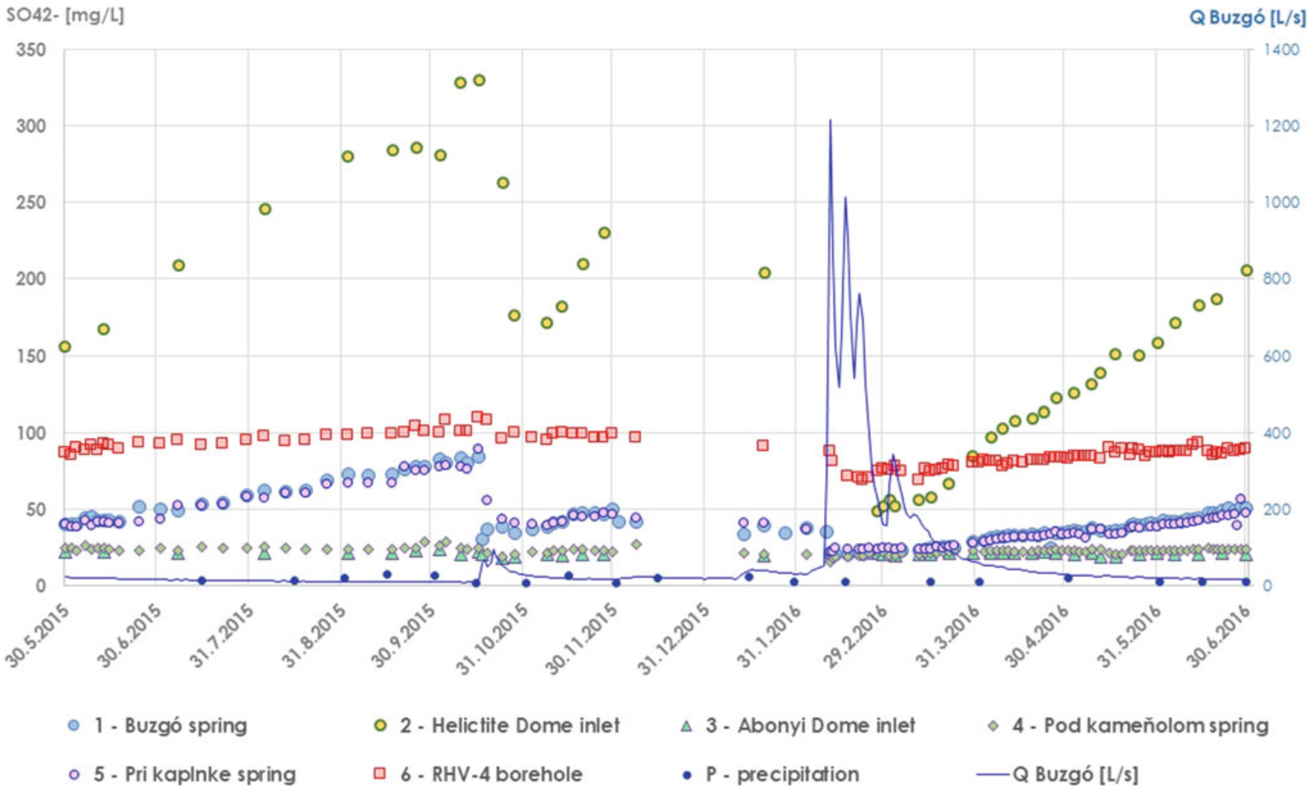

Fig. 4 Content of dissolved sulphates (SO_4^{2-}) in groundwater and precipitation water at different monitored sources within Krásnohorská jaskyňa Cave and its vicinity and Buzgó karstic spring discharge in the period of May 31, 2015–June 30, 2016

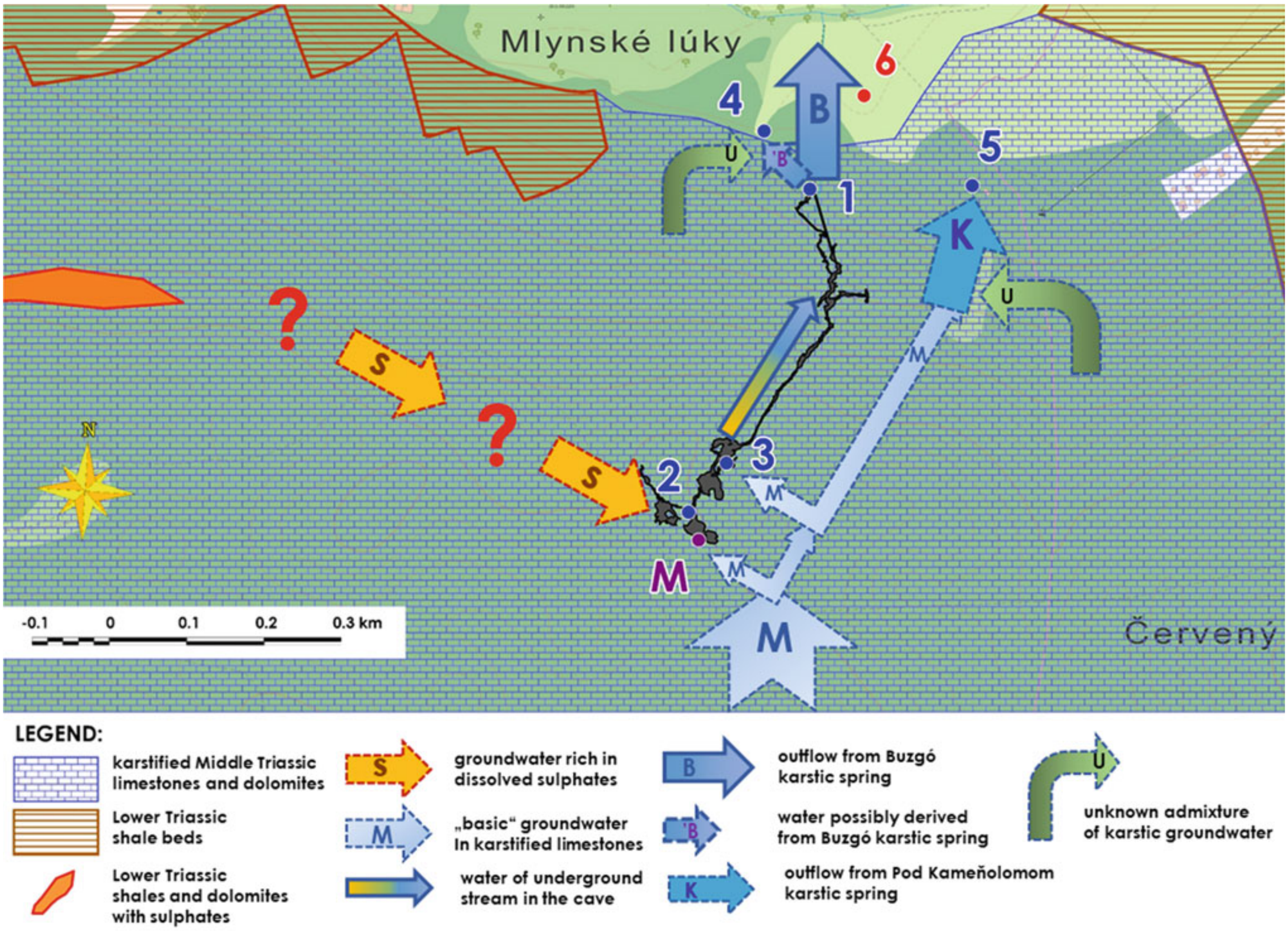

Fig. 5 Conceptual model of groundwater flow in the vicinity of Krásnohorská Cave according to results of detailed water quality monitoring on six groundwater sources. IDs of monitored sites are the same as in Fig. 1 and Tables 1 and 2

Marika lake siphon. Similarity of Buzgó and Pri kaplnke water sulphate content can result from the connection of both Buzgó and Pri kaplnke springs to the same source of sulphate. More probably, Pri kaplnke spring may represent the re-appearance of the Buzgó water on the surface. Another clear connection visible in Fig. 4 is the relation of dissolved sulphates in Pod kameňolomom spring and the inlet in Abonyi Dome (Fig. 5). This is also supported by their similar (but not the same) Ca^{2+} and Mg^{2+} content (Table 2). We should note that dissolved calcium is systematically in some 15 mg L^{-1} higher in Abonyi Dome inlet, while magnesium in only 1–2 mg L^{-1}, but constantly higher in Pod kameňolomom spring. Still, their close relation is evident and these differences should be caused by additional water–rock interaction in the rock mass between Abonyi Dome and the Pod kameňolomom spring. Bajtoš et al. (2017) found that underground inlet from the Helictite Dome with its high and extremely variable sulphate content is bound to geogenic source of sulphates probably from Lower Triassic shales in the area (No. 2; 48.7–330.0 mg L^{-1}; median 161.0 mg L^{-1}). These are diluted according to hydrologic situation (water stage) as shown also in Fig. 4. The relatively high content of sulphates in groundwater of the RHV-4 borehole (No. 6; 68.6–110.0 mg L^{-1}; median 87.8 mg L^{-1}) can also be linked to similar layers, although their presence was not documented in the outcrops nearby. A certain link between the RHV-4 borehole and Helictite Dome inlet waters is outlined by their highest SO_4^{2-} content in the whole dataset. These waters are rich in Mg^{2+} and also less markedly in Na^+ and K^+ in comparison with others. These two sources have markedly high value of rCa/rMg coefficient (0.250 and 0.284), while values in the interval 0.042–0.135 were found for the other groundwater sources. On the other hand, groundwater from the RHV-4 borehole has different (rNa+rK)/(rCa+rMg) coefficient (0.012) than the rest of sampled waters where its values are in the interval 0.007–0.009. This points to more close contact of RHV-4 groundwater with silicates, possibly in Lower Triassic shales of Szin layers. In all cases, variability of parameters analysed in RHV-4 groundwater is much less than that of Helictite Dome inlet which strongly depends on water stage. Bajtoš et al. (2017), based on evaluation of 8 samples, find it probable that water in Helictite Dome inlet is mixed of two endmembers. One of these represents highly mineralised water of small discharge which is diluted—depending on hydrological situation—by different amounts of substantially less mineralised groundwater. The aforementioned study was not concerning groundwater in RHV-4 borehole. Based on information from sampling campaign of this study, we consider similarity of RHV-4 borehole and Helictite Dome inlet waters to be more probably caused by their contact with the same type of layers than their direct physical interconnection.

A close relation, according to sulphate content, seems to be again between the inlet in Abonyi Dome and the Pod kameňolomom spring (Fig. 5). Values of SO_4^{2-} are low and stable in both cases (Table 2), but water in Abonyi Dome inlet is systematically in about 2 mg L^{-1} less in dissolved sulphates. The only exception is the beginning of March, when after the flooding period this ratio is overturned for a very short period and SO_4^{2-} ions in the Abonyi Dome inlet water prevail in 2 mg L^{-1}. In both cases, the mean SO_4^{2-} contents are the lowest from all sampled groundwater sources (21.1 and 22.5 mg L^{-1}).

Total dissolved solids content in precipitation water is low as documented in Table 2, and is in accordance with the results of precipitation quality monitoring in the area. One should note that the way of precipitation sampling on the Soroška monitoring site could not entirely secure representativeness of the analyses results (cumulative samples taken twice a month), especially in HCO_3^- content, but for chloride, nitrate, sulphate contents values in Table 2 are slightly lower than 25-year averages reported in the study of Bodiš et al. (2000). Precipitation monitoring was designed for isotope analyses ($\delta^{18}O$, δ^2H) to reveal water circulation pattern in the area (Fig. 6). It was found that $\delta^{18}O$ values in precipitation water vary in a wide interval from −16.78 to −0.77‰. In individual groundwater sources, $\delta^{18}O$ values were in much narrow range of −10.29 to −7.83‰ (Table 2). Interval from −121.5 to −13.5‰ (span of 108‰) for δ^2H values in precipitation water is more than six times wider than the interval of δ^2H values from individual groundwater sources. For groundwater, we measured 17‰ wide range of δ^2H (from −70.5 to −53.9‰; Table 2). Signs of evaporation are visible in Fig. 6 where two precipitation $\delta^{18}O$ values higher than −5‰ are deviated from global meteoric water line (GMWL; Craig 1961). These samples were taken in hot summer period of July 2015 with low precipitation totals. However, 27 from 29 precipitation samples fit GMWL line together with all the groundwater samples. Mean values of $\delta^{18}O$ in precipitation (−8.78‰) are higher than mean $\delta^{18}O$ values found in individual groundwater sources (range between −9.48 and −9.01‰). In groundwater, infiltrated precipitation waters from the monitored period (2015–2016) should be mixed with precipitation from the previous years. A rough estimate of groundwater mean transit time using McGuire and McDonnell (2006) method was applied here. Using $\delta^{18}O$ values, calculated mean transit time was in the interval between 14 and 36 months. For Buzgó spring groundwater, it is lowest (14 months), followed by RHV-4 and Pri kaplnke spring groundwater (both 18 months), identical result of 27 months was calculated for Pod kameňolom spring and Abonyi Dome inlet. The longest mean transit time of 36 months was estimated for groundwater in Helictite Dome inlet. Tritium content was found to be between 4.5 and 12.7 TU in precipitation (median 7.0 TU) and between 3.7 and 12.7 TU in groundwater sources where individual medians were from 5.7 to 6.7 TU, but any significant pattern was found here. These values correspond to the contemporary tritium content in the atmospheric precipitation (IAEA 2013), and seasonal pattern can be followed mainly in precipitation samples with highest values during the summer period. As for radioactive decay, the lowest tritium values should be assigned to longest mean transit time. Both groundwater form RHV-4 borehole and Helictite Dome inlet have the same tritium content median of 5.7 TU and possibly the slowest circulation. This is followed by Pri kaplnke spring (6.1 TU) and both Buzgó and Pod kameňolomom springs (6.3 TU). Groundwater in Abonyi Dome inlet with 6.6 TU median may present the shortest mean transit time. These mean tritium content differences are less or more featureless compared to the tritium content in precipitation (7.0 TU). Maximal recorded difference of tritium content in individual groundwater samples taken in the same time is 3.05 TU. Apart from major seasonal signal that can be followed on precipitation samples, changes of groundwater tritium content with time are irregular and different for each of the described sources.

Conclusions

Monitoring of water chemistry and isotope composition in the area of Krásnohorská jaskyňa Cave in the Slovenský kras Mts. (Slovakia) in the period of May 2015–June 2016 brought interesting results that could not be achieved by single sample collection. Sampling was performed in 3–9 days intervals, and 573 samples taken from six groundwater sources enabled us **to** recognise their mutual relationship as well as functioning of the entire karstic aquifer system. Precipitation samples taken twice pre month were used to evaluate water input parameters. Snowmelt taking place in February and March 2016 fed the aquifer by strong water input. Flooding lasting two weeks was recorded, with

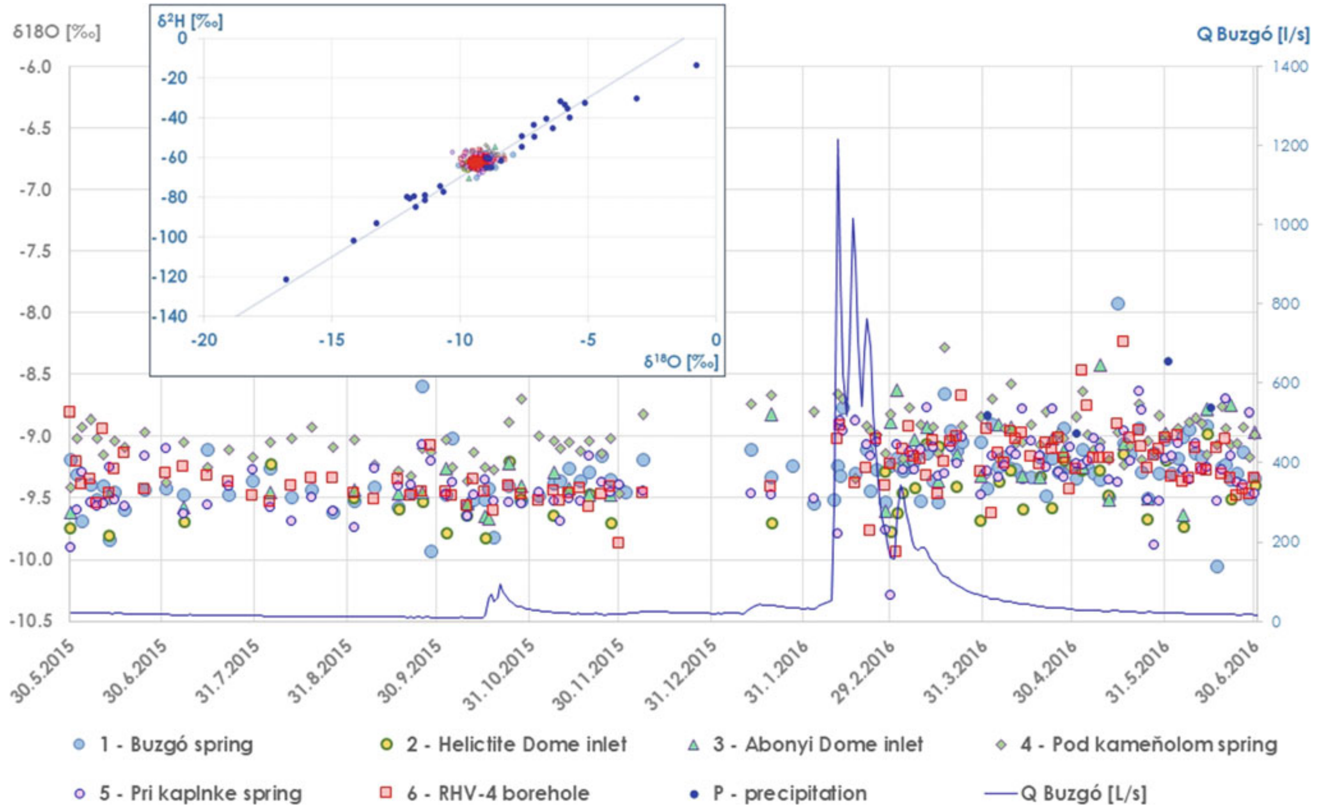

Fig. 6 δ18O and δ2H (‰ V-SMOW) in precipitation water and groundwater at different monitored sources within Krásnohorská jaskyňa Cave and its vicinity in the period of May 31, 2015–June 30, 2016 plotted with global meteoric water line (GMWL)

discharges more than twenty times higher than median value. Study of high water stages impact on water quality could be performed later as well.

Allochthonous components of karstic groundwater quality—those formed outside the karstified limestone and dolomitic aquifer system as NO_3^-, Cl^-, K^+ and Na^+—were nearly uniform in their behaviour over time in all sampled groundwater sources. As for nitrates, any significant pattern was found in the time course of their values. Their input to the karstic system is relatively constant, of some 6.8 ± 1.5 mg L^{-1}. Individual values may slightly vary according to respective circulation differences; the only remarkable feature is constantly lower (in 1.5 mg L^{-1}) content of NO_3^- in groundwater of RHV-4 borehole. Contents of Cl^- and K^+ are also uniform both in time and individual sources, in about 2.3 ± 0.7 and 0.4 ± 0.1 mg L^{-1}. The same can be also stated for Na^+ (1.1 ± 0.3 mg L^{-1}), but in RHV-4 borehole again, sodium content is in only some 0.5 mg L^{-1}, but systematically higher. In this case, presence of silicates in shales seems to have very slight influence. Presence of increased water quantities during flooding period does not influence contents of all mentioned allochthonous components.

Isotopic composition of precipitation water was measured at the top of the karstic plateau, in altitudes where recharge is taking place. Nearly all $\delta^{18}O$ and $\delta^{2}H$ values could be projected to global meteoric water line. Wide interval of $\delta^{18}O$ from −16.78 to −0.77‰ (span of 16.0‰) was found in precipitation. After infiltration processes and further mixing in the aquifer, nearly 7 times narrower $\delta^{18}O$ span of 2.4‰ (interval from −10.29 to s7.83‰) was found in groundwater sources. Still, existing water mixing processes in the karst aquifer system are insufficient to create a homogenous groundwater resource. Time series of isotope composition of individual groundwater sources show irregular distribution along average values. Missing pattern of time development can be explained by differences in water circulation between sampled water sources. Individual mean transit time was estimated between 14 and 36 months for those. Changes of groundwater tritium content in time were also irregular and different for each of the described sources; only major seasonal signal could be followed on precipitation samples. Median value of 7.0 TU was found in precipitation; only slight differences were between medians of individual groundwater sources (5.7–6.7 TU).

Geogenic components of karstic groundwater quality, i.e., HCO_3^-, Ca^{2+}, Mg^{2+} and here also SO_4^{2-}, ions that are dissolved in rock–water interaction inside the karstified limestone and dolomitic aquifer, were most useful in finding mutual links between individual groundwater sources. Three pairs of potentially interconnected monitoring points could be defined according to comparison of time series of these quality components. These were: inlet in Abonyi Dome and Pod kameňolomom spring, Buzgó and Pri kaplnke springs, inlet in Helictite Dome and groundwater in RHV-4 borehole.

Assumption of subsurface water inlet in Abonyi Dome and Pod kameňolomom spring connection is based on similar course and similarly low Mg^{2+} content (3.3 and 5.0 mg L^{-1}), nearly the same course and low $SO_4{}^{2-}$ content (21.1 and 22.5 mg L^{-1}), and perhaps the same estimation of mean transit time from $\delta^{18}O$ values (24.6 months for both). Their differences should be also noted here: water in Abonyi Dome subsurface inlet is in about 40 mg L^{-1} richer in $HCO_3{}^{-}$ concentration and in 16 mg L^{-1} for Ca^{2+} content. Therefore, additional input of merely Ca-HCO_3 water type with lower mineralisation can be supposed here. It should be reaching the feeding channel of Pod kameňolomom spring in the space between the Abonyi Dome and spring orifice. $HCO_3{}^{-}$ and Ca^{2+} concentration decrease in Pod kameňolomom spring during flooding period is probably caused by upraised input of this less mineralised Ca-HCO_3 water during high water stages.

Dissolved sulphate content plays major role in linking Buzgó and Pri kaplnke karstic springs together. It has absolutely the same course and $SO_4{}^{2-}$ content for both groundwater sources (42.1 and 41.7 mg L^{-1}). The same can be observed in magnesium content (9.8 mg L^{-1} in both cases) and its time variations. However, in Pri kaplnke spring, average values of $HCO_3{}^{-}$ and Ca^{2+} content are in 16.4 and 5.9 mg L^{-1} lower than in Buzgó spring. Additionally, increase of $HCO_3{}^{-}$ in 20 mg L^{-1} and of 4 mg L^{-1} in Ca^{2+} was observed during flooding period. We suppose that majority of Pri kaplnke spring water is derived from the main feeding channel of Buzgó spring near its orifice. Pri kaplnke groundwater is also partly fed by another smaller source of Ca-HCO_3 water type with lower mineralisation. In flooding periods, this smaller source is hydraulically blocked and for certain time, Pri kaplnke receives water only form Buzgó spring.

Highest values of $SO_4{}^{2-}$ and Mg^{2+} contents in the whole dataset may lead to linking groundwater of the RHV-4 borehole and Helictite Dome inlet to the same possible source. In all other features, there are more differences than similarities between the RHV-4 borehole and Helictite Dome inlet. $SO_4{}^{2-}$ and Mg^{2+} contents in RHV-4 are stable while they vary lot in Helictite Dome inlet. Calcium content is highest in Helictite Dome inlet and lowest in RHV-4. Important similarity can be marked by in rCa/rMg coefficient. Both in RHV-4 borehole and Helictite Dome inlet, it substantially differs from all the other groundwater sources. On the other hand, groundwater from the RHV-4 borehole has also different (rNa+rK)/(rCa+rMg) coefficient than the rest of sampled waters, what may result from close contact of RHV-4 groundwater with silicates, possibly in Lower Triassic shales of Szin layers. These shales are also supposed to be in Helictite Dome inlet water circulation pattern. Similarity of RHV-4 borehole and Helictite Dome inlet waters results more probably from their contact with the same lithology than from their direct physical interconnection.

Frequent sampling of groundwater chemical and isotope composition in intervals of 3–9 days enabled not only the assessment of water quality reliability in time, but also comparison of individual groundwater sources in the whole karstic aquifer system. Groundwater circulation patterns could be deciphered to such level that can never be reproduced by occasionally performed sampling, especially in karst environment.

Acknowledgements The results of this study could be obtained thanks to the project, coordinated by the European Commission as LIFE11ENV/SK/001023, entitled "Implementation of Sustainable Groundwater Use in the Underground Karst System of the Krásnohorská jaskyňa Cave" (acronym: KRASCAVE). The aim of this the project was to reduce the risk of contamination of drinking water in the underground karst ecosystem Krásnohorská cave through the implementation of innovation activities; the outputs of the project should also serve to reduce the risk of environmental impairment fragile ecosystems, depending on the quantity and quality groundwater. In the KRASCAVE project, the State Geological Institute of Dionýz Štúr Bratislava was acting as coordinating beneficiary and civic association Envi Slovakia Bratislava as associated beneficiaries. In addition to the European Commission, also the Ministry of Environment of Slovak Republic participated in the project co-financing.

References

Bajtoš, P, Malík, P, Repková, R, Máša, B (2017) Geochemické modelovanie tvorby chemického zloženia vody Krásnohorskej jaskyne v Slovenskom krase [Geochemical modelling of karst water chemical composition formation at the Krásnohorská jakyňa cave, Slovak Karst Mts. (Western Carpathians); in Slovak with English summary]. Mineralia Slovaca, 49(2017)1: 73–94

Bakalowicz, M (2005) Karst Groundwater: A Challenge for New Resources. Hydrogeology Journal 13(1):148 160

Bodiš, D, Lopašovská, M, Lopašovský, K, Rapant, S (2000) Chemické zloženie snehovej pokrývky na Slovensku – výsledky 25-ročného pozorovania [Chemical composition of snow pack in Slovakia - the results of 25 years monitoring; in Slovak with English summary]. Podzemná voda VI. (2):162–173

Craig, H (1961) Standard for reporting concentration of deuterium and oxygen-18 in natural waters. Science (133):1833 1834

Erdös, M (1995) Jaskyne, priepasti a vyvieračky severnej časti Silickej planiny. Slovenský kras, Liptovský Mikuláš, 33: 115–127

Fournier, M, Massei, N, Bakalowicz, M, Dussart-Baptista L, Rodet, L, Dupont, JP (2007) Using turbidity dynamics and geochemical variability as a tool for understanding the behavior and vulnerability of karst aquifer. Hydrogeology Journal 15(4):689 704

Gaál, Ľ (2008) Geodynamika a vývoj jaskýň Slovenského krasu. Speleologia Slovaca, 1. Liptovský Mikuláš, Správa slovenských jaskýň, 2008. ISBN 978-80-8064-330-0, 168 p

Goldscheider, N, Drew, D (Eds.) (2007) Methods in Karst Hydrogeology. Taylor & Francis, London, 264 pp

IAEA (2002) Water and Environment Newsletter of the Isotope Hydrology Section, International Atomic Energy Agency. Issue No.16, November 2002: 5

IAEA (2013) International Atomic Energy Agency. Global Network of Isotopes in Precipitation. Water Resources Programme – Global Network of Isotopes in Precipitation. Retrieved from http://wwwnaweb.iaea.org/napc/ih/IHS_resources

Kováčová, E, Malík, P, Švasta, J, Bahnová, N, Pažická, A, Bajtoš, P, Grolmusová, Z (2017) Priestorové zmeny distribúcie mikroklimatických parametrov počas letného režimu prúdenia vzduchu v Krásnohorskej jaskyni [Spatial changes of distribution of microclimatic parameters during the summer ventilation mode in Krásnohorská Cave (Slovak Karst Mts., Slovakia); in Slovak with English summary]. Slovenský kras - Acta Carsologica Slovaca 55(1): 81 102

Kronome, B. Boórová, D (2016) Geologická stavba Silickej planiny pri Krásnohorskej Dlhej Lúke [Geological structure of the Silická planina Plateau near the Krásnohorská Dlhá Lúka; in Slovak with English summary]. Geologické práce, Správy (129):55 78

Malík, P, Gregor, M, Švasta, J, Haviarová D (2011) Interpretácia meraní teploty a mernej elektrickej vodivosti vody v profile podzemného vodného toku Krásnohorskej jaskyne. Slovenský kras/ Acta carsologica Slovaca, 49/1, Liptovský Mikuláš, 41–55

Malík, P, Gregor, M, Černák, R, Bottlik, F, Šutarová, B, Otruba M (2014) Stupeň skrasovatenia horninového prostredia severného okraja Silickej planiny na základe analýzy výtokových čiar. Podzemná voda 20(2), 2014, Slovenská asociácia hydrogeológov, Bratislava, 128 141

McGuire, KJ, McDonnell, JJ (2006) A review and evaluation of catchment transit time modelling. Journal of Hydrology 330 (2006):543 563

Mello, J, Elečko, M, Pristaš, J, Reichwalder, P, Snopko, L, Vass, D, Vozárová, A (1996) Geologická mapa Slovenského krasu 1: 50 000. Ministerstvo životného prostredia, Geologický služba Slovenskej republiky, Bratislava. Map sheet at a scale of 1: 50 000

Mudarra, M, Andreo, B, Barbera, JA, Mudry, J (2013) Hydrochemical dynamics of TOC and NO3- contents as natural tracers of infiltration in karst aquifers. Environmental Earth Sciences 71 (2):507 523

Orvan, J, Vrábľová, M (1986) Rožňava - Horný Vrch, predbežný hydrogeologický prieskum. IHGP Žilina. Manuscript – archive of Geofond, ŠGÚDŠ Bratislava, arch. No. 63001, 69 p

Roda, Š (1964) Jaskyňa Buzgó. Krásy Slovenska, 29, 8, Bratislava, 181 182

Roda, Š (1966) Je najvyšší na svete? Krásy Slovenska, 43, 7, Bratislava, 258–259

Roda, Š, Roda, Š ml., Ščuka, J (1986) Aplikácia fraktálnej analýzy na interpretáciu stopovacích skúšok. Slovenský kras, 24, Liptovský Mikuláš, 61–75

Skřivánek, F (1965) Objev jeskyně Buzgó v Jihoslovenském krasu. Československý kras, 16, Praha, 139 p

Stankovič, J (2003) Mapa Krásnohorskej jaskyne. Archív Štátnej ochrany prírody – Správy slovenských jaskýň Liptovský Mikuláš, map sheet

Stankovič, J, Cílek, V (eds.), Bruthans, J, Cílek, V, Gaál, Ľ, Kovács Á, Rozložník, M, Stankovič, J, Schmelzová, R, Zeman, O, Kováč, Ľ, Mock, A, Ľuptáčik, P, Hudec, I, Nováková, A, Košel, V, Fenďa P (2005) Krásnohorská jaskyňa Buzgó. Speleoklub Minotaurus, Regionálna rozvojová agentúra Rožňava, 150 p

Zwahlen, F (ed) (2004) Vulnerability and risk mapping for the protection of carbonate (karst) aquifers. COST Action 620 Final Report. Office for Official Publications of the European Communities, Luxembourg, 2004–XVIII, pp. 297

Jurassic Carbonate Aquifer—The Most Valuable Fresh Water Resource at the Horn of Africa

Zoran Stevanović and Seifu Kebede

Abstract

Somalia and Ethiopia, two countries of the Horn of Africa, are among the world's poorest when it comes to natural and water resources. Karst aquifers in the eastern part of Ethiopia and northern and south-western parts of Somalia are important local sources of water. They are formed in Jurassic limestones and carbonate and evaporitic rocks of the Eocene age; both are of the platform type and have resulted from the Tethys Sea regression. A Jurassic aquifer provides more fresh water than those from the Eocene and is utilised at several locations. The main consumers are the cities Borama in Somalia and Jijiga in Ethiopia, and water is tapped out in both by the use of well fields. Although limited in extension and groundwater storage, this aquifer can be further developed at many locations, especially those where it is linked to overlying alluviums. Constructing underground dams across river beds of many present temporary streams and storing the water in the upstream alluvium's sections may also contribute to larger and longer recharge of Jurassic aquifers.

Keywords

Karst aquifer • Arid environment • Well field • Jurassic • Horn of Africa

Introduction

Somalia and Ethiopia, two countries of the easternmost part of the Horn of Africa, are among the world's poorest countries as regards natural or, more precisely, any water resources. Due to the prevailing arid climate, in most of the lowlands, rainfed farming is not possible. Irrigation could be a viable alternative if sufficient groundwater is found. As the area is far from major rivers, the main and often only source of drinking water is groundwater, but its uneven distribution and shortage during the drought periods often force people and livestock to migrate in search of water and better areas. The average annual sum of rainfall in study border area between Somalia and Ethiopia is c. 500 mm, but potential evapotranspiration exceeds 2000 mm, and is higher than rainfall in all months of the year (SWALIM 2009; Balint et al. 2012). It is due to high air temperatures (annual average 25 °C), low humidity and winds.

Laureano (2001) states that so far one billion hectares in Africa have been damaged by desertification and that millions of people have been forced to move elsewhere. Such a situation always carries with it a threat of potential conflicts of local, regional, sometimes even international level between permanent and migratory inhabitants, different tribes and various water users (Moenche et al. 2003; Stevanović 2015). The pressure on natural resources and biosphere is likely to only increase in the decades to come, for the two main reasons: climate change and population growth.

The IPCC report (2007) and Solomon et al. (2007) indicates that climate change and global warming represent major threats, especially in the arid region which covers nearly 33% of the Earth's surface (Vaughn 2005). The pressure on aquifers will increase due to climate variations, especially as a result of additional reduction of summer/autumn rainfalls (Treidel et al. 2012; World Bank Group 2016).

The population growth rate in the Horn of Africa is extremely high. In both countries, the population has grown five times when comparing the years 2050–2015 (UN 2015, 2016). There are currently around 115 million citizens that are exposed to uncertainties concerning their water and food supply. Most of the exposed population are living in rural and remote areas. The analyses by Balint et al. (2012),

Z. Stevanović (✉)
Faculty of Mining and Geology, Centre for Karst Hydrogeology at the Department of Hydrogeology, University of Belgrade, Belgrade, Serbia
e-mail: zstev_2000@yahoo.co.uk

S. Kebede
University of Addis Ababa, Addis Ababa, Ethiopia
e-mail: seifukebede@yahoo.com

C. Bertrand et al. (eds.), *Eurokarst 2018, Besançon*, Advances in Karst Science,
https://doi.org/10.1007/978-3-030-14015-1_24

Stevanović and Trivić (2016), Stevanović (2018) show that groundwater specific yield in the region is characterised by values of 1–2 l/s/km^2; such water resources cannot satisfy local water demands, for drinking and cropping. They would be sufficient for the irrigation of only, for instance, 1–2 ha of land per km^2 of the catchment (Stevanović and Papastavrou 2001).

Although not well known and sufficiently explored, some aquifers such as the Jurassic carbonate aquifer could provide more opportunities for local and regional water supply. The objective of this paper is to present its distribution, discharge, actual use for the two cities in bordering area between Somalia and Ethiopia, and Gedo Region in SW Somalia, as well as prospect for further development by constructing subsurface dams in adjacent alluviums for more effective recharge and water storage in underlying or lateral karst aquifers.

Karst Aquifers' Distribution and Properties

Karst aquifers are an important worldwide source of water, but are unequally distributed. The eastern part of the Horn of Africa (Somalia, Ethiopia) is one of the very rare African regions that are characterised by the prevalence of karstified rocks and karstic aquifers. The main aquifers are formed in Jurassic limestones and dominantly evaporitic rocks of the Eocene age (Fig. 1); both are of the platform type and have resulted from the Tethys Sea regression.

The oldest rocks are of Precambrian age (Fig. 2). Different types of gneisses, marble, quartzite, micashists, amphibolite and schists were formed and widely distributed along with granites, depending on the parent material and prevailing temperature and pressure. The Precambrian era was followed by regional folding, uplifting and erosion, and the peneplained basement rocks were covered by conglomerate and sandstone during the Lower Jurassic, which marks the Tethys Sea transgression (Abbate et al. 1994; EGS 1996). Marine sediments were deposited over the regions during the Middle Jurassic. These sediments are predominantly fossiliferous limestone, marl and shale. Toward the end of the Jurassic, gradual uplifting of the shield resulted in sea regression and subsequent erosion of a part of the Jurassic sediments.

The retreat of the sea was followed by the deposition of sandstone, sand and sandy clay of the Yessoma sandstone formation. The Cretaceous sediments range from continental, through lagoonal, to marine.

The exposed land covered by Yessoma sandstone was flooded by a deep sea incursion during the Lower Eocene, when the Auradu limestone was deposited in the eastern part of the Horn of Africa. The sea gradually retreated during the Middle Eocene, causing the deposit of evaporitic facies with

Fig. 1 Distribution of major karstic formations and aquifers of Somalia and Ethiopia (modified from authorised inputs of Stevanovic and Kebede for WOKAM—World Karst Aquifer Map 2017). Legend: NK—non-karstic rocks (Precambrian granites and crystalline rocks, Cretaceous Yessoma Fm. sandstones, Tertiary and Quaternary sediments and basaltic rocks); $J_{2,3}$—Middle and Upper Jurassic carbonate rocks; $E_{1\text{-}3}$—Eocene evaporates and carbonates

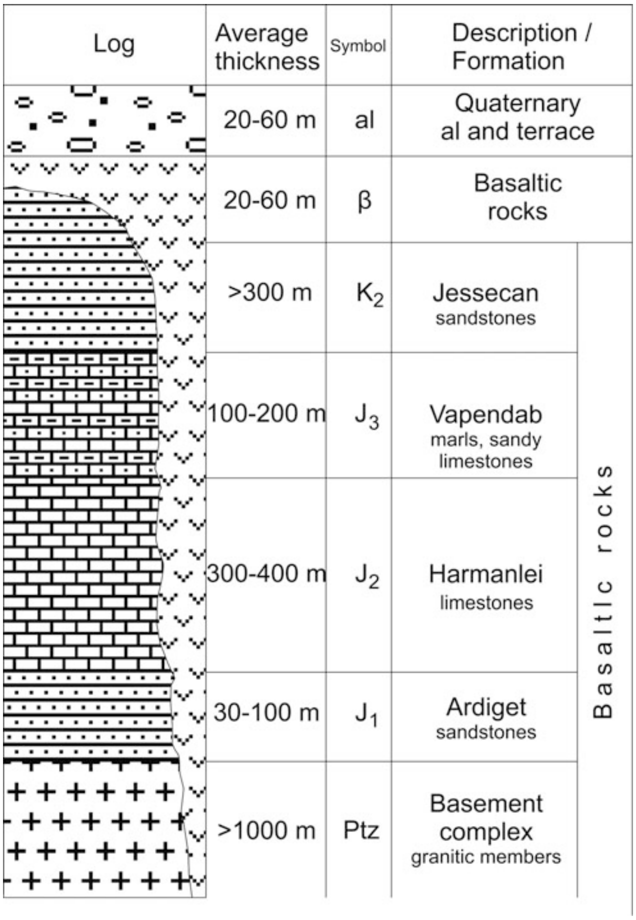

Fig. 2 Litho-stratigraphy column of eastern Ethiopia (based on EGS 1996)

anhydrite, gypsum and marls of the Taleex Formation. Further marine regression during the Upper Eocene resulted in the Karkar Formation deposition in a shallow sea. These three Eocene formations are largely extended over the eastern part of Somalia's provinces Somaliland and Puntland (Failace and Faillace 1986; Basnyat 2007; Balint et al. 2012; Gadain et al. 2016), where Oligocene and Miocene marine sediments were also deposited in a narrow belt along the Indian Ocean.

Even though mostly saline or highly mineralised (TDS mostly >3000 ppm), waters from Eocene evaporitic rocks are broadly used as they represent the sole resource in the easternmost part of Somalia—Bar, Sool and Nugal regions (Muthusi et al. 2009; SWALIM 2009). In contrast, groundwater discharging from the Jurassic karst aquifer is commonly fresh and of very good quality. Unfortunately, the Jurassic aquifer has limited extension in Somalia, with main outcrops located along both sides of the border between Somalia and Ethiopia. Most part of the Jurassic Limestone is buried under thick sequences of other sediments (Angelucci and Barbieri 1981, Fig. 3). Larger extension either as outcrops or covered by younger sediments, Jurassic aquifer has in eastern Ethiopia (Hodwen et al. 1973; EGS 1996; Gebeyehu and Kebede 2012) and southern Somalia (Gedo province) (Abbate et al. 1994). Although Middle to Upper Jurassic formations have different names and some litho-facial diversities (e.g. Hamanlei Fm. in Ethiopia, Fig. 4; Uanei, Baydhabo, Goloda members in Somalia), their hydrogeological properties are relatively similar (Kebede 2013) and they are all categorised as a platform type of karst (Stevanović 2015).

The thickness of aquifer varies from one place to another, mainly due to the lateral change of the facies; the thickest sequence in Somalia is around 200 m, while in Ethiopia they reach a few hundred metres (Fig. 2).

Horizontal and not much deformed limestones do not represent a favourable environment for high infiltration of rainfalls. Main recharge is in zones of more intensive fracturation, and their formation might have been locally influenced by high permeability and good storage capacity. Recharge from erratic rainfall may also occur from water percolating through overlain Yessoma sandstones, very permeable alluvial sediments (Fig. 5) or where basaltic rocks are present overlying the Jurassic limestone formation.

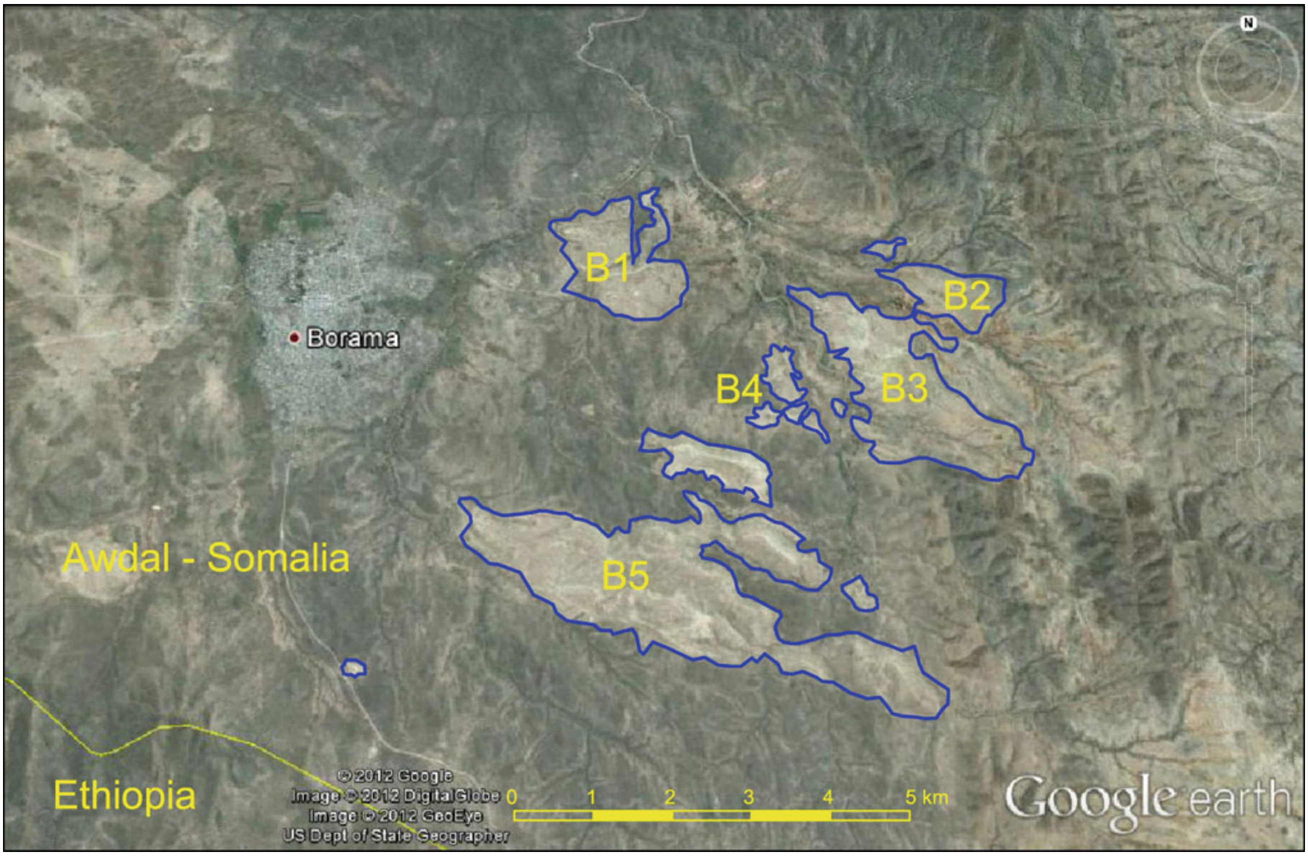

Fig. 3 Disconnected outcrops (labelled by B) in vicinity of Borama city in Somalia, near border with Ethiopia

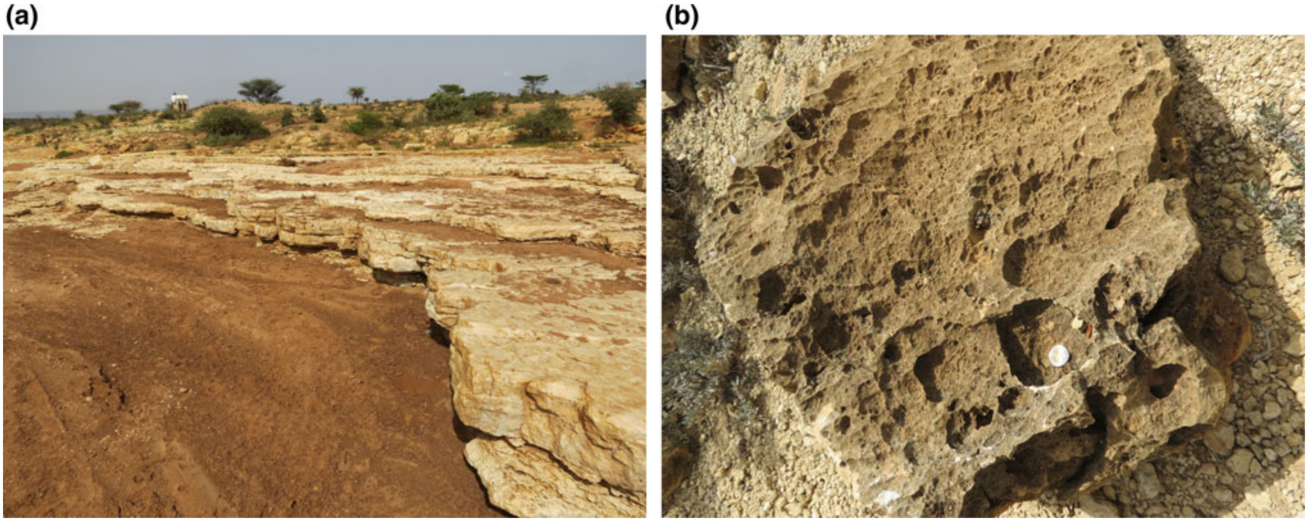

Fig. 4 Horizontal and well-bedded limestones (left) and surficial karstification of Hamanlei Fm. (member of Antalo Group Fm.) in northeast Ethiopia (coin to scale)

Jurassic Aquifer Utilisation

Borama, located just 20 km from the Ethiopian border (Fig. 1), is the largest town in Somalia that utilises the Jurassic aquifer. It currently hosts approximately 150,000 residents, of which only one-fourth are connected to the waterworks' pipeline. The main source of water is in the nearby village of Dhamuuq, where the initial karstic spring has been tapped out (average pumping from the spring's pond: 11.5 l/s), followed by several boreholes that were subsequently drilled from the year 2000 to date.

Their depths vary between 64 and 120 m. The total discharge is 27 l/s, which, together with 6 l/s of tapped spring water, makes for a total of 33 l/s available for drinking water supply. Despite the relatively small capacity, there is clear evidence of local over-extraction. It was indicated that the water table in some wells has depleted by some 13 m during the period 2006–2012 (2 m/year). This could be the effect of limited aquifer distribution and erratic rainfall (Muthusi et al. 2009; Balint et al. 2012).

The quality of water is regularly controlled, and no treatment is applied (not even chlorination). TDS is in the range of 400–1000 ppm, average water temperature is

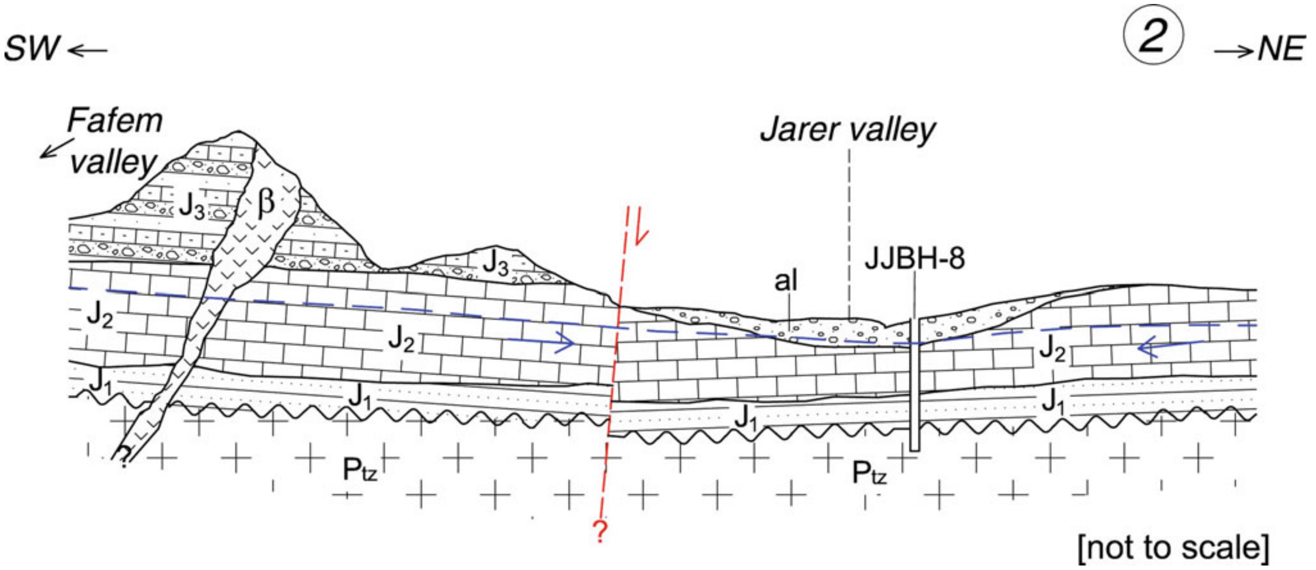

Fig. 5 Hamanlei limestones (J_2) in eastern Ethiopia, sandwiched between underlain Proterozoic (Ptz) and Lower Jurassic sandstones (J_1) and overlain Upper Jurassic (J_3) and basaltic rocks (β). Thick alluvial deposits (al) are well connected to Hamanlei Fm. creating a common groundwater body and enabling effective recharge

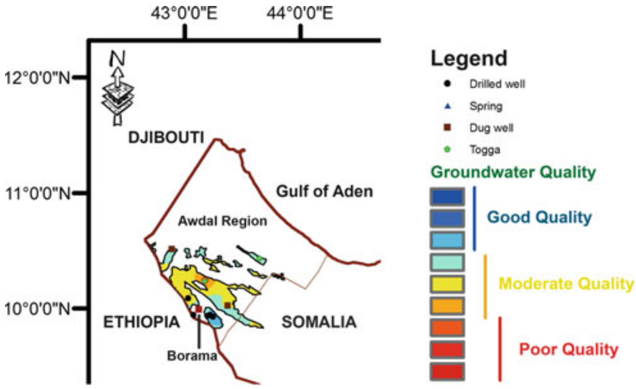

Fig. 6 Outcrops of Jurassic limestones in the NW part of Somalia around Borama town and the water quality zone (moderate to good classes) (according to Balint et al. 2012)

around 26 °C and the prevailing type of water is bicarbonate-sodium (Fig. 6).

Jijiga is the largest town in Ethiopia that taps and utilises the Middle Jurassic (Doggerian) aquifer. The city is also close to the border (Fig. 1) and currently one of the major dwellings in the Somali State Province of Ethiopia. The Jijiga well field (SHAAC 2009) is located near the city, in the alluvial plain of the Jarer River (Fig. 5). In the 1970s, several wells were drilled to the total depth of 70 m. They have very high specific yields (0.6–2.6 l/s per m’ of drawdown). Recent drilling (2009) confirmed the existence of a groundwater table at the average depth of 70 m, while the total drilling depth of most wells is 130 m (Fig. 7). It is noteworthy that the drilling depth has doubled in comparison with that of the 1970s; nevertheless, based on the performed pumping tests, they still yield a good amount of water (specific yield of 1 l/s per m’ of drawdown). The tested water has a low level of mineralisation (TDS is regularly lower than 1000 ppm).

Besides these two cities, many other smaller settlements also utilise the Jurassic aquifer’s water, usually by drilling wells or rarely by tapping springs of relatively small discharges (a few l/s).

The assessment of the Jurassic karstic-fissured aquifer of Uegit (Waajid) Fm. in the Gedo Region in the SW part of Somalia has been carried out (Stevanović and Trivić 2016, Fig. 8).

Fig. 7 Battery of the wells newly drilled for the city of Jijiga

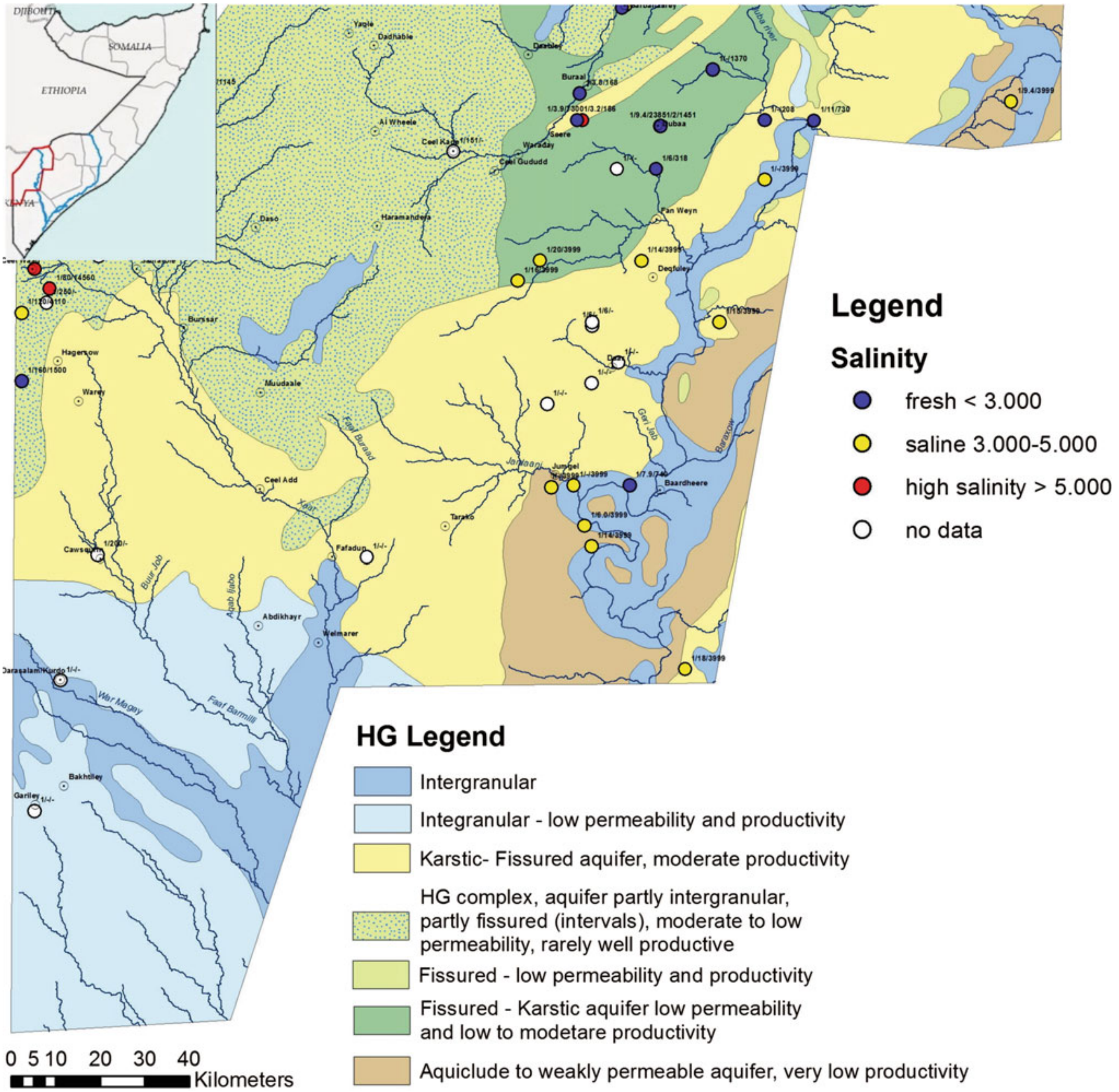

Fig. 8 Hydrogeological sketch map of main aquifer systems and groundwater salinity in the Gedo Region of southern Somalia (after Stevanović and Trivić 2016). Jurassic Uegit (Waajid) Fm. is classified as karstic-fissured aquifer of moderate productivity (yellow colour on the map)

The fissured karstic aquifer of moderate permeability and productivity extends over 10.14 km^2. In the northern part of Gedo, the annual precipitation sum is 320 mm on average, while effective infiltration I_{ef} based on some practical experiences and analogy with karstic terrains of the Northern Africa and Middle East (Stevanović 2015, 2018) is roughly estimated at 22%. This results in potential annual replenishment of 713.6×10^6 m^3 or an equivalent dynamic groundwater flux of 22.6 m^3/s. This theoretical flux is equal to a specific yield of only 2.23 l/s/km^2. Although not high, or even moderate in comparison with karst aquifers' fluxes experienced worldwide, this yield can satisfy the demands of the local population, livestock and agriculture.

Discussion—Further Prospects for Jurassic Aquifer Development

In many arid countries in Africa, problems with the extraction of groundwater that is much greater than its replenishment have caused a total depletion or significant reduction of many aquifers' reserves. It is therefore very important, in all areas with limited groundwater, to determine a safe yield (Burke and Moench 2000; Custodio 2002; Stevanović 2015) and establish monitoring systems for permanent observation of groundwater quantity and quality. This would make it possible to issue warnings to reduce pumping rates, or search for other solutions in water management once over-exploitation is evident. However, talking about a safe yield and sustainable water development in arid environments such as Ethiopia and Somalia does not always seem logical, as most of the water is used for purely humanitarian purposes (Stevanović 2018). For instance, it is not possible to ask for guaranteed and ecological flows when during most of the year there is no flow at all in the river beds (toggas). Nevertheless, an established monitoring network provides for more reliable information about the status of groundwater, the trend of its possible depletion and measures that could be applied in the water practice to amortise the negative effects of water extraction.

Although some evidence of over-extraction of Jurassic aquifer is already evident (e.g. in Borama, Somalia), there are still many locations where sustainable exploitation is possible. This especially concerns southern and SE parts of Ethiopia (Fig. 1), or SW Somalia (Fig. 9) where this aquifer has a large extension. Therefore, an alternative approach of water savings and conservation should be practised in this region.

Nissen-Petersen and Lee (1990) suggest that subsurface dams could represent an optimal solution for storing flood water or water from temporary streams. This kind of structure (a sand dam) is well known in northern and eastern African countries and the Middle East, including Somalia and Ethiopia (Hanson 1987).

Constructing underground dams across river beds of temporary streams and storing the water for longer period of the year in the upstream alluvium's sections (Fig. 9) may also contribute to larger and longer recharge of underlying Jurassic aquifers (Stevanović 2016).

Fig. 9 One of the promising locations for the construction of a subsurface ("sand") dam in the alluvium near Qaaxo (Ethiopia). A subsurface dam can be positioned between the limestone banks of Hamanlei Fm. limestones

Yet another alternative approach to tapping groundwater from the Jurassic Limestone unit is to target zones where overlying Eocene formations (evaporates and Yessoma sandstone) are thin. If such regions are found, the Jurassic formation can be reached by deep wells. Recent deep drilling (500 m wells) in the Ogaden region of Ethiopia shows such a possibility. However, this requires a detailed geological and geophysical survey to map out the overlying formations resting on the Jurassic Limestone.

Conclusions

In many arid regions, including most parts of Ethiopia and Somalia as countries of the Horn of Africa, groundwater represents an essential, sometimes even the sole resource for environmental and economic development. However, due to climate variations and population growth, the pressure on groundwater resources will only increase further. Some mitigation measures should, among others, include a systematic hydrogeological survey, development of new water sources, drilling of humanitarian wells and building of underground dams as most efficient water storage structures.

As a result of their good permeability, productivity of wells and the quality of water, Jurassic aquifers are indicated as one of the most valuable regional water sources. In contrast to other karst aquifers of Eocene age that are widely distributed along northern Somalia, Jurassic aquifers' water has low mineralisation and is therefore suitable for drinking. Along with the two major existing well fields, Borama in Somalia and Jijiga in Ethiopia, there are many other sites that are suitable for opening new sources—in SE Ethiopia, where this aquifer has a large extension, as well as in SW Somalia (Gedo Region). Even drilling wells and constructing ponds and fountain intakes in remote and unpopulated areas help pastoralists and their livestock during severe droughts, which are a common occurrence in region.

Hydrogeological and geophysical surveys should provide support concerning the locations along the temporary streams (togas) that have been found suitable for building underground (storage) dams. The areas where Jurassic aquifers are in lateral contact or under the alluvial deposits are most probable, for two reasons: they would recharge alluviums by subsurface drainage during wet periods, while the water stored in alluviums would recharge the connected karst aquifers during the drought periods.

However, any engineering intervention intended to improve the local water situation should be carried out with caution, following a proper investigation programme, in cooperation with the local population, and by establishing a monitoring system for observing the effects of the implemented technical solution.

References

Abbate E, Sagri M & Sassi FP (with the collaboration of Aden I.H., Arush M.A., Yusuf O.S.), (1994) The geological map of Somalia 1:1,500,000. University of Florence, SELCA, Florence

Angelucci A, Barbieri F et al. (1981) Preliminary report on the Jurassic sequence in the Gedo and Bay Regions (South-western Somalia), Quaderni di Geologia della Somalia 4, pp. 115–154, Univ. Naz. Somalia

Balint Z, Stevanović Z, Gadain H, Milanović S, Trivić B et al. (2012) Hydrogeological survey and assessment of selected areas in Somaliland and Puntland. Technical Report No. W-20, FAO-SWALIM (GCP/SOM/049/EC) Project, Nairobi

Basnyat DB (2007) Water resources of Somalia. Technical Report No W-11, FAO-SWALIM, Nairobi

Burke JJ, Moench HM (2000) Groundwater and society: Resources, tensions and opportunities. Spec ed. of DESA and ISET, UN public. ST/ESA/265, New York. p 170

Custodio E (2002) Aquifer overexploitation. What does it mean? Hydrogeol J 10 (2): 254–277

EGS - Ethiopian Geological Survey (Teffera et al. revised Kazmin et al. (1972), (1996) Geological map of Ethiopia at 1:2,000,000 scale. Geological Survey of Ethiopia, Addis Ababa

Faillace C, Faillace ER (1986) Water quality data book of Somalia. Hydrogeology and water quality of northern Somalia, Vol. 1, Text. GTZ & WDA, Rosdorf

Gadain, H, Stevanovic Z, Upton K, Ó Dochartaigh BÉ (2016) Africa Groundwater Atlas: Hydrogeology of Somalia. British Geological Survey. Accessed 23/07/2018. http://earthwise.bgs.ac.uk/index.php/Hydrogeology_of_Somalia

Gebeyehu A, Kebede S (2012) Geological map of eastern Ethiopia, 1:500.000 compiled under UNESCO and DFID project. Addis Ababa

Hodwen P, Aytenfissa M, Mengesha G (1973) Groundwater in the Ogaden. Geological Survey of Ethiopia, report 880-551-14

Hanson G (1987) Groundwater dam research and development in the Haraghe Region, Ethiopia, NNWC, SIDA, Addis Ababa

IPCC (2007) The Intergovernmental Panel on Climate Change, www.ipcc.ch; www.ipcc.ch/pdf/technical-papers/climate-change-water-en.pdf Accessed 20 Aug 2016

Kebede S (2013) Groundwater in Ethiopia. Features, numbers and opportunities. Springer, Heidelberg, NY, Dordecht, London, 285 p

Laureano P (2001) The water atlas. Traditional knowledge to combat desertification. Bollati Boringhieri edit. Turin. 2nd Edition by UNESCO-ROSTE, Venice, p 437

Moench M, Burke J, Moench Y (2003) Rethinking the approach to groundwater and food security. Water Reports, Vol. 24, FAO, Rome, p 62

Muthusi FM, Mugo MW, Gadain HM (2009) Water Sources Inventory for Central – South Somalia. Technical Report No W-17, FAO-SWALIM (GCP/SOM/048/EC) Project, Nairobi

Nissen-Petersen E, Lee M (1990) Sub-surface and sand storage dams, Harvesting Rainwater in Semi-Arid Africa, Manual no.5, ASAL, Nairobi, p 43

SHAAC Co. (2009) Jijiga well field drilling and pumping test report. Technical document prepared for WAHEEN Drill. Co, December 2009

Solomon S, Qin D, Manning M, Chen Z, Marquis M, Averyt KB, Tignor M Miller HL (eds) (2007) Climate change 2007 – Physical science basis: Contribution of Working group I to the Fourth Assessment report of the IPCC. Cambridge University Press, Cambridge

Stevanović Z, Papastavrou L (2001) Remedial measures in water use practices of drought affected areas. Report. Docum. Fund of FAO Coordination Office for Northern Iraq, Erbil

Stevanović Z (ed) (2015) Karst Aquifers – Characterization and Engineering, Series: Professional Practice in Earth Science, Springer Intern. Publ. Switzerland, p 692

Stevanović Z, Trivić B (2016) Hydrogeological study of Gedo Region, Somalia. Report. Docum. Fund of FAO-SWALIM, Nairobi, p 155

Stevanović Z (2016) Damming underground flow to enhance recharge of karst aquifers in the arid and semi-arid worlds. Environ Earth Sci 75 (1):35 https://doi.org/10.1007/s12665-015-5086-z

Stevanović Z (2018) Karst aquifers in the arid world of Africa and the Middle East – sustainability or humanity? In: Younos T, Schreiber M, KosičFicco K, Kastning EH (eds) Karst Water Environment: Advances in Research, Management and Policy. Series: The Handbook of Environmental Chemistry, vol. 68, Springer, Chem, pp 1–40

SWALIM (2009) Atlas of Somali Water and Land Resources, SWALIM Database, Nairobi

Treidel H, Martin-Bordes JL, Gurdak JJ (eds) (2012) Climate changes effects on groundwater resources. A Global synthesis of findings and recommendations. IAH, Intern. Contrib. to Hydrogeol. vol. 27, CRC/Balkema, p 401

United Nations (2016) The World's population. www.unpopulation.org Accessed 17 Nov 2016

United Nations, Department of Economic and Social Affairs, Population Division (2015). World Population Prospects: The 2015 Revision, DVD Edition

Vaughn MD (2005) Arid Climates. In: Oliver EJ (ed) Encyclopedia of World Climatology. Springer, Dordrecht, pp 85–89

WOKAM Team (2017) World Karst Aquifer Map, 1:40 000 000, BGR, IAH, KIT and UNESCO, https://www.whymap.org/whymap/EN/Maps_Data/Wokam/whymap_ed2017_map_g.html;jsessionid=D3026B51C31E5D17D6C23AAC271B1956.1_cid284?nn=9930710

World Bank Group (2016) High and Dry: Climate change, water, and the Economy. World Bank, Washington, https://openknowledge.worldbank.org/handle/10986/23665 United Nations, 2015, Millennium development goals report. New York, p 75

Hydrochemical and Isotopic Characterization of Karst Aquifer in the Region of Tebessa, Northeast Algeria

Radhia Legrioui, Fethi Baali, Ilhem Abdeslam, Amor Hamad,
Philippe Audra, Didier Cailhol, and Stéphane Jaillet

Abstract

In this work, we present results of the hydrogeological, hydrochemical and isotopic studies on groundwater samples from the karst aquifer in the region of Tebessa, Northeast Algeria. The study area is characterized by a semiarid climate, with a very hot boiling, dry summer and freezing, humid winter. The karstic aquifer system that overlooks this study area is drained by a number of springs; the most important of which are those of Ain Youkous, Ain Troubia, Ain El Megalib, Ain Gaagaa and Ain Sari. They are located at different altitudes and spaced fairly large distances. The karst system has a complex functioning. The hydrochemical data (major ion geochemistry) indicate that these groundwaters are characterized by the dominance of Ca–HCO_3–SO_4 and Ca–Cl–SO_4 water types. The main factors controlling the groundwater composition, its seasonal variations, and the rhythm of recharge are geology, because of the presence of different carbonate formations, and additionally elevation and the rate of karst development. Using stable isotope analysis data, $\delta^{18}O$ and $\delta^{2}H$ relationships show that all waters are meteoric in origin.

Keywords

Hydrochemical • Isotope • Karst aquifer • Tebessa • Algeria

Introduction

The limestone regions of Algeria offer a great diversity of landscapes from the well-watered karsts of the High Atlas Mountains to the little karstified outcrops of the Sahara Desert (Collignon 1991). These are formations that extend over the entire geological scale of the earliest times: the Carboniferous (in the Bechar region), the Triassic (numerous outcrops of gypsum and salt throughout Algeria), Jurassic and Cretaceous (Oran coastal cliffs, Tellian nappes, Tlemcenien domain, Constantinian neritic, Saharan Atlas), Post-nappe Miocene (Bensaoula 2006).

The karst is very abundant in the region of Tebessa (NE Algeria), but it is still poorly known, few works carried out concerning the karst aquifer of the study area (Quinif 1983; Guefaifia 2007; Baali 2007; Fehdi et al. 2015).

This present work focuses on the karst aquifer of the Maastrichtian limestones of the Tebessa's region; based on the sources of water emergence, Ain Youkous, Ain Gaagaa, Ain Troubia, Ain El Mgalib and Ain Sari are considered as an important reserve of water in terms of quality and freshness. Besides, they have become legendary.

Hydrochemical and isotopic analyses have been used to investigate chemical processes that are responsible for the groundwater chemistry and the reconstruction of the origin and recharge mechanisms of groundwaters in recent years.

Description of the study area

Our study area (Hammemt Plain and Tezbent plateau) (Fig. 1) is located in a hydrogeological basin, which is limited by the mountains of Djebel Troubia, Djebel Arour, Djebel Gaagaa, Djebel Draaa el Korratz and Djebel Tezbent. The boundary of the zone can be defined as follows:

Northern limit by the collapse of Tebessa-Morsott,
Eastern limit by the plateau of El Malabiod,

R. Legrioui (✉) · F. Baali · I. Abdeslam · A. Hamad
Laboratory Water and Environment, Department of Earth and Universe Sciences, Tebessa University, Road of Constantine, 12002 Tebessa, Algeria
e-mail: legioui.radhia@yahoo.fr

P. Audra
Polytech' Lab, University of Nice Sophia-Antipolis, 930 route des Colles, 06903 Sophia-Antipolis, Nice, France

D. Cailhol · S. Jaillet
Laboratoire EDYTEM, University Savoie—Mont-Blanc, CNRS, Pôle Montagne, 73376 Le Bourget-du-lac, France

C. Bertrand et al. (eds.), *Eurokarst 2018, Besançon*, Advances in Karst Science,
https://doi.org/10.1007/978-3-030-14015-1_25

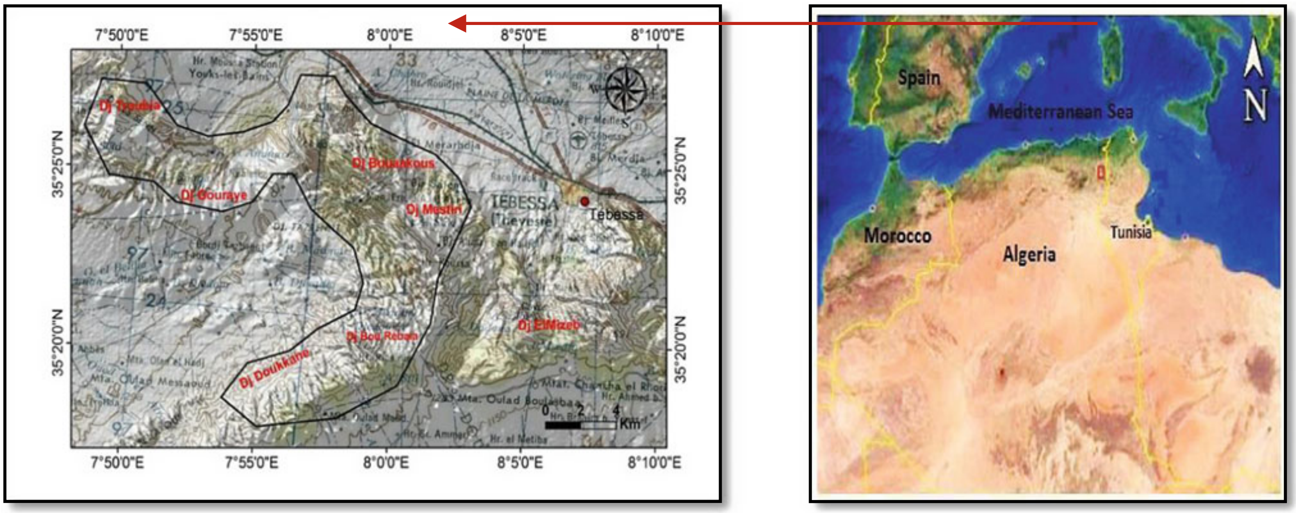

Fig. 1 Geographical situation of the study area

Southern limit by the Synclinal of Chéria,
Western limit by the Syncline of Guerigueur.

Oued Bouakous, which major bed is dug between very steep slopes, joins the Hamamet plain to the Tazbent plateau.

The Oued (“River”) Bouakous deeply cuts in the limestone of the Tezbent plateau, as a steep gorge, a typical karstic reculee, opening to the plain of Hamamet.

The plateau of Tezbent has a roughly planned topography inclined toward SW, with shallow incised wadis (“brooks”), bumped of some marly hills with rounded forms. The altitudes range from 1230 to 1470 m. The edge of the plateau at the northern border reaches 1230–1320 m, which corresponds to the average altitude of the surface. The few characteristics to be retained for their influence on karstification are as follows (Fig. 2).

Geological and Hydrogeological Description

The study area (Fig. 3) is part of the oriental Saharian Atlas close to the Algerian–Tunisian borders; it consists essentially of the followings formations (Vila 1980).

Carbonate formations are represented by important marly limestones layers and marls of Cretaceous to Tertiary. The Turonian outcrops to the north (Dj. Essen, Dj. Gaagaa) are beige limestones, pink with patina, sometimes dark and dotted of hematite. The bases of the Maastrichtian are represented by alternations of well-limbed white limestones, about 60 m thick and gray-to-black clay marl (150 m). The Eocene is composed of marly limestone with flint. To the N of Guerigueur and SE of Youkous and Tezbent, the Eocene is about 50 m thick. Finally, the Miocene deposits mainly conglomerates and sandy sandstones are transgressive over the older formations.

An important Mio-Plio-Quaternary alluvial deposit, which rests inconsistently with the previous formations and thus forms the filling of the depression, is currently the plain. The Quaternary deposits crop out in the northern parts around Dj. Gaagaa and Dj. Tezbent and generally cover the lower zones. The screes accumulate at the foot of the carbonate hillside. The jointing of the limestone combined to acid infiltration allows the formation of a karst aquifer in the carbonate domain.

The region is characterized, like the entire Saharan Atlas, by NE–SW-oriented folds, which result from compressive tectonics corresponding to the Eocene Atlasic phase (Dubourdieu and Durozoy 1950; Vila 1980) and also to faults in normal directions.

The karst aquifer system of the study area is drained by a number of overflow springs; the most important are Ain Troubia, Ain El Megalib, Ain Gaagaa, Ain Youkous and Ain Sari (Table 1) (Fig. 4).

The five sources which have been the object of our study are emergent limestone Maastrichtian. The Youkous spring is the most important of all emerging sources of the limestone ledge, in contact with the marls and marly limestone of the Maastrichtian lower. The emergence of the Gaagaa spring is due to the establishment of a very brittle tectonics generating a well-developed fracturing of the encasing rock and the significant offset of the subsidence of the Hammamet region. Ain Sari is an emerged spring of the upper Maastrichtian limestone fissured from Djebel Draaa el Korratz. The spring of the Ain Troubia is draining Jebel Troubia. The spring of Ain el Mégalib is an important spring of all springs emerging from limestone of the Maastrichtian Jebel Bou Rebaia.

The runoff time series of Oued Bouakous show a close relationship between precipitation and discharge with a relatively short reaction time, from which a relatively close

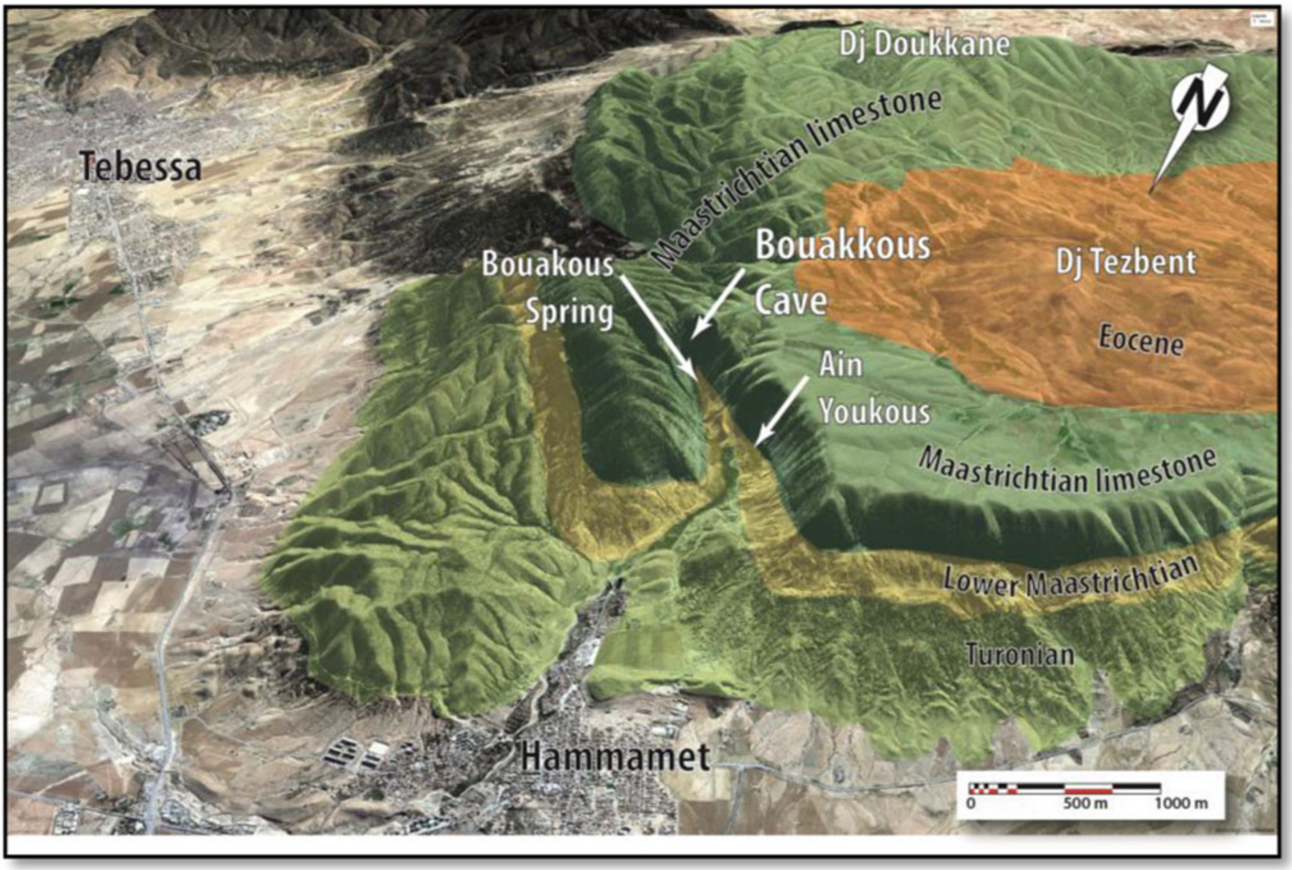

Fig. 2 Sketch of geomorphological surroundings of Youkous

recharge area is deduced. The highest daily flows are generally observed in late winter and early spring, whereas summer and fall storms have no effect on discharge because of the interception by evaporation, (Fig. 5); (Legrioui et al. 2017).

The precipitation records from Tebessa station which is located outside of study area about 30 km, its coordinates (*X* = 419,882.627, *Y* = 3,917,461.059). The flow is measured at Oued Bouakous by the micro-reel gauging technique.

Methodologies

Sampling and Analysis

Groundwater samples were collected into pretreated polyethylene sampling bottles using the standard method of sampling technique for geochemical analysis (APHA 1999). We took a sample of five springs at different altitudes during the 2015–2016 hydrological years, which are draining the Maastrichtian limestone.

Electrical conductivity (EC) and pH were measured in the field. The EC was measured using a conductivity meter Conscan 30—Conscan series. The pH was measured using a pH meter—pH scan 20 pocket—pH scan series, regularly calibrated using two laboratory standards.

Chemical analyses were undertaken at the Water and Environment Laboratory of Tebessa's University and Algerian Water Company (AWC)—Tebessa and Mila. Major cation concentrations (Ca^{2+}, Mg^{2+}, Na^{+}, and K^{+}) were determined by using spectrophotometer HACH DR 2500.

Calibrations for cation analysis were performed using appropriately diluted standards. The laboratory and international reference materials were used as checks for accuracy (Ademoroti 1996).

The analysis of bicarbonate concentrations $\left(HCO_3^{2-}\right)$ was undertaken by titration to the methyl orange endpoint. Concentration of chloride (Cl^{-}) was determined by titration and precipitation of AgCl until silver chromate appeared. Sulfate $\left(SO_4^{2-}\right)$ was determined by precipitation of $BaSO_4$ and then measuring the absorbance with a spectrophotometer.

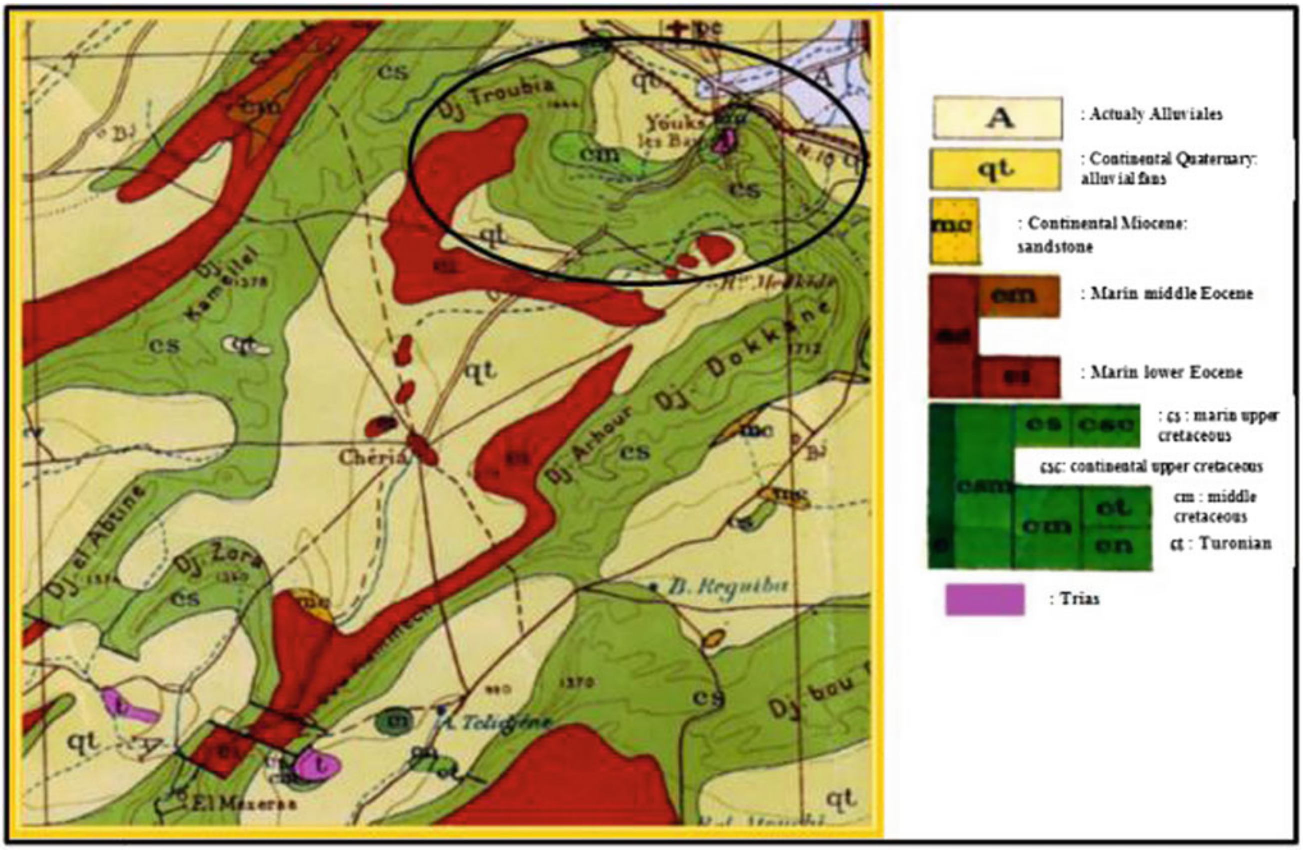

Fig. 3 The geology study of the region from the 1:500,000 scale geological map of the north of Algeria

Table 1 The coordinates of the springs and its variations of flows in 2015/2016

No.	Springs	Coordinates			Discharge (l/s)						
		X (UTM)	*Y* (UTM)	*Z* (m)	08/02	18/04	14/06	09/09	02/12	18/02	15/05
01	Ain Sari	412,264.57	3,915,996.89	1173	0.25	0.5	0.43	0.37	0.29	0.21	0.30
02	Ain youkous	406,063.90	3,919,604.05	1135	1.04	1.70	1.43	1.25	1.00	1.03	0.79
03	Ain Gaagaa	398,836.54	3,917,865.98	1272	0.50	1.00	0.31	0.94	0.71	0.12	0.41
04	Ain EL Mégalibe	402,892.74	3,915,499.65	1279	0.83	2.00	1.05	0.65	1.52	0.21	1.35
05	Ain Troubia	391,367.87	3,923,258.68	1253	1.00	1.66	0.78	1.16	0.95	0.49	0.40

The different water samples have been classified according to their chemical composition using the Piper diagram (Piper 1944). This classification is based on the concentration of the four major anions (bicarbonate, sulfate, chloride and nitrate) and on the four major cations (sodium, potassium, calcium and magnesium).

Using the software diagrams (Simler 2004), the water samples are plotted on a Piper diagram and on a Scholler–Berkaloff diagram.

Oxygen-18 and deuterium groundwater samples were collected in glass phials during February 2016 across the study area. The isotopic analysis of ^{18}O and ^{2}H was carried out in the laboratory of chemistry and isotopes at the University of Gabes, Tunisia. Oxygen isotopes were analyzed using the CO_2–H_2O equilibration method proposed by Epstein and Mayeda (1953), followed by analysis on a mass spectrometer. Hydrogen isotopic ratios were measured on H_2 after the reaction of 10 ml of water with metallic zinc at

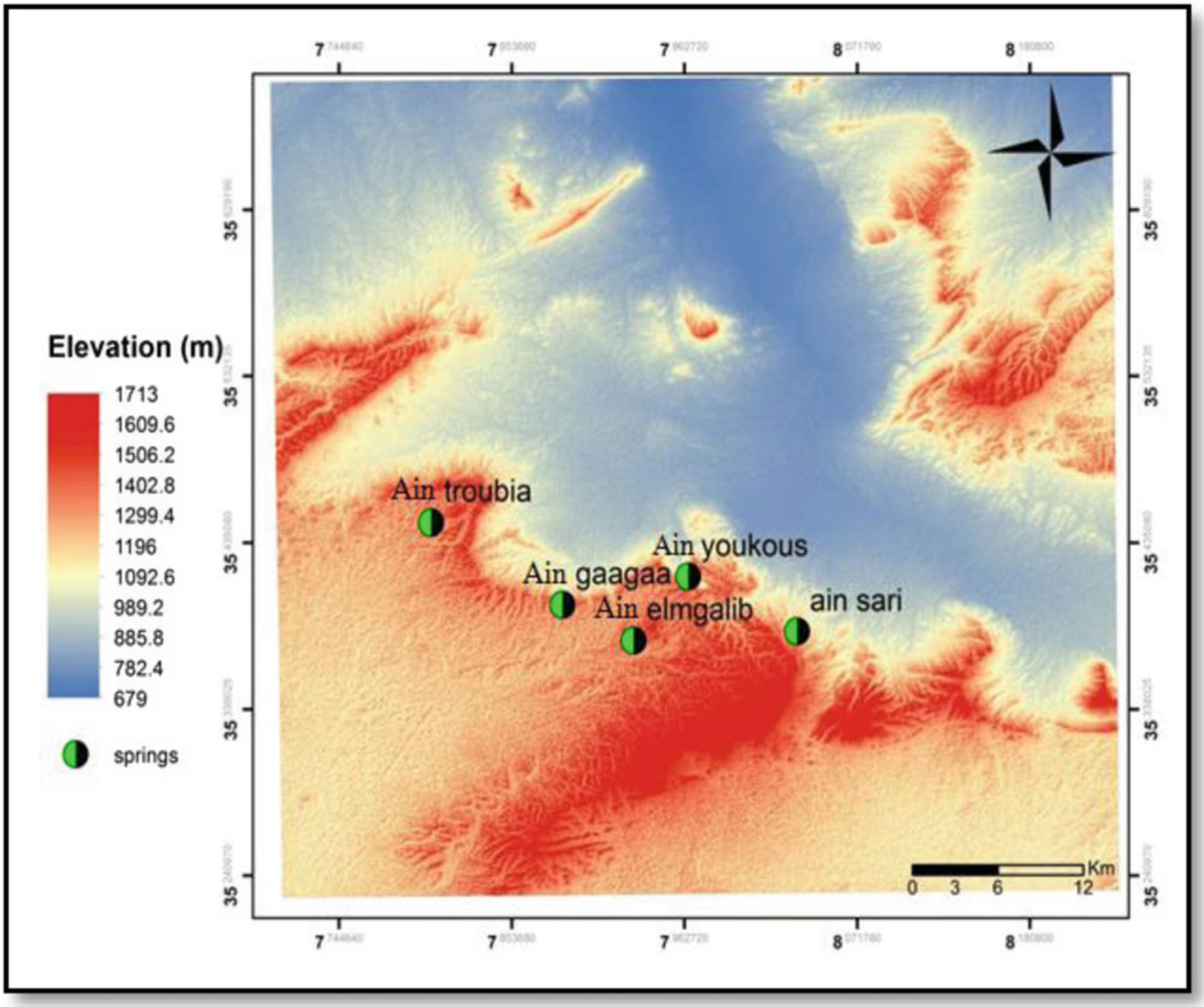

Fig. 4 Location of the springs in the study area

500 °C (Coleman et al. 1982). Oxygen and hydrogen isotopes analyses were reported to δ notation relative to Vienna-Standard Mean Ocean Water (VSMOW), where $\delta = [(R_S/R_{SMOW}) - 1] \times 1000$, R_S represents either the $^{18}O/^{16}O$ or the $^{2}H/^{1}H$ ratio of the sample and RSMOW is $^{18}O/^{16}O$ or the $^{2}H/^{1}H$ ratio of the SMOW. Typical precisions are ±0.1 and ±1.0‰ for oxygen-18 and deuterium, respectively.

Results and Discussion

The physical–chemical and chemical data of all the investigated springs are summarized in Table 2. We discuss the groundwater origin, the water types, the water–rock interactions and the origin of water chemistry.

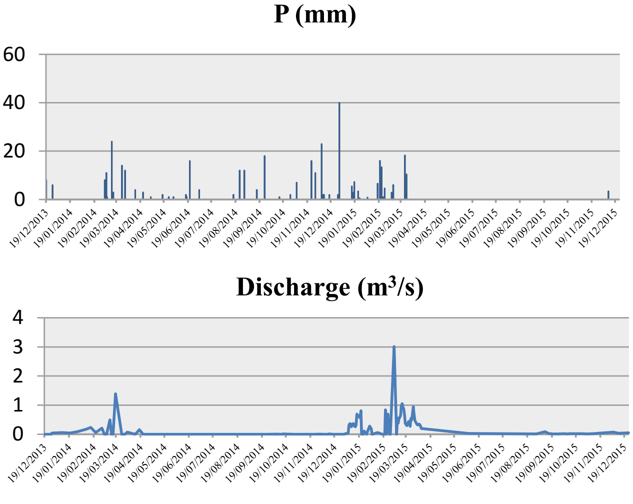

Fig. 5 Rainfall (Tebessa station) and discharge time series at Oued Bouakous

Table 2 Chemical composition (in mg l^{-1}) of groundwater from the study area February 2016

No.	Springs	PH	EC (µs/cm)	Ca^{2+}	Mg^{2+}	Na$^+$	K$^+$	HCO$_3^{2-}$	Cl$^-$	SO$_4^{2-}$	NO$_3^-$
01	Ain Sari	7.2	842	127.45	26.24	55	20	154.94	59.56	168.67	45.45
02	Ain youkous	7.7	198	69.73	5.34	11	1	208.62	14.18	21.67	11.37
03	Ain Gaagaa	7.6	425	85.77	12.64	19	1	281.82	33.22	14.45	14.54
04	Ain EL Mégalibe	7.8	253	45.69	13.12	7	1	153.72	10.64	15.5	21.58
05	Ain Troubia	7.5	422	78.56	21.87	12	1	273.28	168.04	21.67	15.24

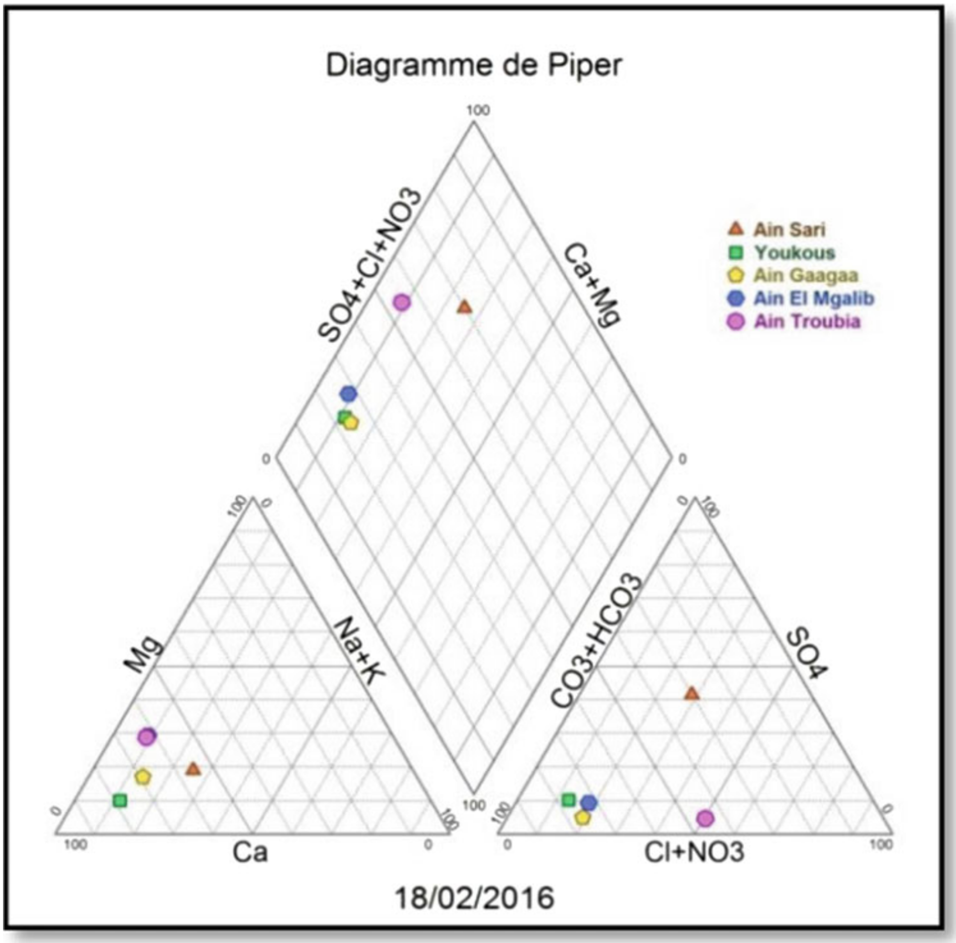
Diagramme de Piper

18/02/2016

Fig. 6 Piper diagrams of the studied springs February 2016

General Hydrochemical Characteristics

The Piper diagram shows a remarkable dominance of calcium (or magnesium) bicarbonate facies in three springs (Youkous, Ain Gaagaa and Ain El Mgalib) which are known to drain areas with carbonate rock (Eocene and Maastrichtian limestone) (Baali et al. 2006), but the facies in Ain Sari source is calcium chloride (or sulfate) because of the leaching of Maastrichtian marls, which contain sulfures (Fig. 6).

Interactions between groundwater and surrounding host rocks are mostly the main processes responsible for the observed chemical characteristics of groundwaters in the study area (Rouabhia et al. 2009; Hamad et al. 2018).

The drawn diagram (Scholler–Berkaloff diagram) for the study period (Fig. 7) mainly confirms a calcium bicarbonate facies, making it possible to say that the mineralization of water is linked to the ions HCO$_3^{-2}$ and Ca^{+2}. Secondarily, we observe a calcium chloride facies.

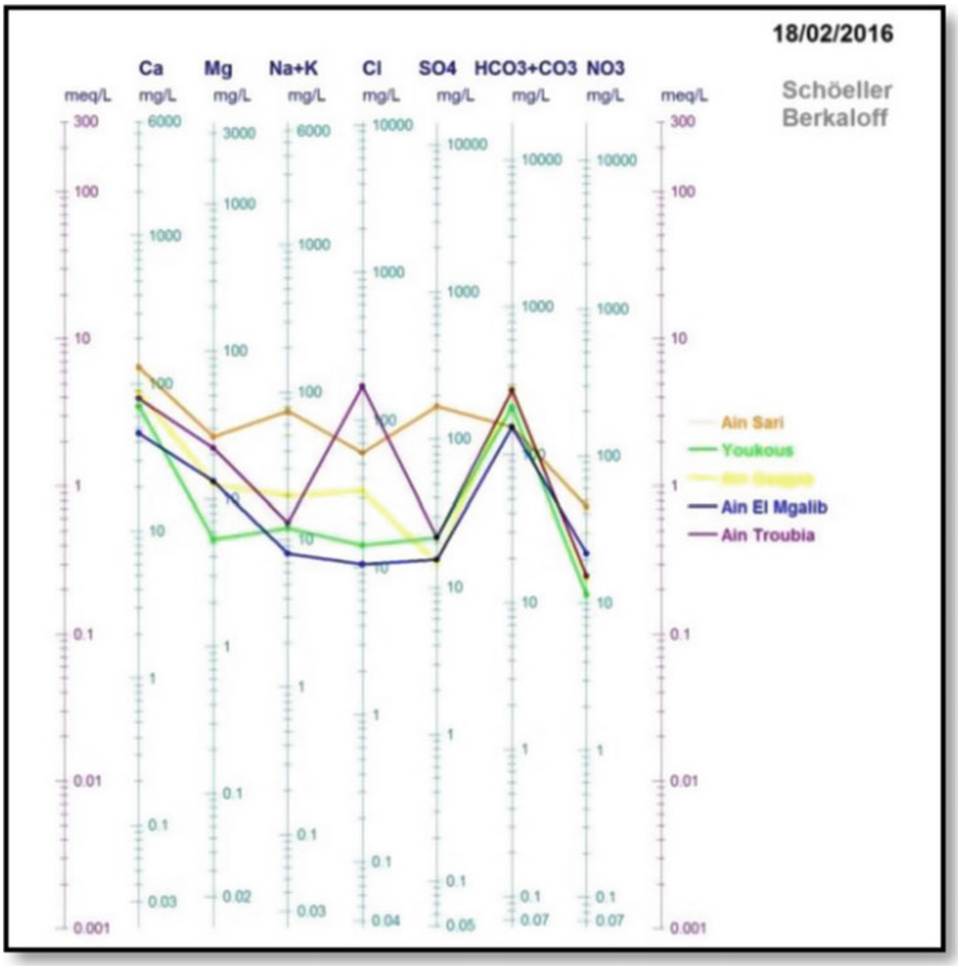

Fig. 7 Schoeller–Berkalof diagrams of the studied springs February 2016

Table 3 Isotopic composition of groundwater measured at springs and spring altitude, February 2016

Samples	Springs	Altitude (m)	$\delta^{18}O$	$\delta^{2}H$
1	A. Sari	1173	−4.9948	−51.9316
2	Youkous	1135	−6.1353	−54.0258
3	Gaagaa	1272	−6.4652	−54.5001
4	A. El Megalibe	1279	−6.7224	−56.9946
5	A. Enneba	1101	−6.3335	−56.8581

Origin and Recharge Mechanisms of Groundwater

The use of stable isotopes is very important in the field of resources assessment (Fontes 1980; Fontes et al. 1986). Stable isotopes of oxygen and hydrogen in groundwater of an active hydrological cycle derive from and reflect the initial isotopic composition of the recharging rainwater.

Stable isotope compositions of water collected from springs are presented in Table 3. Stable isotope values were found to vary for ^{18}O between −6.72 and −4.99 and for ^{2}H between −56.99 and −51.93.

Oxygen and hydrogen isotope composition of the groundwater are plotted in the conventional $\delta^{2}H/\delta^{18}O$ diagram (Fig. 8).

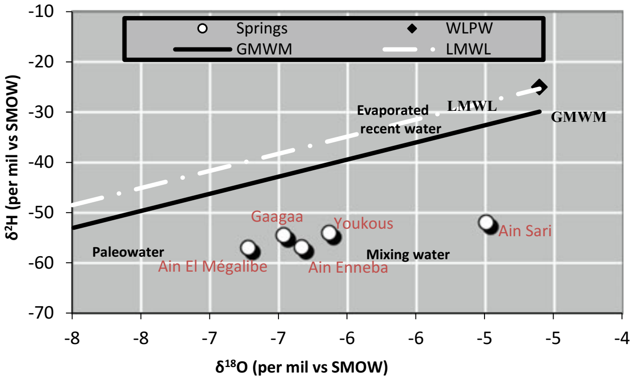

Fig. 8 δ2H versus δ18O relationship for groundwater in the study area, compared to the global meteoric water line (GMWL) (Craig 1961; Rozanski et al. 1993) and to the local meteoric water line (LMWL) of the Sfax and Tunis city (Maliki 2000; Celle et al. 2001)

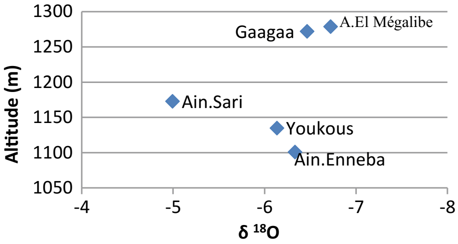

Fig. 9 Relationship between springs altitude and δ18O

In the conventional $\delta^{18}O$ versus $\delta^{2}H$ diagram (Fig. 8), most of the samples plot close to the global meteoric line, suggesting that the groundwater is of meteoric origin (Craig 1961).

The similarity of $\delta^{2}H$ versus $\delta^{18}O$ for springs groundwater samples is not surprising in karst regions and suggests fast infiltration process of the rainfall that recharge the groundwater throughout highly karstified carbonates at high elevations (Fig. 9) (Fehdi et al. 2015; Amor et al. 2018). It also indicates that groundwater is of meteoric origin (Araguas and Diaz Teijeiro 2005).

Conclusions

The study area is a sedimentary terrain consisting limestone, marly limestone and marls. The hydrochemical and isotopic study has been used to characterize the types of water in the region from several modes of interpretation in the usual chemistry, in order to show:

- The water–rock interaction of the aquifer material with carbonates facies.
- The chemical composition of groundwater shows that calcium (or magnesium) bicarbonate facies are derived mainly from dissolution of carbonate rocks along with ion exchange process in the groundwater.
- Water quality in the region has been studied with great particularity, which took into consideration the nature of water from bicarbonates aquifer, which is generally good.
- The results of $\delta^{18}O$ and $\delta^{2}H$ indicate that groundwater from the karst aquifer in the region of Tebessa is of meteoric origin. The studied water samples collected from springs are fed from recharge at the highest elevations.

Acknowledgements The authors thank the anonymous reviewers for their constructive comments. I am grateful to the numerous people who helped me in the preparation of this paper especially laboratory of water and environment at the university of Larbi Tebessi—Tébessa.

I would like also to thank sincerely both my family and friends for their encouragement and support.

Conflict of Interest The author declares that she/he has no conflict of interest.

References

Ademoroti CMA (1996) Standard methods for water and effluents analysis. Fodulex Press Ltd, Ibadan, pp 32–34

Amor H, Riheb H, Fethi B, et al (2018) Conceptual model for karstic aquifers by combined analysis of GIS, chemical, thermal, and isotopic tools in Tuniso-Algerian transboundary basin. Published by Arabian Journal of Geosciences (2018) 11:409 https://doi.org/10.1007/s12517-018-3773-2

APHA (1999) Standard methods for the examination of water and wastewater. 20th ect. APHA, AWWA, WPCF, New York

Araguas LJ, Diaz Teijeiro MF (2005) Isotope composition of precipitation and water vapour in the Iberian Peninsula: first results of the Spanish network of isotopes in precipitation. In: international atomic energy agency—isotopic composition of precipitation in the Mediterranean Basin in relation to air circulation patterns and climate. Int At Energy Agency 1453:173–190

Baali (2007) Contribution à l'étude hydrogéologique, hydrochimique et à la vulnérabilité d'un système aquifère karstique en zone semi-aride. Cas du plateau de Chéria, N. E. Algérien. Thèse de doctorat en sciences, Universite d'Annaba, Algérie

Baali F, Rouabhia AK, Kherici N, Djabri L (2006) Natural chemical tracers of urban pollution: case of born example of application on the area of Algerian Cheria. WRP, LLC ISNB-13: 978-1-887201647-6 Michigan, USA pp 39–45

Bensaoula F (2006) Karstification, hydrogéologie et vulnérabilité des eaux karstiques. Mise au point d'outils pour leur protection (Application aux Monts de Tlemcen – Ouest Oranais), Université de Tlemcen, Tlemcen, 203p

Celle et al (2001) Caract_erisation isotopique des pluies en Tunisie. Essai de typologie dans la r_egion de Sfax. C.R. Acad. Sci. Paris 6, 625e631

Coleman et al (1982) Réduction de l'eau avec du zinc pour l'analyse des isotopes de l'hydrogène. Anal Chem 54:993–995

Collignon B (1991) Les principaux karsts d'Algérie. Congrès SSS. Actes pp. 37–43

Craig H (1961) Isotopic variation in meteoric waters. Science 133, 1702e1703

Dubourdieu and Durozoy (1950) Observations tectoniques dans les environs de Tébessa et de l'Ouenza (Algérie). Bulletin de la Société géologique de France, (V), 20, 4–6, 257-266, Paris

Epstein S, Mayeda T.K (1953) Variations of the JSO/160 ratios in natural waters. Geochim Cosmochim. Acta, 4:213–224

Fehdi CH, Belfar D, Baali F (2015) Characterization of the main karst aquifers of the Tezbent Plateau, Tebessa Region, Northeast of Algeria, based on hydrogeochemical and isotopic data. Environ. Earth Sci. https://doi.org/10.1007/s12665-015-4480-x

Fontes et al (1986) Estimation of long term, diffuse groundwater discharge in the northern Sahara using stable isotope profiles in soil water. J Hydrol 86:315–327

Fontes J (1980) Environmental isotopes in ground water hydrology. In: Fritz J, Fontes J (eds) Handbook of environmental isotope geochemistry. Elsevier, Amsterdam, 1 (A):75

Guefaifia (2007) Identification et caractérisation d'un milieu karstique et sa contribution à l'alimentation d'un champ captant: cas de la zone de Bouakous-Hammamet, région de Tebessa. Thèse de doctorat en sciences, Université d'Annaba, Algérie. 256 p

Hamad A, Baali F, Hadji R, et al (2018) Hydrogeochemical characterization of water mineralization in Tebessa-Kasserine karst system (Tuniso-Algerian Transboundry basin). Euro-Mediterranean J Environ Integr 3(1):7 https://doi.org/10.1007/s41207-017-0045-6

Legrioui R, Baali F, Hamad A, et al (2017) Water Quality At A Karstic Aquifer In The Region Of Tebessa, Northeast -Algeria-. International Conference on Technologies and Materials for Renewable Energy, Environment and Sustainability, TMREES17, 21–24 April 2017, Beirut, Lebanon. Energy Procedia 119 (2017) 356–366. 1876-6102 © 2017 The Authors. Published by Elsevier Ltd

Maliki MA (2000) Etude hydrogéologique, hydrochimique et isotopique du système aquifère de Sfax (Tunisie). Doc Thesis. Tunis II University, Tunis, Tunisia

Piper AM (1944) A graphic procedure in geochemical interpretation of water analysis. Trans AmerGeophys Union, 25(6):914–928; Richmond, VA

Quinif (1983) La reculée et le réseau karstique de Bou Akous (Hammamet, Algérie de l'Est) Géomorphologie et aspects évolutifs. Revue Belge de Géographie, Vol. 4, 89–111

Rouabhia A, Baali F, FehdiCh (2009) Impact of agricultural activity and lithology on groundwater quality in the Merdja area, Tebessa, Algeria. Arab J Geosci, Springer-Verlag, Berlin; Heidlerg. https://doi.org/10.1007/12517-009-0087-4

Rozanski K, Araguas L, Gonfiantini R (1993) Isotopic Patterns in Modern Global Precipitation. In: Continental Isotope Indicators of Climate. American Geophysical Union (monograph)

Simler R (2004) Hydrochemistry Software multilanguage free distribution. Hydrogeology Laboratory of Avignon, Version 2

Vila JM (1980) La chaine alpine de l'Algérie orientale et des confins Algéro-Tunisiens. Thèse de Doctorat- es -sciences, Université, Pierre et Marie curie, Paris VI

Earth Tide Effect in Karstic and Non-karstic Aquifers in the Guinea Gulf

Bernard Collignon

Abstract

During long-term pumping tests in Gabon and Benin, we were surprised to observe large-amplitude tidal signals in boreholes located more than 20 km from the sea. This article describes these tidal signals (maximum amplitude, variation in time and space, phase shift, etc.) and attempts to interpret them. The signal amplitude varies considerably from one aquifer to another (from 2 mm to 110 cm) but is uniform within an aquifer and constitutes a signature. We are therefore seeking to use this signature to characterize the transmissive or capacitive properties of each aquifer. The use of this tool is limited by the difficulty of isolating the piezometric tidal signal among other phenomena that can mask it (pumping, rain, seasonal drying, etc.). Once the tidal signal is properly isolated, it can be used as an indicator of the risk of seawater intrusion. This concern is particularly acute if the aquifer consists of karstified rocks, as the intrusion is likely to extend several kilometres inland. It is therefore essential to be able to distinguish three situations with different levels of risk. Two of these situations have been relatively well documented: earth tides that do not raise a risk of seawater intrusion and ocean tides, which induce a very high risk of karst aquifers in direct contact with the sea. A third case should be added: that of ocean tides that induce periodic pressure variations in captive aquifers. The risk of seawater intrusion is then moderate, even when this tidal signal is very spectacular, as in some confined karst aquifers in Benin.

Keywords

Karst • Earth tide • Ocean tide • Tidal signal measurement and compensation • Seawater intrusion

Introduction

While conducting long-term pumping tests in Gabon and Benin, we were surprised to observe tidal signals in boreholes located more than 20 km away from the sea.

Was it the distant influence of the ocean tide or was it a piezometric effect related to Earth tides? To get to the bottom of it, it was necessary to accumulate experimental data.

This type of observation is often difficult, because, far from the sea, the piezometric tide signal has generally a small amplitude (a few cm, or even a few mm) and thus often goes unnoticed because it is obscured by other phenomena (barometric variations, pump start/stop in a neighbouring well, seasonal variations, etc.).

However, when these parasitic signals are correctly compensated, piezometric tide signals can be observed in many wells. They can then be characterized (amplitude, phase shift, lateral evolution and depth) and used as a signature of the aquifer.

Earth Tides and Ocean Tides

Groundwater is sensitive to two types of tidal effect that have the same astronomical cause (the relative movements of the Earth, Moon and Sun), but fundamentally different hydrogeological mechanism (Table 1).

Ocean tides are the deformation of the hydrosphere caused by the Earth's rotation in the gravitational field of the Moon and the Sun. The vertical deformation of sea level commonly exceeds one metre and can reach about ten metres in areas where the tidal effect is amplified by the topographic configuration of the seabed (as in Brittany or in the St Lawrence River). Such strong water load variations have a strong impact on coastal aquifers, where they induce periodic alternative flows, from the sea to the aquifer and vice versa (Cazenove 1971; Krivic 1982; Cuello et al. 2017). These horizontal groundwater flows can exceed 11 miles in karst

---

B. Collignon (✉)
Urbaconsulting, 198 Chemin d'Avignon, 84470 Chateauneuf de Gadagne, France
e-mail: collignon@urbaconsulting.com

C. Bertrand et al. (eds.), *Eurokarst 2018, Besançon*, Advances in Karst Science,
https://doi.org/10.1007/978-3-030-14015-1_26

Table 1 The impact of Earth tides and sea tides on groundwater levels

	Piezometric tide inside continents (so-called Earth tide)	Piezometric tide along the sea shore (so-called Oceanic tide)
Impacted area	Practically universal, but intensity varies depending on the characteristics of the aquifer (from a few mm to a few dm)	Sensitive only in aquifers close to a large water body (ocean or estuary). Signal damping in porous aquifers limits the phenomenon to a band a few hundred metres along the tidal shore or estuary. However, the impact can be felt several kilometres away in highly transmissive volcanic aquifers (Petit and Leforgeais 2013) and several tens of km from the coast in karst (ZexuanXu et al. 2016)
Water displacement	Essentially vertical movement, by several centimetres or millimetres, of the aquifer and the water it contains	Essentially horizontal movement of the water in the aquifer, from a few m to a few km, depending on transmissivity
Potential impact on groundwater quality	Very limited	Risk of saline intrusion, and this risk is higher when the transmissive properties of the aquifer are high (karst representing the extreme case)
Period (main harmonics)	12 h (Sun tide), 12.4 h (Moon tide) and 14.5 days (resonance between the two aforementioned tides)	
Phase shift	Phase shift from original excitation. Inland, the tidal signal phase is related to the terrestrial tidal phase, a parameter that is costly for field hydrogeologists to measure (it requires a gravimetric observatory nearby) (Rojstaczer and Riley 1990)	At the coast, the tide signal is in phase with the ocean tide, which can be directly measured and observed.
Phase shift within the aquifer	All points in the aquifer have synchronous deformations	Increasing phase shift away from the coast, this variability can be used to determine transmissivity (Ferris 1952)
Amplitude	Relatively uniform amplitude at the scale of an aquifer (so far it is not very heterogeneous); this amplitude can be used to determine the intrinsic properties of the aquifer (Hsiah et al. 1987)	Decreasing rapidly away from the coast; for this reason, a single piezometer is of little use, but variability between two piezometers can be used to determine transmissivity (Ferris 1952)
Variation in amplitude during the lunar month	The ratio of maximum to minimum amplitude is very high (as large as 5)	This ratio is somewhat smaller (between 2 and 3), similar to the ratio along the nearby shoreline

aquifers (ZexuanXu et al. 2016), consequently leading to greater seawater intrusion than that observed in porous aquifers.

Earth tides are the deformation of the Earth's crust following the Earth's rotation in the gravitational field of the Moon and the Sun (Melchior 1978; Melchior and Ducarne 1989). When the Earth's crust deforms, this generates pressure head disturbances caused by dilatation of the aquifer (Hsieh et al. 1987). Head disturbances vary with time and space and induce interstitial pressure variations in the aquifer itself, resulting in piezometric level variations (Hsieh et al. 1987) but limited horizontal groundwater transfers. Such piezometric variations are generally called Earth tides, but it would be better to speak of **piezometric tides**, so as not to confuse them with Earth tides senso strictu, i.e. the earth's crust deformation under the effect of lunar and solar attractions, provoking vertical oscillations of a few tens of cm that affect the entire crust, including aquifers and piezometric divers which cannot therefore measure such Earth tides (because the measuring instrument moves with the aquifer itself).

Data Sources

This study is based on the author's observations of the effects of Ocean and Earth tides in sedimentary aquifers in Gabon and Benin (Fig. 1 and Table 2).

Amplitude of Tide Effects and Experimental Constraints

Oscillations in piezometric levels induced by Earth tides are often of small amplitude, i.e. a few mm or a few cm (see some examples in Table 3). This can make measuring these oscillations difficult because:

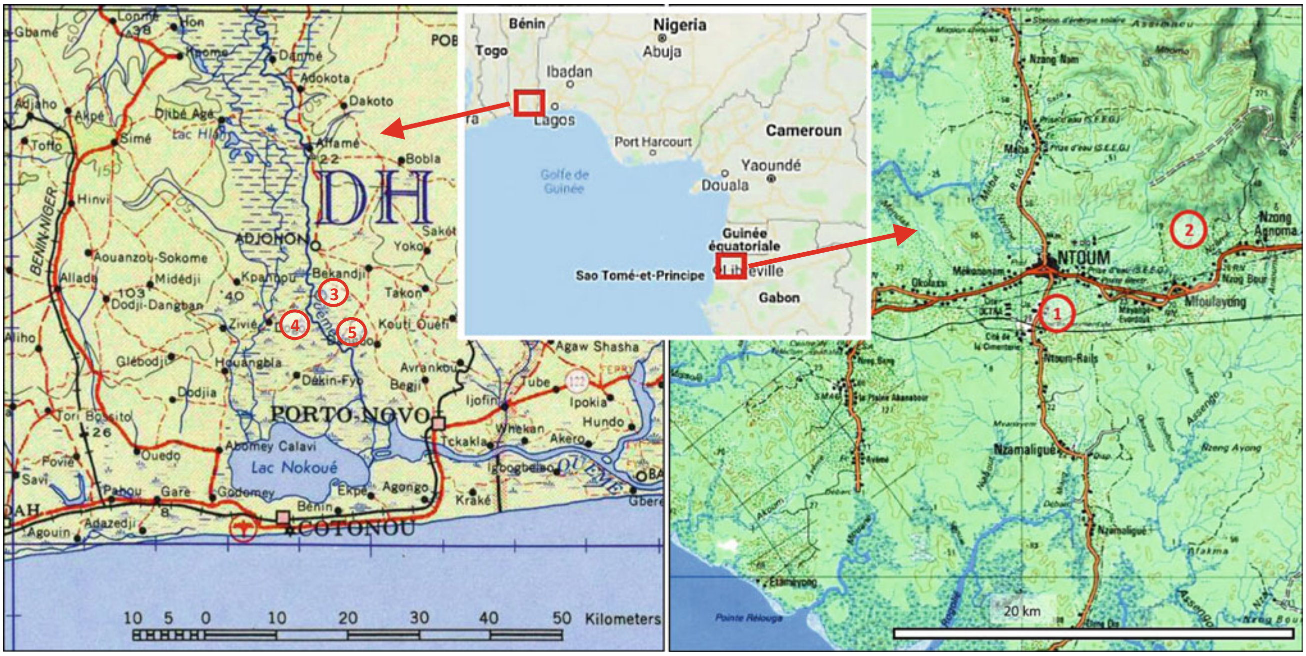

Fig. 1 Cartes Benin and Gabon

Table 2 Main features of the aquifers and well fields (red number refer to Fig. 1)

		Palaeocene coastal aquifer	Madiela limestones	Ndombo sandstones
Country		Benin	Gabon	Gabon
Lithology		Sandy shales, marls and a thick limestone layer	Malry limestones and dolostones	Sandstones and shales
Aquifer extension	km^2	30,000	10,000	10,000
Distance from the sea	km	20–25	20	30
Water table altitude	m asl	0–5	−5 to −10	30–40
Wells		Deep wells (3) Gogbo; (4) Gbeko; (5) Hetin Sota	(1) 7 deep wells (NT1 to NT7)	(2) 6 deep wells (MFL1 to MFL6)
Well depth	m	300–420	180–220	150–160
Aquifer depth	m	370–415	100–210	60–155
Abstraction yield	m^3/day	5000	52,000	30,000
Tide signal amplitude	cm	**80–110**	**1–24**	**1.5–7**
Signal max/min	%	n.a.	160	500

Sources Collignon (1992), Collignon and Ondo (2016)

- the measuring tools do not have a sufficient sensitivity (the basic manual piezometric probes commonly used by field hydrogeologists cannot measure slow variations of less than a few cm);
- they are often obscured by other larger fluctuations (barometric effects, rainfall, pump stop/go in nearby wells, etc.—Figure 2).

Measuring Tide Effects

As a result of these observation difficulties, oscillations in piezometric levels caused by Earth tides often go unnoticed, although they are probably universal. We were able to observe them using two very different instrumental devices:

Table 3 Tide signal features for some aquifers

Area	Aquifer	Well	Max. amplitude (cm)	Min. amplitude (cm)	Semidiurnal tide (h)	Half Lunar month (days)	Phase shift v. Moon (h)
Gabon	Madiela limestones	NT4	24	15	13		3.0
		NT6	8		12.25	n.a.	2.5
	Ndombo sandstones	MFL4	7	1.5	12.24	14.85	−0.1
		MFL3	7	1.4	12.35	14.7	0.0
Benin	Palaeocene marly limestones	GOGBO	90			n.a.	4.3
		GBEKO	110			n.a.	4.3
		HETIN SOTA	80			n.a.	4.3

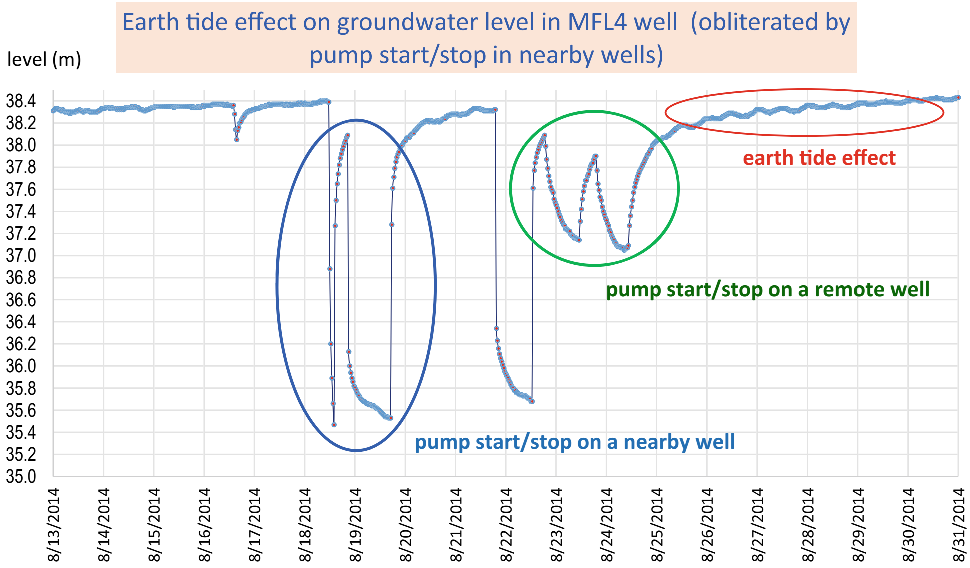

Fig. 2 Tide signal obliterated by pump start/stop

- In Benin, we measured pressure oscillations in artesian boreholes with sealed well heads using two different devices: a conventional Bourdon manometer and a water pressure gauge tube attached to the drilling rig (both devices were accurate to within 5 cm) (Collignon 1992);
- In Gabon, we measured these oscillations using piezoelectric devices that were fitted with good quality barometric compensation mechanisms (Orpheus mini—Ott®) (Collignon and Ondo 2016). Efficient barometric compensation is paramount for taking reliable tide measurements as the barometric effect has the same order of magnitude and may obliterate the tide signal (Rojstaczer and Riley 1990; Toll and Rasmussen 2007); in addition, correcting the barometric effect is not simple (Clark 1965; Toll and Rasmussen 2007). These devices enabled us to record millimetric piezometric variations over 6 boreholes for relatively long periods (3–200 days).

The piezometric signal is distorted by pump start/stop in nearby boreholes (because the observation wells are part of operating wellfields) and by rainfall in karstic aquifers (because the piezometric level reacts quickly to rainfall). To be able to isolate the tidal effect, it is therefore essential to correct these other effects, which we accomplished using a low-pass filter method (Fig. 3) in a similar manner as that described in Hsieh et al. (1987).

Observed Tide Effects in the Guinea Gulf Region

Earth tide-induced piezometric level oscillations are clearly visible in some, but not all, of the boreholes (see Table 3).

The fact that no tidal effects have been observed in other wells in the same aquifer (NT6, NT7, etc.) does not prove

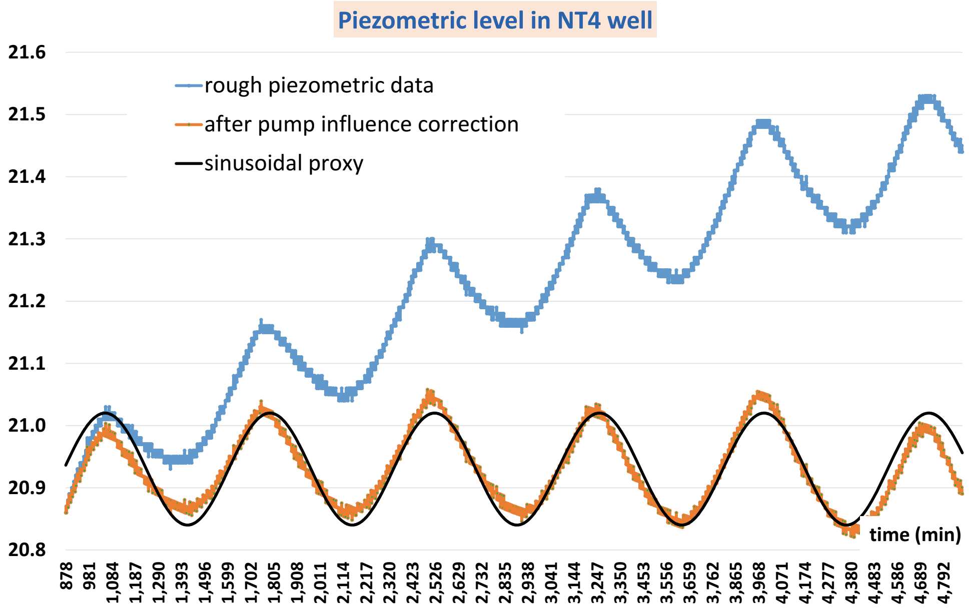

Fig. 3 Tide signal compensated and proxy

that Earth tides have no influence. It is more likely that the tide effect is of small amplitude and therefore indistinguishable from barometric and other noises in the relatively rudimentary signal measurement and processing devices that were used.

Tidal Signal Shape

The shape of the piezometric level oscillation signal is quite close to a 12.42-h period sinusoid, which corresponds to the main harmonic of the Earth tide—M2 semi-diurnal Moon tide signal (Melchior 1978; Hsieh et al. 1987).

In reality, the sinusoidal shape is only a proxy of the tidal signal; however, this approximation is generally sufficient to process the data and, in particular, to measure the amplitude and phase shift of the tide signal (Cazenove 1971). The approximation is even better by combining two sinusoidal signals, corresponding to the tidal waves M2 and S2 (semi-diurnal Moon and Sun tide) (Figs. 4 and 5).

Period

Logically, all astronomical cycles (semi-diurnal, diurnal, semi-lunar, lunar, annual, etc.) should be reflected in the intensity of piezometric oscillations. However, astronomical cycles with the weakest influence are difficult to observe, especially as they are easily obscured by other phenomena (such as temperature and year-long atmospheric pressure changes).

The observations made in Gabon and Benin highlight the following cycles:

- 12.42-h cycles, which correspond to the passages of the Moon (zenith and nadir); this is the most clearly marked cycle, because the Moon is the main contributor to tidal effects (the Moon's influence on tide is approximately two times greater than that of the Sun (Service hydrographique et océanographique de la Marine 1997); this is the length of one of the main Earth tide harmonics, M2 (Melchior 1978);
- 14.5-day cycles, which can be very clearly seen in the changes in piezometric levels in the Mfoulayong boreholes (Fig. 5); it is the resonance period between two of the main Earth tide harmonics, M2 (12.42 h) and S2 (12 h) (Melchior 1978).

Amplitude

The maximum oscillation amplitude varies:

- with the Moon phase (Fig. 5);
- from one aquifer to another (Table 3); it is generally very small (a few mm or cm), as in the Mfoulayong or Tchengue well fields (Gabon); however, it is much larger in the Benin–Togolese coastal aquifer, with oscillations in amplitude of 80–110 cm (Collignon 1992, Fig. 6) (Fig. 6).

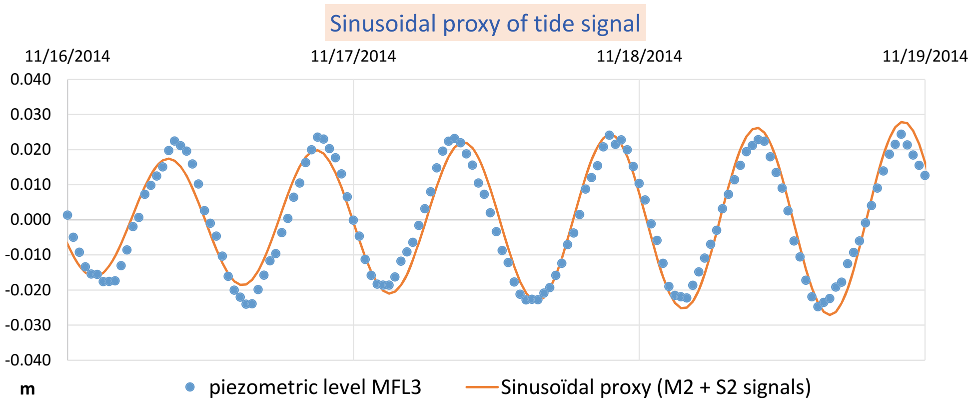

Fig. 4 Sinusoidal proxy of a low amplitude tide signal (MFL3 well—Mfoulayong—Gabon)

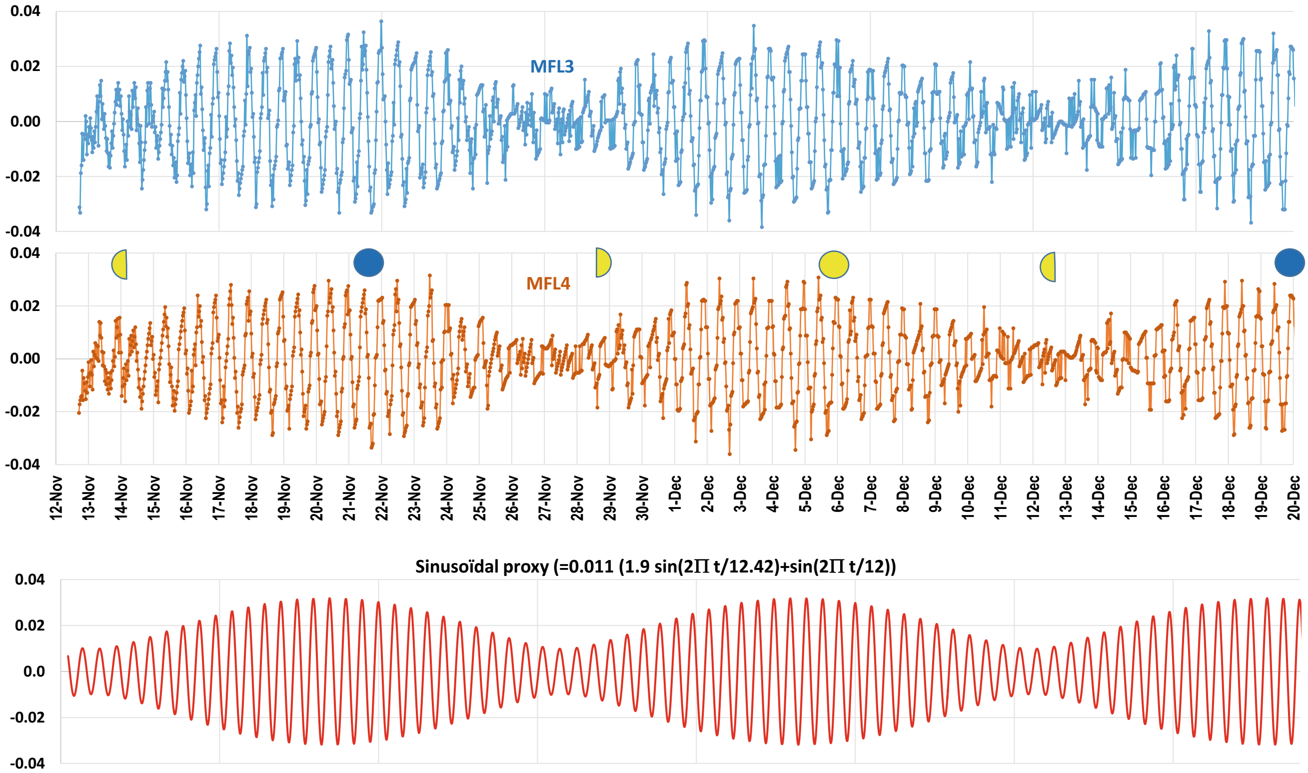

Fig. 5 Tide signal proxy

The maximum oscillation amplitude has the same order of magnitude in the same aquifer (and this suggests that this amplitude is related to the intrinsic properties of the aquifer).

In aquifers influenced by sea tides, the amplitude of the tidal signal is a negative exponential function of distance to the shore line (Ferris 1952; Krivic 1982; Cuello et al. 2017). As a result, the tidal signal gradually damps as it moves inland. This progressive damping can be used to measure an important aquifer parameter: diffusivity—T/S (Krivic 1982). By combining amplitude damping and phase shift, it is possible to estimate transmissivity—*T*—of an infinite aquifer (Ferris 1952). More complex aquifer situations have been extensively modelled, such as aquifers with lateral limits, leakage (Cazenove 1971) or wedge-shaped aquifers (Cuello et al. 2017).

The same argument cannot be applied to the impact of Earth tide on groundwater levels in an aquifer as the intensity of the Earth tide is practically uniform over distances of

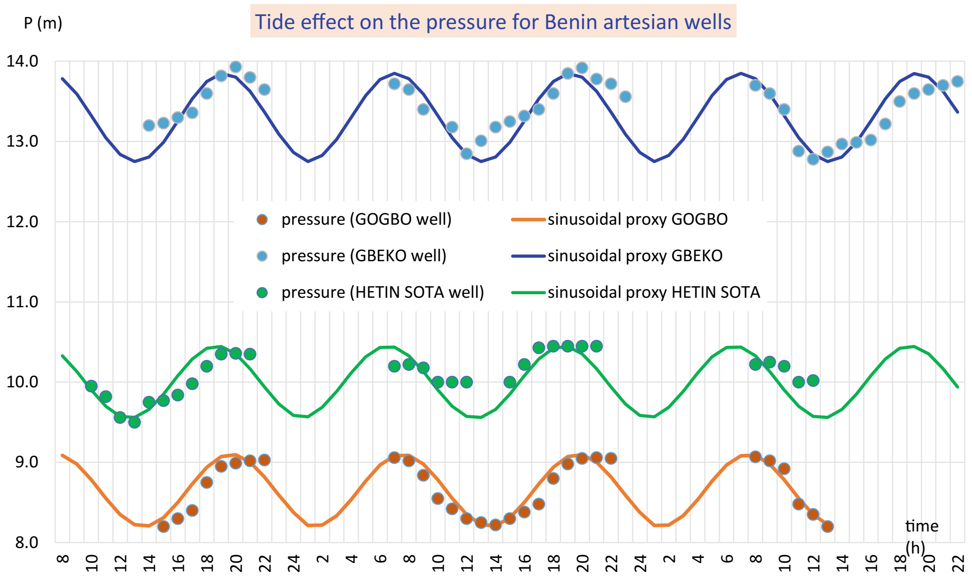

Fig. 6 Tide signals Benin

several kilometres. In the same aquifer, tidal signals of the same amplitude and phase shift are found, which makes it impossible to apply the analytical method developed for ocean tides.

Phase Shift

There is a phase shift between the Earth tide and the water level response in boreholes and piezometers. This phase shift is due, in particular, to the time required for the water to pass from the aquifer to the borehole and vice versa (this is a capacity effect linked to the finite size of the borehole and this effect therefore increases in relation to the diameter of the well) (Hsieh et al. 1987).

Following on from previous work on modelling the impact of earthquakes on water levels in boreholes (Cooper et al. 1965), American researchers modelled the impact of periodic disturbances of the pressure head due to Earth tides (Hsieh et al. 1987). They showed that phase shift (η) was related to transmissivity (T), storage (S), casing radius (r_c), borehole radius (r_w) and disturbance period (τ). The analytical solutions are represented in Fig. 7.

This method would be useful for small-diameter boreholes in shales or sandy clay (low T value). Unfortunately, it is unsuitable for boreholes in highly transmissive aquifers because the duration of the capacity effect is too short. The area of application of this calculation for conventional drilling (13″ 3/8 casing) in sandy aquifers (like Mfoulayong and Port-Gentil in Gabon) with transmissivity in the 1 to 5×10^{-3} m^2/s range is highlighted in blue in Fig. 7. We can see that the phase shift is very small (less than 2° equivalent to 8 min for the M2 component). This is almost imperceptible with the current measuring devices.

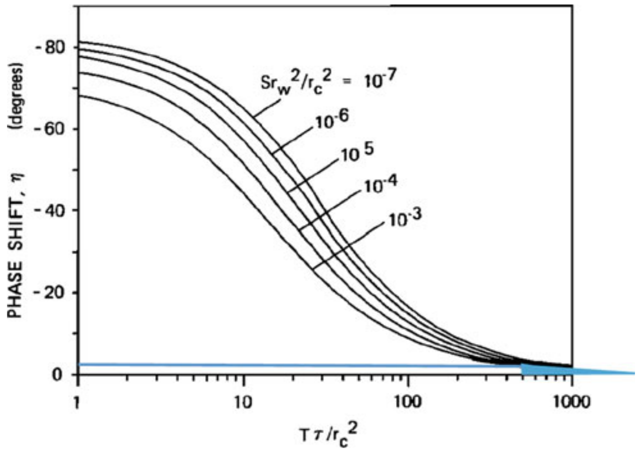

Fig. 7 Hsieh method

Moreover, karstified aquifers (like Ntoum—Gabon and Palaeocene—Benin) have even stronger transmissive properties and thus the method is no longer applicable. Finally, in order to use this method, we would need to measure the exact time of the Earth tide and the equipment required for this (a very good gravimeter) is not part of the field hydrogeologist’s toolbox.

What to Do with Tide Observation in a Well?

Measuring the Main Features of the Aquifer

In aquifers influenced by ocean tides, hydraulic head variations are exerted on the aquifer side and the tidal signal amplitude gradually damps as it travels away from the coast. Simultaneously, its phase shift increases (Cazenove 1971;

Krivic 1982). The damping of the tidal signal and its phase shift can then be used to determine the intrinsic characteristics of the aquifer, particularly its diffusivity (transmissivity/storativity—$\alpha = T/S$. [$L2/T$]). The main aim of this type of study is to evaluate the characteristics of an aquifer where there have been no pumping tests but for which accurate level measurements are available for several piezometers located at a range of distances from the coast (Cazenove 1971).

In aquifers influenced by piezometric tides far from the coast, hydraulic head variations affect the entire aquifer simultaneously and the tidal signal does not travel laterally within the aquifer. It is therefore not possible to use phase or amplitude differences between two piezometers as a tool for estimating diffusivity.

However, accurate level measurements on a single piezometer in an aquifer with very low transmissivity can also be used to determine some of the features of the aquifer. Phase shift has been associated with transmissivity (T) and storativity (S) (Hsieh et al. 1987), with transmissivity having a more prominent influence. Unfortunately, measuring phase shifts requires gravimetric records that are generally unavailable to field hydrogeologists.

Improving Long-Term Pumping Test Accuracy

During long-term pumping tests, the piezometric level gradually drops but after a few tens of hours, the drawdown speed becomes so slow (a few mm per hour) that it is sometimes obscured by piezometric tides far from the coast.

This tidal effect then needs to be corrected (Bélanger 2000; Toll and Rasmussen 2007; Grillot et al. 2015). That is what we had to do to interpret the pumping test carried out on the MFL4 borehole in Gabon (Fig. 8). The correction applied is a simple sinusoid of a 12.4-h period and 1.6-cm amplitude. After tide correction, the depletion curve is ready to use for transmissivity estimation, using the Jacob approximation of Theiss model ($T = 0.183$ discharge/delta $l = 3500$ m^2/day).

Differentiating Between Earth and Ocean Tides to Assess Seawater Intrusion Risk in Karst Aquifers

Ocean tides are a major factor in the seawater contamination of aquifers, especially in karst aquifers, where seawater intrusion is especially extensive. By way of illustration, a brackish water transfer over a distance of 11 miles has been documented in Florida (ZexuanXu et al. 2016).

Piezometric tides far from the coast do not present the same risk because there is very limited horizontal water movement (Fig. 9). When tidal oscillations are observed in a karst aquifer a few or tens of km from the coast, it is therefore of the utmost importance to be able to differentiate between the effects of ocean tides on a coastal aquifer directly connected to the sea, ocean tides on a confined aquifer (where the level of risk is much more limited) and piezometric tides far from the coast (which are not likely to lead to seawater intrusion as horizontal flow is very limited) (Fig. 9b, d and f, respectively).

This is the situation we faced both in Gabon (Ntoum aquifer) and in Benin (Palaeocene aquifer). In both cases, a large amount of water is abstracted from these karst aquifers (for drinking water supply) despite the fact that they are located only a few km from the coast. There are as yet no signs of seawater intrusion although the tidal signal is very clear (Figs. 3 and 6). If this tidal signal turns out to be caused by sea tides, there would be a very high risk of

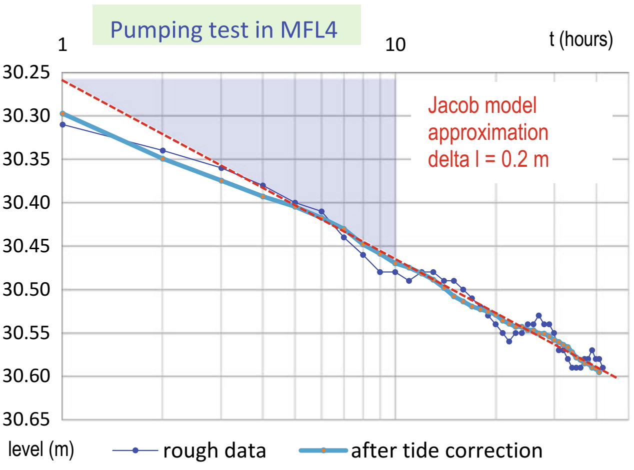

Fig. 8 MFL4 pumping test

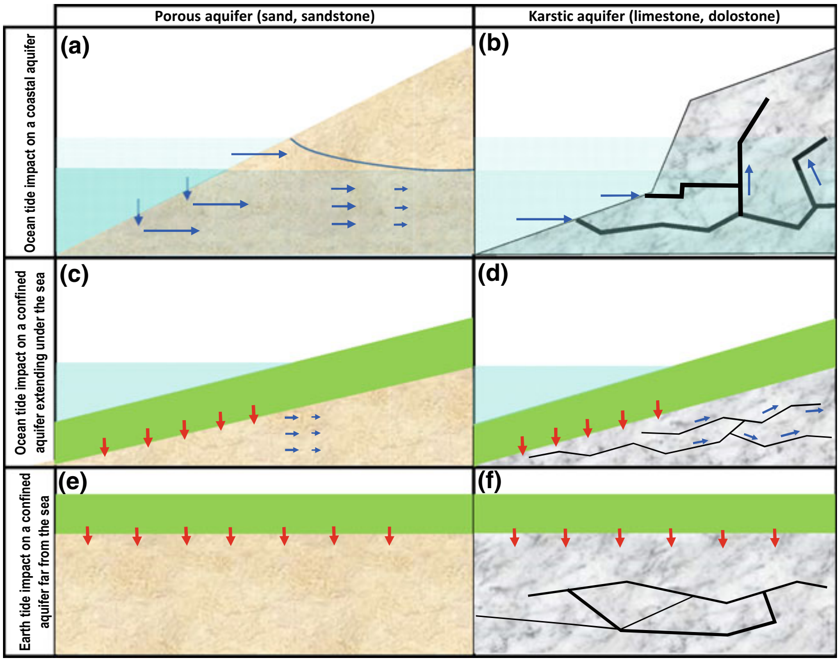

(a) The ocean tide signal causes both a change in load in the part of the aquifer covered by the sea and a horizontal transfer of load and salt water inland. The load transfer is damped in a few hundred meters for daytime tide signals.

(b) The same is true in karstic environments, but the transfer of charge is very little cushioned in ducts more than a few cm wide and the transfer of salt water is effective up to several km from shore.

(c) The ocean tide signal causes a change in load in the part of the aquifer covered by the sea but no transfer of salt water. The horizontal transfer of load inland is cushioned in a few hundred metres for daytime tide signals.

(d) The ocean tide signal causes a change in load in the part of the aquifer covered by the sea but no transfer of salt water. The horizontal transfer of load inland through the karstic conduits is effective over several km.

(e) (f) The terrestrial tidal signal causes uniform load variation in the aquifer and therefore little or no horizontal flux.

Fig. 9 Ocean and Earth impact on porous and karstic aquifers. **a** The ocean tide signal causes both a change in load in the part of the aquifer covered by the sea and a horizontal transfer of load and salt water inland. The load transfer is damped in a few hundred metres for daytime tide signals. **b** The same is true in karstic environments, but the transfer of charge is very little cushioned in ducts more than a few cm wide and the transfer of salt water is effective up to several kilometres from shore. **c** The ocean tide signal causes a change in load in the part of the aquifer covered by the sea but no transfer of salt water. The horizontal transfer of load inland is cushioned in a few hundred metres for daytime tide signals. **d** The ocean tide signal causes a change in load in the part of the aquifer covered by the sea but no transfer of salt water. The horizontal transfer of load inland through the karstic conduits is effective over several kilometres. **e** and **f** The tide signal causes uniform load variation in the aquifer and therefore little or no horizontal flux

seawater intrusion, meaning water abstraction should be reduced and water quality carefully monitored. If this signal is caused by Earth tides, the risk of seawater intrusion can be considered negligible.

Conclusion

In coastal aquifers, the tidal signal is a well-known phenomenon that has been the subject of numerous studies and publications. This is not the case far from the sea, where piezometric tides have a small amplitude and are obliterated by other phenomena. To characterize them, it is essential to have sensitive measuring devices and to filter out interfering signals caused by water abstraction, rainfall or seasonal variations. After good filtering, the tidal signal can be observed in a very large number of continental boreholes (and such phenomenon is probably universal).

At first, we dealt with this signal as a parasite that needed to be filtered out in order to correctly interpret the pumping test results. Subsequently, we considered them as a phenomenon in their own right, likely to provide additional information on the aquifer (as an indicator of seawater intrusion risk or as a key to access the aquifer's intrinsic parameters).

Here again, this research topic has been studied since a long time for coastal aquifers (Boussinecq 1904) but it has not received the same attention for continental aquifers (probably because the tidal signal is weak and therefore more difficult to measure).

The models developed for coastal aquifers (including a lateral change in signal amplitude and phase when moving away from the coast) do not apply to continental piezometric tides. On the contrary, we observed a fairly uniform signal inside the whole aquifer.

We were able to model this signal by a combination of sinusoids whose periods correspond to the lunar and solar semidiurnal tides. The next step in our work will be to link the signal characteristics (amplitude, phase shift, damping at the aquifer boundaries and amplitude variation with depth) with the intrinsic properties of the aquifer.

References

Bélanger, C., 2000. Modélisation numérique d'un essai d'aquifère dans un aquifère à nappe captive soumis à l'effet de marée. Mémoire de Maîtrise ès Sciences Appliquées éd. Montréal: Ecole Polytechnique de Montreal.

Boussinecq J. 1904. Recherches théoriques sur l'écoulement des nappes d'eau infiltrées dans le sol et sur le débit des sources. Journal de mathématiques appliquées, fasc.1.

Cazenove, E. d., 1971. Ondes phréatiques sinusoIdales. La Houille Blanche, Issue 7, pp. 601–616.

Clark, W., 1965. Computing the barometric effeciency of a well. Journal of Hydraulic Engineering, 93, pp. 93–98.

Collignon, B., 1992. Données nouvelles sur l'aquifère paléocène du bassin sédimentaire côtier bénino-togolais. Neuchâtel, 5ème Colloque d'hydrologie en pys calcaire et milieu fissuré.

Collignon, B. & Ondo, C., 2016. Managed Aquifer Recharge (MAR) to Supply Libreville, a Water-Stressed City (Gabon). Dans: P. R. &. C. Bertrand, éd. Eurokarst 2016 - Advances in the Hydrogeology of Karst and Carbonate Reservoirs. Neufchatel: Springer, pp. 273–281.

Cooper, H., Bredehoeft, J. & Papadopulos, L., 1965. The response of well-aquifer systems to seismic waves. Journal of Geophysical Research, 70 (6), pp. 3915–3926.

Cuello, J., Guarracino, L. & L.B. Monachesi, 2017. Groundwater response to tidal fluctuations in wedge-shaped confoned aquifers. Journal of hydrogeology, Volume 25, pp. 1509–1515.

Ferris, J., 1952. Cyclic fluctuations of water level as a basis for determining aquifer transmissivity, Washington: US Geological Survey.

Grillot, J.-C., Clezio, M. L. & Bodoyan, A., 2015. Filtrages piézométriques préliminaires à l'analyse du comportement des eaux souterraines lors des crises sismiques: exemple dans le petit Caucase. Hydrological Science Journal, 40(5), pp. 647–662.

Hsieh, P., Bredehoeft, J. & Farr, J., 1987. Determination of Aquifer Transmissivity From Earth Tide Analysis. Water Resources Research, 23(10), pp. 1824–1832.

Krivic, P., 1982. Transmission des ondes de marée à travers l'aquifère côtier de Kras. Geologie, 25(2), pp. 309–325.

Melchior, 1978. The Tides of the Planet Earth. Elmsford (N.Y.): Pergamon.

P. Melchior & B. Ducarme, 1989. L'étude des phénomènes de marée gravimétrique. Geodynamique, 4(1), pp. 3–14.

Petit, V. & Leforgeais, C., 2013. Evaluation de l'état quantitatif des masses d'eau souterraines de la Réunion, s.l.: BRGM / ONEMA.

Rojstaczer, S. & Riley, F., 1990. Response of the Water Level in a Well to Earth Tides and Atmospheric Loading under Unconfined Conditions. Water Resource Research, 26(8), pp. 1803–1817.

Service hydrographique et océanographique de la Marine, 1997. La marée. Brest: SHOM.

Toll, N. & Rasmussen, T., 2007. Removal of Barometric Pressure Effect and Earth Tides form Observed Water Levels. Groundwater, 45(1), pp. 101–105.

ZexuanXu, Basst, S., Hu, B. & S.C. Barret, 2016. Long distance seawater intrusion through a karst. Scientific reports, 6(32235).

First Outcomes of a Project Dedicated to Monitoring Groundwater Resources in Apulia, Southern Italy

Mario Parise, Luca Benedetto, Michele Chieco, Antonello Fiore, Mina Lacarbonara, Isabella Serena Liso, Costantino Masciopinto, Luca Pisano, Antonietta Riccio, and Michele Vurro

Abstract

The deepest cave in Apulia, an almost entirely karst region in southeastern Italy, has recently been the object of a project aimed at evaluating the quality and quantity of the groundwater resources. The cave system, located in one of the most remarkable karst landforms in the region (Canale di Pirro polje), reaches the water table at a depth of −264 m. Diving explorations brought the total depth of the cave down to −324 m. This contribution illustrates the preliminary activities carried out during the project, with a particular focus on geology, morphology and structural geology of the cave system and surrounding areas, together with hydrogeological research and chemical analyses of the groundwater.

Keywords

Karst • Hydrogeology • Polje • Groundwater resources • Speleology

M. Parise
Department of Earth and Environmental Sciences, University Aldo Moro, Bari, Italy

M. Parise (✉) · L. Pisano
National Research Council, IRPI, Bari, Italy
e-mail: mario.parise@uniba.it

L. Benedetto
CAI GASP, Gioia del Colle, Italy

M. Chieco · A. Riccio
Ass. Qualità dell'Ambiente, Regione Puglia, Bari, Italy

A. Fiore
Autorità di Distretto dell'Italia Meridionale, Valenzano (Bari), Italy

M. Lacarbonara
ARPA, Puglia, Italy

I. S. Liso · C. Masciopinto · M. Vurro
National Research Council, IRSA, Bari, Italy

Introduction

In Apulia, due to lack of significant surface watercourses, groundwater is the main water resource, thus representing an essential factor for society and land development. The concept of water availability is linked not only to quantity of the resource, but also to its quality. Degradation of both surface and subsurface karst and groundwater pollution are largely widespread in the region (Parise and Pascali 2003), with serious consequences for the groundwater quality, also considering the very high vulnerability of the karst Apulian aquifers. Further, the semiarid climate (resulting in scarcity of meteoric recharge to groundwater), and, above all, the uncontrolled overexploitation of water resources, together with the natural configuration of Apulia (a narrow and elongated peninsula), determine a high level of marine intrusion (Tulipano et al. 1990; Tulipano and Fidelibus 2002; Masciopinto and Liso 2016). For all the above reasons, there is an urgent need to monitor the groundwater, in order to preserve and protect the water resources.

In recent years, many efforts have been performed in the attempt to join the outcomes of speleological explorations with the development of scientific research in caves, and several caving activities have caught the attention of mass media and regional administrators. This occurred, for example, in the aftermath of sinkhole collapses, where the role of speleologists was essential to understand the cave development below urbanized areas (Pepe et al. 2013; Parise 2017; Fiore et al. 2018) and to evaluate the residual risk, or with speleologists being the support of many scientific projects. Awareness of the importance of speleological activities, and the need to carry out scientific research in caves, has therefore been acknowledged by Apulia Region. Following the remarkable explorations in 2012 that brought to discover the deepest cave in the region (*Inghiottitoio di Masseria Rotolo*; see Parise and Benedetto 2018), a project funded by Apulia Region was started in 2017. It is dedicated to monitoring of karst groundwater quality and quantity and

C. Bertrand et al. (eds.), *Eurokarst 2018, Besançon*, Advances in Karst Science,
https://doi.org/10.1007/978-3-030-14015-1_27

is carried out through the joint action of scientific research centers, universities, regional bodies and speleologists.

Geological and Hydrogeological Setting

Apulian karst mostly consists of a thick succession of Mesozoic calcareous/dolomitic rocks, forming the Apulian platform foreland, one of the main structural units of the Apennine system (Bosellini and Parente 1994). The main backbone of central Apulia is represented by the Murge plateau, in turn sub-divided into High and Low Murge (Fig. 1). On this latter, *Inghiottitoio di Masseria Rotolo,* the cave object of this study, is located, within one of the most important surficial karst landforms in the region, the *Canale di Pirro* polje. The polje shows an overall length of some 12 km, creating a very elongated landform, bounded on both sides by tectonically controlled ridges (Parise 2006). It reaches on its eastern side the Murgia escarpment, which is the main NW-SE tectonic line separating inland Murge from the Adriatic coastline. High-angle, normal, NNW-SSE, W-E and NW-SE-trending faults (Apennine faults) affect the Cretaceous bedrock (Doglioni et al. 1994; Pieri et al. 1997). The polje direction, on the other hand, has to be ascribed to the family of normal, EW-trending faults marking the boundary between Murge and Salento.

The carbonate bedrock is covered by residual deposits (*terra rossa* and clays derived from past phases of karstification), which at some depressions or at the ridge foothills reach the maximum thickness of a few meters. Several dolines and swallets are present in the *Canale di Pirro*. The whole area, due to the flat topography and cover of residual deposits, becomes periodically flooded after rainstorm events. The main swallow hole is Gravaglione, in the central sector of the polje, that is an elongated depression collecting most of the surface runoff from the head of the catchment. In addition to this, several minor caves and swallow holes are present, even though many of them have been over time

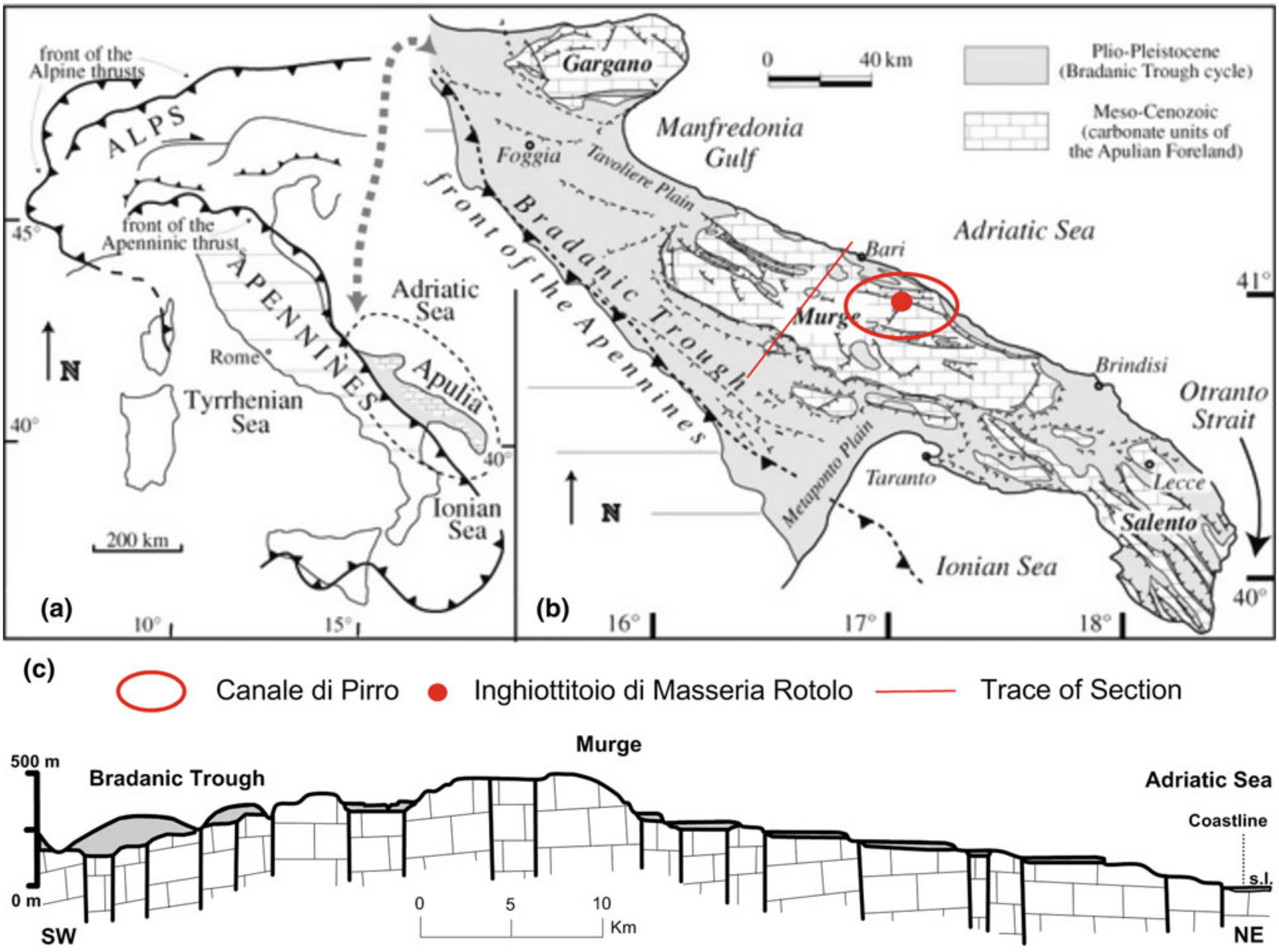

Fig. 1 **a** Schematic map of Italy, with location of Apulia Region; **b** geological sketch of Apulia, showing location of the study area; **c** geological cross section of the Murge plateau (modified after Tropeano and Spalluto 2006)

Fig. 2 Artificial cut, for construction purposes, in the Meso-Cenozoic carbonate rock mass: the epikarst portion, with many fissures and joints, tapering down and filled with residual deposits, is visible. The picture on the right shows also some ancient cavities, entirely filled with terra rossa

infilled by human actions, and locally entirely canceled from the landscape.

As typical of karst regions, Apulia is characterized by a scarce, if not absent, surface hydrography, but it presents a very high effective infiltration rate, especially in the High Murge plateau (Maggiore and Pagliarulo 2004). The thick Mesozoic carbonate successions, indeed, constitute a very extensive hydrogeological structure, and the most important water resource of the region, for both areal extension and the high storage capacity. The water flow is locally affected by the stratigraphic setting and by structural factors. Further, the spatial and vertical distribution of karst landforms, both at the surface and underground, is another controlling factor in the development of the water flow. The Murge carbonate rocks are characterized by almost exclusively secondary permeability, extremely variable in function of the different degree of fracturing and karst dissolution of the rock masses (Fig. 2), which influence the natural groundwater recharge (Grassi 1973).

The Murge carbonate groundwater generally flows under pressure, especially inland, while near the coastline it flows as free water table or confined below sea level. In the Adriatic area, the groundwater flows toward the sea with piezometric gradients ranging from 1% near *Inghiottitoio di Masseria Rotolo* to 0.1–0.5% (average values of gradients, measured from water levels in wells during a hydrologic year; Maggiore 1991) adjacent to the coast. The piezometric head decreases toward the coastline where many freshwater springs are present. Near the coast, the contact between fresh water and salt water takes place through a mixing band which location can be considerably different, determining the conditions for marine intrusion through groundwater salt contamination (Rudnicki 1980; Masciopinto et al. 2017).

Within the Mesozoic carbonate succession, the presence of the deep water table seems to be related to poorly fractured or massive rock intervals or to bituminous limestone levels at different stratigraphic depths (Maggiore and Pagliarulo 2004). One of such bituminous limestone layers was recognized in the Murge stratigraphy, above the Cisalveolina Fallax layer (Mesozoic—Late Cretaceous—Cenomanian) (Luperto Sinni and Reina 1996). It could be the main groundwater physical barrier in the Gioia del Colle and Noci area, located few kilometers inland from *Inghiottitoio di Masseria Rotolo*.

The High Murge plateau is the recharge area, where a variety of endorheic basins collect and convey rainwater into the ground, through sinkholes and the complex network of karst conduits and caves (Parise 2011). In correspondence with the hydrogeological watershed, the piezometric head reaches its maximum value, about 150–175 m a.s.l. (Tulipano 1988; Cotecchia 1993, 2014).

Comparing the major groundwater ions concentration ratios in the Adriatic coast and the High Murge areas by means of the Schoeller's diagram highlights the difference in composition and origin about the waters belonging to these two zones. The High Murge groundwater, with a relatively higher alkaline-earth ions and bicarbonate content, is similar to the rainwater (geochemical composition), while the geochemical trace of the groundwater coastal zone presents a content of "marine" ions (alkaline ions, magnesium, chlorides and sulfates), always higher than the calcium and bicarbonate ions (continental origin) (Maggiore and Pagliarulo 2004).

Ongoing Activities

Inghiottitoio di Masseria Rotolo was originally a very minor swallet, consisting of a 3-m-deep doline at elevation of 300 m a.s.l., with two narrow absorbing sites, at the end of a collector channel, some tens of meters long. As reported in Parise and Benedetto (2018), to which the reader is referred for further details about history of the site, excavation works were started in May 2012 to check the possibility of the presence of a karst system. After some months, in September 2012, a passage wide enough to allow entrance by man was found at the base of the first, 8-m-deep, shaft. The exploration soon made clear the importance and complexity of the cave system: This started with a series of vertical shafts, leading down to a depth of about 100 m below the ground surface. From there, a main sub-horizontal level began, showing at several locations hanging deposits related to past levels of karstification, nowadays suspended above the main cave. This sub-horizontal level develops for a few hundreds of meters, before becoming a meandering canyon-like feature. The cave system then progressively deepens again, reaching its most impressive feature: *Pozzo dei Veneti*, a 20-m large and over 100-m-deep circular shaft, leading down to the water table, at depth of 264 m below the ground surface (i.e., 36 m above the mean sea level). In two different cave diving explorations the maximum documented depth of the system was brought to 324 m below the ground (60 m below the water table). This is where so far the explorations have stopped. The cave system, however, presents other environments where future explorations may bring to new discoveries: Among these, on the opposite side of *Pozzo dei Veneti*, a huge breakdown area marks probably the sector with the clearest evidence of tectonic control on cave development, with likely another branch of the cave system.

The activities in the program during the project include researches in the field of stratigraphy, structural geology, geomorphology, climate in the cave environment and hydrogeology. The first action was to ensure safety of speleologists and scientists, through works at the access site, where a dry-stone wall, built in local limestone rocks, according to the existing regional laws and in the style of the typical rural architecture of the area, was realized (Fig. 3). This was mostly addressed to avoid entrance of stones and earth in the cave during the main floods.

A rain gauge has been installed outside the cave to measure the rainfall, temperature and atmospheric pressure. Besides characterizing the outside climate, these data, with particular regard to rainfall, will be crucial to correlate the water table oscillations with the meteoric recharge. As concerns the cave micro-climate, five sensors to measure temperature and relative humidity have been positioned in the cave, aimed at ascertaining possible variations in different sectors of the cave system. Measured temperatures so far show slight changes, from 14.7 °C (sensor closest to the access) to 15.1–15.3 °C (other sensors).

A new, detailed, survey of the cave system was started, addressed essentially to check the validity of the depth values, with particular regard to the elevation at which the water table is found in the cave. The detailed on-going topographic survey will also be useful to verify the elevation of the deposits, currently suspended above the main sub-horizontal level of development of the system. This is important to identify their possible relationship with ancient phases of speleogenesis and to correlate them with the most significant sub-horizontal levels in other karst systems in the Murge (Castellana-Grotte, Ostuni; see De Waele and Parise 2013).

Geomorphological and structural geological analyses are being performed in the *Canale di Pirro* polje: Several tens of dolines and depressions have been recognized and mapped (Fig. 4), contributing to build a karst geomorphological map of the area and to identify the main sites of water infiltration. Dolines have also been morphometrically analyzed to identify possible structural control on their shape and

Fig. 3 The access to the cave, after the works to ensure safe entrance to the system

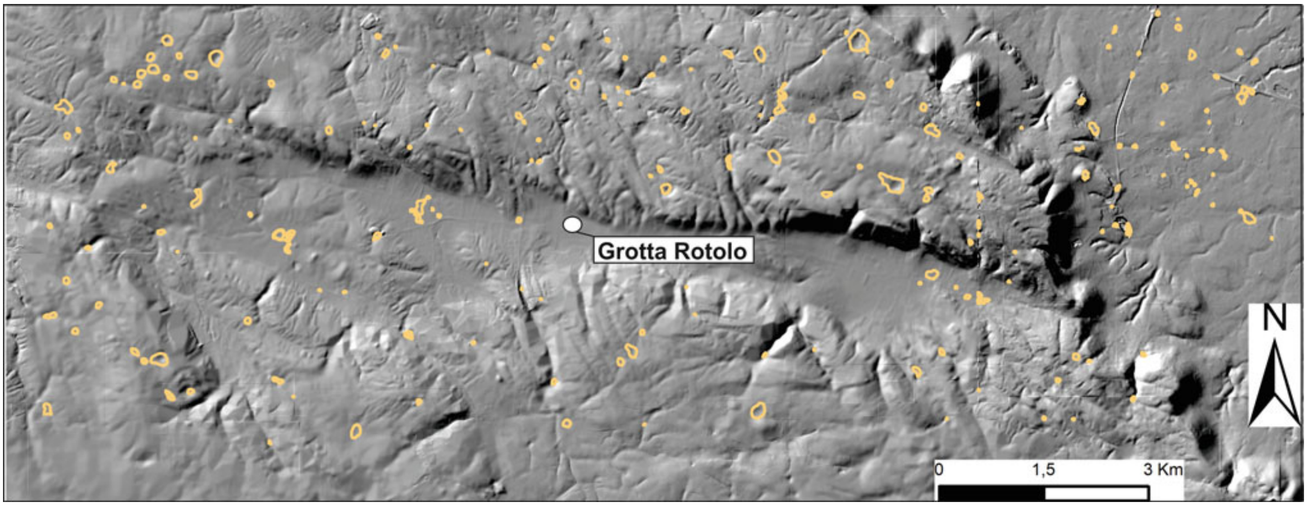

Fig. 4 Doline distributions in the Canale di Pirro polje, shown on a DEM of the area. The features have been extracted through an automatic procedure and validated through digital aerial photograph interpretation and field checks

distribution. Geostructural measurement stations have been performed, both at the surface and within the cave system: The first results show the presence of discontinuity families related to the Apennine faults, but also a significant number of joints belonging to the E-W system, that is the one controlling the polje development.

Samples of the carbonate rock mass have been collected from the ground surface down in the cave system, in order to prepare thin section for petrographic analysis (Fig. 5). This part of the research, aimed at understanding those parts of the carbonate succession within which the cave develops and at identifying the main stratigraphic intervals, has shown so far that the cave develops for the first 110 m of depth within the formation of the Altamura Limestone (Late Cretaceous, Coniacian-Maastrichtian). Continuation of the sampling at greater depths would potentially lead to find the contact with the underlying Bari Limestone (Late Cretaceous, Cenomanian-Turonian).

Monitoring of the water table is being performed through the use of the OTT ecoLog 800, a CTD probe, which essentially consists of three components: a communication unit, a waterproof connection cable and a probe with incorporated data logger (www.ott.com/products/water-level-1/ott-ecolog-800-water-level-logger-848/). The sensors equipping the probe are very reliable and accurate: One measures the groundwater level/pressure (m, cm/bar, psi), another one detects groundwater-specific electrical conductivity (mS/cm or µS/cm), and the third measures the water

Fig. 5 Sampling rocks in the cave system for petrographic analyses

temperature (°C, °F). Eventually, the device estimates the salinity (PSU, ppt) and the TDS (total dissolved solids) values (mg/l), thanks to specific automatic algorithms, based on the specific conductivity.

The sample interval, which is the time delay at which the probe measured values are stored, was set to 1 h. Stored values are then collected by means of an infrared interface (IrDA) using the probe OTT IrDA-Link USB reading head that allows transferring data from the communication unit to a portable computer.

To install the device at *Inghiottitoio di Masseria Rotolo* and to avoid damage related to the difficult transport and installation in the underground environment, the communication unit was further protected with a PVC coating, also to limit excessive humidity contact. Above this PVC coating, a top cap covers the infrared interface, as a further protection. The coating was well anchored to the rock wall, in correspondence with a "window" in the walls of the final shaft (the 100-mt-deep *Pozzo dei Veneti*), about 70 m above the water table. The connection cable, between the communication unit and the probe, was fixed along the rock walls of the shaft, down to the water, where the probe is located about 3 m below the water surface. The hard work of speleologists has permitted to obtain a system for the collection of very important data, needed to carry out the assessment of water parameters inside the cave. Over time, the probe will continue to collect data (until the end of 2018) and their analysis will be essential to evaluate quality and characteristics of the deep water resource.

Two campaigns of water sampling are scheduled during the project: One was done in January 2018, while the second campaign was performed at the end of June 2018, to check any variations in the chemical parameters of water in different seasons. According to the water analysis, carried out following the procedure established by the regional Agency for Protection of the Environment (ARPA Puglia), no problem was registered during January 2018, with all the investigated parameters below the pollution threshold scheduled by regional laws. As concerns the June 2018 campaign, the analyses are still in progress at the moment we write.

A significant effort was done to carry out biospeleological surveys: These are considered of extreme importance not only from the biological standpoint, but also as regards evaluation of the water quality. Previous studies in Apulia have in fact demonstrated that ascertaining the presence of stygofauna in the groundwater could represent a natural indicator of its quality, concerning the possibility of anthropogenic pollution (Masciopinto et al. 2006). At this goal, several campaigns of sampling have been performed: The preliminary outcomes resulted in finding remarkable stygofauna species, never documented before in this part of the region (Inguscio, personal communication).

Future Perspectives

The effective part of the project, after several months of delay due to bureaucratic reasons, eventually started during the fall of 2017. The available data are not enough to draw, at this stage, any definitive conclusion. Nevertheless, the collection of significant amount of different types of data allowed to start depicting the karst system and to delineate in first approximation the likely boundaries of the catchment feeding the system, as well as the response time of the water table to the registered rainfall. The ongoing monitoring, outside the cave and at the water table, and the other activities on structural geology and geomorphology, will concentrate in the next months in the definition of the water catchment and in a deeper characterization of the structural features within the cave, to provide a great amount of data that will definitely improve our understanding of this remarkable karst system of Apulia.

Acknowledgements Luigi Spalluto is kindly acknowledged for the petrographic analyses performed on the thin sections.

References

Bosellini, A. & Parente, M. (1994). The Apulia Platform margin in the Salento peninsula (southern Italy). Giornale di Geologia, 56 (2), 167–177.

Cotecchia, V. (1993). Gestione e salvaguardia delle acque sotterranee in Puglia. Quad. IRSA, 94, 2.1–2.23.

Cotecchia, V. (2014). Le acque sotterranee e l'intrusione marina in Puglia: dalla ricerca all'emergenza nella salvaguardia della risorsa. Memorie Descrittive Carta Geologica d'Italia, 92, 416 pp.

De Waele, J. & Parise, M. (2013). Discussion on the article "Coastal and inland karst morphologies driven by sea level stands: a GIS based method for their evaluation". Earth Surface Processes and Landforms, 38 (8), 902–907.

Doglioni, C., Mongelli, F. & Pieri, P. (1994). The Puglia uplift (SE Italy): an anomaly in the foreland of the Apenninic subduction due to buckling of a thick continental lithosphere. Tectonics, 13, 1309–1321.

Fiore, A., Fazio, N.L., Lollino, P., Luisi, M., Niccoli, M.N., Pagliarulo, R., Perrotti, M., Pisano, L., Spalluto, L., Vennari, C., Vessia, G. & Parise, M. (2018). Evaluating the susceptibility to anthropogenic sinkholes in Apulian calcarenites, southern Italy. In: Parise, M., Gabrovsek, F., Kaufmann, G. & Ravbar, N. (eds) Advances in Karst Research: Theory, Fieldwork and Applications. Geol. Soc. London, sp. publ. 466, 381–396. First published online January 4, 2018, https://doi.org/10.1144/SP466.20.

Grassi, D. (1973). Fondamentali aspetti dell'idrogeologica carsica della Murgia (Puglia), con particolare riferimento al versante adriatico. Geol. Appl. e Idrogeol., 8 (II), 285–313.

Luperto Sinni, E. & Reina, A. (1996). Gli hiatus del Cretaceo delle Murge: confronto con dati offshore. Mem. Soc. Geol. It., 51, 719–727.

Maggiore, M. (1991). Aspetti idrogeologici degli acquiferi pugliesi in relazione alla ricarica artificiale. Proc. Workshop IRSA-Regione Puglia: Trasferimento di tecnologie e metodologie per la gestione delle risorse idriche, Valenzano (Bari), June 10–11, 1991, Quaderni CNR/IRSA, no. 94, Rome, Italy.

Maggiore, M. & Pagliarulo, P. (2004). Circolazione idrica ed equilibri idrogeologici negli acquiferi della Puglia. Geologi e Territorio, 1, 13–35.

Masciopinto, C. & Liso, I.S. (2016). Assessment of the impact of sea-level rise due to climate change on coastal groundwater discharge. Science of the Total Environment, 569–570, 672–680.

Masciopinto, C., Semeraro, F., La Mantia, R., Inguscio, S. & Rossi, E. (2006). Stygofauna abundance and distribution in the fissures and caves of the Nardò (S Italy) fractured aquifer subject to reclaimed water injections. Geomicr. J., 23, 267–278.

Masciopinto, C., Liso, I.S., Caputo, M.C. & De Carlo, L. (2017). An Integrated Approach Based on Numerical Modelling and Geophysical Survey to Map Groundwater Salinity in Fractured Coastal Aquifers. Water, 9, 875.

Parise, M. (2006). Geomorphology of the Canale di Pirro karst polje (Apulia, Southern Italy). Zeitschrift für Geomorphologie N.F. 147, 143–158.

Parise, M. (2011). Surface and subsurface karst geomorphology in the Murge (Apulia, southern Italy). Acta Carsologica, 40 (1), 79–93.

Parise, M. (2017). Engineering-geological studies in artificial cavities, aimed at evaluating the possibility of failures in underground settings. Proc. Int. Congr. Artificial Cavities “Hypogea 2017”, 137–144.

Parise, M. & Pascali, V. (2003) Surface and subsurface environmental degradation in the karst of Apulia (southern Italy). Environmental Geology, 44, 247–256.

Parise, M. & Benedetto, L. (2018). Surface landforms and speleological investigation for a better understanding of karst hydrogeological processes: a history of research in southeastern Italy. In: Parise, M., Gabrovsek, F., Kaufmann, G. & Ravbar, N. (eds) Advances in Karst Research: Theory, Fieldwork and Applications. Geol. Soc. London, sp. publ. 466, 137–153. First published online January 25, 2018, https://doi.org/10.1144/SP466.25.

Pepe, P., Pentimone, N., Garziano, G., Martimucci, V. & Parise, M. (2013). Lessons learned from occurrence of sinkholes related to man-made cavities in a town of southern Italy. Proc. 13th Multidisc. Conf. Sinkholes and Engng. Environ. Impacts of Karst, 393–401.

Pieri, P., Festa, V., Moretti, M. & Tropeano, M. (1997). Quaternary tectonic activity of the Murge area (Apulian foreland, southern Italy). An. Geof., 40, 1395–1404.

Rudnicki, J. (1980). Karst in coastal areas - development of karst processes in the zone of mixing of fresh and saline water (with special reference to Apulia, Southern Italy). Studia Geologica Polonica, 65, 9–59.

Tropeano, M. & Spalluto, L. (2006). Present-day temperature-type carbonate sedimentation on Apulia shelves (Southern Italy). GeoActa, 5, 129–142, Bologna.

Tulipano, L. (1988). Temperature logs interpretation for the identification of preferential flow pathways in the coastal carbonatic and karstic aquifer of the Salento peninsula (Southern Italy). Proc. 21st Congress IAH, 956–961.

Tulipano, L. & Fidelibus, M.D. (2002). Mechanisms of groundwaters salinisation in a coastal karstic aquifer subject to over-exploitation. Proc. 17th SWIM, Delft (The Netherlands), 39–49.

Tulipano, L., Cotecchia, V. & Fidelibus, M.D. (1990). An example of multitracing approach in the studies of karstic and coastal aquifers. Proc. Int. Symp. “Hydrogeologic processes in karst terranes”, IAHS publ. 207, 381–389.